On the interaction between modal behaviour and shear force behaviour of a pneumatic tyre

On the interaction between modal behaviour and contact force development of a pneumatic tyre

Achillefs Tsotras

Abstract

The in-plane phenomena of interaction between the tyre structural response and contact force generation are investigated in this work. The challenges of the physical tyre simulation are identified, primarily associated with the computational load imposed by the need to capture the space distributed mechanisms that prescribe the above interaction. The method of modal expansion and reduction is proposed for the moderation of this load. The theoretical framework for the transformation of a tyre modal representation into a transient contact and shear force generation model is developed. Various modelling approaches are examined with regards to their modal prediction characteristics. Linear and non linear structural features as well as the physical properties that define the broad range modal behaviour are identified. A discretised form of the ring model is derived and combined with a foundation of viscoelastic tread elements for simulating the transient contact behaviour of the tyre. The resulting pattern of the modes' excitation justifies the validity of the modal reduction method and reveals the relative importance of various mechanisms and physical properties in tyre contact behaviour. The interaction between the friction controlled shear slip of the tread, the belt compliance and the sidewall buckling is found to be reflected on the two-dimensional contact pressure distribution patterns. A method able to simulate the dynamic transient rolling and slipping operating conditions is developed, although the small displacement assumption of the modal approach is dropped. The method, which is based on the combined modal-time and space-time domain solutions, is applied on the study of the physical mechanism of the launch process. The examination of the model under steady state kinematic conditions reveals the saturation of the traction force for profound levels of slip, which highlights the contribution of the structural mechanisms on the macroscopically observed shear force performance of the tyre. The variation of the modes' level of excitation, as induced by the operating conditions, is proposed for the capture of the physical properties effect on tyre behaviour and performance.

Keywords:

tyre transient simulation; ring model; tyre modal; tyre tread model; tyre sidewall model;

Acknowledgements

I would like to thank the Aeronautical and Automotive Engineering Department of Loughborough University for offering me a research scholarship, without which it would not have been possible to accomplish the present research work. I would like to thank personally the Head of Department, Professor Richard Stobart, for his decision to support financially my attendance to conferences, where I had the chance to present parts of my work and receive valuable feedback on that.

I would like to thank my research supervisor, Dr. George Mavros, for his scientific contribution and his personal interest in the work, which certainly exceeded his supervising role. For the last three years he has been a real friend, during all the ups and downs of this period.

A big thank you to my University colleagues, Mariapia Lampis, Alex Plianos and Andreas Rousounelos, for standing my nagging about the crashing algorithms and the mysterious simulation results.

My acknowledgements and appreciation to my work colleagues at the Transport iNet project for making the last period of my PhD research very optimistic and for their personal support trying to combine two uncombinable roles.

I would like to thank my mother and to my sister for their continuous support from my initial though of starting a research degree up to the submission. This work would not have been accomplished without the unreserved love and support of my partner, Cristina Arias Pérez, who has stood by me giving me the power to overcome all the difficulties that arose during these three years and the inspiration to complete this experience.

List of Publications

The following journal articles and conference presentations have been based on the present study:

Journal Articles

- *The simulation of in-plane tyre modal behaviour: a broad modal range comparison between analytical and discretised modelling approaches*
  Achillefs Tsotras and George Mavros
  Vehicle System Dynamics, available on line: DOI:10.1080/00423110802635405.

- *A Modal-Based Derivation of Transient Vertical Pressure Distribution along the Tyre-Road Contact*
  Achillefs Tsotras and George Mavros SAE Transactions 2009.

- *Frictional contact behaviour of the tyre: The effect of tread slip on the in-plane structural deformation and stress field development*
  Achillefs Tsotras and George Mavros
  Vehicle System Dynamics, accepted for publication (2009).

- *The interaction between modal behaviour and shear force generation in transient tyre simulation*, submitted for publication (after invitation) to the IAVSD09 Supplement (Special issue of Vehicle System Dynamics).

Conference Presentations

- *Towards the Fast and Accurate Modelling of In-plane Transient Tyre Dynamics*
  George Mavros and Achillefs Tsotras
  Presented at TireExpo 2009, Hamburg, Germany, 17th-19th of February 2009.

- *A Modal-based Derivation of Transient Pressure Distribution along the Tyre-Road Contact*
  Achillefs Tsotras and George Mavros
  Presented at the SAE 2009 World Congress, Detroit, Michigan, USA, 20th-23rd of April 2009.

- *The interaction between modal behaviour and shear force generation in transient tyre simulation*
  Achillefs Tsotras and George Mavros
  Presented at the 21st International Symposium on Dynamics of Vehicles on Roads and Tracks (IAVSD09), Stockholm Sweden, 17th-21st of August 2009.

Table of Contents

Chapter 1

Introduction

1.1 Problem description and work motivation

Since the beginning of the 20th century, the pneumatic tyre has been the dominant solution for the realisation of the rolling contact of the automotive wheels with the ground. Its capability of traction force development, due to the distinctive frictional characteristics of the rubber material, in combination with the vibration insulation properties of its inflated structure gave to the pneumatic tyre a significant advantage in comparison to any other available technical solution. Both the development of the vehicle dynamics engineering and the evolution of the automotive design have been closely coupled with the technical progress in the field of the tyre science. As the output of the vehicles' powertrain was reaching new levels it was the tyre development that allowed or obstructed the parallel progress in the actual performance of the vehicles.

Nowadays the traction potential is just one of the key objectives and challenges that define the design of the automotive tyres. Additional factors like the NVH characteristics, the structural integrity, the load bearing capability and the rolling resistance are just some of the properties and the objectives taken into consideration not only in the development of a new tyre but in its successful integration in the vehicle dynamics platform as well. It is by no surprise that the satisfaction of a broad range of technical requirements constitute a complex engineering problem given especially that in many cases, such as the development of high traction and low rolling resistance forces for example, these characteristics are accomplished by contradicting mechanical properties and design solutions. Today, more than ever, the tyre science tries to define and predict the optimum balance between the contradicting performance characteristics of a modern automotive tyre. Various computational engineering tools and an excessive series of measurements and testing procedures are used in this design optimisation process.

Such is the importance, though, of the pneumatic tyre for the dynamic performance and the NVH rolling behaviour of the vehicle, that it may be reasonably argued that its chassis is designed and developed around the tyres' capabilities, especially for critical applications, such as the motorsport use vehicles. The resulting requirement for the integration of the tyre's and the chassis' design processes in one development platform generates a vital need for the in-common study and mathematical modelling of their interacting performance characteristics. The move of the automotive industry towards the virtual development and virtual testing methods, due to the strict time scales and budgets of the development cycles of the new products, makes the

new vehicles' platforms physically available only towards the latest stages of their design. In effect, most of the engineering development work is accomplished using simulation tools as opposed to physical testing. A new vehicle-tyre combination is tested for refinement and fine-tuning purposes at a stage that it is practically impossible any major change to be implemented. On the above basis, the radically increasing importance of the tyre modelling and simulation science cannot be questioned.

1.2 Tyre modelling background

Historically, as it will be extensively presented in the following chapter, the early attempts for the modelling of the tyre behaviour were focused in its shear force performance. The characteristic development patterns of the tyre forces and moments, as functions of the slip and the vertical load, were already experimentally identified since the early automotive tyre applications and their crucial effect on the dynamic characteristics of the ground vehicles has, since then, motivated numerous attempts for their comprehension and prediction. Furthermore, the repeatability of these patterns, for various tyre designs and a broad range of operating conditions was the key motivation for the early modelling attempts, which, by no surprise, were empirical models. Such attempts led to the widespread adoption of certain analytical expressions that capture accurately the tyre shear force behaviour as it is acquired by experimental measurements. Tyre models based on the same concept, significantly developed developed over the years, still constitute the basic tyre modelling tool widely adopted by the automotive industry.

What the accurate reproduction of the tyre performance measurements cannot, though, offer is an insight in the actual physical mechanisms that prescribe the macroscopically observable behaviour and performance of the pneumatic tyre. Although most of these mechanisms are well known (and to some extent well described in a mathematical way) their non linear nature and their varying, according to the operating conditions, level of contribution to the tyre behaviour have obstructed the development of their mathematical descriptions into tyre models that could be used by the automotive industry. On the other hand, the tyre mechanics science, either industry or academia based, has presented tyre models based on the representation of the respective physical mechanisms which are able to simulate some particular aspects of the tyre performance characteristics within considerable level of fidelity. The significant computational load and time, though, associated with these models, together with the complex process of identification of their parameters, limits the application of them to the detailed research on some individual tyre behaviour characteristics, as opposed to the complete tyre performance and its interaction with the dynamics of the vehicle.

The main reasons for the increased computational effort which is imposed by the physical tyre modelling approaches may be summarised as:

- The tyre structural behaviour is associated with various aspects of the tyre performance, given that the harmonically varying forces of the rolling contact excite a characteristic vibrational response. Accordingly, the modelling representation of the whole tyre cylindrical structure is essential for the capture of the resulting phenomena.

- The contact area, in which the tyre shear forces are developed, corresponds to a small only segment of the tyre circumference. The modelling of the related frictional phenomena imposes, though, the extremely fine representation of this contact section, as it is displaced along the tyre circumference and

varies in shape and dimensions.

Obviously, these two characteristics impose the modelling of the whole tyre structure at a level of detail able to offer an accurate representation of the contact and shear forces, something that increases radically the computational load associated with the respective calculations. Moreover, as it will become apparent in the present study, the interaction of these two behavioral aspects (structural response and shear force development) is a key mechanism that defines the transient performance of the tyre.

The outcome of the above modelling requirements and challenges is the progressive evolution of two distinctive tyre modelling approaches. On one side the simulation requirements of the automotive industry have led to the development of extremely accurate empirical models that can be easily integrated either in the vehicle dynamics or ride and comfort simulation studies. On the other side the tyre science insists on the development of physical models which capture the actual mechanisms of the tyre behaviour. Although such models offer a significant contribution to the industry or academia based tyre R&D activities, their computational load suspends their integration in the general vehicle dynamics simulation platforms.

1.3 The tyre modelling challenge and the scope of the present work

Obviously, the gap between the two tyre modelling approaches, the physical concepts investigated by the tyre science and the macroscopic models used by the vehicle dynamics one, could be bridged by the development of tyre physical models of significantly reduced computational load and simplified parameters' identification procedures. Ideally, such models would offer a physical insight in the behaviour of the tyre as imposed by its physical mechanisms under realistic operating conditions and would additionally allow for the investigation of the tyre's interaction with the dynamic behaviour of the vehicle. Moreover, this approach would enable the integration of the tyre model in the vehicle dynamics one at the very early stages of the chassis design and the parallel development of tyres that would meet the particular specifications and requirements of every application. Apart from the achievement of performance optimisation, the reduction of the necessary physical tests would improve the efficiency of the automotive vehicle development process.

On the above basis, the computationally efficient, physical modelling of one of the predominant interaction mechanisms that defines the transient behaviour and performance of the tyre will be the main topic of the present work. The simulation of the two-dimensional interaction between the structural response and the shear force development of the tyre will be thoroughly investigated. The challenges associated with the particular attempt will be initially identified through an analysis of the most established tyre modelling approaches. This non-exhaustive literature survey will highlight those particular modelling aspects that such an approach should incorporate so as to contribute to the above tyre modelling challenge.

The present work serves as an investigation of the basic steps and modelling enhancements that are necessary for the development of an NVH tyre model into a transient shear force one. Various aspects of this modelling evolvement, even the well established ones, are critically considered against similar approaches and their contribution in the representation of certain characteristics of the tyre behaviour is highlighted. The association of these characteristics with the model's physical properties, examined from the point of view of the achieved computational efficiency, is the key contribution of the study to the tyre modelling science.

Chapter 2

Tyre modelling methods and challenges

This chapter consists of two sections. In the first part a summary of the main tyre modelling approaches is given. This presentation briefly captures the general background, the simulation capabilities and the modelling aims that led to the development of each approach. Although only a brief description is given for every model, their basic characteristics, advantages and limitations become apparent.The presentation also highlights the reasons for the development of the modelling approach which will be presented in the following chapters and identifies the place of this work on the tyre modelling map. For this reason, existing models that exhibit a similarity in the simulation method and in their capabilities with the model developed herein, such as the ring models family, will be presented in more detail.

In the second part of the chapter the discussion will be carried over to a crucial aspect of the tyre behaviour, its viscoelastic properties and their effect on its frictional performance. A brief presentation of the main viscoelastic material characteristics will be attempted, from a historical point of view. The evolution of the established contact and tribological theories will be summarised, together with their applications on the viscoelastic frictional behaviour explanation attempts. The extent of the presentation may surpass the essential one for the present study, it was, though, considered to be beneficiary for the highlight of the current and future tyre research challenges, not only in respect to the simulation techniques, topic covered in the first part of the chapter, but also in respect to the identification and understanding of the physical mechanisms which dictate the tyre behaviour.

2.1 Tyre models and their categorisation

The number of the tyre models in the existing bibliography is significantly high, as the tyre behaviour can be examined from various, different from each other, points of view and consequently the strict categorisation of the tyre models is a challenging task. Moreover, the capture by each approach of the tyre physical mechanisms, the associated computational load and its degree of accuracy are just a few of the factors that have led to the development of numerous hybrid models, matching specific needs and applications. Three main perspectives of categorisation, which are presented in fig. 2.1, may be summarised as:

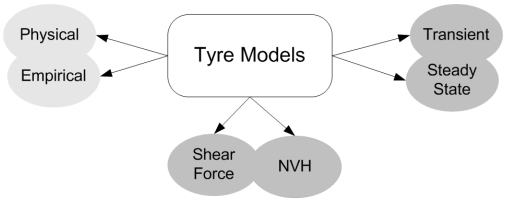

Figure 2.1 – Three criteria of categorisation of the tyre modelling approaches.

1. Categorisation according to the **modelling method**:

   - **Physical models**
     A mathematical description of the physical mechanisms that define the tyre behaviour is sought by such models. The complexity and the non-linearity of these mechanisms, though, dictate the incorporation of radical simplifications in them, the nature of which varies from model to model.
   - **Empirical or experimental models**
     These models attempt to correlate analytical mathematical expressions with ranges of experimental measurements. Common interpolation and extrapolation data-fitting techniques are applied for the prediction of the tyre performance in conditions close to the experimental ones.

2. Categorisation according to the **modelling aim**:

   - **Shear force generation models**
     Such models focus in the prediction of the horizontal shear forces and are commonly incorporated in vehicle dynamics models. The kinematic conditions of the vehicle prescribe the tyre operating conditions, while the generated forces act as dynamic excitation inputs to the vehicle.
   - **NVH models**
     Such models examine the tyre behaviour from the point of view of the structural vibrations, which are excited by the contact-rolling conditions or by the road-profile irregularities. In the low frequency range these models focus in the transmissibility of the vibrations to the vehicle's chassis through the wheel and the suspension. In the higher frequency range, the noise generation and propagation phenomena are studied using the respective models.

3. Categorisation according to the capability of **transient phenomena simulation**:

   - **Steady state models**
     These models examine the tyre performance under constant rolling and slipping operating conditions.
   - **Transient models**
     The response of the tyre to transient operating conditions is examined. The modelling of the interaction between the shear force generation and the structural vibrations phenomena is their common enhancement compared to the steady state ones.

Apparently, tyre physical representation imposes a greater modelling challenge than the respective empirical one, as the tyre behaviour has to emerge through the superposition and the interaction of various

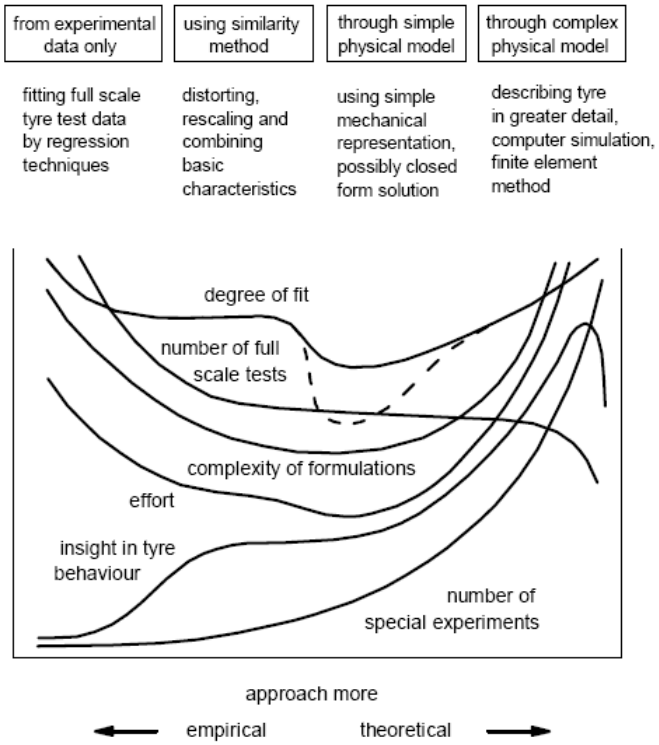

Figure 2.2 – The basic characteristics of the empirical, the physical and the intermediate models, after[1].

physical mechanisms. At the same time, an empirical model may offer much higher accuracy and correlation with the actual tyre behaviour, given that its only requirement is the accurate prediction of certain values. The distance between the pure physical and the pure empirical representations is covered by a vast number of hybrid (intermediate) models, placed closer to the one or to the other approach. The construction and the simulation potential of many of them is comprehensively presented by Pacejka in [1]. The basic characteristics of the intermediate models are presented in fig. 2.2, after [1].

The conceptual difference between the shear force and the NVH physical models, derives from the simplification approach followed in each of the two cases. In the first case an accurate representation of the contact area phenomena is attempted, while the contribution of the out of contact section of the tyre structure is neglected or incorporated in a simplified way. On the other hand, NVH models propose a structural representation of the whole tyre, usually common for the in and out of contact sections. The possible contact is imposed to these studies through the application of the respective boundary conditions or dynamic excitations. Apparently, the above modelling difference imposes a significant difference in the frequency range of the phenomena that may be captured by each of them. The NVH models may cover a broader frequency range, the breadth of which increases with their modelling complexity, as discussed by Reinalter in [2], following the frequency-complexity correlation initially presented in [3] (fig. 2.3).

Trying to follow the complexity induced order, the following presentation of the tyre models will start from the steady state ones. Firstly, the main characteristics of the tyre behaviour, which are captured by such models, will be presented. Historically, the tyre modelling science started as an attempt for the physical identification -in the case of the physical modelling- or the mathematical description -in the case of the

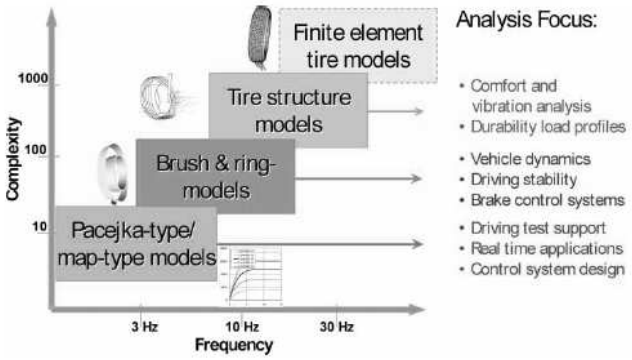

Figure 2.3 – The categorisation of the tyre models, according to their use by the automotive industry. (after [2], originally in [3])

empirical modelling- of the steady state tyre behaviour patterns. Interestingly, although these patterns are easily observed experimentally, the identification of the associated with them physical mechanisms remains one of the greatest challenges of the tyre science, as will be later discussed. The transformation of both kinds of steady state models (physical and empirical) into simple transient ones will be later presented. More advanced transient models, with increased simulation capabilities, will follow, but at the same time it will become apparent that, for reasons related to the computational load of each of them, these advanced models complement but do not substitute the simpler ones.

2.1.1 The basic characteristics of the tyre shear force generation

The steady state tyre shear force development exhibits some basic, characteristic patterns which are summarised in the following:

- **The shear forces as functions of slip**
  Shear force in both the longitudinal and the lateral direction (defined according to the orientation of its crown plane) is primarily a function of the tyre slip. In the first case, the slip value is defined by the difference between the velocity corresponding to the rolling motion and the velocity corresponding to the actual displacement. In the second case (lateral force), the slip is defined as the angle between the displacement velocity and the crown plane orientation [1]. For low slip values, both force functions are linear and proportional. For higher slip values, though, a saturation behaviour can be observed, and a maximum (peak) force slip value can be identified. Further increase of the slip results in a slight decrease of the force value and later in its fixation at a constant value. The plateau-shaped force development with the slip is a vital tyre characteristic and imposes a significant effect on the dynamic behaviour of the vehicle. Typical experimental curves of tyre coefficients of friction with slip are presented in 2.4, after[4].

- **The vertical load effect**
  As the shear force generation is based on a frictional mechanism, both longitudinal and lateral tyre forces increase with the vertical load. Although for most materials a proportional development is

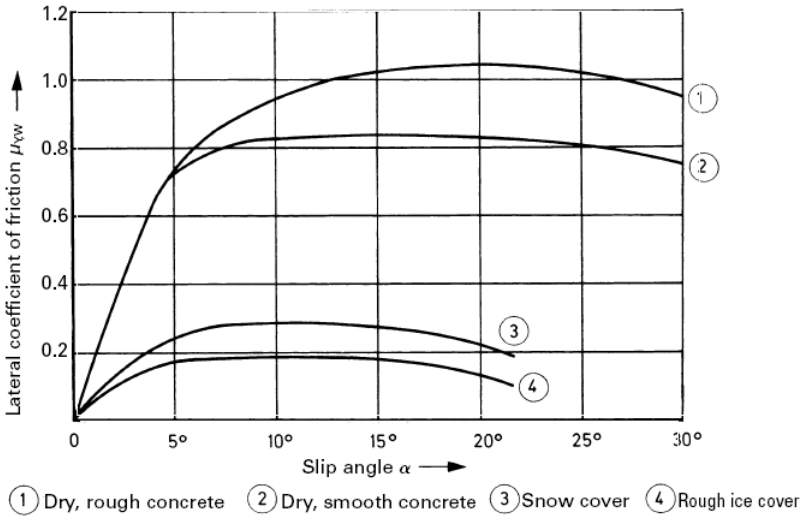

(a) Lateral friction coefficient.

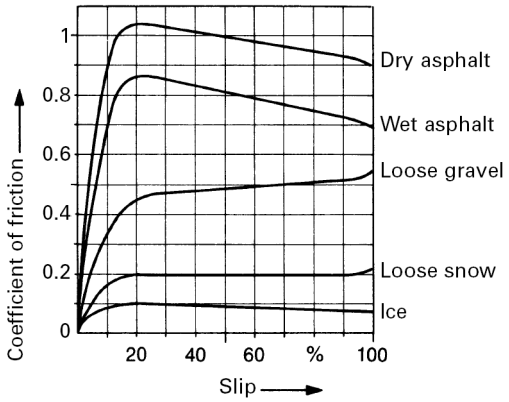

(b) Longitudinal friction coefficient.

Figure 2.4 – Shear force coefficient development with slip, for various road surfaces, after [4].

observed, which corresponds to a constant coefficient of friction, this is not the case for the tyre forces. The force-load function is a non linear one, which corresponds to a decreasing coefficient of friction with the load. The lateral force development with load under constant slip angle, is presented in fig. 2.5, after [4]. The load effects play a major role in the tyre-vehicle interaction as they introduce a range of load transfer associated phenomena.

- **The interaction between the two in-plane forces**
  Although theoretically the friction along the two, vertical to each, tangential to the road develops independently, this is not true in the actual tyre behaviour. The simultaneous development of slip along the two directions (longitudinal slip and slip angle) results is the severe deterioration of both of them. The interaction is presented in fig. 2.6.

- **Aligning moment**
  Apart from the shear forces, the development of the aligning moment is another major performance

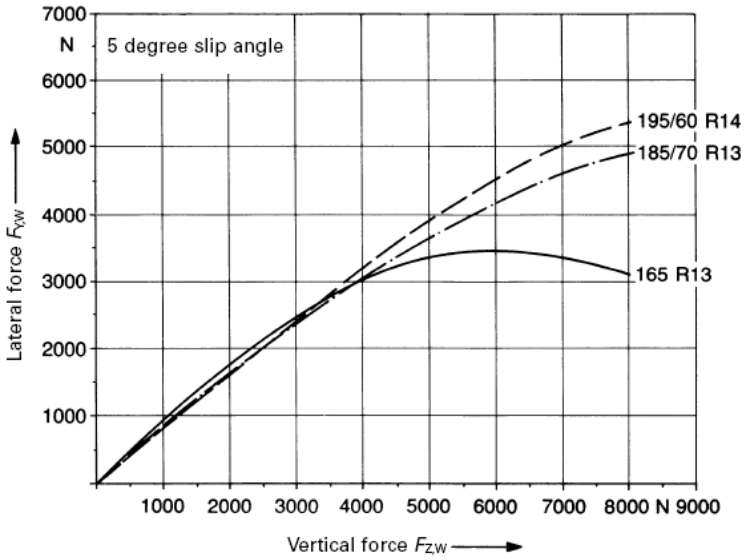

Figure 2.5 – The effect of the vertical force on the lateral force development, after [4].

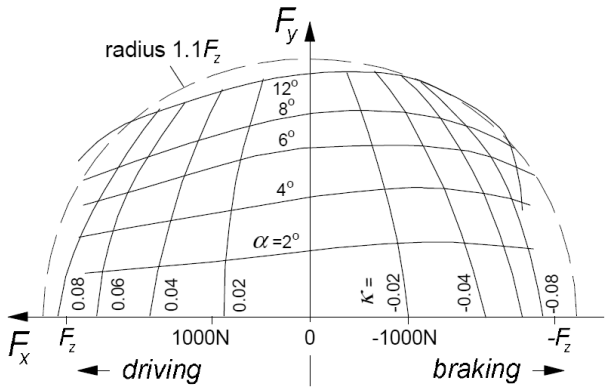

Figure 2.6 – The deterioration of the tyre shear force under combined slip conditions, after [1].

characteristic which tyre shear models attempt to capture. Its reliance on the slip angle, though, is different from the one of the forces. The aligning moment increases with the slip angle, reaches a maximum value and deteriorates radically for a further increase of the slip angle. Some typical aligning moment development functions with the slip angle, for various levels of the vertical load, are presented in fig. 2.7

2.1.2 The empirical steady state shear force models

In the first empirical modelling attempts, experimentally gained data were directly used for the tyre behaviour representation in the form of look-up tables or graphical plots. Early analytical representation models, such as the one presented by Sitchin [5], divided the available data range in zones, in order the most appropriate mathematical function to be applied to each of them. It soon became apparent, though, that the experimental data follow certain mathematical forms for a wide range of vertical load values. Consequently, a force-slip

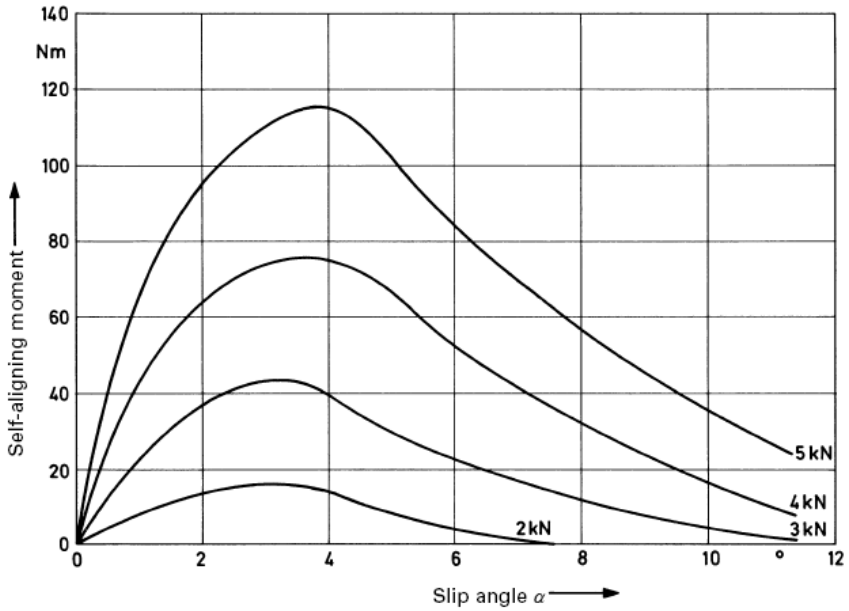

Figure 2.7 – The aligning moment development with the slip angle, after [4].

curve may be adjusted (extrapolated) for different load conditions by the vertical and horizontal magnification and shifting of an initial single curve. In reverse, a "non-dimensionalisation" process of a wide range of curves results in a single one within great accuracy (fig. 2.8). This similarity property was first noticed by Pacejka [6]) while a detailed analysis of it may be found in [7, 8, 1]. A direct result of the similarity property is the capability of using certain analytical mathematical functions not only for the reproduction of the experimentally gained data, but also for the extrapolation of them in tyre operating conditions out of the range of the available data.

The most established empirical tyre model is the Magic Formula one [9, 10], which started as a common project between Delft University and Volvo. The core of the model consists of a combination of basic trigonometric functions and a number of shifting, shape, curvature and peak factors, able to adjust the trigonometric expression so as to match any set of experimental measurements. Magic Formula is able to describe the combined slip tyre performance and aligning moment generation, based on pure lateral and pure longitudinal slip measurements. Many enhancements of the Magic Formula model have been proposed over years, the prediction potential of which now incorporates various effects, such as the camber angle, the turn slip, the ply steer and the tyre conicity. A comprehensive presentation of the Magic Formula model and its numerous variations may be found in [1], together with a description of the identification process of its numerous parameters.

Although the model is still based on a data-fitting procedure, substantial efforts have been put not only into the optimisation of the parameters identification procedure, but also into the possible correlation of them with the tyre physical mechanisms. Such attempts have led to the generation of a number of hybrid, empirical-physical, models, the so called "semi-empirical" ones. Sharp and Bettela in [11] and Sharp in [12] present a systematic analysis of the parameters' identification procedure and the required set of experimental measurements. An identification method based on a finite element model is proposed by Rao

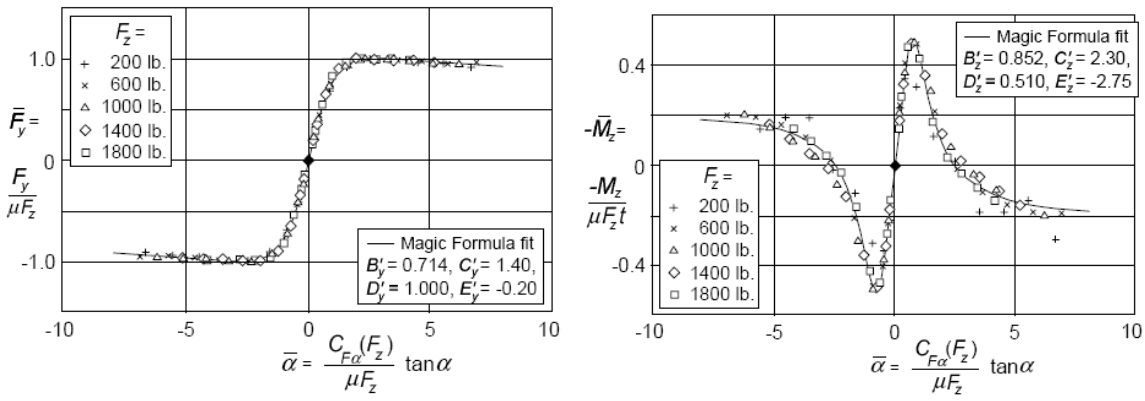

(a) Lateral force

(b) Aligning moment

Figure 2.8 – Lateral force and aligning moment curves for a range of vertical loads after a "non-dimensionalisation" process, after [1]

et al in [13]. The incorporation into the Magic Formula model of external to the tyre factors, such as the road roughness, the weather conditions and the suspension characteristics of the vehicle is discussed by Arosio *et al* in [14]. A genetic algorithm based identification procedure is proposed by Lu and Shih in [15] for the parameters'adjustment to the road characteristics and the vehicle velocity. The most significant enhancement of the Magic Formula model, though, has been the superposition on it of a simplified transient behaviour sub-model, which transforms it into an adjustable and computationally effective low frequency transient model. Such methods have been proposed by Higuchi and Pacejka [16] and by Pacejka and Besselink [17].The actual transient mechanism will be described later, when such simplified transient models will be examined.

2.1.3 The physical steady state models

The physical steady state models offer a simplified representation of the tyre-road interaction phenomena along the contact area, resulting in the macroscopic frictional characteristics described above. The fundamental mechanism of this method is the prediction of at least two distinctive zones of finite length in the contact area. Along one of them the tread of the tyre adheres (stick zone) to the road and along the other one the tread creeps (slip zone). The non-linear dependency of the shear force on the load and the slip are accredited to the variations in the relative length of these zones.

Although physical steady state models may incorporate the deformation compliance of the tyre belt, this is typically accomplished in a simplified way, focusing in its effect on the friction force generation. Such approaches cannot prescribe the development of the vertical pressure distribution along the contact area, which is necessary for the prediction of the transition between the two contact zones. In result, a certain vertical pressure distribution is a priori assumed, in terms of both magnitude and shape. It has been experimentally verified that under common tyre operating conditions, the deviation of the distribution shape from a parabolic/trapezoidal one is insignificant [18, 17] and such a shape is commonly adopted.

The underlying mechanism in every physical steady state approach is the contact stiffness concept, as introduced by Winkler in [19]. He proposed a discretised stiffness foundation for the prediction of the contact

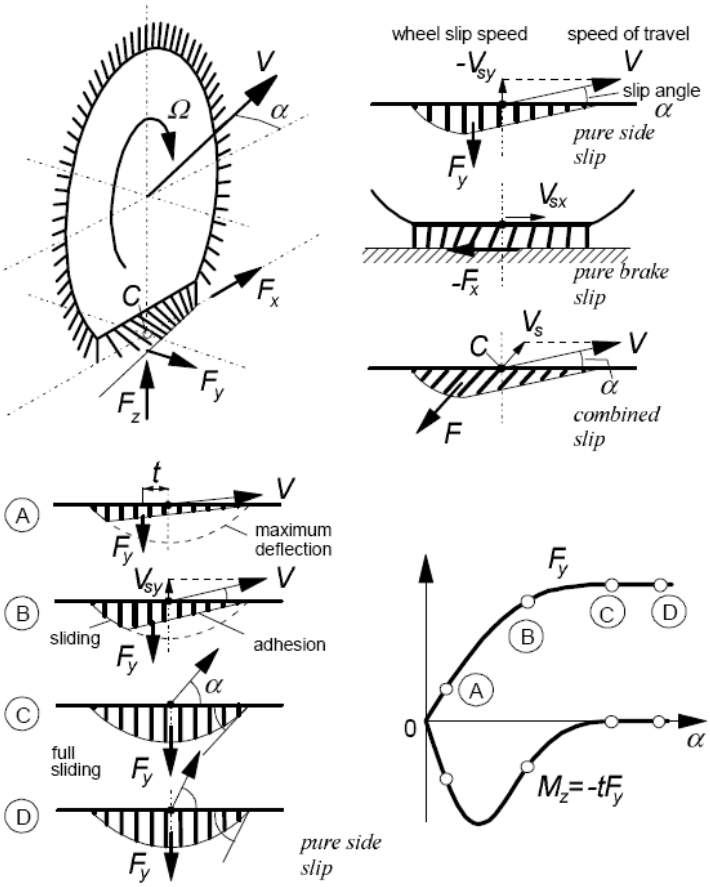

Figure 2.9 – A representation of a brush tyre model (from [1]) and the predicted behaviour of the bristles for an increasing slip angle.

pressure development between two bodies. In the application of the concept in the tyre modelling (brush models family) the stiffness elements are assumed to lie on the road plane, instead of the perpendicular to it direction. Their shear deformation, as the tips of the bristle elements adhere to the road, and their slip offer the development of the two contact zones. The concept is visualized in fig. 2.9. A historically organized survey of the brush models can be found in [20], while a comprehensive analysis of the brush model predicted tyre behaviour is presented in [1]. It should be mentioned that although physically the brush models' theory is based on the discretisation of the tread, the shear force calculation is accomplished in an analytical way, which offers a significant computational advantage over pure tread discretisation approaches.

Sharp and El-Nashar in [21] presented a discretised algorithm based on an approach similar to the one of the brush concept. Every bristle was equipped with radial, tangential and longitudinal stiffness property, and consequently the model could predict the vertical contact pressure distribution. The shear force was numerically calculated following the deformation a bristle along the contact area and calculating its equilibrium position in discretised positions. A stiffness-based model for the prediction of the steady state shear force was also presented by Gim and Nikavresh in a series of articles [22, 23, 24]. The tyre was modelled as a three-dimensional stiffness foundation (radial, longitudinal and lateral) and the approach incorporated their interaction but not the calculation of the contact pressure distribution, which was a priori

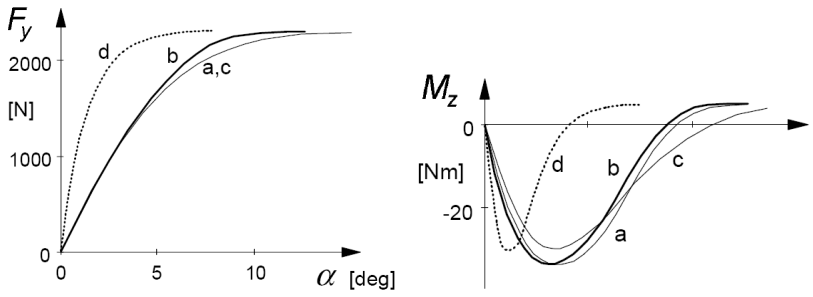

(a) Lateral force (b) Aligning moment

Figure 2.10 – The effect of tyre compliance incorporation on the lateral force and the aligning moment prediction of a series of tread elements (a: string type compliance, b: beam type compliance, c: symmetric parabolic carcass deflection, d: rigid carcass; reprinted from [1], originally in [28])

assumed as a parabolic one. Levin in [25] introduced a brush steady state model with enhanced modelling capabilities, including tread dynamic phenomena, as an inertia property was assigned to each bristle. Two sliding zones (one at the beginning and one at the end of the contact area) were predicted while the shear force generation was based on anisotropic friction properties along the two dimensions and different static and sliding friction coefficients. Lately, Salaani [26] used the brush analytical concept for the construction of a steady state physical model, enhanced by the incorporation of performance parameters derived by the analysis of experimental results.

The brush model approach encompasses a physical conceptual discontinuity in the transition from the adhesional to the sliding zone. Along the first one, the orientation of the bristle deformation and of the shear force is dictated by the wheel velocity direction and the relative to each other bristle stiffness along the two in-plane directions. Along the sliding zone, though, the force orientation is solely dictated by the wheel velocity. A third, transition, zone is introduced by Sorniotti and Velardocchia in [27], where the bristle elements progressively change their orientation from the one to the other. In the same study, the phenomena related to the bristles' stiffness non linearity with the vertical load are accounted for.

The stiffness property of each bristle of a brush model theoretically represents the combined structural stiffness characteristics of both the tread and the belt (carcass) of the tyre. In respect, a crucial evolution of the brush models was the incorporation of a separate belt representing deformation mechanism. Although the particular enhancement concept is associated with the simulation of transient phenomena capability, it also improves the simulation accuracy of the steady state approaches. In fig. 2.10 the effect of the incorporation of different kinds of carcass compliance on a simple brush model is presented, regarding the lateral force and aligning moment prediction.

Sharp in [29] discussed the enriched simulation potential resulting from the addition of lateral, longitudinal and yaw relative flexibility between the bristles' basis and the wheel. Pauwelussen [30] modelled the belt deformation using a string mechanism and combined it with a brush steady state model. The string deformation was expressed through the expansion in the structural eigenvectors (Kernel functions) and the relative participation of the corresponding modes, an approach more common in the NVH models, as will be later discussed.

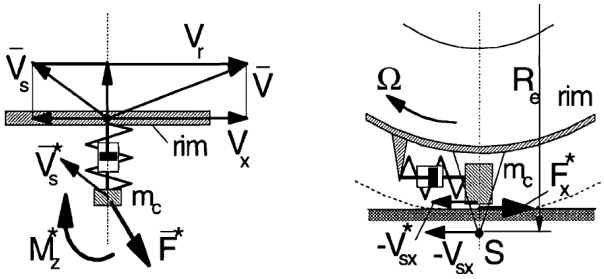

Figure 2.11 – The concept of the inertia equipped translating contact patch, presented by Pacejka and Besselink in [17] for the implementation of the transient behaviour in the Magic Formula model.

2.1.4 The simplified transient shear force models

In this section, tyre models able to represent the tyre behaviour under transient operating conditions will be examined. Simplified dynamic characteristics are incorporated in the models, representing their macroscopic effect on the frictional performance of the tyre. The simplified approach suspends the direct association of macroscopic transient frictional tyre characteristics with the physical dynamic phenomena along the contact area. In physical terms, such models remain steady state ones, but in computational capability terms they may be referred as transient ones.

A major modelling approach for the macroscopic representation of tyre transient behaviour is the single point contact concept, a detailed presentation of which may be found in [1]. According to that, the contact area is deduced to a single contact point which is attached to the wheel through a combined lateral and longitudinal Kelvin-Voigt element. Two first-order time differential equations are derived, one for each in-plane direction of deformation, which describe the slip development as a function of the relative velocities between the contact point and the wheel. The calculated slip values may be used as inputs to any steady state friction model, such as the Magic Formula. This concept was firstly presented by Pacejka and Besselink in [17] and later it was further developed with the addition of the inertia property to the contact point [1].

The time coefficients, calculated by the contact point differential equations, may be explicitly used for the simplified modelling of the transient tyre response. The concept leads to the derivation of the relaxation length property of the tyre [1], representing its first order dynamic behaviour. A high relaxation length value corresponds to a slow, low frequency-like , tyre response, while a low relaxation length corresponds to a fast, high frequency-like, response. Although the relaxation length property is not directly related with any physical one, its easy experimental identification enables the superposition of low frequency range dynamic characteristics to any steady state shear model. Clover and Bernard in [31] extended the relaxation length concept to the study of longitudinal tyre dynamics.

TMeasy is a commercially available semi-empirical tyre model, based on the single contact point concept. The model was initially presented by Rill [33], while the latest version is described in [34]. Apart from the first order dynamic behaviour of the shear forces and aligning moment development, the effects of excessive camber angle and varying vertical load are also accounted for. Starting from the comprehensive steady-state simulation study of Gim and Nikavresh (presented in [22, 23, 24]), a macroscopic transient behaviour was added to it by Gim *et al* [32] leading to the construction of a semi-empirical transient model. The model (fig. 2.12) incorporates analytical functions of physical properties for the force prediction, while the results are fine-tuned according to experimental data fitting process.

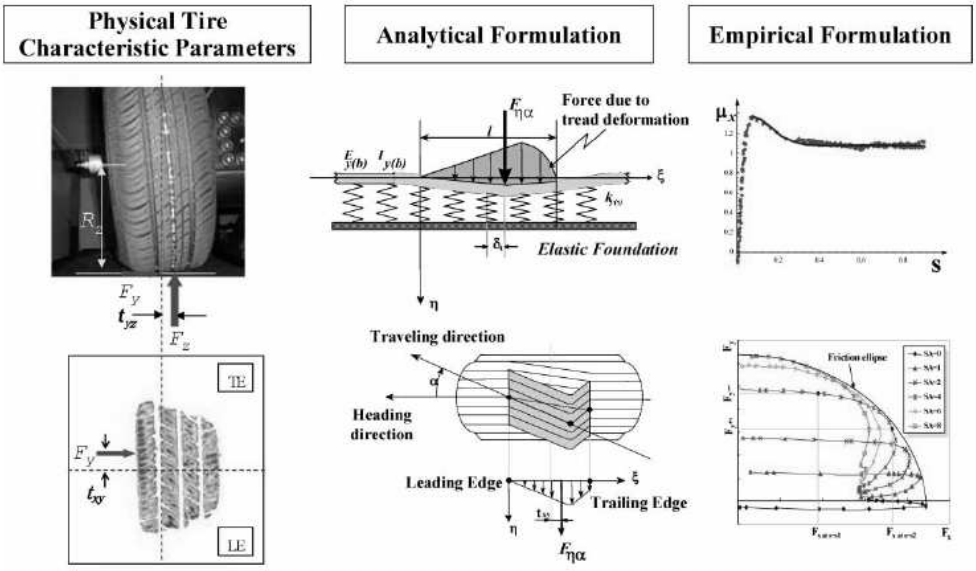

Figure 2.12 – The combination of empirical and physical-analytical methods for the representation of the tyre's force characteristics, in the model, presented by Gim *et al*, after [32].

The availability of continuously increasing computational power moves the centre of attention of the simulation studies towards advanced models with increased physical correspondence, which will be later discussed. At the same time , though, the demand for simplified but accurate shear force models is also increasing, as such models are embedded in the software of the modern chassis electronic control systems (ant-block brake systems, traction and stability control systems, etc.). Such models must be able to simulate in real time the tyre frictional behaviour close to its traction limit, based on a minimum set of easily measured chassis' behaviour values. Other aspects of the tyre behaviour are neglected in favor of the robustness and the computational speed. The implementation of the tyre as a subsystem of a brake stability control system is presented in fig. 2.13, after [35].

As a typical example of this category of models the LuGre friction model may be mentioned. The model, named after the control research groups of the universities of Lund and Grenoble, was initially introduced in [36, 37], as a direct evolution of the Dahl friction model [38], based on a stress-strain like dynamic relationship. The LuGre friction model simulates the basic tyre friction characteristics, such as the velocity dependency, the dynamic (memory) behaviour and the stick-slip motion, all of them associated with the viscoelastic material properties, as will be later discussed. The model was proposed as a dynamic tyre friction model in [39]. Various one dimensional and two-dimensional improvements of the initial model have been proposed, such as the ones described in [40, 41]. The LuGre friction model is comprehensively described by Aström and de Wit in [42], while Liang[43] presents its latest tyre simulation applications.

Moving towards more advanced transient tyre representations, the physical mechanisms correlating representation of the belt dynamic behaviour comes into play. Various models of the carcass deformation have been proposed, since its actual structure is composed by many different materials and exhibits significant anisotropy. As it has been discussed, a first approach is the physical representation of the belt deformation along the contact area as opposed to the structural representation of the complete belt circumference. His-

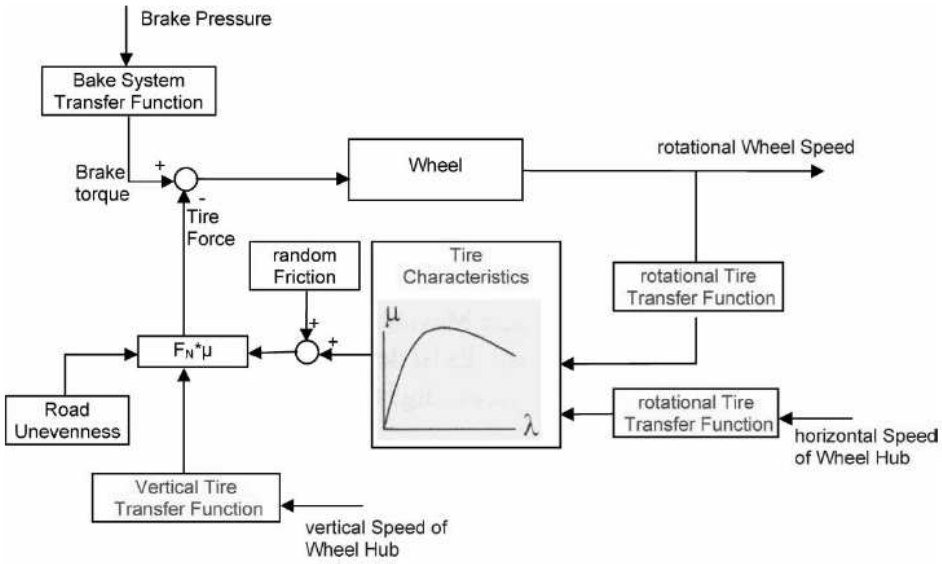

Figure 2.13 – The tyre as part of the ESP control system of the vehicle, after [35]

torically, two analytical mechanisms have been proposed for the capture of this deformation [1]: the string and the bending ones.

The string under tension model was initially introduced by Von Schlippe in [44], while a comparative study of a number of string based shear force transient models can be found in [45]. Single or multiple strings are commonly assumed, while radial and axial stiffness foundations are used for their support and wheel attachment. The string mechanism is commonly incorporated in the calculation of the relative slip velocities along the contact area for the derivation of the models' equations, while Liu *et al* in [46] proposed a method based on the geometrical deformations of the contact area.

The string mechanism introduces a second order differential equation capturing the belt lateral deformation along the tyre circumference. Interestingly, a mathematical expression similar to the one derived by the relaxation length concept is acquired. The combination of a string model derived relaxation length with a Magic Formula tyre is presented by Higuchi and Pacejka in [16]. Both relaxation length concepts (contact point model and string model derived) are incorporated in the commercial software PAC2002 [47], as transient enhancements of the Magic Formula model, able for dynamic simulations up to $12Hz$.

Starting from the discretised contact stiffness physical concept, various transient models have been developed through the incorporation of belt dynamics. The combination of a stretched string with a foundation of brush elements was introduced by Pacejka in [48] for the study of the tyre shimmy phenomenon, while later [49] the inertia effect was incorporated to it. An analytical presentation of the combined string-brush models may be found in [1]. Moreover, the multi-spoke steady state model which was presented by Sharp and El Nashar in [21] has been developed into a transient one by Zhou *et al* in [50].

The incorporation of the bending physical mechanism increases the model's computational load, comparatively to the truss one, as the belt deformation is captured by a fourth-order differential equation. Mastinu and Fainello [51] presented a bending beam based approach, which was later developed in a semi-analytical form by Mastinu *et al* [52]. In general, the bending mechanism based approach broadens the frequency range

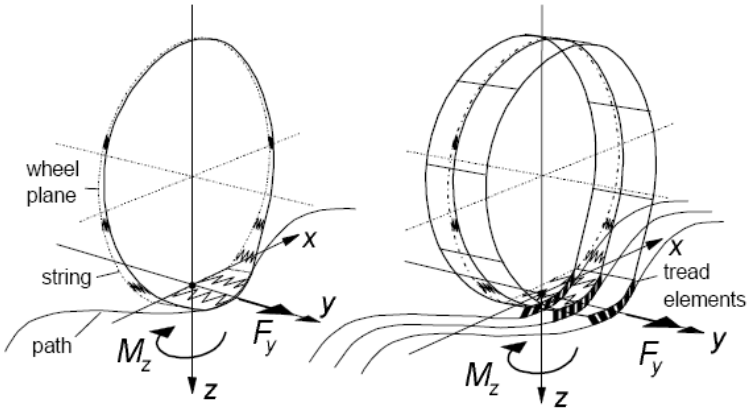

Figure 2.14 – The string mechanism based model (from [1]) in a single and a multiple version, the latter including a tread foundation.

of the model's applicability towards the combined shear and structural NVH phenomena representation, as it will be later discussed in detail. However, before moving the discussion to the modelling of the vibrational behaviour of the tyres, it should be clarified that the term "simplified", which was used for the description of the transient models up to this point, is not derived from their frictional phenomena simulation capability, which may be exceptional. The term refers to the lack of capability of simulating secondary effects related to the structural deformation, which may be acquired only through complete structural models, such as the effects of the rolling velocity, the varying contact area dimensions, etc.

2.1.5 The simplified vibrations models

The vertical vibrational behaviour of the tyre can be easily simulated in case the shear force generation and the contact area phenomena, in general, are neglected. The tyre behaves as a non-linear viscoelastic structure, transmitting to the wheel the excitation imposed by the road profile. The stiffness non-linearity is primarily induced by the sidewall structure of the tyre and its shape variations. In a simplified approach the rotation and the contact area effects are not taken into consideration and the contact may be regarded as a single point boundary condition.

The simplest, linear, model which is used for the modelling of the vertical tyre behaviour is the Kelvin element, consisting of a stiffness and a viscous damping element in parallel configuration. The combination of a number of such elements for the capture of the low frequency radial behaviour of the tyre was investigated by Dunn [54]and later by Olatunbosun and Dunn [55]. Kao [53] proposed the simulation of the tyre vertical behaviour through a pair of combined spring and mass elements, in serial configuration (fig. 2.15), the BAT model. One of the elements corresponds to the sidewall behaviour, while the other one corresponds to the enveloping property (shape conformation of the belt circularity to the road plane).

Although a non linear stiffness property may capture the static vertical deformation behaviour of the tyre and the combination of multiple elements may accurately describe its low frequency radial dynamic behaviour, the applications of such models are limited. Their basic limitation is the lack of capability of coupling with the shear force generation mechanism, of representing the contact area development and of simulating the rolling effects. Such phenomena are vital for the NVH performance and characteristics of the

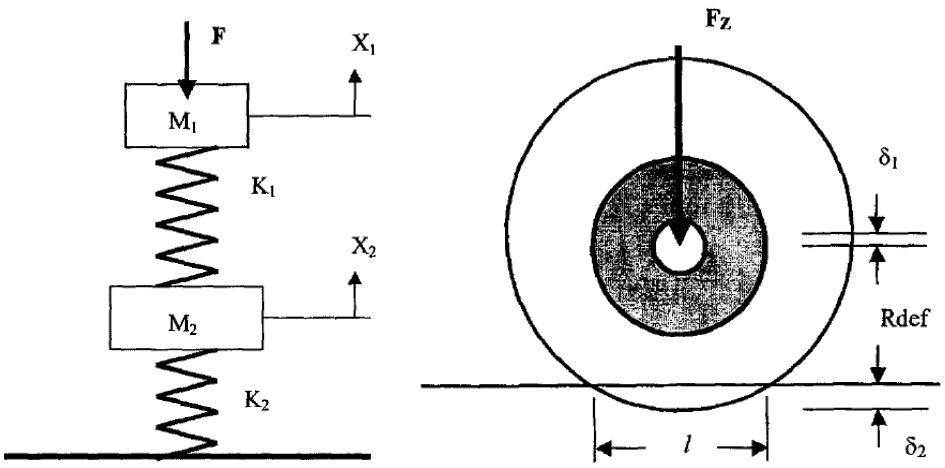

(a) The BAT model.

(b) The displacements corresponding to the two stiffness properties.

Figure 2.15 – The simplified BAT model and the physical analogy of the two stiffness properties, after [53].

tyre, which are studied by the models of the following category.

2.1.6 The advanced transient models

The tyre models examined in this section, approach the tyre as a complete circular (two-dimensional) or cylindrical (three-dimensional) structure. The vibrational behaviour is not deduced any more to its vertical corresponding component but the complete radial, circumferential and out of plane behaviour may be theoretically captured. The possible incorporation of the actual tyre shape into the model enables the simulation of the contact area generation, as imposed by the operating conditions. In result, transient phenomena associated with the interaction between the structural deformation and the shear force generation (shuffle effect, drive-train dynamics, traction/braking induced vibrations, secondary ride phenomena) may be captured by the more advanced models of this category. The broad and enhanced simulation capabilities of these models, though, is usually accompanied by the significant increase of the respective computational load, especially in case such a model is used for the simulation of transient interaction phenomena between the shear force generation and the vibrational behaviour of the tyre.

Although the frequency range of the majority of these models, makes them applicable to both shear force and NVH studies, usually they are developed with a clear orientation towards the one or the other. This has to do with certain simplifications, different in each case, introduced in order to decrease the computational load. Apparently, shear force oriented models incorporate simplifying assumptions on the structural deformation of the belt, while the NVH models assume simplified contact conditions.

Obviously, the frequency range of the tyre NVH behaviour is significantly broader than the range associated with the dynamic behaviour of the vehicle. The shear force generation based interaction between the tyre and the vehicle is captured by a shorter frequency range than the NVH one. In case, though, the contact deformation and the contact area phenomena are studied as part of the vibrational behaviour of the study, instead of being apriori imposed to the model, the shear force generation associated modal range of

interest radically broadens. Moreover, the current development of advanced traction and braking control systems has significantly increased the importance of the high frequency tyre dynamics and their effect on its frictional performance.

Following the study of Sugiyama and Suda [56], the transient tyre models may be categorised according to their degree of belt compliance. Accordingly, rigid belt, flexible belt and detailed discretised modelling categories may be defined, in an increasing frequency range order. These categories will be examined in the following, together with their capability of shear forces prediction.

The rigid ring model

The simplest transient approach, satisfying the circular shape criteria, is the rigid ring model. The model assigns a full set of six spatial degrees of freedom (three translational and three rotational ones) to the carcass circular structure, which is reduced to a two-dimensional (in-plane) ring. All the degrees of freedom are suspended by the sidewall stiffness foundation, attaching the ring to the wheel. Apart from the relative displacement between the wheel and the belt no other deformation pattern is accounted for. The in and out of plane modes of a rigid ring model are presented in figs. 2.16(b) and 2.16(c) respectively.

As a direct result of the ring non flexibility simplification, the contact area development, the effect of the road irregularities and the load related phenomena are omitted from the simulation. Obviously, as the tyre vertical pressure distribution cannot be represented, no physical friction generation mechanism may be incorporated in the model. The modelling discontinuity between the belt deformation and the frictional phenomena, though, allows for the artificial superposition of any macroscopic shear force model to the rigid ring modal behaviour, according to the desired accuracy and the available computational resources.

The rigid ring was firstly proposed as a transient in-plane tyre model by Jagt [57] and Zegelaar [58], while the concept was later extended to the lateral tyre behaviour [59]. Zegelaar *et al* in [60] proposed the in-plane rigid ring model as a simplification of a flexible ring model, which was used for the numerical identification of the common modes. A brush model was used for the derivation of the relaxation length property of the single point contact. As the belt non-deformability would result in the overestimation of the contact stiffness, the concept of the residual stiffness is introduced for the correct static behaviour of the tyre. Zegelaar and Pacejka, in [61], use the quasi-static behaviour of a flexible ring for the derivation of the corresponding to the rigid ring excitation caused by road unevenness. In [62] a rigid ring model equipped with a relaxation length transient shear force sub-model was used for the study of the tyre response to brake torque variations. The potential of the rigid ring model for the representation of the dynamic cornering and braking behaviour of the tyre was experimentally verified by Maurice in [63].

An interesting comparison of the longitudinal simulation performance of three models based on the Magic Formula one was presented by Jansen *et al* in [64]. In particular, a steady state one, a relaxation length transient and a rigid ring equipped model were compared. The study is focused in the simulation of the response to brake force variations induced by a typical ABS braking system. The results indicate that the steady state assumption, cannot be applied above $10Hz$, while the application limit of the relaxation length transient model is in the area of $30Hz$. The rigid ring model was found able to capture higher frequency phenomena.

A relaxation length equipped Magic Formula is also used as a shear force generation sub-model in the commercially available version of the rigid ring model (TNO MF-SWIFT), which is analytically presented in

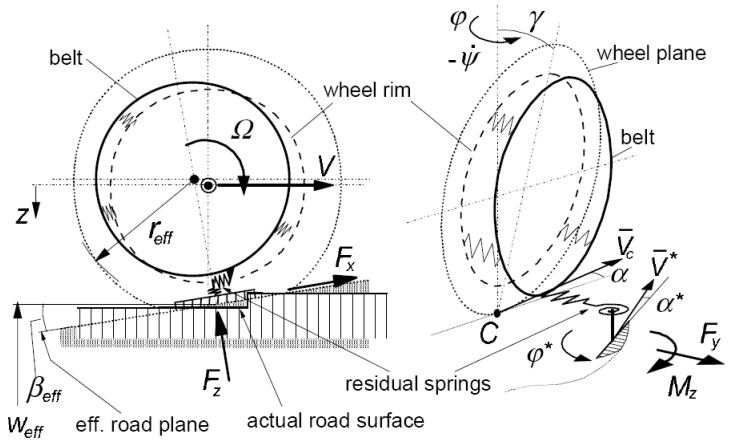

(a) General overview.

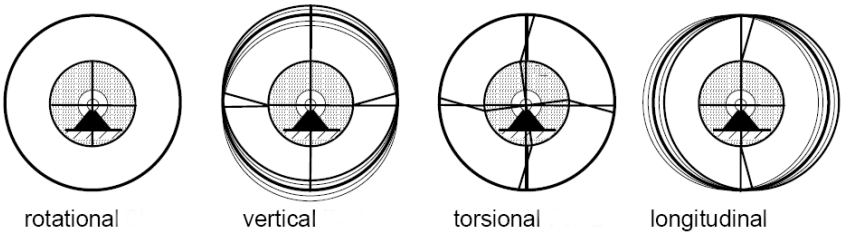

(b) The in-plane rigid modes of the ring.

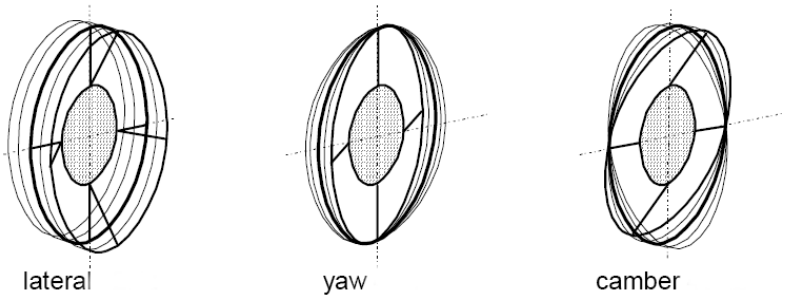

(c) The out-of-plane rigid modes of the ring.

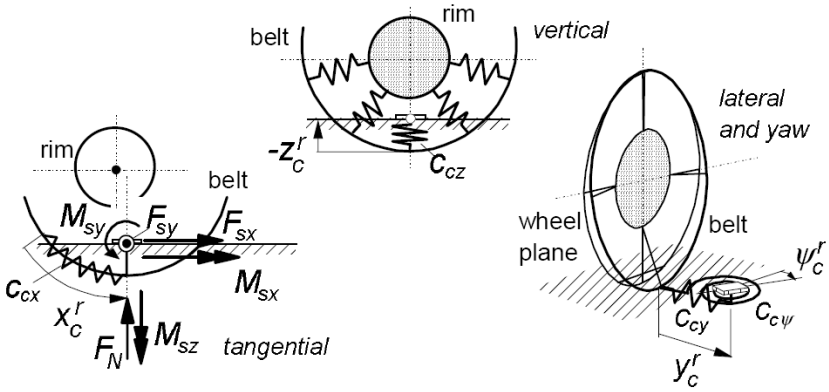

(d) The residual stiffness concept.

Figure 2.16 – Some basic characteristics of the SWIFT model, after [1].

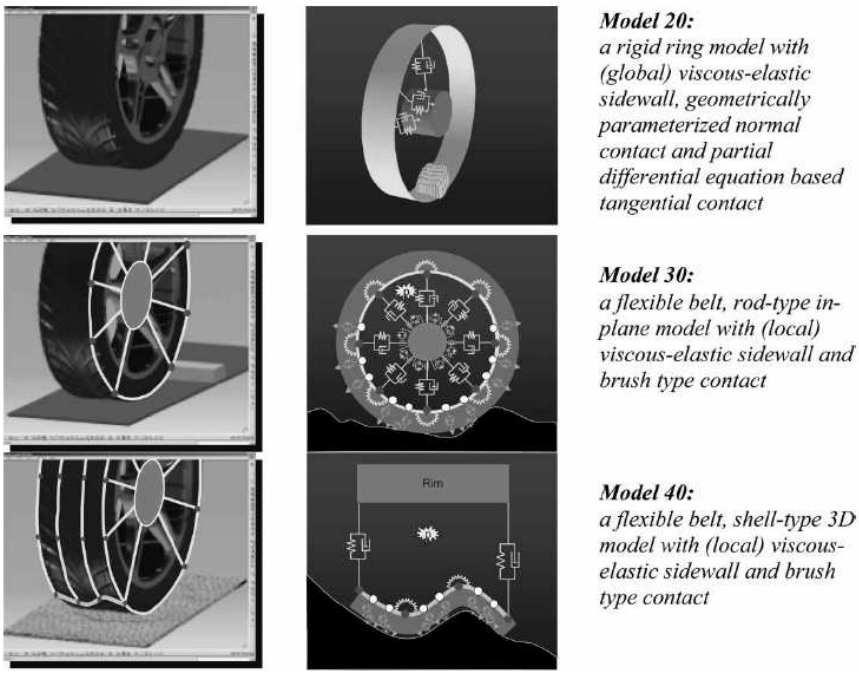

Figure 2.17 – The CDTire family of models, after [68]

[1, 65]. The model (fig. 2.16) is proposed for a broader frequency range of studies ($60-100Hz$) compared to the simple transient Magic Formula ($8Hz$). Interestingly, the simulation of the response to short wavelength road profile irregularities is incorporated in the above model, although the single point contact assumption is retained, using an effective road profile concept. Another rigid ring based semi-empirical transient model is the UniTire, introduced in [66] for real-time applications up to 8Hz. The model, the latest version of which is described in [67], proposes an analytical, polynomial-exponential, relationship between the developed slip and the frictional force. The first member of the CDTire family of models (fig. 2.17) [68], the CDTire 20 one, is also based on a rigid ring approach, combined with a viscous-elastic sidewall and an analytical shear force generation sub-model.

Obviously, the next step in the models development is the incorporation of the belt structural deformation at an in or out of plane level. The belt deformability enables the implementation of the contact deformation and the resulting contact pressure distribution in the simulation process, offering the capability of the representation of the shear force generation through a physical mechanism. This major simulation enhancement offers a physical insight into the interaction between the frictional characteristics and the structural response of the tyre.

It should be highlighted, though, that the calculation of the shear force behaviour of the tyre through the structural deformation mechanism imposes a significant increase in the computational load which is associated with the model. This increase results from the realisation of the contact along a small portion of the tyre's circumference (less than 10% for typical tyre loads according to [18, 1]). Accordingly, the belt deformation has to be examined at an extremely high level of spatial resolution in order an accurate friction generation mechanism to be incorporated in the model. Consequently, although the structural behaviour of

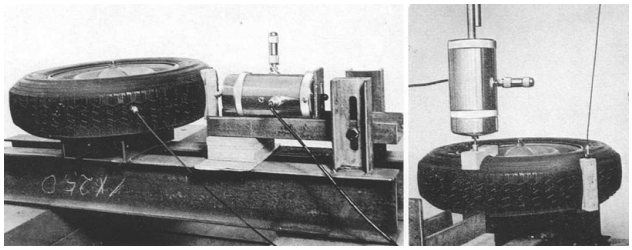

(a) The experimental set up.

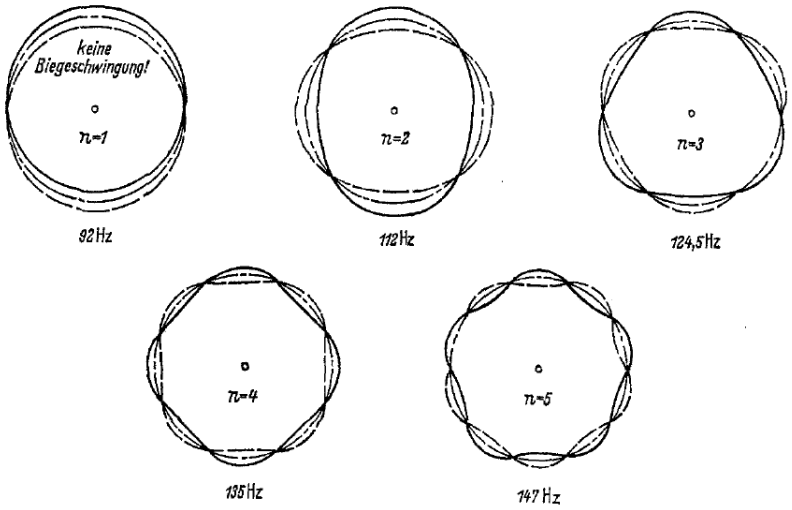

(b) The mode shapes and the natural frequencies.

Figure 2.18 – The modal experiment and the theoretical ring model eigendata, as presented by Böhm in [69].

the tyre has long ago been mathematically modelled and numerous analytical or discretised models have been proposed, this did not lead to the generation of physical shear force tyre models. Such structural models have been traditionally used for the theoretical investigation of the vibrational characteristics of the tyre, but not for detailed investigation the contact area phenomena. As presented in the following, even when the contact tyre vibrational behaviour was to be modelled, simplified boundary conditions were applied (single point contact or constant boundary conditions). Only lately the available computational power has enabled the generation of models that may accurately model both the shear force generation, the structural deformation of the tyre and most important their interaction along the contact area. Following this historical order, the structural vibrations focused tyre models will be firstly presented and the models with the capability of combined frictional and vibrational simulation will follow.

The deformable ring model

Historically, the first analytical structural representation of the tyre belt, from a vibrational point of view, has been the flexible ring on elastic foundation (REF) model foundation. Although the first analysis of the modal behaviour of the ring may be attributed to Hoppe [70], its proposal as a tyre in-plane vibrations simulation tool was accomplished much later (1960's). Tielking [71], Dodge [72], and Clark [73] (all affiliated with Michigan University) presented ring model based studies simultaneously, while almost at the same

time, Böhm [69] verified the correlation between the vibrational characteristics (natural frequencies and mode shapes) of his ring model with the experimental data acquired by him and earlier by Chiesa *et al* [74]. The existing literature is rich in experimental validation studies of ring models, such as the studies presented by Potts *et al* [75], Zegelaar [76], Yam *et al* [77], Guan *et al* [78], Perisse and Hamet [79] and Geng *et al* [80].

Tielking in [71] introduced the inextensibility assumption, leading to the simplification of the ring equations of motion through the coupling of radial and tangential deformation along the ring circumference. Inextensibility is commonly introduced in low frequency range studies. Pacejka, in his contribution to the classic work of Clark [81], introduced the tangential sidewall stiffness in addition to the previously proposed pure radial one. Viscoelastic characteristics were attributed to the ring model by Padovan in [82], a study focused in the standing waves formation.

The analytical ring model remains even today the most established simulation tool of the in-plane tyre vibrational behaviour. This does not source solely from its excellent correlation with the experimental results, but is also related to the straightforward application on it of the modal expansion technique. The double axis symmetry of the ring entitles the expression of its structural mode shapes (the radial and tangential deformation patterns associated with each of the ring's natural frequencies) in an analytical way, using trigonometric functions. Although the response of the tyre is theoretically synthesized by infinite modes, the modal basis is practically reduced to a small number of modes, depending on the frequency range of the model. The structural response of the tyre is expressed by the linear combination of the mode shapes participating in the solution. The method (to be presented and analysed in detail in the following chapters) offers a significant advantage over the representation of the model in the space domain. Using the modal expansion approach the spatial discretisation of the structure is independent from the frequency range of the model, which can be decided upon the simulation aims of the study. Soedel in [83] offers a broad analysis of the method and its capabilities and limitations.

Although the ring model has been presented and used in various tyre simulation studies, the different mathematical expressions proposed for its equations of motion, which will be presented in chapter 3, are certainly confusing. To a great extent, this lack of consistency derives from the various ways in which the ring equations may be acquired as simplifications of the shell equations of motion. The classic work of Leissa [84] offers a detailed presentation of the different assumptions that may be used and the resulting equations of motion.

The ring model ,when proposed as a tyre simulation one, is imposed to the inflation or combined inflation and rotation induced pretensions, which alter its vibrational characteristics. In order such phenomena to be captured by the model, non-linear terms are introduced in the equations, as has been shown by Pacejka in [81], Padovan [82] and Potts [75]. Different approaches may be followed for the derivation of the non-linear terms, a case which is also captured by work of Leissa. Further discussion on the computational effects of the mathematical inconsistency of the ring equation of motions may be found in chapter 3.

The rotation effects

Before examining the application of the contact on the ring models, the theoretical rotation effects should be discussed. The centrifugal force imposes a pretension effect, resulting in a stiffer modal behaviour. Coriolis acceleration on the other hand is associated with more complicated modal effects. Bryan proposed first

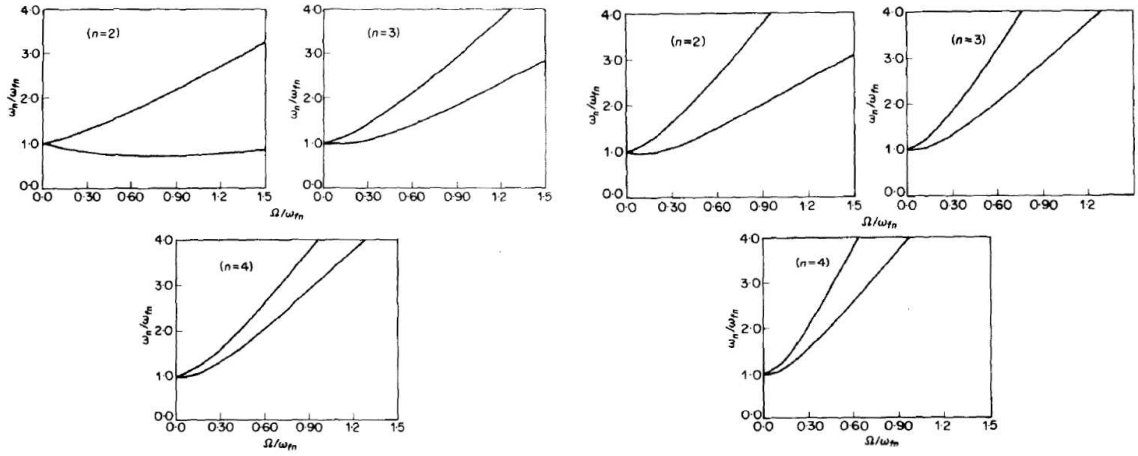

(a) Inextensional modes.

(b) Extensional modes.

Figure 2.19 – The bifurcation effect of the Coriolis acceleration on the inextensional and the extensional modes, as presented in [96]. Both the rotation speed (horizontal axis) and bifurcated natural frequencies (vertical axis) are given as ratios to the stationary natural frequencies for every mode (n).

the equations of the rotating ring in his classic work of investigation of the rotating wine glass [85]. Later, Carrier [86] and Johnson [87] presented improvements to the initial theory.

Coriolis acceleration results in a bifurcated modal behaviour of the structure, compared to the stationary one. Every double mode of the non rotating model is substituted by two rotating ones with the same modal number but with different to each other natural frequencies. These natural frequencies emerge as functions of the stationary ones and the angular velocity. Although, in general, the rotating ring frequencies increase with the velocity, the contrary behaviour may be initially observed in the low velocity range for low modal numbers, a behaviour which, though, depends on the applied modelling assumptions. The bifurcation behaviour of various models of rotating rings or cylindrical structures in general have been analytically derived by Padovan [88] (for prestressed structures), Endo *et al* [89] (in correlation with experimental results), Bickford and Reddy [90] (including shear deformation and rotary inertia), Saito and Endo[91] (for different kinds of cylinder boundary conditions), Lin and Soedel [92] (comparison between thick and thin ring assumptions) and Natsiavas [93] (the effect of the rotation velocity magnitude). The rotational effects on the out of plane modal behaviour of ring structures have been presented by Eley *et al* [94] and Kim and Chung [95].

Focusing in the ring rotation effects from a tyre modelling point of view, their implementation in respective tyre models has been presented by Padovan [97] and Potts [75]. Huang and Soedel [96] presented the centrifugal and Coriolis effects on a ring tyre model (fig. 2.19). The case of a stationary point load applied on a rotating ring was compared to the inverse problem of a rotating excitation on a standing ring. The two responses were found to be in good agreement, for low rotation speed. As the excitation frequency of the rotating excitation, though, approaches the natural frequencies of the stationary model (condition commonly referred as critical speed for the lowest rotation velocity - mode combination) the two cases predict significantly different responses. It should be mentioned that according to their analysis, the rotating ring shows no critical speed, as both pretension and Coriolis acceleration (for high rotation velocities) result in the increase of the natural frequencies with the angular velocity. In the same study it was also concluded that the Coriolis effect is stronger than the pretension one for common tyre rotation conditions and model's

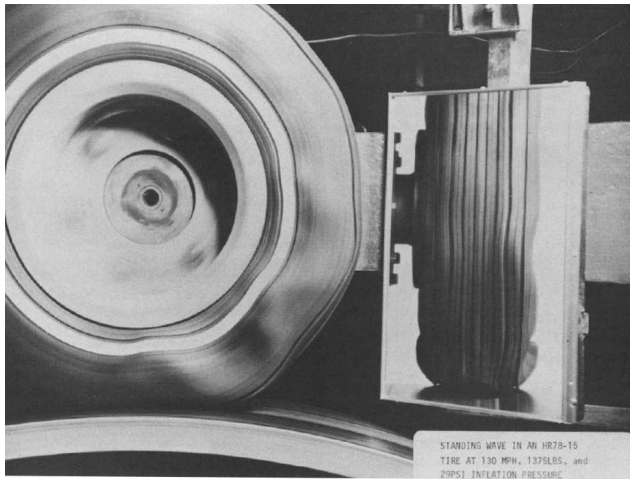

Figure 2.20 – The formation of the tyre standing wave, after [102]

properties. The study was extended by the same authors in [98], where the pretension effect of the inflation pressure was also included and the general response to harmonic and periodic load cases was examined. The coupling of a rotating tyre model with a wheel and a suspension system was latter accomplished by Huang and Hsu [99]. Wei *et al* [100] applied a method initially proposed by Meirovitch [101] for the capture of the transient response of a rotating ring model under a point concentrated excitation.

Typically, the study of the rotation effects has been associated with the prediction of the possible structural instabilities, given that such a condition may be imposed by the contact boundary conditions of a fast rotating tyre. Under the non rotating assumption, where contact rolling is simulated by a rotating excitation on a stationary structure, instability is commonly associated with the critical speed and the standing wave formation, as it may be observed by a stationary observer (fig. 2.20). This approach (stationary tyre - rotating excitation) was followed by Tielking [71] and later by Soedel [103], although the latter study assumed a thin shell model, instead of the ring one. When, though, the rotation effects are incorporated into the structural models, the examination of the possible instability occurrence is not easy, as the natural frequencies are derived by non-linear, different for every mode, functions of the rotation velocity (fig. 2.19). The existence or not of a critical speed and a resulting instability behaviour for a rotating ring model has been for long a topic of contradicting theoretical simulation results. In most cases, such results could not be experimentally verified, as the coexistence of the viscoelastic damping mechanism practically suspends the unstable behaviour.

Padovan [88] using a rotating prestressed cylinder model predicted the existence of a critical speed and an unstable behaviour. Extending this approach, he added the viscoelastic effects on a standing wave formation study [82]. Endo *et al* [89] proposed a different set of equations of motion to theoretically support their experimentally gained conclusions that no instability was identified in the behaviour of a rotating ring. Bickford and Ready [90] supported the above conclusion in their theoretical study. Lin and Soedel [92], though, showed that rotation may cause the extensional ring modes to be associated with lower frequencies than flexural ones and that the non-prediction of instability by the previous researchers was a result of incomplete inclusion of the rotation in the equations of motion. The theoretical prediction or not of the rotation induced instability depends on the followed modelling approach, as has been discussed by Kim and

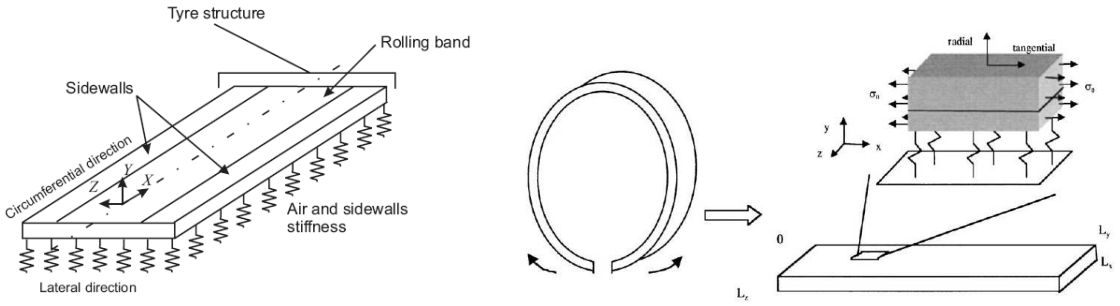

(a) The model proposed by Kropp, after [108].

(b) The evolution of the Kropp model to a two layers structure, after [109].

Figure 2.21 – The plate models developed by Kropp and Larsson.

Chung in [95]. Focusing in the usual tyre modelling ring models and properties, the instability case was investigated by Huang and Soedel in [96] and a non existence of a critical speed was predicted. The coupling, though, of the tyre model with a suspended wheel [99] introduces the possibility of an unstable behaviour, although in rotation velocities out of the range of interest for automotive applications. Doorman [104] presented an instability analysis on a similar system, expressing the equations of motion in a non-rotating system of axis. A comprehensive presentation of the rotation phenomena implementation in a modal model has been included in the work of Soedel [83].

Other modal models and their NVH simulation potential

The simulation of the tyre vibrational behaviour is not accomplished purely by ring based models. Other two-dimensional and three-dimensional models have been proposed for the capture of the tyre deformation. A three-dimensional, thin shell model, for example, was proposed by Soedel in [103] for the study of the standing wave phenomena of a rolling tyre and a toroidal membrane model was described by Saigal *et al* in [105].

As the interest of the studies moves from the vibrations related, low frequency range, towards the noise related, high frequency one, the effects of the circularity and the inflation pretension on the modal behaviour fade and the bending mechanism of the belt becomes the dominant factor. Accordingly, a two-dimensional plane plate is the common modelling approach in the frequency range above the one associated with the ring behaviour. The model properties that affect the modal behaviour in each frequency range has been discussed by Perisse *et al* [106] and by Muggleton *et al* [107]. The ring and plate models were compared with experimentally gained modal data by Perisse and Hamet [79]. Better frequency correlation was exhibited by the ring model in the low frequency range and by the plate model in the higher one.

Kropp in [110] proposed an orthotropic, pretensioned, planar plate model for the simulation of high frequency tyre modal behaviour, including both the circumferential belt and the sidewalls (fig. 2.21(a)). Later the model was further developed by Larsson and Kropp [109] and a tread representing, plate layer (fig. 2.21(b)) was added.This approach was used by Dinkova and Kropp [111] for the simulation of the modal behaviour of a truck tyre. In the plate model proposed by Muggleton *et al* [107] the vertical to each other tread and sidewall plates are connected by a stiffness foundation fig. 2.22. Pinnington and Briscoe [112]

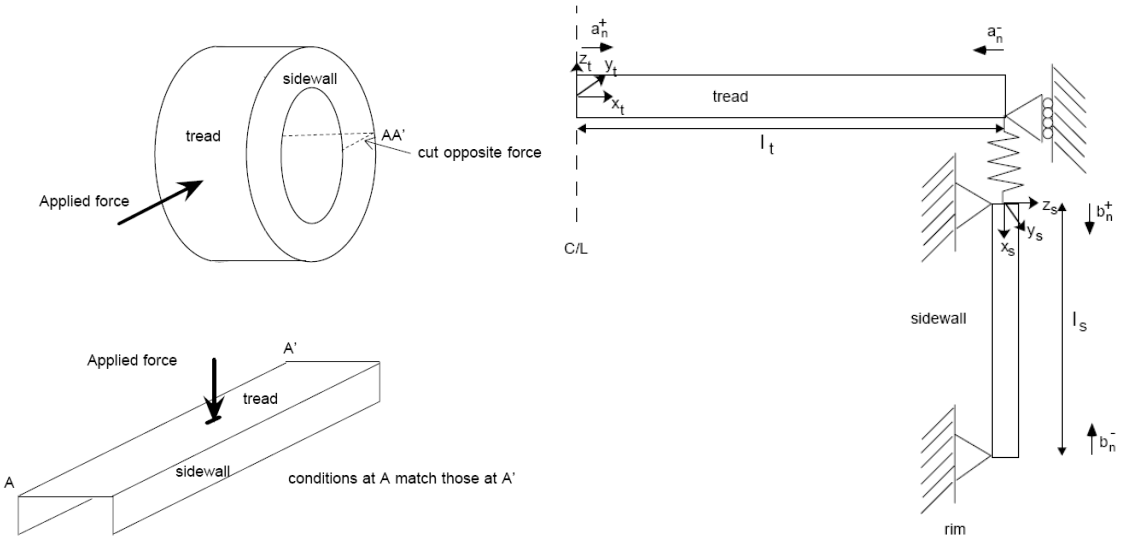

(a) Overview.

(b) Representation of a section.

Figure 2.22 – The plate model proposed by Muggleton, after [107].

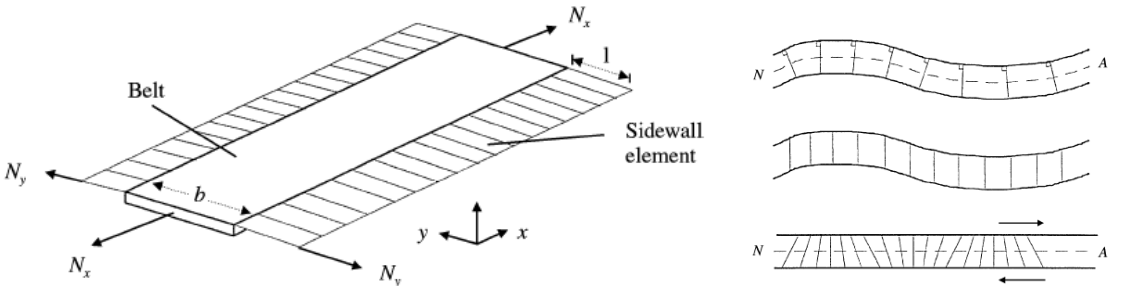

(a) The model used for the derivation of the wave equation.

(b) The bending, shear and rotational belt waves.

Figure 2.23 – The wave model of Pinnington and Briscoe, after [112].

proposed the modelling of the tyre vibrational behaviour using waves propagating along the belt, which was modelled, together with the sidewall, as a plane plate (fig. 2.23). In the latest development of this approach [113, 114] the geometrical effect of the belt and the sidewall curvatures is also included in the equations used for the wave derivation.

Moving the discussion from the analytically expressed models to the discretised ones, it should be mentioned that the modal expansion and reduction techniques can be also applied to such models, decoupling the space discretisation from the modal range of the model. In general, the discretised models which are used for the capture of the tyre modal behaviour are different from the high number of degrees of freedom models that are used for the detailed representation of the response of the structure to contact induced excitation, that will be later presented. The discretised modal models represent basic geometrical and material characteristics that affect the tyre modal behaviour. In respect, the necessary, for the accurate capture of the vibrational characteristics, number of elements is much lower than the number of elements required to represent the contact behaviour of the model.

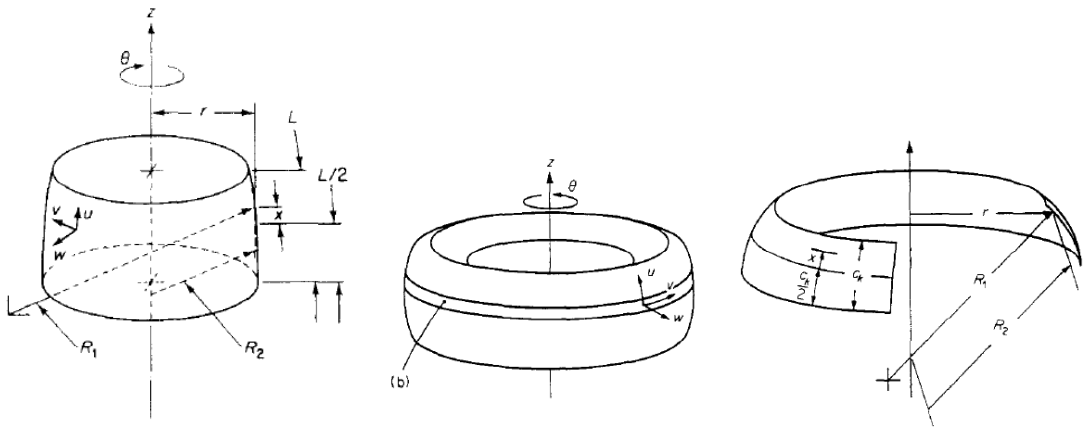

(a) The curved finite element developed by Chang *et al*, after [115].

(b) The tyre as a doubly curved thin shell, after [116].

Figure 2.24 – The finite element used by Chang *et al* for the simulation of the tyre modal behaviour and the representation of the tyre as doubly curved thin shell of revolution.

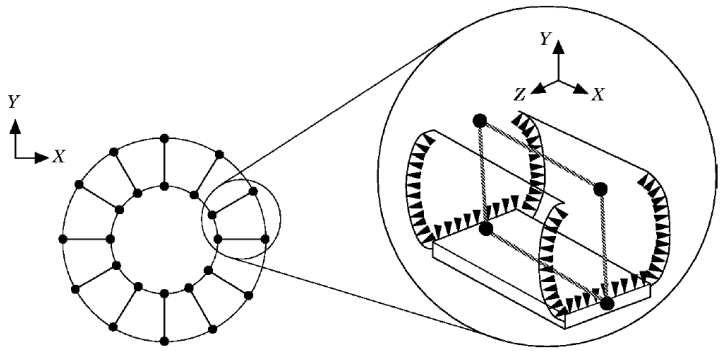

Figure 2.25 – The discretised modal model proposed by Mousseau and Hulber, after [117].

Chang *et al* [115] used a thin, doubly-curved, axisymmetric, shell element for the tyre belt representation (fig. 2.24). The derived model was modally expanded for the calculation of the dynamic behaviour of a radial tyre, under a traveling sinusoidal point excitation. The modal prediction of the model was correlated with a respective ring one in [116], where also both of them were used for the study of the transition from the modal behaviour of a tyre mounted to a fixed wheel to the one of a tyre mounted to a free wheel. Mousseau and Hulbert [117] presented a discretised modelling approach, assigning membrane under tension properties to the sidewall and a beam-bending behaviour to the belt (fig. 2.25).

The contact implementation in the NVH models

The tyre modal behaviour acquired by the theoretical models and validated by experimental work was used in numerous studies for the investigation of rolling contact related vibrational phenomena, such as the above described standing wave formation [103, 97]. The road contact though, apart from a dynamic excitation, also imposes a boundary (non penetration) condition and, as such, alters the modal characteristics of the tyre. Soedel and Prasad in [118], proposed a theoretical method for the prediction of the tyre modal behaviour

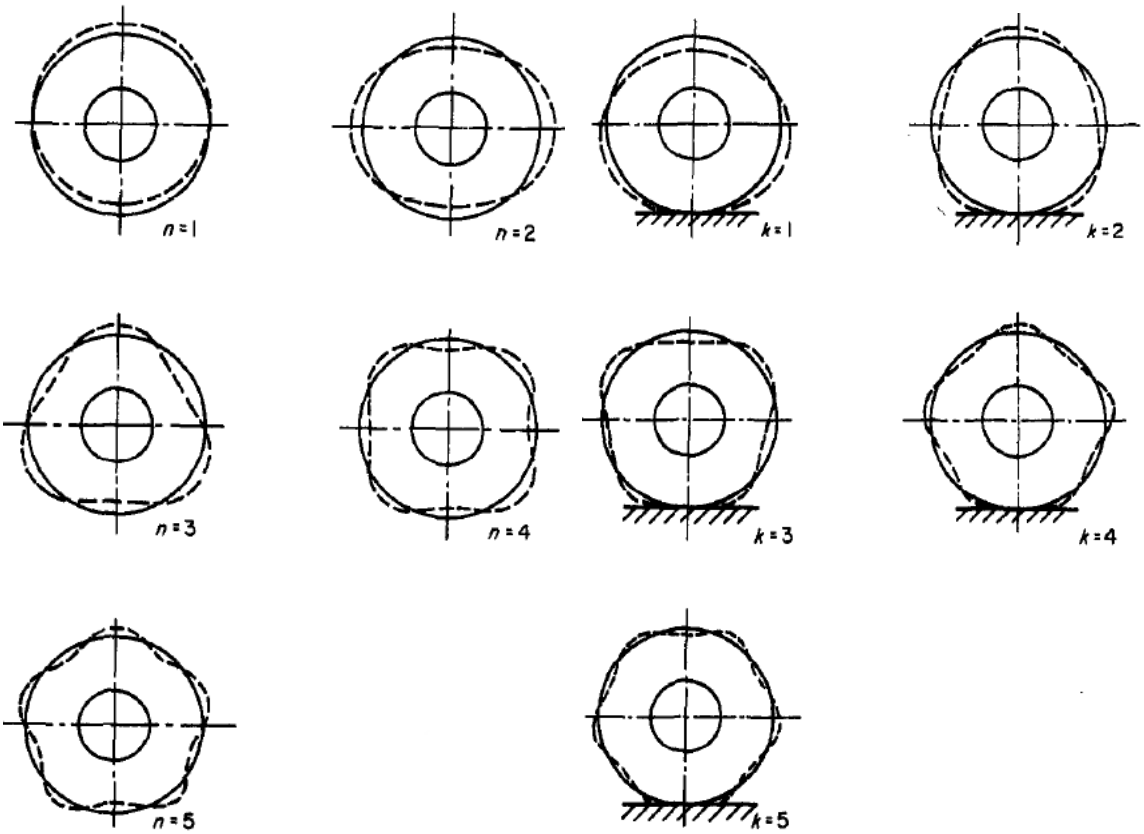

(a) The non-contact mode shapes.

(b) The contact mode shapes.

Figure 2.26 – The non-contact mode shapes and their transformation under contact conditions, under [118].

under point contact boundary conditions, based on the non-contact one, as acquired by any theoretical or experimental method. A bifurcation-like splitting of the modes was predicted, induced by their orientation fixation according to the position of the contact along the circumference. Applying a similar method, Huang [119] and Huang and Su [120] calculated the modal characteristics of a rotating, pretensioned, ring tyre model, under point, vertical and vertical/tangential respectively, contact boundary conditions.

Kung *et al* dropped the single contact point assumption in their study of the effect of the tread pattern on the tyre modal response [121]. The point excitation was firstly upgraded to a line one, characteristically modelled as an knife edge along the axial dimension, and later to a series of edges along the tyre circumferential direction, corresponding to contact area of finite dimensions(fig. 2.27). The study took also into consideration the contact pressure distribution along and across the contact area for the calculation of the excitation force at every point. The important step towards the combined shear forces and structural response simulation was the adoption of the contact stiffness foundation concept. The contact in not realised any more by road adherence boundary conditions but a discretised stiffness foundation is introduced between the belt and the road, in a way similar to the respective steady state tread modelling approach (presented in section 2.1.3). Furthermore, and in contrast to the steady state application of the concept, the foundation may now extend to two dimensions, enabling the physical and transient derivation of the contact pressure

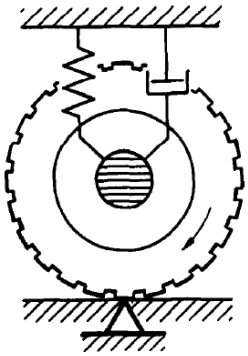

(a) Single point excitation.

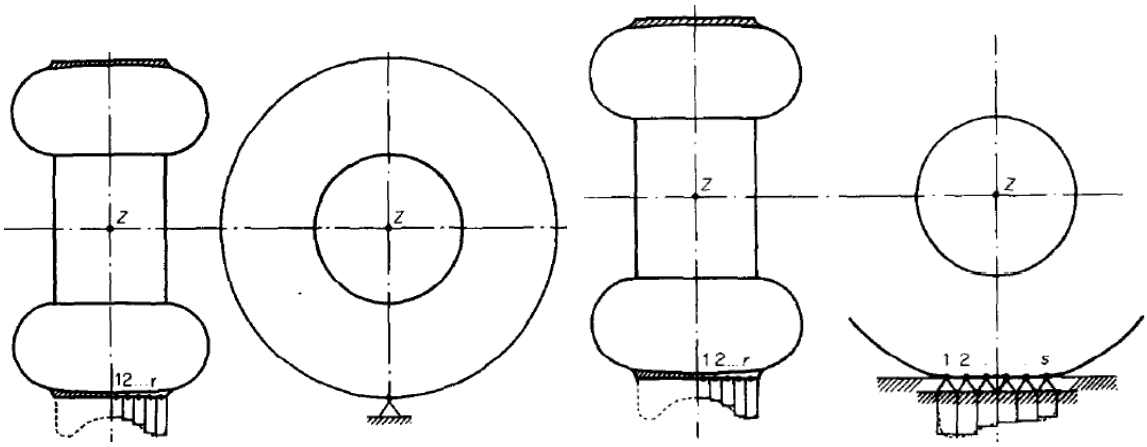

(b) Multi point, single knife edge excitation.

(c) Multi point, multi knife edge excitation.

Figure 2.27 – Visualization of the knife edges concept introduced by Kung *et al* for the study of the tread patten induced excitation, after [121].

distribution.

Zegelaar in [76] used a two-dimensional stiffness foundation for the study of the contact modal characteristics of a ring model, while a similar model was proposed by Zegelaar and Pacejka [61] for the study of the frictionless rolling of a tyre over a cleat. A similar approach was followed by Kim and Savkoor [122] for the study of frictional steady state rolling of a tyre on a plane road surface. Rustighi and Elliot [123], presented a ring model study where the dynamic road excitation was calculated as a function of the surface roughness and the rolling velocity. The model was extended to a three-dimensional one by Rustighi *et al* in [124], where the analytical ring model was substituted by a respective finite element formulation. The contact stiffness concept has been also combined with plate models for the simulation of the high frequency contact dynamics. The tangential road interaction and friction phenomena are neglected in this high frequency category of contact models. Such studies, focused in the tyre noise generation, have been presented by Kropp [110], by Larsson and Kropp [109] and by Andersson and Kropp [125]. An enhanced advanced approach was proposed by Wullens and Kropp in [108], where the belt plate model was coupled to a tread representing one. The contact behaviour of the latter plate was modelled using an elastic half-space, under a uniform normal pressure, in contact with the rough road surface. Lopez *et al* [126] presented a vibration

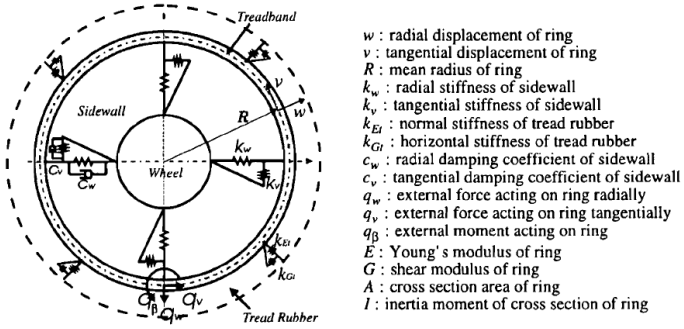

(a) The model and its properties, after [122].

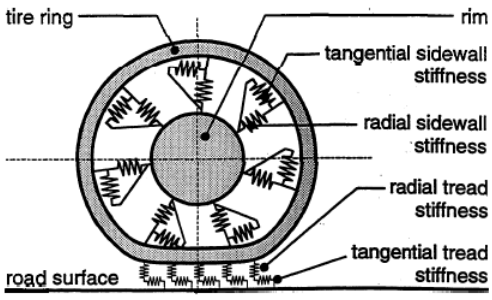

(b) The model under road contact deformation, after [76].

Figure 2.28 – The combination of the ring on elastic foundation belt model with the contact stiffness foundation.

model where the effect of the structural non linearity, exposed by the contact deformation, is also captured by the modal model, which is then excited by the road roughness.

From the modal models to the complete tyre behaviour modelling: Challenges and difficulties

Summarising the above discussion on the modelling of the tyre vibrational behaviour, it may be concluded that the structural modal characteristics and the effects of contact and rotation on them may be captured by various models. The arising question, though, is why given the computational efficiency of the above modal representations, such models have not been further developed to include the simulation of the shear force generation. The answer to this question may be given through the analysis of the additional modelling challenges associated with the physical shear force calculation.

In contrast to the vertical contact reaction, the transient shear force generation cannot be directly transformed into a modal excitation problem. The friction is a non linear force, the value of which does not depend only on the structural response of the belt but also on the shear motion (slip) characteristics. These characteristics change radically over time and the transient shear force generation can only be acquired in the time domain of calculation as opposed to the frequency one. The computational advantage of the belt behaviour representation in the modal (frequency) domain is lost, as the solution has to be acquired through a numerical simulation process over time. The case is further discussed by Wullens and Kropp in [108], where a mixed modal-time simulation method is also proposed.

Using a model based on a modal representation for the combined tyre simulation, the vertical pressure distribution (a necessary input for the friction model) is derived by the contact induced structural deformation. Although the modal basis necessary to capture this structural response under pseudo-static contact equilibrium conditions can be easily identified the derivation of a similar modal basis under transient contact conditions is difficult. The varying contact area dimensions and belt deformation continuously change the vertical contact pressure distribution, together with the necessary breadth of the modal basis which is able to capture these physical changes. An obvious answer would be that an extended modal basis, including higher modes, would definitely increase the accuracy of the model. Given though that such a modal basis extension certainly increases the computational load of the model, the appropriate modal basis breadth cannot be easily derived.

Continuing on the above, the frequency range of the tread-road interaction mechanism, must be identified in order the belt modal basis to be accordingly expanded or reduced. The frictional contact of the tyre, though, imposes a very wide frequency range of excitation. The road roughness and profile irregularities, the stick-slip shear motion of the tread and the friction force non linearity theoretically correspond to step excitation patterns and in order to be captured by a modal domain model an infinite frequency breadth is theoretically necessary. In reality, though, the range of the excited belt modes is not exactly the same with the theoretical frequency range of the excitation. The energy dissipation, induced by the various damping mechanisms of the tyre, deduces the actual number of modes participating in the belt response and the associated frequency range. The tyre damping mechanisms are related to the viscoelastic properties of the tyre, which are present in both the belt and the tread structures. Whether the response corresponding to a certain modal excitation will be present in the total tyre response or not, depends on the damping coefficient of that mode. The tyre viscoelastic mechanisms, on the other hand, are difficult to be identified and accurately modelled as they depend on a number of factors that cannot be practically included in the model, such as the thermal behaviour. For the above reasons, the uncertainty associated with the modal range able to represent the interaction between the frictional and structural tyre phenomena is the main reason that suspends the application of the modal models on the combined simulation approaches.

Another factor which is believed to suspend the use of the modal based models for the shear force generation modelling is the actual nature of the contact deformation. Although contact takes place in a small portion of the tyre's circumference, the respective radial deformation in this area is high. Moreover, the physical mechanism which controls this deformation is a non linear one, due to the sidewall buckling behaviour. If a linear sidewall stiffness is assumed for the contact behaviour of the tyre, the contact pressure overestimation severely deduces the accuracy of the acquired results. Characteristically, Miege and Popov in [127] predict a 44% higher contact stiffness value than the experimental one, under a linear sidewall approach. It is evident that the resulting contact pressure distribution cannot be used for the accurate simulation of the shear force generation. Böhm, in his original study [69], presented the sidewall geometry effect on the sidewall stiffness, as did Zegelaar and Pacejka in [61] and Pinnington in [128]. In all these studies, a membrane mechanism is used for the capture of the sidewall behaviour. Such a mechanism, though, may only be incorporated in a space domain calculation, since it requires the derivation of the belt deformed dimensions. Accordingly, the simulation of the tyre's contact behaviour cannot be accomplished solely in the modal domain and a intermediate step of sidewall behaviour calculation in the space domain is necessary.

An apparent solution to the above problem would be the use of the in-contact modal data for the belt representation instead of the ones corresponding to an undeformed condition. The procedure may be based on either experimental or theoretical modal data (as described in section 2.1.6). The contact, in this case, is not treated as an external excitation to the model, as its effect has already been incorporated in the modal expression of it. If steady or within a certain range contact deformation or boundary conditions are applied, this method significantly improves the accuracy of the predicted response to other excitation inputs (torque, road irregularities). If, though, the contact deformation and the contact area are to be predicted by the model, or a broad range of operating conditions are to be applied to it, such an approach cannot be used. Obviously, the transient simulation potential of the model is deduced when the contact boundary conditions are not calculated as part of the total response of the system but are a priori induced to the model. Especially in case where the variations of the contact conditions are believed to play an important role in

the development of the transient phenomena (e.g. shuffle effects, coupling of the tyre and the suspension dynamics) the computational expensive method of the on-the-run calculation (in the space domain) of the contact variations is the only valid approach. The above discussion could similarly cover the incorporation of the rotation effects on the modal characteristics. Although the effects of the rotation under constant angular velocity may be easily incorporated into a modal model (see section 2.1.6), when this model is to used for the response calculation across a range of angular velocity values, the modal expansion should be either repeated or a computational error should be accepted. On the other hand, the rotation effects are embedded in the space domain expression of the equations of motion and accordingly, a varying angular velocity value may be accounted for without any further computational requirement [129].

It is clear from the above discussion that the evolution of a tyre structural models into combined vibrational and shear force generation one is not a straight forward task. Characteristically, even when such a physical modelling approach is chosen for the belt deformation, an indirect link with the shear force generation mechanism is chosen. The second member of the CDTire family [68], the CDTire 30 (fig. 2.17), consists of a flexible ring on a viscoelastic sidewall foundation to which a brush model shear force model is coupled. Kim *et al* [130] proposed a three-dimensional model that is based on a modally expressed belt model and a discretised two-dimensional contact stiffness foundation. The approach, though, uses a pseudo-transient contact interaction algorithm which reduces the modal content of the interaction to a shape conformation corresponding one.

A slightly different, modal based, approach for the modelling of the tyre transient behaviour was proposed by Guan *et al* in [131]. Instead of using the experimentally gained modal data for the identification of the physical properties of a model, these data (natural frequencies and mode shapes) were directly used for the construction of the modal basis. This method was used in [132] for the modelling of the tyre vertical properties, while in [133] a detailed analysis on the frictional contact interaction with the road, including the enveloping behaviour, was presented. The model was developed further in [134] by the addition of a non linear sidewall foundation. A similar approach was used by Guan *et al* [135] and by Shang *et al* [136] for the simulation of the transient cornering behaviour of the tyre. This method, which is summarised by Guan *et al* in [67], overcomes the dilemma of the appropriate belt structural model, but at the same time its accuracy is directly dependent on the breadth of the experimental range. In many cases, as it will be discussed in chapter 4, the experimentally observed frequency range is not broad enough to capture the contact area phenomena which affect the tyre-road shear interaction.

Although the coupled modelling of the, expressed in the modal domain, transient behaviour of the tyre with the shear force generation has not flourished, a different approach to the same problem has started to develop rapidly. The increasing level of the broadly available computational power has enabled the generation of models based on the space domain discretisation and calculation of the belt and its combination with a similarly discretised tread foundation. Although such discretised approaches are not a new idea (similar models have been proposed in [137, 138, 139]), only lately has the available computational power been sufficient for the adoption by them of a high enough level of discretisation that may lead to the accurate shear force prediction. Such models will be presented in the following section.

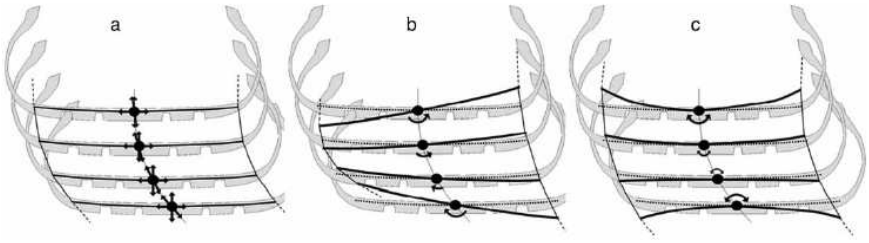

(a) The degrees of freedom of the belt nodes.

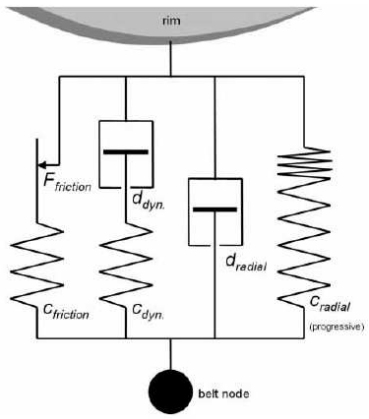

(b) The radial sidewall foundation.

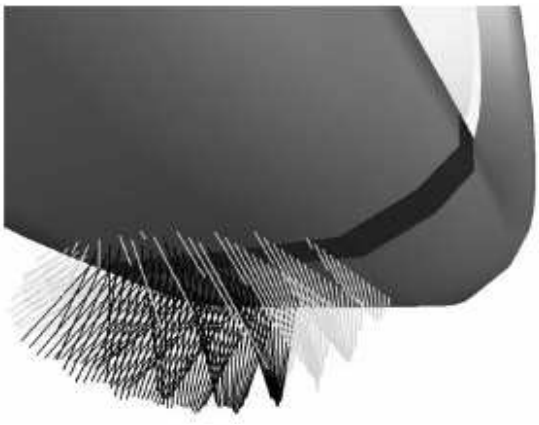

(c) The calculated contact pressure distribution during a parking manoeuvre.

Figure 2.29 – Some basic characteristics of the FTire model, after [140].

The discretised models

Theoretically, the accuracy of such models depends on the conformation of their modelling approach to the actual tyre physical mechanisms and their degree of discretisation. The space-time domain calculation is theoretically able to capture and represent various aspects of the tyre transient behaviour, including the changing dimensions of the contact area, the response to road profile irregularities, the effect of drivetrain and torque variations and the physical coupling with the vehicle dynamics behaviour through the wheel and the suspension.

A discretised, three-dimensional, tyre modelling approach, able to capture both the tyre structural behaviour and the contact area frictional phenomena, was developed by Mavros in [129]. The belt model was composed by discrete nodes, to which three-dimensional degrees of freedom were attached, and stiffness elements modelled their interaction. The contact was realised by viscoelastic elements, attached to the belt nodes. Although the model was able to capture the pressure distribution development, a data fitting process of a parabolic pressure model was preferred, so that the distribution accuracy did not directly depend on the degree of discretisation. A similar approach is followed by the third member of the CDTire family [68], the CDTire 40, which is based on a discretised, three-dimensional, flexible shell structure, combined with a brush type contact (fig. 2.17).

An advanced, three-dimensional, discretised tyre model which is proposed for both ride and shear force studies is the FTire (fig. 2.29), presented in [140, 141]. Three translational degrees of freedom are assigned

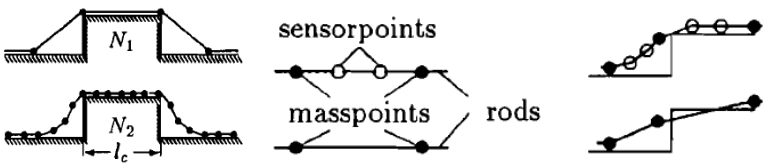

(a) The effect of the degree of discretisation on the prediction of deformation of a tyre running over a road irregularity.

(b) The scattering of the massless sensor points into the discretised structure.

Figure 2.30 – The discretisation effect on the deformation accuracy and the concept of the scattered sensor points, after [142].

to each of the belt nodes while both torsional and bending compliance around the circumferential axis are accounted for (fig. 2.29(a)). The nodes are connected to the wheel through a viscoelastic foundation, the radial part of which is presented in 2.29(b). Contact is realized through a discretised non-linear stiffness and damping foundation in radial , tangential and lateral direction. The degree of tread discretisation is higher than the belt one, as typically 10–100 tread bristles correspond to each belt node. The contact pressure distribution is calculated by the model and fed to the tread friction law, which is able to simulate stick-slip phenomena. Simplified thermal and tread-wear sub-models may be incorporated to the model. The proposed frequency range of application of the model extends to $\sim 150Hz$.

A obvious consequence of the space discretised physical modelling approach is that the level of discretisation is directly related to the frequency range of the model. As a high degree of discretisation is necessary for the capture of the contact area phenomena, the associated broad frequency range makes the numerical simulation computationally heavier as higher order dynamics are involved. The computational load increases radically not only because of the higher frequency of the modes (resulting in smaller calculation time steps) but also because of their stiffer behaviour, induced by the damping mechanism. The effect of the damping mechanism and distribution on the modes' stiffness behaviour is analysed in chapter 3. Here, it should be mentioned that although damping finally deduces the participation of the high frequency modes in the response, their effect on the computational process and the associated load remains present. This issue has been treated by Oertel in [142], where a method for the decoupling of the space discretisation from the modal range of the model is proposed. Firstly, the sufficient degree of discretisation for the accurate prediction of the tyre response to short wavelength road unevenness is investigated. Secondly, a network of massless nodes is introduced into the discretised belt structure, scattered into the mesh of the inertia-equipped nodes. The massless nodes do not introduce additional differential equations, as their state is expressed by pure algebraic ones. The order of the system is not increased by the existence of the additional network of the "sensor" points, although the deformation of them can be calculated. The high degree of space discretisation enables the prediction of the transient contact pressure distribution and the resulting shear forces. The modal behaviour of the structure, though, is captured by the layer of the inertia equipped nodes, which shows a significantly coarser discretisation. The above idea of the sensor nodes network has been developed into a commercial simulation software, named RMOD-K, presented in its various development stages in [142, 143, 144].

Apparently, the next step in the development of the discretised models is related to the application of

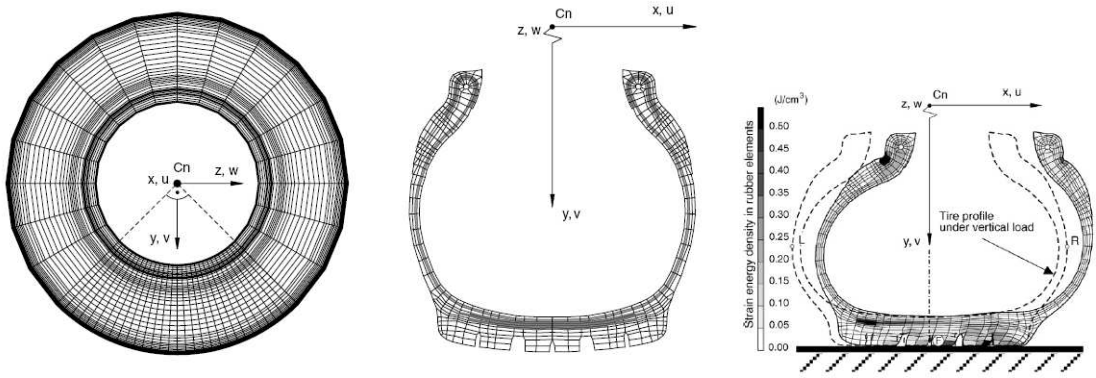

(a) The model discretisation.

(b) The road contact deformation.

Figure 2.31 – A typical FEM tyre model and the contact induced deformation, after [145].

pure Finite Element Method (FEM) on the shear force calculation. Although similar studies already exist, the approach cannot yet be proposed as a tyre simulation one, given that the associated computational load restricts its application to the study of specific contact interaction phenomena. As the available computational resources increase, such models may be proposed not only as structural studies of the tyre deformation, but as complete tyre models, able to simulate the tyre behaviour for a time period, which is sufficiently long in order such a model to be coupled with a transient vehicle dynamics one.

It should be mentioned that if the space discretisation level exceeds a certain limit, the tyre-road interaction cannot be modelled any more as an interaction between two smooth surfaces. The tread pattern effects, the local stiffness behaviour of the tread viscoelastic materials and the road roughness must be taken into consideration and their effect on the shear force generation has to be modelled (see section 2.2.3). The mathematical modelling of such concepts of the tyre behaviour is a sector of intensive scientific research, as the physical mechanisms that control the viscoelastic materials behaviour and their contact with rough surfaces haven't been interpreted yet. A brief summary of the current level of understanding of these mechanisms, together with their historical evolution from a contact mechanics point of view, is attributed in section 2.2. The lack of established and experimentally verified modelling methods of such mechanisms impose a barrier to the transformation of FEM models into physical tyre simulation tools, which is probably more difficult to overcome than their computational load and requirements.

In the early discretised approaches, a substantial effort was put in the incorporation of the physical effects of the structural shape on the tyre behaviour, with the minimum number of required elements. The already mentioned approach of Chang *et al* [115], or the ones of Noor *et al* [146] and Danielson *et al* [139] are characteristic examples. As the available computational power was increasing, the studies focused in the modelling of the anisotropy and the detailed contact behaviour. A computational effective method for the synthesis of such an element, incorporating the structural anisotropy and non-homogeneity of the tyre, was proposed by Burke and Olatunbosun in [147]. Moreover, a number of FEM models has been proposed for the study of particular aspects of the tyre contact behaviour, such as the localised deformation prediction [148], the wear mechanism [149], the structural strength of the belt [150] and the interaction with deformable surfaces [151, 152]. Such studies use commercially available finite element software packages which offer elements able to represent the distinctive viscoelastic behaviour of the typical materials used for the tyre

construction (e.g. the hyperelastic element of the NASTRAN/PATRAN commercial FEM software).

A FEM model constructed by hyperelastic elements was proposed by Pelc [145] (fig. 2.31) for the study of the in-contact tyre deformation caused by three-dimensional static loading conditions, while a survey of similar approaches may be found in [153]. FEM based models able to simulate the transient shear force generation have been proposed by Kabe and Koishi [154], and by Chae *et al* [155, 156]. As the degree of discretisation increases, FEM tyre algorithms are focused in the local frictional interaction between the tread blocks and the road surface, in an attempt to associate the tyre frictional characteristics with the actual tread pattern and the local viscoelastic deformation. Such a finite element modelling approach, which associated the tread pattern design with a stiffness matrix, has been presented by Braghin *et al* [157]. The model is used to predict both the vertical contact reactions and the local shear forces. A dynamic, viscoelastic, contact model of a tread block, based on finite element discretisation, was also presented by Liu *et al* in [158]. Nakajima in [159] presented a simulation study of tyre traction on various road surfaces, based on the finite element method predicted deformation of the tread blocks. A discussion on the current level of understanding of the tread pattern effect on the macroscopically observed and experimentally measured tyre behaviour is presented by Mundl *et al* in [160].

Identification of parameters and experimental fine tuning of the models

A summary of the various tyre modelling approaches which were presented in the previous sections is attributed in table 2.1, following an order defined by their complexity and modelling potential. Obviously the number of tyre models is so high that an excessive overlap in regards to their uses and applications is generated. This overlap makes the question of which model should be preferred, for a certain simulation task or virtual testing project, difficult to be answered. The confusion is intensified by the different sets of parameters that have to be identified (according to different experimental procedure) for the use of each model. Moreover, every tyre model needs a specific procedure in order to be incorporated in an on-purpose developed or commercially available vehicle dynamics simulation software.

An attempt to overcome the above issues was made introducing a standard virtual test procedure [161]. Although this concept does not offer a solution to the different parameters' identification method required by each model, it may offer directions on the simulation capabilities and computational efficiency of certain combinations of tyre models with vehicle dynamics ones. The standardized virtual testing concept has been provoked by the TMPT research group ([162]), located in the Technical University of Vienna, composed by representatives from both the academia and the tyre/automotive industry. Combinations of simulation packages and tyre models (based on experimental results offered by the tyre industries) are tested according to standard simulation procedures. The acquired results may be directly compared, offering the special characteristics, the advantages and the shortcomings of each combination. The accomplished work and the further aims of the group are described in [163].

It can be concluded from the above sections that none of the described models may be regarded as a pure physical one as all of them incorporate an empirical process: actual tyre measurements or other experiments are necessary for the identification of their parameters. The procedure compensates for the physical mechanisms that were neglected or simplified by the model's concept and consequently the process varies from model to model. The successful parameters' identification is vital for the acquisition of accurate simulation results and a possible non correlation between them and the experimental data usually originates from a

Empirical models	- Sitchin [5] - **Magic Formula** (Pacejka *et al*) [1,9,10]
Empirical models with physical enhancements	- Based on the **Magic Formula concept**: Sharp & Betella [11], Sharp [12], Arosio [14]
Steady state physical models	- Based on the **brush concept**: Pacejka [1], Sharp & El Nashar [21], Gim & Nikavresh [22,23,24], Salaani [26], Sornioti & Velardocchia [27], Sharp [29], Pauwelussen [30]
Simplified transient shear force models	- **Relaxation length concept**: Pacejka [1], Clover & Bernard [31] - **Magic Formula-single point contact**: Pacejka & Besselink [17] **Magic Formula-string model**: Higuchi & Pacejka [16] - **TM Easy** (Rill) [33,34] - **Multi-spoke based models**: Gim *et al.* [32], Zhou *et al* [50] - **Lu Gre models** [39,40,41,42,43] - **PAC2002** [47] - **Brush-string model**: Pacejka [1,49] - **Brush-string model-inertia properties**: Pacejka [49] - **Bending beam model**: Mastinu & Fainello [51], Mastinu *et al* [52]
Simplified vibration models	- **Stiffness-Viscous elements concept**: Dunn[54], Dunn & Olatunbosun [55] - **BAT model** (Kao) [53]
Circular vibration models	- **Flexible ring concept**: Tielking[71], Dodge [72], Clark [73], Böhm [69], Chiesa *et al* [74], Potts [75], Zegelaar [76], Yam *et al* [77], Guan [78], Perisse & Hamet [79], Geng *et al* [80], Clark [81], Padovan [82], Soedel [83] - **Thin shell model**: Soedel [103], Chang *et al* [115] - **Toroidal membrane model**: Saigal *et al* [105] - **Plate model**: Kropp [110], Muggleton *et al* [107], Pinnington & Briscoe [112,113,114] - **Bending beam-membrane sidewall model**: Mousseau & Hulbert [117] - **Vibration models under contact conditions**: Soedel & Prasad [118], Huang [119], Huang & Su [120], Kung *et al* [121], Zegelaar [76], Rustighi & Elliot [123], Larsson & Kropp [109], Dinkova & Kropp [110], Andersson & Kropp [125], Lopez *et al* [126], Wullens & Kropp [108] - **Vibration models under rotation conditions**: Padovan [97], Huang & Soedel [96,98], Huang & Hsu [99], Wei *et al* [100], Soedel [83]
Physical transient shear force models	- **Rigid ring concept**: Zagt [57], Zegelaar [58], Maurice [59,63], Zegelaar *et al* [60], Zegelaar & Pacejka [61], **TNO-MF SWIFT** [1,65], **UniTire** [66,67], **CD Tire 20** [68] - **Flexible ring concept**: Zegelaar *et at* [60], Zegelaar & Pacejka [61], Kim & Savkoor [122], **CDTire 30** [68] - **models with direct modal belt representation**: Kim [130], Guan [131,132,133], Shang *et al* [136] - **Discretised models**: Padovan & Paramadilok [137], Faria *et al* [138], Danielson *et al* [139], Mavros [129], **CDTire 40** [68], **FTire** (Gipser) [140,141], **RMOD-K** [142,143,144]
FEA based models	Bozdog & Olson [148], Cho & Jung [149], Kabe *et al* [150], Oida *et al* [151], Shoop *et al* [152], Kabe & Koishi [154], Cae *et al* [155,156], Braghin *et al* [157], Liu *et al* [158], Nakajima [159], Mundl [160]

Table 2.1 – A summary of the basic tyre simulation approaches and some representative models.

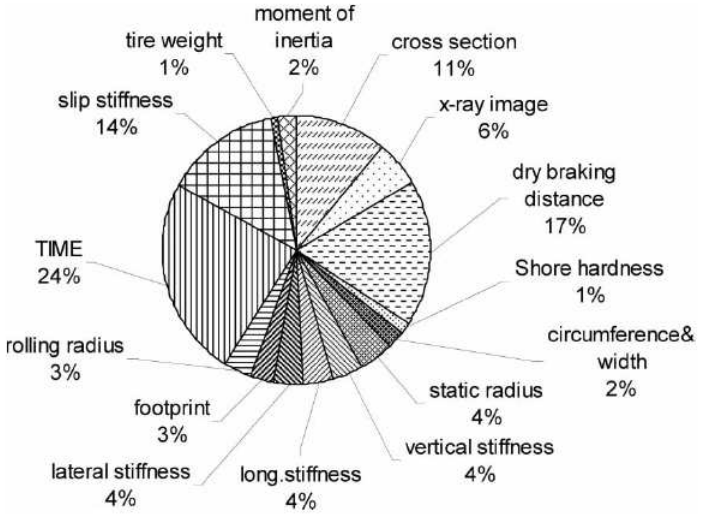

Figure 2.32 – The relative cost of the identification of the tyre properties which are commonly used by semi-empirical models, after [164].

wrong identification method. The importance of the parameter's identification is highlighted in the accompanying literature of all the advanced physical or semi-empirical tyre models, while all of them incorporate software applications specially designed for the correct implementation of the parameters' identification data. Moreover, the commercial success of a tyre model is to a great extent defined by the correct design of the identification method, and the associated time and cost resources that are required. The relative cost of the various identification procedures is presented by Mundl and Duvernier in [164].

A comparative presentation of some commercially established transient models may be found in [165], following the above discussed standardized virtual testing concept. Actual experimental data were used for the validation of the models and the required identification procedures. The tyre models were combined with different, multi-body-systems, commercial software packages. Under the above followed categorization, four of the models belong to the simplified transient family (TM-easy, MF-tyre, PAC2002, Uni-Tire) and three models belong to the advance transient family (SWIFT, F-Tire and RMOD-K, in increasing complexity order). The conclusions drawn by that study [165] may be regarded as summarising the current trends of the tyre simulation research: Although the simplified models exhibit satisfying simulation accuracy in the low frequency range, accompanied by a relatively easy parameters' identification process, the demand for models that combine accurate and physical representation of the interaction between the structural deformation and the shear force generation, is evident for studies extending to the tyre behaviour in the higher frequency range.

2.2 The tyre behaviour from a viscoelastic materials science and contact mechanics point of view

In the previous section, the tyre behaviour was examined from the simulation strategy point of view. Although the simulation potential and the limitations of a broad range of models was comprehensively exam-

ined, little insight was offered into the actual physical mechanisms that control the macroscopically observed tyre behaviour. In the following sections the framework of the physical mechanisms that define the tyre-road frictional interaction will be investigated and presented from a historical point of view. The importance of the incorporation of this analysis is promoted and amplified by the previously identified current trend of the tyre simulation science towards the understanding and capture of the behaviour defining mechanisms. Consequently the identification and understanding of the broad physical background of these mechanisms is a necessary initial stage of the design of any physical modelling strategy or concept.

The tyre-road interaction is primarily defined by two major physical mechanisms:

- Its materials viscoelasticity.
- The road surface roughness and the micro-scale contact characteristics.

Interestingly, although the effect of both of them has been long ago experimentally identified, as will be presented in the following discussion, none of them has been fully understood and mathematically modelled. Moreover, the interaction between these two mechanisms is regarded as one of the most challenging problems for the modern science

2.2.1 Basic properties of a viscoelastic material

Setting a starting point, the physical behaviour of a viscoelastic material has to be identified. The classic work of Ferry [166] offers a valuable guidance on the topic. In general, a material is defined as ideally elastic when its stress and strain are proportional to each other and but one independent from the time rate of application of the other. This proportional relationship is captured in the law of Hooke. In contrast, a material is defined as ideally viscous when the stress is proportional to the time rate of the applied strain, but independent from the level of strain. This behaviour is described by the law of Newton. A material which combines both the elastic and the viscous behaviour is defined as viscoelastic.

In reality, none of the ideal pure elastic or viscous behaviour can be found in solids. All materials exhibit viscoelastic characteristics, being closer to the one or to the other idealized cases. Polymers, materials which are typically used for the tyre manufacture, show, though, a behaviour in which both characteristics are profound. The relationship between the stress and the strain in a viscoelastic material is a dynamic function of time. In fig. 2.33, for example, the strain development with time is presented as the response to a constant stress excitation. It is evident that the strain level increases in a non linear way with the time of stress application. This characteristic behaviour can be explained in an oversimplified way by the chain-like shape of the polymer's molecules (fig. 2.34). When a tension is applied to the polymer, these chains elongate and align with the direction of the stress, a process which needs a finite time to be activated.

The time dependency of the mechanical behaviour of the viscoelastic materials is typically summarized in the stress relaxation and creep properties (fig. 2.35). When an excitation of constant strain is applied to a viscoelastic material the resulting stress deteriorates with the time and asymptotically reaches a constant value. The decrease of the stress level with time is named stress relaxation (fig. 2.35(a)). In accordance, when a constant stress is suddenly applied to a viscoelastic material, the resulting strain increases with the time, and asymptotically reaches a constant value. The increase of the strain level with the time is named creep (fig. 2.35(b)). Apparently, in contrast to the common elastic behaviour, the definition of the elastic

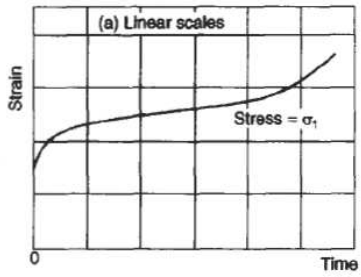

Figure 2.33 – The strain response over time of a viscoelastic material to the application of a constant stress, after [167].

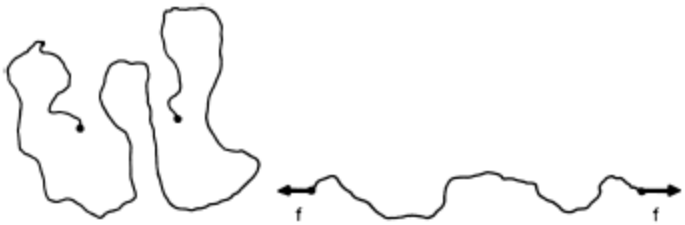

Figure 2.34 – A polymer molecule, in initial (left) and under stress condition (right), after [168].

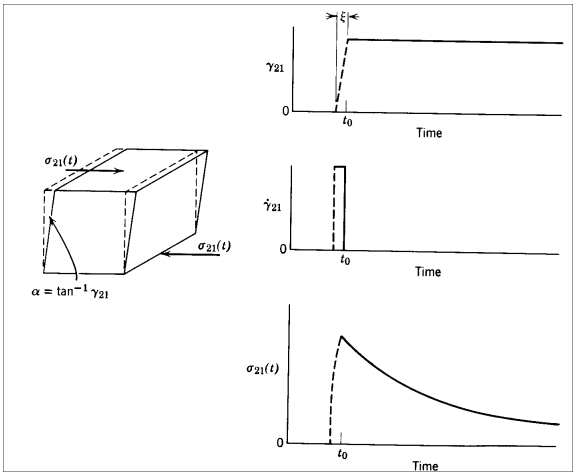

(a) The imposed shear strain, its time rate and the stress relaxation mechanism.

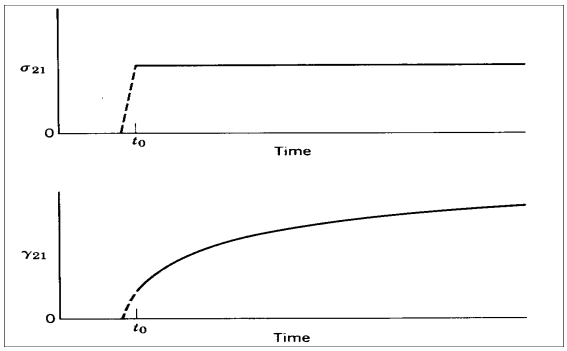

(b) The imposed shear stress and the creep mechanism.

Figure 2.35 – The viscoelastic shear relaxation and creep mechanisms, after [166].

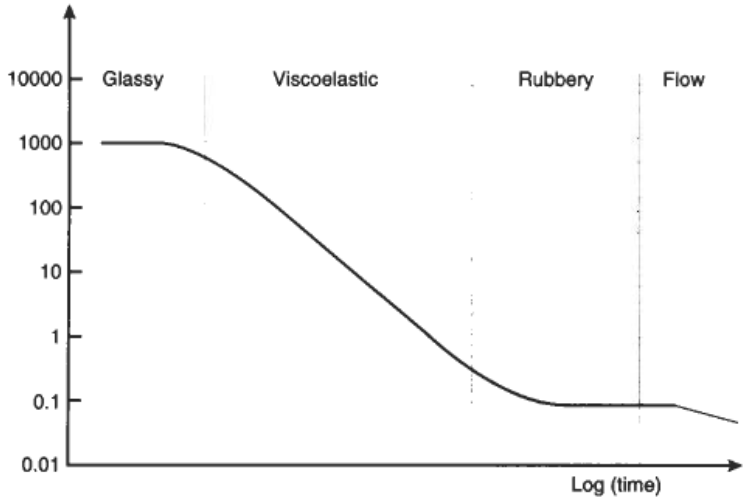

Figure 2.36 – The material elastic modulus as a function of the loading time, after [167].

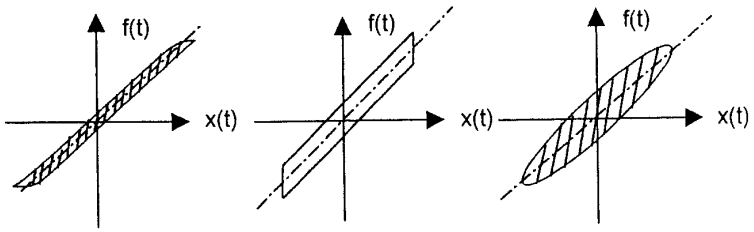

Figure 2.37 – Three different variations of the stress-strain relationship from the loading to the recovery phases, after [169].

modulus of a viscoelastic material incorporates the effect of time (fig. 2.36). As an increase in the application time of a load (stress) results in an increase in the resulting deformation (strain), the elastic modulus of the material decreases with the time. As is it is presented in fig. 2.36 the range of the elastic modulus can theoretically extend from a very high, glassy material corresponding value to a very low, flow-behaviour corresponding, one.

A direct result of the viscoelastic property, which is characteristically reflected in the tyre behaviour, is the non correspondence between the deformation and the recovery phases of a finite time loading process. The stress-strain relationship varies from the one phase to the other and this variation reflects the energy dissipation mechanism of the viscoelastic material (fig. 2.37). Moreover, when not only the magnitude of the load but also the application time exceed certain limits, a permanent deformation may be exhibited by the viscoelastic material.

The dynamic behaviour of a viscoelastic material is also exhibited under the application of a harmonic, stress or strain, excitation. The resulting response is not in phase with the excitation (fig. 2.38) and it may be decoupled in two components, one being in phase with the excitation and one 180° out of phase. The constant of the in phase component transfer function is named storage modulus and reveals the portion of

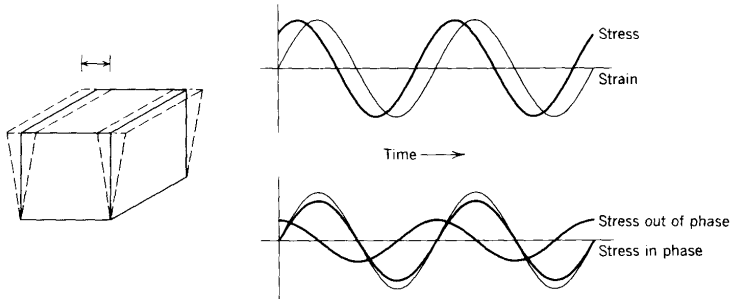

Figure 2.38 – The stress response of a viscoelastic material to a harmonic strain excitation, after [166]

the energy that is stored and recovered by the material during a cycle. The constant of the out of phase transfer function is called loss modulus and reveals the portion of the energy that is dissipated in every cycle. None of the modulus properties has a constant value but both of them are functions of the excitation frequency. Their ratio is called loss tangent and offers an indication of the energy dissipation across the frequency range of interest.

The dependency of the storage and loss modulus, expressed respectively as the real and the imaginary parts of the complex elastic modulus, on the excitation frequency is presented in fig. 2.39. In the low frequency range the material exhibits a rubber-like behaviour transforming into a glass-like one, in the frequency increases. The behaviour may be divided in two respective zones, in which the storage modulus exhibits modest value variation. The transition between these two characteristic behaviors takes place in a certain frequency range (transition region), in which the storage modulus increases radically. The loss modulus initially increases with the frequency, reaches a maximum value in this transition region, and decreases after that. In result, the loss tangent exhibits a parabolic development with the frequency. The maximum value is placed in the transition region, and the loss tangent deteriorates rapidly in the rest of the frequency range.

Viscoelasticity imposes a temperature dependence similar to the rate or duration of excitation one. In the low temperature range, the viscoelastic material shows a glassy behaviour, similar to the one corresponding to a high frequency excitation, while in the high temperature range, the material behaviour becomes rubber-like, similar to the low frequency one. This behaviour is captured in fig. 2.40. The transition between the two characteristic behaviour patterns of the viscoelastic material, the glassy and the rubbery, although it is not a step one, can be identified in the range of a certain temperature value. The glass transition temperature is an important viscoelastic material property which offers a certain indication of the material behaviour. The elastic and loss modulus of various materials in the range of the glass transition temperature is presented in fig. 2.41. The elastic modulus (fig. 2.41(a)) decreases sharply, while the loss modulus (fig. 2.41(b) exhibits a parabolic behaviour and reaches its maximum value for the glass temperature.

The characteristic correspondence between the temperature and the frequency (time) effects on the mechanical properties of a viscoelastic material enables their interchange in an experimental study. This is evident in fig. 2.42, where experimental data acquired for the same range of loading duration but in different temperatures, are used for the derivation of a common curve, called master curve. Consequently, the master curve may extend to a much broader time or temperature range than the one that may be experimentally studied. A common transformation is the one corresponding to the glass transition temperature, the WLF

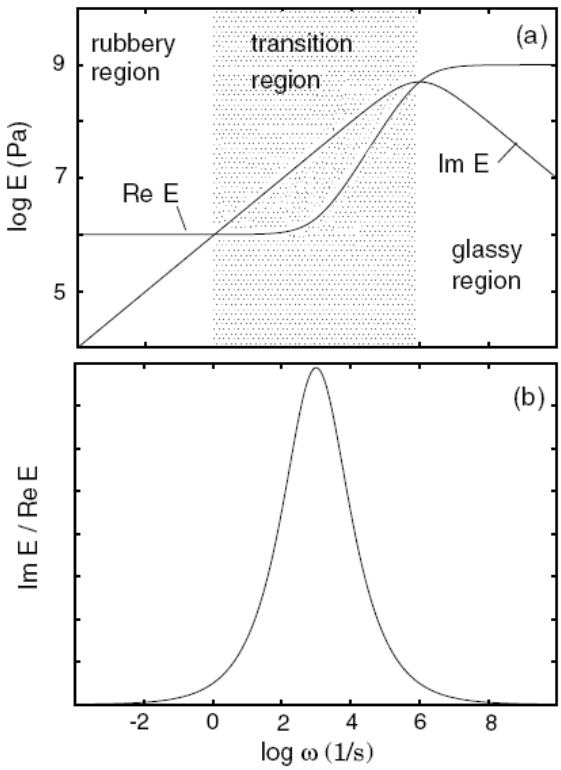

Figure 2.39 – The storage modulus, the loss modulus and their ratio (loss tangent) as functions of the excitation frequency, after [170]

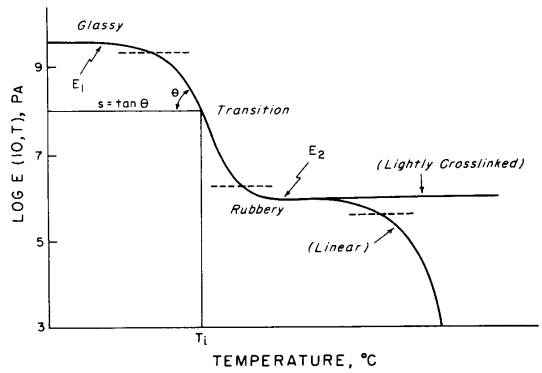

Figure 2.40 – The material elastic modulus as a function of the temperature, after [166].

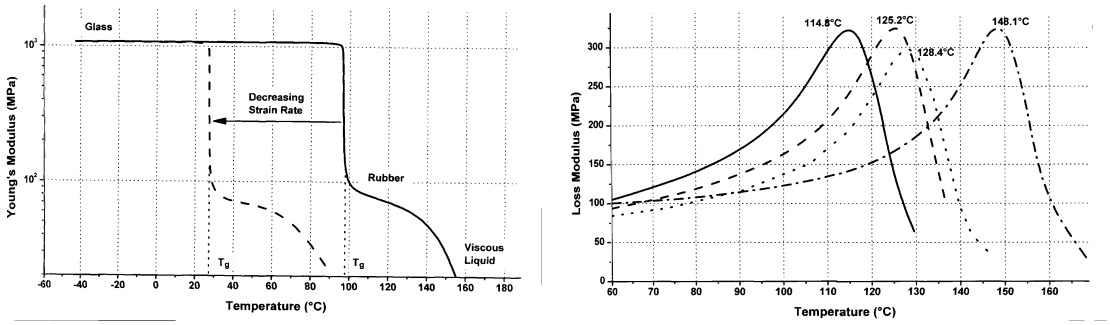

(a) The young modulus variation.

(b) The shear loss modulus variation.

Figure 2.41 – The variation of the mechanical properties of the viscoelastic materials in the area of the glass temperature, after [171].

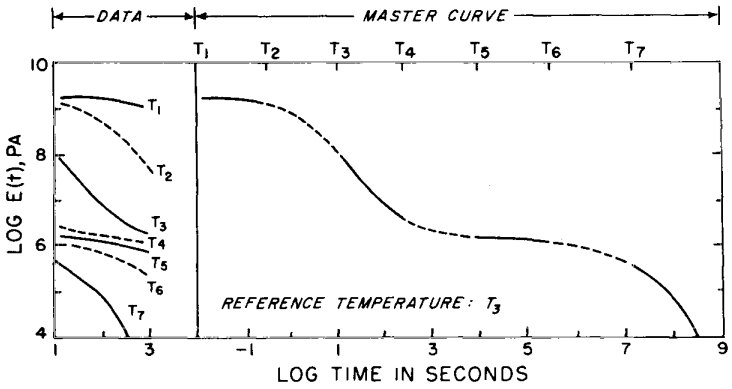

Figure 2.42 – The construction of an elastic modulus - time - temperature master curve from experimental data acquired at different temperatures, after [172].

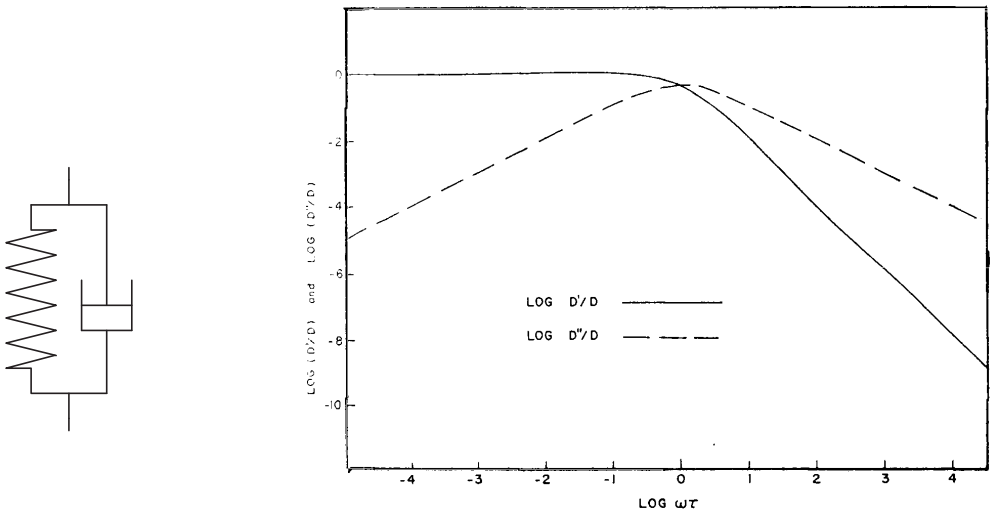

(a) The representation of the element.

(b) The predicted response, after [172]. (D:steady state strain, D': storage strain, D":loss strain)

Figure 2.43 – The Voigt viscoelastic element and its behaviour.

transformation, which was firstly proposed by Williams, Landel and Ferry, in their classic work [173]. A detailed analysis of the time and temperature effects correspondence may be found in [166].

Models of viscoelastic materials

Apparently the modelling of the viscoelastic behaviour is a challenging task. In practice and under a linear assumption, a stiffness model captures the elastic behaviour and a viscous damping model captures the viscous one. The different combinations of these simple elements result in different viscoelastic modelling approaches. The simplest of them are the combination of two elements (one elastic and one viscous) in parallel (Kelvin-Voigt element, fig. 2.43(a)) or in serial configuration (Maxwell-Voigt element, fig. 2.44(a)). The excitation frequency dependency of the storage and loss modulus of each of them is respectively presented in figs. 2.43(b) and 2.44(b).

Obviously the viscoelastic behaviour of the above linear models does not correlate accurately with the actual one. These simple models may only predict one transition region, while the real material exhibit more, one of them corresponding to the rubber to liquid transition and the others introduced by the mixture of different viscoelastic material in the final compound. Moreover, even if the actual viscoelastic behaviour of the material is accurately captured in the transition region, severe deviation will be observed away from this point. The combination of a higher number of parallel and serial models (the generalised models, fig. 2.49) has been proposed for the enhancement of the simulation accuracy across a broad range of conditions.

The actual energy dissipation mechanism and its simplification assumptions

In the above discussion it was assumed that the energy dissipation mechanism may be fully captured by a mechanism generating a force proportional to the time rate of strain (viscous analogy). The actual mechanism though exhibits a dynamic (memory equipped) behaviour and the calculation of the damping

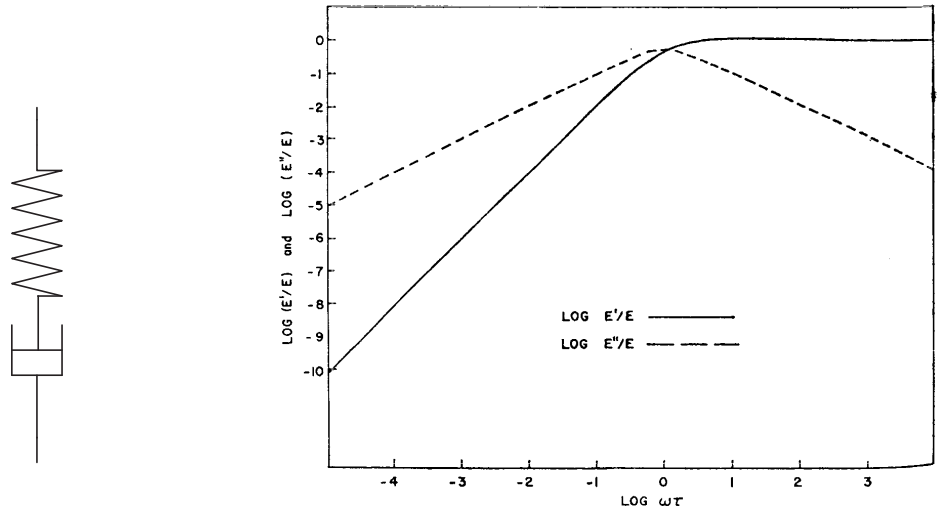

(a) The representation of the element.

(b) The predicted response, after [172].(D:steady state stress, D': storage stress, D":loss stress)

Figure 2.44 – The Maxwell viscoelastic element and its behaviour.

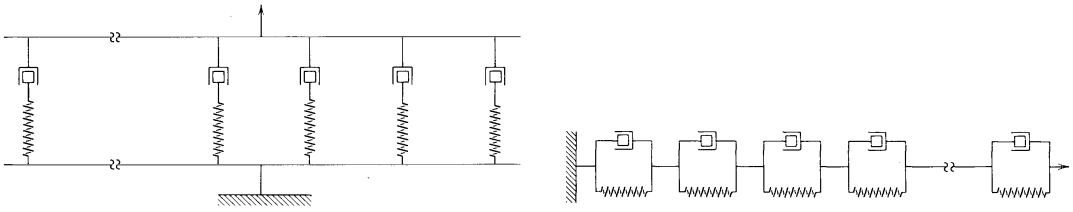

(a) The generalized Voigt element.

(b) The generalized Maxwell element.

Figure 2.45 – Generalized viscoelastic elements, after [166].

force should be accomplished by a time integration of a state variable, not explicitly associated with the strain time rate (velocity). The latter was actually an assumption proposed by Lord Raleigh in 1896 [174] and commonly adopted since then for various damping modelling purposes. A summary of the most important non-viscous dissipation models may be found in [175]. The uncertainty related to the actual mechanism and the circumstances under which the mechanism may be deduced to the viscous one has been comprehensively discussed by Adhikari and Woodhouse [176, 177].

Viscosity (velocity-analogous force) is not the only non-memory modelling approach. As it is discussed in [169], the viscous mechanism introduces a direct frequency dependency of the amount of energy loss per cycle, something not correlating with the actual material's behaviour. A hysteretic energy dissipation mechanism compensates for this shortcoming of the viscous one. The constant proportionality coefficient of the strain rate, proposed by the viscous model, is divided by the frequency excitation in the case of forced vibration. Due to its mathematical expression, hysteretic damping mechanism cannot be applied neither to the free structural vibration case nor for the calculation of the response in the time domain. Ribeiro *et al* [178] proposed a unified, viscous and hysteretic, modelling approach entitling the simulation of the dissipation mechanism in the time domain.

The actual tyre energy dissipation mechanism is difficult to be identified, although its effect is apparent on both shear force generation and energy dissipation phenomena. Holding the friction related discussion for the following section, the rolling resistance of the tyre constitutes the most observable effect related to the tyre energy dissipation. Although a viscous damping mechanism is assumed in the majority of the models, as summarised in [18], the non linear velocity dependence of the rolling resistance experimentally confirms the coexistence of both dissipation mechanisms (viscous and hysteretic) in the tyre structure. A survey of the followed approaches for the modelling of tyre damping mechanism can be found in the work of Miege and Popov [127].

Various approaches have been proposed for the incorporation of the tyre structural energy dissipation mechanism in the tyre models. Lu and Segel [179] assumed a radial hysteretic mechanism embedded in the tyre sidewall for the study of the rolling resistance development. The low predicted values, in comparison to the experimental results, prove that dissipation is also associated with belt deformation and contact area phenomena. A similar, radial foundation only, approach is followed by Stutts and Soedel for their string under tension model [180]. Padovan [82], in contrast, proposed a viscous mechanism associated with both belt and sidewall structure. Miege and Popov in [127] assume a equally distributed, in terms of modes, damping property as they associate each mode of their analytical ring model with the same damping ratio. Kim and Savkoor [122], motivated by the small dependence of the rolling resistance on the velocity, associated tyre damping with a hysteretic mechanism, incorporated in a flexible ring model. Miege and Popov comment in [127] that in the low frequency range the nature of the assumed damping model (viscous or hysteretic) does not affect much the predicted modal behaviour.

Popov and Geng [181] and Geng *et al* [80] investigated the validity of common tyre damping related assumptions, based on experimental results and a complex modes identification procedure. The linearity and reciprocity (property related to the interchangeability between the positions of excitation application and response measurement) were the first characteristics to be verified. The common viscous assumption, associated with the structure description by real modes, was found to be valid in the frequency range up to 200Hz, but complex modes have to be used for the modal expression of the tyre deformation in the higher

than that frequency range. The legitimacy of the application of Rayleigh's small damping approximation and the resulting simplifications (see [174, 182, 176, 177]) are comprehensively discussed in the same study.

Tyre linearity is experimentally proved by Guan *et al* [78], where different excitation methods are compared in respect to their linearity proof capability. In the same study, cross ply tyre construction was found to result in higher damping coefficients than radial construction. This conclusion is in accordance with the rolling resistance difference between tyres following each of the construction method, proving the interaction between rolling resistance and structural damping. The decrease of the damping ratios with the inflation pressure was also verified. The inflation pressure dependency of the damping ratios was also experimentally concluded by Yam *et al* [77] and by Kim *et al* [183].

The tyre damping mechanisms and their effect on its modal characteristics will be further analysed in chapter 3, where also the validity of many of the above modelling assumptions and simplifications will be further investigated.

2.2.2 The contact and tribological behaviour of the viscoelastic materials

Having briefly presented the basic characteristics of the viscoelastic materials and the related modelling approaches, the discussion here moves to their contact behaviour and the friction force development.

Historically, Leonardo Da Vinci was, according to Dowson [184], the first who observed that the sliding friction force between two solids is proportional to the vertical load and independent from their phenomenal contact area. His tribological experiments (fig. 2.48(a)) were described in his classic *Codex Atlanticus* and *Codex Arundel* work. Isaac Newton [185] reached the same conclusions also through his experimental studies. These observations, which are still regarded as the two basic characteristics of friction force, are known today as the Amontons or Coulomb laws of friction, after the two pioneers of tribology who reached the same conclusions [186, 187]. Coulomb proposed various surface roughness representations in order to support the sliding friction development (fig. 2.48(b)), but Euler was the first to propose a certain model for the roughness, the triangular asperities one [188, 189]. Dowson in [184] offer a comprehensive review of the early steps of the science of tribology.

Even since those early experimental investigations it was evident that the actual contact and the frictional interaction between two solids do not take place in the nominal macroscopic contact area, but in a small portion of it, defined by the load and the surface roughness. This observation led to the development of two different study approaches in the science of tribology. The first approach investigates the actual, physical interaction between the asperities of the two surfaces and identifies the mechanisms that define the developed forces, often at a molecular level (nano-tribology and nano-scale friction [190, 191]). This approach aims at the mathematical formulation of the friction mechanisms. The second approach investigates the friction mechanics from a macro-scale point of view. The experimentally observable tribological behaviour of the materials is studied as a function of the imposed physical conditions of interaction (velocity, pressure, temperature). The challenge of this approach is the synthesis of an accurate model, able to capture the various factors of the friction development even if this model is not directly related to the actual physical mechanisms. A comprehensive and comparative survey of the main macroscopic models may be found in the work of Al-Bender and Swevers [192].

In this discussion, a brief summary of the evolution of the contact mechanics theories will be firstly attempted. The macroscopic frictional behaviour of the viscoelastic materials will be later discussed. Finally

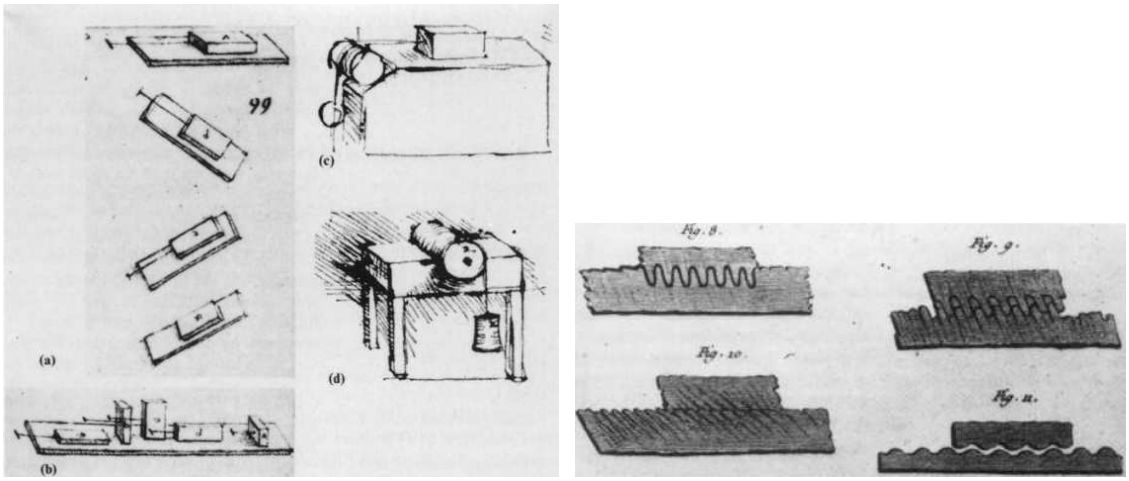

(a) The friction experiments of da Vinci, as presented in *Codex Atlanticus* and *Codex Arundel*.

(b) The sketches of Coulomb, on the effect of surface roughness on friction.

Figure 2.46 – The pioneering studies of friction, after [184].

the interaction and the possible overlap of the two approaches, examined from the point of view of the tyre shear force development, will be investigated, according to the still developing theories.

A brief introduction to the theories of contact mechanics

The start of the modern contact mechanics science is associated with the investigation of a scientific paradox. Hertz, in [193], derived an analytical solution for the elastic frictionless contact of a sphere. The calculated pressure distribution was an ellipsoidal one, the so called -*Hertzian*- pressure distribution. This distribution predicts the development of a contact area which is proportional to the applied load, raised to the 2/3 power. Given that the real contact between two surfaces takes place at the top of the surface roughness asperities, the real contact area between two, even phenomenally smooth, surfaces may be assumed as following the above power law. As research progress, though, started associating the friction force with the real contact area between two surfaces [194, 195, 196], the physical background of the experimentally established proportional dependency of the friction force on the vertical load, could not be verified.

Bowden and Tabor, in their classic work, *The Friction and Lubrication of Solids* [197], proposed a theory for the justification of the above paradox. The actual contact area between the two surfaces was believed to be so small that the elastic deformation pressure limit of the softest of the two materials is always reached. The resulting plastic flow makes the real contact area proportional to the load. The plasticity contact theory, though, could not justify the non proportionality in the case of repeated contacts.

A radical theory was proposed by Archard [199, 198] for the explanation of the paradox, based on the realisation of the contact at multiple levels of asperities, representing the surface roughness. The key assumption of Archard's theory is that the increase of the vertical load does not result in the magnification of the already existing contact areas, but in the multiplication of the number of the contacts, as finer levels of asperities come in contact. If this assumption is combined with the elastic Hertzian contact a proportional contact area (or force) development with load is predicted. Archard's model may be regarded as the first, simplified, description of a fractal surface model many years before such theories were applied to contact

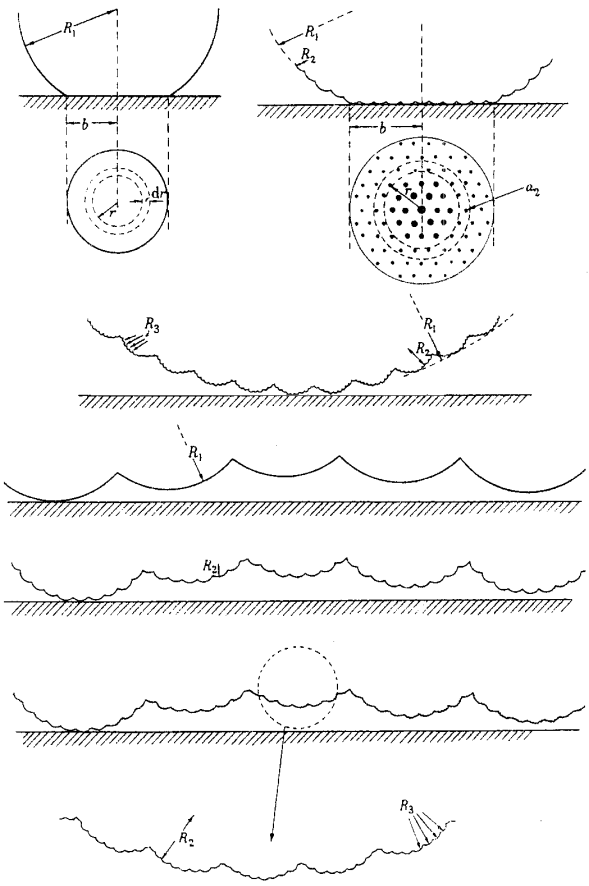

Figure 2.47 – The multiple levels of asperities-on-asperities roughness model proposed by Archard, after [198].

physical representations.

Greenwood and Williamson in [200] reached a similar conclusion to the above, assuming a more generic statistical distribution (Gaussian) of the asperities' heights. The asperity was defined as a point higher than its neighboring ones, a process emerging from experimental measurements of the surface roughness. This model leads to the prediction of a perfect proportionality between the load and the number of contacts. In contrast to Archard's approach, the area of the existing contacts increases with the load, but the addition of new contacts keeps the average area value constant. In result, the proportionality between the real contact area and the applied load was not attributed to the possible plastic deformation of the asperities but to the distribution of the surface roughness.

As it became obvious soon, the accurate measurement and mathematical description of the surface micro-roughness was necessary for a further development of the tribology theories and the respective science, the *topography*, attracted significant interest. Whitehouse and Archard in [201] approached the surface roughness as a random profile, fully described by its height distribution and its autocorrelation function. Moreover, experimental results showed that the majority of the materials may be described by a Gaussian height distribution and an exponential autocorrelation function. Greenwood in [202] extended the above approach to a two-dimensional one, modelling the surface roughness as a two-dimensional random noise

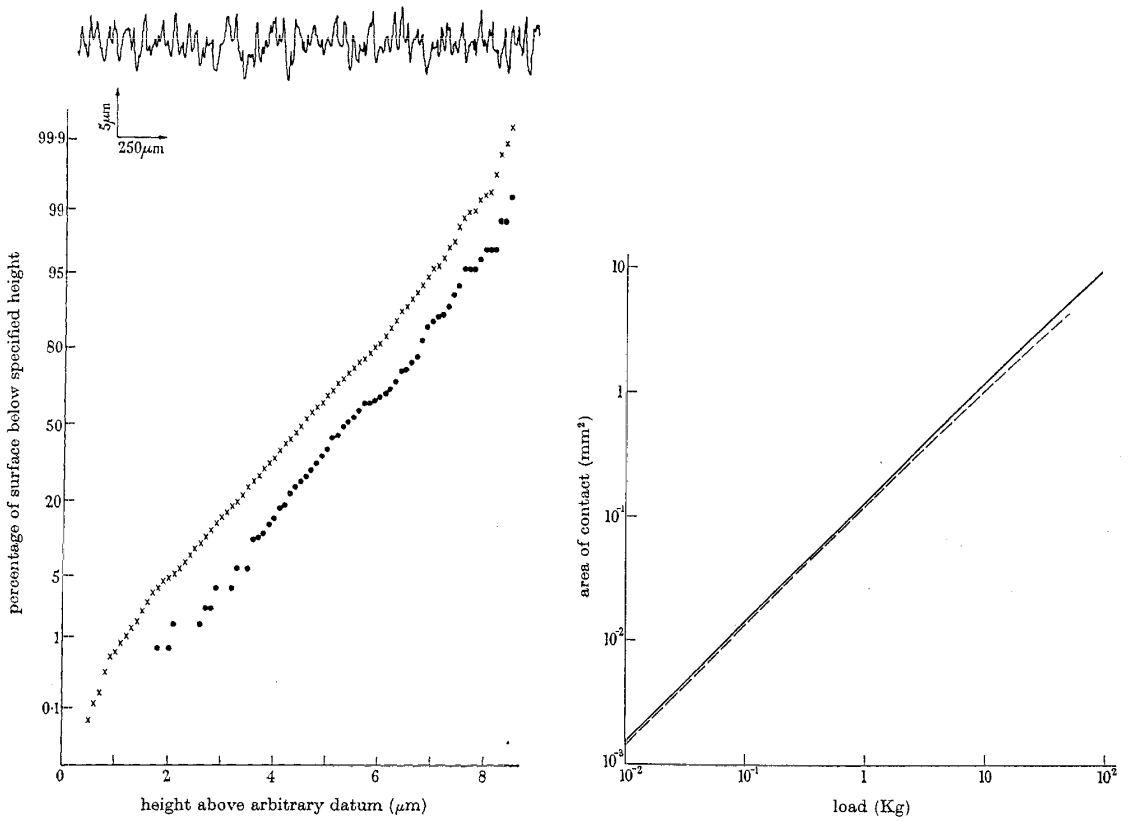

(a) The experimentally derived, Gaussian, height distribution of the measured heights (×) and the peaks' heights (•) of a surface.

(b) The predicted real contact area as a function of the load for $10cm^2$ (solid line) and $1cm^2$ (dashed line) nominal areas. The load proportionality and the insignificant effect of the nominal area are apparent.

Figure 2.48 – The contribution of the Greenwood-Williamson study to the first contact mechanics theories, after [200].

signal. The work of Greenwood and Wu [203] may be regarded as the final member of this group of topology theories. Greenwood, 35 years after his statistical surface topology approach [200], redefines the concept of the asperity and decouples that from the experimentally measured sequence of summits and peaks,as the statistical description of the surface roughness depends directly on the measuring method (accuracy and sampling length).

At that point of the tribology progress, a phenomenologically different science, the geography, lent a breakthrough mathematical tool to the topography: the fractal theory. The concept was initially proposed for the mathematical description of the brownian motion and the islands' coastline [206, 207] and was quite later applied to the case of the surface roughness [208]. The definition of a fractal surface (according to the Weierstrass-Mandelbrot function) may be found in the classic work of Mandelbrot [209, 210]. Two basic properties of this function define its significance for the topography: the properties of self-similarity and self-affinity [210]. The roughness shape of a surface is repeated for increasing levels of magnification, different in each dimension. Numerous topography and surface roughness fractal models have been proposed [211, 212], each of them leading to a respective contact mechanics theory [213]. Interestingly, Ciavarella *et al* [205] used a fractal based contact theory to prove the original Greenwood-Williamson concept, although the originally

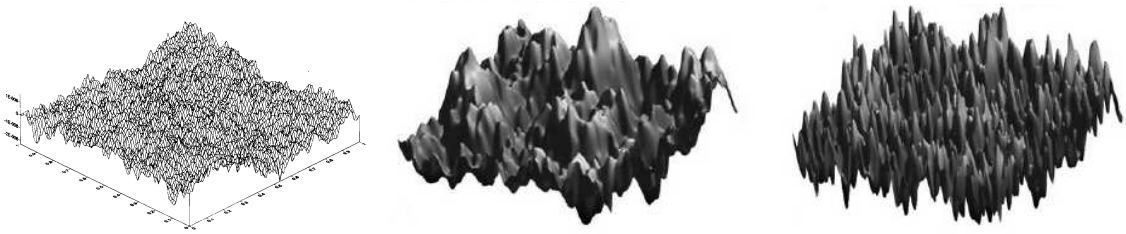

Figure 2.49 – A scan of a rough surface, after [204] and two fractal surfaces constructed using the Weierstrass-Mandelbrot mathematical model, after [205].

used for that statistical methods are affected by the measuring resolution.

The late progress of science enabled the study of surface topology and contact mechanics at a molecular level and various theories emerged, associating the frictional behaviour with atomic level physical mechanisms [214], such as the atomic vibrations. A survey of the most important of them may be found in [215, 190, 191]. Although the description of the micro- and nano-scale friction theories diverges from the aims of this presentation, the multi-level and multi-dimensional dependency of the friction physical mechanisms on the surface roughness is the conclusion that should be highlighted in regards to the tyre-road physical interaction.

The viscoelastic friction as an experimental science

The obvious question arising from the above discussion, is to what extent the analytical contact theories are able to offer the computational background for the accurate representation of the macroscopically observable frictional behaviour and especially the one of the viscoelastic materials. Before trying to give an answer to that question, the actual viscoelastic friction characteristics, as identified by the macro-scale, experimental studies should be presented.

The first uses of the physical rubber were associated with its high elastic deformability, in the temperature range above the transition one and not with its frictional properties. As Roberts has characteristically written [216], early motorists were hardly troubled by skidding problems of the road tyres given that travel speed was limited by the vehicle design and the poor road conditions. The frictional behaviour of the polymers had attracted minimal scientific interest before 1940's. By then, though, basic characteristics of it, such as its dependency on the sliding velocity and temperature, had been experimentally identified. Ariano [217] and Derieux [218] mentioned the increase of the friction coefficient with the sliding velocity, while Ariano comments also its decrease with the temperature friction. The surface transformation (conditioning and abrasive wear) of soft rubber materials had been also observed, as had also been the load dependence of the friction coefficient [218].

A systematic experimental study was accomplished by Schallamach [219] and a mechanism for the theoretical support of the similar to the above results was proposed. His theory was based on a molecular activation mechanism: The rubber molecules are in adhesional contact with the surface and may jump to the next adhesional position only after an energy barrier (activation energy) is overcome. The sufficient energy for that is provided by the temperature rise. The friction increase with the velocity was attributed to the conditioning of the rubber surface, resulting in the increase of the contact area. The molecular activation mechanism may be regarded as the first hint for the association of the viscoelastic friction with the

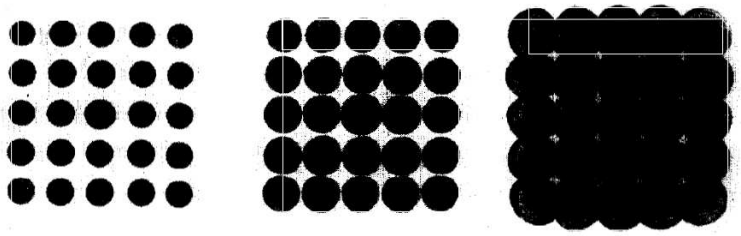

(a) The spherical asperities contact model.

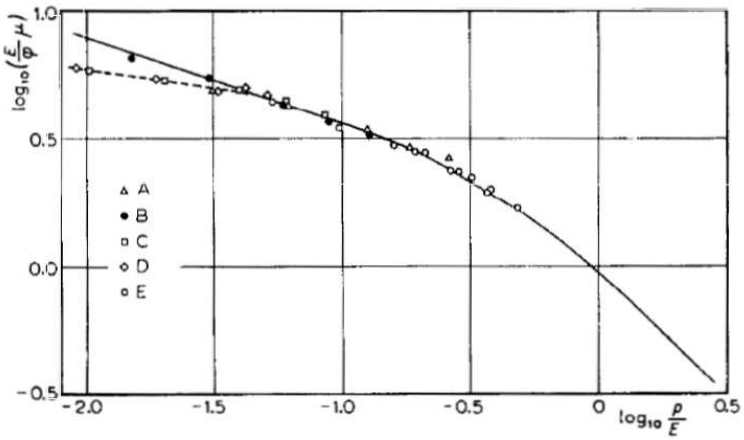

(b) The theoretical and experimental dependency of the friction coefficient on the load.

Figure 2.50 – The initial viscoelastic contact model presented by Schallamach, for the explanation of the load effect on the friction coefficient, after [220].

viscoelastic material properties, given that the respective energy theories for the viscous flow had already been proposed.

Schallamach in [220], tried also to associate the viscoelastic materials coefficient of friction with the load, proposing a physical mechanism. According to that, the viscoelastic contact is realised at the edges of similar to each other spherical asperities, following the classic Hertz deformation law, and the actual contact area is predicted by a load function, similar to the one of the other materials. As the load increases, though, the profound deformation of the viscoelastic materials results in the rapid decrease of the tangential distance between the asperities and any further increase of the contact area is suspended (fig. 2.50). That theory could be regarded as an oversimplified one according to the modern standards, offered, though, a first coupling between the tribological behaviour and the bulk properties of the viscoelastic materials.

Although the initial viscoelastic tribology models associated the frictional phenomena with the adhesional mechanisms of the actual contact area, the profound bulk deformation, imposed by the sliding motion, very soon led to new theories based on that. Some of the early experimental studies on the association of the sliding friction with the hysteretic deformation losses may be found in [221, 222]. The deformation mechanism is, theoretically, the sole source of friction in the case of sliding on a lubricated surface. In the case of a dry surface, the ratio of the adhesional to the deformational contribution of the friction is a function of the sliding velocity and the temperature.

The next fundamental step in the evolution of the viscoelastic friction theories was based on the experi-

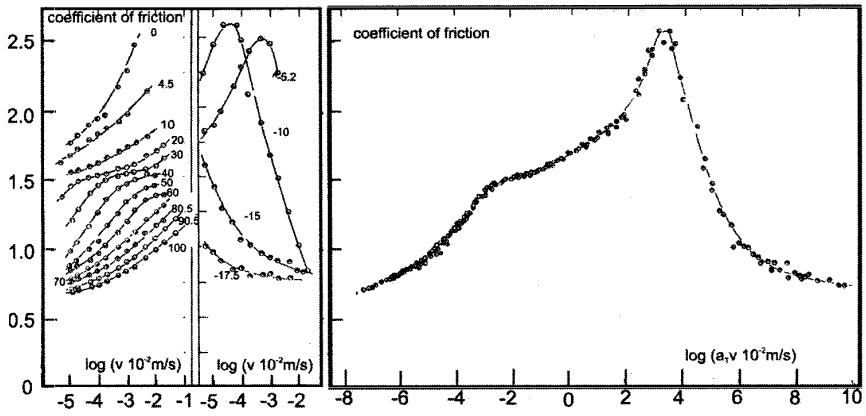

Figure 2.51 – The construction of a friction coefficient master curve, after [223].

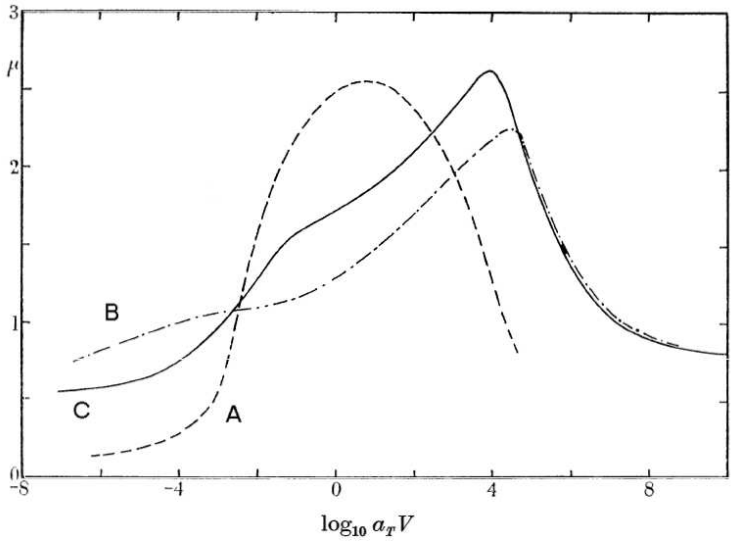

Figure 2.52 – Master curves of the sliding friction coefficient of a rubber material on three different surfaces; A: on smooth glass, B: on a silicon carbide surface(rough) and C: on powder covered silicon carbide [224])

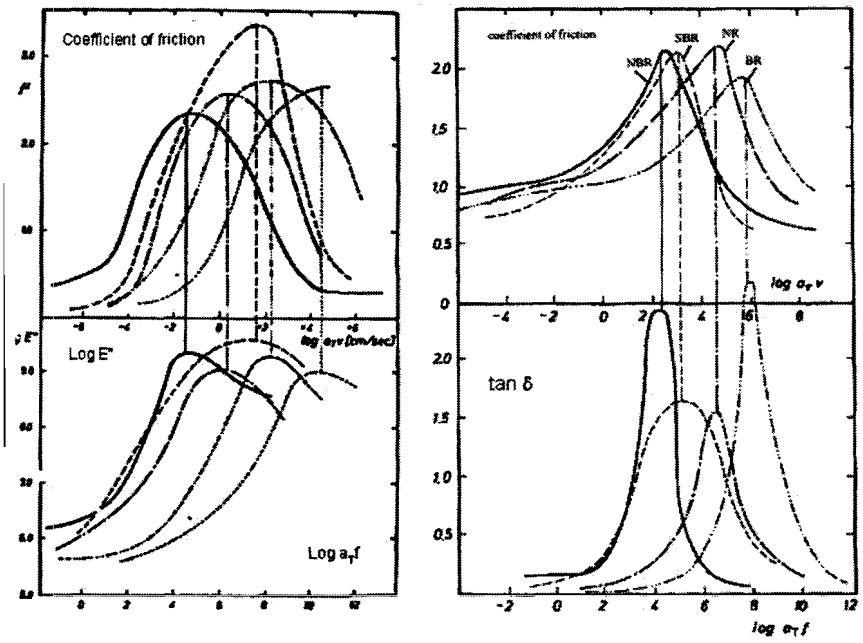

Figure 2.53 – The correspondence between the loss modulus and the maximum values of the adhesional sliding friction coefficient (left) and the correspondence between the loss tangent and the maximum values of the hysteretic friction coefficient (right), after [223].

mental measurements of Grosch [224]. He concluded that the coefficients of sliding friction measured across a range of temperatures and velocities can be represented by a single master curve (fig. 2.51), through the WLF transformation [173], in a way similar to the elastic modulus master curve (fig. 2.42). Moreover, Grosch investigated the effect of surface roughness on the shape of the master curve. In the case of sliding on a smooth surface, the curve shows a single maximum value (curve A of fig. 2.52), the position of which (in the common temperature-velocity axis) lies in a constant distance from the maximum value of the loss modulus (in the common temperature-frequency axis). This distance corresponds to a molecular level length value (derived as the velocity to frequency ratio), which prescribes the molecular mechanism of the adhesional friction. Many theories were proposed trying to describe the actual mechanism, a summary of which can be found in [216].

In the case of sliding on a rough surface, the coefficient of friction master curve exhibits a different shape (curve B of fig. 2.42). Although the adhesion-related peak may be identified, the total curve shape is defined by a second peak which develops at a higher temperature-velocity value and corresponds to a higher coefficient of friction. The distance of this second peak value from the frequency at which loss tangent reaches its maximum value corresponds to the distance between the asperities of the rough surface. In other words, the frictional behaviour associated with the second peak is the contribution of the deformation induced energy dissipation. The above correspondence between the frictional and the viscoelastic properties is presented in figs. 2.53 and 2.54. Interestingly, when the rough surface is covered with a powder media which theoretically suspends the adhesional mechanism contribution the first peak disappears and only the deformation-related one (curve C of fig. 2.52) may be observed. Accordingly, the coefficient values decrease across the whole temperature-velocity range.

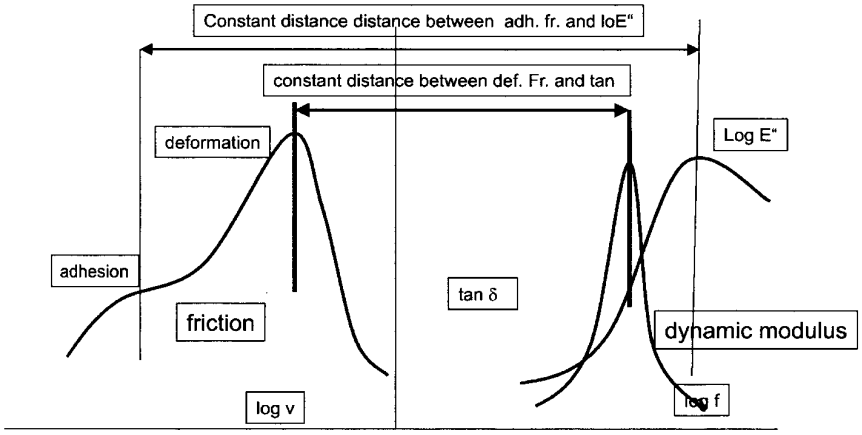

Figure 2.54 – The correlation between the friction and deformation maximum values, after [223].

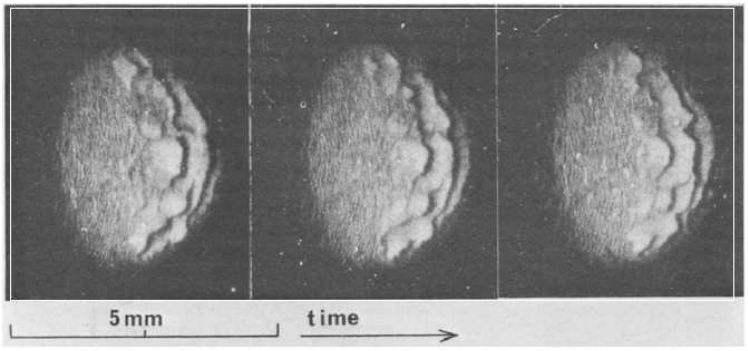

Figure 2.55 – The formation of the "Schallamach" waves on a rubber surface as the photographic lens slides on it, after [225]

A significant step towards the understanding of the macroscopic rubber sliding mechanism was made by Schallamach and presented in [225]. He observed that, under certain conditions, actual sliding does not occur between a soft viscoelastic material and a hard surface (in accordance to the first molecular theory presented by him!). In contrast, deformation waves propagate along the contact area, forcing the viscoelastic material to detach form the surface and to adhere to it at a different position. The formation of the "Schallamach waves" is based on a pure hysteretic mechanism and the process incorporated excessive deformation of the viscoelastic material.

At the same period the viscoelastic theories of adhesion were enhanced with the contribution of Johnson, Kendall and Roberts [226]. They observed that the viscoelastic contact between a sphere and a plane surface cannot be described by the classic contact theory of Hertz (see section 2.2.2). Molecular attraction not only increases the magnitude of the contact area in comparison to the one predicted by the Hertzian theory, but also increases the attachment force to a value higher than the applied load. The energy mechanism of the transformation of the above contact equilibrium into a sliding one and the conditions leading to the generation of the propagation waves have been discussed in the review paper of Barquins [227].

2.2.3 From the laboratory experiments of rubber specimens to the tyre shear force simulation

As soon as the basic characteristics of the viscoelastic tribological behaviour were experimentally identified, great research effort was put in the association of them with the tyre traction performance, from the vehicle dynamics point of view. Such an early coupling attempt was made by Savkoor [228]. Topics such as the tread pattern and the macroscopic contact deformation effects on the developed stress distribution, the identification of the contribution of the adhesional and hysteretic friction mechanisms and the road surface properties factor were mentioned. A little later, Ludema [229] proposed four viscoelastic friction mechanisms defining the tyre traction behaviour: the adhesion, the bulk deformation, the viscous properties and the tear mechanism. Putting aside the contribution of the structural deformation and the contact pressure distribution, as mechanical inputs, the correspondence between the experimentally derived viscoelastic friction of the materials used for tyre tread manufacture and the macroscopic shear force performance of the tyre is difficult to be defined for a number of reasons:

- The materials' tribological experiments are accomplished under strictly controlled velocity conditions, for reasons of measuring accuracy and repeatability. Tread shear motion, though, covers a broad range of sliding velocity values, which cannot be accurately measured or calculated. Under rolling-slipping conditions, the tread accelerates and decelerates rapidly as it crosses the stick (adherence) and slip zones of the contact area.

- Similarly, the temperature conditions are also controlled and the sliding velocity is limited to values that no significant increase due to the friction occurs. This is not true, though, for the actual tyre operation as severe heating is caused by the sliding process, severely affecting the friction development mechanism. The friction induced temperature change as a function of the sliding speed is presented in fig. 2.56). The transient sliding contact conditions excite a dynamic heat generation and dissipation mechanism, which is difficult to be measured or simulated.

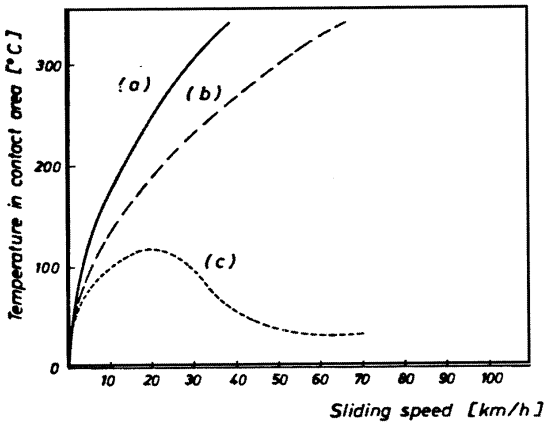

Figure 2.56 – The measured surface temperature as a function of the sliding speed, after [223]

- The actual surface roughness of the road cannot be reproduced in the laboratory and its effect cannot be mathematically simulated. Although the roughness can be measured down to a level defined by the accuracy of the applied methods, the actual physical mechanism associating each level of roughness with a certain frictional contribution has not been yet identified, neither is the actual level magnification to which such an association should be extended to. Moreover, the existence of particle and liquid debris changes the effective road roughness and changes radically its tribological properties.

Grosch in [223] presents the current level of understanding of the association between the experimentally measured tribological characteristics of the tread materials and the frictional behaviour of the tyre. The tyre shear force development as a function of the slip may, to some extent and across a certain velocity range, be correlated with the tread material master curve. In terms of temperature, though, such a direct association cannot be proposed. Although the effect of the temperature increase (due to friction) may be superimposed on the macroscopic temperature and velocity operating conditions, the actual measurement of the transient temperature field across the contact area raises a challenge. Interestingly, the load effect on the friction coefficient may be accounted for using the respective associated temperature increase and the resulting transpose of the problem to a new conditions' section along the master curve. This observation leads to the idea of a physical mechanism of interaction between the macroscopic non linear load effect on the tyre friction with the contact area thermal phenomena. Apparently, such a study of the local micro-scale tribological and thermal effects cannot be accomplished using the smooth road assumption and he physical effects of the road multi-level roughness have to be incorporated in that.

Having already briefly referred to the fractal theory based representations of the surface roughness, the obvious question is to what extent a typical road surface may be mathematically represented using such an approach. Various studies have given a positive answer to this question, offering the fractal properties of different types of road surface [231, 232, 233]. The development of advanced roughness measurement techniques and the analytical representation of the results, enables the correlation between the experimental results and the simulation studies of the friction force as a function of the road multi-level roughness. Such studies may be developed following either a discretised or an analytical tread representation approach.

The discretised studies of the roughness contribution to the viscoelastic friction may be regarded as a further development of the mechanisms proposed for the association of the tyre structural deformation with

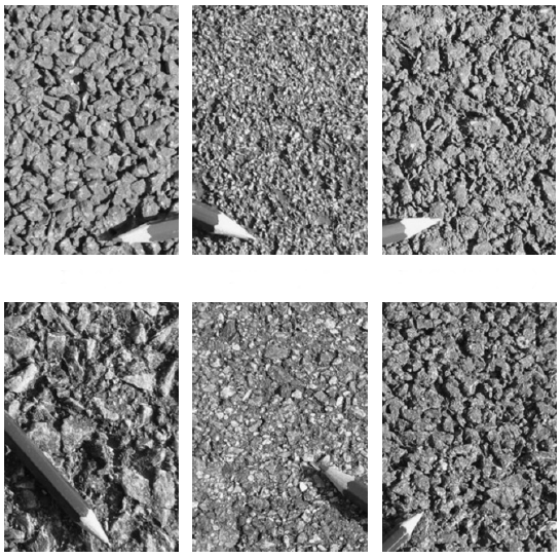

Figure 2.57 – Roughness of some typical road surfaces, after [230].

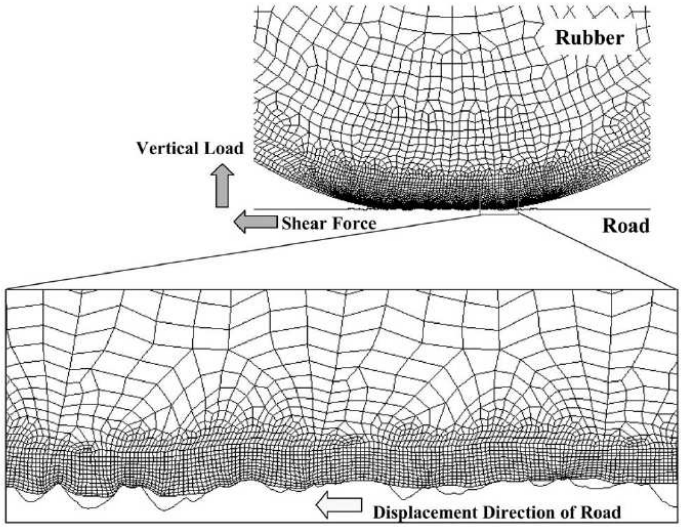

Figure 2.58 – Simulation of a deformed tread block sliding on a rough surface, after [234]

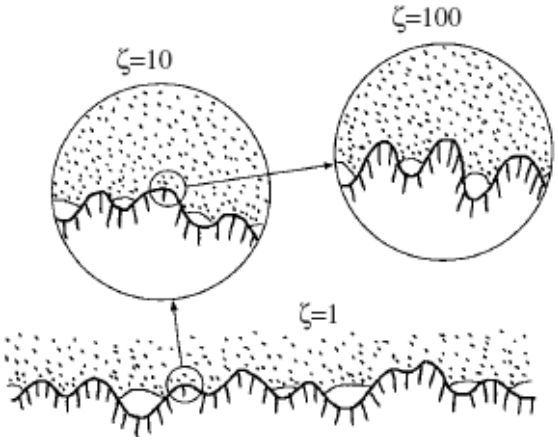

Figure 2.59 – The viscoelastic material - surface roughness contact model of Persson, after [170]

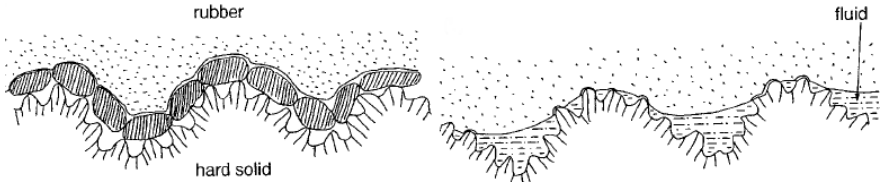

Figure 2.60 – The effect of dust contamination and water on the roughness friction model of Persson, after [239]

.

the friction force development (discussed in section 2.1.6). Kuwajima *et al* in [234] developed a FEM based contact model 2.58 for the prediction of the viscoelastic material sliding behaviour on an rough surface and the calculation results were correlated with experiential results. Hofstetter *et al* [235] presented a FEM based study of a tread block, subject to a stress field generated by its sliding on a rough surface.

The discretised modelling of the sliding friction on a rough surface using a multi-level roughness representation is suspended by the level of the discretisation coarseness. The contribution of only a few of the levels of roughness may be practically examined and the generation of friction cannot be associated only with them. As discussed by Persson *et al* [236], the attempts for correlation between certain levels of roughness, identified by empirical sand filling methods, and road frictional characteristics have failed.

The incorporation of a broad range of roughness levels in a friction model may be better addressed by the analytical representation of the surface. Kluppel and Heinrich [237] proposed an analytical mechanism coupling the sliding friction of tyres with the hysteretic losses caused by the fractal road surface. The model was used in [238] for the capture of the non linear tyre friction dependence on the vertical load and velocity, in correlation with a typical brush model predicted tyre characteristics.

Persson in [240] introduced a viscoelastic contact theory, which incorporates both the bulk deformation of the material by the roughness asperities and the adhesional attraction between the two surfaces (fig. 2.59) and following a similar approach a friction model was proposed by Persson and Tossati [241]. The pressure and velocity dependency of the friction were attributed to their effect on the conformation of the viscoelastic material to the fractal surface roughness. A transient dynamic expression of the same dependance was given in [242]. The decrease of the sliding coefficient of friction in the case of water or dust debris on the

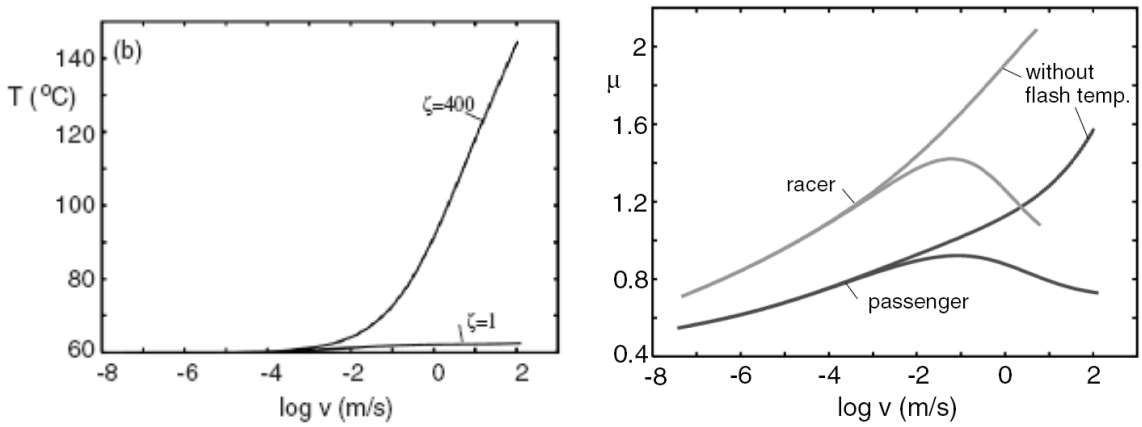

(a) The predicted temperature increase as a function of the sliding velocity, for two magnification levels.

(b) The predicted coefficient of friction as a function of the sliding velocity, for two typical tyre tread compounds, with and without the incorporation of temperature increase.

Figure 2.61 – The predicted sliding induced temperature increase and its effect on the friction coefficient, after [170].

road surface was accredited to the partial suspension of this deformation mechanism [239] (fig. 2.60). A comprehensive discussion on the present level of understanding of the effect of the surface roughness on the frictional performance may be found in [236].

According to Persson[170] and in agreement to the concluding remarks of Grosch [223], the present trends of the viscoelastic friction research focus in the exploration of the slip and load related phenomena through the local temperature effects and the roughness based mechanisms (fig. 2.61). In general, the predicted temperature increase effect of the sliding speed activates more roughness levels in the friction mechanism (fig. 2.61(a)). Interestingly, although a steady increase of the friction coefficient with the velocity is theoretically predicted, the incorporation of the local temperature effects changes radically this pattern and the coefficient decreases for sliding velocities above $1cm/sec$ (fig. 2.61(b)). In other words, the local temperature increase results in the tyre operation along a much wider section of the friction master curve, as the correlation of figs. 2.52 and 2.61(b) reveals.

It is evident from the above discussion that the attribution of viscoelastic friction special characteristics to a local deformation and thermal mechanism is at the moment the centre of attention of the tyre research activity in regards to the physical identification of the process. Both analytical and discretised approaches may contribute to that, as the first approach exhibits better computational performance in regards to the multi-level roughness induced deformation, while the second approach can represent more accurately the transient dynamic deformation characteristics of the material and the associated propagation of the generated heat. The transformation of such approaches, though, into accurate and robust tyre simulation tools is still suspended by the ignorance of the actual transient phenomena that take place in the tyre-road contact area. The local micro-slip and stick behaviour of the tread material, as it enters and exits the contact area, and the propagation of the related dynamic phenomena to the rest of the tyre structure have not been identified to a sufficient extent in order to be incorporated in surface roughness based tyre models. Further research on the tyre dynamic behaviour is expected to demystify the physical tyre traction mechanism and to enable the transformation of the above promising material friction models into tyre ones.

2.3 Basic conclusions from the tyre models survey

From the above analysis it may be concluded that the latest challenges of the tyre science can be met only by the development of advanced physical models, acting as an integration platform for the advanced tread viscoelastic representations. Such a modelling combination is able offer an insight into the interaction between the thermal phenomena of the viscoelastic friction and the tyre's transient performance, as captured by its macroscopic behaviour. It became clear as well that the physical study of this interaction necessitates a very fine space discretisation of the tyre contact area, as the kinematic and dynamic conditions vary significantly across and along it. This particular requirement generates the biggest barrier to the widespread adoption of such models by the vehicle dynamics science, which is their computational load. In parallel, the complex identification procedures of the physical models' properties make their integration in vehicle models a difficult and time consuming task, which often has to be repeated even for slight tyre design modifications. A certain gap among the tyre modelling methods may be identified, due to the lack of computational efficient physical models with a simple and straightforward process of parameters' identification.

It may be also argued that a certain category of physical models qualifies well for meeting the above requirements. These are the models that propose a modally expanded and reduced belt structural representation, acquired through either a theoretical belt model (e.g. [144]) or experimental data (e.g. [134]). The combination of such a belt model with a discretised tread representation may lead to a computationally efficient physical tyre model which can be used for transient, time-domain, simulation purposes. Indeed, such a modelling approach has already been presented in various tyre simulation studies (e.g. [76, 122, 144, 134, 130]), which have been proposed for the capture of the interaction between the structural and the shear force related phenomena of the tyre performance.

As it has been extensively discussed in section 2.1.6, the frequency range of the modal base of such a structural model which is able to offer a sufficient level of accuracy of the tyre transient phenomena simulation cannot be strictly defined, as it depends on the operating conditions that are imposed to the model by the vehicle dynamics modelling platform. Although in the case of an experimentally derived modal basis the complete available range is obviously used for the belt representation, the definition of the sufficient modal range in the case of a theoretically derived modal basis is not easy and certainly corresponds to key gap in the available literature.

Attempting to fill this gap, a number of belt models, which represent the basic physical mechanisms that control the belt structural deformation, will be compared in regards to their modal prediction characteristics. The actual effect and the importance of the various physical mechanisms and model properties on the modal behaviour of each of them will be highlighted across a broad frequency range. Although the capability of the examined representations to capture the actual tyre modal behaviour has been experimentally verified in various studies (e.g. [79]), the actual mechanisms and properties that affect the level of correlation across the frequency range have not been sufficiently examined.

As a second step, the present study will attempt to identify the actual modal range which is excited by the tyre operating conditions. Using the well established ring model the participation of the structural modes in the contact deformation will be examined. The analysis of the physical mechanisms, properties and conditions that control the balance between the contact simulation accuracy and the computational load of a modally reduced model is a key contribution of the present work.

The simulation of the large displacement rolling operating conditions using a modal based model is

commonly accomplished through pseudo-transient methods, kinematically superimposing the transient conditions to the tyre rigid motion (e.g. [130]). Indeed, the simulation of real transient conditions in the mixed modal-time domain methods, necessary to capture the frictional phenomena, has not been previously addressed. In the present study the theoretical framework for the simulation of dynamically induced, time domain transient conditions is developed. Moreover, the method may be proposed as applicable on various dynamic problems of engineering where certain deformation patterns are imposed by the operating conditions, allowing for the significant modal reduction of the respective model.

Finally, the identification of the effect of the physical properties of the tyre on its performance characteristics, through the sensitivity of the excited modes to them, is proposed as a concept. Certain operating conditions affect the degree of excitation of certain modes, while the effect of the physical properties on the modal characteristics is easier to be derived (experimentally or theoretically) than their respective effect on the performance characteristics. The method is believed to be capable of capturing the properties-performance association, based on the excited physical mechanisms. It is suggested that some of the experimental measurements which are necessary for the capture of the variation of the performance characteristics of the tyre as a function of the structural properties could be substituted by a respective experimental or simulation modal work.

2.4 Methodology and structure of the work

The present work is divided in three distinctive chapters, which correspond to the three major intermediate modelling steps towards the simulation of the rolling operating conditions.These steps may be summarised as:

- the modelling of the modal characteristics of the tyre and the structural deformation phenomena
- the simulation of the frictional contact of the tread and the interaction with the belt deformation
- the simulation of the large displacement, transient, contact operating conditions and the shear force development as a function of the macroscopic slip

The comparative examination of the tyre structural models is based on the predicted by them modal characteristics, as the modal expansion of the tyre structure is a major component of the present approach. The ring on elastic foundation model is used as a comparison basis, given that its good correlation with the actual low frequency in-plane modal behaviour of the tyre has been experimentally verified. Starting from the simple analytical rectilinear models, the string under tension and the bending beam ones are examined, as both of them correspond to basic mechanisms of the tyre structural behaviour. The differences in the strain development between the rectilinear and the circular modelling approaches is highlighted. The sensitivity of the ring modal characteristics to its physical properties is examined and the modal zones, in which the properties' effects are predominant, are identified. The modal prediction characteristics of simple discretised models, composed by rectilinear elements, are presented and the respective effect of discretisation is analysed.

Using the ring model, the incorporation of the inflation pressure effects in the modal prediction, through the circumferential pretension and membrane sidewall mechanisms, is examined. The combined modal behaviour of the wheel and the tyre belt is presented, as it is also the effect of the rotation on the modal

characteristics. The discussion of the simulation of the tyre structural behaviour is completed by the analysis of the energy dissipation mechanisms. Applying simplified damping models, the capability of the prediction of the experimentally identified damping behaviour is examined. This chapter offers the theoretical background for the incorporation of various physical factors and mechanisms in a tyre structural model and their effect across a broad modal range. In result, the actual range of the modal prediction correlation of the proposed models is identified and physically justified.

In the second chapter, the ring model is used for the simulation of the frictional contact behaviour of the tyre. For this purpose, its analytical structural expression is transformed into a discretised one and coupled with an also discretised tread foundation. This foundation consists of pairs of, vertical to each other, Kelvin-Voigt elements and is capable of predicting the possible shear slip of the tread on the road surface, as imposed by the vertical load, its viscoelastic properties and the frictional conditions. The resulting two-dimensional pressure distribution fields are acquired for a range of operating conditions and the effect of the buckling sidewall on the tread contact behaviour is identified. The interaction between the belt deformation, the tread frictional slip and the imposed load will be found to capture the mechanism of the horizontal pressure distribution development and justify some contradicting to each other observations and results of the existing studies, in regards to that.

The modelling potential of the modal reduction method is investigated, by the examination of the contact induced excitation of the modes across their range and the developed pattern of their participation in the deformation solution. Furthermore, the accuracy of the model is examined as a function of the operating conditions and the degree of modal reduction. These results, accompanied by the effect of the degree of modal reduction on the computational load, prescribe the applicability and the computational efficiency characteristics of a modally expanded structural model on the capture of the contact behaviour of the tyre.

The major theoretical challenge of the transformation of the contact model into a transient rolling one, is that the small displacement assumption, associated with the linearity of the modal expansion method, cannot be regarded to remain valid. This problem is tackled by the simulation framework which is developed in the following chapter, where the simulation of the rolling conditions is examined. A double level simulation algorithm is proposed, which retains the computational efficiency of the modal expansion for the calculation of the deformational response of the system, but combines that with a space domain calculation of its large displacement rigid motion.

Based on that approach, the launch physical mechanism of the tyre is investigated and the friction and damping effects on the interaction between the translational and the rotational motions is highlighted. The dynamic model may be simplified for the simulation of kinematic steady state slipping conditions and the typical saturation development of the tyre force with the slip is predicted. The latter tyre behaviour characteristic, given that it has been acquired using a simplified tread friction law, proves that the contribution of the structural phenomena of the tyre to its macroscopically observed shear force non linearities is significant. Finally, the effects of the rolling and slipping conditions on the structural response is examined by the respective variations of the modes' level of excitation. Comparing that with the corresponding to the contact static conditions modal excitation, certain conclusions on the physical properties which prescribe the rolling and frictional interaction are drawn.

Chapter 3

The simulation of tyre in-plane modal behaviour

In this chapter the simulation of the tyre modal characteristics will be investigated. The natural frequencies and deformation mode shapes, as they are predicted according to different modelling approaches, will be comparatively presented. This comparison is crucial for the rest of the work, given that the belt deformation under various tyre operating conditions will be calculated by its modally expanded representation. Moreover, the comparison will not be limited to the low frequency range but it will cover the total one as the actual modal content of the belt response will be later examined.

Both analytical and discretised belt representations will be investigated. In the first case, the modal contribution of basic mechanisms, such as the bending and axial stiffnesses and the string under tension one, will be presented. The ring on elastic foundation model will be comprehensively presented, as it plays a crucial role in the whole study. Comparing the ring modal prediction capabilities with the respective ones of the simple rectilinear assumptions, the effect of the incorporation of the circularity in the model will be identified. Moreover, using the ring model, the influence of the physical properties on the modal characteristics will be analysed. Basic discretised modelling approaches will be later presented, in correlation to the analytical ones. The implementation of similar physical mechanisms in discretised and analytical models will be investigated, as will also be the actual effect of the discretisation on the modal characteristics.

Using the ring on linear elastic foundation model as a basis, a physical mechanism that simulates the shape and inflation pressure non linear factors on the sidewall stiffness will be presented. The modal prediction of the resulting nonlinear ring model, as a function of the inflation pressure, will be investigated and compared to the linear one. The ring model will be also used for the study of the theoretical modal effect of the assignment of rotational and translational degrees of freedom to the wheel.

Finally the modal effect and the simulation techniques associated with two crucial mechanisms of the actual tyre behaviour, the rotation and the energy dissipation will be investigated. In regards to the rotation, the theoretical background of its modelling incorporation will be presented, but also the computational error of its possible omittance will be examined along the frequency range. The tyre energy dissipation will be studied through various damping models and ways of implementation into the physical structural representation. The effect of each of the different approaches on the damping coefficients of the modes will

be discussed.

3.1 The modal range of interest and the basic modelling approaches

Prior to presenting and comparing the various methods and techniques for the simulation of the tyre belt modal behaviour, the frequency range across which such a comparison will be attempted should be investigated. Typically, the tyre modal behaviour can be assumed to develop as a pure in-plane one in the frequency range up to 400Hz [79]. In the higher frequencies range the tyre response is three-dimensional and the vibration modes incorporate also an axial deformation component [108]. A large number of tyre transient phenomena is mainly associated with in-plane physical mechanisms. Longitudinal traction and braking, straight line rolling resistance, response to road profile irregularities and the transmission of them to the rest of the vehicle through the suspension, are phenomena for which the tyre in-plane dynamics is the significant factor and the out-of plane ones may be neglected for computational reasons. Respectively, it is a common practice that the two-dimensional study approach is extended to a frequency range in which the actual tyre behaves as a three-dimensional structure.

As it has already been discussed in section 2.1.6, the bandwidth of the tyre transient behaviour, from a physical modelling perspective, is difficult to be identified. Although excitations such as noise generation and macro-scale road irregularities may be associated with certain frequencies, these frequencies cannot directly constitute the model's bandwidth. The accurate prediction of the contact reaction stress field, necessary for the shear forces simulation, requires the representation of the contact area generation. The required modal/frequency range for the capture of the above mechanism cannot be a priori determined as it depends on the actual contact boundary conditions and their space distribution. The not so obvious effect of the space distribution of the excitation on the model's modal range is presented in fig. 3.1. A ring modal model, to be later presented, is used for the representation of the deformation induced by the contact between the tyre with a plane surface (fig. 3.1(a)) or a point cleat (fig. 3.1(b)). It may be observed that the simulation of the second case requires a broader modal range than the plane surface one.

An additional obstacle for the determination of the optimum structural model of a tyre is that the experimentally identified modal range is narrowed by damping phenomena and practical restrictions related to the measuring methods [106]. Practically, tyre modal data in the range up to 500Hz can be experimentally extracted, a range which is not sufficient for the simulation of the contact phenomena, as will be explained in chapter 4. In result, tyre modal behaviour cannot be explicitly associated with a certain modelling approach. Consequently, different modal simulation approaches have to be compared along a broad frequency range. The actual breadth and its association with the accuracy of the simulation results will be gradually investigated in the following chapters.

The followed modal simulation approaches may be divided in three basic categories:

- **Analytical rectilinear models**
- **Analytical circular models**
- **Discretised models**

In the first case the modal contribution of the tyre circularity is neglected and instead the effect of the basic stiffness mechanisms is captured. The belt is modelled as a rectilinear structure, in terms of its

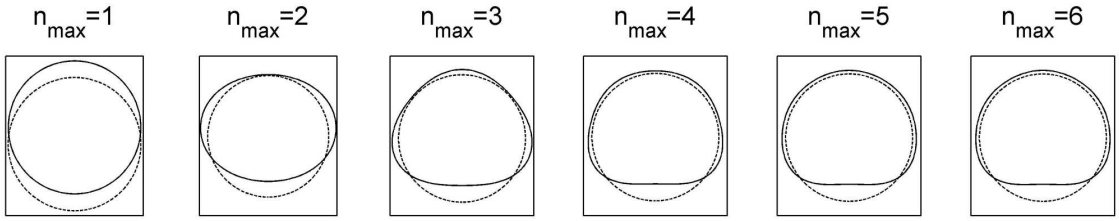

(a) Road excitation.

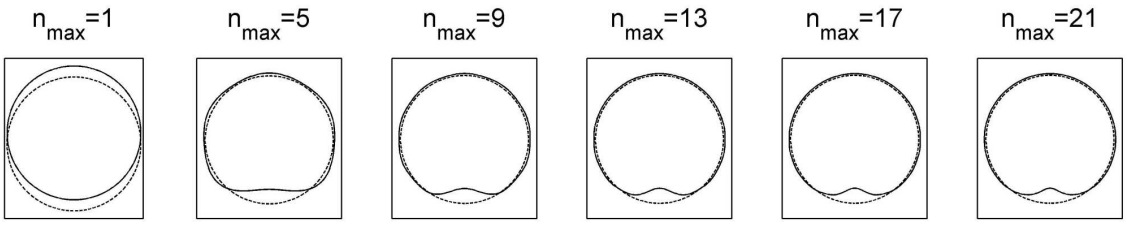

(b) Point excitation.

Figure 3.1 – The required modal range for the solution convergence of the steady state response calculation. The n_{max} number refers to the upper limit of the radial modal range of the model.

stiffness behaviour, with common degrees of freedom, though, assigned to its ends. From a computational point of view this is the simplest in-plane belt representation as the only degree of freedom of every point is assigned to its vertical deformation. In the second case, the representation is enhanced by the theoretical interaction between the two in-plane degrees of freedom (horizontal/vertical or radial/tangential). The ring model is the most established model of this category and for this reason its modal behaviour will be used as a comparison basis for the first, rectilinear, approach. The effect the incorporation of this interaction on the modal characteristics will be outlined.

The third, discretised, approach will be discussed in direct correlation to the analytical ones. Simple models will be examined, in order an analytical representation of their stiffness mechanism to be also available. In this way the actual effect of the discretisation on the predicted modal characteristics may be identified and highlighted.

3.2 Analytical rectilinear models

Historically [1], two basic physical mechanisms have been proposed for the capture of the tyre belt structural deformation:

- The string under tension model
- The bending beam model

The modal characteristics analysis will start from these two approaches, as the two respective mechanisms are called to describe the, vertical to their axis, vibrational behaviour of the rectilinear models. In both cases the models are combined with a distributed linear stiffness foundation, representing the contribution of the radial sidewall one to the modal behaviour.

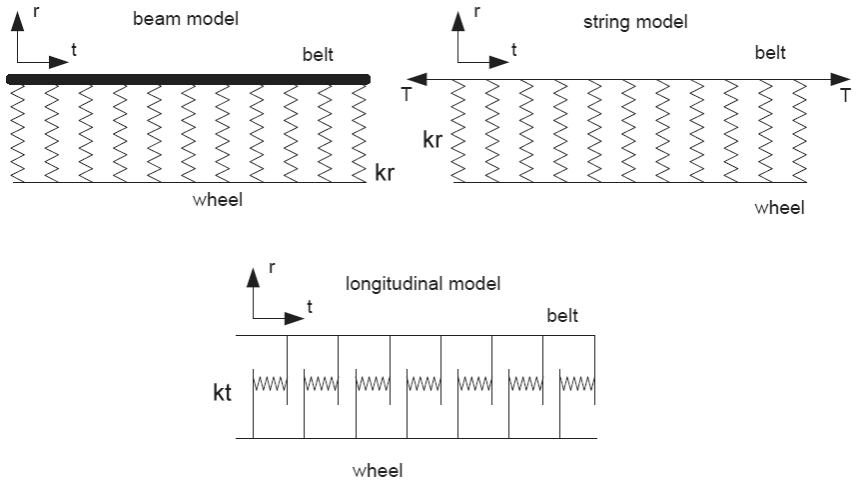

Figure 3.2 – The analytical rectilinear models of the belt radial and tangential deformation.

3.2.1 The string under tension model

The string on elastic foundation is a fundamental model of the radial modal behaviour of the tyre, as it is presented in the review work of Mundl [164], while over the years numerous studies have associated the low frequency range behaviour of the tyre with a string under tension or a membrane mechanism [49, 105]. Perisse *et al* [106] validated experimentally the string-like low order modal behaviour of the tyre. The differential equation of the transverse vibrations of the combined string-sidewall mechanism, normalised to its length, may be written as:

$$-T\frac{\partial^2 u_r}{\partial(s)^2} + k_r \cdot u_r + \rho \cdot A\frac{\partial^2 u_r}{\partial \mathrm{t}^2} = 0 \tag{3.1}$$

where:

T	the string tension force
s	the circumferential length variable
u_r	the belt radial deformation, as analytical function of the circumferential position (s)and the time (t)
$\frac{\partial}{\partial}$	partial derivative
R	the belt radius
θ	the central angle
k_r	the radial sidewall stiffness, normalised to the circumferential length
ρ	the belt material density
A	the cross-section area of the belt
t	the time

The tension force, as induced by the inflation pressure, may be calculated as:

$$T = P_0 \cdot R \cdot b \tag{3.2}$$

P_0 the inflation pressure
b the belt width

It should be highlighted that for the calculation of the string tension force the belt is assumed to retain its circular shape, although this assumption is later dropped in favor of the rectilinear one. The circular assumption permits the expression of the length variable s of the belt arch as a function of the central angle:

$$s = R \cdot \theta \Rightarrow \frac{\partial}{\partial s} = \frac{1}{R}\frac{\partial}{\partial \theta} \tag{3.3}$$

Differential equation 3.93 may be now written as:

$$-\frac{P_0 \cdot b}{R}\frac{\partial^2 u_r}{\partial(\theta)^2} + k_r \cdot u_r + \rho \cdot A\frac{\partial^2 u_r}{\partial \mathrm{t}^2} = 0 \tag{3.4}$$

The above expression is a separable partial differential equation with time and space components. The time function $e^{\iota \cdot \omega \cdot \mathrm{t}}$, where $\iota = \sqrt{-1}$, may be proposed as a solution to the time component. Regarding the space one, a harmonic function is used for the capture of the deformation [243], as a function of the modal number of each mode, which corresponds the number of complete deformation periods along the structure. Moreover, in the present approach such a harmonic function must be able to describe the in-plane deformation of a double axis symmetry structure. For this reason, a characteristic modal concept [83] of the ring models, to be later described, is applied. Every natural frequency or mode is associated with two vibration shapes, being orthogonal to each other. The concept of modes duplicity, although not justified by a rectilinear structure, is essential for the representation of any in-plane orientation of the response:

$$u_r(\theta, \mathrm{t}) = \cos\left(\mathrm{n}(\theta - \varphi)\right) \cdot \mathrm{e}^{\iota \cdot \omega \cdot \mathrm{t}} \tag{3.5}$$

from which the two mode shapes may be derived as:

$$u_r^1(\theta, \mathrm{t}) = \cos\left(\mathrm{n}(\theta - \varphi^1)\right) \cdot \mathrm{e}^{\iota \cdot \omega \cdot \mathrm{t}} \tag{3.6}$$

$$u_r^2(\theta, \mathrm{t}) = \cos\left(\mathrm{n}(\theta - \varphi^2)\right) \cdot \mathrm{e}^{\iota \cdot \omega \cdot \mathrm{t}} \tag{3.7}$$

where:
n the modal number of the mode
ω the natural frequency
φ the mode shape orientation angle

The different orientation angles of the two components of the double mode (φ^1 and φ^2 respectively) enables the rotation of it according to the excitation. The rotation of the response, although it is not predicted by a rectilinear structure, is a vital characteristic of the modal behaviour of a double axis symmetry one. As no particular orientation of the mode shapes of the circular belt is physically preferable, the global orientation of the mode shape couples may be arbitrarily selected. Their necessary property of orthogonality, though, imposes the following relationship to their relative to each other orientation:

$$\varphi^1 - \varphi^2 = \frac{\pi}{2 \cdot n} \tag{3.8}$$

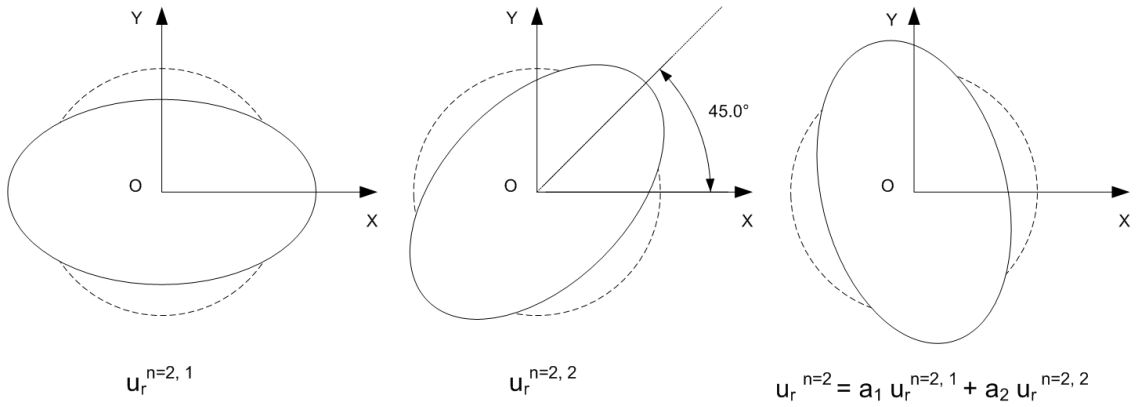

Figure 3.3 – The composition of an arbitrary orientation of the n=2 mode as a linear combination of two modes of certain orientation.

The rotation of a particular mode shape according to the excitation is achieved by the linear combination of the respective components, as it is presented in fig. 3.3.

Substituting the proposed solution to eqn. 3.4, the characteristic equation may be derived, as a second order polynomial equation:

$$\frac{P_0 \cdot b}{R} n^2 + k_r - \omega^2 \cdot \rho \cdot A = 0 \tag{3.9}$$

By solving that the natural frequency of every "double" mode, as a function of the modal number, emerges:

$$\left.\begin{matrix}(3.4)\\(3.5)\end{matrix}\right\} \Rightarrow \omega = \sqrt{\frac{P_0 \cdot b}{R \cdot \rho \cdot A} n^2 + \frac{k_r}{\rho \cdot A}} \tag{3.10}$$

3.2.2 The bending beam model

The equation that describes the transverse vibrations of a bending beam [243], including the distributed radial sidewall stiffness, may be written as:

$$E \cdot I \frac{\partial^4 u_r}{\partial (R \cdot \theta)^4} + k_r \cdot u_r + \rho \cdot A \frac{\partial^2 u_r}{\partial \mathrm{t}^2} = 0 \tag{3.11}$$

where additionally to eqn.3.93:

- E the elastic modulus of the material
- I the cross section second moment of inertia, $I = b \cdot d^3/12$

A solution similar to the above is proposed and the characteristic equation reads:

$$\frac{E \cdot I}{R^4} n^4 + k_r - \omega^2 \rho \cdot A = 0 \tag{3.12}$$

Apparently, the same principles with the string rectilinear model apply in regards to the duplicity of the mode shapes. The natural frequencies of the modes are given by the following equation:

$$\omega = \sqrt{\frac{E \cdot I}{R^4 \cdot \rho \cdot A} n^4 + \frac{k_r}{\rho \cdot A}} \tag{3.13}$$

3.2.3 The combination of the string and beam models

As both string and bending mechanisms contribute to the actual modal behaviour of the tyre belt, an obvious next step is the combination of both mechanisms in one model. The respective equation reads:

$$\frac{E \cdot I}{R^4} \frac{\partial^4 u_r}{\partial \theta^4} + \frac{P_0 \cdot b}{R^2} \frac{\partial^2 u_r}{\partial \theta^2} + k_r \cdot u_r + \rho \cdot A \frac{\partial^2 u_r}{\partial \mathrm{t}^2} = 0 \tag{3.14}$$

while the respective natural frequencies are given by the equation:

$$\omega = \sqrt{\frac{E \cdot I}{R^4 \cdot \rho \cdot A} n^4 + \frac{P_0 \cdot b}{R \cdot \rho \cdot A} n^2 + \frac{k_r}{\rho \cdot A}} \tag{3.15}$$

3.2.4 The tangential modes of the rectilinear models

In the above rectilinear approaches, the vertical/radial modes of vibration were presented. Although a horizontal/tangential vibrations model may be adopted, this will correspond to an independent modal behaviour, not coupled or interacting with the first one. The longitudinal vibration behaviour of a prismatic bar [243] is proposed, which, with the inclusion of a tangential distributed stiffness foundation, reads:

$$-E \cdot A \frac{\partial^2 u_t}{\partial s^2} + k_t \cdot u_t + \rho \cdot A \frac{\partial^2 u_t}{\partial \mathrm{t}^2} = 0 \tag{3.16}$$

where:

u_t the belt tangential deformation, as analytical function of the circumferential position (s)and the time (t)

k_t tangential sidewall stiffness, normalised to the circumference length

A solution form similar to the radial one is proposed for the derivation of the tangential modes. The respective natural frequencies are given by the equation:

$$\omega = \sqrt{\frac{E}{R \cdot \rho} n^2 + \frac{k_t}{\rho \cdot A}} \tag{3.17}$$

3.3 Analytical circular models

The main difference between the rectilinear representations and the circular ones is that in the second case the interaction between the radial and the tangential deformation of the structure is included in the model. The ring model is the most established representative of this approach, which captures the coupling between the bending behaviour in the radial direction and the extensional one in the tangential direction. The ring equations of motion may be derived from a sequence of simplifications applied on the thin shell equations, imposed by an in-plane, closed structure of steady curvature [83]. As, though, different simplification methods

have been proposed for the derivation of the thin shell equations from the solid body ones, many variations of the ring model exist. A systematic survey of the various thin shell modelling concepts may be found in [84]. The approach proposed by Love [244] and extended by Soedel [83] will be used in this study. Love's equations of motion of an one-dimensional (arch) thin shell of revolution [83] read:

$$-\frac{\partial^2 M_{ss}}{\partial s^2} + \frac{1}{R_s} N_{ss} + \rho \cdot d \frac{\partial^2 u_r}{\partial t^2} = 0; \tag{3.18a}$$

$$-\frac{\partial N_{ss}}{\partial s} - \frac{1}{R_s} \frac{\partial M_{ss}}{\partial s} + \rho \cdot d \frac{\partial^2 u_t}{\partial t^2} = 0; \tag{3.18b}$$

where:

N_{ss}	the tension (membrane) pressure of the arch
M_{ss}	the bending moment of the arch, normalised to its length and width
s	the length variable along its central axis
R_s	the curvature radius of the arch

The above force and moment terms correspond to the following strains:

$$\kappa_{ss} = \frac{M_{ss}}{D^*} \tag{3.19a}$$

$$\epsilon_{ss} = \frac{N_{ss}}{K^*} \tag{3.19b}$$

where:

D^*	the bending stiffness
K^*	the tension (membrane) stiffness
κ_{ss}	the bending strain
ϵ_{ss}	the tension (membrane) strain

The above stiffness values are functions of the material properties and the dimensions of the structure:

$$D^* = \frac{E \cdot d^3}{12} \tag{3.20a}$$

$$K^* = E \cdot d \tag{3.20b}$$

where d is the height (on the radial direction) of the belt cross section. The strain and deformation terms are coupled using the following equations:

$$k_{ss} = -\frac{\partial^2 u_r}{\partial s^2} + \frac{1}{R_s} \frac{\partial u_t}{\partial s} \tag{3.21a}$$

$$\epsilon_{ss} = \frac{\partial u_t}{\partial s} + \frac{1}{R_s} u_r \tag{3.21b}$$

Eqns. 3.21 capture the coupling between the two deformation patterns predicted by the ring model, the radial and the tangential one. The effect of this coupling on the modal behaviour of the model will be analysed in the following sections.

The arch radius of curvature along the ring circumference is constant ($R = R_s$) and the position coordinate (s) may be deduced to a respective angular one, as it has already been assumed for the rectilinear models. For reasons of agreement of the equations form to the rectilinear models one, the effect of the width of the ring cross section (b), is introduced in the equations:

$$D = D^* \cdot b \tag{3.22a}$$

$$K = K^* \cdot b \tag{3.22b}$$

The ring equations of motion (3.18) may be written as:

$$\frac{D}{R^4}\left(\frac{\partial^4 u_r}{\partial\theta^4} - \frac{\partial^3 u_t}{\partial\theta^3}\right) + \frac{K}{R^2}\left(u_r + \frac{\partial u_t}{\partial\theta}\right) + k_r \cdot u_r + \rho \cdot A\frac{\partial^2 u_r}{\partial \mathrm{t}^2} = 0 \tag{3.23a}$$

$$\frac{D}{R^4}\left(\frac{\partial^3 u_r}{\partial\theta^3} - \frac{\partial^2 u_t}{\partial\theta^2}\right) - \frac{K}{R^2}\left(\frac{\partial u_r}{\partial\theta} + \frac{\partial^2 u_t}{\partial\theta^2}\right) + k_t \cdot u_t + \rho \cdot A\frac{\partial^2 u_t}{\partial \mathrm{t}^2} = 0 \tag{3.23b}$$

The above couple is a linear system of separable partial differential equations, and each of them may be separated into one time and one spatial component, in which both radial and tangential deformations are present. The proposed solutions read:

$$u_r(\theta, \mathrm{t}) = \mathrm{U_r}(\theta) \cdot \mathrm{e}^{\iota\omega\cdot\mathrm{t}} = \mathrm{R^m} \cdot \cos\left(\mathrm{n}(\theta - \varphi)\right) \cdot \mathrm{e}^{\iota\omega\cdot\mathrm{t}} \tag{3.24a}$$

$$u_t(\theta, \mathrm{t}) = \mathrm{U_t}(\theta) \cdot \mathrm{e}^{\iota\omega\cdot\mathrm{t}} = \mathrm{T^m} \cdot \sin(\mathrm{n}(\theta - \varphi)) \cdot \mathrm{e}^{\iota\omega\cdot\mathrm{t}} \tag{3.24b}$$

where:

U	belt deformation, as analytical function of the circumferential position (θ)
R^m	the radial deformation amplitude of the mode shape
T^m	the tangential deformation amplitude of the mode shape

The co-existence of both radial and tangential deformations in the mode shapes of a mode is the significant difference of this approach from the rectilinear ones. In the latter ones, as the modes were independently associated with pure vertical or horizontal deformation, the deformation amplitude of each mode shape could be arbitrarily chosen and was assumed as equal to unit. In the case of the circular models, though, as every mode is associated with both of the deformation patterns, the terms R^m and T^m may be still arbitrarily chosen but their ratio is a characteristic property of each mode. Substituting the deformation expressions (eqn. 3.147) in the system of the equations of motion 3.23 and rewriting them in a matrix form, it is derived:

$$\begin{bmatrix} C_1 & C_2 \\ C_3 & C_4 \end{bmatrix} \times \begin{bmatrix} R^m \\ T^m \end{bmatrix} = \begin{bmatrix} 0 \\ 0 \end{bmatrix} \tag{3.25}$$

where:

$$C_1 = \frac{D}{R^4}n^4 + \frac{K}{R^2} + k_r - \rho \cdot A \cdot \omega^2 \tag{3.26}$$

$$C_2 = C_3 = \frac{D}{R^4}n^3 + \frac{K}{R^2}n \tag{3.27}$$

$$C_4 = \left(\frac{D}{R^4} + \frac{K}{R^2}\right)n^2 + k_t - \rho \cdot A \cdot \omega^2 \tag{3.28}$$

Setting the determinant of the coefficient matrix of eqn. 3.25 equal to zero, the characteristic equation of the system is derived:

$$\begin{vmatrix} C_1 & C_2 \\ C_3 & C_4 \end{vmatrix} = 0 \Rightarrow C_1 \cdot C_4 - C_2 \cdot C_3 = 0 \Rightarrow \Lambda_4 \cdot \omega^4 + \Lambda_2 \cdot \omega^2 + \Lambda_0 = 0 \tag{3.29}$$

where:

$$\Lambda_4 = \rho \cdot A^2 \tag{3.30}$$

$$\Lambda_2 = -\rho \cdot A\frac{D}{R^4}n^4 - \rho \cdot A\left(\frac{D}{R^4} + \frac{K}{R^2}\right)n^2 - \rho \cdot A\left(\frac{K}{R^2} + k_r + k_t\right) \tag{3.31}$$

$$\Lambda_0 = \left(\frac{D\left(\frac{D}{R^4} + \frac{K}{R^2}\right)}{R^4} - \frac{D^2}{R^8}\right)n^6 + \left(\frac{D \cdot k_t}{R^4} - \frac{2 \cdot D \cdot K}{R^6}\right)n^4 \tag{3.32}$$

$$+ \left(\left(\frac{D}{R^4} + \frac{K}{R^2}\right) \cdot \left(k_r + \frac{K}{R^2}\right) - \frac{K^2}{R^4}\right)n^2 + k_t\left(k_r + \frac{K}{R^2}\right) \tag{3.33}$$

A conceptual difference between the rectilinear and the circular models is the order of the corresponding characteristic equations. The ring model equation is a fourth order polynomial one in respect to ω_j which may be written as a second order one in respect to ω_j^2. In result, four vibration modes are associated with each modal number, which emerge, though, as two modal couples. The two modes of each modal couple, share the same natural frequency and similar mode shapes rotated to each other to an orthogonality derived angle, in agreement with the double modes concept discussed in the rectilinear models analysis. The two couples, though, are associated with different natural frequencies and different mode shapes, in respect to their radial to tangential deformations ratio. The frequencies of the modal couples are given by:

$$\omega_1^2 = \frac{B - \sqrt{\Delta}}{2 \cdot A \cdot R^4 \cdot \rho} \tag{3.34a}$$

$$\omega_2^2 = \frac{B + \sqrt{\Delta}}{2 \cdot A \cdot R^4 \cdot \rho} \tag{3.34b}$$

where:

$$B = D \cdot n^4 + (D + K \cdot R^2)n^2 + K \cdot R^2 + R^4(k_r + k_t) \tag{3.35a}$$

and:

$$\begin{aligned}\Delta = & D^2 \cdot n^8 + (2 \cdot D^2 - 2 \cdot D \cdot K \cdot R^2) n^6 \\ & + \big(D^2 + K^2 \cdot R^4 + 12 \cdot D \cdot K \cdot R^2 + 2 \cdot D \cdot R^4 (k_r - k_t)\big) n^4 \\ & + \big(2 \cdot K^2 \cdot R^4 - 2 \cdot D \cdot K \cdot R^2 - 2 \cdot R^4 (D + K \cdot R^2)(k_r - k_t)\big) n^2 \\ & R^4 \big(K + R^2 (k_r - k_t)\big)^2\end{aligned} \tag{3.35b}$$

Typically, the double mode associated with the low frequency value, ω_1, exhibits a predominant radial deformation, while the double mode associated with the high frequency value, ω_2, is mainly associated with the tangential deformation. For this reason the modes corresponding to the first value are named radial ones, while the modes corresponding to the second value are named tangential ones. This correspondence will be also followed in the present study and the indices 1 and 2 will be substituted by *rad* and *tang* from now on. Substituting the calculated natural frequencies to one of the eqns. 3.25 the ratio of the radial to the tangential deformation amplitudes (T^m/R^m) of every mode may be calculated:

$$(\rho \cdot A \cdot \omega^2 + C_1) R^m + C_2 \cdot T^m = 0 \tag{3.36a}$$

$$C_3 \cdot R^m + (\rho \cdot A \cdot \omega^2 + C_4) T^m = 0 \tag{3.36b}$$

It may be derived for the two mode shapes of every modal number n:

$$\left(\frac{T^m}{R^m}\right)_{rad} = \frac{B_s - \sqrt{\Delta_s}}{2\left(\frac{D\cdot}{R^2} n^3 + K \cdot n\right)} \tag{3.37a}$$

$$\left(\frac{T^m}{R^m}\right)_{tang} = \frac{B_s + \sqrt{\Delta_s}}{2\left(\frac{D\cdot}{R^2} n^3 + K \cdot n\right)} \tag{3.37b}$$

where:

$$B_s = -\frac{D}{R^2} n^4 + \left(K + \frac{D}{R^2}\right) n^2 - K - R^2 (k_r - k_t) \tag{3.38}$$

and

$$\Delta_s = \frac{\Delta_n}{R^4} \tag{3.39}$$

The first five radial and tangential mode shapes are presented in fig. 3.4.

3.3.1 The zero modes of the ring

The modal number (n_j) of the jth mode prescribes the number of the complete periods of the characteristic deformation which can be identified along the ring circumference in the associated mode shape. This number

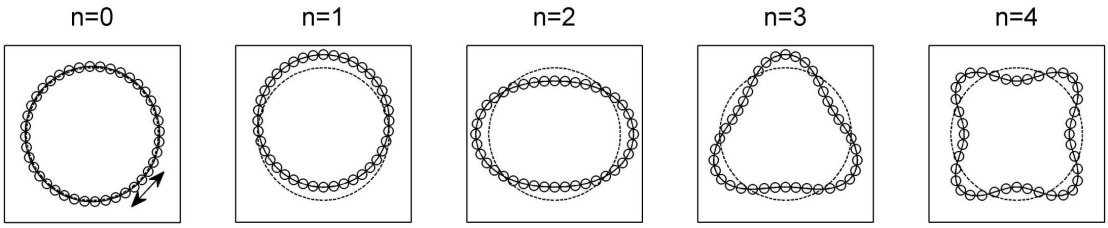

(a) radial mode shapes

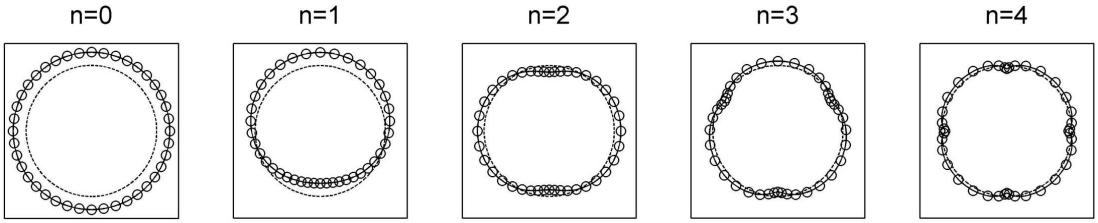

(b) tangential mode shapes

Figure 3.4 – Ring model mode shapes

is the same for both the radial and the tangential deformations of the mode(fig. 3.4). The examination of the zero modes, though, requires a slightly different approach. The substitution of $n = 0$ in the mode shape functions (eqns. 3.147) leads to:

$$u_r^{n=0} = R_{n=0}^m \cdot \cos\big(0(\theta - \varphi)\big) = R_{n=0}^m \tag{3.40a}$$

$$u_t^{n=0} = T_{n=0}^m \cdot \sin\big(0(\theta - \varphi)\big) = 0 \tag{3.40b}$$

The modal calculation resulting from the above substitution, though, is not complete, as it can only predict one zero mode corresponding to a constant radial deformation and another zero mode corresponding to a tangential one.Every mode of a double axis symmetry structure evolves as a double one, with the same frequency but orthogonal mode shapes. The orientation angle φ of them can be arbitrarily selected as long as the relative to each other orthogonality condition is satisfied:

$$\varphi^2 = \varphi^1 - \frac{\pi}{2 \cdot n} \tag{3.41}$$

Accordingly, the corresponding to the angle φ_1 mode shape functions may be now written as:

$$u_r^{n=0,\varphi^1} = R_{n=0}^m \cdot \cos\big(0(\theta - \varphi^1)\big) = R_{n=0}^m \tag{3.42a}$$

$$u_t^{n=0,\varphi^1} = T_{n=0}^m \cdot \sin\big(0(\theta - \varphi^1)\big) = 0 \tag{3.42b}$$

The corresponding to the angle φ^2 mode shape functions can be written as:

$$u_r^{n=0,\varphi^2} = R_{n=0}^m \cdot \cos\big(n(\theta - \varphi^2)\big) = R_{n=0}^m \cdot \cos\left(n \cdot \theta - n \cdot \varphi^1 + \frac{n \cdot \pi}{2 \cdot n}\right) = R_{n=0}^m \cdot \cos\left(n \cdot \theta - n \cdot \varphi^1 + \frac{\pi}{2}\right) \tag{3.43a}$$

$$u_t^{n=0,\varphi^2} = T_{n=0}^m \cdot \sin\left(n(\theta - \varphi^2)\right) = T_{n=0}^m \cdot \sin\left(n \cdot \theta - n \cdot \varphi^1 + \frac{n \cdot \pi}{2 \cdot n}\right) = T_{n=0}^m \cdot \sin\left(n \cdot \theta - n \cdot \varphi^1 + \frac{\pi}{2}\right) \quad (3.43b)$$

and substituting $n = 0$ in the above:

$$u_r^{n=0,\varphi_2} = R_{n=0}^m \cdot \cos\frac{\pi}{2} = 0 \quad (3.44a)$$

$$u_t^{n=0,\varphi_2} = T_{n=0}^m \cdot \sin\frac{\pi}{2} = T_{n=0}^m \quad (3.44b)$$

In conclusion, one of the zero modes exhibits constant radial deformation but zero tangential one, while the second zero mode exhibits constant tangential deformation but zero radial one. Substitution of $n = 0$ in eqns 3.28 leads to:

$$C_1 = -\frac{K}{R^2} - k_r \quad (3.45)$$

$$C_2 = C_3 = 0 \quad (3.46)$$

$$C_4 = -k_t \quad (3.47)$$

$$(3.48)$$

The characteristic equation is expressed as:

$$(\rho \cdot A)^2 \omega_{n=0}^4 + \rho \cdot A(C_1 + C_4)\omega_{n=0}^2 + C_1 \cdot C_4 = 0 \quad (3.49)$$

$$(\rho \cdot A\omega_{n=0}^2 + C_4) \cdot (\rho \cdot A\omega_{n=0}^2 + C_1) = 0 \quad (3.50)$$

and the corresponding frequencies are:

$$\omega_1^{n=0} = \sqrt{\frac{k_t}{\rho \cdot A}} \quad (3.51a)$$

$$\omega_2^{n=0} = \sqrt{\frac{K + k_r \cdot R^2}{R^2 \cdot \rho \cdot A}} \quad (3.51b)$$

The radial zero mode frequency ($\omega_1^{n=0}$) is a function of the tangential sidewall stiffness only, while the tangential zero mode frequency ($\omega_2^{n=0}$) is a function of the ring membrane stiffness and the radial sidewall one. Examining the associated mode shapes, the fact that $C_2 = C_3 = 0$ and the form of the characteristic equation (3.50), allow only one of the eqns. 3.36 to be able to predict the mode shape of each of the zero mode frequencies, as the other transforms into an identity. In result, the constant deformation of each of the zero modes refers to the supplementary deformation pattern to the one it is named after. The radial zero mode (eqn. 3.51a) exhibits constant tangential deformation (eqn. 3.44), while the tangential zero mode (eqn. 3.51b) exhibits constant radial one (eqn. 3.42). Both of them are presented in fig. 3.4.

3.3.2 The rigid modes of the ring

In the previous analysis, the ring model was theoretically attached to a fixed wheel through the sidewall stiffness foundation. The omission of this foundation enables the free in-plane motion of the ring, which is composed by a rotational and a translational component. In regards to the predicted modal behaviour, the ring free motion corresponds to two of the frequencies having zero values, while the associated mode shapes express the free motion of the ring. The term rigid is used for these modes, as no ring deformation is developed.

Examining the mode shapes in fig. 3.4, it could be proposed that the rotational rigid mode emerges from the radial $n = 0$ one, by the omission of the tangential sidewall stiffness. The omission or not of the radial stiffness does not affect the particular mode, as it is not associated with any radial motion or deformation. The translational rigid mode evolves from the $n = 1$ mode and its prediction necessitates the omission of both of the sidewall foundations. Substituting $n = 1$, $k_r = 0$ and $k_t = 0$ in eqn. 3.34, it is derived:

$$\omega_1^{n=1} = 0 \tag{3.52a}$$

$$\omega_2^{n=1} = \frac{2 \cdot K \cdot R^2 + 2 \cdot D}{R^4 \cdot \rho \cdot A} \tag{3.52b}$$

Obviously the translational rigid modes emerges from the first, (radial $n = 1$) mode. Although the tangential $n = 1$ mode is affected by the sidewall omission, it still corresponds to a stress/strain (deformational) condition for the ring.

The rigid modes prediction capability is a crucial characteristic of the ring model, especially if it is combined with a non-linear sidewall structure. In that case, the linear foundation is omitted and the sidewall effect is imposed to the ring as a force excitation. Although the above, simple, form of the ring equations of motion predicts the rigid modes, more complicated ring models, as it will be later discussed, have to be carefully examined in respect to this characteristic.

3.3.3 The pretension effect

The ring model may capture the bending mechanism of the tyre belt and the circularity induced interaction between the radial and the tangential deformations, the actual modal behaviour of the tyre, though, incorporates another major mechanism, the membrane one, induced by the inflation pretension. As it has been discussed in section 2.1 and in various published studies [105, 106, 183], the low frequency range modal behaviour of the tyre is defined by the inflation pretension effects and this behaviour is captured by various implementations of the string/membrane mechanisms in the model. Although the inflation dependent behaviour is usually associated with the sidewall mechanism, its effect on the circumferential belt behaviour cannot be neglected. Only the latter one will be examined here, while a sidewall inflation dependent physical mechanism will be later presented.

Many different methods have been proposed for the incorporation of the pretension induced non linearity in the ring model, in accordance to the various forms of its equations of motion and a comprehensive analysis of the topic may be found in the classic work of Leissa [84]. In the majority of the ring model studies ([119, 79, 245, 123] the incorporation of the pretension effect follows the approach described by Endo *et al* in [89] or by Huang and Soedel in [96]. According to this approach, an additional, inflation pressure

(P_0) induced, strain term is incorporated in the model, which is given by the following equation:

$$\epsilon_{ss}^{pretension} = \frac{1}{2R^2} \quad \left(u_r + \frac{\partial u_t}{\partial \theta}\right)^2 + (\frac{\partial u_r}{\partial \theta} - u_t)^2\Bigg) \tag{3.53}$$

The actual derivation of the pretensioned ring equations of motion can be found in [84, 96, 83, 100] and is omitted from the presentation. Their final form reads:

$$\frac{D}{R^4}\left(\frac{\partial^4 u_r}{\partial \theta^4} - \frac{\partial^3 u_t}{\partial \theta^3}\right) + \frac{K}{R^2}\left(u_r + \frac{\partial u_t}{\partial \theta}\right) \underline{+\frac{P_0 \cdot b}{R}\left(u_r + 2\frac{\partial u_t}{\partial \theta} - \frac{\partial^2 u_r}{\partial \theta}\right)} + k_r \cdot u_r + \rho \cdot A\frac{\partial^2 u_r}{\partial \mathrm{t}^2} = 0 \tag{3.54a}$$

$$\frac{D}{R^4}\left(\frac{\partial^3 u_r}{\partial \theta^3} - \frac{\partial^2 u_t}{\partial \theta^2}\right) - \frac{K}{R^2}\left(\frac{\partial u_r}{\partial \theta} + \frac{\partial^2 u_t}{\partial \theta^2}\right) \underline{+\frac{P_0 \cdot b}{R}\left(u_t - 2\frac{\partial u_r}{\partial \theta} - \frac{\partial^2 u_t}{\partial \theta}\right)} + k_t \cdot u_t + \rho \cdot A\frac{\partial^2 u_t}{\partial \mathrm{t}^2} = 0 \tag{3.54b}$$

where the underlined terms correspond to the pretension effect. The frequencies of the modes, radial and tangential, associated with every modal number are given by eqn. 3.34, where the B_n and Δ_n terms may be expressed as functions of the corresponding non pretensioned terms according to the following equations:

$$B^{pretension} = B + 2 \cdot P_0 \cdot b \cdot R^3 \cdot (n^2 + 1) \tag{3.55}$$

$$\Delta^{pretension} = \Delta + 16 \cdot R^3 \cdot P_0 \cdot b \cdot n^2 (P_0 \cdot b \cdot R^3 + n^2 \cdot D + K \cdot R^2) \tag{3.56}$$

while the mode shapes are given by eqn. 3.36, the B_s and Δ_s terms of which are:

$$B_s^{pretension} = B_s \frac{n^2 \cdot D + K \cdot R^2}{n^2 \cdot D + K \cdot R^2 + 2 \cdot P_0 \cdot b \cdot R^3} \tag{3.57}$$

$$\begin{aligned} \Delta_s^{pretension} =& \Delta_s - \frac{4 \cdot P_0 \cdot b \cdot (K \cdot R^2 - n^2 \cdot K \cdot R^2 + k_r \cdot R^4 - k_t \cdot R^4 - n^2 \cdot D + D \cdot n^4)^2}{R \cdot (n^2 \cdot D + K \cdot R^2 + 2 \cdot P_0 \cdot b \cdot R^3)^2} \\ & \cdot (n^2 \cdot D + P_0 \cdot b \cdot R^3 + K \cdot R^2) \end{aligned} \tag{3.58}$$

The above method, though, introduces an anomaly in the predicted modal behaviour, which usually remains unnoticed by the ring model studies. As it is obvious in the pretensioned equations of motion (3.54), the pretension factor $P_0 \cdot b/R$ is multiplied with non derivated deformation terms (u_r and u_t), in a similar way to the sidewall stiffness factors (k_r and k_t). Consequently, the ring rigid modes cannot be anymore predicted by the omission of the sidewall stiffness. The torsional mode (radial $n = 0$) frequency for the pretensioned model is given by the equation:

$$\omega_1^{n=0} = \sqrt{\frac{k_t}{\rho \cdot A} + \frac{P_0 \cdot b}{R \cdot \rho \cdot A}} \tag{3.59}$$

A non zero frequency is obviously predicted in the case of the tangential sidewall omission. Similarly, the substitution of $n = 1$, $k_r = 0$,$k_t = 0$ in eqn. 3.34a for the pretensioned case leads to:

$$\omega_1^{n=1} = \frac{P_0 \cdot b}{A \cdot R \cdot \rho} \neq 0 \tag{3.60}$$

The drawn conclusion is that the sidewall stiffness-like incorporation of the pretension effect prevents the prediction of both of rigid modes of the ring, in case the sidewall foundation is omitted.

In case the above terms are dropped from the equations of motion, the rotational rigid mode prediction is re-established, but a new anomaly in the prediction of the translational rigid one is generated. An imaginary, instead of zero, value is predicted for the $\omega_{1|rad}$ frequency. The same anomaly is introduced by the possible omission of the respective deformation term only from the tangential equation of motion(3.54b). Furthermore, as it is concluded by Leissa [84], many ring models fail to predict the existence of the rigid modes, even without the incorporation of the pretension effect. The experimental results presented in the same work, though, reveal that the effect of the pretension not only on the $n = 0$ and $n = 1$ modes but on the whole low frequency range is insignificant. In conclusion, the complete omission of the pretension effect from the $n = 0$ and $n = 1$ modes could be proposed for the rigid mode prediction capability re-establishment, without the introduction of a significant computational error.

3.3.4 The inextensibility assumption

A very common ([60, 122, 80]), experimentally validated, simplification of the analytical ring model is the inextensibility assumption, which was introduced by Tielking in [71]. According to it, the membrane strain of the ring is omitted and the radial and tangential deformations are additionally coupled by the following equation:

$$u_r = -\frac{\partial u_t}{\partial \theta} \tag{3.61}$$

The derivation of the ring equations of motion under the inextensible assumption has been presented by Soedel [83] for the simple, excluding the pretension and sidewall effects, case. Here, the equations of motion of the inextensible model, including the above effects will be derived, so that its modal characteristics may be directly compared to the respective ones of the extensible model. As the membrane strain is suspended, the terms that correspond to it have to be eliminated from the equations of motion 3.18. In order to do so, eqn. 3.54a is solved for the tension stress corresponding terms. The time derivative of the expression is then substituted in eqn.3.54b. In detail:

$$(3.54a) \Rightarrow \frac{K}{R^2}\left(\frac{\partial u_t}{\partial \theta} + u_r\right) = -\frac{D}{R^4}\left(\frac{\partial^4 u_r}{\partial \theta^4} - \frac{\partial^3 u_t}{\partial \theta^3}\right) - \frac{P_0 \cdot b}{R}\left(u_r + 2\frac{\partial u_t}{\partial \theta} - \frac{\partial^2 u_r}{\partial \theta^2}\right) - k_r \cdot u_r - \rho \cdot A \frac{\partial^2 u_r}{\partial \mathrm{t}^2} \tag{3.62}$$

$$\Rightarrow \frac{K}{R^2}\left(\frac{\partial u_r}{\partial \theta} + \frac{\partial^2 u_t}{\partial \theta^2}\right) = -\frac{D}{R^4}\left(\frac{\partial^5 u_r}{\partial \theta^5} - \frac{\partial^4 u_t}{\partial \theta^4}\right) - \frac{P_0 \cdot b}{R}\left(\frac{\partial u_r}{\partial \theta} + 2\frac{\partial^2 u_t}{\partial \theta^2} - \frac{\partial^3 u_r}{\partial \theta^3}\right) - k_r \frac{\partial u_r}{\partial \theta} - \rho \cdot A \frac{\partial^2 u_r}{\partial \mathrm{t}^2} \tag{3.63}$$

$$\left\{ \begin{array}{c} (3.54b) \\ (3.63) \end{array} \right\} \Rightarrow$$

$$\frac{D}{R^4}\left(\frac{\partial^6 u_t}{\partial \theta^6} + 2\frac{\partial^4 u_t}{\partial \theta^4} + \frac{\partial^2 u_t}{\partial \theta^2}\right) + \frac{P_0 \cdot b}{R}\left(\frac{\partial^4 u_t}{\partial \theta^4} + 2\frac{\partial^2 u_t}{\partial \theta^2} + u_t\right) - k_r \frac{\partial^2 u_t}{\partial \theta} + k_t \cdot u_t + \rho \cdot A\left(\frac{\partial^2 u_t}{\partial t^2} - \frac{\partial^4 u_t}{\partial \theta^2 \partial \mathrm{t}^2}\right) \tag{3.64}$$

As it is evident from eqn. 3.64 the inextensibility assumption reduces the system of the equations of motion to one equation. The derived equation of motion is a sixth order one if it is expressed as a function

Model Physical Properties[a]			
elastic modulus	E	$[\frac{kg}{m \cdot s}]$	10.4×10^9
density	ρ	$[\frac{kg}{m^3}]$	8.1×10^3
radius	r	$[m]$	0.3
belt section height	d	$[m]$	3.1×10^{-3}
belt section width	b	$[m]$	15.2×10^{-2}
inflation pressure	P_0	$[Pa]$	2.2×10^5
radial sidewall stiffness	k_r	$[\frac{kg}{m \cdot s^2}]$	192.9×10^6
tangential sidewall stiffness	k_t	$[\frac{kg}{m \cdot s^2}]$	648.7×10^5

[a] after [76]

Table 3.1 – The physical properties of the model.

of the tangential deformation or a fifth order one if it is expressed as a function of radial deformation. Following the usual procedure, a harmonic function may be proposed for the mode shape deformation description. The inextensibility assumption results in the following coupling between the radial and the tangential deformations of the mode:

$$\left\{ \begin{array}{c} u_t(\theta, \mathrm{t}) = \mathrm{T^m} \cdot \sin\big(\mathrm{n}(\theta - \varphi)\big) \cdot \mathrm{e}^{\iota \cdot \omega \cdot \mathrm{t}} \\ u_r(\theta, \mathrm{t}) = -\dfrac{\partial \mathrm{u_t}}{\partial \theta} \end{array} \right\} \Rightarrow \left\{ \begin{array}{c} u_t(\theta, \mathrm{t}) = \mathrm{T^m} \cdot \sin\big(\mathrm{n}(\theta - \varphi)\big) \cdot \mathrm{e}^{\iota \cdot \omega \cdot \mathrm{t}} \\ u_r = -n \cdot T^m \cdot \cos\big(n(\theta - \varphi)\big) \cdot e^{\iota \cdot \omega \cdot \mathrm{t}} \end{array} \right\} \tag{3.65}$$

The ratio of the radial to the tangential mode shape amplitudes is equal to the modal number of the mode:

$$\frac{R^m}{T^m} = \frac{-n \cdot T^m}{T^m} = -n \tag{3.66}$$

In regards to the zero modes, the inextensibility obviously prevents the development of the breathing mode deformation pattern but does not affect the torsional one. Following eqn. 3.66 the radial and the tangential deformations exhibit equal amplitudes for $n = 1$, while for $n > 1$ the tangential component of the mode shape decreases proportionally to the modal number.

The characteristic equation of the inextensible ring model reads:

$$\frac{D}{R^4}(-n^6 + 2n^4 - n^2) + \frac{P_0 \cdot b}{R}(n^4 - n^2 + 1) + k_r \cdot n^2 + k_t + \rho \cdot A(\omega^2 + n^2 \cdot \omega^2) = 0 \tag{3.67}$$

$$\Rightarrow \omega = \sqrt{\frac{\dfrac{E \cdot I}{R^4} n^2(n^2 - 1)^2 + \dfrac{P_0 \cdot b}{R} n^2(n^2 - 1) + k_r \cdot n^2 + k_t + \dfrac{P_0 \cdot b}{R}}{\rho \cdot A(n^2 + 1)}} \tag{3.68}$$

3.4 The modal behaviour prediction of the analytical models

In this section the modal prediction characteristics of the analytical models will be comparatively presented. The modal behaviour imposed by the two basic mechanisms of the rectilinear models will be examined, together with the ring one, in its various forms. The circularity induced coupling between the deformation patterns will be highlighted in regards to its modal contribution and the effect of the model's physical properties will be analysed. The physical properties, which are used in the calculation of the modal characteristics

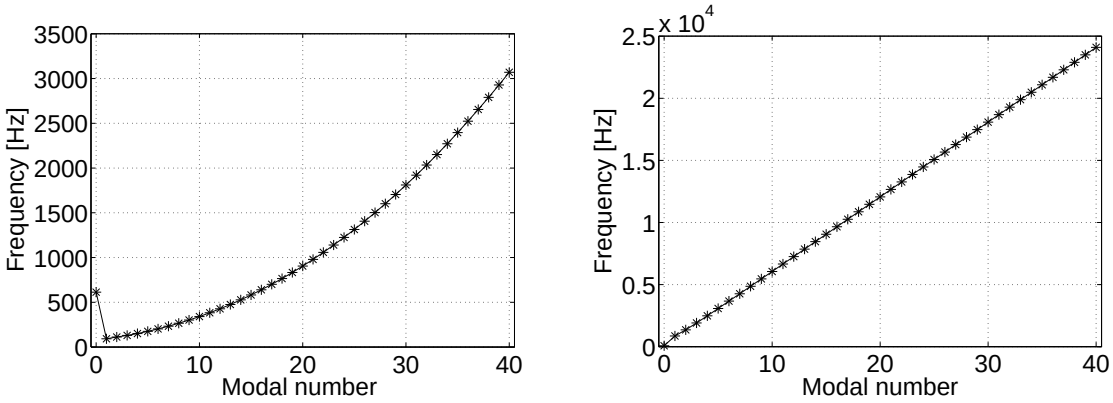

(a) Radial modal group.

(b) Tangential modal group.

Figure 3.5 – The respective frequency ranges of the examined modal groups.

are given in table 3.1.

As it has been discussed in section 3.3.1, the zero modes of the ring exhibit a deformation pattern which is complementary to the one they are named after, (pure radial deformation for the tangential $n = 0$ -breathing mode- and pure tangential deformation for the radial $n = 0$ -torsional mode-). As the main mechanism that affects their mode shape development coincides with the one prescribing the complementary to theirs modal group, zero modes will be examined as belonging to that: the breathing -zero tangential- mode will be incorporated in the radial modal group examination, while the torsional -zero radial- in the tangential one.

The comparison of the models will be accomplished in two stages:

- Firstly, the models will be compared in regards to the predicted natural frequencies.
- Next, the relative development of the radial and the tangential deformations of the circular models will be discussed.

3.4.1 Modal sensitivity analysis of the ring model

In order the ring model to be used as a comparison basis, the physical mechanisms that define its modal behaviour across the frequency range should be identified. This may be accomplished through the capture of the effect of the ring's properties on its modal characteristics and its natural frequencies in particular. Imposing a range of percentage variations (-25% to $+25\%$) to some of the basic physical properties of the model, the corresponding deviation of the natural frequencies along the modal range is monitored and the range in which the influence of each of the properties is dominant is identified. The examined properties are:

- The inflation pressure
- The material elastic modulus
- The sidewall radial stiffness
- The sidewall tangential stiffness

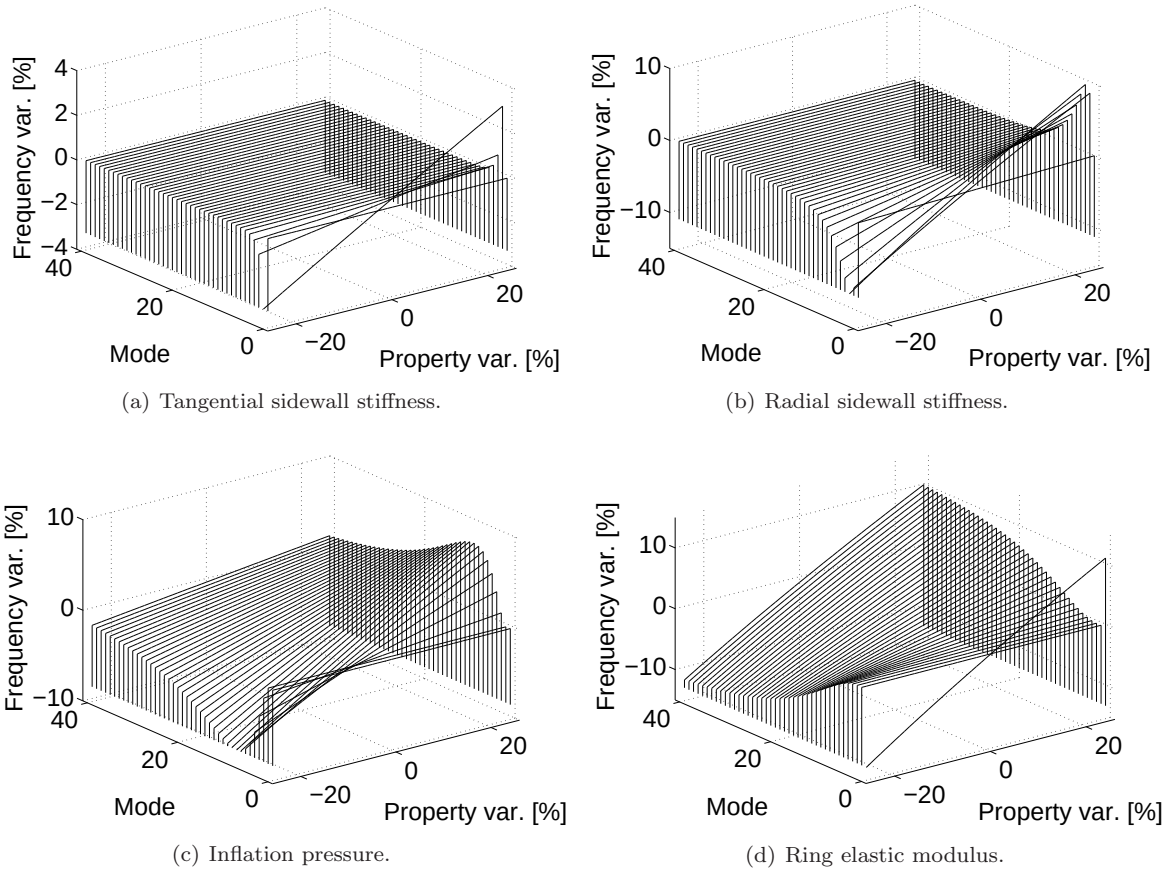

(a) Tangential sidewall stiffness.

(b) Radial sidewall stiffness.

(c) Inflation pressure.

(d) Ring elastic modulus.

Figure 3.6 – The sensitivity of the ring model radial modes to the basic model properties.

The modal range up to the 40th mode, of both the radial and the tangential modes will be examined, as this range has been found capable of capturing the influence of the properties, without though, this range being indicative of a sufficient tyre modelling breadth, something that will be examined in the following chapters. The sensitivity analysis will be presented in regards to the modal number of the modes and the respective frequencies of them are presented in fig. 3.5.

Radial modes sensitivity

The sensitivity of the frequencies of the radial modes is firstly examined, in fig. 3.6, where the zero -breathing- mode is also included. It is obvious that each of the properties can be associated with a certain zone of the modal range, in which its influence is predominant. Tangential sidewall stiffness affects the natural frequencies of the first few modes only. The highest influence is identified for the $n = 2$ mode, and the effect can be neglected for the $n > 3$ modes. The radial sidewall stiffness is the predominant property in the next zone,the corresponding variation to which reaches its maximum value for the n=3 mode, but covers a broader range (up to the $n = 10$ mode) than the tangential one. The effect of inflation pressure becomes predominant in the low to medium modal range, with maximum variation identified around the $n = 10$ mode, while significant dependence can be observed up to the $n = 20$ mode. The elastic modulus of the material has

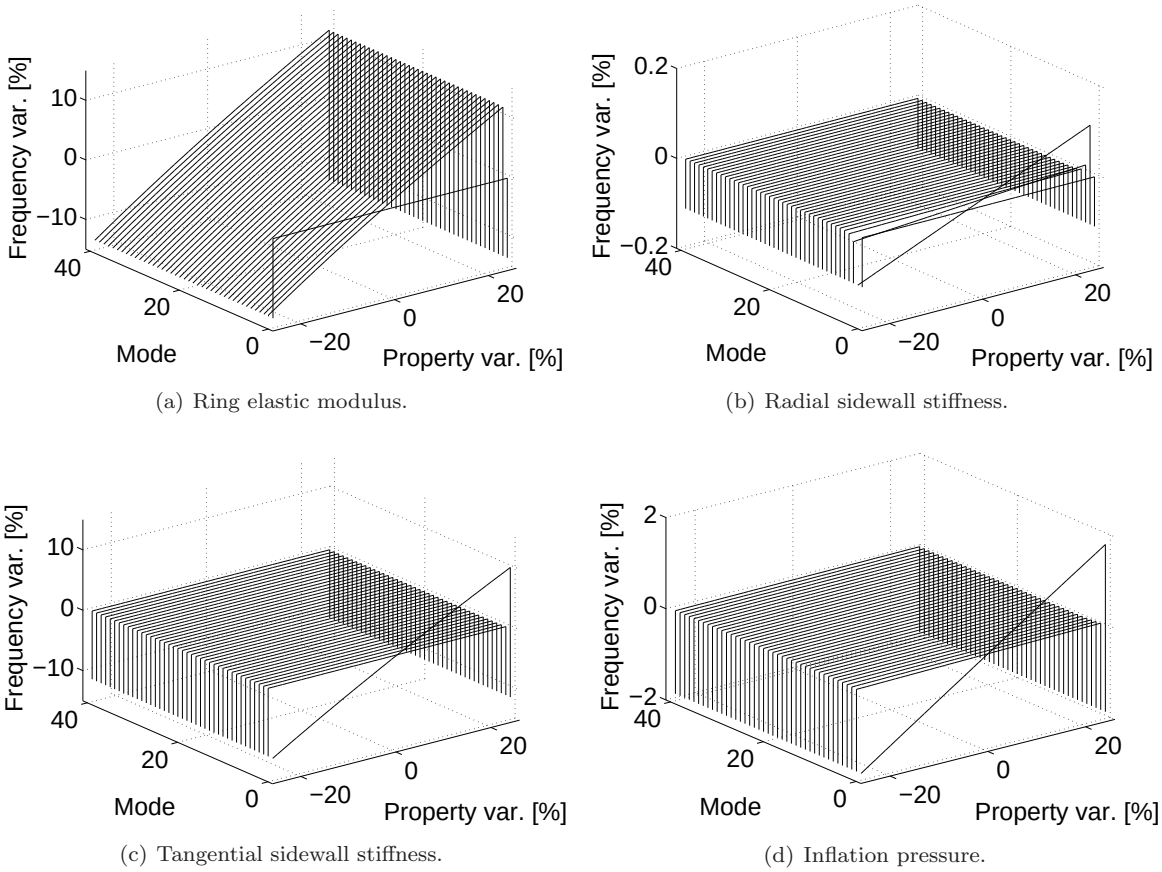

(a) Ring elastic modulus.

(b) Radial sidewall stiffness.

(c) Tangential sidewall stiffness.

(d) Inflation pressure.

Figure 3.7 – The sensitivity of the ring model tangential modes to the basic model properties.

an asymptotically increasing effect with modal number, being the sole frequency factor in the $n > 20$ modal range. Its effect is insignificant in the low modal range, apart from the breathing mode, the frequency of which is controlled by the elastic modulus and insignificantly affected by the radial sidewall stiffness property. The above analysis is in agreement with the experimental tyre model identification procedure, presented in [106]. According to that, pretension (expressed in the ring model by the sidewall and the inflation effect) is the dominant property when it comes to low frequency modal behaviour, while bending stiffness (property directly proportional to the material elastic modulus) dominates higher frequencies.

Tangential modes sensitivity

As the frequency range of the tangential modal group significantly exceeds the experimentally observable range (fig. 3.5(b)), the analysis of the second modal group sensitivity to the model's properties cannot be experimentally verified. At the same time, though, this range shows no practical interest for common tyre studies, as will be made clear in chapter 4. Numerical results are presented in fig. 3.7. Torsional mode frequency is controlled by the tangential sidewall stiffness and slightly affected by the pretension. The rest of the modes exhibit a strong dependency on the elastic modulus, quantitatively equal along the frequency

range. is the influences on the natural frequencies of the tangential group, an effect equal across the whole modal range (fig. 3.7(a)).

3.4.2 The frequencies prediction of the rectilinear models

The natural frequencies of the first 41 modes ($n = 0$ to $n = 40$) of the rectilinear models are examined and compared to the respective radial ring ones (fig. 3.8). Both the frequency values and their percentage deviation from the ring ones are presented. The string model shows an almost linear increase in the frequency values with the modal number, along the whole modal range, while the bending model shows a parabolic one, similar to the frequency development of the ring model (fig. 3.8(a)). In result the deviation of the string model increases with the modal number, while the deviation of the bending model remains almost constant. Interestingly, the frequencies predicted by the combined beam-string model exhibits an excellent correlation to the ring model ones, along the whole modal range.

Examining the percentage deviation of the frequency values from the ring corresponding ones (fig. 3.8(b)), it is evident that all the rectilinear models underestimate the breathing frequency and overestimate the $n = 1$ one at an almost equal level. As the modal number increases, the string model deviation becomes negative (underestimation) for $n \geq 6$ and the percentage underestimation raises steadily. In contrast, the two bending mechanism incorporating models exhibit a broad range frequency agreement with the ring one. Initially, the simple bending model underestimates the frequencies' values but this underestimation degrades parabolically, while the combined model exhibits a slight overestimation, also decreasing with the modal number.

The significant breathing mode frequency divergence of the rectilinear models results from their incapability of capturing the actual physical mechanism associated with the breathing deformation pattern (fig. 3.4). The constant radius increase along the tyre circumference imposes an extensional strain condition, which is suspended by the respective ring stiffness (elastic modulus) and insignificantly by the radial sidewall one, given that the effect of the elastic modulus on the breathing frequency is the dominant one (figs. 3.6(b) and 3.6(d)). In contrast, the breathing-like deformation mode of the rectilinear models, corresponds to a constant vertical displacement along their length, which is solely suspended by the sidewall foundation.

A difference in the physical mechanism is also responsible for the $n = 1$ mode natural frequency overestimation of the rectilinear models. As it is obvious by the observation of the associated mode shape (fig. 3.4(a)), both radial and tangential sidewall foundations resist to the deformation pattern. In the case of the rectilinear representation, though, the suspension of the deformation associated with one full wavelength is apparently accomplished by the radial (vertical) stiffness foundation only, along the whole model's length. The higher natural frequency of the rectilinear models emerges from the higher stiffness value of the radial foundation in comparison to the tangential one (table 3.1), increasing the stiffness induced resistance to the deformation pattern.

Two basic conclusions may be drawn from the frequency convergence between the ring and rectilinear models in the high frequency range. The first one is that the bending stiffness becomes the dominant mechanism which controls the modal behaviour of both the rectilinear and the ring models. The effect of the omission of the rest of the ring model stiffness mechanisms (extensional stiffness, tangential sidewall stiffness, pretension) deteriorates and may be neglected above a modal number. Accordingly, the absence of the bending stiffness mechanism deteriorates the validity of the string model, as the modal number increases. Moreover, the predominant dependence of the ring model on the elastic modulus (fig. 3.6(d) is related to the

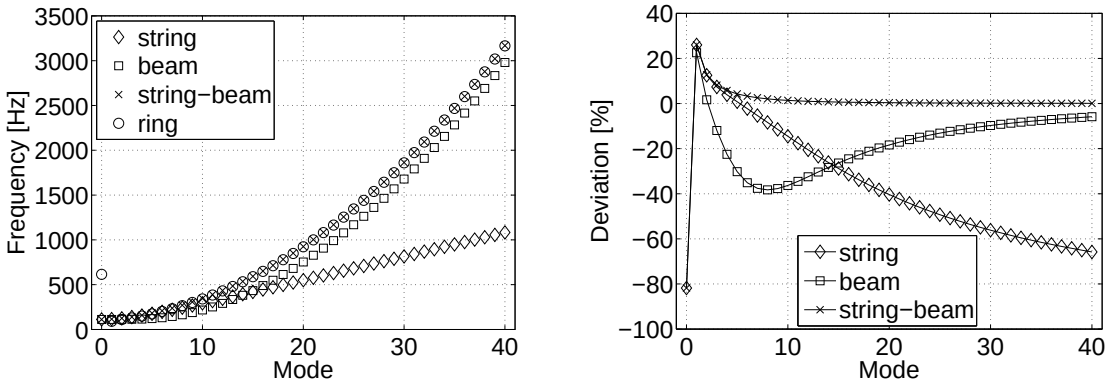

(a) Frequency values.

(b) Percentage variation from the ring model.

Figure 3.8 – The natural frequency prediction of the rectilinear belt models in comparison to the ring model one.

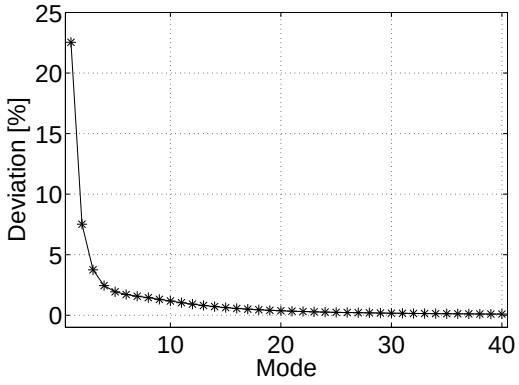

Figure 3.9 – The percentage frequency deviation of the rectilinear bending model from the non-pretensioned ring one.

resulting bending stiffness mechanism and not to the extensional (membrane) one, as only the first one is depicted in the beam rectilinear models. The second conclusion is associated with the decreasing effect of the belt circularity as the modal number increases. Although a circular representation should be preferred for the capture of the low frequency range modal behaviour a rectilinear one may be used in the high frequency range. Similar conclusions have been experimentally drawn by Perisse and Hamet [79] and Perisse *et al* [106]. Furthermore, the above discussion justifies the application of the plate models on the high frequency range simulation studies, as for example proposed by Kropp [110] and Pinnington [128].

Focusing in the middle frequency range, the in common examination of the profound deviation between the ring and the rectilinear bending models and the good correlation between the ring and the beam-string rectilinear ones, proves that the significant effect of the circumferential pretension across this range. The above comparison, though, cannot capture the possible importance of the circularity effect incorporation. In order the latter to be captured, the frequencies predicted by a simple bending rectilinear model are compared to a ring one, omitting the pretension effect from the latter (fig. 3.9). Interestingly, the rectilinear model overestimates the frequencies of the whole modal range but the overestimation reduces with the modal number. This development pattern of this overestimation is similar to the one describing the deviation of the beam-string rectilinear model from the complete ring one (fig. 3.8(b)). The coupling between the radial

and the tangential deformation offers a "relaxation" mechanism to the model, reducing the total stress and respectively the natural frequencies of the modes.

As it will be later discussed, the decreasing with the modal number effect of the omission of the tangential deformation capability may be attributed to the decrease of the participation of the tangential deformation component in the respective ring mode shapes. A second interesting result from the above analysis is that since the low frequency range deviation of the beam-string model from the ring one was attributed to the omission of the circularity, the string physical mechanism (even in its rectilinear assumption) may be regarded as able to capture the pretension effect to the same extent with the pretensioned ring model. This conclusion will be used later, when a similar mechanism will be proposed for the modelling potential enhancement of a discretised beam model (section 3.5.4).

Summarizing the frequency prediction performance of the rectilinear models, in comparison to the ring one, the following conclusions may be drawn:

- The rectilinear models underestimate the breathing mode frequency and overestimate the $n = 1$ one as the corresponding ring physical mechanisms cannot be captured.
- The predicted frequencies of any rectilinear approach converge to the ring ones as the modal number increases, if the approach incorporates the bending mechanism. The effect of the omission of the other ring physical mechanisms decreases and the bending stiffness becomes the predominant property.
- The superposition of the string mechanism on the bending one, captures satisfactorily the frequency behaviour of the ring.
- The circularity omission results in stiffer modal behaviour in the low to medium modal range, but the effect decreases for higher modes.

3.4.3 Ring models

As it has already been discussed (section 3.3) various forms of the ring model have been proposed for the capture of the tyre modal behaviour. The frequency prediction of some of them will be here investigated. In particular, the following model variations will be examined:

- The extensible ring (eqns. 3.23).
- The pretensioned extensible ring, in its complete form (eqns. 3.54).
- The pretensioned extensible ring in its simplified form (eqns 3.54, omitting the stiffness-like terms).
- The inextensible pretensioned ring(eqn. 3.64).

In fig. 3.10 the radial frequencies predicted by the above ring models are presented, together with the relative percentage deviation of them from the frequencies of the complete, extensible and pretensioned, ring model. All of them predict a parabolic development pattern with the modal number and although a good correlation of values between them is predicted, the omission of the pretension leads to the underestimation of the frequency values. As the examination of the percentage deviation (fig. 3.10(b)) reveals, the highest deviation is associated with the exclusion of the pretension effect and can be mainly identified in the middle

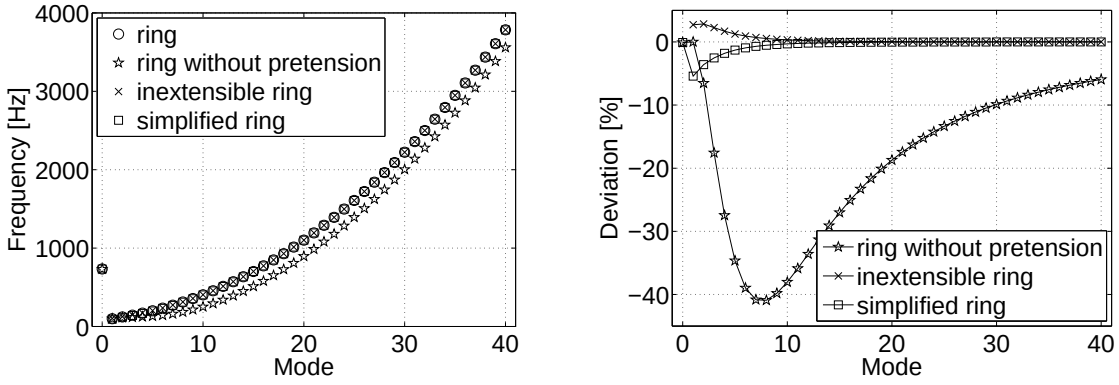

(a) Frequency values.

(b) Percentage frequency deviation.

Figure 3.10 – The natural frequency prediction of the ring-based models, in comparison to the pretensioned, extensible ring one.

modal range. In the low range, a slight relative frequency underestimation of the simplified pretensioned form is observed, as also a slight overestimation of the inextensible one. Predictably, as a similar bending mechanism is incorporated in all models, the deviation diminishes in the high modal numbers section of the range.

A further analysis of the modal prediction differences between the ring models may be attempted through the examination of their mode shapes deformation patterns. The radial to tangential deformation ratios for the whole modal range are presented in fig. 3.11(a) and their percentage deviation from the complete ring model is depicted in fig. 3.10(b). A similar development pattern of the deformation ratios may be identified in all of them. An almost equal radial and tangential participation is observed in the $n = 1$ mode shapes but the tangential participation decreases with the modal number and its value in the high modal number modes becomes insignificant. The mode shapes can be assumed as asymptotically tending to pure radial deformation ones. The decreasing with the modal number tangential deformation component of the ring modes, justifies the improving frequency correlation between the ring and the rectilinear bending models (figs. 3.8(b) and 3.9). The omission of the tangential deformation strain component from the rectilinear models becomes an insignificant frequency deviation factor of them from the ring ones in the high modal number range.

Accordingly, the frequencies deviation of the inextensible ring may be justified by the nature of the respective modelling assumption. As the membrane strain of the ring is suspended, the tangential deformation is only derived by the respective bending strain component and practically calculated by the integration of the radial deformation (eqn. 3.61). Obviously, the relative tangential to relative deformation is lower than the rest of the ring models and the level of the percentage underestimation increases with the modal number, following the development of deformation patterns corresponding to increased strain conditions (higher modes). The same physical mechanism difference is depicted in the frequencies deviation (fig. 3.10(b)). The suspension of the membrane strain imposes a stiffening effect on the model, which is more profound in the low modal number range, where the tangential deformation component was supposed to reach its maximum value (fig. 3.11(a)). As, though, the tangential deformation component decreases with the modal number, the relative stiffening effect on the inextensible ring becomes insignificant.

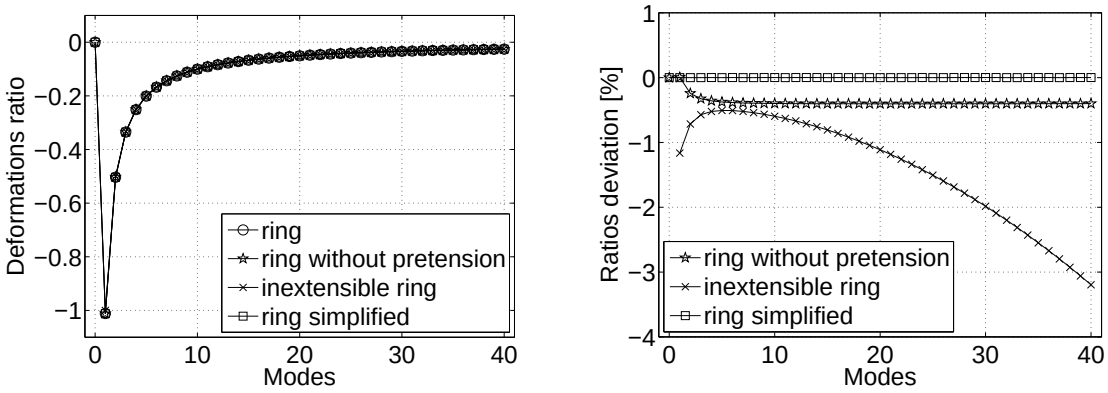

(a) The deformation ratios.

(b) The percentage deviation of the deformations' ratios.

Figure 3.11 – The tangential to radial ratio of deformation magnitudes of the radial modes, as a function of the modal number, for the various ring models and in comparison to the complete ring one.

3.4.4 Tangential modal behaviour

Moving to the analysis of the tangential modes prediction characteristics, it should be mentioned that the respective range of frequencies is much broader than the radial one (fig. 3.5). The experimental identification of these modes is difficult, as the tyre damping mechanisms suspend their excitation.

As it has been discussed in section 3.2.4, the tangential modal behaviour may be incorporated in the rectilinear models, by the superposition of an extensional stiffness mechanism (truss), in a non-interacting with the radial behaviour way. Consequently, the tangential strain does not couple the radial and the tangential deformations and the tangential modes, which emerge as additional ones, correspond to pure tangential deformation shapes. The radial modes remain unaffected in regards to their frequencies and deformation patterns. In agreement with the analysis of the previous section, the coupling of different deformation patterns by the strain relaxes the stiffness of the structure and the possible absence of this mechanism results in a stiffer modal behaviour. In the particular case, the frequency range predicted by the rectilinear tangential model is so broader than the ring one, that the superposition approach cannot be regarded as a valid one (fig. 3.12(a)).

The ring model variations, on the other hand, show excellent frequency correlation to each other, throughout the examined modal range (fig. 3.12(b)), as the effect of the simplification or the complete absence of the pretension mechanism on the tangential modes is insignificant. The above may be justified by the minor dependency of the tangential group on the pretension property (fig. 3.7(d)). Apparently, the inextensible ring model does not predict a tangential modal group.

The analysis of the tangential modal prediction of the ring models is completed with the comparison of the radial to tangential deformation ratios for each mode. This is accomplished in fig. 3.13. Similarly to the radial group (fig. 3.11(a)), equal radial and tangential deformations are predicted for the $n = 1$ mode, above which, the radial component asymptotically tends to zero. The tangential modes are practically associated with pure tangential mode shapes, above a modal number. The zero mode included in fig. 3.13 corresponds to the torsional mode, which of course does not incorporate radial deformation. The radial relative deformation prediction of the various ring models show excellent correlation to each other and only

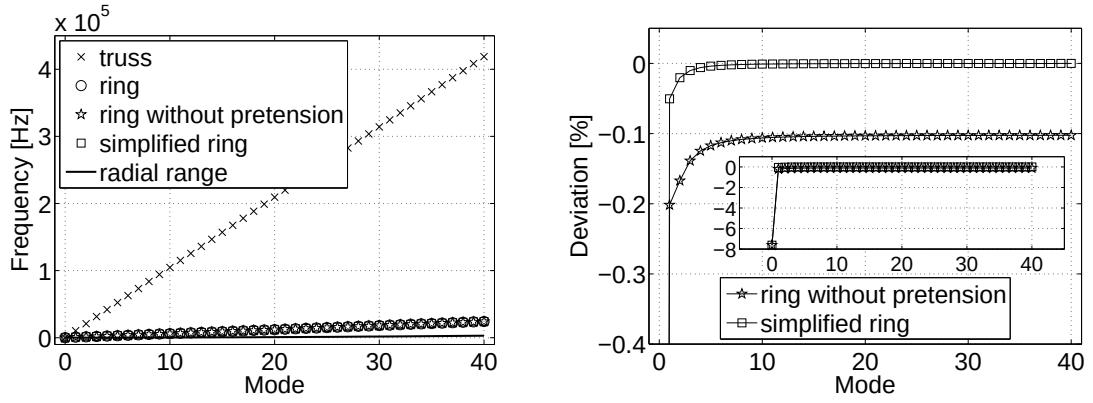

(a) Frequency values.

(b) Percentage deviation from the complete ring model.

Figure 3.12 – The tangential modes frequencies as predicted by the rectilinear truss model and the various ring models.

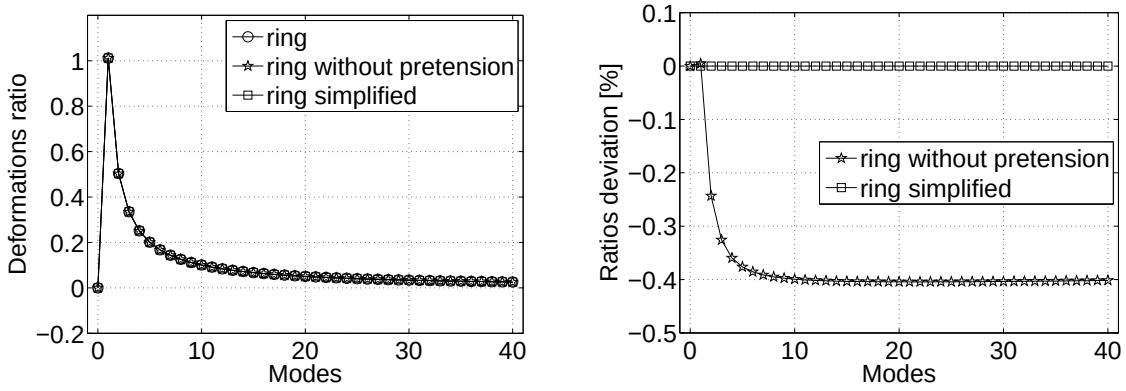

(a) The deformation ratios.

(b) The percentage deviation of the deformations' ratios.

Figure 3.13 – The radial to tangential ratio of deformation magnitudes of the tangential modes, as a function of the modal number, for the various ring models and in comparison to the complete ring one.

the no pretensioned model shows a steady, but insignificant, relative deviation.

An important difference between the radial and the tangential modal groups may be identified in the relative orientation (direction) of the deformation components. It is observed (figs. 3.11(a) and 3.13(a) that the radial and tangential deformations have opposite orientation (signs) in the radial mode shapes but similar in the tangential ones. The physical meaning of that is presented in fig. 3.14, where the deformations' relative orientation of the $n = 2$ mode shape is presented for the radial and the tangential modes. The direction of the tangential deformation which is predicted by the tangential mode corresponds to a more intensive stress condition than the radial mode corresponding one, as it is opposite to the physical reaction of the structure. In the case of the radial mode the two deformations act as a relaxation mechanism for each other, while in the case of the tangential mode, their coexistence is competitive to each other, increasing the total stiffness of the mode. The above mechanism is obviously in agreement with the prediction of a higher radial mode frequency than the the tangential one.

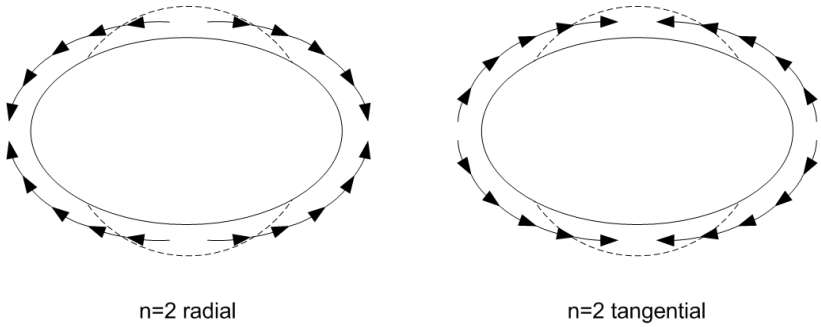

Figure 3.14 – The relative to each other orientation of the radial and the tangential deformations in the radial and the tangential modes cases.

3.5 Discretised belt modelling approaches

It is very common in tyre models, a belt structure to be combined with a discretised tread foundation. This is an obvious reason for the adoption of an also discretised belt representation approach, which allows for its direct coupling with the tread one. Apparently, the categorisation of a model as a modal or a space discretised one, refers to the followed method for its response calculation, as the modal behaviour of the structure defines the transient response in both cases. Many times, though, as the space domain solution does not incorporate the clear statement of the modes' excitation, the modal characteristics of such models are overlooked. For this reason, the modal behaviour of some common discretised belt representations will be here examined in comparison to the respective analytical one.

For reasons related to the stability of the solution the use of elements representing the circular shape of the tyre belt (such as the arch elements) is usually avoided. As a high degree of discretisation is imposed by the need for accurate contact area representation, the circular shape of the tyre can be adequately reconstructed by rectilinear elements, attached to each other under a relative angle. Many different types of elements have been proposed in tyre simulation studies, each of them aiming at the capture of specific aspects of the tyre behaviour. A brief summary of the main discretised approaches has been presented in section 2.1.6 of chapter 2. From the point of view of the present study, the modal prediction characteristics of the discretised models are investigated, in comparison to corresponding analytical ones. For this reason, such elements are chosen, that their physical mechanism can be modelled by either an analytical or a discretised approaches.

As discussed in section 2.1.3 of chapter 2, Pacejka in [1] categorised the physical modelling approaches according to their belt deformation mechanism. The possible inclusion or not of the bending stiffness in the model was found to be crucial for the predicted behaviour. In accordance to that, two simple elements are initially selected for the study of the modal characteristics of the discretised models:

- A linear axial truss element is selected for the study of the excluding the bending stiffness case.
- An extensible linear beam element is chosen for the study of the including the bending stiffness case.

These two elements and the deformation degrees of freedom respectively assigned to their nodes are presented in fig. 3.15.

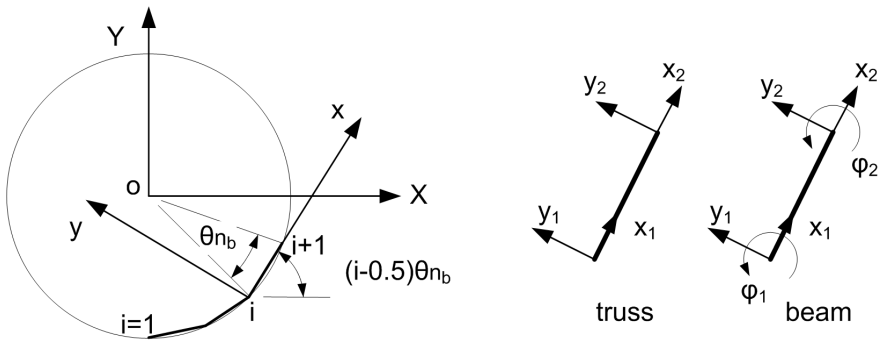

Figure 3.15 – The representation of the belt by rectilinear elements and the degrees of freedom of the truss and the beam elements.

3.5.1 The modal prediction of the discretised belt models

Prior to the analysis of the particular modal behaviour of the two discretised models, some general modal characteristics of the discretised approaches should be highlighted. Many of the differences between them and the respective analytical representations may be justified by these basic characteristics.

A significant modal property of the discretised models is the coupling between the radial and the tangential deformations. Although the vertical and horizontal degrees of freedom of a single element are decoupled, with non interacting terms in the inertia and stiffness matrices, the rotation of the elements prior to their assembly changes the case. If the same elements were assembled in a rectilinear form, such coupling would not be predicted for the complete structure and the modes would still emerge as pure radial or tangential, in accordance to the behaviour of the rectilinear analytical models. The angular transformation of the elements and the composition of the total matrices of the structure will be presented in the following.

The stiffness and inertia matrices of every element have to be transformed from the local system of axis of it to the global one of the belt, the origin of which coincides with the centre of the wheel (fig. 3.15). Assuming that the first node lies on the negative vertical semi-axis, the transformation angle is given by the following equation:

$$\varphi_{g\to l} = \left(i - \frac{1}{2}\right)\theta_{n_b} = \left(i - \frac{1}{2}\right)\frac{2\cdot\pi}{n_b} \tag{3.69}$$

where:

$\varphi_{g\to l}$	the local to global system transformation angle
i	the element or node index
n_b	the total number of elements

The local to global transformation may be written as:

$$\mathbf{K}_{global} = \mathbf{T}^T\left(\varphi_{g\to l}\right)\cdot\mathbf{K}_{local}\cdot\mathbf{T}\left(\varphi_{g\to l}\right) \tag{3.70a}$$

$$\mathbf{M}_{global} = \mathbf{T}^T\left(\varphi_{g\to l}\right)\cdot\mathbf{M}_{local}\cdot\mathbf{T}\left(\varphi_{g\to l}\right) \tag{3.70b}$$

where:

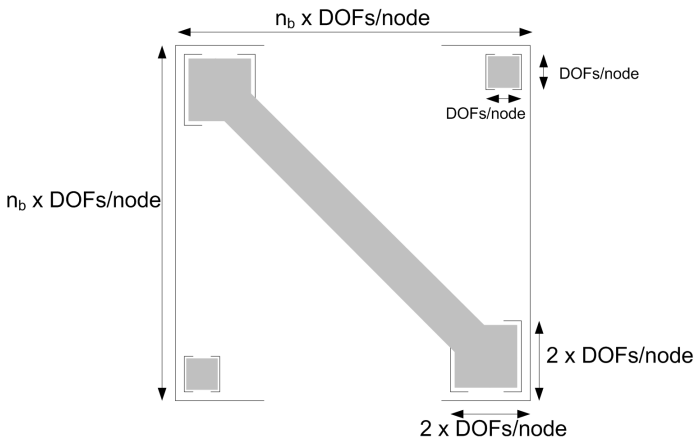

Figure 3.16 – The pseudo-diagonal form of the inertia and stiffness matrices of the discretised models.

K_{global}	the stiffness matrix in the global system of axis
M_{global}	the inertia matrix in the global system of axis
K_{local}	the stiffness matrix in the local system of axis
K_{local}	the inertia matrix in the local system of axis
T^T	the transpose of the global to local transformation matrix
θ_i	the central angle of the ith belt node

The actual form of the transformation matrix will be later, examined for each particular element. The global matrices are composed, adding the elements of the stiffness and inertia of the elements'matrices which correspond to the same degrees of freedom. Given that each element is attached only to its previous and following ones, the process results in a pseudo-diagonal matrix, presented in fig. 3.16. Their total dimensions are equal to the total number of degrees of freedom, which is calculated by the product of the number of the nodes (n_b) with the number of degrees of freedom assigned to each of them ($DOFs/node$). The two sub-matrices in the upper right and bottom left areas of the matrices (fig. 3.16) emerge as a result of the closed geometry of the structure (the first node of the first element, coincides with the last node of the last element).

The sidewall stiffness is incorporated in the model as a discretised foundation. One radial and one tangential stiffness element are assigned to each node of the structure, connecting that to a theoretical respective point of the wheel. The stiffness value of each element is derived from the analytical stiffness value and the degree of discretisation:

$$k_{r/t}^{i} = k_{r/t}\frac{2 \cdot \pi \cdot R}{n_b} \tag{3.71}$$

The undamped equation of motion of the structure, in its homogenous form, reads:

$$\mathbf{M}_{global} \cdot \ddot{\mathbf{u}} + \mathbf{K}_{global} \cdot \mathbf{u} = 0 \tag{3.72}$$

where $\mathbf{u}(t)$ is the $n_b \times DOFs/node$ deformations' vector. In agreement with the respective analytical ex-

pressions, the solution $\mathbf{u}(t) = \mathbf{U} \cdot e^{\iota \cdot \omega \cdot \mathrm{t}}$is proposed:

$$3.72 \Rightarrow (\mathbf{K}_{global} - \omega^2 \cdot \mathbf{M}_{global})\mathbf{U} \cdot e^{\iota \cdot \omega \cdot \mathrm{t}} = 0 \tag{3.73}$$

$$\Rightarrow (\mathbf{K}_{global} - \omega^2 \cdot \mathbf{M}_{global})\mathbf{U} \tag{3.74}$$

The natural frequencies of the structure are acquired by the solution of the characteristic equation of the system:

$$|\mathbf{K}_{global} - \omega^2 \mathbf{M}_{global}| = 0 \tag{3.75}$$

Substituting each natural frequency in eqn. 3.73 the mode shapes of the structure are calculated.

The sparse form of the model's matrices, makes the solution of eqn. 3.75 difficult, especially when a high number of elements (n_b) is assumed. The topic, although of outstanding importance for the numerical calculation of the discretised models response, surpasses the aims of the present analysis. Wilkinson in [246] offers a systematic approach to the solution of the respective eigen-analysis problem.

The eigenvectors of the discretised model capture the deformation shape of the modes and each of their elements corresponds to one degree of freedom. The total number of the predicted modes of a discretised structure is equal to the total number of the degrees of freedom and the model's transformation from its space to modal representation may be regarded as a domain transformation. An eigenvector basis (matrix) can be accordingly composed as each column of it corresponds to one eigenvector:

$$\tilde{\mathbf{\Psi}}_{(n_b \times \frac{DOFs}{node}) \times (n_b \times \frac{DOFs}{node})} = \left[\mathbf{\Psi}_1 \cdots \mathbf{\Psi}_j \cdots \mathbf{\Psi}_{n_b \times \frac{DOFs}{node}}\right] = \left[\begin{bmatrix} U_1^1 \\ \vdots \\ U_{i,\kappa}^1 \\ \vdots \\ U_{n_b \times \frac{DOFs}{node}}^1 \end{bmatrix} \cdots \begin{bmatrix} U_1^j \\ \vdots \\ U_{i,\kappa}^j \\ \vdots \\ U_{n_b \times \frac{DOFs}{node}}^j \end{bmatrix} \cdots \begin{bmatrix} U_1^{n_b \times \frac{DOFs}{node}} \\ \vdots \\ U_{i,\kappa}^{n_b \times \frac{DOFs}{node}} \\ \vdots \\ U_{n_b \times \frac{DOFs}{node}}^{n_b \times \frac{DOFs}{node}} \end{bmatrix}\right] \tag{3.76}$$

where:

$\tilde{\mathbf{\Psi}}$	the eigenvectors matrix
n_b	the number of nodes
$\mathbf{\Psi}_j$	the jth mode eigenvector
$U_{i,\kappa}^j$	the deformation of the κth degree of freedom of the ith node, as predicted by the eigenvector of the jth mode

The eigenvectors' matrix bears a characteristic property: it diagonalises the stiffness and inertia matrices of

the structure, according to the equations:

$$\mathbf{M}^m = \tilde{\mathbf{\Psi}}^T \cdot \mathbf{M} \cdot \tilde{\mathbf{\Psi}} \tag{3.77}$$

$$\mathbf{K}^m = \tilde{\mathbf{\Psi}}^T \cdot \mathbf{K} \cdot \tilde{\mathbf{\Psi}} \tag{3.78}$$

$$\tag{3.79}$$

and

$$\mathbf{M}^m(j_1, j_2) = \begin{Bmatrix} m^m_{j_1},\ j_1 = j_2 \\ 0,\ j_1 \neq j_2 \end{Bmatrix} \quad , \qquad \mathbf{M}^m(j_1, j_2) = \begin{Bmatrix} m^m_{j_1},\ j_1 = j_2 \\ 0,\ j_1 \neq j_2 \end{Bmatrix} \tag{3.80}$$

where:

$\mathbf{M}^m$	the modal inertia matrix of the model
$\mathbf{K}^m$	the modal stiffness matrix of the model
m^m_j	the modal mass of the jth mode
k^m_j	the modal stiffness of the jth mode

The parenthesis indexes define the position of the elements in the respective matrices. The natural frequency of each mode may be derived from them as:

$$(\omega_j)^2 = \frac{k^m_j}{m^m_j} \tag{3.81}$$

Examining the total range of the derived modes, it is observed that the ones with modal number $n \geq 1$ exist as duplicates, while the $n = 0$ modes exist as singular ones, a result of the double axis symmetry of the tyre structure. The duplicate modes have equal to each other natural frequencies but their mode shapes exhibit a relative orientation angle $\pi/2n$. The importance of this relative orientation has been discussed in the presentation of the analytical models (section 3.2.1), where the modes' duplicity and the orientation angle was a priori imposed and not physically emerging as it happens here. The total number of the zero modes equals the number of degrees of freedom per node (t), while their singular existence can be attributed to their associated deformation, which shows no orientation property.

In order the double axis symmetry of the discretised models to preserved an even number of elements (n_b) is required, resulting in an even number of total degrees of freedom ($n_b \times DOFs/node$) and an equal number of total modes. As the $DOFs/node$ zero modes appear once, the rest of the modes, $n_b \times DOFs/node - DOFs/node = (n_b - 1)DOFs/node$, emerge as categorised into modal groups, $DOFS/node$ in number, each of them consisting of $n_b - 1$ modes. The concept of the modal groups of the discretised models can be proposed as an extension of the modal group study approach (radial and tangential) of the analytical ring models:

Definition:*A modal group is a sequence of modes with strictly increasing or decreasing modal number, the deformation of which follows a particular development pattern.*

Each of the $n_b - 1$ modes of each group, should be predicted as a double one, something contradicting

with their odd total number. In result, the modes with modal number ranging from $n = 1$ to $n = n_b/2 - 1$ emerge as double while the $n = n_b/2$ mode emerges as single one. The above may be summarized as:

$$n_b \text{ elements} \rightarrow (DOFs/node \times n_b) \text{ DOFs} \rightarrow (DOFs/node \times m) \text{ modes} \rightarrow DOFs/node \text{ modal groups} \rightarrow$$

$$\frac{DOFs}{node} \times \begin{cases} 1 \times \ n = 0 \text{ mode} \\ 2 \times \{n = 1 \ ... \ n = \dfrac{n_b}{2} - 1\} \text{ modes} \\ 1 \times \ n = \dfrac{n_b}{2} \text{ mode} \end{cases} \tag{3.82}$$

3.5.2 The truss discretised model

Two degrees of freedom (x_1 and x_2 in fig. 3.15) are assigned to the truss element, as every node is associated with its axial deformation capability. The stiffness and inertia matrices of the element are:

$$\mathbf{K}_{truss}^{local} = \frac{E \cdot A}{l} \begin{bmatrix} 1 & -1 \\ -1 & 1 \end{bmatrix} \tag{3.83a}$$

$$\mathbf{M}_{truss}^{local} = \frac{\rho \cdot A \cdot l}{6} \begin{bmatrix} 2 & 1 \\ 1 & 2 \end{bmatrix} \tag{3.83b}$$

The nodes of a deformed belt are displaced not only in the axial for the rectilinear elements direction but also in a vertical to it direction. The angular transformation of the matrices results in the doubling of the degrees of freedom of every node, as the vertical degree of freedom(, y_1 and y_2 in fig. 3.15) is generated:

$$\text{axial DOF} \rightarrow \begin{Bmatrix} \text{horizontal} & \text{DOF} \\ \text{vertical} & \text{DOF} \end{Bmatrix} \tag{3.84}$$

The transformation matrix reads:

$$\mathbf{T}_{truss}\left(\varphi_{g \rightarrow l}\right) = \begin{bmatrix} \cos\varphi_{g \rightarrow l} & \sin\varphi_{g \rightarrow l} & 0 & 0 \\ 0 & 0 & \cos\varphi_{g \rightarrow l} & \sin\varphi_{g \rightarrow l} \end{bmatrix} \tag{3.85}$$

The above procedure introduces an artificial deviation in the dynamic behaviour of the complete structure. As discussed in [247], the process is correct for the stiffness property, as the axial stress-strain mechanism of the element is responsible for both the horizontal and the vertical expressions of it. The initial axial stiffness is decoupled into the horizontal and the vertical ones by the transformation matrix. The same concept, though, cannot be applied to the inertia property. The horizontal and the vertical inertia forces develop independently from each other and they do no interact. The vertical inertia behaviour cannot be assumed as emerging from the axial one. The application of the same transformation on the inertia matrix introduces an extremely stiff dynamic behaviour of the structure. The inertia property of each of the two vertical degrees of freedom must be assumed as equal to the initial, axial, one. Interestingly, a similar concept is

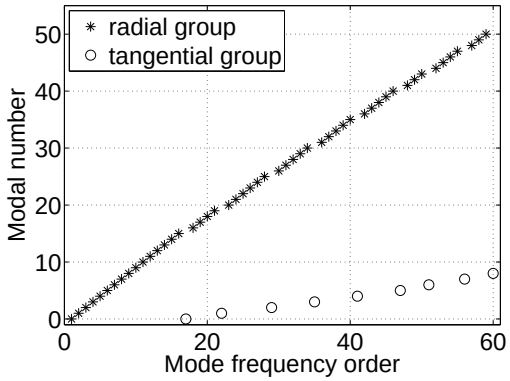

Figure 3.17 – The frequency defined order of the first 60 (radial and tangential) modes of the ring model.

incorporated in the ring equations of motion (eqns. 3.18), where equal inertia terms are assumed for both of them. The duplication of the inertia related terms should not be accomplished by the angular transformation as a decomposition of the axial property. In contrast, equal inertia terms to the axial ones should be initially incorporated in the element' inertia matrix, the dimensions of which are accordingly increased:

$$\mathbf{M}_{truss}^{local} = \frac{\rho \cdot A \cdot l}{6} \begin{bmatrix} 2 & 0 & 1 & 0 \\ 0 & 2 & 0 & 1 \\ 1 & 0 & 2 & 0 \\ 0 & 1 & 0 & 2 \end{bmatrix} \tag{3.86}$$

For reasons of agreement a similar dimensions increase is applied to the stiffness matrix, although in this case the additional terms are zero:

$$\mathbf{K}_{truss}^{local} = \frac{E \cdot A}{l} \begin{bmatrix} 1 & 0 & -1 & 0 \\ 0 & 0 & 0 & 0 \\ -1 & 0 & 1 & 0 \\ 0 & 0 & 0 & 0 \end{bmatrix} \tag{3.87}$$

The transformation matrix is now responsible for the change of the angular orientation of the elements but not for the increase of their dimensions and number of degrees of freedom:

$$\mathbf{T}_{truss}\left(\varphi_{g\to l}\right) = \begin{bmatrix} \cos\varphi_{g\to l} & \sin\varphi_{g\to l} & 0 & 0 \\ -\sin\varphi_{g\to l} & \cos\varphi_{g\to l} & 0 & 0 \\ 0 & 0 & \cos\varphi_{g\to l} & \sin\varphi_{g\to l} \\ 0 & 0 & -\sin\varphi_{g\to l} & \cos\varphi_{g\to l} \end{bmatrix} \tag{3.88}$$

Continuing the above discussion, the form of the truss element matrices can be directly associated with the analysis presented in section 3.4, related to the effect of the strain and deformation suspensions. The case of the truss element without the vertical degrees of freedom (2×2 dimensions) corresponds to the

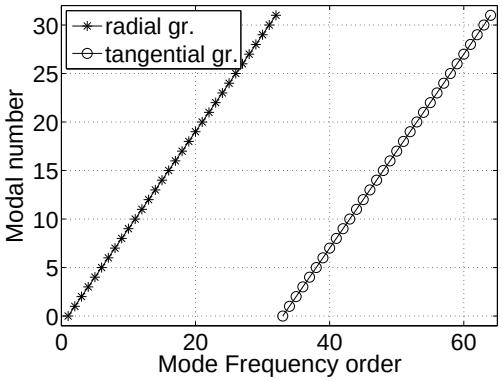

Figure 3.18 – The modal groups of the truss model.

suspension of the respective deformation, while the case of the truss element including the vertical degrees of freedom not. Since the stiffness mechanism in both cases is equivalent, the first case results in a much stiffer modal behaviour of the structure. Examining them from a physical mechanism point of view, the second case offers an additional deformation component to the strain, resulting in a "relaxation" mechanism associated with a less stiff dynamic behaviour. The choice of the second approach for the following analysis does not actually derive from the association of the tyre structure with the one or the other model but with the observation that the extensional beam model incorporates both vertical and axial degrees of freedom, sensed as strain components by the structure. In order this element to be proposed as a corresponding to an enhanced (bending stiffness including) mechanism and a comparison between their modal predictions to have physical meaning, the complete (4×4) truss matrices are adopted by the present study.

The truss model modal groups

Summarizing the above discussion (section 3.5.1), the modal behaviour of the truss model is expected to develop in two modal groups, combining both radial and tangential deformation in the corresponding mode shapes. The complete ring model (eqns. 3.54) will be used as a comparison basis. For this reason, the sixty lowest frequency modes of the ring model, are presented in fig. 3.17, according to their frequency order and the modal group categorization. It is evident that although the two modal groups (radial and tangential) develop as scattered into each other, the majority of the low frequency modes belong to the radial modal group.

A truss model composed by 62 elements will be initially examined, the modes of which develop in 2 modal groups of 32 modes, covering the modal number range from $n = 0$ to $n = 31$. The frequency order of the whole modal range is presented in fig. 3.18. The deformation amplitude ratios (T^m/R^m for the first group and R^m/T^m for the second one) are presented in figs. 3.19(a) and 3.19(b) respectively. Obviously, the modes of the first group exhibit predominant radial deformation and thus the group is named radial group, while the second group is mainly associated with tangential deformation and thus named tangential group. Following the analysis method of the ring model modal behaviour, the breathing zero mode is incorporated in the radial group and the torsional zero mode in the tangential one.

A significant difference between the truss and the ring models in the prediction of the modal groups'

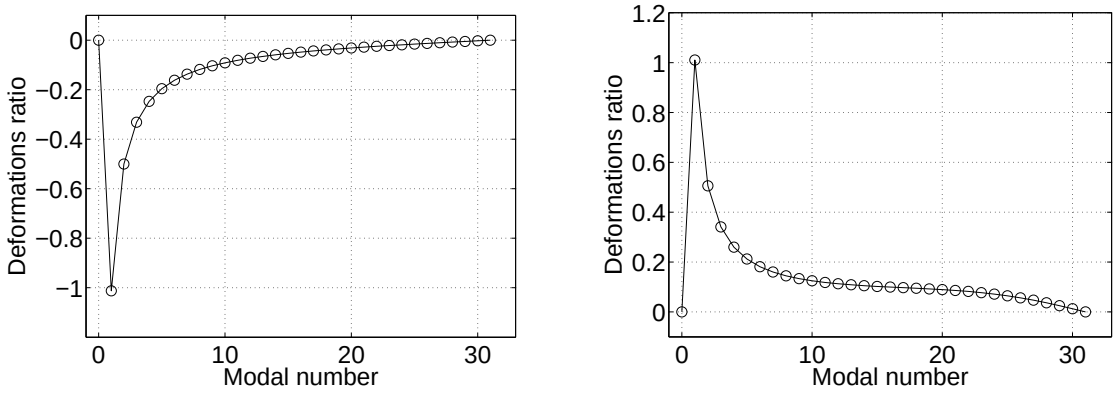

(a) Tangential to radial deformation ratios of the radial modes.

(b) Radial to tangential deformation ratios of the tangential modes.

Figure 3.19 – The relative deformations of the two modal groups predicted by the truss model.

development can be identified in the respective figures, 3.18 and 3.17. The truss modal groups do not scatter into each other, as happens in the analytical ring case, but they develop sequentially. The tangential group starts after the completion of the radial one. As, though, the number of modes composing each group depends on the number of elements, the frequency order of the tangential modes is directly related to the degree of discretisation level, ranging from $\frac{n_b}{2} + 2$ to $n_b + 2$. This observation should be taken into account when a modal reduction method is applied on such a model, based on the criterion of frequency order of the modes.

The percentage deviation of the truss model predicted radial frequencies from the ring ones is presented in fig. 3.20(a). Good correlation can be observed for the breathing and $n = 1$ modes, but as the modal number increases, the truss model frequencies are significantly lower. The percentage deviation increases rapidly for the low modal number modes (more than 50% for the $n = 7$ mode) and asymptotically moves towards 100% for the high modal number modes. The conclusion that the truss model predicts a severely lower frequency range for the radial modal group may be objectively drawn.

The truss model radial frequency underestimation may be justified by the radial modes sensitivity analysis of the ring model (fig.3.6). Although the sidewall stiffness mechanism exists in the truss model, this is not true for the inflation pretension effect and the ring bending stiffness. The good correlation of the $n = 1$ mode could be attributed to the sidewall mechanism, while the correlation of the breathing mode may be justified by both the sidewall and extensional stiffness of the elements. The lack of pretension, though, radically deteriorates the values of the middle range frequencies, while the absence of the bending stiffness is responsible for the severe devastation of its frequency correlation to the ring model, in the high modal range.

The percentage deviation of the tangential to radial deformation ratios from the ring ones is presented in fig. 3.20(b). An increasing underestimation of the tangential deformation component is observed throughout the modal range. The tangential deformation diminishes for the maximum modal number mode. As the deviation range extends from 0% to 100% throughout the modal range, the deviation of a certain mode is a function of the total number of the available modes.

The frequency deviation of the tangential modal group from the ring one is presented in fig. 3.21(a).

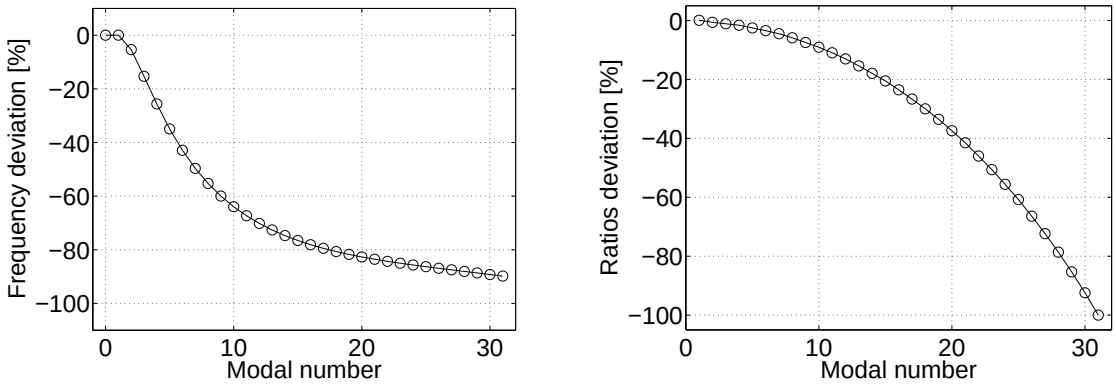

(a) Relative percentage deviation of the frequencies of the radial modes predicted by the truss model from the corresponding ring ones.

(b) Relative percentage deviation of the tangential to radial deformations ratio ($\frac{T_n}{R_n}$) of the radial modes predicted by the truss model from the corresponding ring ones.

Figure 3.20 – Relative modal behaviour of the truss model radial group to the corresponding ring one.

In this case only the torsional mode frequency is slightly underestimated, while the rest of the frequencies are overestimated. The level of deviation, though, is lower, in absolute terms, than the one of the radial group. Interestingly, maximum deviation is not exhibited by the mode of the highest modal number, as in the radial group, but a relative deviation plateau (maximum value) is reached, above which the deviation values decrease.

Given that the predominant deformation of this modal group is the tangential one (figs. 3.11(a) for the ring model and 3.19(b) for the truss one), the existence of the extensional stiffness mechanism in the truss elements justifies the better correlation between the two models, compared to the one of the radial group. The fact that although basic stiffness factors such as the pretension and the bending mechanism are omitted, the frequencies are overestimated is a characteristic effect of the discretisation process and will be later examined in detail.

Comparing the deviation of the R_n/T_n deformations ratios of the truss model from the ring one, a similar, plateau including, overestimation development is identified. Initially, an increasing overestimation is predicted, up to a maximum value corresponding to a modal number lower than the highest available one. The overestimation decreases radically and turns into underestimation towards the end of the modal range. Zero radial deformation is predicted for the last -highest- mode of the group. The relative radial deformation range from equal to the ring model participation to zero associates the radial deformation of a certain mode with the total number of elements, a common behaviour with the tangential deformation component of the radial modes.

Summarising the modal behaviour of the truss model in comparison to the ring one, two basic characteristics should be taken into consideration, in regards to its physical mechanism justified modal characteristics:

- Although two modal groups are predicted, one with radial and one with tangential predominant deformation, they emerge in strictly sequential frequency order and not scattered into each other.

- The radial group frequencies and tangential deformation are both severely underestimated, compared to the ring ones, as the lack of pretension and bending stiffness mechanisms limit the modal range of

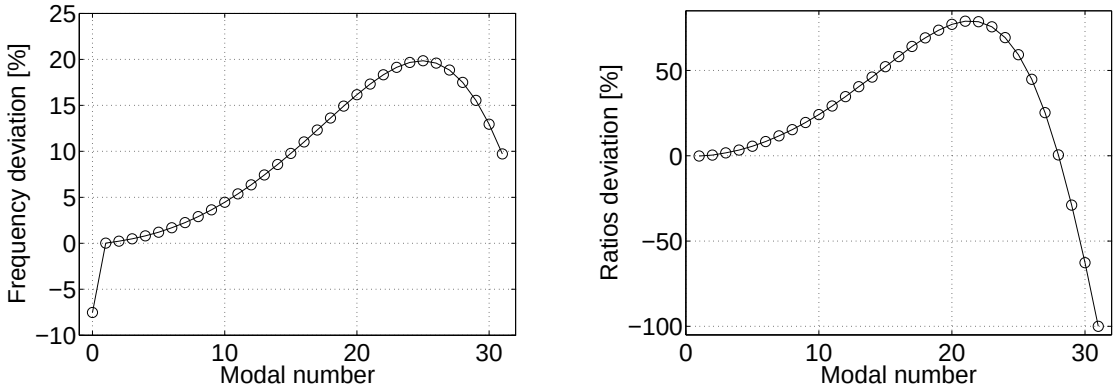

(a) The relative percentage deviation of the frequencies of the truss model tangential modes from the corresponding ring ones.

(b) The relative percentage deviation of the radial to tangential deformations ratio ($\frac{R_n}{T_n}$) of the truss model tangential modes from the corresponding ring ones.

Figure 3.21 – The relative modal behaviour of the truss model tangential group to the corresponding ring one.

acceptable correlation to the first modes.

The truss model discretisation effect

Although the underestimation of the radial modes frequencies has a physical explanation, associated with the absence of certain stiffness mechanisms from the truss model, the overestimation of the tangential cannot be satisfactory attributed to a physical mechanism. Additionally, it is evident that both frequency and shape deviation of a certain mode form the corresponding ring one, depends on its position in the total range of available modes. The discretised models introduce a direct effect of the total number of elements on the predicted modal prediction characteristics.

In order to identify the discretisation effect and to separate it from the effect of the physical mechanisms absence, a ring model without bending stiffness and pretension mechanism will be used for the comparison. Such a structure incorporates the same physical mechanisms with the truss model, the extensional stiffness and the sidewall foundations, but, being an analytical model, lacks the effect of the discretisation. A gradually increasing number of elements will be assumed for the truss model ($n_b = 60,\ 80,\ 100,\ 120,\ 140,\ 160,\ 180$ and 200) so that the effect of the relative position of a certain mode in the predicted modal range can be identified. The frequencies of the first 200 radial modes of the analytical ring-derived structure are also presented for comparison. The breathing mode is excluded from the investigation, as its deviation from the ring model is insignificant.

The complete frequency range of the radial modal group is presented in fig. 3.22(a) for increasing number of truss model elements, while the first 30 modes are presented in fig. 3.22(b). The frequency range of the analytical model asymptotically tends towards an upper limit value which is defined by the physical properties of the model. The frequency range of the discretised models also extends to a certain limit, although non asymptotically, independently from the number of elements/modes. As an equal, properties defined and discretisation independent, total frequency range is associated with both of the models, the frequency value of the intermediate modes is defined by the discretisation. Consequently, the total number of elements prescribes the discretisation effect on each of the modes. Moreover, the effect is profound for the

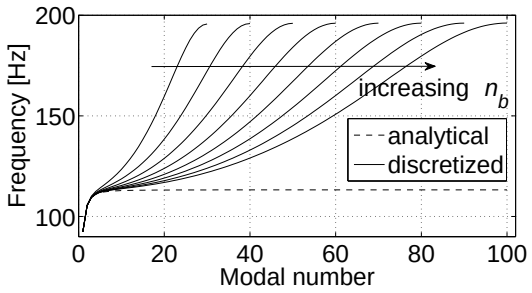

(a) The total frequency range.

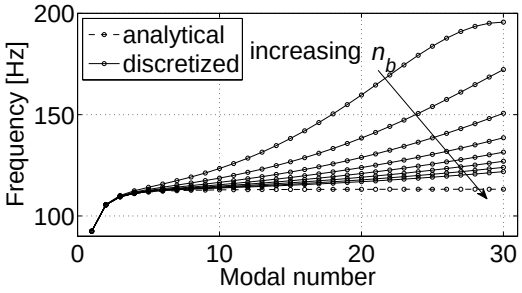

(b) The frequency range of the $n = 1$ to $n = 30$ modes.

Figure 3.22 – The truss model discretisation effect on the prediction of the radial natural frequencies for an increasing total number of elements.

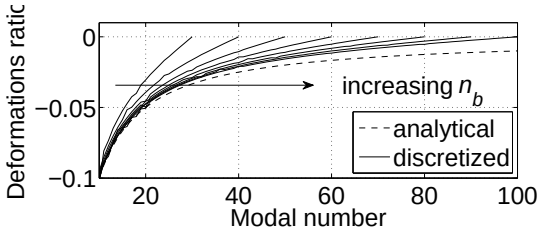

Figure 3.23 – The effect of the discretisation on the ratio of the tangential to the radial deformation of the radial group mode shapes.

modes close to the upper limit of the modal range, but insignificant in the initial section of it.

Assuming that reduction process based on a modal number cut-off limit is to be applied to such a model, the correlation to the analytical representation improves with the degree of discretisation and the frequency range which corresponds to the modal one narrows. This is evident in fig. 3.22(b)), where the associated frequency range of the $n = 1$ to the $n = 30$ modal range is presented for an increasing level of discretisation.

The discretisation affects also the development of the tangential to radial deformation ratio across the modal group, presented in fig. 3.23. In general, the discretised models underestimate, in terms of absolute values, the participation of the tangential deformation. For any number of elements, though, the range of the deformations' ratio of extends to the whole range from equal participation (always predicted for the $n = 1$ mode) to zero tangential participation (always predicted for the highest available mode). This is evident in both fig. 3.20(b) and fig. 3.23 where the deformation ratios of the whole modal group (starting from $n = 10$) is presented for various discretisation levels. Examining a certain mode the closer its modal number is to the upper limit of the total modal range the closer to zero will be the predicted tangential participation. Similarly to the frequencies case, the discretisation effect is more profound for the modes close to the upper modal number limit of the group.

Moving the discussion to the discretisation effect on the tangential group modal characteristics, the fact that this group lies in the second half of the total modal range seems to induce a completely different, almost contrary, frequency development. The complete range frequency-modal correspondence for the same degrees of discretisation with the radial group are presented in fig. 3.24(a), where the frequencies predicted by the analytical ring derived model are also presented for comparison reasons. The major difference of the tangential group modal development from the radial one is that the total frequency range of the group is

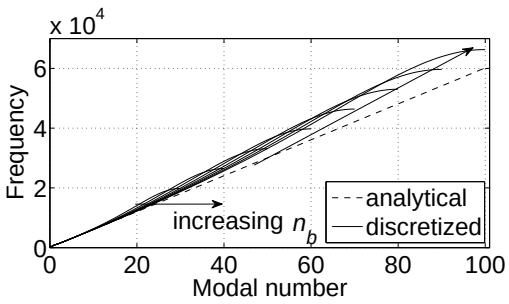

(a) The total frequency range.

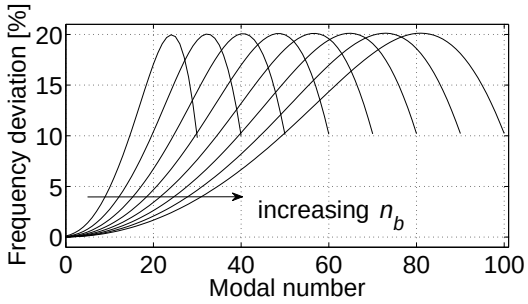

(b) The frequency range of the $n = 1$ to $n = 30$ modes.

Figure 3.24 – The truss model discretisation effect on the prediction of the tangential natural frequencies for increasing total number of elements.

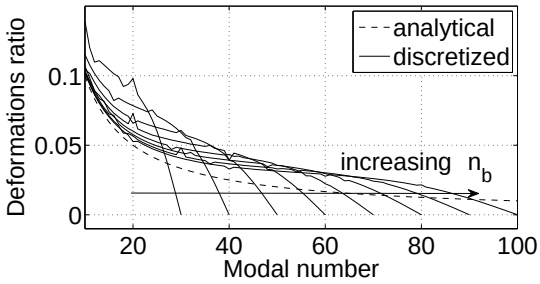

Figure 3.25 – The effect of the discretisation on the ratio of the radial to the tangential deformation of the tangential group mode shapes.

not constant but depends on the number of elements. The increase of this number does not result only in the increase of the modal number range but also in the increase of the respective frequency range.

The truss models overestimate the frequencies also of the tangential group, while, in a way similar to the radial one, the level of overestimation increases radically above a certain modal number, related to the total number of elements. Although this behaviour may be observed across the greatest part of the modal range, a contradicting behaviour may be observed towards the upper limit of the modal range of each model.The frequency rate of change with the modal number decreases and the predicted frequencies of the last part of the modal range appear as lower than the ones predicted by truss models composed by a higher number of elements. The above is evident in fig. 3.24(b) where the percentage deviation of the frequencies of all the truss models from the corresponding analytical model ones is presented. The decrease of the percentage overestimation in the last portion of the modal range is evident in all models. Interestingly, although the frequency deviation of a certain mode is a function of the discretisation, throughout the modal range, this is not true in this last portion, as the maximum percentage deviation and the deviation of the last (maximum modal number) mode are insignificantly affected by the degree of discretisation.

The discussion on the discretisation effect of the truss model tangential group comes to an end with the presentation of the deviation of the radial to the tangential deformations' ratio (fig. 3.25). An initial overestimation of the radial component which transforms into underestimation towards the upper limit of the modal group is apparent for all the discretised cases. In agreement with the radial group behaviour, the whole range from equal ($n = 1$) to zero ($n = n_{max}$) radial participation is covered for each of the models.

Combining these two characteristics, an increase in the number of elements/modes results in a moderate initial ratio overestimation, transforming into a moderate underestimation towards the upper modal limit.

Summarising the analysis of the truss models' discretisation effect, some basic conclusions can be drawn in regards to its necessary consideration when the modal prediction of such a model is to be validated or justified:

- The truss discretisation effect may be identified as an artificial stiffening mechanism of increasing with the modal number magnitude, for both radial and tangential groups. In the radial group, it is accompanied by an underestimation of the relative tangential deformation, but in the tangential one an initial overestimation followed by an underestimation in the last section is observed.
- The magnitude of the effect on a certain mode does not actually depend on its modal number or frequency, but on its order across the predicted modal range. In result, the effect may be deteriorated by the broadening of the available range, through the increase of the number of elements composing the structure.
- The increase of the discretisation degree, broadens the modal range of both radial and tangential groups. An increase of the respective frequency range, though, can be identified only for the tangential group.
- The effect of the discretisation on the radial group is more profound than the effect on the tangential one.

3.5.3 The beam discretised model

As the lack of the bending stiffness mechanism devastated the modal prediction capability of the truss based model compared to the analytical ring one, the investigation of the model composed by rectilinear beam elements shows great interest. As it was highlighted in the truss model analysis, the degrees of freedom increase should not be induced by the angular transformation process, but by their incorporation in the element's initial matrix expression. In accordance, the proposed beam element, does not include only the rotational and vertical deformation terms, associated with the bending mechanism, but also the extensional deformation term (fig.3.15). The additional terms correspond to the superposition of the truss element's axial stiffness terms, decoupled, in the single element case, from the bending stiffness ones. The angular transformation process will induce the coupling between the bending and extensional deformation patterns for the complete structure, as discussed in section 3.5.1.

The stiffness and inertia matrices of the non extensional beam are:

$$\mathbf{K}_{beam} = \frac{E \cdot I}{l^3} \begin{bmatrix} 12 & 6l & -12 & 6l \\ 6l & 4l^2 & -6l & 2l^2 \\ -12 & -6l & 12 & -6l \\ 6l & 2l^2 & -6l & 4l^2 \end{bmatrix} \tag{3.89a}$$

$$\mathbf{M}_{beam} = \frac{\rho \cdot A \cdot l}{420} \begin{bmatrix} 156 & 22l & -54 & -13l \\ 22L & 4l^2 & 13l & -3l^2 \\ 54 & 13l & 156 & -22l \\ -13l & -3l^2 & -22l & 4l^2 \end{bmatrix} \tag{3.89b}$$

After the incorporation of the truss-like axial deformation degree of freedom, the above matrices read:

$$\mathbf{K}_{beam} = \begin{bmatrix} \frac{EA}{l} & 0 & 0 & -\frac{EA}{l} & 0 & 0 \\ 0 & \frac{12EI}{l^3} & \frac{6EI}{l^2} & 0 & -\frac{12EI}{l^3} & \frac{6EI}{l^2} \\ 0 & \frac{6EI}{l^2} & \frac{4EI}{l} & 0 & -\frac{6EI}{l^2} & \frac{2EI}{l} \\ -\frac{EA}{l} & 0 & 0 & \frac{EA}{l} & 0 & 0 \\ 0 & -\frac{12EI}{l^3} & -\frac{6EI}{l^2} & 0 & \frac{12EI}{l^3} & -\frac{6EI}{l^2} \\ 0 & \frac{6EI}{l^2} & \frac{2EI}{l} & 0 & -\frac{6EI}{l^2} & \frac{4EI}{l} \end{bmatrix} \tag{3.90a}$$

$$\mathbf{M}_{beam} = \frac{\rho \cdot A \cdot l}{420} \begin{bmatrix} 140 & 0 & 0 & 70 & 0 & 0 \\ 0 & 156 & 22l & 0 & 54 & -13l \\ 0 & 22l & 4l^2 & 0 & 13l & -3l^2 \\ 70 & 0 & 0 & 0 & 140 & 0 \\ 0 & 54 & 13l & 0 & 156 & -22l \\ 0 & -13l & -3l^2 & 0 & -22l & 4l^2 \end{bmatrix} \tag{3.90b}$$

The transformation form the local system of each element to the global one of the structure, affects the displacement deformations terms but not the rotational ones. Thus, the transformation matrix reads:

$$\mathbf{T}_{beam} = \begin{bmatrix} \cos\varphi_{g\to l} & \sin\varphi_{g\to l} & 0 & 0 & 0 & 0 \\ -\sin\varphi_{g\to l} & \cos\varphi_{g\to l} & 0 & 0 & 0 & 0 \\ 0 & 0 & 1 & 0 & 0 & 0 \\ 0 & 0 & 0 & \cos\varphi_{g\to l} & \sin\varphi_{g\to l} & 0 \\ 0 & 0 & 0 & -\sin\varphi_{g\to l} & \cos\varphi_{g\to l} & 0 \\ 0 & 0 & 0 & 0 & 0 & 1 \end{bmatrix} \tag{3.91}$$

Apart from the discretisation related effects, which will be later discussed, the only physical mechanism difference between the beam model behaviour and the analytical ring one is the lack of the pretension effect from the first one. This is expected to be mainly depicted in the middle modal range, where the inflation non linearity effect seems to maximize (fig. 3.6(c)).

The beam model modal groups

According to the analysis of section 3.5.1, the attribution of three degrees of freedom to each node of the beam-based structure results in the prediction of three modal groups (section 3.5.1). The three degrees of freedom of the beam element, though, do not correspond to different deformation patterns. The vertical to the element's axis deformation and the rotational one (fig. 3.15) are coupled to each through a derivative

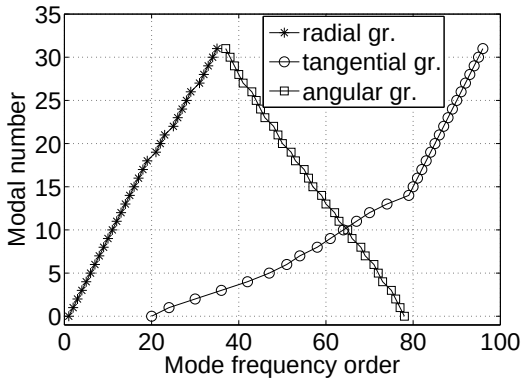

Figure 3.26 – The modal groups of the beam model.

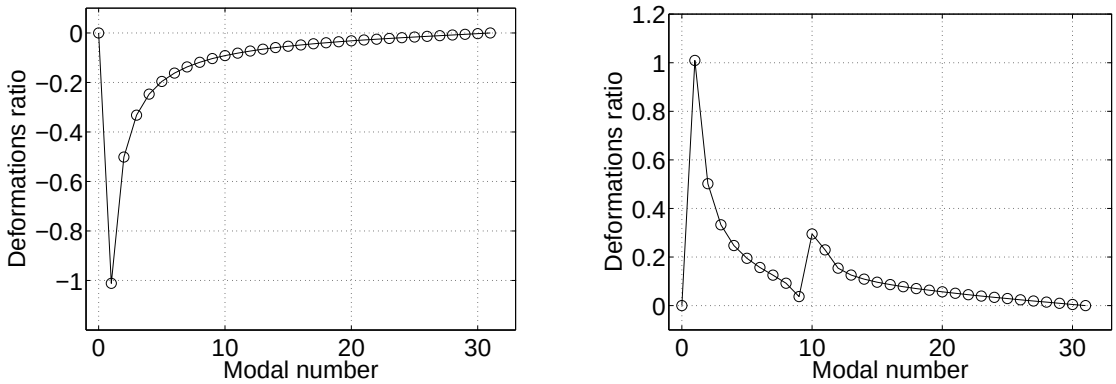

(a) The tangential to radial deformation ratios of the radial modes.

(b) The radial to tangential deformation ratios of the tangential modes.

Figure 3.27 – The relative deformations of the two first modal groups of the beam model.

equation:

$$\tan(\theta) = \frac{\partial u_t}{\partial u_r} \Rightarrow \theta \simeq \frac{\partial u_t}{\partial u_r} \tag{3.92}$$

Consequently, the existence of the angular deformation in the matrices of the element offers no additional degree of freedom to the ones predicted by the extensional ring model, the radial and the tangential displacements.

The frequency order of the modes is presented in fig. 3.26, where the formation of the three modal groups is evident. Moreover, the radial and the tangential groups develop as scattered into each other, in a way similar to the corresponding modal groups of the ring models (fig. 3.17). The position of the tangential modes along the frequency defined modal order is not directly affected by the number of elements, and their positions correlate to the ring predicted ones. This characteristic offers a qualitative correlation between the modal prediction of these two approaches, in contrast to the behaviour of the truss discretised model.

The characterization of the first two modal groups as radial and tangential ones is justified by the ratios of the corresponding deformations, presented in fig. 3.27. The relative direction (sign) and the magnitude

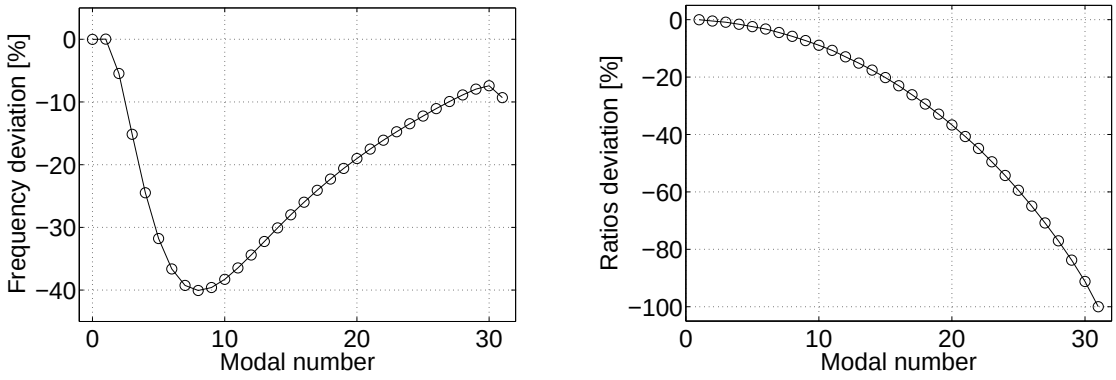

(a) The relative percentage deviation of the radial modes frequencies of the beam model from the respective ring ones.

(b) The relative percentage deviation of the tangential to radial deformations ratio ($\frac{T_n}{R_n}$) of the beam model radial modes from the respective ring ones.

Figure 3.28 – The relative modal behaviour of the beam model radial group to the respective ring one.

of the deformation exhibit a satisfactory correlation to the respective ring modal groups (figs. 3.11(a) and 3.13(a)). Similarly to the truss discretised model, the deformation ratios of both groups extend from equal to zero participation of the supplementary deformation along the modal range, a discretisation related effect that will be later discussed. A small deviation in the ratio development, observed in the middle of the modal range, is attributed to an eigenanalysis computational error, introduced by the close existence of modes belonging to two modal groups (tangential and angular) with convenient modal numbers and frequencies, something that imposes a critical condition to any numerical eigenanalysis method [246]. The deviation area can be identified in fig. 3.26 as the intersection of the two groups.

The third modal group develops sequentially after the completion of the radial one. Although in fig. 3.26, the name angular is inherited from the third distinctive degree of freedom of every node, the associated mode shapes do not always reveal the angular deformation as the primal one. It should be highlighted that in this modal group the frequency-defined order of the modes is contrary to the modal number defined one. This modal development pattern, though, objects to the generic physical mechanism, according to which the frequency of any structural mode increases with the modal number. As this third modal is artificial induced by the element's matrices and its behaviour does not coincide with the physical one, it will be dropped from the further study of the beam model modal characteristics.

The radial group modal behaviour is presented in fig. 3.28, in comparison to the ring corresponding one. In general, the beam model underestimates the natural frequencies along the whole modal range (fig. 3.28(a)). As it is expected, the level of underestimation increases for the low modal numbers, reaches a maximum value and decreases above that. This parabolic behaviour coincides with the development of the inflation pretension effect across the modal range (fig. 3.6(c)). The decrease in the deviation level for higher modal number can be justified by the predominant bending stiffness effect as the modal number increases (depicted as an elastic modulus dependency in fig. 3.6(d)), a stiffness mechanism accurately captured by the beam model. In terms of magnitude, the frequency deviation of the beam model is significantly lower than the truss model one. Although equal levels of underestimation are exhibited by both models for low modal numbers, the existence of the bending mechanism improves significantly the prediction characteristics of the

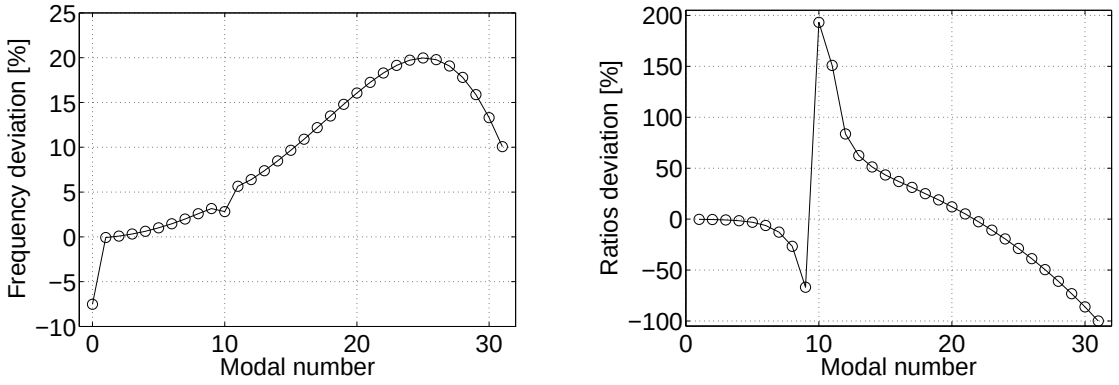

(a) The relative percentage deviation of the tangential modes frequencies of the beam model from the respective ring ones.

(b) The relative percentage deviation of the radial to tangential deformations ratio ($\frac{R_n}{T_n}$) of the beam model tangential modes from the respective ring ones.

Figure 3.29 – The relative modal behaviour of the beam model tangential group to the respective ring one.

beam model in the high modal number zone of the modal range.

The tangential deformation component of the radial mode shapes is lower than the respective ring model one (fig. 3.28(b)). Similarly to the development of the truss model radial group, the deviation increases with the modal number, ranging from the zero value (perfect correlation of the participation) to the complete absence of tangential deformation.

The tangential modal group behaviour is compared with the respective ring one in fig. 3.29. Apart from the torsional zero mode frequency, which is underestimated compared to the ring one for reasons associated with the absence of the pretension effect, all the other tangential frequencies are overestimated. The percentage overestimation increases up to a maximum value, towards the end of the tangential group, after which it deteriorates. The behaviour is similar to the truss model one and as it will later discussed, is induced by the discretisation effect. The deviation of the radial deformation participation in the mode shapes, though, develops a different pattern (fig. 3.29(b)). The percentage level of deviation initially drops, but suddenly increases for a specific value, after which it deteriorates again. The behaviour is largely affected by the computational error induced by the coexistence of the tangential and angular groups in close frequencies and modal numbers, which prevents the drawing of conclusion related to the associated physical mechanisms.

Summarizing the physical mechanism induced deviation of the beam model from the ring one, the following remarks should be highlighted:

- Both radial and tangential modal groups are represented and their deployment pattern correlates well with the ring model predicted one. A third, artificial, modal group develops as a result of the inclusion of the rotational deformation of the node as a distinct degree of freedom in the element's matrix.

- The frequencies of the radial modal group are underestimated, especially in the middle modal range as a direct consequence of the pretension effect absence. The degree of underestimation decreases for higher modal numbers, as bending becomes the predominant mechanism.

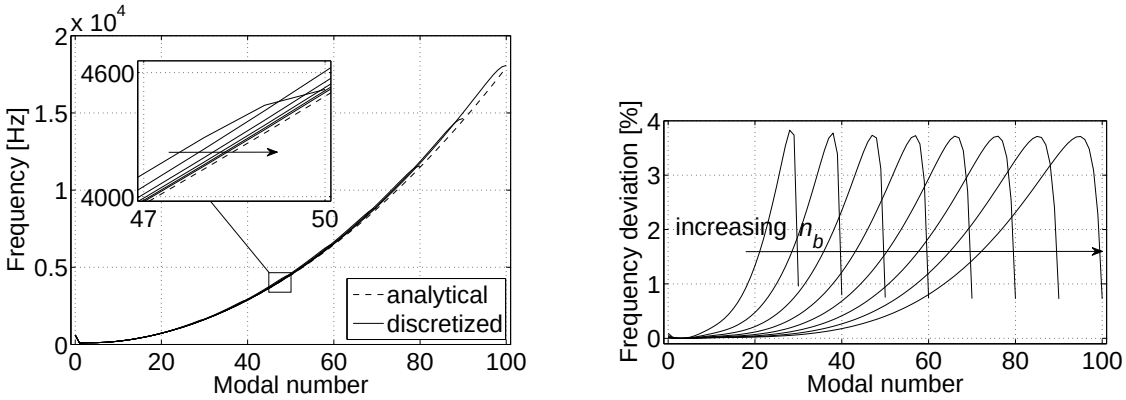

(a) The complete range of frequencies of the radial modes, for increasing number of elements.

(b) The percentage deviation of the beam model frequencies from the respective ring ones.

Figure 3.30 – The effect of beam discretisation on the prediction of the radial natural frequencies for increasing number of elements.

The beam model discretisation effect

Similarly to the truss model analysis, many characteristic differences of the beam model modal prediction from the respective ring one cannot be attributed to an absence or difference of a physical mechanism between them. The increasing underestimation of the tangential deformation with the modal number across the radial modal group, and the modal behaviour (frequencies and deformations) of the tangential one cannot be justified by the absence of the inflation pretension. For this reason, the discretisation effects will be examined, in order to be determined if they can offer a satisfactory justification. Similarly to the truss respective investigation, beam models with gradually increasing number of elements ($n_b = 60, 80, 100, 120, 140, 160, 180$ and 200), will be compared to a non pretensioned ring model.

The complete range of the natural frequencies of the radial modal group is presented in fig. 3.30(a), together with the frequency prediction of the ring model. The percentage frequency deviation from the latter one of each of the beam models is presented in fig. 3.30(b). In general, all the discretised models predict a, similar to the ring model, parabolic development of the frequencies with the modal number and a slight overestimation can be identified in all of them. Interestingly, as it can be observed in the second figure, although the percentage overestimation increases towards the upper limit of the available modal range, a radical drop in the overestimation level is identified in the last section of it. The maximum percentage of overestimation is equal for any discretisation level, as is also the percentage value corresponding to the last mode. A similar behaviour was identified for the tangential modal group of the truss models.

Apart from the apparently smaller deviation magnitude from the corresponding analytical solution, another major difference between the radial modal group prediction of the beam and the truss model must be highlighted. As it has been observed (fig. 3.22(a)) the predicted frequency range in the truss case does not depend on the discretisation level and the total number of modes, although the latter significantly affects the deviation from the analytical solution of a certain examined mode. In the beam case, though, the total breadth of frequency range of the radial group increases almost proportionally to the number of elements and the resulting modal range.

The discretisation effect on the tangential deformation component of the radial mode shapes is presented

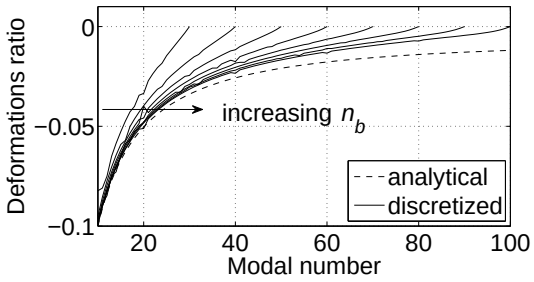

Figure 3.31 – The effect of the discretisation on the ratio of the tangential to the radial deformation of the radial group mode shapes.

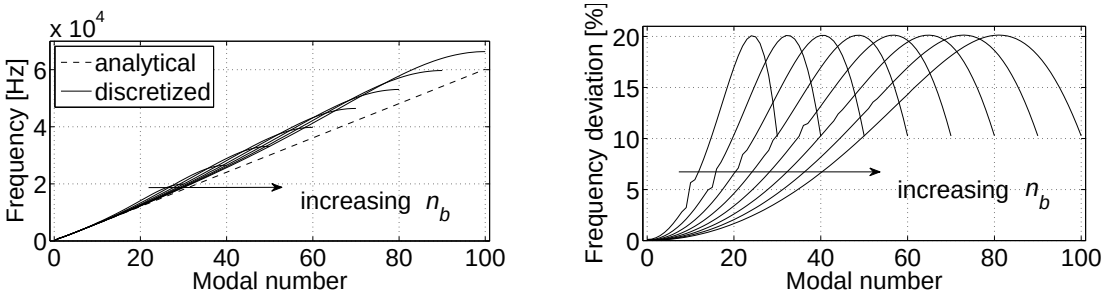

(a) The complete range of frequencies of the tangential modes, for increasing number of elements.

(b) The percentage deviation of the beam model frequencies from the respective ring ones.

Figure 3.32 – The effect of beam discretisation on the prediction of the tangential natural frequencies for increasing number of elements.

in fig. 3.31. In contrast to the frequencies prediction, the behaviour is similar to the one of the truss model radial group (fig. 3.20(b)), in both qualitative (underestimation) and quantitative terms. Independently from the number of elements, the whole relative participation range, from equal to zero, is covered. This results in increasing underestimation level with the degree of discretisation, for a particular mode. The relative tangential to radial deformation values tend asymptotically to the analytical model ones, also presented in fig. 3.31, as the number of elements increases.

Moving the discussion to the tangential modal group, a similar to the radial group development pattern may be identified (fig. 3.32). Quantitatively, though, higher deviation levels than the ones of the radial group can be observed. The behaviour shows very good correlation with the one predicted by the truss model tangential modal group, in both overestimation development patterns and magnitudes. This may be justified not only by the equal physical mechanism representing the extensional deformation of the elements (which primarily defines the modal behaviour of the tangential modal group), but also by the similar modelling capture of this mechanism by both elements (eqns. 3.87 and 3.90).

The effect of the discretisation on the participation of the radial deformation in the mode shapes of the group (fig. 3.33), is difficult to be identified for the already discussed computational reasons. Detracting the deviation pattern associated with this anomaly, the, already identified (fig. 3.27(b)), underestimation trend follows the, commonly observed, mode deviation dependency on its relative to the upper modal limit position in the modal range.

Summarizing the effect of discretisation on the beam model modal prediction some basic conclusions

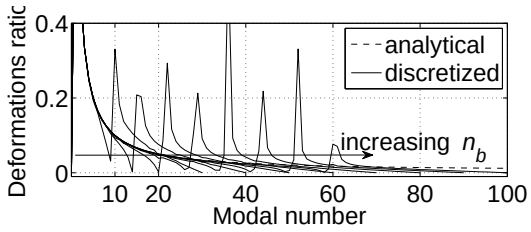

Figure 3.33 – The effect of the discretisation on the ratio of the radial to the tangential deformation of the tangential group mode shapes.

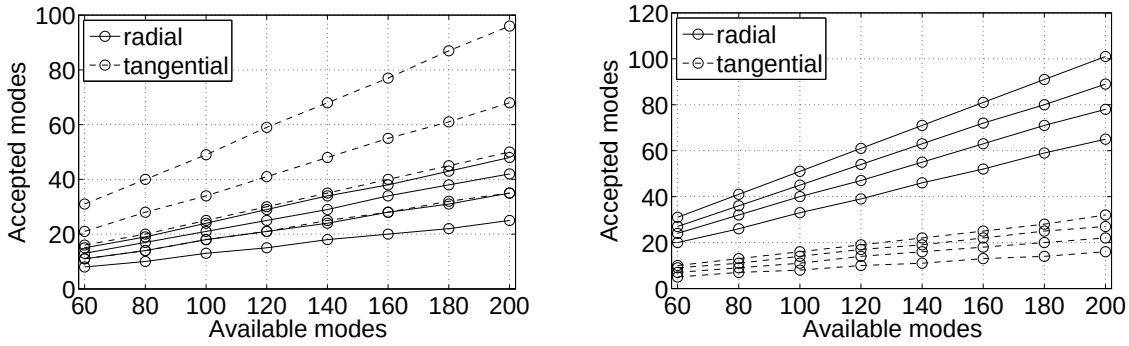

(a) Truss model modes fulfilling a 5, 10, 15, 20% criteria.

(b) Beam model modes fulfilling 1, 2, 3, 4% criteria.

Figure 3.34 – The number of modes satisfying a criteria of certain deviation from the corresponding analytical frequencies, as a function of the total number of available modes.

must be highlighted, especially in comparison to the corresponding ones drawn by the examination of the truss model:

- Similarly to the truss model, the discretisation imposes an artificial stiffening effect and a reduction of the supplementary relative deformation on both modal groups of the beam model. The effect on a particular mode does not depend on its modal number or frequency, but on its relative position (order) across the predicted modal range. Consequently, this effect can be deduced by an increase of the discretisation level.

- The frequency ranges of both the radial and tangential modal groups increase proportionally to the respective modal ranges and the degree of discretisation. In the truss case, though, the frequency range of the radial group was found to be independent of the modal range.

- The discretisation effect is more profound on the tangential modal group, in comparison to the radial one. The contrary conclusion was drawn in the truss model case.

In the preceding analysis, it has been multiply emphasized for both truss and beam models that the deviation from the respective analytical behaviour increases in a non linear way with the modal number and is magnified towards the upper limit of the available modal range. If a cut off frequency or modal number limit is to be chosen as an initial step for the application of a modal reduction method on a discretised model, the above conclusion should be taken into severe consideration.

The increase of the discretisation degree broadens the modal range in which the related phenomena may be considered as insignificant. Moreover, it may be proposed that the number of modes that meet a criteria of certain percentage deviation from the respective analytical frequencies is proportional to the total number of elements. This is presented in fig. 3.34, where various values of percentage frequency deviation are proposed as criteria for the modes of the truss (fig. 3.34(a)) and the beam models (fig. 3.34(b)).

3.5.4 The enhanced beam discretised model

It may be argued that if the study of a highly discretised beam model is limited to the low-medium modal range, the effect of the discretisation is insignificant and the only factor that makes the predicted modal behaviour divert from the one of the analytical ring is the lack of the pretension mechanism (fig. 3.28(a)). Although the pretension effect can be generally described as a stiffening one, an increase of the elastic modulus cannot be proposed as a compensating solution. As it is obvious in figs. 3.6(c) and 3.6(d), the effect of the two properties (inflation pressure and material modulus) is associated with different zones of the modal range and, moreover, the effect of the elastic modulus does not deteriorate in the high modal number range. In result, a possible attempt for correlation between the beam and ring models medium modal range behaviour through a correction of the elastic modulus value would result in an excessive increase of the high modal number frequencies and the stiffening of the structure's behaviour.

A method based on a physical mechanism will be proposed for the capture of the inflation effect by the beam model. The method is based on the superposition of a linear, inextensible, string under tension element, on the beam element's stiffness matrix. Such a mechanism has been proposed as an analytical rectilinear belt representation in section 3.2.1. The differential equation which describes the transverse vibrational behaviour of the string element along its length is similar to eqn. 3.93, dropping the sidewall corresponding term:

$$T\frac{\partial^2 u_y}{\partial x^2} = \rho A\frac{\partial^2 u_y}{\partial t^2} \tag{3.93}$$

where:

T	the tension force
u_y	the transverse deformation
y	the direction transverse to the axis of the string
x	the dimension along the axis of the string
ρ	the material density
A	the cross-section area

In order to express the string mechanism described by eqn. 3.93 in a discretised way, a rectilinear string element of equal length (l) to the beam one is proposed, sharing the same nodes. The two degrees of freedom of each string element (to which the deformation term u_y of eqn. 3.93 applies to) coincide with the vertical to the element's axis degrees of freedom of the beam. The superposition of the string element is characteristically presented in fig. 3.35. Although the string element is assumed to be a rectilinear one, the calculation of its tension force is based on an arc-shaped assumption, with the same radius with the belt circumference (R). The tension force is given by eqn. 3.93, which is repeated here:

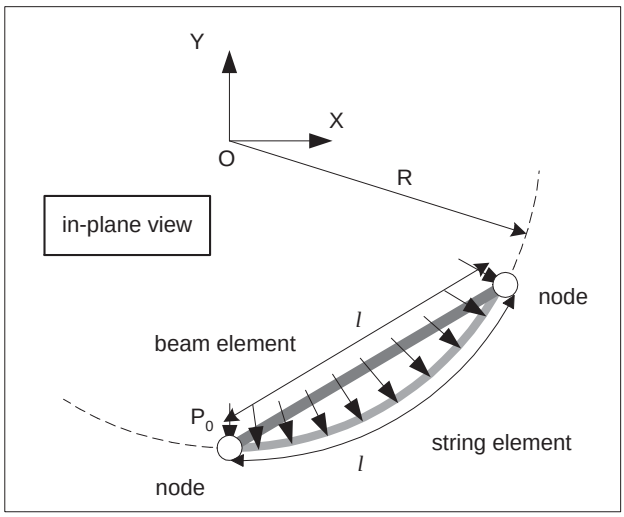

Figure 3.35 – The combined bean and string element.

$$T = P_0 \cdot R \cdot b \tag{3.94}$$

where:

P_0	the inflation pressure
R	the belt radius
b	the belt width

The differential eqn. 3.93 now reads:

$$\frac{\partial^2 u_y}{\partial x^2} = \frac{\rho \cdot d}{P_0 \cdot b} \frac{\partial^2 u_y}{\partial t^2} \tag{3.95}$$

For the expression of the string element behaviour in an equivalent to the stiffness way, a linear interpolation method [248] is assumed along the element. The process is similar to the one followed for the derivation of the truss element stiffness matrix, although in this case the interpolated deformation (U_y) lies in the direction vertical to the element's axis. The deformation function along the may be written as:

$$u_y(x,t) = u_y^1(t) + x\frac{u_y^2(t) - u_y^1(t)}{l} \Rightarrow u_y(x,t) = (1 - \frac{x}{l})u_y^1(t) + \frac{x}{l}u_y^2(t) \tag{3.96}$$

where u_y^1 and u_y^2 are the deformation values of the two nodes, and x the position along the element's axis.The emerging expression for the stiffness matrix reads:

$$K_{string} = \frac{P_0 \cdot R \cdot b}{l} \begin{bmatrix} 1 & -1 \\ -1 & 1 \end{bmatrix} \tag{3.97}$$

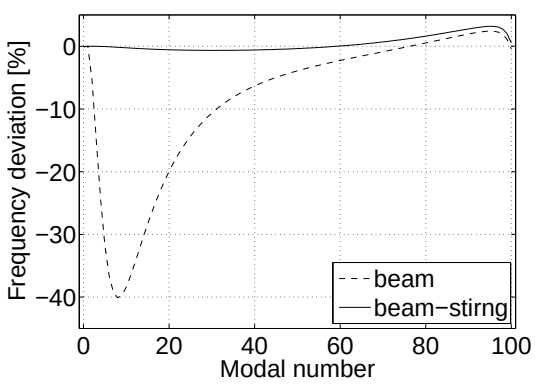

(a) The frequency deviation of the radial modes.

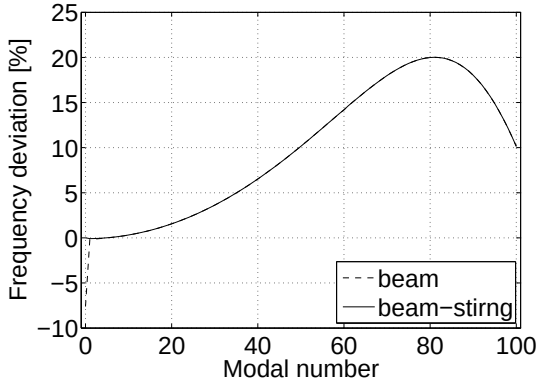

(b) The frequency deviation of the tangential modes.

Figure 3.36 – The frequency deviation of the radial and the tangential modes predicted by the combined beam-string discretised model from the pretensioned ring one.

The updated stiffness matrix of the beam element, incorporating the inflation-dependent contribution of the string element, reads:

$$K^{local}_{beam-string} = \begin{bmatrix} \frac{EA}{l} & 0 & 0 & -\frac{EA}{l} & 0 & 0 \\ 0 & \frac{12EI}{l^3} + \frac{P_0 Rb}{l} & \frac{6EI}{l^2} & 0 & -\frac{12EI}{l^3} - \frac{P_0 Rb}{l} & \frac{6EI}{l^2} \\ 0 & \frac{6EI}{l^2} & \frac{4EI}{l} & 0 & -\frac{6EI}{l^2} & \frac{2EI}{l} \\ -\frac{EA}{l} & 0 & 0 & \frac{EA}{l} & 0 & 0 \\ 0 & -\frac{12EI}{l^3} - \frac{P_0 Rb}{l} & -\frac{6EI}{l^2} & 0 & \frac{12EI}{l^3} + \frac{P_0 Rb}{l} & -\frac{6EI}{l^2} \\ 0 & \frac{6EI}{l^2} & \frac{2EI}{l} & 0 & -\frac{6EI}{l^2} & \frac{4EI}{l} \end{bmatrix} \tag{3.98}$$

The inertia matrix remains that of the beam element, described by eqn. 3.90b.

The percentage frequency deviation of the radial and the tangential modal groups, predicted by the enhanced model, from the complete (pretensioned) ring model is respectively presented in figs. 3.36(a) and 3.36(b). It is evident that the frequency correlation of the radial group has been significantly improved, especially in the middle range, where the effect of the pretension is dominant (fig. 3.6(c)). An insignificant deviation along the modal range can be observed and only a slightly increased frequency overestimation can be identified, in the high modal, final, portion. The frequency deviation of the tangential group remains though constant, as it is mainly attributed to the discretisation effect and not to any physical mechanism difference. Moreover the radial deformation associated with the tangential modal group is not profound (fig. 3.27(b) and the change to the stiffness mechanism related to it hardly affect the frequency prediction of the group. The significantly improved correlation of the torsional zero mode should be, though, mentioned.

3.6 Summary of the modal behaviour of the belt models

Having completed the presentation of the basic belt modelling approaches and before moving to the analysis of other factors affecting the tyre modal behaviour, a brief summary of the basic conclusions drawn from the

above analysis may be useful.

The relative to each other modal behaviour of the proposed models develops on the basis that either the suspension of a strain component (deformational degree of freedom) or the incorporation of an additional stiffness mechanism impose a stiffening effect, while the addition of a deformation pattern or the drop of a stiffness mechanism contribution result in the "relaxation" (stiffness decrease) of the modal behaviour. Moreover, the development of the deviation of each model from the complete ring one, along the modal range, may be justified by the modal sensitivity analysis (section 3.4.1) of the latter one. In the case of the discretised models, the discretisation stiffening effect has to be taken into consideration, especially in case the examined modes lie close to the upper limit of the available range.

- **Rectilinear models**
  The radial (vertical) rectilinear model overestimates the natural frequencies, compared to a ring model with similar stiffness mechanisms, as its strain lacks the coupling between the radial and the tangential deformation. The overestimation is profound in the low modal range modes, the mode shapes of which predict a significant tangential deformation pattern. In terms of stiffness properties incorporation, the omission of bending stiffness (rectilinear string model) results in increasing underestimation with modal number, while the omission of string stiffness (rectilinear beam model) mainly affects the medium modal range. Both development trends are in absolute agreement with the ring modal sensitivity analysis. In the case of the tangential (extensional) rectilinear model, the overestimation of the frequencies is so severe that its comparison with the ring model is meaningless.

- **Ring models**
  An inextensible, membrane strain lacking, ring model exhibits frequency overestimation in the low modal range, where the ring coupling between the radial and the tangential deformation of the complete model is more intense. The lack of the membrane strain also imposes the underestimation of the tangential deformation, the degree of which increases with the modal number. In terms of stiffness mechanism incorporation, the effect of the pretension mechanism drop may be identified mainly in the middle radial modal range. In the high modal range, both of the above frequency deviation effects (tangential strain suspension and pretension absence) deteriorate, as the radial bending mechanism becomes the predominant modal factor. All the ring models, able to predict a tangential modal group, correlate well to each other in terms of frequencies values and deformation patterns.

- **Truss model**
  Both radial and tangential modal groups are predicted, although their sequential deployment pattern does not correlate with the scattered one of the ring model, nor does the corresponding frequency range prediction of the radial group. Radial frequencies are severely underestimated along the modal range and the degree of underestimation increases with the modal number. The absence of bending (mainly) and the pretension (secondarily) stiffness mechanisms are responsible for the deviation magnitude increasing pattern. The slight frequency overestimation of the tangential modal group, though, is not imposed by a physical mechanism but by the discretisation effect.

- **Beam model**
  Three modal groups are predicted, two of which correlate adequately with the radial and the tangential

ones of the ring model, in terms of deployment pattern and characteristic deformations, and a third one, artificially imposed by the form of the element's matrices. The radial frequencies correlate well with the ring ones, especially in the high modal range. The middle range frequency underestimation can be attributed to the lack of the pretension mechanism, and the frequency prediction potential is radically improved by the incorporation of a string physical stiffness mechanism to the model. The tangential modal group characteristics are similar to the truss model tangential group, as the stiffness mechanism associated with the dominant tangential deformation is satisfactorily captured by the element's stiffness matrix.

3.7 The sidewall related modal effect of the inflation pressure

The modal effect of the inflation pressure is not limited to the circumferential pretension of the belt, presented in section 3.3. Acting on the tyre sidewall, air pressure directly influences the sidewall stiffness through a non linear mechanism. This effect is intensified by the sidewall profile shape variations imposed by the inflated equilibrium of the tyre at different values of radius.

The actual tyre sidewall is a relatively thin structure composed by several cord layers of high tensile strength but small bending stiffness, covered by a thin rubber surface. This morphology justifies the choice of a membrane or string (in terms of tyre cross section) mechanism in order to represent the, geometry and pressure related, inflation dependency of the radial stiffness of the tyre. This dependency develops through their non-linear effect on the magnitude and orientation of the sidewall tension force. A discretised formulation combining a string-based sidewall and a beam-based belt can be found in [117], while a complete modal study using a tyre model incorporating a string/beam based sidewall is presented in [128]. The concept of the inextensible membrane based sidewall will be analysed in the following for the capture of the sidewall-related effect of the inflation pressure on the ring modal behaviour. Prior to that, though, the response calculation of a modally expended belt model will be presented, as the process is crucial not only for the calculation of the inflation deformation but also of the operational response of the tyre which will be examined in the following chapters.

It should be noted that another effect of the inflation is related to the vibrational coupling between the belt and the quantity of air which is contained in the tyre cavity. Although this coupling does affect slightly the modal characteristics of the tyre, its main effect is related to the acoustics behaviour as opposed to the structural one. The air coupling phenomena play a predominant role in the generation of the tyre rolling noise but not in the actual traction or structural performance characteristics. For this reason, the air coupling phenomena will be excluded from the present analysis. Gautin and Ropers in [249] describe some of the simulation tools which have been developed by the tyre industry for the study of the noise related air coupling effects.

3.7.1 The transient response calculation of a modally expanded ring model

Although space domain numerical methods for the calculation of the belt response, as prescribed by the ring equations of motion, exist (for example the finite differences method presented by Wijnant and De Boer in [245]) ring and analytical in general models are commonly associated with methods based on their modal expansion. The reason for that will become obvious in chapter 4, when such an approach will be combined

with a modal reduction method for the improvement of the computational efficiency of the model. The response calculation of a modally expanded ring structure has been thoroughly presented by Soedel in [83] and a brief summary of the main aspects of the method will be given in the following, in order the calculation of the inflation response to be explained.

In general, the transient response of a modally expanded structure can be expressed in the space-time domain as the superposition of the mode shape functions of the structure, each of them multiplied with a respective modal participation factor. The space and time factors of the response are decoupled, as the mode shapes offer the space deformation pattern of it but remain constant over time, while the participation factors (time functions) offer the transient nature of the response. For the linear ring case, given that its analytical nature theoretically imposes an infinite number of modes, it may be proposed:

$$u_{r/t}(\theta, \mathrm{t}) = \sum_{\mathrm{j}=1}^{\infty} \eta_{\mathrm{j}}(\mathrm{t}) \cdot \mathrm{U}_{\mathrm{r/t}}^{\mathrm{j}}(\theta) \tag{3.99}$$

where:

$u_{r/t}$	the radial/tangential deformation response functions
η_j	the modal participation factor of the jth mode
$U_{r/t}^{j}$	the radial/tangential deformation functions of the mode shape of the jth mode

The time history of each modal participation factor, $\eta_j(t)$, is calculated by a respective second order differential equation of time:

$$\ddot{\eta}_j + \lambda_j \dot{\eta}_j + \omega_j^2 \eta_j = f_j^m(\mathrm{t}) \tag{3.100}$$

where:

λ_j	the modal damping coefficient of the jth mode
f_j^m	the modal force of the jth mode

Rewriting the above differential equation in the form:

$$R \cdot \rho \cdot d \cdot \Gamma_j \cdot \ddot{\eta}_j + R \cdot \rho \cdot d \cdot \Gamma_j \cdot \lambda_j \dot{\eta}_j + R \cdot \rho \cdot d \cdot \Gamma_j \cdot \omega_j^2 \cdot \eta_j = f_j^{m'}(\mathrm{t}) \tag{3.101}$$

where:

$$\Gamma_j = \int_0^{2\pi} \left[\left(U_r^j(\theta) \right)^2 + \left(U_t^j(\theta) \right)^2 \right] \mathrm{d}\theta \tag{3.102}$$

The coefficients of eqn. 3.101 are the modal properties of the system:

$$m_j^m = R \cdot \rho \cdot d \cdot \Gamma_j, \text{ modal mass} \tag{3.103}$$

$$c_j^m = R \cdot \rho \cdot d \cdot \Gamma_j \cdot \lambda_j, \text{ modal damping} \tag{3.104}$$

$$k_j^m = R \cdot \rho \cdot d \cdot \Gamma_j \cdot \omega_j^2, \text{ modal stiffness} \tag{3.105}$$

where: m_j^m the modal mass of the jth mode
c_j^m the modal damping of the jth mode
k_j^m the modal stiffness of the jth mode

Eqn. 3.101 can be rewritten as:

$$m_j^m \cdot \ddot{\eta}_j + c_j^m \cdot \dot{\eta}_j + k_j^m \cdot \eta_j = f_j^{m'}(\mathrm{t}) \tag{3.106}$$

By transferring the units of the response $[m]$, predicted by eqn. 3.99, from the deformation (u) to the participation factors (η), the modal mass, the modal damping and the modal stiffness may be expressed in units of mass, damping coefficient and stiffness respectively ($[kgr]$, $[N \cdot sec/m]$ and $[N/m]$). The modal force of eqn. 3.101 is calculated as:

$$f_j^{m'}(\mathrm{t}) = \mathrm{R} \int_{\theta=0}^{2\pi} \big(\mathrm{p_r}(\mathrm{t},\theta) \cdot \mathrm{U_r^j}(\theta) + \mathrm{p_t}(\mathrm{t},\theta) \cdot \mathrm{U_t^j}(\theta)\big)\mathrm{d}\theta \tag{3.107}$$

where $p_r(\theta,\mathrm{t})$ and $p_t(\theta,\mathrm{t})$ are the excitation pressures functions (or forces normalised to the tyre width and circumferential length). In respect, the modal force term in the above equation may be expressed in $[N]$. Obviously, in order to be consistent with the circumferentially length only normalised form of the ring equations of motion (eqn. 3.23), eqn. 3.101 should be multiplied with the ring width b and accordingly the excitation forces could be expressed as length normalised values. Taking into account this consideration, the simple form of the factors differential equation (3.100) can be used, as far as the modal forces are calculated according to:

$$f_j^m(\mathrm{t}) = \frac{\mathrm{R}}{\mathrm{b} \cdot \mathrm{m_j^m}} \int_0^{2\pi} \big(\mathrm{q_r}(\theta,\mathrm{t}) \cdot \mathrm{U_r^j}(\theta) + \mathrm{q_t}(\theta,\mathrm{t}) \cdot \mathrm{U_t^j}(\theta)\big)\mathrm{d}\theta \Rightarrow \tag{3.108}$$

$$f_j^m(\mathrm{t}) = \frac{1}{\mathrm{b} \cdot \rho \cdot \mathrm{d} \cdot \Gamma_\mathrm{j}} \int_0^{2\pi} \big(\mathrm{q_r}(\theta,\mathrm{t}) \cdot \mathrm{U_r^j}(\theta) + \mathrm{q_t}(\theta,\mathrm{t}) \cdot \mathrm{U_t^j}(\theta)\big)\mathrm{d}\theta \tag{3.109}$$

where additionally, q_r and q_t are the circumferential length normalised ring excitation forces.

3.7.2 The simulation of the tyre inflation

The computational advantage of the above described modal-time domain calculation for the inflation response is obvious, if the form of the respective excitation is considered. The tangential component of it is zero, while the radial one is constant function in regards to the time and angle variables:

$$q_r^{inf}(\theta,\mathrm{t}) = \mathrm{P_0} \cdot \mathrm{b} \tag{3.110a}$$

$$q_t^{inf}(\theta,\mathrm{t}) = 0 \tag{3.110b}$$

Accordingly, the modal force expression may be simplified in the following:

$$f_j^m = \frac{R}{b \cdot m_j^m} \int_{\theta=0}^{2\pi} \big(P_0 \cdot r \cdot U_r^j(\theta)\big) \mathrm{d}\theta = \frac{R \cdot P_0}{b \cdot m_j^m} \int_{\theta=0}^{2\pi} U_r^j(\theta) \mathrm{d}\theta \tag{3.111}$$

Substituting in the above modal force expression the typical harmonic mode shape function (eqn. 3.5), it is derived:

$$f_j^m(\theta, \mathrm{t}) = \frac{\mathrm{R} \cdot \mathrm{P_0}}{\mathrm{m_j^m}} \int_{\theta=0}^{2\pi} \mathrm{R_j^m} \cos\big(\mathrm{n_j}(\theta - \varphi)\big) \mathrm{dt} \tag{3.112}$$

$$\Rightarrow f_j^m(\theta, \mathrm{t}) = \left\{ \begin{array}{r} 0, \quad n_j \neq 0 \\ \dfrac{P_0 \cdot R \cdot R_j^m \cdot 2\pi}{m_j^m}, \quad n_j = 0 \end{array} \right\} \tag{3.113}$$

The above equation associates the inflation procedure with the excitation of a sole mode, the zero tangential (breathing) one, as the other zero mode, the radial (torsional) one, exhibits no radial deformation (section 3.3.1). In other words, the ring response to the inflation pressure excitation may be captured by the breathing mode participation history. The modal mass of the breathing mode is calculated as:

$$m_{br} = \rho \cdot d \cdot R \int_{\theta=0}^{2\pi} (R_{br}^m)^2 \mathrm{d}\theta = \rho \cdot d \cdot R \cdot 2\pi \cdot (R_{br}^m)^2 \tag{3.114}$$

where R_{br} correspond to the deformation magnitude of the breathing mode shape. The respective modal force may be written as:

$$\left\{ \begin{array}{l} 3.113 \\ 3.114 \end{array} \right\} \Rightarrow f_{br}^m = \frac{P_0 \cdot R \cdot 2\pi \cdot R_{br}^m}{\rho \cdot d \cdot R \cdot 2\pi \cdot (R_{br}^m)^2} = \frac{P_0}{\rho \cdot d \cdot R_{br}^m} \tag{3.115}$$

The breathing participation factor is calculated by the differential eqn. 3.100:

$$\ddot{\eta}_{br} + \lambda_{br} \dot{\eta}_{br} + \omega_{br}^2 \eta_{br} = \frac{P_0}{\rho \cdot d \cdot R_{br}^m} \tag{3.116}$$

while the respective radial deformation is calculated as:

$$u_r^{br}(\mathrm{t}) = \eta_{\mathrm{br}}(\mathrm{t}) \cdot \mathrm{R_{br}^m} \tag{3.117}$$

and the equilibrium (steady state) deformation as:

$$3.99 \Rightarrow u_r^{br}|_{eq.} = \eta_{br}|_{eq.} \cdot R_{br} \tag{3.118}$$

$$\Rightarrow u_r^{inflation} = \frac{P_0}{\rho \cdot d} \tag{3.119}$$

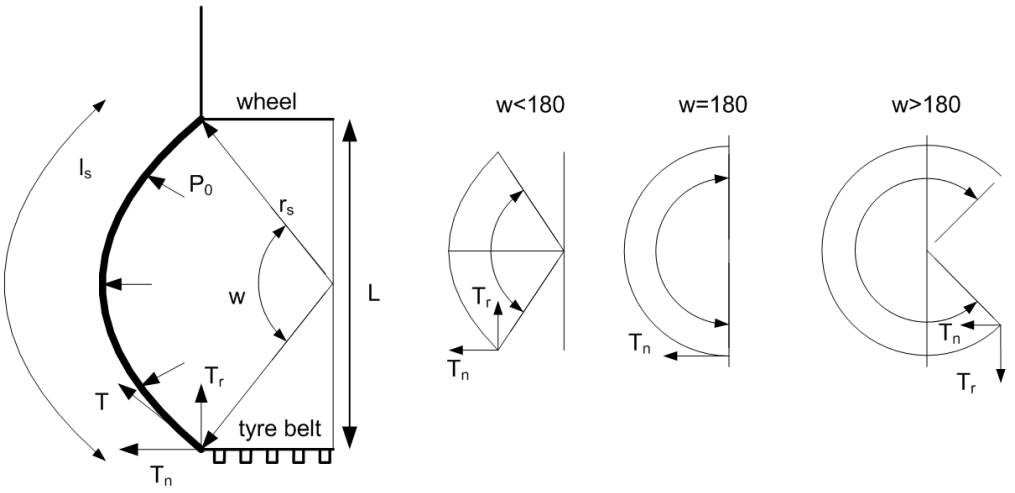

Figure 3.37 – The cross section of the membrane radial sidewall mechanism and the resulting force direction for various deformation shapes of it.

It may be concluded from the above analysis that under the linear -small deformation- assumption, the calculation of the inflation equilibrium deformation of the ring deduces to an algebraic equation (3.119). In reality, though, the validity of the above sequence of calculations could be argued, as the breathing mode frequency derived from the application of the modal expansion method under non inflated conditions cannot be assumed as valid for the inflated tyre under various pressure values, mainly due to the sidewall nonlinearity. The inflation dependency (geometrical and pressure) of the sidewall stiffness affects the breathing frequency. In order this non linearity to be captured, a membrane sidewall model will be introduced in the above calculation procedure.

3.7.3 The inextensible membrane sidewall mechanism

The sidewall of the tyre is modelled as an inextensible membrane surface of radius r, constrained by the cylindrical structure of the wheel and the cylindrical circumference of the belt. A cross section of the complete model is presented in fig. 3.37, together with the tension force and its radial and lateral components for various geometries of the membrane. The total tension force and its normalised to the length of the tyre circumference value are given by the following equations:

$$T_{membrane} = P_0 \cdot 2 \cdot \pi \cdot R \cdot r_s \tag{3.120}$$

$$q_{membrane} = P_0 \cdot r_s \tag{3.121}$$

The calculation of the membrane curvature may be derived from fig. 3.37 and the solution of the following

system of equations:

$$\left.\begin{array}{c} \dfrac{w}{l_s} = \dfrac{1}{r_s} \\ \sin\dfrac{w}{2} = \dfrac{L}{2\cdot r_s} \end{array}\right\} \Rightarrow \sin\frac{l_s}{2\cdot r_s} = \frac{L}{2\cdot r_s} \tag{3.122}$$

where additionally:

- L the radial distance between the belt and the wheel
- w the central angle of the sidewall arc
- l_s the circumferential length of the string arch

It is evident from the above equations that although the membrane force is proportional to the inflation pressure, its dependency on the membrane shape is a non linear one. The radial term of its magnitude is calculated as:

$$q_r^{membrane} = -P_0 \cdot \frac{l_s}{w} \cdot \cos\frac{w}{2} \tag{3.123}$$

In order the membrane sidewall mechanism to be incorporated in the ring model, the linear sidewall stiffness term (k_r) is dropped from the radial equation of motion 3.54a and the radial term of the membrane force ($q_r^{membrane}$) of both sidewall structures is regarded as an external radial excitation. Eqn. 3.54a is substituted by the following one, given that both sidewalls of the tyre offer the same force contribution:

$$\frac{D}{R^4}\left(\frac{\partial^4 u_r}{\partial\theta^4} - \frac{\partial^3 u_t}{\partial\theta^3}\right) + \frac{K}{R^2}\left(u_r + \frac{\partial u_t}{\partial\theta}\right) - \frac{P_0\cdot b}{R}\left(\frac{\partial^2 u_r}{\partial\theta} - 2\frac{\partial u_t}{\partial\theta} - u_r\right) + \rho\cdot A\frac{\partial^2 u_r}{\partial t^2} = 2\cdot q_r^{membrane} \tag{3.124}$$

The equation:

$$L = R + u_r - R_w \tag{3.125}$$

where R_w is the wheel radius offers the coupling between the ring equations of motion and the membrane geometry equation (3.122). It should be mentioned that the non linear nature of the membrane equation prevents its direct solution and a numerical method has to be used for that. The second equation of motion, related with the tangential deformation of the ring, remains the same, as the linear tangential sidewall stiffness mechanism remains unchanged.

3.7.4 The inflation of the non linear sidewall model

In order the inflation effect to be captured by the non linear sidewall equipped model, the sidewall and the circumferential sections of it are examined independently from each other. The modal expansion method is applied on the non radial sidewall stiffness equation of motion (eqn. 3.124), where though, the inflation effect on the circumferential modal behaviour is retained. The respective breathing natural frequency is given by the equation:

$$\omega_{br} = \sqrt{\frac{K + P_0\cdot b}{R\cdot\rho\cdot A}} \tag{3.126}$$

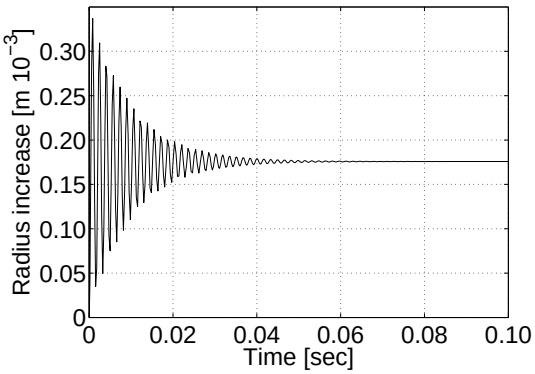

Figure 3.38 – The increase of the ring radius as a response to a step inflation pressure excitation, $P_0 = 2.2 \cdot 10^5 \frac{N}{m^2}$.

The differential equation of the breathing mode participation factor reads:

$$\ddot{\eta}_{br} + \lambda_{br} \cdot \dot{\eta}_{br} + \omega_{br}^2 \cdot \eta_{br} = \frac{P_0}{\rho \cdot d \cdot R_{br}} + 2\frac{R_{br}^m}{m_{br}^m} \int_{\theta=0}^{2\pi} q_r^{membrane} \cdot U_r^{br} \mathrm{d}\theta \tag{3.127}$$

$$\Rightarrow \ddot{\eta}_{br} + \lambda_{br} \cdot \dot{\eta}_{br} + \omega_{br}^2 \cdot \eta_{br} = \frac{P_0}{\rho \cdot d \cdot R_{br}^m} - 2\frac{P_0}{b \cdot \rho \cdot d}\frac{l_s}{w} \cos\frac{w}{2} \tag{3.128}$$

Obviously, the effect of the inflation induced geometrical changes on the modal characteristics of the ring circumference are neglected, and the process earns its validity by the small deformation (linear) consideration.

The calculation of the inflation deformation is based on a time domain discretised simulation algorithm; each time step consists of two basic calculation steps:

- In the space domain, the radial deformation, derived in the previous time step, is used for the calculation of the wheel to belt radial distance (eqn.3.125) and the corresponding to it radial membrane force value (eqns.3.122 and 3.123).
- Based on the above excitation, a numerical method is used for the solution of the differential equation 3.128 and the calculation of the instant value of the breathing participation factor. The respective radial deformation is calculated through eqn. 3.117.

A membrane arc length (l_s) value of $122mm$ is chosen for the application of the above process. Choosing also a wheel diameter value of $381mm$ ($15in$) an initial (deflated) wheel to belt distance (L) equal to $109.5mm$ is derived. The breathing mode damping coefficient is arbitrarily chosen, as the damping effect will be discussed in a following section (3.10) and its value does not affect the steady state solution. The radius increase as a function of time is presented in 3.38, for a step inflation pressure excitation $P_0 = 2.2 \cdot 10^5 N/m^2$. The steady state radius increase imposed by a range of inflation pressure values is given in fig. 3.39. The almost proportional radius increase validates the linear assumption induced by the modal expansion procedure.

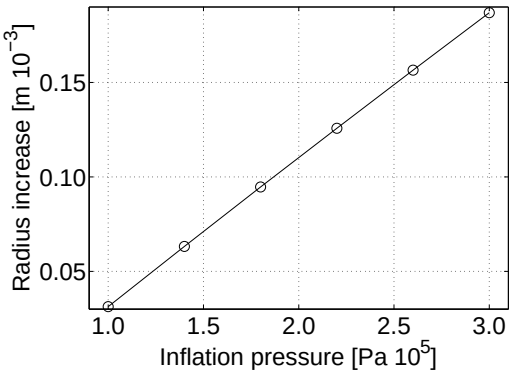

Figure 3.39 – The steady state radius increase as a function of the inflation pressure.

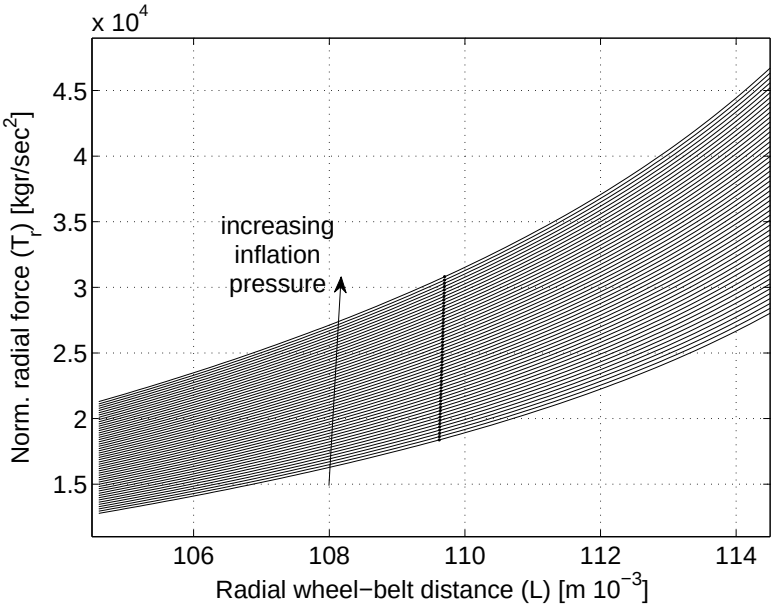

Figure 3.40 – The radial sidewall force (length normalized) as a function of the wheel to belt distance, for various values of the inflation pressure, in a range from -25% to $+25\%$ of the nominal value $P_0 = 2.2 \cdot 10^5 N/m^2$. The ring equilibrium deformations for each pressure value is also noted.

3.7.5 The effect of the inflation on the modal characteristics

In order the non linear effect of the inflation to be captured by the calculation of the modal behaviour, the modal expansion method has to be applied to a model which incorporates the related effects on both the belt circumference and the sidewall. For this reason an equivalent radial stiffness value is derived for every inflation equilibrium condition and the modal expansion is accomplished for this (linear) value assumption. The linearisation process comprises of the following steps:

1. For each value of inflation pressure, the equilibrium deformation is calculated, according to the procedure described in section 3.7.4.

2. For a range of deformation values in the area of the equilibrium one, the radial inflation force (T_r) is

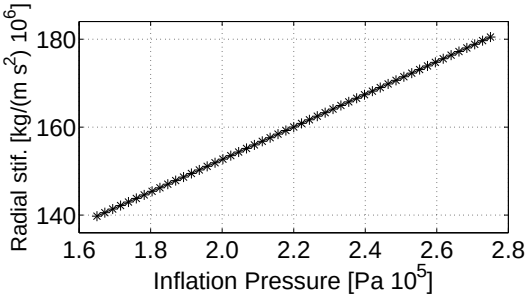

Figure 3.41 – The radial sidewall stiffness (length normalized) as a function of the inflation pressure, as derived from the linearisation procedure.

calculated. Such force plots are presented in fig. 3.40.

3. Each of the force-radial distance plots is interpolated by a polynomial expression.

4. The derivative of every polynomial expression is analytically derived and the value of this derivative for the deformation value corresponding to the ring equilibrium (fig. 3.40) is the equivalent radial sidewall stiffness (fig. 3.41).

5. The sidewall radial stiffness values are substituted in eqn. 3.54a and the modal expansion method is applied.

The radial sidewall stiffness which is derived by the above process for the nominal pressure $P_0 = 2.2 \cdot 10^5 N/m^2$ correlates well with the linear sidewall stiffness of table 3.1 and based on this observation the above proposed membrane dimensions may be validated. For the capture of the complete (sidewall including) inflation effect along the modal range, a modal sensitivity analysis (similar to the ones accomplished in section 3.4.1) is applied according to the above steps. A $\pm 25\%$ variation of the nominal pressure value is imposed and the emerging stiffness values are presented in fig. 3.41. Comparing the effects of the pressure and the membrane shape variation (through the distance effect) it may be concluded that the first factor is the predominant one and that the variation of the ring radius bears an insignificant effect on the sidewall stiffness.

The percentage deviation of the frequencies is presented in fig. 3.42. Comparing that with the pressure sensitivity of the linear model 3.6(c), it is evident that the significant stiffness dependency on the inflation pressure, is depicted in the pressure sensitivity analysis of the ring. The range of influence is significantly broader while the new sensitivity deployment corresponds to the superposition of the pressure and sidewall sensitivities of the ring model. The conclusion that the inflation pressure effect in the low modal number range is related more to the respective sidewall contribution than the circumferential belt one may be drawn.

3.8 The incorporation of the wheel in the modal behaviour

In all the stages of the above analysis, the tyre model was regarded as attached to a wheel, the degrees of freedom of which were suspended (fixed wheel). For reasons that will become later apparent (chapter 5), this assumption is dropped for the simulation of the large displacement operating conditions and the modal behaviour of the combined wheel-tyre system is used. The transition from the fixed wheel case to the one

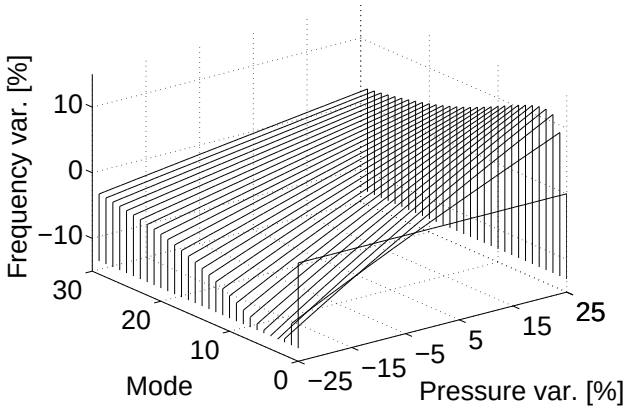

Figure 3.42 – A revised calculation of the sensitivity of the inflation pressure on the ring model natural frequencies, including the sidewall stiffness nonlinearity.

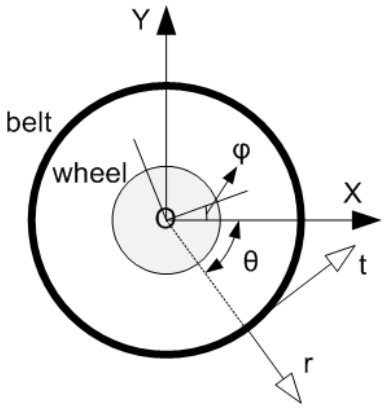

Figure 3.43 – The wheel and the belt systems of reference.

allowing its free vertical motion has been presented by Kung *et al* in [116],for a simplified version (see section 3.3.3) of the extensible ring model. Zegelaar *et al* in [60] and Zegelaar and Pacejka in [61] presented the modal combination of the free wheel with an inextensible ring tyre model. Here the free wheel including modal behaviour of a complete (pretensioned and extensible) ring model will be examined.

Prior to the extraction of the combined wheel-belt modal behaviour from the corresponding equations of motion, the theoretical differences from the fixed wheel case should be highlighted. The transition from the fixed to the free wheel case is associated with the addition to the system of three in-plane degrees of freedom, two of them corresponding to the horizontal and vertical translational motions and one of them corresponding to the rotational motion of the wheel. Apparently, the introduction of the three degrees of freedom results in the generation of three additional modes. The increase of the number of modes is of course qualitatively identified as in both cases (fixed or free wheel) the analytical ring structure theoretically corresponds to infinite modes. These three modes will predict the participation of the wheel in the associated mode shapes. Moreover, the unsuspended wheel results in the generation of three rigid modes of the system, without requiring the omission of the sidewall mechanism for that. Each of the rigid modes corresponds to the in-common motion of the wheel and the ring as dictated by each of the added degrees of freedom.

Including the interaction with the belt as an excitation, the wheel equations of motion may be written as:

$$m_w \cdot \ddot{u}_X^w = F_X^{b\to w} \tag{3.129}$$

$$m_w \cdot \ddot{u}_Y^w = F_Y^{b\to w} \tag{3.130}$$

$$I_w \cdot \ddot{u}_\Phi^w = M^{b\to w} \tag{3.131}$$

where:

m_w	the mass of the wheel
I_w	the in-plane moment of inertia of the wheel
u_X^w	the horizontal displacement of the wheel
u_Y^w	the vertical displacement of the wheel
u_Φ^w	the wheel angle of rotation
$F_X^{b\to w}$	the total horizontal force excitation from the belt to the wheel
$F_Y^{b\to w}$	the total vertical force excitation from the belt to the wheel
$M^{b\to w}$	the moment excitation from the belt to the wheel

The ring equations of motion may be respectively rewritten as:

$$\frac{D}{R^4}\left(\frac{\partial^4 u_r}{\partial\theta^4} - \frac{\partial^3 u_t}{\partial\theta^3}\right) + \frac{K}{R^2}\left(u_r + \frac{\partial u_t}{\partial\theta}\right) - \frac{P_0\cdot b}{R}\left(\frac{\partial^2 u_r}{\partial\theta} - 2\frac{\partial u_t}{\partial\theta} - u_r\right) + \rho\cdot A\frac{\partial^2 u_r}{\partial t^2} = f_r^{w\to b}(\theta) \tag{3.132a}$$

$$\frac{D}{R^4}\left(\frac{\partial^3 u_r}{\partial\theta^3} - \frac{\partial^2 u_t}{\partial\theta^2}\right) - \frac{K}{R^2}\left(\frac{\partial u_r}{\partial\theta} + \frac{\partial^2 u_t}{\partial\theta^2}\right) - \frac{P_0\cdot b}{R}\left(\frac{\partial^2 u_t}{\partial\theta} + 2\frac{\partial u_r}{\partial\theta} - u_t\right) + \rho\cdot A\frac{\partial^2 u_t}{\partial t^2} = f_t^{w\to b}(\theta) \tag{3.132b}$$

where:

$f_r^{w\to b}(\theta)$	the distributed radial force applied from the wheel to the belt
$f_t^{w\to b}(\theta)$	the distributed tangential force applied from the wheel to the belt

In order the interaction between the wheel and the belt to be captured by the radial and tangential sidewall mechanisms, the wheel displacement will be expressed in the radial/tangential system of reference, in which the ring equations of motion are also expressed. The transformation of the wheel displacement from the one system to the other (presented in fig. 3.43) depends on the the central angle (θ) of the examined belt point:

$$\begin{bmatrix} u_r^w \\ u_t^w \end{bmatrix} = \begin{bmatrix} \cos\theta & \sin\theta \\ -\sin\theta & \cos\theta \end{bmatrix} \cdot \begin{bmatrix} u_X^w \\ u_Y^w \end{bmatrix} + \begin{bmatrix} 0 \\ R\cdot u_\Phi^w \end{bmatrix} \Rightarrow \tag{3.133}$$

$$u_r^w = \cos\theta\cdot u_X^w + \sin\theta\cdot u_Y^w \tag{3.134a}$$

$$u_t^w = -\sin\theta\cdot u_X^w + \cos\theta\cdot u_Y^w + R\cdot u_\Phi^w \tag{3.134b}$$

The interaction forces (normalised to the ring circumferential length) for the same point may be expressed as:

$$f_r^{b\to w}(\theta) = k_r(u_r - u_r^w) \tag{3.135a}$$

$$f_t^{b\to w}(\theta) = k_t(u_t - u_t^w) \tag{3.135b}$$

3.8.1 The translational motion coupling between the wheel and the ring

Examining the translational motion of the wheel first, the force expressions of the wheel equations of motion (eqns. 3.129 and 3.130) will be expressed according to the deformation interaction described by eqn. 3.135. The transformation of the normalized force terms from the radial/tangential to the horizontal/vertical system of axis reads:

$$\begin{bmatrix} f_X^{b\to w}(\theta) \\ f_Y^{b\to w}(\theta) \end{bmatrix} = \begin{bmatrix} \cos\theta & -\sin\theta \\ \sin\theta & \cos\theta \end{bmatrix} \cdot \begin{bmatrix} f_r^{b\to w}(\theta) \\ f_t^{b\to w}(\theta) \end{bmatrix} \Rightarrow \tag{3.136}$$

$$f_X^{b\to w}(\theta) = \cos\theta \cdot f_r^{b\to w}(\theta) - \sin\theta \cdot f_t^{b\to w}(\theta) \tag{3.137a}$$

$$f_Y^{b\to w}(\theta) = \sin\theta \cdot f_r^{b\to w}(\theta) + \cos\theta \cdot f_t^{b\to w}(\theta) \tag{3.137b}$$

The total horizontal force may be written as:

$$F_X^{b\to w} = R\int_{\theta=0}^{2\pi} f_X^{b\to w}(\theta)\mathrm{d}\theta \tag{3.138}$$

and substituting the above expressions in it, it is derived:

$$\Rightarrow F_X^{b\to w} = R\int_{\theta=0}^{2\pi} \Big(\cos\theta\cdot\big(k_r(u_r - \cos\theta\cdot u_X^w + \sin\theta\cdot u_Y^w)\big) - \sin\theta\cdot\big(k_t(u_t + \sin\theta\cdot u_X^w - \cos\theta\cdot u_Y^w - R\cdot\phi^w)\big)\Big)\mathrm{d}\theta \tag{3.139}$$

$$\begin{aligned} \Rightarrow F_X^{b\to w} =& R\cdot k_r\int_0^{2\pi}\cos\theta\cdot u_r(\theta)\mathrm{d}\theta - R\cdot k_r\cdot u_X^w\int_0^{2\pi}\cos^2\theta\mathrm{d}\theta \\ &+ R\cdot k_r\cdot u_Y^w\int_0^{2\pi}\cos\theta\cdot\sin\theta\mathrm{d}\theta - R\cdot k_t\int_0^{2\pi}\sin\theta\cdot u_t(\theta)\mathrm{d}\theta \\ &- R\cdot k_t\cdot u_X^w\int_0^{2\pi}\sin^2\theta\mathrm{d}\theta + R\cdot k_t\cdot u_Y^w\int_0^{2\pi}\sin\theta\cdot\cos\theta\mathrm{d}\theta \\ &+ R^2\cdot k_t\cdot\phi^w\int_0^{2\pi}\sin\theta\mathrm{d}\theta \end{aligned} \tag{3.140}$$

The above expression is considerably simplified , given that:

$$\int_{\theta=0}^{2\pi} \sin\theta \mathrm{d}\theta = 0 \tag{3.141}$$

$$\int_{\theta=0}^{2\pi} \cos\theta \cdot \sin\theta \mathrm{d}\theta = \frac{1}{2}\int_{\theta=0}^{2\pi} \sin 2\theta = 0 \tag{3.142}$$

$$\int_{\theta=0}^{2\pi} \cos^2\theta \mathrm{d}\theta = \frac{1}{2}\int_{\theta=0}^{2\pi} (1+\cos 2\theta)\mathrm{d}\theta = \frac{1}{2}2\pi + \frac{1}{2}\int_{\theta=0}^{2\pi} \cos 2\theta \mathrm{d}\theta = \pi \tag{3.143}$$

$$\int_{\theta=0}^{2\pi} \sin^2\theta \mathrm{d}\theta = \frac{1}{2}\int_{\theta=0}^{2\pi} (1-\cos 2\theta)\mathrm{d}\theta = \frac{1}{2}2\pi - \frac{1}{2}\int_{\theta=0}^{2\pi} \cos 2\theta \mathrm{d}\theta = \pi \tag{3.144}$$

In result, the force expression 3.140 may be written as:

$$F_X^{b\to w} = -R\cdot\pi\cdot u_X^w(k_r+k_t) + R\cdot k_r \int_{\theta=0}^{2\pi} \cos\theta \cdot u_r(\theta)\mathrm{d}\theta - R\cdot k_t \int_{\theta=0}^{2\pi} \sin\theta \cdot u_t(\theta)\mathrm{d}\theta \tag{3.145}$$

The substitution of the above force expression in the wheel differential equation of horizontal motion (eqn. 3.129) results in:

$$m_w \ddot{u}_X^w + R\cdot\pi\cdot u_X^w(k_r+k_t) - R\cdot k_r \int_{\theta=0}^{2\pi} \cos\theta \cdot u_r(\theta)\mathrm{d}\theta + R\cdot k_t \int_{\theta=0}^{2\pi} \sin\theta \cdot u_t(\theta)\mathrm{d}\theta = 0 \tag{3.146}$$

Similarly to the previously examined modal data calculation cases (sections 3.2 and 3.3), the following solution forms are proposed:

$$u_r(\theta,\mathrm{t}) = \mathrm{R^m}\cdot\cos\left(\mathrm{n}(\theta-\varphi)\right)\cdot \mathrm{e}^{\iota\omega\cdot\mathrm{t}} \tag{3.147a}$$

$$u_t(\theta,\mathrm{t}) = \mathrm{T^m}\cdot\sin\left(\mathrm{n}(\theta-\varphi)\right)\cdot \mathrm{e}^{\iota\omega\cdot\mathrm{t}} \tag{3.147b}$$

and respectively the horizontal wheel displacement may be written as:

$$u_X^w(t) = X_w^m \cdot e^{\iota\cdot\omega\cdot\mathrm{t}} \tag{3.148}$$

Substituting eqns. 3.147 and 3.148 in the wheel equation of motion (3.146), it is derived:

$$-m_w\cdot\omega^2\cdot X_w^m + \pi\cdot R(k_r+k_t) - R\cdot k_r\cdot R^m \int_{\theta=0}^{2\pi} \cos\theta\cdot\cos\big(n(\theta-\varphi)\big)\mathrm{d}\theta + R\cdot k_t\cdot T^m \int_{\theta=0}^{2\pi} \sin\theta\cdot\sin\big(n(\theta-\varphi)\big)\mathrm{d}\theta = 0 \tag{3.149}$$

Given that:

$$\int_{\theta=0}^{2\pi} \cos\theta \cdot \cos\big(n(\theta-\varphi)\big) = \frac{1}{2}\int_{\theta=0}^{2\pi} \cos\big((1-n)\theta - n\cdot\varphi\big)\mathrm{d}\theta + \frac{1}{2}\int_{\theta=0}^{2\pi} \cos\big((1+n)\theta + n\cdot\varphi\big)\mathrm{d}\theta = \left\{ \begin{array}{r} 0, \quad n\neq 1 \\ \pi\cdot\cos\varphi, \quad n=1 \end{array} \right\} \tag{3.150}$$

$$\int_{\theta=0}^{2\pi} \sin\theta \cdot \sin\big(n(\theta-\varphi)\big) = \frac{1}{2}\int_{\theta=0}^{2\pi} \cos\big((1-n)\theta - n\cdot\varphi\big)\mathrm{d}\theta - \frac{1}{2}\int_{\theta=0}^{2\pi} \cos\big((1+n)\theta + n\cdot\varphi\big)\mathrm{d}\theta = \left\{ \begin{array}{r} 0, \quad n\neq 1 \\ \pi\cdot\cos\varphi, \quad n=1 \end{array} \right\} \tag{3.151}$$

In result, the horizontal displacement of the wheel, as predicted by the jth mode, may be written as:

$$X_w^m = \left\{ \begin{array}{r} \dfrac{\pi\cdot R\cdot\cos\varphi(k_r\cdot R^m - k_t\cdot T^m)}{\pi\cdot R(k_r+k_t) - \omega^2\cdot m_w}, \ n=1 \\ 0, \ n\neq 1 \end{array} \right\} \tag{3.152}$$

According to the above equation, a horizontal wheel displacement is predicted for the the $n = 1$ modes (radial and tangential), while the wheel remains stationary, in terms of horizontal translation, for the rest of the modes.

An equivalent procedure may be applied for the prediction of the vertical translational motion of the wheel (3.130).The proposed vertical wheel deformation function of the jth mode reads:

$$u_Y^w(t) = Y_w^m \cdot e^{\iota\cdot\omega\cdot \mathrm{t}} \tag{3.153}$$

and the calculated amplitude is:

$$Y_w^m = \left\{ \begin{array}{r} \dfrac{R\cdot\pi\sin\varphi(k_r\cdot R^m - k_t\cdot T^m)}{\pi\cdot R(k_r+k_t) - \omega^2\cdot m_w}, \ n=1 \\ 0, \ n\neq 1 \end{array} \right\} \tag{3.154}$$

Similarly to the horizontal case, only the $n = 1$ modes predict a possible vertical displacement of the wheel.

Following the analysis of section 3.2, every mode is incorporated twice in a modal basis in order this basis to be able to capture any possible orientation of the mode shape. The global orientation of the two modes may be arbitrarily chosen, as long as their relative to each other orientation condition described by eqn. 3.8 is satisfied. For the $n = 1$ modes this condition implies a $\pi/2$ relative angle between the two modes. Moreover, the selection of the 0 and $\pi/2$ *rad* values, entitles the modal decomposition of the horizontal and

vertical wheel displacements:

$$X_w^{m,j} = \left\{ \begin{array}{r} \dfrac{R \cdot \pi (k_r \cdot R_j^m - k_t \cdot T_j^m)}{\pi \cdot R(k_r + k_t) - \omega_j^2 \cdot m_w},\ \varphi = 0 \\ 0,\ \varphi = \dfrac{\pi}{2} \end{array} \right\},\ j:\ n = 1,\ \text{radial/tangential} \tag{3.155}$$

and

$$Y_w^{m,j} = \left\{ \begin{array}{r} 0,\ \varphi = 0 \\ \dfrac{R \cdot \pi (k_r \cdot R_j^m - k_t \cdot T_j^m)}{\pi \cdot R(k_r + k_t) - \omega_j^2 \cdot m_w},\ \varphi = \dfrac{\pi}{2} \end{array} \right\},\ j:\ n = 1,\ \text{radial/tangential} \tag{3.156}$$

Hence, each of the two cases, $\varphi = 0$ and $\varphi = \frac{\pi}{2}$, is associated with pure horizontal or pure vertical wheel displacement for the radial and tangential $n = 1$ modes.

3.8.2 The rotational motion coupling between the wheel and the ring

Moving the discussion to the rotational wheel motion, the total moment applied from the belt to the wheel may be written as:

$$M^{b \to w} = R \int_{\theta=0}^{2\pi} R \cdot f_t^{b \to w} \mathrm{d}\theta \tag{3.157}$$

The substitution of the expressions 3.134b and 3.135b in the above and the application of the simplifications described by eqn. 3.144 results in:

$$\Rightarrow M^{b \to w} = R^2 \cdot k_t \int_0^{2\pi} u_t \mathrm{d}\theta - R^3 \cdot \phi^w \cdot k_t \cdot 2\pi \tag{3.158}$$

The integral $\int_0^{2\pi} u_t(\theta)\mathrm{d}\theta$ is equal to zero for all the modes, the tangential deformation of which may be expressed as a harmonic function of the central angle (θ). According to the discussion of section 3.3.1, the only mode for which the deformation is non zero and not described by a harmonic expression is the radial $n = 0$ (torsional) mode. It may be written:

$$\int_0^{2\pi} u_t^j \mathrm{d}\theta = \left\{ \begin{array}{r} 2\pi \cdot T_j^m \cdot e^{\iota \cdot \omega_j \cdot \mathrm{t}},\ j: n = 0,\ \text{radial} \\ 0\ ,\ j: \text{every other mode} \end{array} \right\} \tag{3.159}$$

Consequently and in regards to the rotational motion, the wheel and the belt interact only through the excitation of the torsional mode. The wheel rotational response is written as:

$$u_\Phi^w(\mathrm{t}) = \Phi_{\mathrm{w}}^{\mathrm{m}} \cdot \mathrm{e}^{\iota \cdot \omega \cdot \mathrm{t}} \tag{3.160}$$

The substitution of the moment expression, the ring tangential (3.147b and wheel angular (eqn. 3.159) deformations of the jth mode), in the wheel equation of rotational motion (3.131), leads to the following:

$$-\omega \cdot I_w \cdot \Phi_w^m + 2\pi R^3 \cdot k_t \cdot \Phi_w^m - R^2 \cdot k_t \cdot T^m \int_{\theta=0}^{2\pi} u_t \mathrm{d}\theta = 0 \tag{3.161}$$

$$\Rightarrow \Phi_w^{m,j} = \left\{ \begin{array}{r} \dfrac{2\pi \cdot R^2 \cdot k_t \cdot T_j^m}{2\pi \cdot R^3 \cdot k_t - \omega_j^2 \cdot I_w},\ j : n = 0,\ \text{radial} \\ 0\ ,\ j : \text{every other mode} \end{array} \right\} \tag{3.162}$$

In result, no rotational wheel motion is predicted for all modes, apart from the radial zero one (torsional), which is the only mode, the deformation of which, entitles the moment interaction between the wheel and the ring. In correlation to the form of eqns. 3.155 and 3.156, the wheel rotation may be written as:

$$\Phi_j = \frac{2\pi \cdot R^2 \cdot k_t \cdot T_j^m}{2\pi \cdot R^3 \cdot k_t - \omega_j^2 \cdot I_w},\quad j : n = 0,\ \text{radial} \tag{3.163}$$

Summarising the analysis up to this point, it has been proved that the translational interaction between the wheel and the ring is captured by the radial and tangential $n = 1$ modes, while the rotational one is captured the radial $n = 0$ mode. The fact that the wheel does not participate in the mode shapes of the rest of the modes, enables the application of the fixed wheel analysis for the study of them. Similar conclusions have been drawn by the analysis of Kung *et al* [116] and Zegelaar *et al* [60], for the simplified models proposed in the respective studies.

3.8.3 The wheel-ring interacting modes

In the previous section, although the modes of wheel and belt interaction were identified, the nature of these modes, in terms of frequencies and deformation magnitudes, was not acquired. The analysis of these modes will be attempted in this section.

The rigid modes prediction potential

The horizontal modes of interaction will be firstly examined and the ring equations of motion which include the interaction with the wheel (3.132) will be used. The system of reference transformation of the wheel displacement, expressed by eqn. 3.133, is applied for the corresponding mode shape amplitudes which, after the substitution of eqns. 3.155 and 3.156 in them, may be written as:

$$R_w^{m,1} = \cos\theta \cdot X_w^{m,1} = \cos\theta \cdot \frac{R \cdot \pi(k_r \cdot R_1^m - k_t \cdot T_1^m)}{\pi \cdot R(k_r + k_t) - \omega_1^2 \cdot m_w} \tag{3.164a}$$

$$T_w^{m,1} = -\sin\theta \cdot X_w^{m,1} = -\sin\theta \cdot \frac{R \cdot \pi(k_r \cdot R_1^m - k_t \cdot T_1^m)}{\pi \cdot R(k_r + k_t) - \omega_1^2 \cdot m_w}. \tag{3.164b}$$

where:

R_w^m	the modal amplitude of the wheel displacement projected on the radial direction
T_w^m	the modal amplitude of the wheel displacement projected on the tangential direction

Moreover, the conditions $n = 1$ and $\varphi = 0$ simplify the expression of the mode shape functions' amplitudes:

$$U_r^1(\theta) = R_1^m \cdot \cos\theta \tag{3.165a}$$

$$U_t^1(\theta) = T_1^m \cdot \sin\theta \tag{3.165b}$$

The substitution of the above expressions in eqns. 3.132 results in:

$$\begin{bmatrix} C_1 & C_2 \\ C_3 & C_4 \end{bmatrix} \cdot \begin{bmatrix} R_1^m \\ T_1^m \end{bmatrix} = \begin{bmatrix} 0 \\ 0 \end{bmatrix} \tag{3.166}$$

where:

$$C_1 = \frac{D}{R^4} + \frac{K}{R^2} + k_r - \frac{\pi \cdot R \cdot k_r^2}{\pi \cdot R(k_r + k_t) - w_1^2 \cdot m_w} - \omega_1^2 \cdot \rho \cdot A \tag{3.167a}$$

$$C_2 = C_3 = \frac{D}{R^4} + \frac{K}{R^2} + \frac{R \cdot \pi \cdot k_r \cdot k_t}{\pi \cdot R(k_r + k_t) - \omega_1^2 \cdot m_w} + 2\frac{P_0 \cdot b}{R} \tag{3.167b}$$

$$C_4 = \frac{D}{R^4} + \frac{K}{R^2} + k_t - \frac{\pi \cdot R \cdot k_t^2}{\pi \cdot R(k_r + k_t) - w_1^2 \cdot m_w} - \omega_1^2 \cdot \rho \cdot A \tag{3.167c}$$

The respective characteristic equation is:

$$\begin{vmatrix} C_1 & C_2 \\ C_3 & C_4 \end{vmatrix} = 0 \Rightarrow C_1 \cdot C_4 - C_2 \cdot C_3 = 0 \tag{3.168}$$

The above equation is a third order one and is theoretically able to predict the three horizontal motion modes. Obviously one of them corresponds to the horizontal rigid mode, while the other two ones are the deformational modes. Rewriting eqn. 3.168 in a polynomial form, though, reveals a constant term equal to:

$$P_0 \cdot \frac{-4 \cdot b(K \cdot R^2 \cdot k_r + P_0 \cdot b \cdot R^3 \cdot k_r + k_r \cdot R^4 \cdot k_t + k_r \cdot D + K \cdot R^2 \cdot k_t + P_0 \cdot b \cdot R^3 \cdot k_t + D \cdot k_t)}{R^5 \cdot (k_r + k_t)} \tag{3.169}$$

which prevents the existence of the zero frequency as a solution of the characteristic equation and in result suspends the prediction of the rigid mode. The expression of the constant term as a product of the inflation pressure, reveals the association of the above issue with the pretension term of the equations of motion. As the vertical motion coupled modes are prescribed by a similar equation, a respective term will suspend the prediction of the vertical rigid mode.

In order to examine the rotational rigid mode prediction potential, the wheel rotation amplitude is expressed as:

$$T_j^w(\theta) = R\Phi_j = \frac{2\pi \cdot R^3 \cdot k_t \cdot T_j^m}{2\pi \cdot R^3 \cdot k_t - \omega_j^2 \cdot I_w}, \quad j : n = 0, \text{ radial} \tag{3.170}$$

while the ring deformations are written as:

$$U_r^j(\theta) = 0, \quad j : n = 0, \text{ radial} \tag{3.171a}$$

$$U_t^j(\theta) = T_j, \quad j : n = 0, \text{ radial} \tag{3.171b}$$

Substituting the above in the tangential ring equation of motion (3.132b) it is derived:

$$-\omega_j^2 \cdot \rho \cdot A + k_t(T_j^m - \frac{2\pi \cdot R^3 \cdot k_t \cdot T_j^m}{2\pi \cdot R^3 \cdot k_t - \omega_j^2 \cdot I_w}) + \frac{P_0 \cdot b}{R} T_j^m = 0, \quad j : n = 0, \text{ radial} \tag{3.172}$$

Apparently, the pretension related term($\frac{P_0 \cdot b}{R} T_j^m$, $j : n = 0$, radial) prevents the prediction of the rotational rigid mode.

An explicit solution to the above problem does not exist. Here, a similar solution to the one proposed in section 3.3.3 for the fixed wheel model rigid modes prediction will be followed and the inflation pretension terms will be dropped from the system's equation for the calculation of the $n = 0$ and $n = 1$ modes.

The translational coupled modes

Returning to the equations describing the $n = 1$ coupled modes (3.164-3.168), the omission of the pretension terms will only affect the $C_2 = C_3$ term of the characteristic equation (3.168), which, instead of eqn. 3.167b, is now given by:

$$C_2 = C_3 = \frac{D}{R^4} + \frac{K}{R^2} \tag{3.173}$$

The two non zero solutions may be described by an expression similar to 3.34. In this case the terms B and Δ emerge as:

$$B_1^{coupled} = B_1 + \frac{(k_r + k_t)R^4}{2} \frac{m_b}{m_w} \tag{3.174a}$$

$$\Delta_1^{coupled} = D_1 + \frac{(k_r + k_t)R^4}{2} \frac{m_b}{m_w} \big((4 \cdot D + 4 \cdot K \cdot R^2)(k_r + k_t) - 2 \cdot R^4 (k_r - k_t)^2 \big) \tag{3.174b}$$

where:

B_1, D_1	the equivalent $n = 1$ term of the fixed wheel case (eqn. 3.35)
m_b	the ring mass, calculated by the equation: $m_b = 2 \cdot \pi \cdot R \cdot A \cdot \rho$

The respective mode shape deformation amplitude ratios ($\frac{T_1}{R_1}$) are also given by an expression similar to 3.37, where the terms $B_{s|1}$ and $\Delta_{s|1}$ emerge as:

$$B_{s|1}^{coupled} = B_{s|1} + \frac{R^2 \cdot m_b (k_r - k_t) \cdot (k_r \cdot R^4 + K \cdot R^2 + D)}{R^4 \cdot m_b \cdot k_r - 2 \cdot K \cdot m_w \cdot R^2 - 2 \cdot D \cdot m_w} \tag{3.175a}$$

$$\Delta_{s|1}^{coupled} = \Delta_{s|1} \tag{3.175b}$$

where $B_{s|1}$ and $\Delta_{s|1}$ the fixed wheel case corresponding terms of eqn. 3.37 for $n = 1$.

The wheel horizontal displacement is calculated by the substitution of the natural frequencies and the deformation amplitudes of the mode shapes in eqn. 3.155. Its analytical expression is omitted as its form does not allow for any conclusions to be drawn and for this reason the following numerical investigation of them is proposed. Setting as an initial case the one of equal wheel and belt masses, the table 3.2 may be derived, using the properties of table 3.1.

	Frequencies $[Hz]$		Deformation ratios		
	fixed wheel	free wheel	fixed wheel $\frac{T}{R}$	free wheel $\frac{T}{R}$	free wheel $\frac{X}{R}$
$\omega_{1\|rad}$	92.4	130.7	-1.01	-1.02	-0.51
$\omega_{1\|tang}$	855.9	856.0	0.99	0.99	-0.01

Table 3.2 – The affected by the incorporation of the wheel modes and their characteristics.

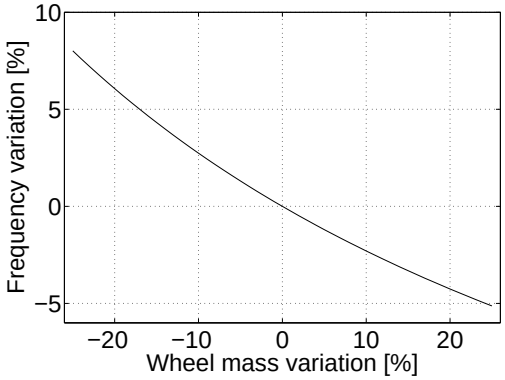

Figure 3.44 – The frequency sensitivity of the $n = 1$ radial mode to the variation of the wheel mass value.

Apparently the wheel modal participation is mainly depicted in the radial mode, the natural frequency of which has increased from $92.4Hz$ to $130.7Hz$. The tangential deformation remains almost unaffected, while the wheel displacement magnitude is half of the radial one of the belt and the direction of the two deformations is opposite, as the ring and the wheel vibrate in anti-diagonal mode. The tangential $n = 1$ mode has hardly been affected by the wheel modal incorporation, in both frequency and mode shape terms. Accordingly, the predicted wheel deformation value is insignificant.

The application of the modal sensitivity analysis method, presented for the fixed wheel case in section 3.4.1, reveals a similar sensitivity of the fixed and free wheel $n = 1$ modes to the ring properties. This may be attributed to the equivalent deformation patterns in both cases. As depicted in table 3.2, the tangential to radial ring deformation ratio has hardly been affected by the wheel motion incorporation. Whether the wheel remains stationary or develops various relative levels of horizontal displacement affects the level of stress induced to the ring (which is depicted in the resulting frequency variation) but not the deformation pattern, retaining equal sensitivity to the ring properties.

The sensitivity of the radial coupled mode of the free wheel model to the wheel mass in terms of frequency value and relative deformations will be examined, as the tangential mode sensitivity has been found to be insignificant. The radial mode frequency sensitivity is depicted in fig. 3.44 and the corresponding relative deformation variations in fig. 3.46. In accordance to the analysis of section 3.4.1, a $\pm 25\%$ variation is imposed to the wheel mass value, setting the equal ring and wheel mass case as the nominal one ($m_w = 7.18kg$, $I_w = 0.65kg \cdot m^2$), and the resulting percentage deviation of the examined values is monitored. The increase of the wheel mass is found to significantly affect the natural frequency of the mode, the value of which

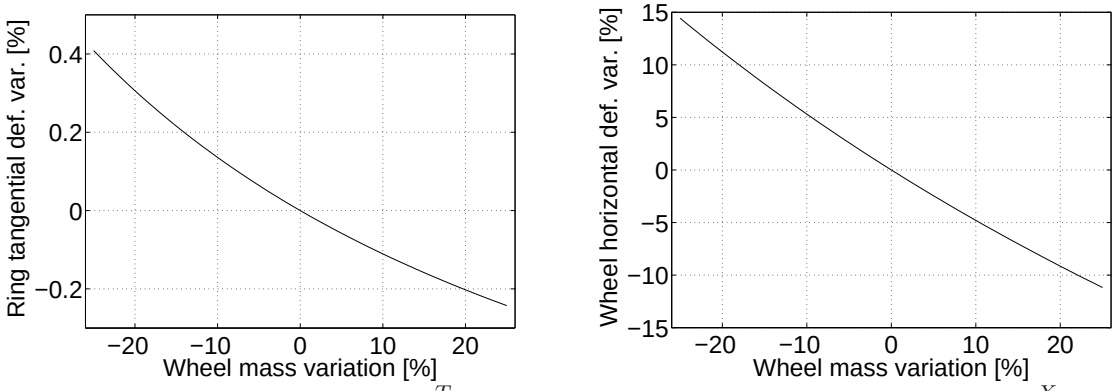

(a) Tangential ring deformation $\frac{T}{R}$.

(b) Horizontal wheel displacement $\frac{X}{R}$.

Figure 3.45 – The sensitivity of the $n = 1$ radial mode shape on the wheel mass variation.

decreases with the mass, as does the wheel deformation in absolute terms. The wheel inertia suspends the relative wheel to ring displacement, decreasing the participation of the wheel deformation in the mode shape. Accordingly, as the wheel and ring displacements are of opposite direction, its suspension decreases the respective level of stress of the system, leading to lower frequency values. The fixed wheel case could be regarded as the special case of infinite wheel inertia, as the frequency asymptotically reaches the fixed wheel corresponding value and wheel deformation diminishes. In contrast, as the wheel mass decreases, their opposite displacement is intensified and the level of stress increases, as does the natural frequency of the mode.

The rotational coupled mode

Moving the discussion to the rotational coupled mode, eqn.3.172 is rewritten after the omission of the pretension terms:

$$-\omega_j^2 \cdot \rho \cdot A + k_t(T_j - \frac{2\pi \cdot R^3 \cdot k_t \cdot T_j}{2\pi \cdot R^3 \cdot k_t - \omega_j^2 \cdot I_w}) = 0,\ j : n = 0,\ \text{radial} \tag{3.176}$$

$$\Rightarrow \rho \cdot A \cdot I_w \cdot \rho \cdot \omega_j^4 - (k_t \cdot I_w + 2\pi \cdot R^3 \cdot k_t \cdot \rho \cdot A)\omega_j^2 = 0 j : n = 0,\ \text{radial} \tag{3.177}$$

Apparently, the above equation, apart from the zero solution, predicts one more, which is given by the equation:

$$w_j^{coupled} = \sqrt{\frac{k_t \cdot I_w + 2\pi \cdot R^3 \cdot k_t \cdot \rho \cdot A}{I_w \cdot \rho \cdot A}} j : n = 0,\ \text{radial} \tag{3.178}$$

Given that the ring moment of inertia corresponds to:

$$I_b = 2 \cdot \pi R \cdot A\rho \cdot R^2 = 2 \cdot \pi \cdot A \cdot R^3 \tag{3.179}$$

the frequency may be rewritten as:

$$w_j^{coupled} = \sqrt{\frac{k_t}{\rho \cdot A} + \frac{I_b}{I_w}\frac{k_t}{\rho \cdot A}}\, j : n = 0, \text{ radial} \tag{3.180}$$

$$\Rightarrow w_j^{coupled} = \omega_j \cdot \sqrt{1 + \frac{I_b}{I_w}}\, j : n = 0, \text{ radial} \tag{3.181}$$

where $\omega_{0|rad}$ is the fixed wheel radial $n = 0$ (torsional mode) frequency (eqn. 3.51a). Interestingly, the participation of the wheel in the torsional mode increases the corresponding frequency with the square root of the moments of inertia ratio. The corresponding wheel to ring deformation ratio is given by:

$$\left\{ \begin{array}{c} (3.163) \\ (3.178) \end{array} \right\} \Rightarrow \Phi_w^{m,j} = -\frac{2\pi \cdot \rho R^3}{I_w}\frac{T_j^m}{R} = -\frac{I_b}{I_w}\frac{T_j^m}{R}\, j : n = 0, \text{ radial} \tag{3.182}$$

The wheel angle of rotation is opposite to the ring one, while the ratio of their rotation magnitudes is inversely proportional to their ratio of inertia moments.

Following the analysis of the translational coupled modes, a similar physical mechanism may be identified in the rotational interaction case. As the wheel inertia increases, its rotational deformation decreases and the frequency of the mode is reduced. The fixed wheel case corresponds to a wheel with infinite inertia. Decreasing wheel inertia, on the other side, entitles the wheel rotation, which is associated with a pronounced stress condition for the system. The latter is depicted in the relative increase of the associated frequency.

Considering the equal wheel and ring moments of inertia case as the nominal one, it is obvious that the rotational deformations will be equal in absolute terms (eqn. 3.182), while the respective frequency will be the one of the fixed wheel case, multiplied by a $\sqrt{}$ coefficient (eqn. 3.181). The sensitivity of the two modal characteristics to the variation of the wheel inertia can be acquired from the above simple equations. Its presentation, though, in a way equal to the translational modes analysis, reveals that the frequency sensitivity is equal to sensitivity of the translational mode to the wheel mass, while the angular deformation sensitivity is more intense than the respective horizontal one to the wheel mass.

Summarizing the modal effect of the transition from the fixed wheel case to the free wheel one, the following conclusions may be drawn:

- The transition is associated with the generation of three rigid modes (two translational and one rotational).
- Each of radial $n = 0$ and $n = 1$ modes split in one rigid and one coupled mode, the latter associated with relative out of phase vibrational motion (translational or rotational) between the wheel and the ring. The tangential n=1 mode, is insignificantly affected by the wheel incorporation and a minimal wheel translation is predicted. All the other modes of the ring remain equal to the fixed wheel case.
- The increase of the wheel mass and inertia decrease the coupled modes frequencies (for reasons of reduced stress condition) and the participation wheel deformation in the associated mode shapes.

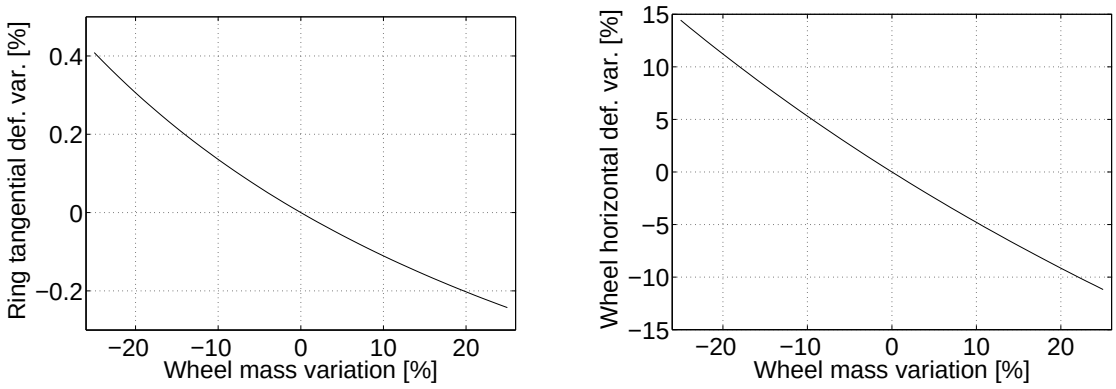

(a) Frequency sensitivity.

(b) Wheel angular deformation sensitivity.

Figure 3.46 − The sensitivity of the $n = 0$ radial mode on the wheel inertia variation.

- The incorporation of the pretension effect in the ring equation of motion prevents the prediction of the rigid modes and for this reason the pretension terms should be accordingly dropped from the respective modes.

3.9 The rotation effects on the modal prediction characteristics

The rotation affects the modal behaviour of the tyre through the induced centrifugal and coriolis accelerations. Although the centrifugal acceleration imposes a stiffening effect, similar to the inflation induced pretension, the Coriolis effect is more complicated, as it will be explained in the following. At a theoretical level, the rotational effects will be briefly presented, as the topic has been comprehensively analysed in a number of published studies (see section 2.1.6).

In the present analysis the rotation effects will be examined from a point of view related to the imposed numerical deviation of the predicted modal behaviour from the non rotating case. As the incorporation of the rotational effects results in the association of a modal basis with a certain angular velocity value, this basis is not valid for different values of it. In the present study, though, the transient tyre behaviour will be examined along a velocity range, so the knowledge of the imposed deviation of the modal characteristics is vital. Using the stationary modal data as a comparison basis, the centrifugal and coriolis induced deviation levels will be acquired as a function of the rotation velocity. Later the critical velocity prediction potential of the ring tyre model will be examined, in relation to the incorporation or not of the rotational phenomena.

3.9.1 The deviation of the modal behaviour of the rotating model from the stationary one

The centrifugal force terms may be expressed in their length normalised form as [96]:

$$q_r^{centrifugal} = \rho \cdot A \cdot \Omega^2 \left(u_r + 2\frac{\partial u_t}{\partial \theta} - \frac{\partial^2 u_r}{\partial \theta} \right) \tag{3.183}$$

$$q_t^{centrifugal} = \rho \cdot A \cdot \Omega^2 \left(u_t - 2\frac{\partial u_r}{\partial \theta} - \frac{\partial^2 u_t}{\partial \theta} \right) \tag{3.184}$$

while the Coriolis terms are:

$$q_r^{Coriolis} = -\rho \cdot A \left(\Omega^2 \cdot u_r + 2 \cdot \Omega \cdot \frac{\partial u_t}{\partial t} \right) \tag{3.185}$$

$$q_t^{Coriolis} = -\rho \cdot A \left(\Omega^2 \cdot u_t - 2 \cdot \Omega \cdot \frac{\partial u_r}{\partial t} \right) \tag{3.186}$$

The incorporation of the above terms in the pretensioned ring equations of motion 3.54, results in a new pair of equations, which describe the ring behaviour in an also rotating with it system of axis:

$$\frac{D}{R^4}\left(\frac{\partial^4 u_r}{\partial \theta^4} - \frac{\partial^3 u_t}{\partial \theta^3}\right) + \frac{K}{R^2}\left(u_r + \frac{\partial u_t}{\partial \theta}\right) + \frac{P_0 \cdot b}{R}\left(u_r + 2\frac{\partial u_t}{\partial \theta} - \frac{\partial^2 u_r}{\partial \theta}\right) + k_r \cdot u_r + q_r^{cent.} + \rho \cdot A \frac{\partial^2 u_r}{\partial \mathrm{t}^2} + q_r^{Cor.} = 0 \tag{3.187a}$$

$$\frac{D}{R^4}\left(\frac{\partial^3 u_r}{\partial \theta^3} - \frac{\partial^2 u_t}{\partial \theta^2}\right) - \frac{K}{R^2}\left(\frac{\partial u_r}{\partial \theta} + \frac{\partial^2 u_t}{\partial \theta^2}\right) + \frac{P_0 \cdot b}{R}\left(u_t - 2\frac{\partial u_r}{\partial \theta} - \frac{\partial^2 u_t}{\partial \theta}\right) + k_t \cdot u_t + q_t^{cent.} + \rho \cdot A \frac{\partial^2 u_t}{\partial \mathrm{t}^2} + q_t^{Cor.} = 0 \tag{3.187b}$$

It is evident that the pretension term of the rotation modal contribution has a stiffening effect, similar to the inflation one. The Coriolis terms, though, impose a substantial change to the differential equations, as they are not separable differential equations any more. Hence, the typical solution forms given by eqn. 3.147 cannot be proposed. A more generic solution form is [83]:

$$u_r(\theta, \mathrm{t}) = \mathrm{R}^{\mathrm{m}} \cdot \mathrm{e}^{\iota(\mathrm{n} \cdot \theta + \mathrm{w} \cdot \mathrm{t})} \tag{3.188}$$

$$u_t(\theta, \mathrm{t}) = \mathrm{T}^{\mathrm{m}} \cdot \mathrm{e}^{\iota(\mathrm{n} \cdot \theta + \mathrm{w} \cdot \mathrm{t})} \tag{3.189}$$

The above expressions are substituted in the equations of motion, which are rewritten in a matrix form,

similar to eqn. 3.25. The respective matrix elements are:

$$C_1 = \frac{D}{R^4}n^4 + \left(\frac{P_0 \cdot b}{R} + \rho \cdot A \cdot \Omega^2\right) n^2 + \frac{K}{R^2} + \frac{P_0 \cdot b}{R} + k_r - \rho \cdot A \cdot \omega^2 \tag{3.190}$$

$$C_2 = i\left(\frac{D}{R^4}n^3 + (\frac{K}{R^2} + \frac{2 \cdot P_0 \cdot b}{R} + 2 \cdot \rho \cdot A \cdot \Omega^2)n) - 2 \cdot \Omega \cdot \rho \cdot A\omega_j\right) \tag{3.191}$$

$$C_3 = -C_2 \tag{3.192}$$

$$C_4 = \left(\frac{D}{R^4} + \frac{K}{R^2} + \frac{P_0 \cdot b}{R} + \rho \cdot A \cdot \Omega^2\right) n^2 + k_t + \frac{P_0 \cdot b}{R} - \rho \cdot A \cdot \omega^2 \tag{3.193}$$

The characteristic polynomial emerges as:

$$\Lambda_4 \cdot \omega^4 + \Lambda_2 \cdot \omega^2 + \Lambda_1 \cdot \omega + \Lambda_0 = 0 \tag{3.194}$$

The coriolis induced presence of the first order term, cancels the duplicity of the modes and four individual eigenvalues emerge from the characteristic polynomial, corresponding to four different modes. The term bifurcation is commonly used for the description of the phenomenological splitting of each of the double modes into two different ones. It should be noticed, though, that the bifurcation does not alter the radial or tangential nature of the modes, which adopt the primal deformation pattern of the initial mode.

The magnitude of the rotation effects on the pretensioned, extensible ring model is numerically investigated in fig. 3.47 for the $n = 0$ to $n = 8$ radial modes. As the level of deviation of the modal behaviour from the stationary one is to be examined, the percentage deviation of the emerging frequencies from the stationary ones is monitored, along a reasonable range of rotation velocity values, corresponding to a rolling tyre with translational velocity up to 100 km/h. The individual contribution of the pretension and coriolis terms is presented, together with the combined effect.

In general, the total deviation increases with the velocity in a non linear way. The centrifugal component exhibits a parabolic development with the velocity, while the coriolis component develops almost linearly along the velocity range, for both of the bifurcated branches. For the torsional ($n = 0$) mode, no bifurcation is predicted by the coriolis effect incorporation and a single frequency mode is predicted, corresponding to a lower velocity value than the stationary one. The arithmetically equal stiffening centrifugal effect, though, results in an insignificant total rotation effect.

For the $n > 0$ modes, the coriolis effect is maximum for $n = 1$ and decreases with the modal number. In contrast, the centrifugal effect is insignificant for the $n = 1$ mode and increases with the modal number. In result, excluding the torsional mode, the coriolis effect is the predominant one for the first modes while the centrifugal effect is the predominant for higher modal number modes, leading to a pure pretension induced rotational effect above a modal number. Examining a broader modal range, the two deviation components are presented in fig. 3.48 for a constant rotation velocity, corresponding to the upper limit of the examined range ($100km/h$). Evidently, the coriolis deviation component decreases rapidly with the modal number, following an exponential deployment and reduces to insignificant values for $n > 10$. The centrifugal contribution to the deviation is, presumably, in agreement with the ring sensitivity to the variation of the inflation induced pretension, presented in section 3.4.1 (fig. 3.6(c)). The effect initially increase, reaches a maximum in the $n = 10$ area and asymptotically tends to zero above that. The total effect, emerges as the superposition of

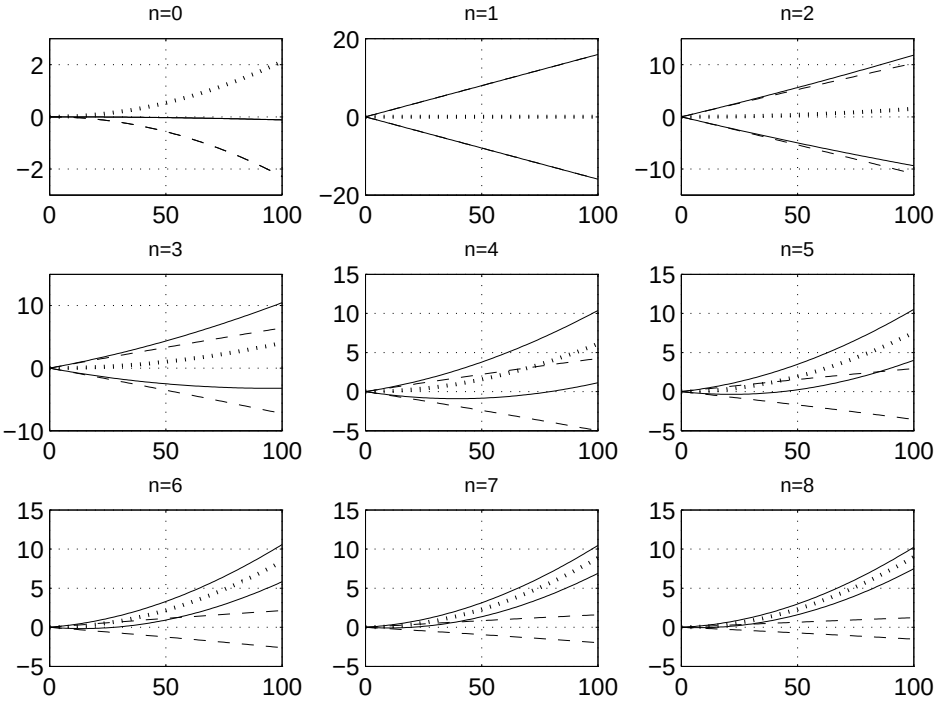

Figure 3.47 – The development of the rotation effects development with the velocity, for the $n = 0$ to $n = 8$ radial modes. (horizontal axis: travelling velocity (km/h), vertical axis: percentage frequency deviation, dotted line: centrifugal effect, dashed line: coriolis effect, solid line: combined effect)

the two components and reaches its maximum value, controlled by the coriolis component, for the $n = 1$ mode. Both of the rotational effects asymptotically vanish with the modal number.

A similar analysis is attributed for the rotational effects on the tangential modes. The percentage deviation induced by each of the rotational contributions to that is presented in fig. 3.49 for the $n = 0$ to $n = 8$ modes. A significant difference from the radial modes case is that the effect in this case is in general one order weaker. A linear development pattern of the coriolis component and a parabolic one of the pretension component may be identified, with the exception of the breathing ($n = 0$) mode, for which both contributions show a parabolic development with the velocity. In contrast to the radial $n = 0$ case, the coriolis frequency effect on the breathing mode is increasing and is added to the pretension one . The coriolis effect remains stronger than the pretension throughout the examined modal range, a significant difference from the radial effect deployment. The $100km/h$ velocity effect along a broad ($n = 0$ to $n = 40$) tangential modal range is presented in fig. 3.50. The total effect, in this case, is controlled by the coriolis component, as the pretension one is constant and insignificant. Obviously, the latter could be concluded by the respective sensitivity analysis of the group (fig. 3.7(d) in section 3.4.1). In result, the, similar to the radial group, exponentially decreasing coriolis effect defines the total degree the deviation, resulting in an asymptotically vanishing effect.

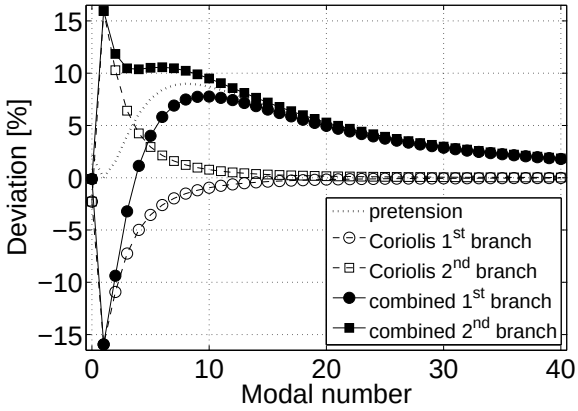

Figure 3.48 – The percentage deviation of the radial natural frequencies across the $n = 1$ to $n = 40$ nodal range for the rolling velocity value of $100km/h$.

3.9.2 The critical speed and standing wave prediction potential

The effect of the rotation is not fully depicted by the modes bifurcation and the frequency variation. A respective change may be identified in the development of the associated mode shapes. Examining them from a stationary point of view, the deformation patterns seem as travelling along the ring circumference, in contrast to the stationary case where the whole ring vibrates in an simultaneous mode. The rotation velocity of every mode shape is different from the angular velocity of the ring (Ω), but it is a function of it. The calculation of the rotation velocity of the mode shapes has been thoroughly presented in [83, 96] and will be only briefly presented in the following.

The central angle variable, θ, of the rotating system of reference is transformed to the respective variable of the stationary one(Θ), using the equation:

$$\Theta = \theta + \Omega \cdot t \tag{3.195}$$

In respect, the radial and tangential mode shape functions of eqns. 3.188 and 3.189 respectively are transformed into the following stationary system expressions:

$$u_r(\Theta, \mathrm{t}) = \mathrm{R^m} \cdot \mathrm{e}^{\iota\left(\mathrm{n}\cdot\Theta+(\omega-\mathrm{n}\cdot\Omega)\mathrm{t}\right)} \tag{3.196}$$

$$u_t(\Theta, \mathrm{t}) = \mathrm{T^m} \cdot \mathrm{e}^{\iota\left(\mathrm{n}\cdot\Theta+(\omega-\mathrm{n}\cdot\Omega)\mathrm{t}\right)} \tag{3.197}$$

The real part of the above functions, is the deformation pattern acquired by a stationary observer. In result, the rotational motion of the pattern may be examined by the observation of a certain point of the mode

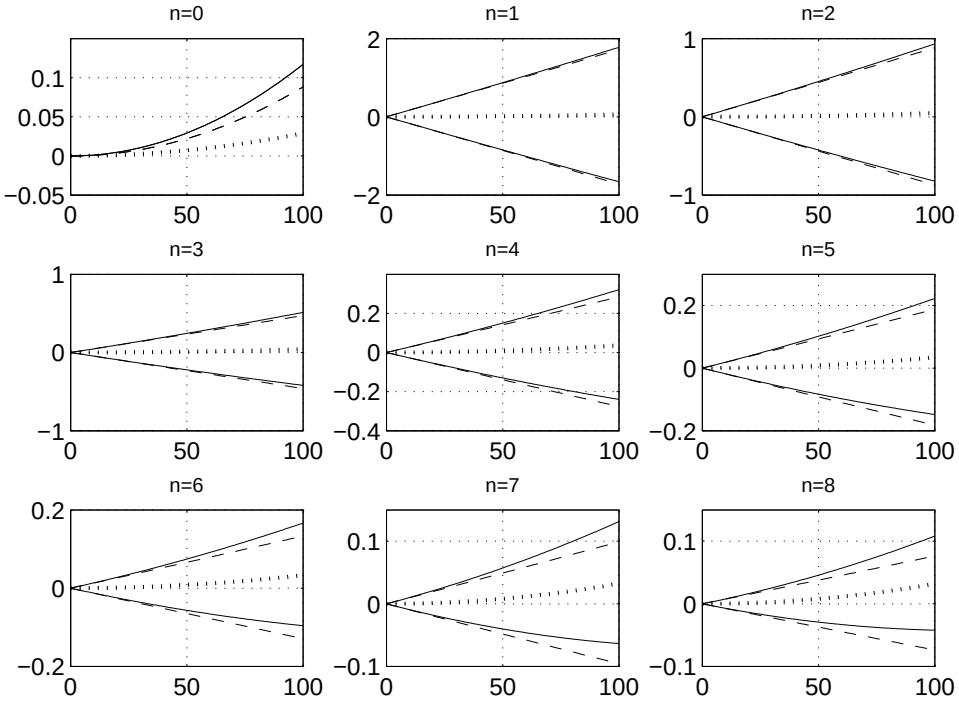

Figure 3.49 – The development of the rotation effects development with the velocity, for the $n = 0$ to $n = 8$ tangential modes. (horizontal axis: travelling velocity (km/h), vertical axis: percentage frequency deviation, dotted line: centrifugal effect, dashed line: coriolis effect, solid line: combined effect)

shape, corresponding to a constant real value of the functions:

$$\begin{aligned} &Re\big[U(\Theta,\mathrm{t})\big] = \mathrm{Re}\Big[\cos\big(\mathrm{n}\cdot\Theta + (\omega - \mathrm{n}\cdot\Omega)\mathrm{t}\big) + \iota\cdot\sin\big(\mathrm{n}\cdot\Theta + (\omega - \mathrm{n}\cdot\Omega)\mathrm{t}\big)\Big] = \text{constant} \\ &\Rightarrow \cos\big(n\cdot\Theta + (\omega - n\cdot\Omega)\mathrm{t}\big) = \text{constant} \\ &\Rightarrow n\cdot\Theta + (\omega - n\cdot\Omega)\mathrm{t} = \kappa\cdot\pi + \theta_{\mathrm{i}}, \qquad \mathrm{k} = 0,1,2,... \end{aligned} \tag{3.198}$$

The angular velocity of the monitored point is calculated as:

$$\Omega_{ms} = \frac{\mathrm{d}\Theta_{ms}}{\mathrm{dt}} = \Omega - \frac{\omega}{n} \tag{3.199}$$

In general, three distinctive cases may be identified by the stationary (global) observer, regarding the propagation direction of the mode shapes:

$$\begin{aligned} &\Omega_{ms} > 0 \Rightarrow \text{forwards travelling wave} \\ &\Omega_{ms} < 0 \Rightarrow \text{backwards travelling wave} \\ &\Omega_{ms} = 0 \Rightarrow \text{stationary (standing) wave} \end{aligned} \tag{3.200}$$

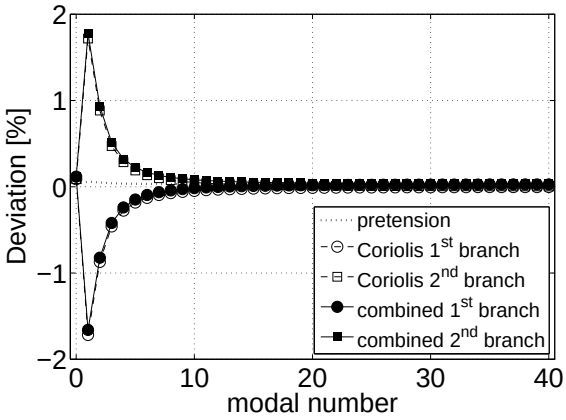

Figure 3.50 – The percentage deviation of the tangential natural frequencies throughout the $n = 1$ to $n = 40$ nodal range for the rolling velocity value of $100km/h$.

It should be noted that in the above derivation of the deformation pattern velocity, the value ω corresponds to the eigenvalues, as predicted by the solution of the characteristic polynomial (eqn. 3.194) and not to their absolute values (natural frequencies)which were presented in figs. 3.47 and 3.49. The signs of the eigenvalues cannot be neglected in the calculation of the global angular velocity of each deformation pattern. Neglecting the rotation effects, each mode corresponds to two opposite constant eigenvalues ($\pm\omega_j$). Consequently, the global propagation velocity of the deformation pattern as a function of the ring velocity is given by the following linear equations:

$$\Omega_{ms}^{1^{st}\text{ branch}} = \Omega + \frac{\omega_j}{n_j} \tag{3.201a}$$

$$\Omega_{ms}^{2^{nd}\text{ branch}} = \Omega - \frac{\omega_j}{n_j} \tag{3.201b}$$

The last case of eqn. 3.200, the standing wave formation, is crucial for the tyre behaviour, as the respective deformation corresponds to a resonance operating condition that may cause the structural failure of the tyre.

The above couple of equations corresponds to the same deformation pattern propagating to the positive or negative direction. Assuming a positive direction for the ring rotation, the propagation velocity magnitude of both waves increases with the ring velocity and a standing wave will emerge from the positive eigenvalue equation (eqn. 3.201b). The linearity of eqn. 3.201b imposes the existence of a ring velocity corresponding to a standing wave formation for each of the radial or tangential modes. These velocities are presented in fig. 3.51 for a range of modal numbers from $n = 1$ to $n = 40$. For the radial modes, the standing wave rolling velocity exhibits a parabolic dependency on the modal number, while the minimum velocity value ($\simeq 225km/h$) is observed for the $n = 8$ mode. The lowest rotation speed speed at which a standing wave (of any mode) is generated is named *critical speed* [103]. Tangential standing waves, in contrast, correspond to standing wave velocities which lie out of the range of interest for common automotive applications.

If the rotation effects are incorporated in the eigenvalues calculation, eqn. 3.199 losses its linearity. The rotation effects on the eigenvalues and the corresponding effects on the wave propagation velocity are

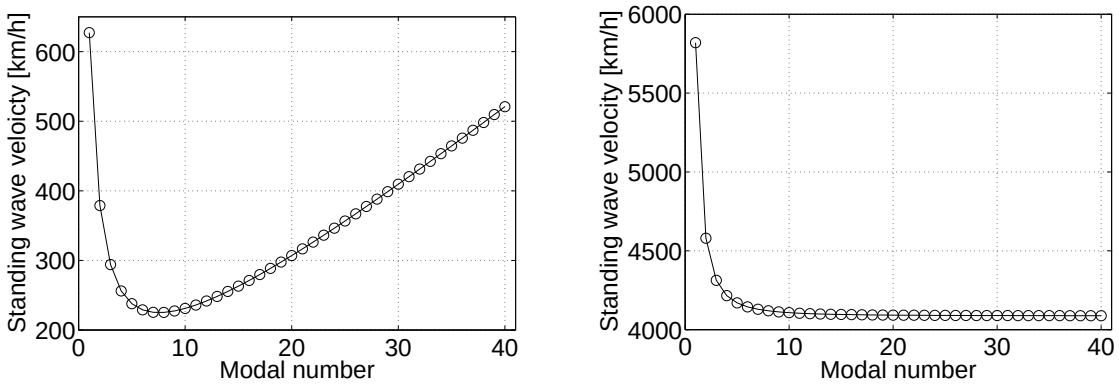

(a) Radial modes.

(b) Tangential modes.

Figure 3.51 – The rolling velocity corresponding to standing wave formation of every radial/ tangential mode, neglecting the rotation effects on the modal characteristics.

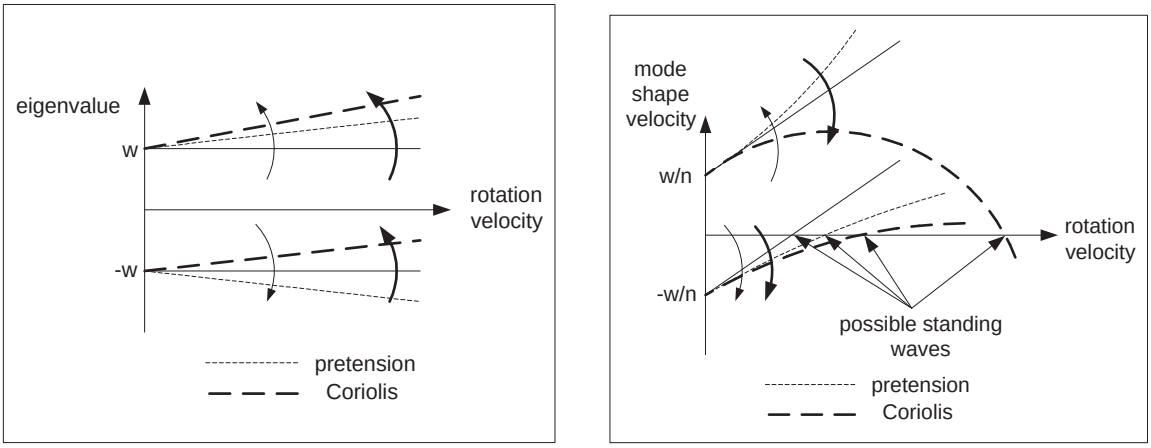

(a) Frequencies.

(b) Mode shape rotation velocity.

Figure 3.52 – The effects of rotation on the eigenvalues and the rotation velocity of the mode shapes, by a stationary observer, for the radial ring modes.

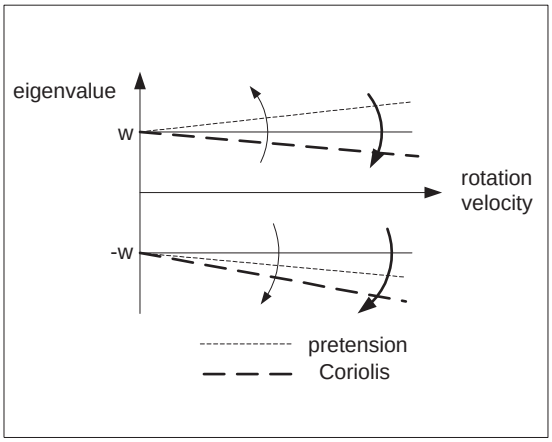

(a) Frequencies.

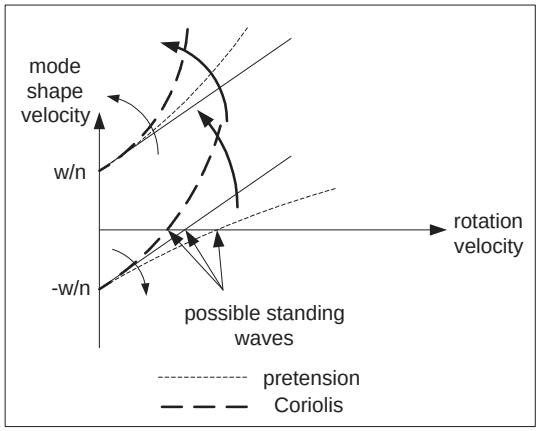

(b) Mode shape rotation velocity.

Figure 3.53 – The effects of rotation on the eigenvalues and the rotation velocity of the mode shapes, by a stationary observer, for the tangential ring modes.

summarized in figs. 3.52 and 3.53 for the radial and the tangential modes respectively. Examining the radial modal group, the centrifugal pretension results in the increase of the positive eigenvalue and the decrease of the negative one. In result, both forwards and backwards travelling waves propagate faster, and the standing wave formation velocity of the latter one accordingly increases. Coriolis acceleration imposes the increase of the positive eigenvalue but has a similar effect on the negative one. Consequently, the corresponding to the first one velocity of standing wave formation increases while, theoretically, a standing wave may be generated by the decrease of the (initially positive) propagation velocity of the shape associated with the negative value. Examining the rotational effects on the tangential modes, a similar to the radial case effect of the pretension may be identified, resulting in the same consequences for the rolling velocity of the standing wave formation. The effect of Coriolis acceleration, though, is the contrary one, as both positive and negative eigenvalues decrease. Consequently, the standing wave formation velocity which is associated with the positive eigenvalue decreases.

It should be highlighted that the above theoretical effects of the rotation on the standing wave formation velocities do not guarantee the existence of such a velocity. The non linear development of the wave propagation velocities (figs. 3.52(b) and 3.53(b)) may suspend them from being zeroed, for any rolling velocity value. Furthermore, the investigation of the standing waves formation has to be limited to a certain rolling velocity range in which the initial equations of motion may be assumed as valid and the solutions of the characteristic equations remain real values.

As an application of the above theoretical analysis, the rotation effects on the wave propagation velocity of the radial and tangential $n = 4$ mode shapes are presented in figs. 3.54 and 3.54 respectively. The examined velocity range is limited to the $1000km/h$ value. As expected, the velocity branch which is associated with the negative radial eigenvalue increases by the introduction of the pretension effect but decreases by the introduction of the Coriolis one. A combined increasing behaviour is identified, as the pretension influence is stronger than the Coriolis one. In the case of the velocity branch associated wit the positive eigenvalue, both effects result in the decrease of the propagation velocity and the pretension effect is the predominant one also in this case. Interestingly, although the individual incorporation of the pretension or the Coriolis effect

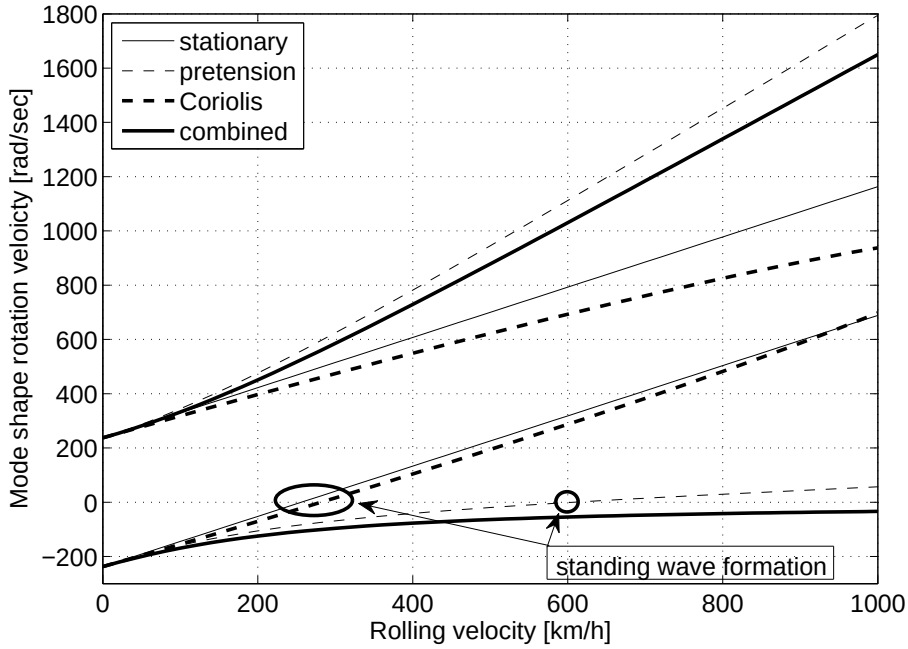

Figure 3.54 – The rotation velocity of the 4th radial mode deformation pattern, as measured by a stationary observer.

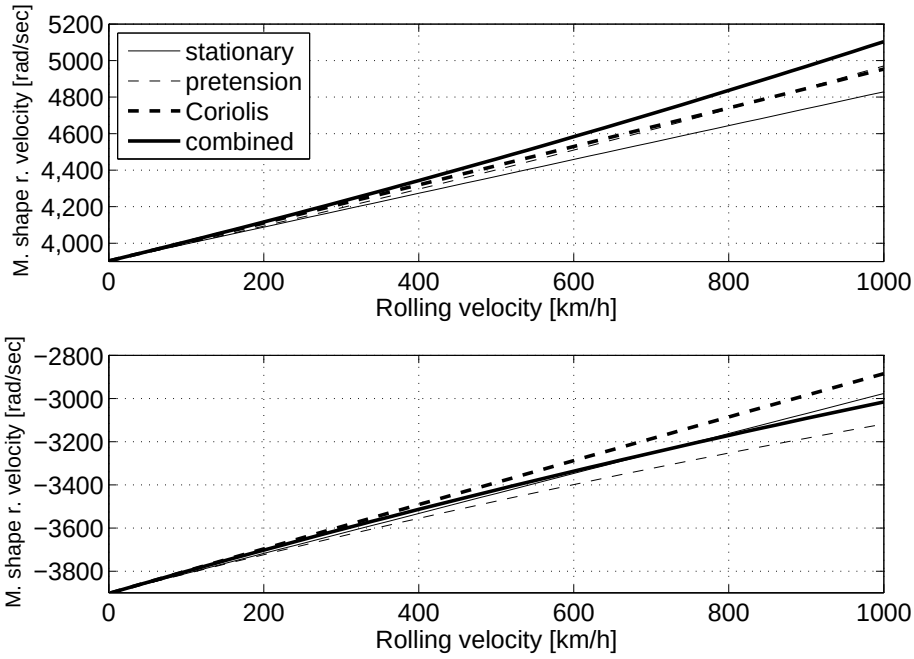

Figure 3.55 – The rotation velocity of the 4th tangential mode deformation pattern, as measured by a stationary observer.

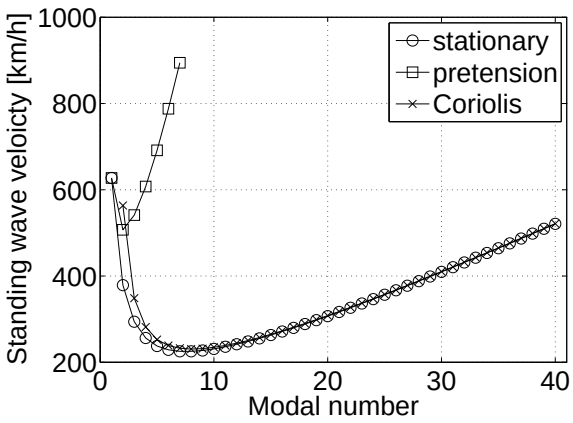

Figure 3.56 – The rotation velocity at which each standing wave is formed, in the cases of the stationary modal assumption, the Coriolis and the pretension effects incorporation.

increases the standing wave formation velocity, their combined effect seems to suspend its generation, as the propagation velocity asymptotically reaches a negative value. In the case of the tangential mode shapes propagation velocities, the branch associated with the negative eigenvalue increases by the influence of the rotational effects, while the branch corresponding to the positive eigenvalue exhibits an equal decreasing and increasing effect of the pretension and the Coriolis acceleration respectively, resulting in an insignificant total variation. Across the examined velocity range, no standing wave formation is predicted by the tangential modes.

Examining the same velocity range for the whole $n = 1$ to $n = 40$ modal range, the rolling velocity which corresponds to the standing wave formation is presented in fig. 3.56, including the two rotation effects. For comparison reasons the standing wave velocity of the stationary modal approach is also presented in the same figure. All the standing wave cases in the specific range are associated with the positive radial eigenvalue. The coriolis effect on the first mode is so profound that the existence of the standing wave is prevented, while for the following modes, the deviation of the stationary model predicted velocity value is small. The pretension results in an insignificant change of the $n = 1$ standing wave velocity, but a tremendous increase in the velocity of the rest of the modes. Characteristically, the formation velocity of the $n \geq 8$ standing wave exceed the examined range. The combination of the two rotation phenomena suspends the formation of any standing wave up to the $1000km/h$ limit.

3.9.3 Summary of the rotation effects on the modal behaviour

Summarising the rotation effects on the modal behaviour prediction, it may be concluded that the centrifugal acceleration introduces a stiffening pretension effect while the coriolis acceleration cancels the duplicity of the modes. Rotation effects are more profound in the radial modal group than the tangential one but their strength deteriorates with the modal number in both cases. Examining the radial modal group behaviour in detail, the Coriolis effect becomes maximum for the first mode, while the centrifugal effect reaches its maximum for a higher modal number. Both effects deteriorate as the modal number increases further. The incorporation of the rotation effect in the modal prediction of the ring model and especially of the pretension one, increases the rotation velocity of the standing wave formation or suspends completely the standing wave

generation.

The above analysis of the rotation effects on the modal behaviour prediction should be examined under the consideration that any rotation velocity variation from the one at which the eigenanalysis has been accomplished introduces a modal data calculation error. The desired accuracy of the modal basis, in respect, defines the range of velocity across which the model may be assumed as valid. Moreover, given that the modal deviation is a function of the modal number, the range of the modal basis is crucial for the determination of the total error. Although the above results should be re-examined after the investigation of the necessary tyre model modal range (chapters 4 and 5), it is obvious that the significant magnitude of the rotation effects on the low modal number zone cannot be countered by the modal reduction process.

3.10 The damping effect

The modelling of the energy dissipation mechanism of the tyre structure will be discussed in this section. The incorporation of an accurate damping mechanism in the model is crucial for the simulation of the tyre phenomena related to the energy dissipation, such as the rolling resistance. As discussed in the first chapter, the variety of the materials used for the tyre construction and their profound viscoelastic behaviour makes the modelling of the total dissipation behaviour difficult. In the following, the effect of some common tyre damping modelling assumptions on the modal behaviour prediction will be identified and the possible justification of them through published modal data characteristics will be attempted.

3.10.1 The generalised energy dissipation mechanism and its common assumptions

In contrast to the inertia and stiffness properties of a structure, a deterministic physical approach for the capture of the structural energy dissipation mechanisms does not exist. In general, a damping force depends on the deformation history of the structure and for this reason it may be expressed as a convolution integral of a dissipation (*relaxation*) function over a state variable (*generalised coordinate*) [175]. Applying this approach on the tyre structure, it may be proposed:

$$f_{r/t}^{damping}(\theta,\mathrm{t}) = \int_{-\infty}^{\mathrm{t}} \mathrm{G_{r/t}}(\theta,\mathrm{t}-\tau)\cdot \mathrm{u_{r/t}^{s.v.}}(\theta,\tau)\mathrm{d}\tau \tag{3.202}$$

where:

$f_{r/t}^{damping}$	the radial or tangential damping force analytical function
$G_{r/t}(\theta,\mathrm{t})$	the dissipation functions
$u_{r/t}^{s.v.}$	the generalised state variables

The only inviolable condition for the above function is the non negative energy dissipation, which may be expressed as:

$$\int_0^{2\pi} u_{r/t}^{s.v.}(\theta,\mathrm{t})\cdot \mathrm{f_{r/t}^{d}}(\theta,\mathrm{t})\mathrm{d}\theta \ \geq 0 \tag{3.203}$$

Assuming that the dissipation function can be written as the product of a space distribution function and a time one, the latter one defining the memory property of the damping mechanism, eqn. 3.202 transforms into:

$$f_{r/t}^{damping}(\theta, \mathrm{t}) = \mathrm{G}_{\mathrm{r/t}}^{\mathrm{s}}(\theta) \int_{-\infty}^{\mathrm{t}} \mathrm{G}_{\mathrm{r/t}}^{\mathrm{s}}(\mathrm{t}-\tau) \cdot \mathrm{u}_{\mathrm{r/t}}^{\mathrm{s.v.}}(\theta, \tau)\mathrm{d}\tau \tag{3.204}$$

The most common assumption related to the time function of the dissipation mechanism is the viscous one, initially proposed by Lord Rayleigh in [174]. According to that, the time function is the δ-Dirac one and the generalised coordinate refers to the deformation velocity. In result, dissipation mechanism loses its memory effect and depends only on the instantaneous velocity values:

$$f_{r/t}^{damping}(\theta, \mathrm{t}) = \mathrm{G}_{\mathrm{r,t}}^{\mathrm{s}}(\theta) \int_{-\infty}^{\mathrm{t}} \delta(\tau) \cdot \mathrm{u}_{\mathrm{r/t}}^{\mathrm{s.v.}}(\mathrm{t}-\tau)\mathrm{d}\tau = \mathrm{G}_{\mathrm{r/t}}^{\mathrm{s}}(\theta) \cdot \dot{\mathrm{u}}_{\mathrm{r/t}}(\theta, \tau) \tag{3.205}$$

In regards to the space function of the dissipation mechanism, the most common assumption is the reciprocity one. According to that, the damping mechanism allows for the interchange between the excitation and the response positions in a structure. The damping linearity and reciprocity are tyre properties which are experimentally verified in a number of studies, such as [78, 181, 80].

The damping mechanism significantly affects the modal characteristics of the structure, in terms of both eigenvalues and eigenvectors prediction. In general, complex values emerge for both of them, in contrast to the imaginary eigenvalues ($s^{eig} = \iota \cdot \omega^2$) and real eigenvectors (Ψ) of the undamped stationary structure. The imaginary part of the eigenvalues captures the frequency of the free oscillatory response, similarly to the undamped case, but its actual value is different (lower) from the respective undamped one. The real part captures the intensity of the energy dissipation. The imaginary part may be absent from the eigenvalue and in this case the free response shows no oscillatory behaviour (over-critically damped modes). The general eigenvalue form may be written as:

$$s^{eig} = -\omega \cdot \zeta \pm \iota \cdot \omega\sqrt{1-\zeta^2} \tag{3.206}$$

$$\Rightarrow s^{eig} = -\omega \cdot \zeta \pm \iota \cdot \omega^d \tag{3.207}$$

where:

- ω^d the damped frequency
- ω the undamped frequency
- ζ the damping ratio

and the following cases may be identified:

$$\zeta < 1 \Rightarrow \text{subcritical (oscilatory) response pattern}$$
$$\zeta = 1 \Rightarrow \text{critical (oscilatory) response pattern}$$
$$\zeta > 1 \Rightarrow \text{overcritical (non} - \text{oscilatory) response pattern}$$

The complex nature of the eigenvectors results in the coupled time and space domains response. Practically, the mode shapes develop as propagating waves in contrast to the stationary ones of the real eigenvectors. The similarities between the effects of rotation and damping on the modal characteristics of the structure are obvious and further analysis on the topic may be found in the work of Huang and Soedel [96] and in the books of Ewins[169] and Maia *et al* [250].

3.10.2 The damping proportionality assumption

An important aspect of the dissipation mechanism is its space deployment and distribution. The most commonly assumed pattern is the damping proportionality. According to that, the damping mechanism coexists with the mass or stiffness structural properties, in a parallel configuration to theirs. The mass proportionality correlates adequately with the friction induced dissipation mechanism, while the stiffness one corresponds to the material bulk property [182]. Interestingly, both of these dissipation mechanisms are strongly present in the tyre structure, given its multi-layer structure and its viscoelastic materials construction.

Rewriting the ring equations of motion in a generalised way and incorporating the viscous damping force terms, it may be proposed:

$$\mathbf{L}^{\mathrm{s}}_{\mathrm{r/t}}(\mathrm{u_r}, \mathrm{u_t}) + \mathbf{L}^{\mathrm{d}}_{\mathrm{r/t}}\left(\frac{\partial \mathrm{u_r}}{\partial \mathrm{t}}, \frac{\partial \mathrm{u_t}}{\partial \mathrm{t}}\right) + \mathrm{f}^{\mathrm{inertia}}_{\mathrm{r/t}} = 0 \tag{3.208}$$

where:

$\mathbf{L}^{\mathrm{s}}_{\mathrm{r/t}}$	the stiffness force partial differential operator to θ
$\mathbf{L}^{\mathrm{d}}_{\mathrm{r/t}}$	the viscous damping force partial differential operator to θ
$f^{inertia}_{r/t} = \rho \cdot A \frac{\partial^2 u_{r/t}}{\partial t^2}$	the inertia force

The stiffness proportionality may be expressed as:

$$\mathbf{L}^{\mathrm{d}}_{\mathrm{r/t}} = \beta_{\mathrm{d}} \frac{\partial}{\partial \mathrm{t}}(\mathbf{L}^{\mathrm{s}}_{\mathrm{r/t}}) \tag{3.209}$$

while mass proportionality as:

$$\mathbf{L}^{\mathrm{d}}_{\mathrm{r/t}} = \gamma_{\mathrm{d}} \cdot \rho \cdot \mathrm{A} \frac{\partial \mathrm{u_{r,t}}}{\partial \mathrm{t}} \tag{3.210}$$

where β_d and γ_d are the proportionality coefficients. For the simple ring equations of motion (eqns. 3.23a and 3.23b) the stiffness proportional concept can be rewritten as:

$$\begin{aligned} \mathbf{L}^{\mathrm{s}}_{\mathrm{r}} &= \frac{D}{R^4}\left(\frac{\partial^4 u_r}{\partial \theta^4} - \frac{\partial^3 u_t}{\partial \theta^3}\right) + \frac{K}{R^2}\left(u_r + \frac{\partial u_t}{\partial \theta}\right) + k_r \cdot u_r \Rightarrow \\ \mathbf{L}^{\mathrm{d}}_{\mathrm{r}} &= \beta_d \cdot \frac{\partial}{\partial \mathrm{t}}\left(\frac{D}{R^4}\left(\frac{\partial^4 u_r}{\partial \theta^4} - \frac{\partial^3 u_t}{\partial \theta^3}\right) + \frac{K}{R^2}\left(u_r + \frac{\partial u_t}{\partial \theta}\right) + k_r \cdot u_r\right) \end{aligned} \tag{3.211}$$

$$\begin{aligned}
\mathbf{L}_{\mathfrak{t}}^{\mathrm{s}} &= \frac{D}{R^4}\left(\frac{\partial^3 u_r}{\partial\theta^3} - \frac{\partial^2 u_t}{\partial\theta^2}\right) - \frac{K}{R^2}\left(\frac{\partial u_r}{\partial\theta} + \frac{\partial^2 u_t}{\partial\theta^2}\right) + k_t \cdot u_t \Rightarrow \\
\mathbf{L}_{\mathfrak{t}}^{\mathrm{s}} &= \beta_d \cdot \frac{\partial}{\partial \mathfrak{t}}\left(\frac{D}{R^4}(\frac{\partial^3 u_r}{\partial\theta^3} - \frac{\partial^2 u_t}{\partial\theta^2}) - \frac{K}{R^2}(\frac{\partial u_r}{\partial\theta} + \frac{\partial^2 u_t}{\partial\theta^2}) + k_t \cdot u_t\right)
\end{aligned} \tag{3.212}$$

An important consequence of the proportionality property is the derivation of real eigenvectors, which are similar to the ones of the undamped model. This may be better explained if the model is expressed in a discretised (matrix) form and the equation of motion is written as:

$$\mathbf{M} \cdot \ddot{\mathbf{u}}(t) + \mathbf{C} \cdot \dot{\mathbf{u}}(t) + \mathbf{K} \cdot \mathbf{u}(t) = 0 \tag{3.213}$$

where:

$\mathbf{u}$	the DOFs deformation vector
$\mathbf{M}$	the inertia matrix
$\mathbf{C}$	the damping matrix
$\mathbf{K}$	the stiffness matrix

As it has been discussed in section 3.5.1 the eigenvectors' matrix of a structure diagonalise the inertia and stiffness matrices, offering the modal mass and stiffness properties of every individual mode. The proportionality property may be written as:

$$\mathbf{C} = \beta_d \cdot \mathbf{K} + \gamma_d \cdot \mathbf{M} \tag{3.214}$$

Applying a similar diagonalisation procedure to the proportional viscous damping matrix it may be written:

$$\tilde{\mathbf{\Psi}}^T(\beta_d \cdot \mathbf{K} + \gamma_d \cdot \mathbf{M})\tilde{\mathbf{\Psi}} = \beta_d \cdot \tilde{\mathbf{\Psi}}^T \cdot \mathbf{K} \cdot \tilde{\mathbf{\Psi}} + \gamma_m \tilde{\mathbf{\Psi}}^T \cdot \mathbf{M} \cdot \tilde{\mathbf{\Psi}} = \beta^m \cdot \mathbf{K}^m + \gamma^m \cdot \mathbf{M}^m \tag{3.215}$$

Evidently, the linear combination of the stiffness and inertia matrices results in a matrix that can be also diagonalised by the same eigenvectors' matrix. In physical terms, the incorporation of the proportional viscous damping mechanism does not affect the eigenvectors of the structure and the damping properties of the modes can be decoupled from each other, similarly to the modal mass and stiffness properties (see section 3.5.1):

$$c_j^m = \beta_j^m \cdot k_j^m + \gamma_j^m \cdot m_j^m \Rightarrow \tag{3.216}$$

$$\lambda_j = \frac{c_j^m}{m_j^m} = \beta_j^m \cdot \omega_j^2 + \gamma_j^m \tag{3.217}$$

The damping ratio of each mode is expressed by a function of the proportionality coefficients and the undamped natural frequencies:

$$\zeta = \frac{\beta \cdot \omega}{2} + \frac{\gamma}{2 \cdot \omega} \tag{3.218}$$

The validity of the proportionality assumption for the tyre belt structure has been experimentally examined by Popov and Geng [181] and by Geng *et al* [80]. A certain frequency limit exists (typically $\sim 200Hz$), up to which the imaginary part of the eigenvectors is insignificant, leading to the conclusion that the damp-

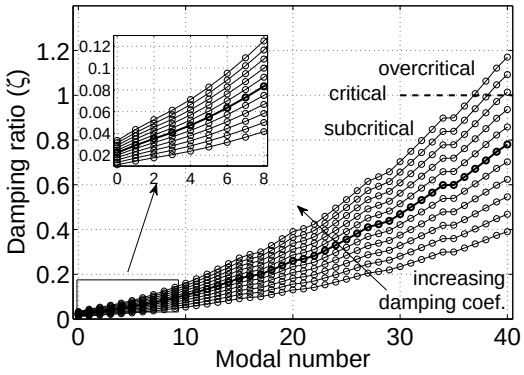

(a) Damping ratios.

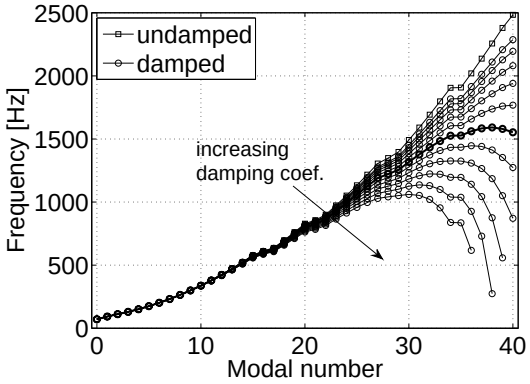

(b) Natural frequencies.

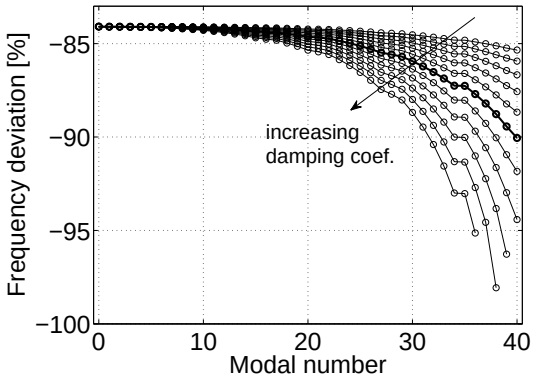

(c) Natural frequencies percentage deviation.

Figure 3.57 – The effect of the stiffness proportional viscous damping on the modal characteristics.

ing spatial distribution pattern does not deviate much from the proportional one. The imaginary part of the eigenvectors in the higher frequency range, though, is profound and the assumption cannot be further justified.

Based on the definition of the modal damping ratio (eqn. 3.218), the stiffness and mass proportionality effect across the modal range is examined in figs. 3.57 and 3.58 respectively. As it may be concluded from eqn. 3.218, in the case of stiffness proportionality the values of the damping ratio increase with the modal number, following the similar development of the natural frequencies. In result,for any value of the damping coefficient, there is a modal number above which the behaviour of the model becomes overcritically damped. For the graphical representation of the above pattern, a value of β_d equal to $6 \cdot 10^{-5}$ is chosen, together with a variation range from -50% to $+50\%$. This value was arbitrarily selected in order the emerging low modal number damping ratios to agree with published experimental values. Explicitly, values up to 10% were measured by Kim *et al* ([183]) for a number of different tyres, ratios between 7% and 8% were experimentally acquired in [79, 106] by Perisse and Hamet and Perisse *et al*, while values lower than 4% are presented by Yam *et al* in [77] and by Guan *et al* in [78]. The damped frequencies of the subcritical modes of every damping level case are presented in fig. 3.57(b) in comparison to the undamped ones, while the percentage deviation of them from the last is plotted in fig. 3.57(c). Obviously the damping effect increases with the

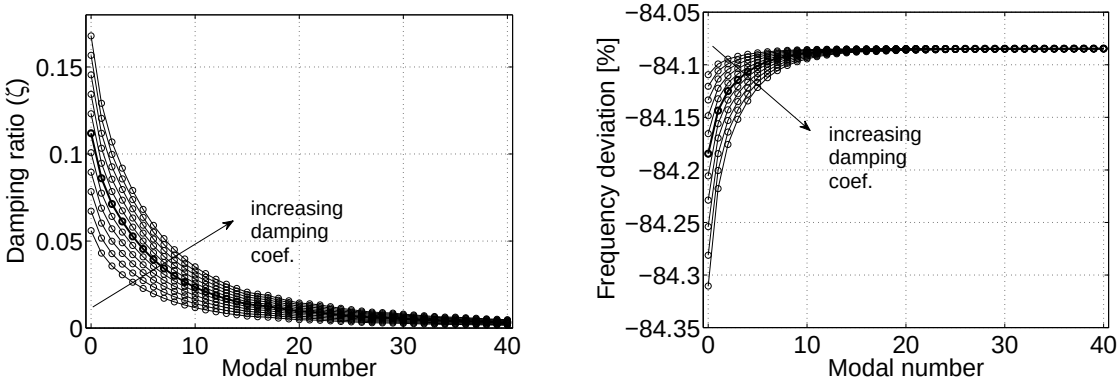

(a) Damping ratios.

(b) Natural frequencies percentage deviation.

Figure 3.58 – The effect of the mass proportional viscous damping on the modal characteristics.

modal number, while towards the critical mode the increasing frequency order of the modes is abrogated, as the corresponding frequencies decrease radically.

The damping ratios of the mass proportional damping cases are presented in fig. 3.58(a), where a contrary development pattern to the stiffness proportionality corresponding one may be observed (nominal value $\gamma_d = 400$). The damping ratio values decrease with the modal number and asymptotically reach the zero ratio value. Damping coefficients that correspond to a range of damping ratios between 5% to 16% for the first mode range, result in a lower than 1% ratio value near the upper limit of the examined modal range. A similar asymptotic behaviour is observed for the frequency deviation of the damped frequencies from the undamped ones (fig. 3.58(b)).

Apparently, the question, that the above plots try to give an answer to, is whether any of the above proportional damping mechanisms is able to describe the experimentally captured damping behaviour of the tyre. Apparently, only a narrow modal range may be experimentally monitored, something that suspends the comparison of the proposed damping mechanism with the actual one. The reason for this narrowness, though, is directly related to the increase of the damping ratio with the modal number [77, 106, 79, 251, 78, 80] something that prescribes a stiffness proportional-like physical mechanism.

A closer examination of the published tyre modal damping data, though, leads to the conclusion that the identified damping pattern is not strictly monotonous, as predicted by the above simple proportionality assumptions. Although an increasing damping factor with the mode number is in generally observed, this pattern does not apply to the beginning of the modal range. In [77], for example, the $n = 2$ mode is more heavily damped than the following 5 modes, although the increasing ratio order applies for all the $n >= 3$ modes. A similar behaviour can be observed in [78] and [79]. Accordingly, the natural frequency of the $n = 0$ mode is identified as higher than the $n = 1$ one in [252] and the $n = 1$ mode damping ratio is higher than the following three ones in [80]. Obviously, none of the proportional damping models can accurately represent the damping development pattern on its own, especially in the low modal range, as both of them exhibit a clear monotonous behaviour. A combination of the two models, though, may capture the representation of the experimentally observed change in the evolution pattern from the initial decreasing to the general increasing one. A data fitting procedure can identify a combination of mass and stiffness proportionality coefficients that accurately represents a an experimentally acquired pattern.

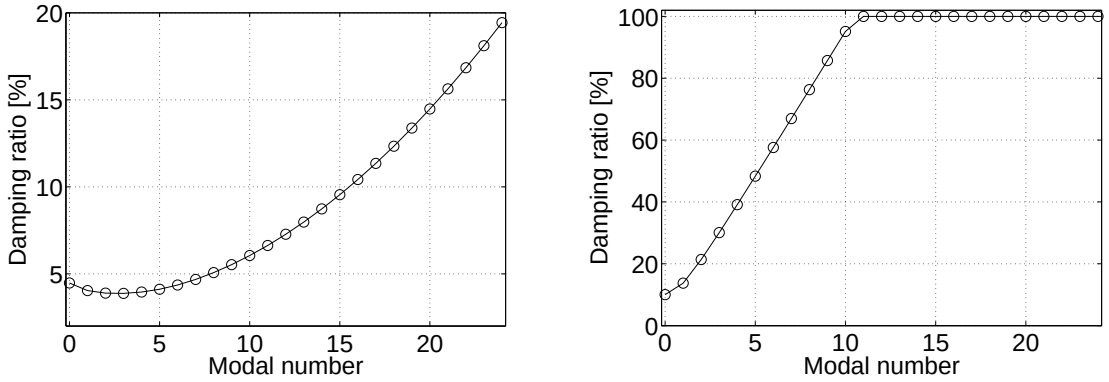

(a) Radial damping ratios.

(b) Tangential damping ratios.

Figure 3.59 – The damping ratios of the first 25 radial and tangential modes resulting from a viscous proportional damping mechanism ($\beta_d = 6 \cdot 10^{-5}$ and $\gamma_d = 400$).

As an example of such a combination, the modal damping ratio values resulting from the coefficients $\beta_d = 6 \cdot 10^{-5}$ and $\gamma_d = 400$ are presented in fig. 3.59. Obviously the combination of the two mechanisms of proportionality may capture the above described parabolic pattern. The range of the first 25 radial and tangential modes are examined with the first ones being sub-critically damped across the whole range and the second ones being over-critically damped above the $n = 10$ mode.

3.10.3 Non proportional (reduced) damping mechanisms

The dropping of the damping proportionality assumption, something that is necessary for the investigation of the damping development across a broad modal range, requires a different study approach. The eigenanalysis is based on the transformation of the $n_b \times DOFs/node$ degrees of freedom double order system into a respective $2 \times n_b \times DOFs/node$ degrees of freedom single order one. The transformation is commonly called state-space analysis [250]:

$$\mathbf{M} \cdot \ddot{\mathbf{u}}(t) + \mathbf{C} \cdot \dot{\mathbf{u}}(t) + \mathbf{K} \cdot \mathbf{u}(t) = 0 \Rightarrow \mathbf{A}^{ss} \cdot \dot{\mathbf{u}}^{ss}(t) + \mathbf{B}^{ss} \cdot \mathbf{u}^{ss}(t) = 0 \tag{3.219}$$

where:

$$\mathbf{A}^{ss} = \begin{bmatrix} \mathbf{C} & \mathbf{M} \\ \mathbf{M} & \mathbf{0} \end{bmatrix}, \ \mathbf{B}^{ss} = \begin{bmatrix} \mathbf{K} & \mathbf{0} \\ \mathbf{M} & \mathbf{0} \end{bmatrix} \text{ and } \mathbf{u}^{\text{ss}} = \begin{bmatrix} \mathbf{u} \\ \dot{\mathbf{u}} \end{bmatrix} \tag{3.220}$$

The above equation represents a generalised eigenanalysis problem, the solution of which is a set of $2 \times n_b \times DOFs/node$ real (overcritical modes) or complex (subcritical modes) eigenvalues, existing in conjugate pairs, following the general eigenvalue form of eqn.3.206. Given the double axis symmetry of the tyre structure, a damping non proportional distribution may only correspond to a different damping contribution between the belt and the sidewall. In the existing tyre modelling literature, the damping non proportionality is commonly introduced by the omission of the property from the circumferential belt and its sole presence in the sidewall mechanism. Such models have been proposed by Lu and Segel [179] and by Stutts and Soedel [180].

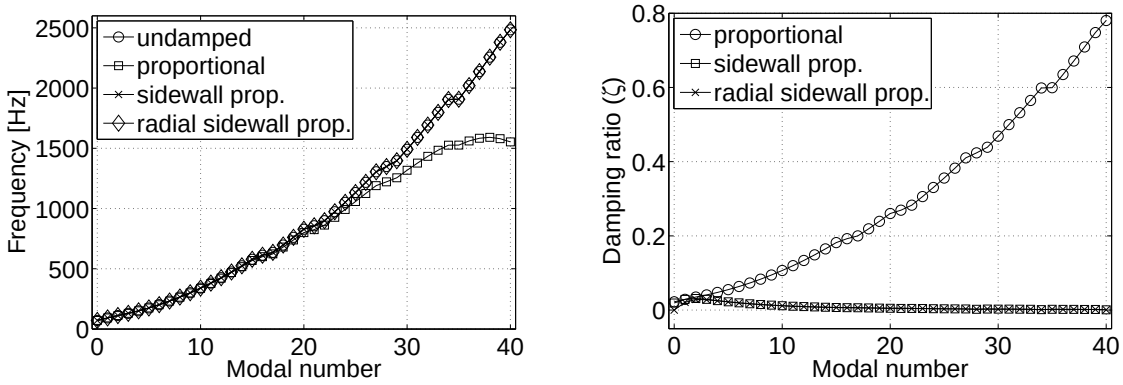

(a) Frequencies.

(b) Damping ratios.

Figure 3.60 – The modal prediction of two non proportionally damped models, the sidewall only stiffness proportional and the pure radial stiffness proportional ones, in comparison to the stiffness proportional and the undamped ones.

The effect of two reduced damping mechanisms on the frequencies is captured in fig. 3.60. The sidewall stiffness and the radial sidewall stiffness proportional damping cases are examined, in comparison to the total stiffness proportional one, while all cases correspond to a proportionality coefficient value $\beta_d = 6 \cdot 10^{-5}$. Both reduced models result in an insignificant deviation of the natural frequencies from the respective undamped ones. This can be justified by the fact that the tangential stiffness mechanism of the belt circumference is the dominant stiffness mechanism of the structure. Accordingly, the magnitude of the damping effect which is observed in the general stiffness proportional case is determined by it. Examining the corresponding to each case damping ratios, the increasing with the modal number pattern of the proportional case is not present in the non proportional ones. Both reduced damping cases follow an initially increasing ratio pattern only up to the third mode (radial $n = 2$), after which the damping ratios decrease and asymptotically vanish. Consequently, the non proportional distribution should be examined not only as a possible source of damping magnitude variations but also as a source of different development patterns along the examined modal range.

3.10.4 The small damping assumption

A more generic study approach which may be followed, even in the case of the non viscous dissipation mechanism, is based on the assumption that the damping forces remain modest. The *small damping* property, as it usually called [174, 182, 176, 177], cannot be defined in mathematical or quantitative terms but could be regarded as being described by a minor deviation of the vibrational behaviour from the respective undamped one. Practically, the property can be identified through the damping ratio values and the assumption may be regarded as valid in the damping behaviour cases described by the typical tyre damping ratio values experimentally identified [183, 77, 79, 106, 183]. The studies of Popov and Geng [181] and Geng *et al* [80] investigate the validity of the assumption in a more systematic way. The importance of the small damping property for the followed modelling approach was firstly proposed by Rayleigh in [174]. He proved that the modal characteristics of a viscous, lightly damped structure may be approached by a perturbation method applied on the modal eigendata of the undamped one.

The modal data of the jth mode of the damped structure can be calculated as:

$$\omega_j^d \simeq \pm\omega_j + \iota \cdot \frac{1}{2} \cdot \mathbf{C}^m(j,j) \tag{3.221a}$$

$$\Psi_j^d \simeq \Psi_j + \iota \cdot \sum_{k=1,\ k\neq j}^{k=m} \frac{\omega_j \cdot \mathbf{C}^m(j,k)}{\omega_j^2 - \omega_k^2} \Psi_k \tag{3.221b}$$

where:

$omega_j^d$	the damped natural frequency
$omega_j$	the undamped natural frequency
$C^m(j,k)$	the jth horizontal line and kth vertical row element of the modal damping matrix
m	the total number of modes, equal to the dimensions of the matrix
Ψ_j	the jth eigenvector
Ψ_j^d	the jth damped eigenvector

According to the above equations,the complex natural frequencies consist of a real part, equal to the undamped eigenvalue, and an imaginary part corresponding to the diagonal terms of the modal damping matrix. Accordingly, the real part of the mode shapes is equal to the undamped one, while the imaginary part is a function of the other undamped mode shapes, weighted to favor the influence of the close to the examined one modes. The validity of the approximation is experimentally proved by Geng *et al* in [80], for at typical heavy vehicles tyre. Woodhouse in [182], extended the above approach from the viscous simplification to any energy dissipation mechanism, under the linearity and small damping conditions.

3.10.5 Hysteretic damping

Another damping model which is used for the capture of the tyre energy dissipation mechanism, is the hysteretic one. As discussed in [169] and [250], the viscous damping model, overestimates the dependence of the real structures dissipation mechanism on the oscillation frequency. Even in the case of viscoelastic materials, that such a dependence is one of their characteristic properties, the dependency is not as profound as described by a velocity proportional model. The above is proved by the sub-proportional increase of the tyre rolling resistance with the velocity.

For a single degree of freedom oscillator, hysteretic damping could be expressed in a similar to the viscous case velocity proportional term, which, though, would be inverse proportional to the driving frequency:

$$m \cdot \ddot{u} + \frac{h}{\omega}\dot{u} + k \cdot u = F \cdot e^{\iota \cdot \omega \cdot \mathrm{t}} \Rightarrow m \cdot \ddot{u} + k(1 + \iota \cdot \zeta^h)u = F \cdot e^{\iota \cdot \omega \cdot \mathrm{t}} \tag{3.222}$$

where, ζ^h represents the hysteretic damping ratio, commonly called loss factor. The equation that describes the forced response of a hysteretically damped discretised model reads:

$$\mathbf{M} \cdot \ddot{\mathbf{U}} + \iota \cdot \mathbf{C} \cdot \mathbf{U} + \mathbf{K} \cdot \mathbf{U} = 0 \tag{3.223}$$

In the proportional case, the complex frequency values are calculated as:

$$(\omega^d)^2 = \omega^2(1 + \iota \cdot \zeta^h) \tag{3.224}$$

where:

$$\zeta^h = \beta_d + \frac{\gamma_d}{\omega^2} \tag{3.225}$$

An interesting approach to the study of hysteretically damped free response is presented in [178], where a common approach is proposed for a viscous, hysteretic or any relative combination of them damping mechanism. Under this approach, the natural frequency of a hysteretically damped system could be calculated as:

$$\omega^d = \sqrt{\frac{1 + \sqrt{1 + (\zeta^h)^2}}{2}}\ \omega \tag{3.226}$$

Although in the majorities of the tyre modelling attempts the viscous damping approach is followed, hysteretically damped tyre models have been presented. Kim and Savkoor in [122] introduced such a damping model into their flexible ring tyre study. Although Miege and Popov in [127] comment that in the low frequency range, no significant difference results in the low frequency range modal behaviour from the adoption of a viscous or a hysteretic mechanism.

3.10.6 Conclusions on the tyre damping mechanism modelling

In this section a number of tyre damping modelling mechanisms was examined, together with their effect on the simulation of the tyre modal characteristics. Starting from the general damping concept, the viscous model was derived and simplified through its proportional assumption. The stiffness proportionality was found to result in an increasing with the modal number pattern of damping ratios and the structure becomes over-critically damped above a modal number. The mass proportionality was found to impose a contrary effect and the damping ratios of the modes follow a decreasing with the modal number development pattern. Examining a number of published experimental studies, a general stiffness-like behaviour is identified in all of them, but this model alone cannot capture the actual damping behaviour in the low modal number range, where a contrary development pattern is identified.

The low modal number zone damping behaviour may be captured by the superposition of a mass-proportional damping mechanism on the stiffness one. Given though that the proportionality assumption may be dropped, various damping spatial distributions are able to represent a similar low modal range damping ratios development pattern. Retaining the double axis symmetry of the damping property's spatial distribution, the difference between the circumferential and the sidewall damping properties is the most common deviation from the proportional distribution. The hysteretic damping mechanism was briefly presented given that the sub-proportional increase of the rolling resistance of the tyre with the velocity could be explained by such a mechanism and accordingly hysteretically damped tyre models may be found in the literature.

The most important result that may be drawn from the examination of the experimentally acquired modal damping data is that the small damping assumption may be regarded as valid up to a certain modal number. Following the latest damping theories, this condition is sufficient for the simulation of the tyre damping behaviour according to the viscous assumption, even if a number of other conditions cannot be verified. The error associated with this approach increases with the modal number, as the actual structural behaviour diverges from the small damping case.

3.11 Summary of the chapter

The simulation of the modal behaviour of the tyre structure was investigated in terms of natural frequencies and deformation mode shapes prediction. The proposed modelling approaches were examined across a broad modal range, as the breadth of the modal basis which is sufficient for the accurate capture of the structural mechanisms of the tyre behaviour will be examined in the following chapters. The analytical ring on elastic foundation model was used as a comparison basis, given that, at least in the low frequency range, its correlation with the tyre modal behaviour has been experimentally established. Some common ring model variations, the basic rectilinear models and the corresponding to them discretised representations were analysed and the physical structural mechanisms captured or neglected by them were identified, together with the physical properties that support the development of them. Based on that, the modal range of agreement between the modelling approaches was identified, something that will later lead to their possible applicability or not on the simulation of the complete tyre performance.

The primal vibrational mechanism of a ring model is the bending behaviour of its circumference. Due to its circular shape, the bending strain is composed by both radial and tangential deformation contributions. Two series of modes are predicted by the ring model, one of them primarily exhibits a radial deformation while the other exhibits a tangential one. For ring properties corresponding to the actual tyre structure, the first group is associated with lower natural frequencies than the second one. It was found that both groups predict a decreasing with the modal number participation in the mode shapes of the deformation supplementary to the one they are named after. This participation starts from an almost equal to their primal one and progressively reduces with the modal number. Above a certain number, the radial modal group exhibits pure radial deformation and the tangential modal group pure tangential one. Examining the effect of the physical properties on the modal data, although the tangential modal group is primarily affected by the extensional stiffness of the circumference (defined mainly by the elastic modulus), in the case of the radial group various properties define the modal behaviour. Its low modal range is affected by the sidewall stiffness, the medium one by the inflation pretension, while above a certain modal number only the bending stiffness (defined again by the elastic modulus) affects the modal characteristics.

The above, briefly described, modal characteristics of the ring model were found able to theoretically justify the modal prediction differences of the rectilinear models. Obviously, a rectilinear model cannot offer the coupling between the two deformation patterns, something that, assuming similar structural mechanisms, leads to a stiffer modal behaviour that the ring one, especially in the low modal range where the coupling of the patterns is significant. Two physical mechanisms were examined, the bending and the string under tension ones. It was found that the first one exhibits excellent correlation with the ring model in the high modal range, where the behaviour of the ring becomes a pure bending one. For the same reason the string

under tension mechanism exhibits an increasing with the modal number deviation. A general conclusion that may be drawn from the above is that the simulation of the low and medium range behaviour of the tyre, requires a combination of deformation patterns and properties' effects. In the high modal number range, though, the bending mechanism and the radial deformation pattern are the only contributions to the tyre response, and the rest of the mechanisms may be neglected.

The simulation of the tyre modal characteristics using discretised approaches based on rectilinear elements capturing the same physical mechanisms with the respective analytical ones was also examined. It was found that the combination of the elements under a relative angle to each other is able to represent the coupling between the radial and the tangential deformation components. Assuming a similar physical mechanism, the analytical ring and the discretised model predict similar modal characteristics in the low modal number range. A significant deviation, though, emerges close to the upper limit of the discretised model's available modal range, mainly corresponding to a profound stiffer behaviour of the latter one. Obviously, this modal zone should be dropped from a respective modal basis and the degree of discretisation should be high enough in order the required modes not to lie close to the upper modal limit of the model.

Based on the ring model, the modal effect of three mechanisms was analysed: the non linear sidewall, the incorporation of the wheel in the modal expansion and the effects of the rotation. A membrane mechanism was proposed for the capture of the inflation and shape effects of the sidewall on the tyre behaviour, as an enhancement to the ring model. The incorporation of the wheel affects three modes of the ring model resulting in either an out of phase deformational behaviour, or a common (ring and wheel) rigid mode one. The effects of the wheel properties on these modes were examined as was also the rigid modes prediction capability of the ring model variations. The rotation was found to affect the ring behaviour through the coriolis and centrifugal accelerations. Given that the contribution of both of them is a non linear one, the modal expansion may be accomplished for a particular value of the angular velocity, introducing a computational error if the same modal basis is used across a range of angular velocities. The magnitude of this error depends not only on the properties and the velocity value but also varies according to the modal number. It was found that the rotation phenomena primarily affect the low modal number modes and deteriorate in the high modal number range, a conclusion which supports the above argument that the low-medium tyre modal representation is more demanding in terms of mechanisms and effects that should be considered, compared to the high one. Finally, the effect of the common energy dissipation mechanisms on the predicted modal behaviour was also analysed. The correlation of the experimentally acquired damping characteristics with the damping coefficient development pattern predicted by the simplified assumptions was investigated.

In the following chapters the range of the excited modes under common tyre operating conditions will be identified and the necessity or not of the incorporation of the above mechanisms and modal behaviour factors will become apparent, together with the possible validity of the proposed modelling approaches.

Chapter 4

The simulation of tyre in-plane contact behaviour

The simulation of the tyre in-plane contact behaviour will be investigated in this chapter. The process is based on the tyre modal characteristics which where highlighted and analysed in chapter 3, while it may be proposed as the first step of the simulation of the rotating tyre operating conditions that will follow in chapter 5.

Firstly, the challenges associated with the contact simulation are identified and, based on them, the modelling methodology is composed. As it will emerge from the discussion of the contact simulation requirements, the discretised, independent form the belt, tread representation is vital for the capture of the contact phenomena. For this reason, the contact behaviour of a single radial tread element will be initially examined. The reasons that impose its extension to a two-dimensional (radial-tangential) element will be discussed. Later, the discretised tread foundation will be combined with an also discretised belt ring model and the simulation of the contact behaviour of the complete tyre model will be presented.

The tyre contact and the development of the two-dimensional contact pressure distribution will be examined from two different points of view. Firstly, the related physical mechanisms will be identified, together with the effect of the tyre properties and the level of applied load. The interaction between the contact pressure distribution fields and the belt strain development will be analysed. Based on that, the tread frictional behaviour and the belt deformation will be linked to each other. In result, the physical mechanism of the tangential pressure distribution development will be investigated, as a function of the tyre properties and the road friction potential.

Secondly, the contact behaviour of the tyre will be examined from a computational point of view.The sufficient modal range, which should be used for the simulation of the belt deformation will be discussed. The accuracy and the capability of the capture of the previously identified physical mechanisms will be used as criteria for the modal reduction. The correspondence of certain aspects of the contact behaviour to the participation of certain modes in the solution basis will be identified and discussed. In conclusion, the interaction mechanism between the development of the two-dimensional contact pressure distribution field, the belt response and the frictional potential of the road surface is presented in parallel to the necessary modal range for its simulation.

4.1 Challenges of the tyre contact behaviour modelling

The tyre-road interaction is a process which involves various physical mechanisms and geometrical effects. The relative contribution of these, depends on the physical properties of the tyre and the magnitude of the applied load. As a first step to the simulation of the contact behaviour, these mechanisms should be identified and accurate but also computationally efficient methods for their capture should be proposed.The most important of these mechanisms are briefly described in the following.

Belt compliance

The contact between the tyre and the road exhibits significant differences from the one of a rigid disk. Although the contact between a rigid structure and a plane surface may be theoretically realised by a single point, this is not true in the case of the actual tyre. The profound structural deformation of the tyre results in the realisation of the contact across an area of significant dimensions. Moreover, as the tyre geometry conforms to the road plane along this area, its circular shape transforms into a plane one. The contact area dimensions vary according to the applied load and also dynamically change under transient tyre operating conditions. This transient deformation of the belt must be precisely captured by a physical tyre model as it affects the development of the tyre shear force through the also changing vertical contact pressure distribution. A pretensioned ring model will be used here as a belt representation, given that certain aspects of the low frequency range modal behaviour of the tyre cannot be captured by more simplified approaches.

Sidewall nonlinearity

Apart from the compliance of the tyre's circular shape, a significant contact behaviour nonlinearity is imposed by the deformation of the sidewall section. The membrane-like structure exhibits a profound buckling deformation which affects both the magnitude and the direction of the tension force. Although the inflation pressure bears a proportional effect on this force, the shape variation affects the force development in a highly non linear way. The sidewall buckling results in the decrease of the radial sidewall stiffness as the deformation increases something that certainly affects the contact pressure distribution development. Following the membrane model based analysis of the inflation effects on the tyre modal behaviour, which was presented in chapter 3, a discretised approach will be proposed for the capture of the contact sidewall phenomena. A foundation of inextensible string elements will be coupled to the ring model and attach that to the wheel.

Inflation pressure effects

The inflation pressure does not impose only a stiffening effect to the modal characteristics of the tyre but also contributes to the contact equilibrium establishment. Being a constant radial excitation, it offers a significant resistance to the deformation of the belt and balances the applied to the wheel load. In respect, the inflation pressure defines to a great extent the contact behaviour of the tyre and should be incorporated in the simulation process prior to the contact.

Structural viscoelasticity

The energy dissipation mechanism of the tyre structure affects its contact behaviour and actually enables the establishment of the equilibrium. Although its effect on the rotational behaviour of the tyre is more significant, as it defines certain aspects of that, such as the rolling resistance mechanism, its incorporation in the contact simulation cannot be ignored. The stress and strain of the belt depend on both the stiffness and damping mechanisms, given that the contact conditions are applied in a dynamic way.

Tread viscoelasticity and shear slip motion development

The tread section of the tyre that contacts the road surface has different properties and material characteristics than the belt section of it. These differences certainly affect the contact behaviour and should also be incorporated in the modelling procedure. Moreover, the tread characteristics and the shear force development are to a great extent defined by its viscoelastic properties (section 2.2 of chapter 2), which impose a time rate dependency on the contact phenomena. Moreover, the tread-road interaction is associated with the development of a profound shear slip motion. This motion exhibits a localised step-change nature as, depending on the conditions, certain adherence and slip zones develop along the contact area. The location and the relative magnitude of these zones vary and influence the macroscopically observable transient frictional contact behaviour of the tyre.

Although from a computational point of view, contact boundary conditions may be imposed directly to the belt structure, the above modelling requirements dictate the independent and also discretised modelling representation of the tread. In the following, the tread simulation approach will be firstly analysed. Later, the developed tread foundation will be incorporated in the complete tyre model and the contact simulation algorithm and results will be presented.

4.2 The simulation of the tread contact behaviour

The discretised tread representation may be regarded as deriving from the concept of the contact stiffness foundation, introduced by Winkler [19] (see section 2.1.3 of chapter 2). This concept practically substitutes the binary contact boundary condition (contact/no contact) between two points of the contacting bodies with a progressive relative approach of them, which is controlled by a foundation of stiffness elements of minimal initial length, vertical to the two surfaces. From the numerical simulation point of view, the introduction of the contact stiffness concept addresses the artificial local oscillatory behaviour resulting from the non penetration contact law. According to that law, the possible penetration of the one body into the other is accounted for by correcting its position and placing the penetrating point on the boundary of the second body. This correction, though, imposes a structural deformation to the penetrating body (in the case of course that it is not a rigid one) and the whole structure responds to that. A sequence of successive contact and separation conditions results in an artificial oscillation especially in the case that the damping mechanism of the structure cannot absorb the imposed excitation. This numerically stiff behaviour is commonly treated by the contact stiffness foundation concept.

The introduction of the above contact modelling approach in the tyre simulation has resulted in the development of the brush models family [1]. According to these models, the bristles' orientation does not

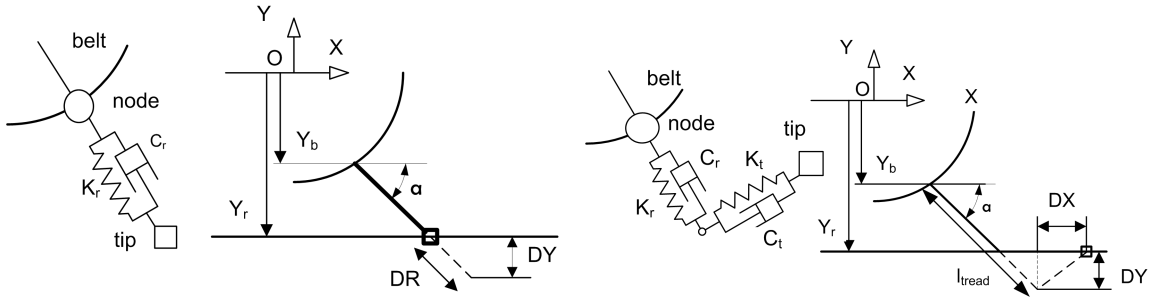

(a) Radial element. (b) Radial-tangential element.

Figure 4.1 – The contact deformation of a radial and a tangential-radial tread element.

depend on the belt response and any deformation of them sources from the shear frictional interaction between their tips and the road surface. The superposition of a vertical contact pressure distribution on the bristles' foundation leads to the development of a distributed tyre friction model. The concept has been analytically discussed in chapter 2. A vertical contact stiffness foundation, coupled with a flexible belt model has been proposed by Shiobara *et al* in [253] for the calculation of the contact stiffness foundation. Developing the above concept further, two-dimensional contact stiffness foundations, attached to a ring model, have been presented by Zegelaar [76], Kim and Savkoor [122] and Kim *et al* [130]. In these studies the orientation of the elements deviates from the initial radial or vertical one, as a result of the belt response. Mavros in [129] proposed a Kelvin-Voigt viscoelastic variation of the two-dimensional stiffness foundation concept in order to implement the tread viscoelasticity effects in the simulation of the tyre behaviour.

The frictional contact behaviour of such an element will be examined in the following and the significant modelling differences between a single radial and a combined radial and tangential element will be identified and discussed.

4.2.1 The radial tread element

The concept of the viscoelastic Kelvin-Voigt tread element is presented in fig. 4.1 together with the contact induced deformation. The element will be firstly examined in its single radial form (fig. 4.1(a)) and later in its double radial and tangential one (fig. 4.1(b)). In both cases, the elements do not impose any moment reaction to the belt and only contact forces result from their contact deformation.

A certain combination of belt response and road profile define kinematically the deformation of a single tread element and its respective time rate, while, obviously, the resulting contact force lies on the element's axial direction. This kinematic definition of the element's state allows the development of its tangential deformation, only as a component of the total axial one. Any shear slip motion of the element's tip which does not derive from the kinematic conditions would correspond to a kinematic violation and cannot be considered. In result the friction conditions of the interaction cannot affect the tangential deformation of the bristle and the single element cannot be used for the simulation of the frictional tread contact. Such a tread model, though, may be used for the calculation of the vertical pressure distribution, assuming that all the elements within the contact remain vertical to the road surface. This approach is proposed in the tyre contact simulation study of Shiobara *et al* [253].

The contact geometry of fig. 4.1(a) prescribes:

$$\Delta Y_t = Y_r - (Y_b + l_t \cdot \sin\alpha) \tag{4.1}$$

$$\Delta \dot{Y}_t = \dot{Y}_r - (\dot{Y}_b + l_t \cdot \cos\alpha \cdot \dot{\alpha}) \tag{4.2}$$

The horizontal and vertical components of the reaction force may be calculated by the axial deformation and the element's orientation:

$$\Delta R_t = \Delta Y_t \cdot \sin\alpha \tag{4.3}$$

$$\Delta \dot{R}_t = \Delta \dot{Y}_t \cdot \sin\alpha + \Delta Y_t \cdot \cos\cdot\dot{\alpha} \tag{4.4}$$

$$F_t = K_r^t \cdot \Delta R_t + C_r^t \cdot \Delta \dot{R}_t \Rightarrow \tag{4.5}$$

$$F_{tX} = F_t \cdot \cos\alpha \tag{4.6}$$

$$F_{tY} = F_t \cdot \sin\alpha \tag{4.7}$$

where :

DY_t	the vertical deformation of the element
Y_r	the vertical global coordinate of the road profile at the contact point
Y_b	the vertical global coordinate of the attachment node
l_t	the initial axial length of the tread element
α	the global orientation of the tread element
DR_t	the axial deformation of the tread element
F_t	the contact force applied to the belt point along the tread element direction
F_{tX}	the global horizontal contact force
F_{tY}	the global vertical contact force
K_r^t	the axial stiffness of the element
C_r^t	the axial viscous damping coefficient of the element

4.2.2 The radial-tangential tread element

The capability of modelling the friction effect on the shear motion and horizontal deflection is added to the tread representation by the introduction of a second Kelvin-Voigt element. This element is regarded as dimensionless initially and attached to the free tip of the radial element, in tangential to it orientation (fig. 4.1(b)). The contact problem becomes kinematically unconstrained and the additional degree of freedom, associated with the displacement of the tangential element tip, is controlled by the frictional interaction between the tread element and the ground. In result, a friction-regulated shear slip motion, which is affected by but not derived from the vertical kinematic conditions, may be developed by the tread representation.

The study of the tread element behaviour is better accomplished using global, vertical and horizontal

to the plain road, coordinates, instead of the radial and tangential ones. The vertical contact deformation (and deformation velocity) remain kinematically constrained, as in the single element case, and are therefore calculated using eqn. 4.1. The horizontal (shear) deformation, though, is dynamically derived by a differential equation of the horizontal displacement degree of freedom.

The transformation between the radial/tangential expressions (or better the axial and the vertical to it ones, as the belt deformation may in general impose a different direction to the tread element from the radial one) and the global horizontal/vertical expressions of the deformation vector for each of the tread element reads:

$$\begin{bmatrix} \Delta R_t \\ \Delta T_t \end{bmatrix} = \mathbf{T}(\alpha) \cdot \begin{bmatrix} \Delta X_t \\ \Delta Y_t \end{bmatrix} \tag{4.8}$$

where the transformation matrix is:

$$\mathbf{T}(\alpha) = \begin{bmatrix} \cos\alpha & \sin\alpha \\ -\sin\alpha & \cos\alpha \end{bmatrix} \tag{4.9}$$

	ΔT_t	the tangential (vertical to the axial) tread deformation
and additionally:	ΔX_t	the combined horizontal tread deformation
	ΔY_t	the combined vertical tread deformation

Assuming that:

$$\mathbf{K} = \begin{bmatrix} K_r^t & 0 \\ 0 & K_t^t \end{bmatrix} \tag{4.10}$$

is the matrix of the radial and tangential stiffness properties (K_r^t and K_t^t respectively), the radial and tangential stiffness forces applied to the belt ($F_{t,r}^s$ and $F_{t,t}^s$ respectively) may be expressed as:

$$\begin{bmatrix} F_{t,r}^s \\ F_{t,t}^s \end{bmatrix} = \mathbf{K} \cdot \begin{bmatrix} \Delta R_t \\ \Delta T_t \end{bmatrix} = \mathbf{K} \cdot \mathbf{T}(\alpha) \cdot \begin{bmatrix} \Delta X_t \\ \Delta Y_t \end{bmatrix} \tag{4.11}$$

$$\begin{bmatrix} F_{tX}^s \\ F_{tY}^s \end{bmatrix} = \mathbf{T}^T(\alpha) \cdot \begin{bmatrix} F_{t,r}^s \\ F_{t,t}^s \end{bmatrix} = \mathbf{T}^T(\alpha) \cdot \mathbf{K} \cdot \mathbf{T}(\alpha) \cdot \begin{bmatrix} \Delta X_t \\ \Delta Y_t \end{bmatrix} = \begin{bmatrix} K_{11}(\alpha) & K_{12}(\alpha) \\ K_{21}(\alpha) & K_{22}(\alpha) \end{bmatrix} \begin{bmatrix} \Delta X_t \\ \Delta Y_t \end{bmatrix} \tag{4.12}$$

The damping forces are calculated by a procedure equivalent to the above one. The deformations velocities are given by the time differentiation of eqn. 4.8:

$$\begin{bmatrix} \Delta \dot{R}_t \\ \Delta \dot{T}_t \end{bmatrix} = \dot{\alpha} \cdot \dot{\mathbf{T}}(\alpha) \cdot \begin{bmatrix} \Delta X_t \\ \Delta Y_t \end{bmatrix} + \mathbf{T}(\alpha) \cdot \begin{bmatrix} \Delta \dot{X}_t \\ \Delta \dot{Y}_t \end{bmatrix} \Rightarrow \tag{4.13}$$

$$\begin{bmatrix} \Delta \dot{R}_t \\ \Delta \dot{T}_t \end{bmatrix} = \dot{\alpha} \cdot \begin{bmatrix} -\sin\alpha & \cos\alpha \\ -\cos\alpha & -\sin\alpha \end{bmatrix} \cdot \begin{bmatrix} \Delta X_t \\ \Delta Y_t \end{bmatrix} + \mathbf{T}(\alpha) \cdot \begin{bmatrix} \Delta \dot{X}_t \\ \Delta \dot{Y}_t \end{bmatrix} \Rightarrow \tag{4.14}$$

$$\begin{bmatrix} \Delta \dot{R}_t \\ \Delta \dot{T}_t \end{bmatrix} = \dot{\alpha} \cdot \mathbf{T}(\alpha) \cdot \begin{bmatrix} 0 & -1 \\ 1 & 0 \end{bmatrix} \cdot \begin{bmatrix} \Delta X_t \\ \Delta Y_t \end{bmatrix} + \mathbf{T}(\alpha) \cdot \begin{bmatrix} \Delta \dot{X}_t \\ \Delta \dot{Y}_t \end{bmatrix} \tag{4.15}$$

Assuming that the respective damping properties matrix is:

$$\mathbf{C} = \begin{bmatrix} C_r^t & 0 \\ 0 & C_t^t \end{bmatrix} \tag{4.16}$$

the damping forces may be written as:

$$\begin{bmatrix} F_{tX}^d \\ F_{tY}^d \end{bmatrix} = \mathbf{T}^T(\alpha) \cdot \mathbf{C} \quad \dot{\alpha} \cdot \mathbf{T}(\alpha) \cdot \begin{bmatrix} 0 & -1 \\ 1 & 0 \end{bmatrix} \cdot \begin{bmatrix} \Delta X_t \\ \Delta Y_t \end{bmatrix} + \mathbf{T}(\alpha) \cdot \begin{bmatrix} \Delta \dot{X}_t \\ \Delta \dot{Y}_t \end{bmatrix} \Rightarrow \tag{4.17}$$

$$\begin{bmatrix} F_{tX}^d \\ F_{tY}^d \end{bmatrix} = \mathbf{T}^T(\alpha) \cdot C \cdot \mathbf{T}(\alpha) \cdot \begin{bmatrix} 0 & -\dot{\alpha} \\ \dot{\alpha} & 0 \end{bmatrix} \begin{bmatrix} \Delta X_t \\ \Delta Y_t \end{bmatrix} + \mathbf{T}^T(\alpha) \cdot C \cdot \mathbf{T}(\alpha) \cdot \begin{bmatrix} \Delta \dot{X}_t \\ \Delta \dot{Y}_t \end{bmatrix} \Rightarrow \tag{4.18}$$

$$\begin{bmatrix} F_{tX}^d \\ F_{tY}^d \end{bmatrix} = \begin{bmatrix} C_{11}^1 & C_{12}^1 \\ C_{21}^1 & C_{22}^1 \end{bmatrix} \cdot \begin{bmatrix} \Delta X_t \\ \Delta Y_t \end{bmatrix} + \begin{bmatrix} C_{11}^1(\alpha) & C_{12}^1(\alpha) \\ C_{21}^1(\alpha) & C_{22}^1(\alpha) \end{bmatrix} \cdot \begin{bmatrix} \Delta \dot{X}_t \\ \Delta \dot{Y}_t \end{bmatrix} \tag{4.19}$$

Finally, the vector of the contact forces may be written as:

$$\begin{bmatrix} F_{tX} \\ F_{tY} \end{bmatrix} = \begin{bmatrix} F_{tX}^s \\ F_{tY}^s \end{bmatrix} + \begin{bmatrix} F_{tX}^d \\ F_{tY}^d \end{bmatrix} \tag{4.20}$$

In the general case where the tread element is considered to be inertia-equipped, the horizontal motion of the tread tip is defined by a second order differential equation of the form:

$$F_X^{b \to t} + F_{friction} = m_t \cdot \Delta \ddot{X} \Rightarrow -F_{tX} + F_{friction} = m_t \cdot \Delta \ddot{X} \tag{4.21}$$

where:

$F_X^{b \to t}$	the horizontal force applied form the tread element to the tip
$F_{friction}$	the friction force

For typical automotive tyres the tread mass is negligible compared to the belt one and the tread inertia effect on the contact behaviour is insignificant compared to the stiffness and damping ones. Moreover, as it has been proved in [129], the difference in the tyre simulation results following the inertia and inertia-less approaches is ignorable. Eqn. 4.21, under the inertia-less assumption reads:

$$-F_{tX} + F_{friction} = 0 \Rightarrow \tag{4.22}$$

$$C_{11}^2 \cdot \Delta \dot{X}_t + C_{12}^2 \cdot \Delta \dot{Y}_t + (K_{11} + \dot{a} \cdot C_{11}^1)\Delta X_t + (K_{12} + \dot{a} \cdot C_{12}^1)\Delta Y_t - F_{friction} = 0 \Rightarrow \tag{4.23}$$

$$\Delta \dot{X}_t = -\big(C_{12}^2 \cdot \Delta \dot{Y}_t + (K_{11} + \dot{a} \cdot C_{11}^1)\Delta X_t + (K_{12} + \dot{a} \cdot C_{12}^1)\Delta Y_t + F_{friction}\big)/C_{11}^2 \tag{4.24}$$

The horizontal (shear) deformation of the element is calculated by the time integration of the above derived

relative horizontal velocity between the tip and the respective belt node:

$$\Delta X_t = \int_{time\ step} \Delta \dot{X}_t \mathrm{dt} \tag{4.25}$$

Respectively, the contact forces (as sensed by the belt nodes) are given by the following equations:

$$F_{cY} = -\big(C_{21}^2 \cdot \Delta \dot{X}_t + C_{22}^2 \cdot \Delta \dot{Y}_t + (K_{21} + \dot{a} \cdot C_{21}^1)\Delta X_t + (K_{22} + \dot{a} \cdot C_{22}^2)\Delta Y_t \tag{4.26}$$

$$F_{tX} = -F_X^{b \to t} = F_{friction} \tag{4.27}$$

4.2.3 Initiation of contact

A search algorithm is incorporated in the tread contact model for the identification of the contact initiation conditions between a tread element and the ground. The algorithm compares the global vertical position of the tread tip with the road level, taking into consideration the non penetration requirement. The calculation of the position of a tread element's tip takes into account possible residual deformations induced by recent contacts:

$$Y_t = Y_b + (l_t + \Delta R_t)\ \sin a + \Delta T_t \cdot \cos a \tag{4.28}$$

where in this case ΔR_t and ΔT_t correspond to the possible residual deformations from a previous contact.

When a tread tip location dictates its penetration into the road, the vertical position of it is corrected in order to coincide with the road level and the respective vertical deformation is applied to the Kelvin-Voigt element. The horizontal global velocity of the tip is initially assumed to be zero, i.e. the tip momentarily comes to a halt as it establishes contact with the road. Its possible further shear motion depends on the friction force development. The above may be summarised as:

$$Y_t\ <\ Y_r \Rightarrow contact \Rightarrow \left\{ \begin{array}{c} Y_t = Y_r \\ \dot{X}_t = 0 \end{array} \right\} \tag{4.29}$$

where $\dot{X}_t$ is the global horizontal velocity of the tread tip.

4.2.4 Loss of contact

A force criterion is used for the termination of the contact, given that no attraction force may be developed between the tread and the road surface. The contact reaction force must satisfy the following inequality as long as its contact persists:

$$F_{tY} \geq 0 \tag{4.30}$$

On termination of the contact, both radial and tangential elements progressively return to their initial length (l_t for the radial element and 0 for the tangential one). Since this rebound motion does not depend on the global orientation angle (a) of the tread element, the differential equations are solved in the respective local radial/tangential system of reference in the interest of computational efficiency. The transformation from

the global horizontal/vertical system to the radial/tangential one is accomplished at the contact loss moment and offers the initial conditions for the differential equations governing the expansion of the bristles back to their free length:

$$C_r^t \cdot \Delta\dot{R}_t + K_r^t \cdot \Delta R_t = 0 \tag{4.31}$$

$$C_t^t \cdot \Delta\dot{T}_t + K_t^t \cdot \Delta T_t = 0 \tag{4.32}$$

The elements are considered to have reached their free length when their local deformation reduces below a pre-specified limit and the above equations are made redundant for the following steps.

4.2.5 Friction force

Various friction laws may be incorporated in the horizontal interaction between the tread and the road. The simple Coulomb one is chosen as a starting point. The law may be described as:

$$F_{friction} = \left\{ \begin{array}{lll} F_{static}, & \dot{X}_t = 0, & F_{static} \leq (\mu \cdot F_{tY}) \\ \text{sign}(F_{static})\ \mu \cdot F_{tY}, & \dot{X}_t = 0, & F_{static} > (\mu \cdot F_{tY}) \\ -\text{sign}(\dot{X}_t)\ \mu \cdot F_{tY}, & \dot{X}_t \neq 0 & \end{array} \right\} \tag{4.33}$$

where μ is the coefficient of sliding friction. The global horizontal velocity of the tip, $\dot{X}_{tread}$, may be calculated by the equation:

$$\dot{X}_t = \dot{X}_b + \Delta\dot{X} \tag{4.34}$$

where $\dot{X}_b$ is the horizontal global velocity of the respective belt node. The static friction, F_{static}, is calculated by the equilibrium equation of the tread tip (eqn. 4.24), assuming a zero velocity value $\dot{X}_t = 0$:

$$(4.24) \xrightarrow{(4.34)} \dot{X}_t - \dot{X}_b = \frac{-(C_{12}^2 \cdot \Delta\dot{Y}_t + (K_{11} + \dot{\alpha} \cdot C_{11}^1)\Delta X_t + (K_{12} + \dot{\alpha} \cdot C_{12}^1)\Delta Y_t + F_{friction})}{D_{11}^2} \tag{4.35}$$

$$\xrightarrow[F_{friction}=F_{static}]{\dot{X}_t=0} F_{static} = C_{12}^2 \cdot \Delta\dot{Y}_t + (K_{11} + \dot{\alpha} \cdot C_{11}^1)\Delta X_t + (K_{12} + \dot{\alpha} \cdot C_{12}^1)\Delta Y_t - C_{11}^2 \cdot \dot{X}_b \tag{4.36}$$

The non-linear (step) nature of the friction law adds a significant complication to the numerical simulation of the tread motion. The magnitude of the friction force is a function of the vertical load but independent from the slip velocity. In result, the friction force may impose a change to the direction of the motion, something that does not correspond to the physical sliding behaviour. The tread slip velocity is calculated as:

$$\begin{array}{l} (4.24) \xrightarrow{(4.33),(4.34)} \dot{X}_t = \\ \dfrac{C_{11}^2 \cdot \dot{X}_b - C_{12}^2 \cdot \Delta\dot{Y}_t - (K_{11} + \dot{\alpha} \cdot C_{11}^1)\Delta X_t - (K_{12} + \dot{\alpha} \cdot C_{12}^1)\Delta Y_t + sign(\dot{X}_t)\mu \cdot F_{tY}}{C_{11}^2} \end{array} \tag{4.37}$$

Given that $C_{11}^2 < 0$, the case in which:

$$\dot{X}_t \cdot \left(C_{11}^2 \cdot \dot{X}_b - C_{12}^2 \cdot \Delta\dot{Y}_t - (K_{11} + \dot{\alpha} \cdot C_{11}^1)\Delta X_t - (K_{12} + \dot{\alpha} \cdot C_{12}^1)\Delta Y + sign(\dot{X}_t)\mu \cdot F_{tY}\right) > 0 \qquad (4.38)$$

imposes an artificial self excited oscillation to the tread tip, as a result of the self-conserved loop of successive changes of velocity and friction directions, always opposing to each other. In other words the horizontal velocity of the element cannot reach a zero value, an essential requirement for the transition between the slipping and the adhesional zones. A similar, friction-induced, stability problem in tyre tread simulation has been described by Oertel [142] and by Zimmer and Otter [254].

The problem of the numerically induced oscillation is typically overcome in the above studies by a regularised friction function, according to which a zone of progressive transition between the two constant values of opposite signed kinematic friction forces is introduced in the zero velocity area. Such an approach, though, would certainly affect the model's behaviour in the, critical for the present study, phase of the near-standstill equilibrium. In order not to introduce any deviation in the friction law, an additional criterion is introduced, according to which a tread tip cannot change its direction of shear global velocity in two successive simulation steps. Every value of tread global velocity, $\dot{X}_t$, predicted by the eqn. 4.37 is compared with the respective value of the previous simulation step. If a change of direction is identified, the tip is considered to adhere to the road and its horizontal position is constrained for the present step:

$$\dot{X}_t \cdot \dot{X}_t^* \begin{cases} \geq 0 \Rightarrow \dot{X}_t\text{: accepted}, & F_{friction} = -\text{sign}(\dot{\text{X}}_\text{t})\mu \cdot \text{F}_\text{tY} \\ < 0 \Rightarrow \dot{X}_t = 0\ , & F_{friction} = F_{static} \end{cases} \qquad (4.39)$$

where $\dot{X}_t^*$ refers to the velocity value at the previous time-step.

4.2.6 Contact behaviour of a single tread element

Prior to the incorporation of the above described contact algorithm in the tyre belt model, an insight into its contact simulation potential is attempted through the examination of two simple contact case studies of a single tread element:

1. A vertical, harmonic velocity excitation is applied to the belt node while the free end of the bristle is assumed to be initially in road angular contact, under zero deformation condition.
2. The node follows a circular trajectory with constant angular velocity. The initially not in contact element establishes and later terminates its road contact.

Both of the above cases are examined under different surface frictional conditions in order the effect of the shear force development potential on the contact interaction to become evident. The tread physical properties which are used are given in table 4.1.

Case study 1: Vertical velocity excitation of the belt node

The contact behaviour of the tread element, under a constant angle of orientation ($\alpha = \pi/4$), is depicted in fig. 4.2 for various values of the friction coefficient ($\mu = 0, 0.2, 0.5$). A sinusoidal vertical velocity excitation is

Tread Physical Properties[a]			
radial stiffness	K_r^t	$[\frac{kgr}{sec^2}]$	3.02×10^5
tangential stiffness	K_t^t	$[\frac{kgr}{sec^2}]$	1.01×10^5
radial damping coefficient	$C_r = c_d \cdot K_r^t$	$[\frac{kgr}{sec}]$	
tangential damping coefficient	$C_t = c_d \cdot K_t^t$	$[\frac{kgr}{sec}]$	
	c_d, single element	$[sec]$	0.025
	c_d, tyre model	$[sec]$	0.0025
initial radial length	l_t, single element	$[mm]$	100
	l_t, tyre model	$[mm]$	10
[a] stiffness values according to the distributed tread properties given in [61], assuming distribution of each property in 200 tread elements.			

Table 4.1 – The physical properties of the tread

imposed to the belt (fig. 4.2(a)) and the contact behaviour is examined for a full time period of it. As it has been presented in section 4.2.2, when a two-dimensional radial-tangential tread element is in ground contact under an orientation angle $\alpha \neq \pi/2$ both vertical and horizontal deformations emerge, while the development of the second may be suspended by the friction force. The developed slip displacement is maximum for the non-frictional surface case (fig. 4.2(b)), something that could be also predicted from eqn. 4.24 substituting $F_{friction} = 0$. In the case of a positive coefficient of friction ($\mu = 0.2$) the tip departs from the initial contact position, but the developed slip distance is smaller. For friction coefficients higher than a critical one the tip adheres to its initial contact position, as the static friction force may reach values that completely suspend the sliding motion. This critical value is a function of the contact angle and the viscoelastic properties of the tread.

The magnitude of the horizontal component of the reaction force increases with the coefficient of friction (4.2(c)). Interestingly, a similar effect is imposed to the vertical component of the reaction force, given that both of them develop as functions of both the horizontal and vertical deformations (section 4.2.2). In accordance, a friction-less contact results not only in zero shear force but also in a lower vertical reaction one, compared to the frictional cases. The reaction forces predicted by the single radial tread element are also presented in the same plot. In this case, both horizontal and vertical deformation components are kinematically derived and independent from the surface friction potential. The developed force magnitudes in this case are higher, especially for the horizontal component.

The contact behaviour is significantly affected by the damping property and for this reason the contact reaction forces do not follow precisely the harmonic pattern of the kinematic excitation but a relative phase angle is exhibited by their development. Accordingly, the forces reach their maximum values before the belt node reaches its lowest position and the contact is terminated before the node reaches its initial position. Although the residual deformations in the higher coefficient of friction cases are higher, their time rates of decrease is the same in all cases, as the rebound process depends on the tread properties only (eqns. 4.31 and 4.32). The single radial element residual deformation is higher than the one of the combined element.

Case study 2: Circular motion of the belt node

The rotational motion of the belt node around a theoretical wheel centre axis is investigated in this case. Two values of angular velocity -$\omega = 1 rad/sec$ and $\omega = 5 rad/sec$ (anti-clockwise)- and three values of friction

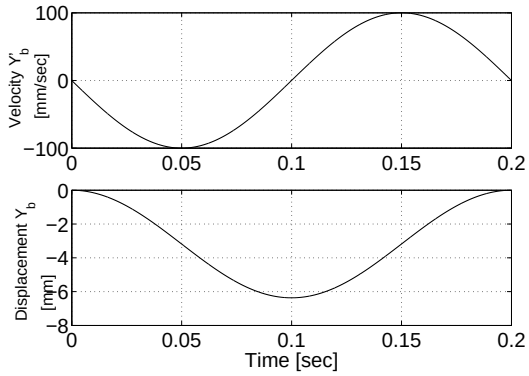

(a) The vertical velocity and displacement of the node.

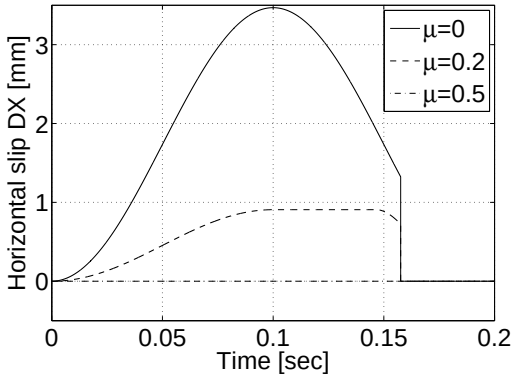

(b) The horizontal shear displacement (slip) of the tread tip, measured form the initial contact position.

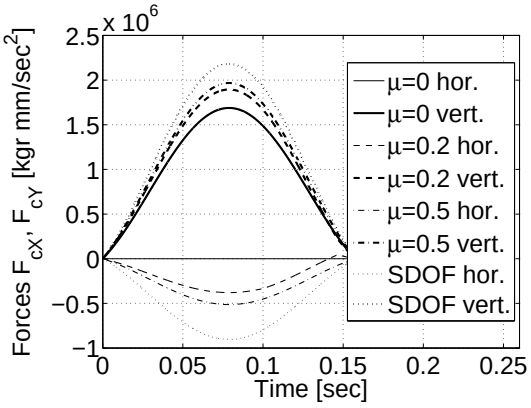

(c) The vertical and horizontal reaction forces.

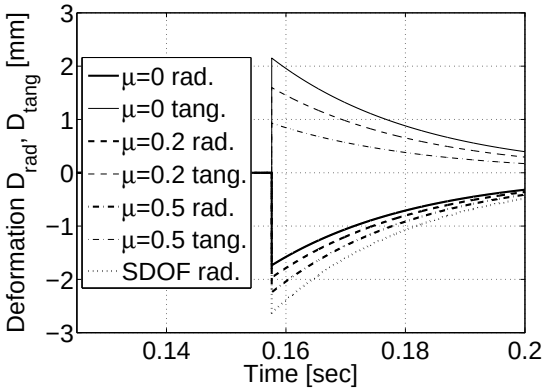

(d) The recovery of the radial and tangential degrees of freedom after the termination of the contact.

Figure 4.2 – The 1st case study tread deformation and contact forces for three different values of the friction coefficient ($\mu = 0, 0.2, 0.5$).

coefficient -μ = 0, 0.2 and 0.5- are examined and presented in fig. 4.3. In every subfigure, the horizontal axis refers to the global orientation angle of the element and its positive direction also corresponds to the time history of the motion.

The friction force incommodes the tread slip displacement and velocity ($\dot{X}_{tread}$) during the first phase of the contact (downwards vertical motion of the node). In result, higher values of negative horizontal deformation are developed (fig. 4.3(b)), as the tread tip cannot follow the horizontal motion of the node. Interestingly, though, a contrary effect is identified during the second phase of the contact (upwards vertical motion of the node). As the vertical deformation and load decrease, the friction force apparently does the same and a recovery motion (deformation decrease) is exhibited by the tread. The higher friction coefficient case is associated with a higher maximum value of horizontal recovery velocity, a result of the higher amount of energy stored by the element deformation mechanism during the first phase of the motion.

The effect of the varying, along the contact, angle of orientation is evident in figure 4.3(b), where in the non frictional and the low friction-low velocity cases, the horizontal deformation (DX_t) changes direction during the second phase of the contact. This change is promoted by the continuously varying values of the horizontal stiffness and damping coefficients which develop as functions of the orientation angle. The high

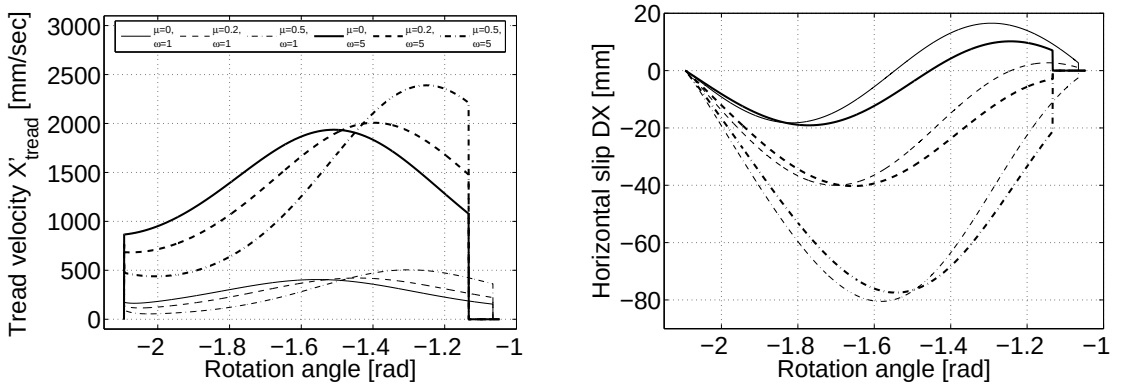

(a) The global slip velocity.

(b) The horizontal shear deformation.

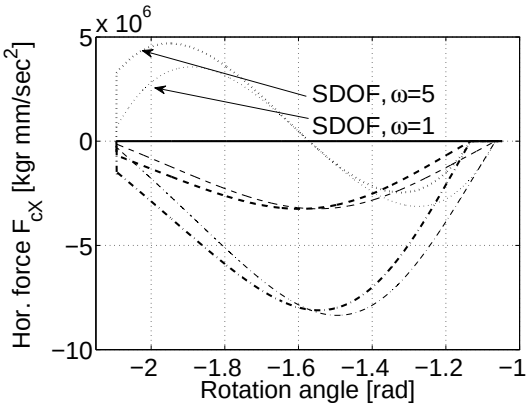

(c) The horizontal reaction force.

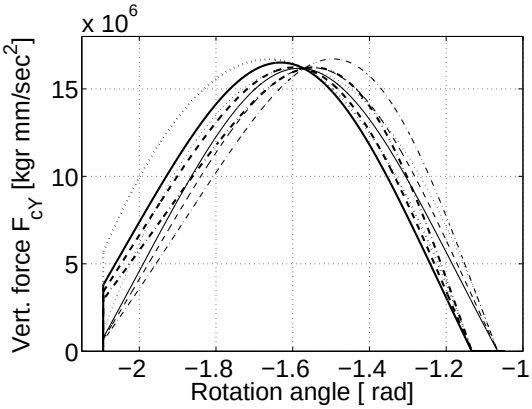

(d) The vertical reaction force.

Figure 4.3 – The behaviour of the contact element in the 2nd case study, for three different friction coefficients and two values of the base rotation velocity. (all subfigures follow the legend of (a), while (d) also follows the additional legend of (c))

level of the horizontal deformation, which is associated with the higher friction cases, suspends a respective change of the horizontal deformation direction. As a direct effect of the damping property of the element, a higher angular velocity shortens the duration of the contact.

The developed shear force is presented in fig. 4.3(c) for all the examined cases, also in comparison to the single radial element. Obviously, the effect of the friction potential on the magnitude of the shear forces is significant, while, due to the damping mechanism, higher (in absolute terms) force values are developed during the first phase of the contact, than the ones of the second phase. A respective behaviour is exhibited by the development pattern of the vertical reaction forces (fig. 4.3(d)), where, though, a closer correlation between all the cases may be observed. The contradicting to the above shear force prediction of the radial element should be highlighted. In this case, the direction of the force is defined by the orientation angle of the element, resulting in the harmonic variation of the force along the contact (negative in the first phase and positive in the second one).

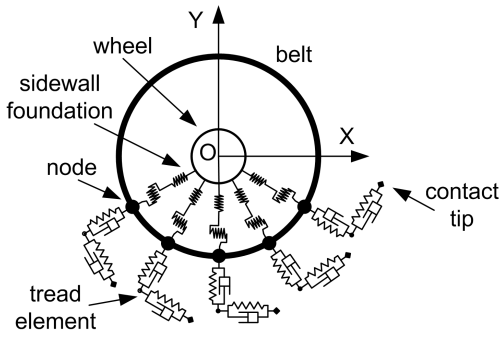

Figure 4.4 – The combined belt and tread foundation model.

4.3 The combined belt-tread model

The above described tread foundation may be theoretically coupled with any in-plane tyre belt model, applying to it a space distributed field of contact excitations. Obviously, a discretised belt model would offer a computationally easier modelling of the interaction between the belt and the tread representations, especially in the case that a space domain method of solution is to be followed. In general, the belt and tread degrees of discretisation are different and it is very common in such models (e.g. FTire [141] and CDTire [68]) a much finer discretisation to be chosen for the tread foundation in case the contact area frictional phenomena are to be captured. The direct correspondence between the tread and the belt, realised by the attachment nodes, is substituted by a force and deformation interface. This interface calculates the excitation of a single belt node by the superposition of the contact forces generated by a number of tread elements and at the same time calculates the belt deformation corresponding to the treat attachment points, between two successive nodes, applying an interpolation method. Although this approach offers a significant improvement of the accuracy, compared to the equal belt and tread discretisation, the latter method will be used in the present study, as it highlights the physical interaction mechanism between the belt and the tread contact behaviours.

One of the main research questions of the present study is the theoretical validation of a transient physical tyre model based on a modal expansion and reduction technique, for reasons associated with its computationally efficiency but also with the identification of the mechanisms of interaction between the excited modes and the performance characteristics. Although such techniques may be applied to both analytical and discretised space representations, as it was presented in chapter 3, an analytical one will be chosen here. Such a model allows for the space discretisation process to be decoupled from the modal expansion method which remains based on the analytical formulation of the model. The belt structure will be described by a discretised belt model but its modal characteristics evolve from its analytical mathematical expression. Although the following analysis will be based on the pretensioned ring on elastic foundation model, the conclusions that will be drawn will justify the possible applicability or not of the other modal simulation approaches presented in chapter 3 on the simulation of the tyre contact behaviour.

An overview of the complete tyre model is given in fig. 4.4. The actual contact simulation is accomplished in the time domain and the loading conditions are progressively applied over time. For reasons that will become later obvious (especially in chapter 5), the simulation process is significantly simplified assuming a vertical kinematic excitation of deformation instead of a load one. Moreover, for similar reasons, the wheel

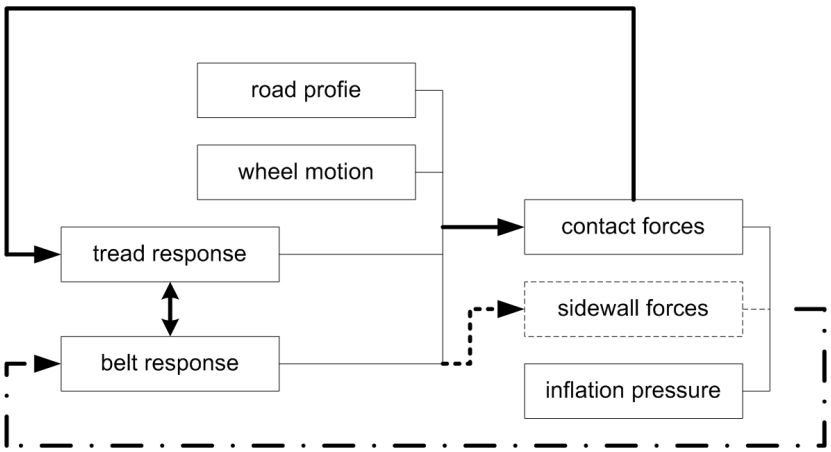

Figure 4.5 – The flowchart of a single time step of the contact algorithm. (solid line: space domain calculation, dashed-dotted line: modal domain calculation, dashed line: non linear sidewall related calculation)

position remains fixed and the wheel-road approach is accomplished by the road level variation. Practically, the level of the road rises according to a constant time rate of approach, until the required degree of vertical deformation (approach) or resulting load has been achieved. Prior to that, the inflation pressure has been applied to the model and the respective equilibrium has been established. The dynamic inflation of the ring model has already been presented in sections 3.7.2 and 3.7.4 for the linear and the non linear sidewall cases respectively. As it was highlighted, the process of inflation leads to a minor radius increase but it is necessary in the non linear sidewall case for the identification of the sidewall equilibrium geometry. Obviously, after the required level of approach or load has been reached, sufficient additional time is offered for the contact equilibrium establishment.

An overview of the calculations composing a single time step of the simulation algorithm (presented in fig. 4.5) prescribes the coupling pattern of the algorithm subcomponents that will be later analysed. The deformation response of the in-contact tread elements and the belt nodes deformation, as calculated in the previous time step, are brought forward. Combining them with the road kinematic characteristics (which theoretically capture both the wheel kinematic condition -velocity and displacement- and the road profile changes), the contact reaction forces are calculated. The contact reaction forces are used for the space-domain derivation of the tread response. In parallel, the belt excitation is composed by the contact forces (as sensed by the belt nodes), the inflation pressure and the possible contribution of the non linear sidewall mechanism. The belt modal response is calculated and later transformed into the respective space domain deformation.

4.3.1 The excitation and response of the discretised ring model

The modal expansion of the analytical ring model has been presented in section 3.3 of chapter 3. The method derived the natural frequencies and the analytical expressions of the mode shapes of the structure 3.147. These expressions will be here transformed into their respective discretised form. Moreover, since the calculation of the tread contact forces is based on the horizontal/vertical system of reference, a similar expression should be adopted by the discretised mode shapes. The transformation of the deformation (U) of a belt point at a central angle θ, as predicted by the jth mode shape, from the radial/tangential system

to the horizontal/vertical one may be written as:

$$\begin{bmatrix} U_X^j(\theta) \\ u_Y^j(\theta) \end{bmatrix} = \begin{bmatrix} \cos\theta & -\sin\theta \\ \sin\theta & \cos\theta \end{bmatrix} \cdot \begin{bmatrix} U_r^j(\theta) \\ U_t^j(\theta) \end{bmatrix} \tag{4.40}$$

The application of a constant discretisation along the belt circumference leads to the following expression for the central angle of each node, assuming that the $i = 1$ node lies on the negative vertical global semi-axis:

$$\theta_i = -\frac{\pi}{2} + (i-1)\frac{2 \cdot \pi}{n_b}, \qquad 1 \leq i \leq n_b \tag{4.41}$$

where n_b is the number of belt nodes. Hence, the analytical expression of a mode shape function may be substituted by a vector one, composed by the horizontal and the vertical deformations of the belt nodes:

$$\boldsymbol{\Psi}_j = \begin{bmatrix} U_{X,i=1}^j(\theta_1) \\ U_{Y,i=1}^j(\theta_1) \\ \vdots \\ U_{X,i}^j(\theta_i) \\ U_{Y,i}^j(\theta_i) \\ \vdots \\ U_{X,i=n_b}^j(\theta_{n_b}) \\ U_{Y,i=n_b}^j(\theta_{n_b}) \end{bmatrix} \tag{4.42}$$

The mode shape matrix (modal basis) is composed by the mode shape vectors of all the modes that participate in the response calculation:

$$\tilde{\boldsymbol{\Psi}} = \begin{bmatrix} \boldsymbol{\Psi}_1 & \cdots \boldsymbol{\Psi}_j & \cdots \boldsymbol{\Psi}_{n_m} \end{bmatrix} \tag{4.43}$$

The calculation of the response of a modally expanded ring model has been briefly presented in section 3.7.2 of chapter 3, using the analytical mode shape expressions. Here, the respective discretised expressions will be derived. The excitation force, in the particular case, is composed by the superposition of the contact forces, the inflation pressure and the possible non linear sidewall contribution:

$$\mathbf{F}_{2n_b \times 1}(t) = \mathbf{F}_{inflation}(t) + \mathbf{F}_{contact}(t) + \left\{\mathbf{F}_{sidewall}(t)\right\} \tag{4.44}$$

The modal response calculation retains the linear nature of the space domain described structural stiffness. The response to multiple excitations can be either calculated through the summation of the excitation vectors (as proposed in eqn. 4.44) or through the superposition of the individual to each excitation responses. In the above equation the contact excitation is a transient one, but the inflation pressure remains constant over time. The incorporation of the inflation to the excitation vector at every single time step may be omitted and the respective steady state response (deformation) may be applied to the belt structure. Obviously,

this computational simplification cannot be applied to the non linear sidewall case, where the radial sidewall force (and the respective response) is a non linear function of the deformation. In this case, the inflation forces are given by the following transformation:

$$\begin{bmatrix} F^i_{inf,X} \\ F^i_{inf,Y} \end{bmatrix} = \mathbf{T}(\theta_i) \cdot \begin{bmatrix} P_0 \cdot b \frac{2\pi \cdot R}{n_b} \\ 0 \end{bmatrix} \tag{4.45}$$

where $F^i_{inf,X/Y}$ is the inflation force of the ith node, along the X/Y direction and $P_0 \frac{2\pi \cdot R}{n_b}$ is the inflation radial force corresponding to each node.

Following a form similar to the one of the mode shapes, the force vector may be written as:

$$\mathbf{F}(t) = \begin{bmatrix} F_{X,i=1} \\ F_{Y,i=1} \\ \vdots \\ F_{X,i} \\ F_{Y,i} \\ \vdots \\ F_{X,i=n_b} \\ F_{Y,i=n_b} \end{bmatrix} \tag{4.46}$$

where $F_{X,i}$ and F_{Y^i} are the horizontal and vertical force components corresponding to the ith node of the ring. The transformation of the analytical expression of the modal excitation into the respective discretised one, is based on the theoretical equivalence between the cross product of two space discretised vectors and the integration of the analytical value over the same length or distance:

$$\Gamma_j = \int_{\theta=0}^{2\pi} [(U^r_j)^2 + (U^t_j)^2] \mathrm{d}\theta = \frac{2\pi}{\mathrm{n_b}} \mathbf{\Psi}^{\mathrm{T}}_{\mathrm{j}} \cdot \mathbf{\Psi}_{\mathrm{j}} \tag{4.47}$$

The transformation may be now written as:

$$f^m_j(\mathrm{t}) = \frac{R \cdot \int_{\theta=0}^{2\pi} \left(q_r(\mathrm{t},\theta) \cdot \mathrm{U^j_r}(\theta) + \mathrm{q_t}(\mathrm{t},\theta) \cdot \mathrm{U^j_t}(\theta) \right) \mathrm{d}\theta}{b \cdot R \cdot \rho \cdot d \cdot \Gamma_j} \Rightarrow \tag{4.48}$$

$$f^m_j = \frac{R \cdot \frac{2\pi}{n_b} \mathbf{\Psi}^T_j \cdot \mathbf{q}}{b \cdot R \cdot \rho \cdot d \frac{2\pi}{n_b} \mathbf{\Psi}^T_j \cdot \mathbf{\Psi}_j} = \frac{\mathbf{\Psi}^T_j \cdot \mathbf{q}}{b \cdot \rho \cdot d \cdot \mathbf{\Psi}^T_j \cdot \mathbf{\Psi}_j} \Rightarrow \tag{4.49}$$

$$f^m_j = \frac{\mathbf{\Psi}^T_j \frac{n_b}{2\pi \cdot R} \mathbf{F}}{b \cdot \rho \cdot d \cdot \mathbf{\Psi}^T_j \cdot \mathbf{\Psi}_j} = \frac{1}{\frac{2\pi \cdot R \cdot b \cdot \rho \cdot d}{n_b}} \frac{\mathbf{\Psi}^T_j \cdot \mathbf{F}}{\mathbf{\Psi}^T_j \cdot \mathbf{\Psi}_j} \Rightarrow \tag{4.50}$$

$$f^m_j = \frac{n_b}{m_b} \frac{\mathbf{\Psi}^T_j \cdot \mathbf{F}}{\mathbf{\Psi}^T_j \cdot \mathbf{\Psi}_j} = \frac{1}{m^i_b} \frac{\mathbf{\Psi}^T_j \cdot \mathbf{F}}{\mathbf{\Psi}^T_j \cdot \mathbf{\Psi}_j} \tag{4.51}$$

where m_b^i is the mass property corresponding to each of the belt nodes. The modal participation factors may be calculated by differential equations similar to the ones of the analytical approach (eqn. 3.100):

$$\ddot{\eta}_j + \lambda_j \cdot \eta_j + \omega_j^2 \cdot \eta_j = f_j^m \tag{4.52}$$

Accordingly, the transformation of the deformation and velocity responses from the modal domain into the space one may be written as:

$$\mathbf{u}(t) = \mathbf{\Psi} \cdot \tilde{\eta} \tag{4.53}$$

$$\dot{\mathbf{u}}(t) = \mathbf{\Psi} \cdot \dot{\tilde{\eta}} \tag{4.54}$$

where the deformation and deformation velocity vectors ($\mathbf{u}$ and $\dot{\mathbf{u}}$ respectively) follow the same space discretisation pattern with the mode shapes and $\tilde{\eta}$ is the vector of the modal participation factors of the modal basis modes:

$$\tilde{\eta} \begin{bmatrix} \eta_1(t) \\ \vdots \\ \eta_{n_m}(t) \end{bmatrix} \tag{4.55}$$

Finally, the global position of a belt node (i), as used in section 4.2 for the calculation of the tread contact forces, may be expressed as:

$$X_b = R \cdot \cos\theta_i + u_{X,i} \tag{4.56}$$

$$Y_b = R \cdot \sin\theta_i + u_{Y,i} \tag{4.57}$$

The tread orientation angle, a, of eqn. 4.28, which is also used for the calculation of the tread's global stiffness and damping values (section 4.2.2), is also derived through the belt modal response. This angle is primarily a function of the rotation of the belt node around the wheel centre, $a_{rotation}$, as induced by the belt response:

$$\alpha_{rotation} = \arctan(\frac{u_r}{u_t}) \tag{4.58}$$

A secondary possible contribution to the angle a may exist, expressed by the deviation (torsional) of the tread's orientation from the vertical to the belt's tangent at the attachment point. Practically, this deviation corresponds to the rotation of the tread element around the node and for the ring model it may be calculated as:

$$\alpha_{torsion} = -\frac{1}{R}\frac{\partial u_r}{\partial \theta} \tag{4.59}$$

The total global orientation angle (a) is given by the following equation:

$$\alpha = \theta + a_{rotation} + a_{torsion} \tag{4.60}$$

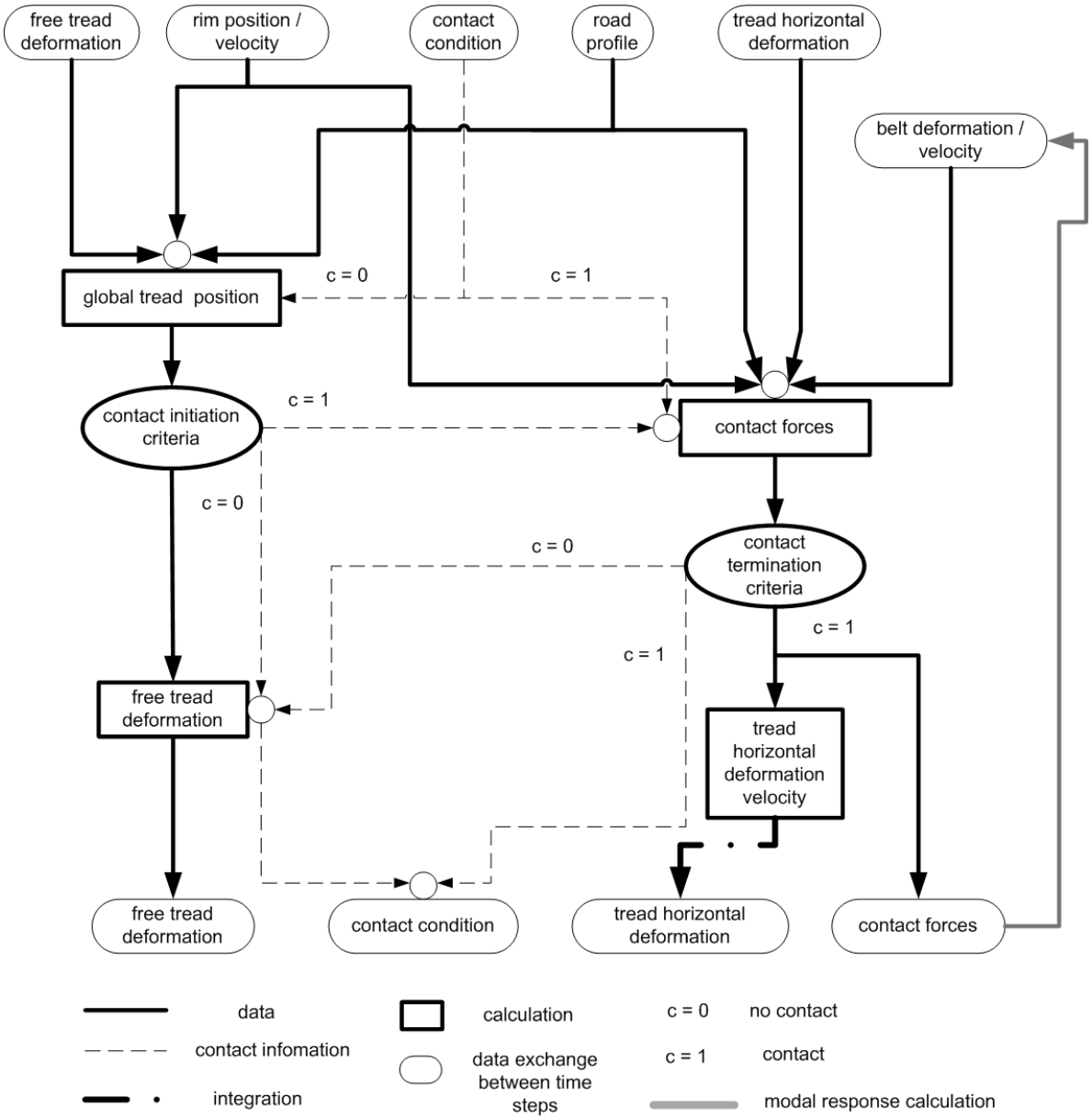

Figure 4.6 – The flowchart of the contact algorithm.

4.3.2 The flowchart of the contact algorithm

Having completed the analysis of the various sections of the algorithm, the computational flowchart of a single time step (fig. 4.6) may be synthesised:

1. The global positions (Y_t) of the out-of-contact ($c = 0$) tread elements are calculated (eqn. 4.28).
2. The possible contact of them is examined using the criterion described by eqn. 4.29 and the initial contact conditions of the same equation are applied to the elements for which the criterion is satisfied.
3. The vertical deformation and deformation velocity (ΔY_t and $\Delta \dot{Y}_t$ in eqns. 4.1 and 4.2 respectively), the friction force ($F_{friction}$, eqn. 4.33)and the tip shear relative velocity ($\Delta \dot{X}_t$, eqn. 4.24) are calculated for all the in-contact ($c = 1$) tread elements.
4. The satisfaction of the contact continuation condition (eqn. 4.30) is examined for all the in-contact elements and the possible termination of contact is verified.
5. The transformation from the horizontal/vertical (ΔX_t, ΔY_t) to the radial/tangential (ΔR_t, ΔT_t) deformation system is applied to elements that step out of the contact (eqn. 4.8) and the residual deformation is calculated (eqns. 4.31 and 4.32) for the elements that still exhibit significant deformation.
6. For the in-contact elements, the tread slip displacement (relatively to the deformation position) is derived by the integration of the shear velocity (eqn. 4.25).
7. The contact reaction forces applied to the contact belt points (F_{tY} and F_{tX} in eqns. 4.26 and 4.27 respectively) are calculated and the excitation vector ($\mathbf{F}$, eqn. 4.44) is composed including (in the non linear sidewall case) the contribution of the inflation pressure and the sidewall tension (T_r, eqn. 4.64, section 4.3.4).
8. The modal force of each mode is derived (f_j^m, eqn. 3.108) and the modal participation factors (η_j) are calculated through the equation 4.52.
9. The belt response ($\mathbf{u}$) and deformation velocity ($\dot{\mathbf{u}}$) in the space domain are derived (eqn. 4.53).

4.3.3 The tyre contact stiffness and the effect of the load on the pressure distribution shape

Moving to the application of the above described contact algorithm, the deformation is imposed to the model over a time of $0.4sec$, assuming a constant velocity of road approach. A further time of $0.1sec$ is provided for the contact equilibrium establishment. The resulting deformation rate is sufficiently low in order the magnitude of the damping forces to remain modest and the stiffness interaction mechanism between the belt and the tread deformations to be mainly captured. A friction coefficient $\mu = 0.5$ is chosen for the cases in which no different value is explicitly mentioned. The ring physical properties summarised in table 4.1 are used and the damping coefficients predicted in section 3.10.2 (under the viscous stiffness and mass proportionality assumption with coefficient values of $\beta_d = 6 \cdot 10^{-5}$ and $\gamma_d = 400$) are applied, as they

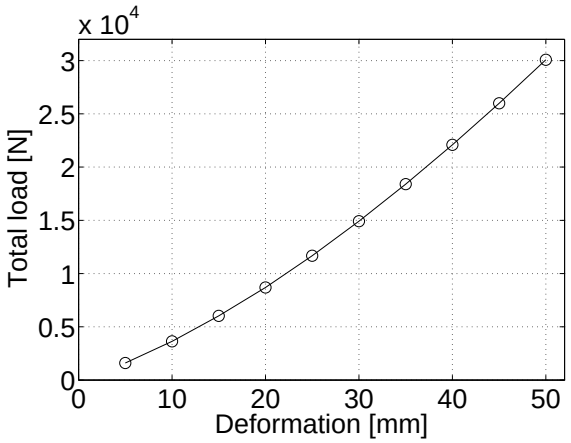

Figure 4.7 – The increase of the tyre load and the tyre vertical deformation.

were found to predict a satisfactory modal damping ratios correlation with the majority of the experimental studies.

The total contact stiffness of the tyre is derived (fig. 4.7), by the summation of the equilibrium vertical reaction forces for various values of wheel-road approach, measured from an initial tangential and no-load relative position. The model captures the contact non linearity of the tyre, which is depicted by the increasing contact stiffness. This behaviour has been experimentally verified in numerous studies [255, 256, 117, 53, 145, 1, 18] and is imposed by the increasing portion of the tyre circumference that conforms to the road plane surface as the wheel and the road approach each other.

The development of the vertical contact forces along the contact length is presented in fig.4.8 for various levels of wheel-road relative approach. Both the contact length and the reaction forces increase with the imposed deformation. Apart from the forces magnitude, though, a significant change in the distribution shape of the forces may be observed. The initial parabolic (convex) shape transforms into a trapezoidal one as the load increases, a change that is in agreement with various experimental results [255, 257, 256, 258, 18]. The increase of the level of approach does not result in a proportional increase of the force values as both the extension of the contact length and the shape evolution affect the values of the developed forces. The maximum values of the reaction force along the contact area (for the cases examined in fig. 4.8) are presented in fig. 4.9 as a function of the total load. It is obvious that the rate of the force increase drops as the load increases. A similar conclusion has been experimentally drawn by Hall *et al* in [258].

The respective development of the horizontal contact forces is presented in fig. 4.10. A full period-like harmonic shaped distribution along the contact length is predicted, becoming maximum (in absolute terms) near the contact edges and reducing down to zero around the symmetry axis. The predicted inwards (towards the symmetry axis) force direction has been experimentally verified in numerous studies, summarised in [228] and [18]. As the circular shape of the belt conforms to the plane road surface, the belt slides away from the centre of the contact. The developing friction force, though, reacts to this displacement generating the inwards horizontal stress field. As the load increases, no significant change in the shape of the horizontal forces field can be identified, in contrast to the vertical one.

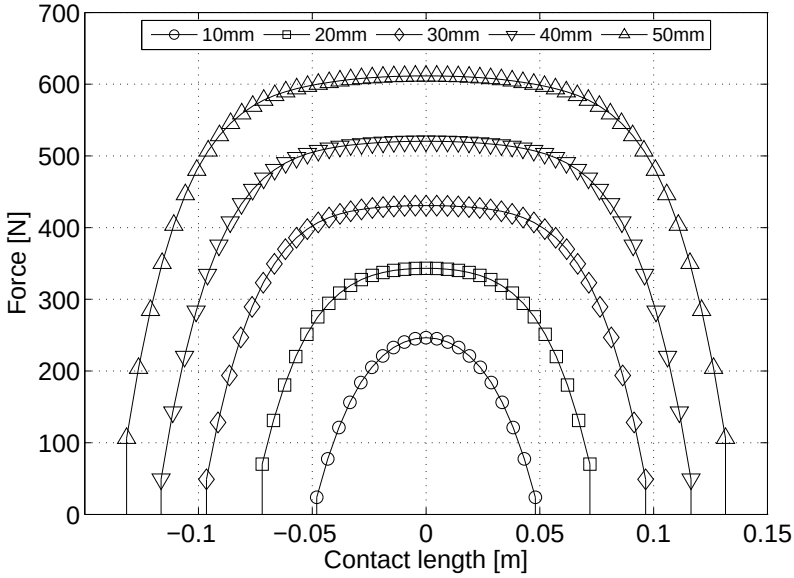

Figure 4.8 – The development of the vertical contact forces field with the imposed level of deformation.

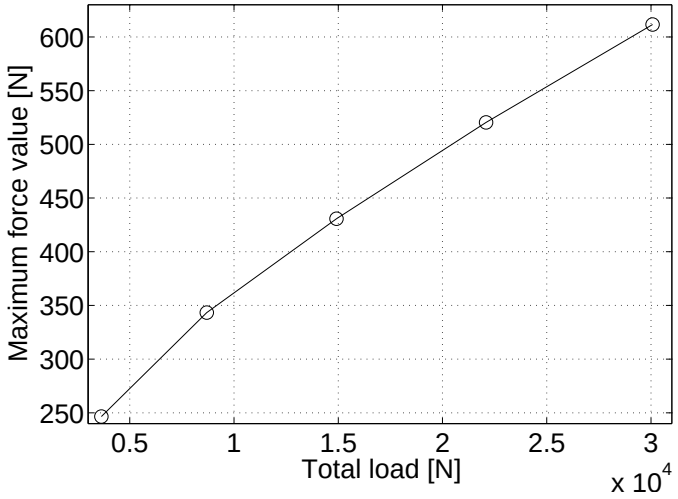

Figure 4.9 – The maximum value of the contact reaction force along the contact area as a function of the total load.

4.3.4 Sidewall nonlinearity and its effect on the pressure distribution

It is well known that although the ring model offers an excellent prediction of low frequency modal behaviour of the tyre, the predicted contact stiffness is overestimated. Characteristically, Miege and Popov in [127] notice a 44% higher contact stiffness value predicted by a ring model, compared to the experimental results acquired using a truck tyre. The main reason for this overestimation is the sidewall non linear behaviour of the tyre which cannot be captured by a linear sidewall equipped ring model. The geometrical buckling of the membrane-like sidewall structure as the deformation increases, reduces the radial force in comparison to the respective value predicted by the linear model.

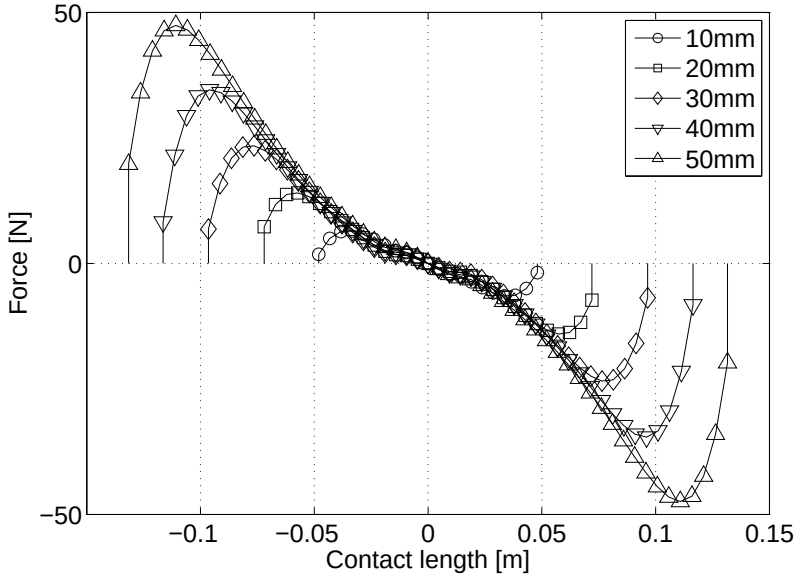

Figure 4.10 – The development of the horizontal contact forces field with the imposed level of deformation.

Apart from the magnitude, though, the linear sidewall model fails to capture the actual sidewall behaviour in terms of force direction as well. The actual membrane tension force of the sidewall exhibits a radially inwards direction, no matter whether the belt deforms in a radial inwards or outwards direction. Only in the case of an excessive inwards radial deformation, exceeding the levels corresponding to the typical tyre operation and applicability of the model, does the sidewall force exhibit an outwards direction. In respect, for typical tyre deformation levels the road contact reaction and the sidewall force are both counterbalanced by the inflation pressure. In the linear sidewall case, though, the sidewall force exhibits an inwards direction only as long as the radial deformation exceeds the theoretical undeformed length of the sidewall structure. As typically the contact conditions impose an inwards radial deformation that in the contact area place the belt radially inwards, the predicted sidewall force exhibits an outwards direction. In result, both sidewall force and inflation pressure are supposed to counterbalance the road reactions, something that violates the actual tyre behaviour. The above are summarised in fig. 4.11.

Typically, the sidewall shape nonlinearity is represented by a membrane-based physical mechanism, as it was proposed by Böhm in [69]. A similar concept of an inextensible discretised string foundation will be used here, based on the membrane concept presented in section 3.7.3 of chapter 3. The discretisation is necessary for the capture of the varying sidewall behaviour along the model's circumference, as induced by the contact deformation. The cross section and side views of a single string element are presented in fig. 4.12. Its tension force, normalised to the length of the ring circumference, is proportional to the inflation pressure and its radius of curvature:

$$T = P_0 \cdot r_s \tag{4.61}$$

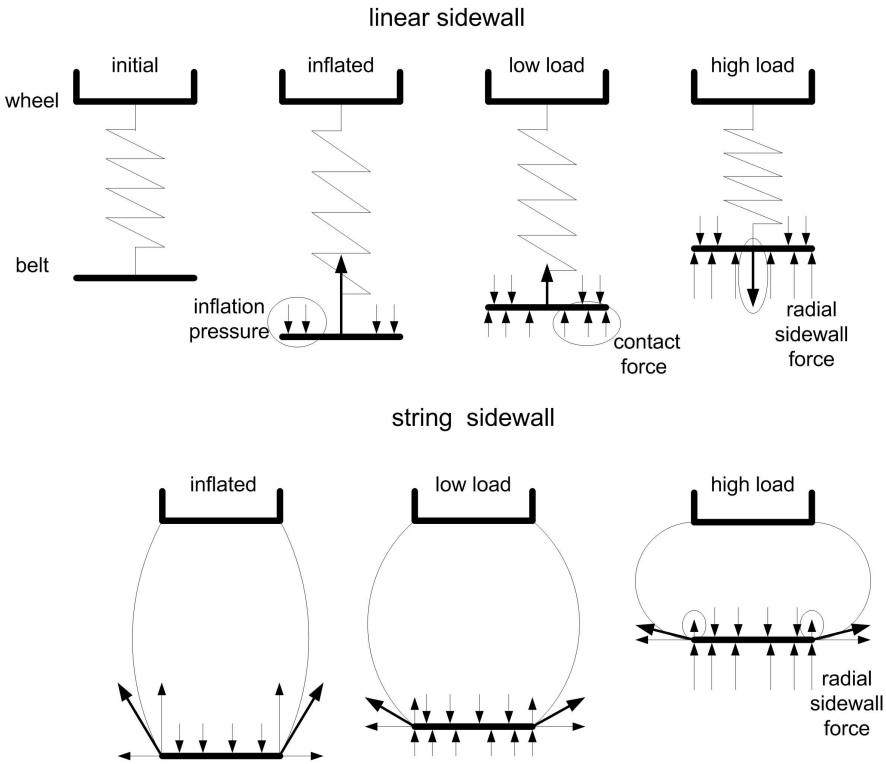

Figure 4.11 – The difference in the direction and the magnitude of the sidewall radial forces predicted by the linear stiffness and the string sidewall mechanisms.

while the string geometry, as presented in fig. 4.12, may be described by the following system of equations:

$$\left.\begin{aligned} \frac{\pi - 2w}{l_s} &= \frac{1}{r_s} \\ \cos w &= \frac{L}{2 \cdot r} \end{aligned}\right\} \;\rightarrow\; L(\pi - 2w) = 2l_s \cdot \cos w \tag{4.62}$$

where :

T	the string force, circumference length normalized
T_r	the in-plane component of the string force
T_n	the out-of-plane component of the string force
L	the distance between wheel and belt string attachment points
P_0	the inflation pressure
r_s	the radius of the string
l_s	the length of the string
w	the angle between the wheel axis of symmetry and the direction vertical to the in-plane projection of the string (see fig. 3.37)

In contrast to the membrane mechanism proposed for the study of the ring inflation process (section 3.7.3 of chapter 3) the distance between the wheel and belt string attachment points cannot be calculated by the

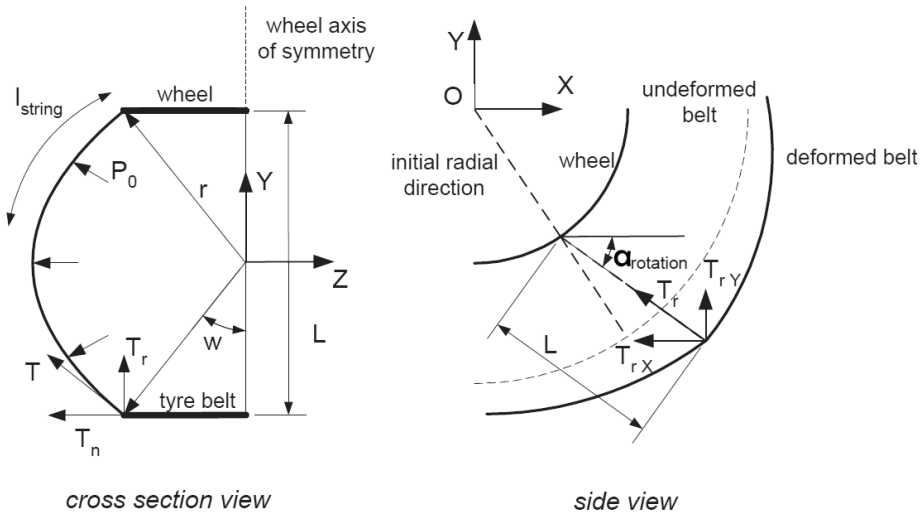

Figure 4.12 – A single string element in cross section and side view.

eqn. $L_i = R + u_{r,i} - R_w$, as the belt deforms in both radial and tangential directions. In accordance, the point's distance is calculated by the following equation:

$$L_i = \sqrt{((R - R_w) \cdot \cos\theta_i + u_{X,i})^2 + (R - R_w) \cdot \sin\theta_i + u_{X,i})^2} \tag{4.63}$$

The nonlinear equation 4.62 of every string element is solved using an iteration algorithm in every time step. The angle w_i is calculated for the instantaneous distance value (L_i) and the in-plane component of the string force is given by the equation:

$$T_r = P_0^* \cdot l_s \frac{\sin w}{\pi - 2w} \tag{4.64}$$

where P_0^* is the discretisation-normalized inflation pressure, which eliminating the effect of the discretisation from the force calculation:

$$P_0^* = P_0 \frac{2 \cdot \pi \cdot R}{n_b} \tag{4.65}$$

The in-plane component of the string force lies on the direction of the string element, as it can be observed in the side view of fig. 4.12and it contributes to both vertical and horizontal node forces, according to the angle $a_{rotation}$ (fig. 3.37). This angle expresses the relative angular orientation of the belt node to the corresponding wheel attachment point:

$$T_{rX}^i = T_r \cdot \cos(\theta_i + \alpha_{rotation}^i) \tag{4.66}$$

$$T_{rY}^i = T_r \cdot \sin(\theta_i + \alpha_{rotation}^i), \quad 1 \leq i \leq n_b \tag{4.67}$$

Finally, the sidewall force vector (similar to eqn. 4.46) is composed by the sidewall forces of all the belt

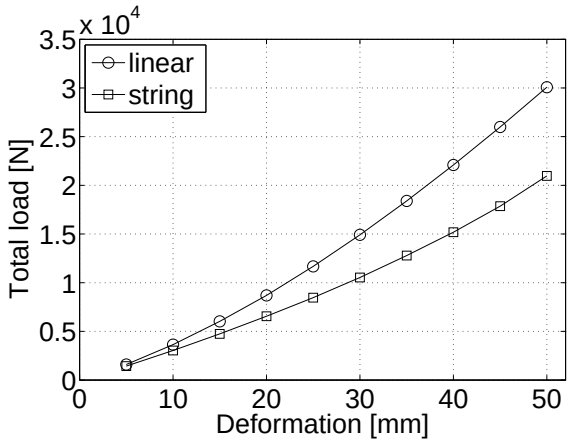

Figure 4.13 – The increase of the tyre load and the tyre vertical deformation in both linear and non linear sidewall cases.

nodes.

The total contact stiffness of the non linear sidewall model is presented in fig. 4.13, in comparison to the linear one. The pattern of the increasing stiffness with the deformation may be identified also in the non linear model, but in this case the stiffness values are significantly lower than the respective linear model ones. The relative difference increases with the deformation, as the buckling behaviour becomes profound and ranges from from 10% for the $5mm$ deformation case to 30% for $50mm$ one.

The vertical contact forces fields, under the non linear sidewall assumption, are presented in fig. 4.14 for the same vertical deformation values with the ones examined in fig. 4.8 (linear sidewall model). Comparing the two cases, it is obvious that the non linear sidewall model predicts lower force values and the magnitude difference increases with the deformation level. Another significant variation develops as the level of deformation increases. Although both models predict a parabolic distribution shape for modest contact deformations, a concave formation develops in the middle of the contact area for the string model, the amplitude of which increases with the deformation. The concave formation in the $50mm$ case affects the distribution shape along the whole contact length, which significantly deviates from the respective trapezoidal one of the linear model.

The concave-shaped vertical distribution and the corresponding to it inwards belt deformation pattern have been experimentally observed and analysed by Akasaka *et al* [259]. According to them, this behaviour is associated primarily with the bending behaviour of the belt and secondarily with the inwards direction of the shear force in the neighboring contact area. Under the current modelling approach and for the particular physical properties, this characteristic deformation shape develops only for the non-linear sidewall model. This conceptual difference may be further explained through fig. 4.11. As the inwards directed contact deformation increases, the radial sidewall force becomes outwards directed for the linear sidewall model and reaches its maximum value in the centre of the contact area. The sidewall pushes the belt against the road and prevents any shape deviation from the one imposed by the strict conformation to the road plane surface. In the string sidewall case, though, the inwards radial deformation along the contact area corresponds to a variation of the inwards directed sidewall force and moreover, its magnitude decreases with the deformation, allowing for the development of the shape deviation of the belt from the one induced by the plane road surface.

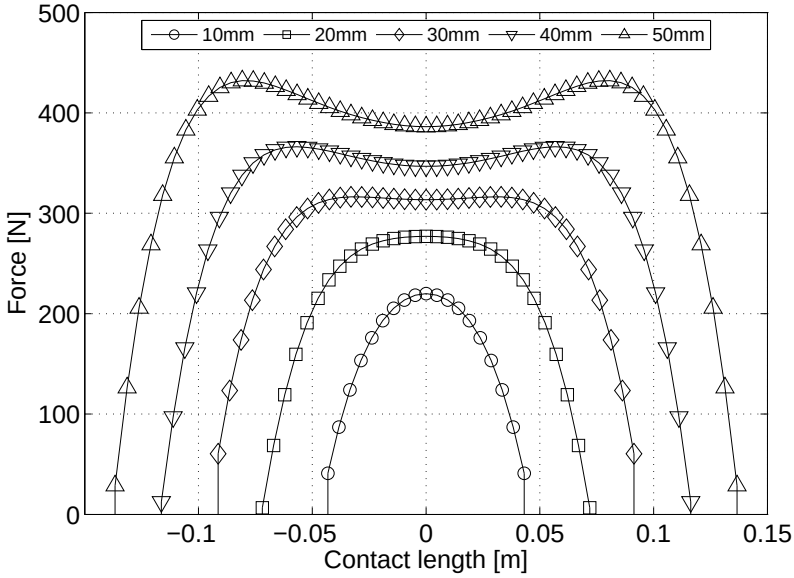

Figure 4.14 – The development of the vertical contact forces field with the imposed level of deformation in the non linear sidewall model.

A certain load applied to the linear model is counterbalanced by the air pressure supported by the bending stiffness of the belt and the sidewall stiffness. In result, a modest bending deformation is sufficient for the generation of the support force. In the string case, though, the action of the air pressure is supported by the bending stiffness but deteriorated by the inwards sidewall force. In result, a higher bending deformation is necessary for the generation of the sufficient force. In any case, the bending and sidewall deformation mechanisms do not develop independently, as they share a common platform of application, which is the tyre belt. The tyre properties define the equilibrium belt deformation which corresponds to a certain relative ratio of contribution of the two mechanisms. The effect of the possible concave formation on the frictional interaction between the tread and the road will be later analysed.

4.3.5 Inflation pressure contact effects

As it has been highlighted, the main load support action is carried over by the inflation pressure and secondarily by the tyre deformation mechanisms. In support of that, Hall *et al* in [258] experimentally proved that the maximum contact pressure along the contact length exceeds the inflation pressure by a factor ranging between 1.5 and 2.0 independently from the tyre load. Practically, the additional support necessary to counterbalance the increasing load is provided by the increase of the contact area magnitude. Obviously in the examined case, the linear deformation mechanism of the model, apart from the string radial sidewall one, imposes an increasing with the load maximum contact pressure value, as can be identified in fig. 4.14.

Three inflation values (P_0 =1.7, 2.2 and 2.7 $\cdot 10^5 Pa$) are examined in regards to the increase of the

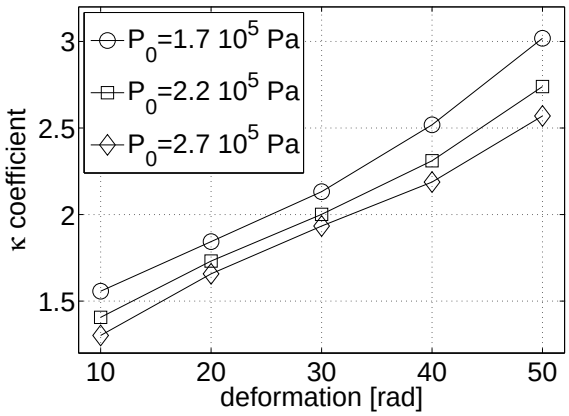

Figure 4.15 – The ratio of the maximum contact force to the inflation one for the range of the examined deformation cases and three inflation pressures.

maximum contact pressure value with the imposed load. The respective ratio is calculated by the equation:

$$\frac{F_{tY}|_{max}}{P_0 \cdot b\frac{2 \cdot \pi \cdot R}{n_b}} \tag{4.68}$$

The ratios across the range of the imposed deformations are presented in fig. 4.15. The ratio values increase almost linearly with the deformation while they decrease with the inflation pressure. Their development, though, is not proportional to the deformation one, as a 5 times increase of the imposed deformation (resulting in a more intensive increase of the corresponding load according to fig. 4.13) results in an average 2 times increase of the maximum contact force.

The actual effect of the inflation pressure on the forces distribution shape is presented in fig. 4.16 where a $40mm$ deformation is applied on the non linear sidewall model, inflated to the three examined pressure. Apart from the increase in the reaction force magnitudes along the contact length, a shape transformation can be also identified. As the inflation pressure increases, the concave formation is smoothed out and the distribution transforms into a trapezoidal shaped one. The increased inflation force pushes radially outwards the belt and increases the load that the particular level of deformation can support.

4.3.6 The belt deformation mechanism

The structural deformation of the belt along its circumference, as imposed by the contact conditions, is presented in figs. 4.17(a) (horizontal) and 4.17(b) (vertical), where the respective contact length is also marked. The horizontal deformation develops according to a symmetrical, outwards directed distribution. Its values within the contact length are, though, moderate and the predominant deformation along the contact is the vertical one(fig. 4.17(b)). The maximum horizontal deformation occurs at a $\pm\pi/4$ angle, measured from the vertical line of symmetry, which lies well outside the in-contact section of the belt.

The vertical deformation decreases rapidly towards the edges of the contact length (fig. 4.17(b)), after reaching its maximum value in the centre of it. A small increase is noticed at a $\pm\pi/2$ angle from the

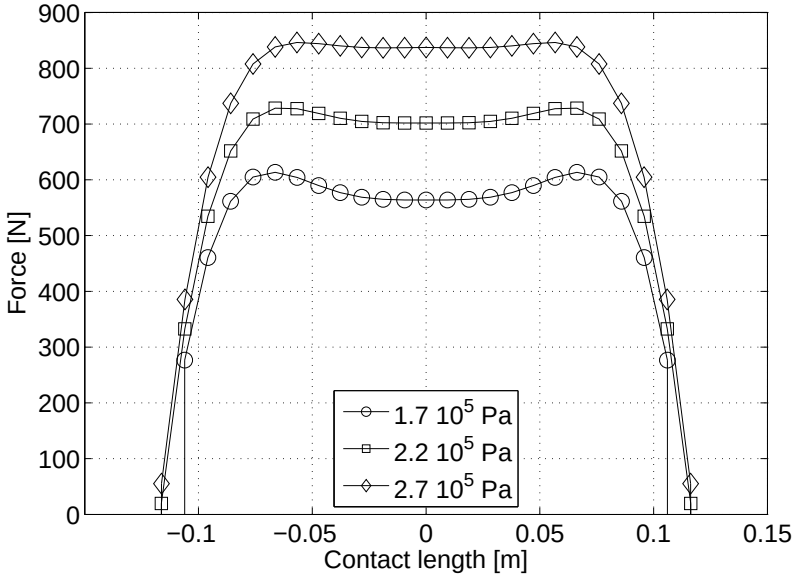

Figure 4.16 – The development of the vertical contact forces field with the inflation pressure in the non linear sidewall model.

symmetry line, which is justified by the lower value of tangential sidewall stiffness compared to the radial one. Interestingly, the minimum vertical deformation is predicted at a point symmetrical to the centre of the contact, a direct effect of the increasing stiffness with the radial wheel to belt distance. The predicted distribution shapes of the vertical deformation correlate well with the experimental ones presented in [260].

An insight into the vertical deformation of the belt in the region of the contact is accomplished by presenting the vertical distance of the belt relative to the road level (fig. 4.18). The radially inwards deformation pattern of the belt, associated with the concave contact force distribution shape, develops even for moderate deformation levels, although it is limited to a small angle range around the axis of symmetry and in general the convex deformation shape is dominant along the contact. As the load increases, the concave section broadens and the dominant deformation shape transforms from convex to concave. This transformation affects not only the vertical but also the horizontal contact pressure distribution in the area, as it will be later discussed, after the analysis of the tread contact behaviour.

4.3.7 Friction potential and tread slip development

The shear slip motion of the tread tips along the contact surface is examined here as a function of the friction potential of the road surface. For this reason, a constant vertical deformation of $40mm$ is applied to the non linear sidewall model and the tread slip behaviour in the non frictional case ($\mu = 0$) is compared to the respective ones in two frictional cases ($\mu = 0.01$ and $\mu = 0.1$). The displacement history - as measured from the initial points of contact- of some tread elements along the contact semi-length is presented in fig. 4.19. The numbers next to each slip plot refer to the order of the element: for the particular value of the applied deformation the contact length incorporates 25 tread elements, assuming a 200 elements belt discretisation. Accordingly, the 1st element corresponds to the centre of the contact length while the 13th one to the right

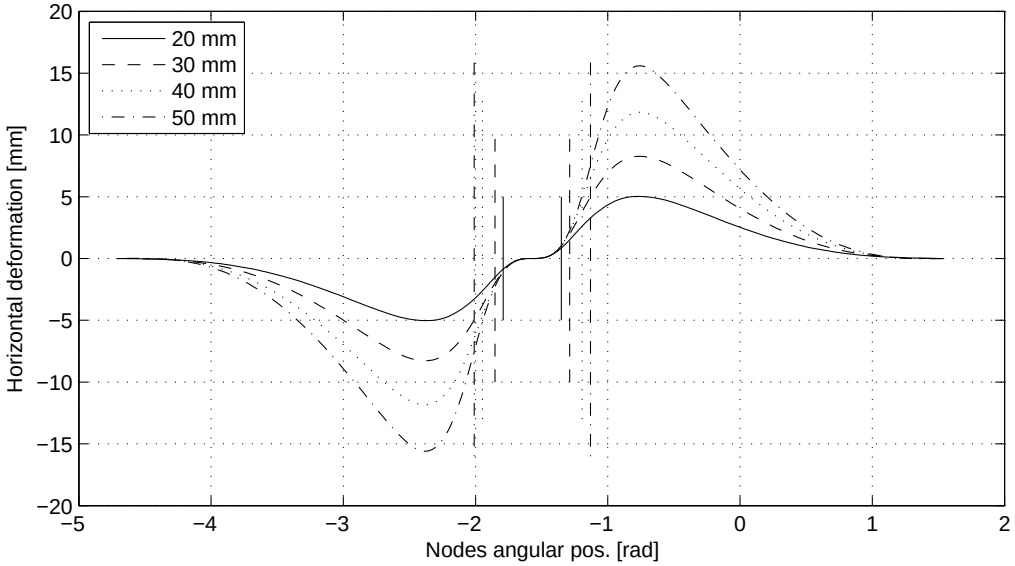

(a) Horizontal deformation.

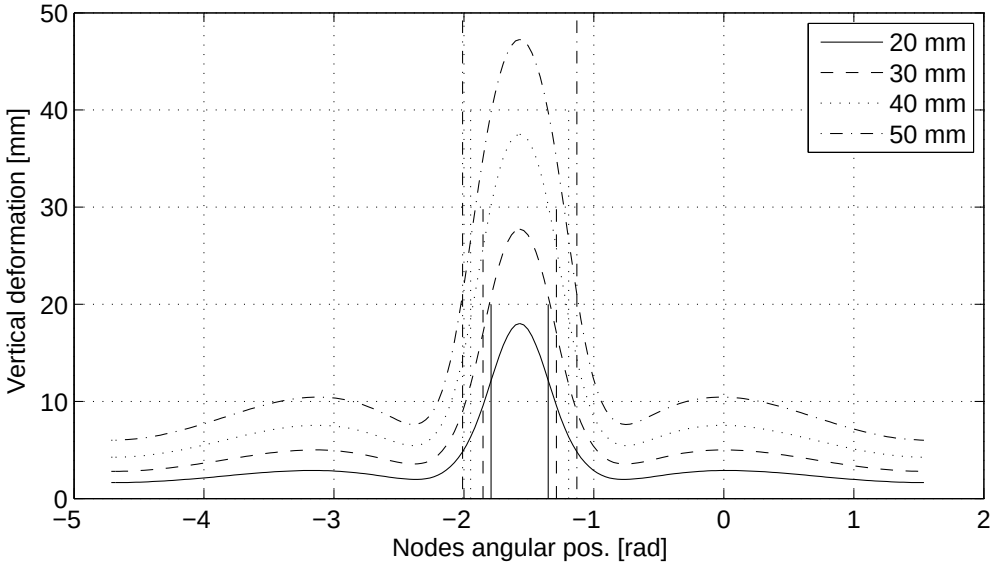

(b) Vertical deformation.

Figure 4.17 – The belt deformation along its circumference for various levels of vertical deformation level.

edge of it.

In general, the slip displacement has an outwards direction along the contact area and its value increases as we move from the centre to the edges of it, reaching its maximum one for elements in the outer zone of the contact. In the non-frictional case (fig. 4.19(a)), a rebound motion may be identified, especially for the elements close to the contact centre, as the displacement reaches a maximum value but later stabilises at a lower one. This final value is slightly negative for the 2nd element, as the tip reaches a standstill at a

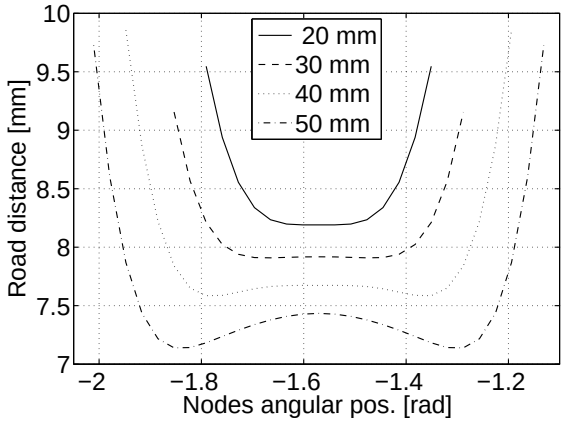

Figure 4.18 – The vertical distance of the belt circumference from the road level.

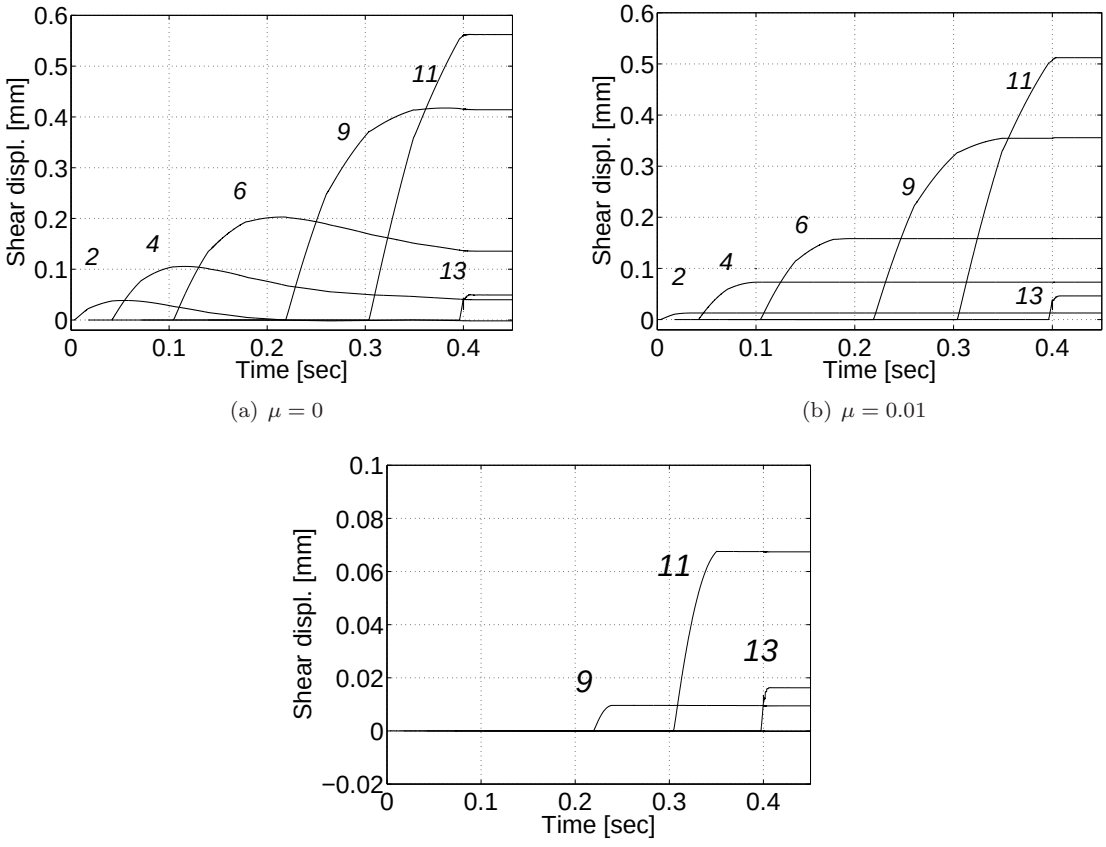

(a) $\mu = 0$

(b) $\mu = 0.01$

(c) $\mu = 0.1$

Figure 4.19 – The shear displacement (slip) of the tread tips, measured from the initial contact position, for three different values of the friction coefficient (μ).

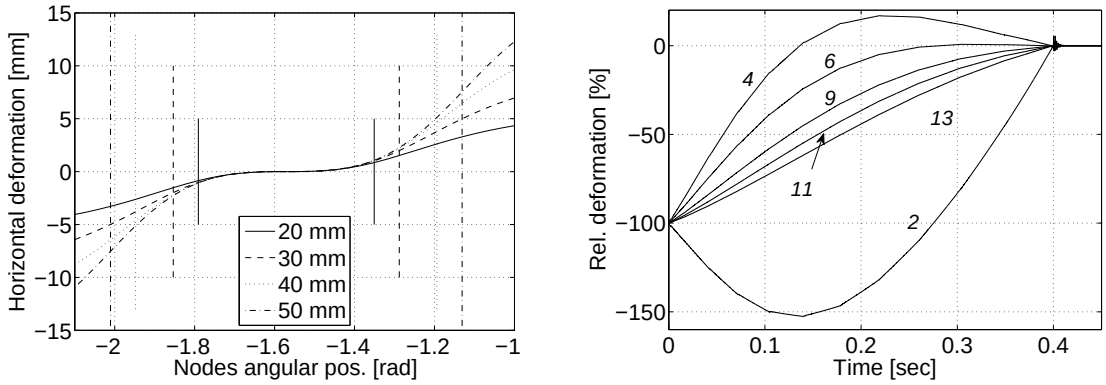

(a) The equilibrium horizontal deformation of the belt in the region of the contact, for five different values of the vertical deformation.

(b) The deformation history of the nodes corresponding to the previously examined tread elements, presented as percentage deviations from the final equilibrium values of them.

Figure 4.20 – The deformation of the belt in the area of the contact. ($\mu = 0$)

position closer to the centre than the initial contact point.

The presence of friction is in general associated with lower shear displacement and the rebound motion is also suspended (fig. 4.19(b)). Although the maximum slip values for the first elements (2nd, 4th, 6th) are lower than the respective ones in the non-frictional case, the final equilibrium values are higher, as the rebound motion is absent. For the elements that this rebound motion was small or insignificant (9th, 11th) the final displacement values appear to be lower, compared to the non-frictional case ones.

As the coefficient of friction increases further (fig. 4.19(c)), the elements closer to the centre of the contact length lock at their initial contact positions, as the developed friction is high enough to completely suspend their slip motion. For $\mu = 0.1$ the 2nd, 4th and 6th elements lock at their initial contact positions, while the rest of them develop displacements, which are, though, much smaller compared to the ones of the lower friction cases.

In general, for every case of tyre-road interaction, there is a value of friction coefficient for which the tread shear slip motion is completely suspended along the contact. In result, any further increase of the coefficient does not introduce any variation in the tyre stress and strain development as no change in the dynamic interaction exists. It may be concluded that the areas close to the edges of the contact may develop shear displacement for a broader range of tribological conditions, as the frictional locking appears firstly in the region close to the centre of the contact.

The above described behaviour and conclusions are in agreement with the work of Maurice and Savkoor [261], in which the areas towards the edges of the contact exhibit a higher tendency to slip. Furthermore, a number of experimental and simulation studies (summarised in [18, 1]) locate the slip development primarily at the edges of the contact area and the adhesion zones at the centre of it.

4.3.8 The belt-tread interaction mechanism

The tread slip behaviour is not determined only by the vertical load and the road frictional potential, but also by its interaction with the belt deformation. The tread tendency to outwards slip motion (fig. 4.19) is

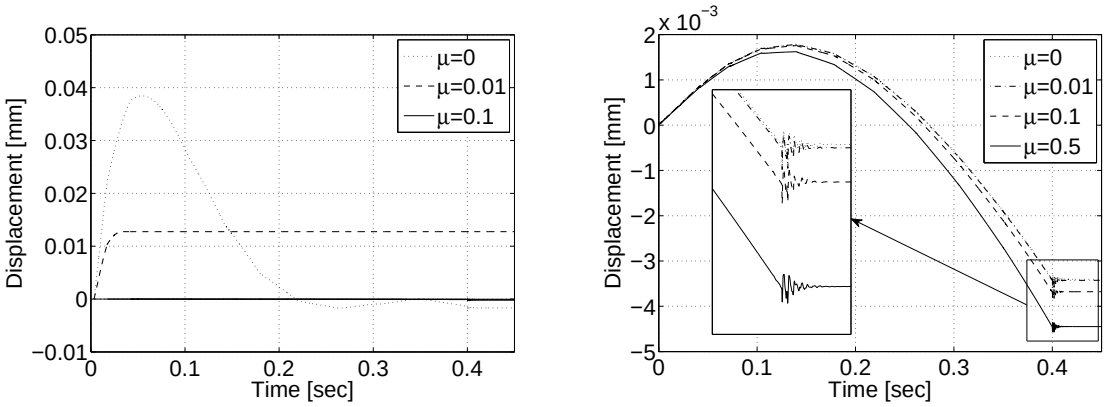

(a) Slip (b) Deformation

Figure 4.21 – The tread slip and the belt deformation histories corresponding to the 2nd contact point, for different values of the friction coefficient.

obviously a direct result of the respective deformation pattern of the belt (fig. 4.17(a)). The value of the belt horizontal deformation increases as we move from the centre to the edges of the contact length as it may be observed in fig. 4.20(a).

An insight into the above interaction between the belt deformation and the tread slip is attempted by the examination of the deformation of the particular nodes corresponding to the above examined tread elements. This is accomplished in fig. 4.20(b), for the non-frictional case, where the horizontal deformation of each node is presented as the percentage ratio to its final, equilibrium value. The respective rebound motion of the 2nd, the 4th and the 6th nodes may be observed. Moreover, the 2nd node exhibits a horizontally inwards final deformation. No rebound motion may be observed for the rest of the nodes. This rebound motion of the central belt zone is associated with the concave formation in the same area (fig. 4.18), as the upwards belt movement results in a horizontally inwards one (shrinkage).

Based on the above, a friction induced discrepancy between the rebound motion of the belt and the respective one of the tread foundation may be identified. Although the friction force development may suspend the rebound motion of the tread, this is not true for the rebound motion of the belt nodes. The friction force cannot prevent the formation of the concave pattern, although it can slightly affect its magnitude. The bending mechanism which governs the concave formation, also discussed in [259], is present independently from the tribological conditions. It is apparent, though, that certain conditions exist for which the tip rebound or even its complete shear displacement may be suspended, although the belt nodes bounce back, as the concave deformation pattern is formed. This is presented in fig. 4.21, where the tread tip and the belt node displacements of the second contact element are examined (figs. 4.21(a) and 4.21(b) respectively), for various values of the friction coefficient.

This interaction is significant for the contact behaviour of the tyre and prescribes the development mechanism of its tangential contact reaction field. In the central zone, the road-imposed reaction force becomes outwards directed (positive), as the rebound (inwards) motion of the tread zone is suspended. Moving along the contact half-length, the point where no further tread rebound motion is observed in the frictionless case, coincides with the change in the contact force direction, for any value of the coefficient of friction. From that point the tangential contact field receives its generally observed inwards direction, in

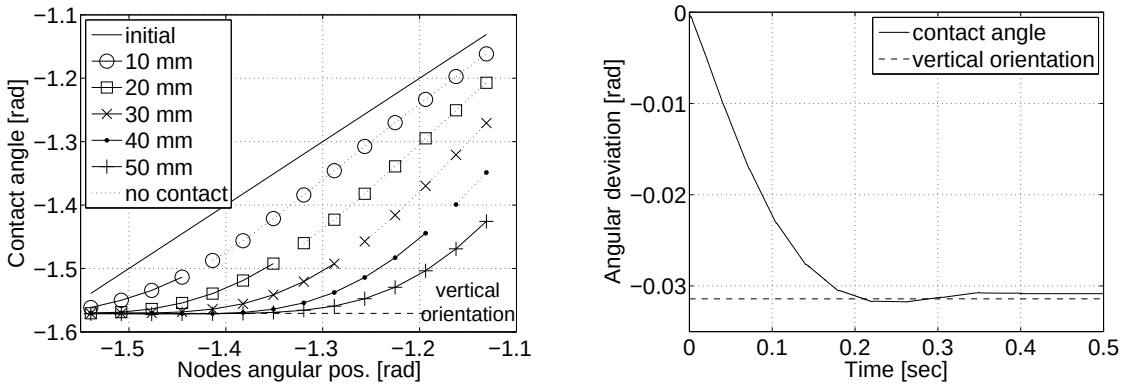

(a) The orientation angle of the in-contact tread elements for various deformation levels.

(b) The deviation history of the orientation of the 2nd tread element from its initial, radial, orientation.

Figure 4.22 – The effect of the contact on the orientation of the tread elements ($\mu = 0$).

correlation to the measurements presented in [18]. The development of this mechanism, associated with the change in the contact force direction along the contact semi-length, is suspended in the case of high friction, in which the positive slip motion of the elements is in general obstructed (fig. 4.19(c)) and the contact reaction is directed inwards along the contact length.

The present analysis offers an explanation for an observed discrepancy between various published experimental studies. Although a good agreement among them can be identified for the shape of the vertical pressure distribution and the vertical belt deformation, this is not true for the respective horizontal ones. As discussed by Pottinger [256], the frictional contact of a solid cylinder would result in pure inwards directed contact forces emerging from the conformation of its circular shape to the plane surface. In the case of the tyre, though, some experimental results of static and slow rolling contact indicate an outwards directed forces field ([256, 258] while other studies, summarized in [228, 18], indicate exactly the opposite. As it has been highlighted, the contact stress direction is dictated by the belt contact deformation mechanism. When the dominant mechanism is the solid disk-like one, the belt deformation is outwards directed and an opposite to that contact stress field is observed. When the predominant mechanisms, though, are the relaxation of the radial, inflation-induced, tension and the bending one, the deformation is directed towards the centre of the contact and radially inwards, resulting in outwards tangential contact stresses, even for the whole contact area (e.g. [256, 260]).

The behaviour of the model presented in this study is primarily defined by the first of the two mechanisms, in correlation to the majority of the experimental measurements [18], while the second mechanism can be identified only in the central concave zone. In the case of a real tyre, though, its physical properties, the carcass design and the belt-tread interaction will define the predominant mechanism and the relative amplitude of the two zones. An experimentally acquired transition between these two zones may be found in the work of Akasaka [255].

4.3.9 The effect of the contact angle

Up to this point, the effect of the contact angle on the belt and tread interaction has been omitted from the analysis. It is apparent, though, that the belt deformation from a circular to a planar profile, as it conforms to the road plane, transforms the initially radial orientation of the tread elements to an almost perpendicular one, according to the analysis presented in section 4.3.1 . Moreover, their horizontal and vertical stiffness values and damping characteristics vary as functions of the contact angle. The actual effect of the orientation change on the contact phenomena is directly related to the relative radial and tangential properties of the tread element.

The equilibrium contact angle of the 14 tread elements of the contact area (2nd to 15th) is presented in figure 4.22(a) for the five load cases. In the same plot the elements participating in the contact are marked. Apart from the apparent orientation change towards the perpendicular one, in every case a larger deviation from the perpendicular orientation may be observed for the elements located near the edge of the contact length. Moreover, this deviation increases with the dimensions of the contact length, resulting in a broader range of contact orientation angles.

Interestingly, the orientation of the contact elements is also affected by the concave deformation pattern. In fig. 4.22(b) the angular deviation history of the orientation of the 2nd contact element is presented. The deviation is calculated from the initial radial orientation, while the deviation value corresponding to perpendicular orientation is also plotted for reasons of comparison. As the belt node participates in the formation of the concave pattern, the element's orientation may decrease further than $-\pi/2$. It's final value, though, depends on the -relative to the concave's central plateau- location of the node.

4.3.10 The mechanism of the horizontal pressure distribution development

It is evident from the above analysis that the horizontal contact stress field development is a highly non linear function of the interaction between the two-dimensional belt deformation and the frictional behaviour of the tread, in regards to its possible shear slip displacement. In fig. 4.23 the evolution of the horizontal contact stress field is presented as a function of the friction coefficient, for a constant vertical deformation of $40mm$. The mechanism of the stress field generation may be summarized in the following:

- An almost symmetrical stress distribution along the contact semi-length is predicted for a limited friction potential. The distribution corresponds to an outwards directed stress field at the inner section and an inwards directed one at the outer section. During the initial phase of the contact an outwards directed slip displacement is developed along the whole contact length. This is imposed by a similar deformation pattern of the belt, as its circular shape conforms to the contact plane. The initially moderate vertical load cannot generate friction forces sufficient to suspend this slip. As the deformation increases, the developing concave pattern of the belt induces a horizontally inwards motion to the central nodes. The friction force now is higher, as the vertical load has increased, and may resist to the belt-induced, rebound motion of the tread. The resulting contact stress field for the affected section of the belt is an outwards directed one. In contrast, the outer part of the contact semi-length, is not affected by the concave deformation pattern. The belt displacement in this case remains outwards directed during the contact realisation. The developed friction force reacts to this motion, resulting in the inwards stress direction.

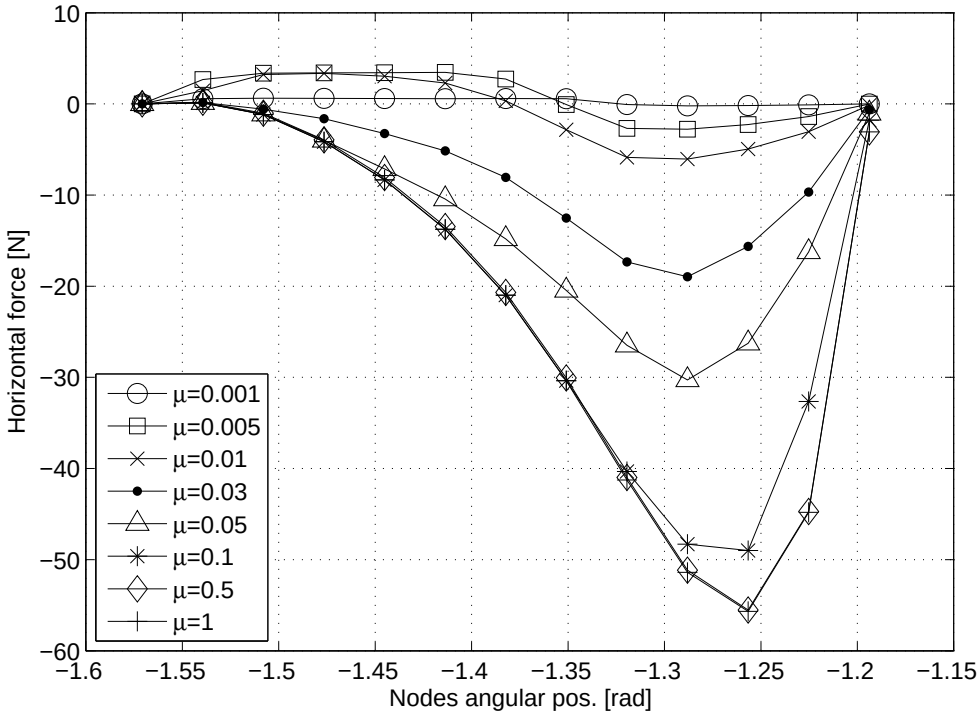

Figure 4.23 – The development of the shear reaction forces along the contact semi-length, as a function of the friction coefficient.

- As the coefficient of friction increases, the tread slip diminishes and the stress values in both zones (inwards and outwards) are in general pronounced. In the central zone, the slip may still develop during the initial phase, but the later suspension of the rebound motion leads to a slight increase in the stress values, compared to lower friction coefficient cases. The stress increase is higher, though, in the outer zone, as the outwards directed deformation of the belt is directly retarded by the enhanced friction potential.

- A further increase of the coefficient of friction results in the radical expansion of the zone associated with the inwards directed stress field along the contact semi-length. The tread slip starts to be suspended (frictional lock) for the central elements and the effect is extended to the rest of the contact area, as the coefficient raises, emerging in the profound increase of the inwards directed stress values.

- The stress field converges to a final distribution of values, when the coefficient of friction reaches a value that prevents the slip development along the whole contact length. From that point, the stress field becomes insensitive to any further increase in friction coefficient.

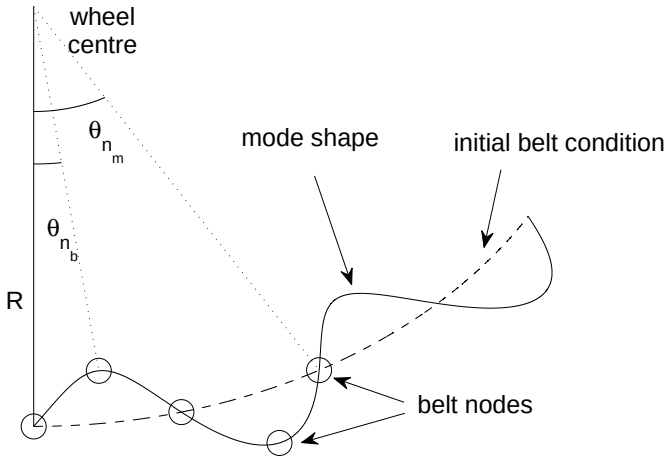

Figure 4.24 – The relationship between the space discretisation and the modal range in a complete model.

4.4 The modal behaviour and modal reduction effects on the tyre contact

In the above analysis the physical mechanisms of the tyre contact behaviour were examined using a modally expanded ring model, but the actual effect of the modal basis breadth on the acquired solution was not discussed. In this section, the tyre contact behaviour is examined from the associated modal content point of view. Firstly, the development of the modal participation factors is presented as a function of the imposed deformation for the linear and the non linear sidewall models. As a second step, the modal reduction of the model is discussed and the respective effects on the accuracy and the computational load are identified.

4.4.1 The complete modal model

The complete modal representation, in the case of a finite element model, may be easily derived: the space discretisation determines the total number of the degrees of freedom which is equal to the total number of modes that the model can predict. The transformation of the model from the space domain to the complete expression of it in the modal domain is simply a coordinates transformation.

In the case of the analytical ring model, though, the correspondence between the two domains is neither direct nor obvious. Theoretically, the ring model may be expanded to an infinite number of modes. The application of the space discretisation does not alter the analytical nature of the model and the number of modes remains independent from the discretisation level. Given that the belt discretisation has been associated with the tread elements attachment points, a first deviation attempt from the infinite modal basis could be derived from the modal expression of the smallest wavelength that may be captured by the space discretisation. As it may be observed in fig.4.24, a sequence of 5 ring nodes can describe the harmonic deformation of the wave length of a mode shape, with the last of the nodes being shared with the following

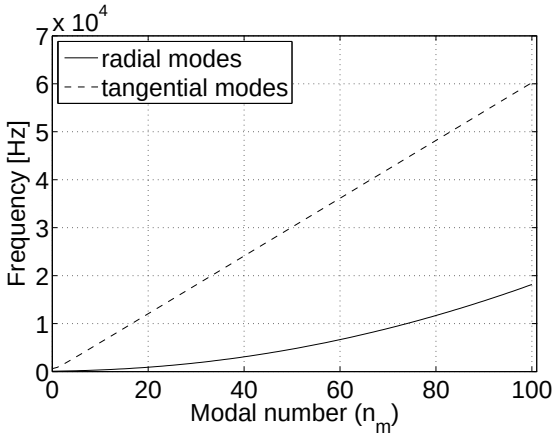

Figure 4.25 – The total frequency range of the complete model.

wave pattern. The statement of the above observation using the respective central angles reads:

$$\left.\begin{aligned}\theta_n &= \frac{2\pi}{n}\\ \theta_{n_b} &= \frac{2\pi}{n_b}\end{aligned}\right\} \xrightarrow{\theta_{n_{max}}=4\cdot\theta_{n_b}} n_{max} = \frac{n_b}{4} \tag{4.69}$$

θ_n	the modal wavelength angle
θ_{n_b}	the discretisation angle
n_{max}	the maximum modal number
n_b	the total number of nodes

Assuming a ring model discretised to 400 nodes, the respective range of the modal numbers of the modes that could be described by it is $n = [0, \dots 100]$. Given that the $n > 0$ modes need to be incorporated twice in the modal base (rotated to a relative to each other angle of $\pi/(2 \cdot n)$), the modal basis would theoretically be composed by 201 radial and 201 tangential modes. The respective frequency range is presented in fig.4.25. Obviously, the frequency range extends to values that not only exhibit limited practical interest for the tyre structural deformation and transient response but also introduce significant problems to the associated numerical calculations.

The emerging huge computational load is not only associated with the number of modes, as each of them corresponds to a column of the matrix $\tilde{\mathbf{\Psi}}$, but also with the assumed frequency range, imposing the use of an extremely small time step for the simulation process. Moreover, a damping property distribution corresponding to a physical one, such as the stiffness proportional distribution, results in an increasing modal damping coefficient with the modal number (see section 3.10 of chapter 3). In result, all the modes above a critical frequency value exhibit an overcritical behaviour which imposes problems of stability associated with the numerical simulation of stiff problems. On the other hand, the overcritical modal behaviour suspends the participation of the modes in a transient solution for reasons related to the excitation energy of these modes. In order, though, to justify the modal reduction of the basis by physical and not computational reasons, the modal content of the contact equilibrium should be examined.

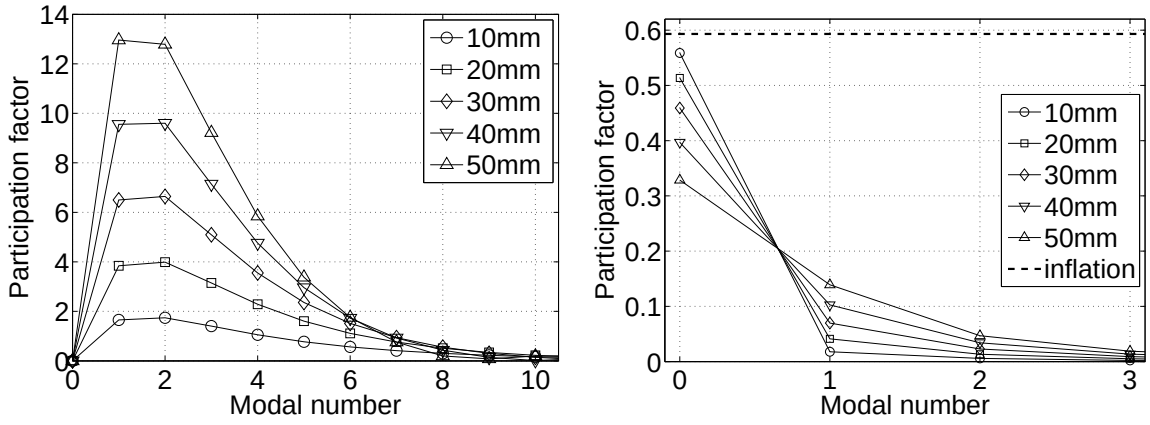

(a) Radial modes

(b) Tangential modes

Figure 4.26 – The radial and tangential modes participation factors for every load/deformation case.

4.4.2 The modal content of the contact deformation

Starting from a linear sidewall model, the absolute values of the contact equilibrium modal participation factors, as derived by eqn. 3.100, are presented in fig. 4.26 for both radial and tangential modes and for the various values of deformation. An important conclusion that may be drawn is that the participation of the modes decreases with the modal number and asymptotically reaches insignificant values. This pattern validates the use of a modally reduced model for the capture of the contact deformation of the tyre, composed by the omission of the high modal number zones. Furthermore, comparing radial and tangential modes with the same modal number, the participation of the second ones is much lower. Apparently, the contact deformation is primarily associated with the radial low and medium modal zones. Combining the above finding with the ones of chapter 3 it may be concluded that the contact of the tyre depends on all the physical properties of the ring structure, as it excites modes sensitive to the sidewall stiffness, the inflation pretension and the bending behaviour. Moreover, the mode shapes of the particular modes have been found to exhibit significant coupling of the radial and tangential deformation components, something that deduces the applicability of the rectilinear modal representations. The above conclusions justify the adoption of the pretensioned ring model, in contrast to the simplified models, for the construction of a modal basis able to represent the tyre contact behaviour.

The $n = 1$ and $n = 2$ radial modes exhibit the highest participation which increases with the level of the imposed deformation (fig. 4.26(a)). For a low deformation level, the maximum participation corresponds to the $n = 2$ mode but for a high one the maximum participation value is assigned to the $n = 1$ mode. The maximum tangential mode participation factor corresponds to the $n = 0$ mode (fig.4.26(b)), and is associated with the inflation process. Interestingly, the contact corresponding $n = 0$ participation is lower than the inflation corresponding one, as the contact deformation is associated with a radius decrease, in contrast to the inflation process. The effect of the deformation level on the participation of the $n > 0$ modes is, though, the contrary one, following the obvious -increasing with it- participation development.

In order to highlight the correspondence between the contact pressure distribution shape and the modal content of the deformed belt the effect of the magnitude is removed from both the contact force values

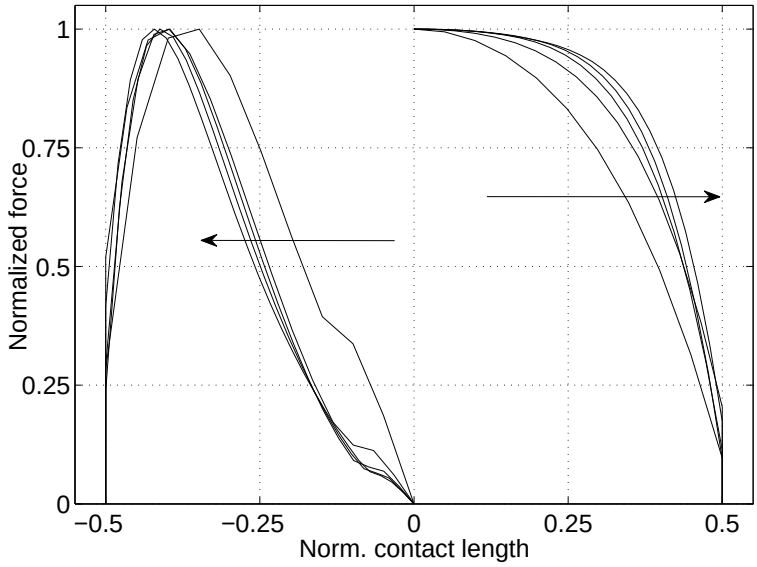

Figure 4.27 – The effect of the deformation level on the horizontal and vertical contact pressure distribution shape. (The arrows indicate the deformation increase)

and the modal participation factors. For every deformation level of figs. 4.8 and 4.10 the force values are normalised with respect to the respective vertical or horizontal maximum value along the contact. In accordance, the modal participation factors are normalised in respect to the maximum radial or tangential factor of each deformation case. The resulting pressure distributions are presented in fig.4.27. The shape transformation from a parabolic into a trapezoidal one with the deformation increase is evident. No significant shape transformation emerges in the horizontal pressure distribution case. The position of the maximum horizontal value of which is slightly transferred towards the edge of the contact length as the deformation increases.

The corresponding to the deformation levels relative modal participation factors are presented in figs. 4.28(a) and 4.28(b) for the radial and the tangential groups respectively. Interestingly, the lower the imposed deformation the broader is the range of the excited modes. Although for any load case, the relative participation values decrease with the modal number, this decrease is intensified by the deformation. The participation of higher modal number tangential modes, in contrast, is promoted by the deformation increase. Given, though, that their absolute values are insignificant compared to the respective radial ones, the conclusion that a broader modal range should be assigned to the simulation of the low load/deformation tyre operating conditions may be reached.

An explanation of this modal participation development pattern is attempted through the comparison of the shape of the deformed belt in the contact area with the mode shapes. This is accomplished in fig.4.29 for a low ($10mm$) and a high ($50mm$) deformation cases and the first ten radial mode shapes. Their deformation magnitude has been normalised to the corresponding belt deformation for easier shape comparison. As it may be observed, the belt deformation pattern along the contact length correlates better with the $n_m = 5$ mode shape in the low load case, while it correlates better with the $n = 3$ one in the high load case. This difference may be justified not only by the contact deformation nonlinearity but also by the relative to each

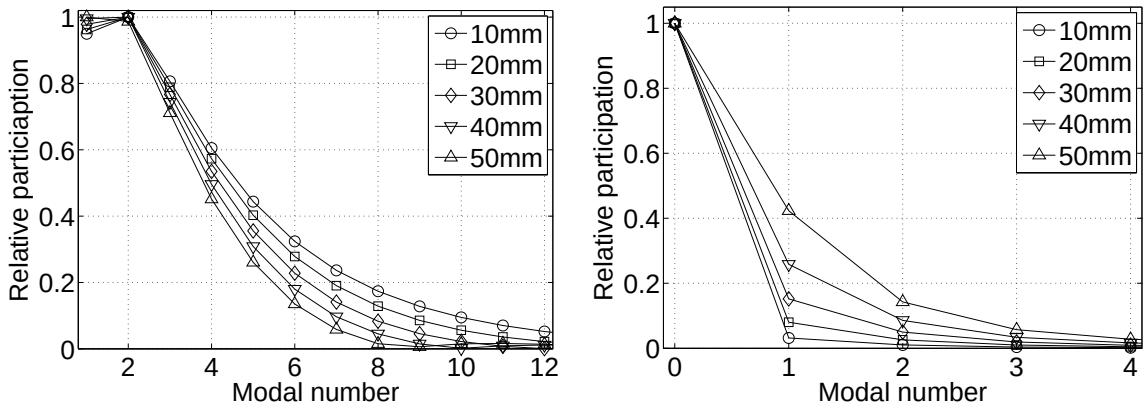

(a) Radial modes.

(b) Tangential modes.

Figure 4.28 – The radial and tangential modes participation factors for every load/deformation case.

other wavelength of the mode shapes and the contact area dimensions increase with the deformation level.

The shape correlation with a higher modal number mode shape in the low deformation case can offer an explanation to the excitation of a relatively broader range of modes (fig.4.28(a)). It should be noticed that although the belt deformation pattern correlates well with a particular mode shape, the similarly high participation factors of the nearby modes reveals their equal importance for the deformed belt shape representation. In other words, the contact deformation may be associated with a certain mode shape, but its representation is associated with a broader modal range which favours, though, the participation of its modal region.

The above conclusions may be summarised by the examination of the time history of the $n_m = 3$ and $n = 5$ participation factors, presented as normalised to their maximum values in fig.4.30. The time history of the normalized deformation is also plotted for easier comparison of the modal participation developments. The 5th radial mode follows closely the development rate of the deformation in the early stage of the contact, while the development of the 3rd one exhibits an initial delay during the low deformation phase.

4.4.3 The effect of the non linear sidewall on the contact modal content

The effect of the incorporation of the non linear sidewall mechanism in the prediction of the belt deformation and the resulting contact force distribution have been analysed in section 4.3.4. Here, those effects will be examined through the corresponding variation of the participation of the modes in the equilibrium deformation. Following an approach similar to the one presented in the linear model case, the deformation magnitude effect is removed from the response and the shape of the contact forces distribution is isolated in fig. 4.31. The transformation of the initial parabolic to the final concave shape is obvious, but no significant shape variation from the linear case emerges for the horizontal distribution. The respective difference in the belt deformation shape between the linear and the non linear sidewall cases is presented in fig. 4.32

The modal content of the variation of the deformed belt shape is examined using the ratios of the evolving participation factors to the respective ones of the linear sidewall model. Obviously, in order the two models to be directly comparable, the linear one in this case has been modally expanded excluding the radial sidewall stiffness.The sidewall effect has been introduced as an external, deformation dependent,

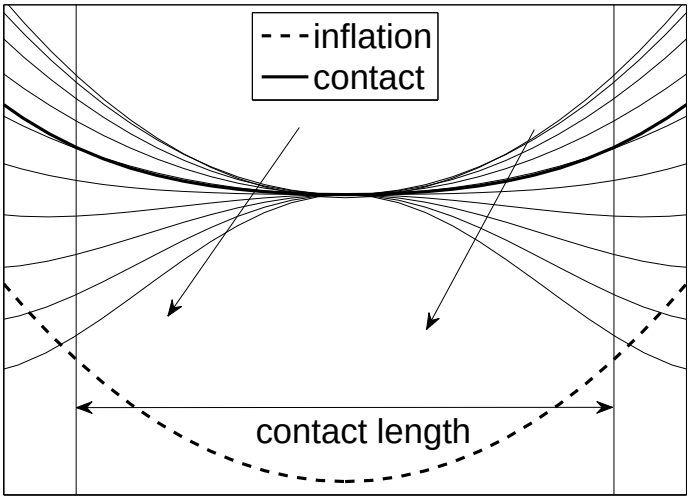

(a) $10mm$

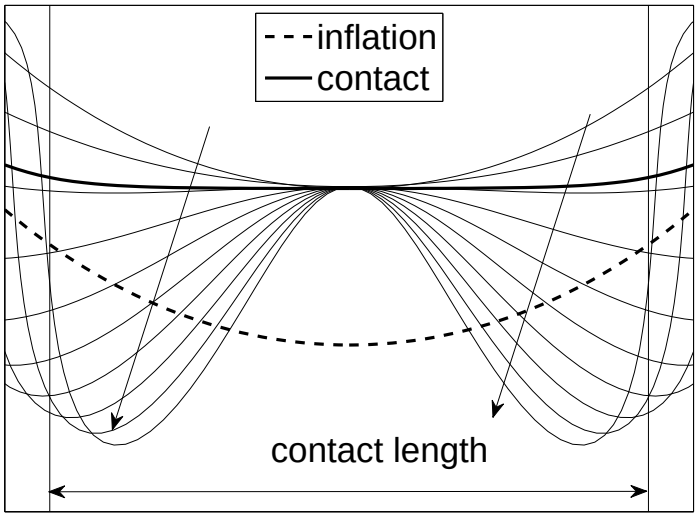

(b) $50mm$

Figure 4.29 – The comparison of the deformed belt shape with the $n = 1$ to $n = 10$ radial mode shapes, in the low and high deformation cases.

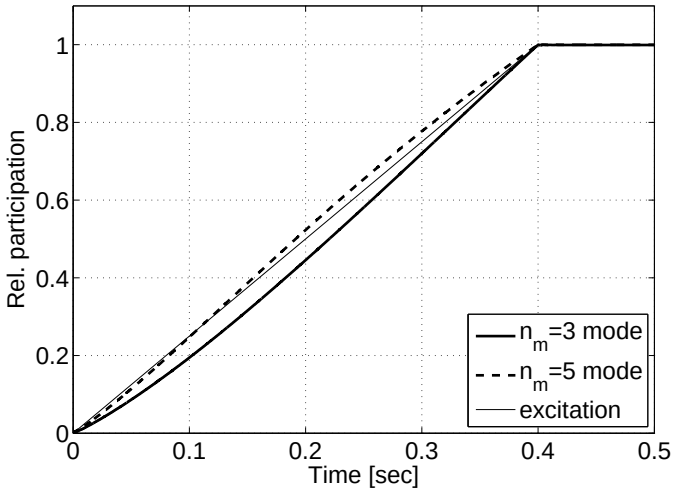

Figure 4.30 – The normalised participation history of the $n_m = 3$ and $n_m = 5$ radial modes.

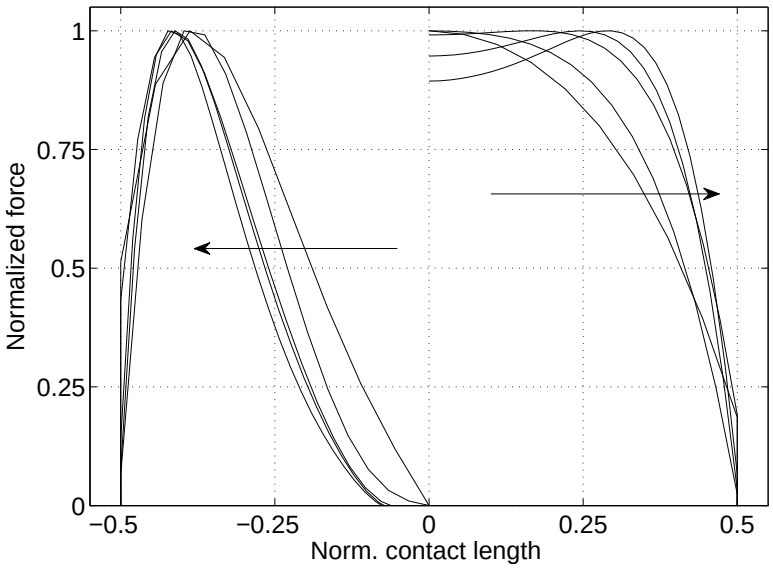

Figure 4.31 – The effect of the deformation on the distribution shape, under the non linear sidewall assumption. (the arrows indicate the deformation increase)

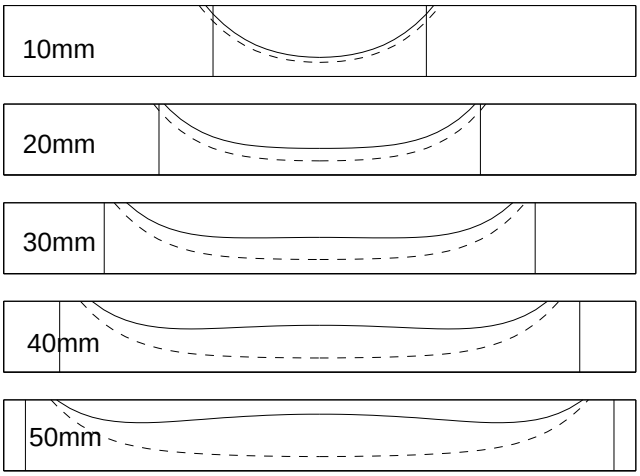

Figure 4.32 – The belt deformation along the contact in the linear and the non linear sidewall cases.

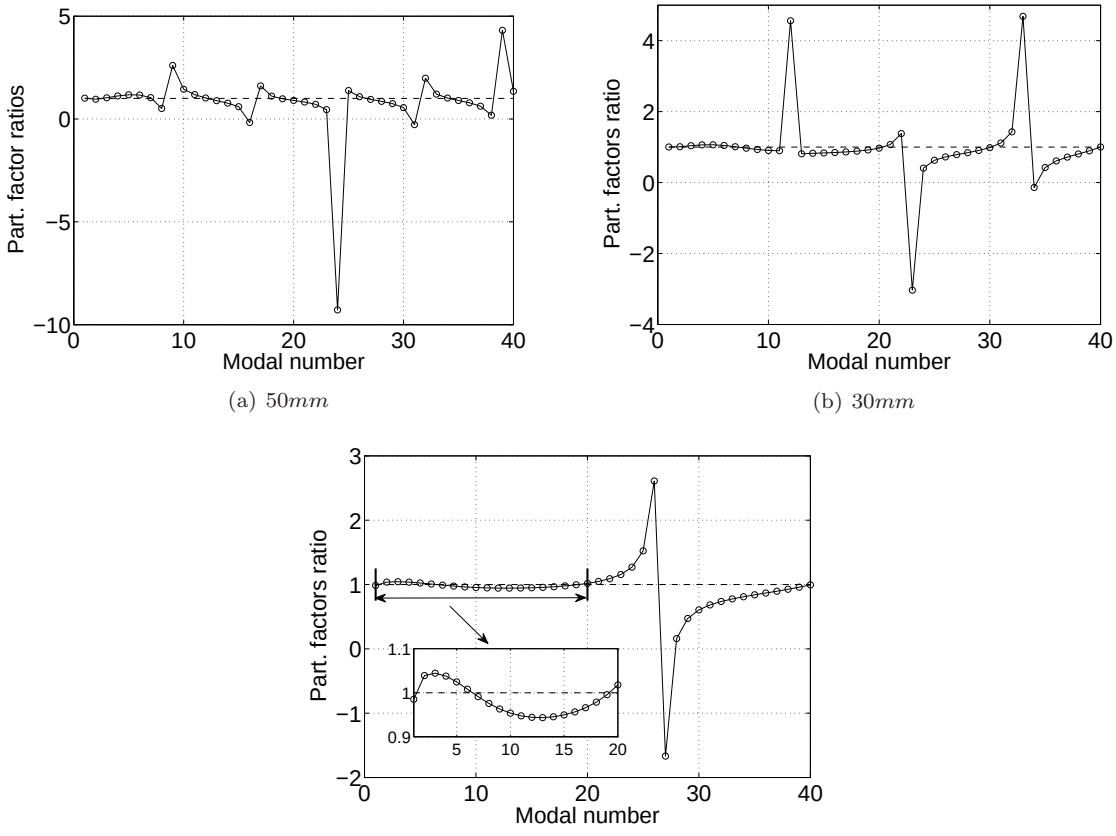

(a) $50mm$

(b) $30mm$

(c) $10mm$

Figure 4.33 – The modal participation factors ratios of the non linear sidewall and the linear sidewall models.

Frequency range [Hz]	Radial modes	Tangential modes
110	2	0
130	3	0
150	4	0
180	5	0
400	11	0
600	15	0
800	18	1
1000	21	2

Table 4.2 – Modal range - frequency range correspondence.

excitation. Three deformation levels are examined: 10, 30 and 50mm. The buckling behaviour of the non linear sidewall intensifies the radially inwards belt deformation (evident in all cases of fig.4.32). The profound radial compliance is reflected on the higher participation values of the modes with modal numbers from $n = 2$ to $n = 6$ and the decreased participation of the $n = 7$ to $n = 19$ ones for the 10mm case (fig.4.33(c)), while similar changes (successive zones of participation increase and decrease) may be also identified in the low modal range of the other deformation cases (figs. 4.33(a) and 4.33(b)). The radical ratio deviation that follows the development of these zones corresponds to the generation of the central concave deformation pattern and the accompanying shape effects in the surrounding area. Further similar ratio anomalies are repeated at higher modal numbers.

Interestingly, the effect of the concave shape formation is associated with higher modal number mode shapes in the low deformation case. The first ratio peak, is identified in the $n = 26$ mode (1401HZ) region in the 10mm case. The extension of the concave formation to a larger area around the contact centre, as the load level increases, results in the respective ratio peak of lower modal number modes. The first peak value in the = 30mm case corresponds to the $n = 12$ (570Hz) mode, while in the 50mm case the $n = 9$ (239Hz) mode exhibits a similar radical deviation. It is evident that the accurate representation of the contact behaviour associated with the non linear sidewall mechanism necessitates a broader modal range in the low deformation cases, where, though, the concave pattern of the belt deformation is moderate. The above conclusion is in agreement with the previously identified correspondence between the load level and the excited modal range of the linear model. In general, the load increase magnifies the dimensions of the portion of the belt circumference which is affected by the imposed deformation. In result, the belt shape correlates better with the waveform predicted by a lower order mode shape, as its deformation pattern covers an increased circumferential length.

4.4.4 The effect of the modal reduction on the simulation accuracy

Having identified the modal range breadth that is able to capture the contact behaviour of the belt and the associated deformation phenomena, the effect of the modal reduction on the simulation accuracy may be investigated. Such effects will be examined in terms of both total load prediction and contact pressure distribution shape and magnitudes. The correspondence between the frequency and the modal range of the modal basis, resulting from the application of various degrees of reduction is summarised in table 4.2 .

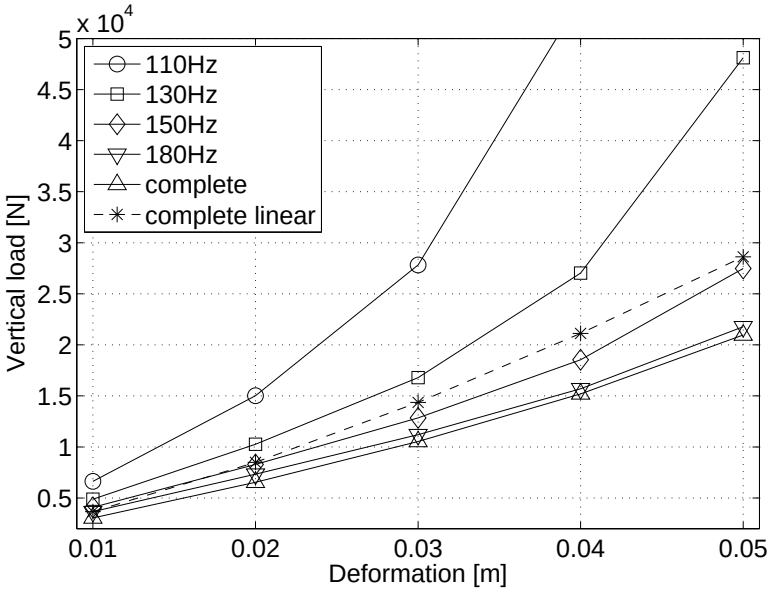

Figure 4.34 – The total vertical load as a function of the imposed deformation for various degrees of reduction.

Tyre contact stiffness

The total vertical load predicted by the non linear sidewall model is presented in fig. 4.34 as a function of the imposed deformation, for various levels of the modal reduction. Obviously, the shorter the frequency range, the stiffer the predicted contact behaviour becomes, as the deduction of modes corresponds to the decrease of the compliance capability of the model. Characteristically, the contact behaviour for a frequency range narrower than $150Hz$ is stiffer than the one of the linear sidewall model (also presented in fig.4.34 for comparison reasons). In other words, the effect of the modal reduction to the three first radial and breathing modes cancels out the buckling sidewall effect, in term of total contact stiffness.

As it is expected, the deviation of the total load from the one predicted by the complete model increases with the level of deformation. Examining, though, the percentage deviation in each deformation case as a function of the reduction degree (fig. 4.35), a different pattern is observed. Starting from an excessive degree of reduction, an extremely narrow frequency range ($150Hz$- 2 radial modes) results in a higher load overestimation in the high deformation case than in the low deformation one (350% in the $50mm$ case compared to 120% in the $10mm$ case). The deviation associated with the high load case, though, decreases radically. For a frequency range limit between $150Hz$ and $300Hz$, a larger deviation is predicted for the $10mm$ deformation compared to the $50mm$ one. It is obvious that the broader modal range which is associated with the low deformation level(fig.4.28(a)), results in a higher computational error if a common degree of reduction is applied to all the deformation cases. The examination of the contact stiffness supports the previously drawn conclusion that the lower the induced load or deformation level, the broader is the sufficient modal range of the model for the achievement of a certain accuracy degree.

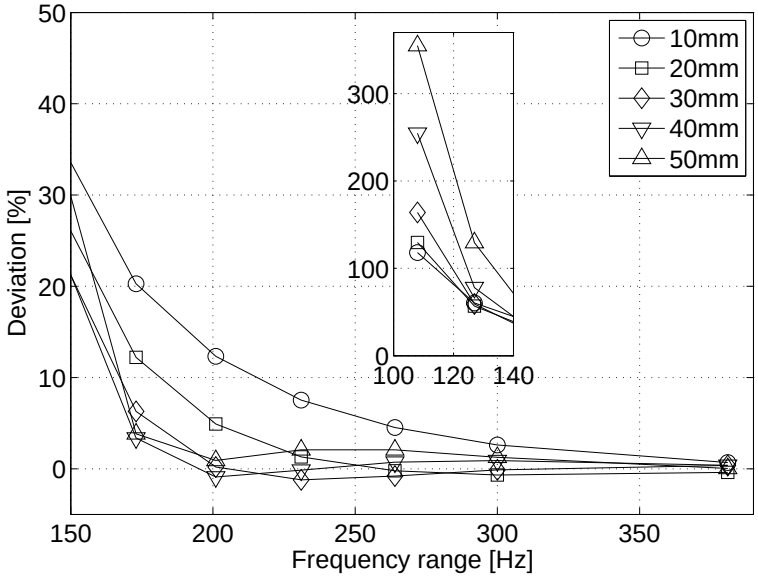

Figure 4.35 – The load percentage deviation from the complete model as a function of the frequency range of the solution.

Vertical contact force distribution

Moving the discussion from the effect of the modal reduction on the total contact stiffness to the force distribution along the contact length, the vertical force fields for 4 reduced models are presented in figs. 4.36(a) and 4.36(b) for the $10mm$ and the $50mm$ deformation cases respectively. The distributions predicted by the complete model is also plotted for comparison reasons. Starting from the first case, it may be observed that the reduction results in an overestimation of the force values in the central zone and a respective underestimation in the outer zones. This behaviour may be physically justified by the incapability of the prediction of the belt shape conformation to the plane road surface. As the force values in the central contact area are much higher than the ones at the edges of it, the effect of the overestimation is the predominant one leading to the similar effect on the total contact stiffness. The shape effect of the reduction in the high deformation case is more complicated because of the profound concave formation. The reduced models underestimate the force values at the contact edges, or even predict a shorter contact area ($400Hz$ case). Moving towards the centre of the contact, though, the deviation pattern depends on the actual model and the possible correlation between the deformed belt at the particular position and the mode shape waveforms.

The examination of the reduction effect through the percentage force deviation from the complete model along the contact (fig. 4.37) reveals its agreement with the above enounced association between the degree of accuracy achieved by a reduced model and the level of deformation. As in both cases equally reduced models are examined, the percentage deviation in the high deformation case is lower, ignoring the local effect of the contact length variation. Accordingly, the possible requirement of a 5% maximum percentage deviation along the contact is fulfilled by a $600Hz$ range of solution in the $50mm$ deformation case and by a$1000Hz$ one in the $10mm$ case.

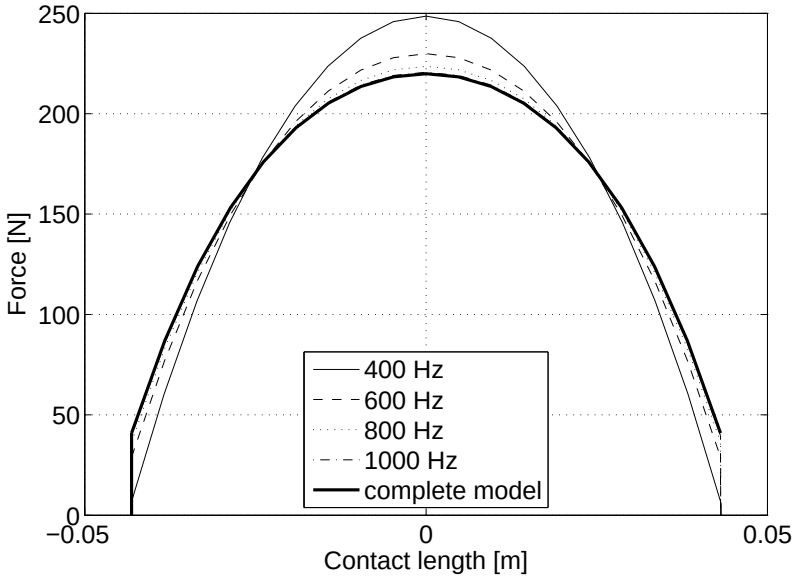

(a) $10mm$

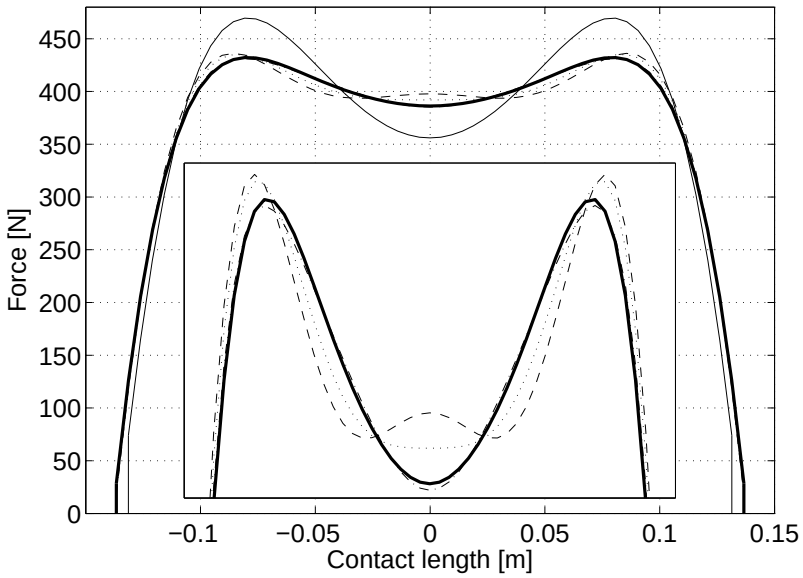

(b) $50mm$

Figure 4.36 – The vertical force distribution for various levels of modal reduction.

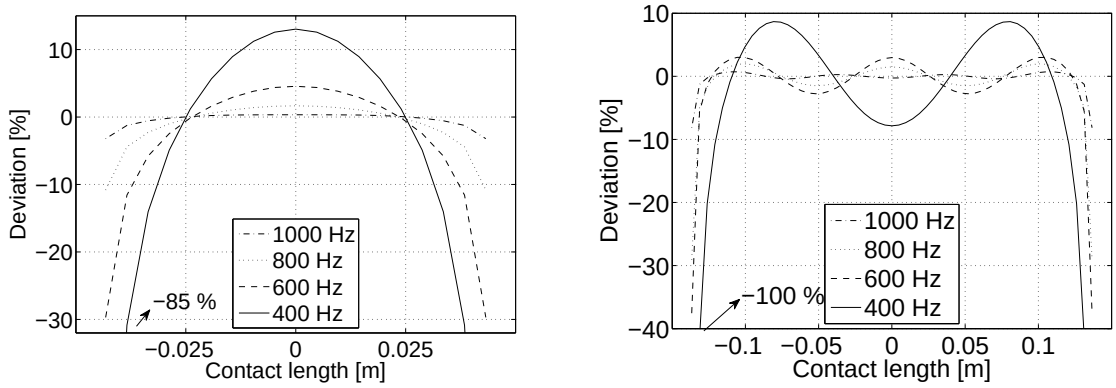

(a) $10mm$ (b) $50mm$

Figure 4.37 – The deviation of the vertical pressure distribution from the complete model corresponding one, for various levels of modal reduction.

Horizontal contact force distribution

The effect of the modal reduction on the horizontal forces distribution is presented in fig. 4.38 for the deformation cases examined in the respective vertical cases. Underestimation at the edge of the contact transforming into an overestimation is the observed pattern in the low deformation case, similarly to the vertical deviation. Once again, no certain deviation pattern can be identified in the high deformation case, close to the central area which is affected by the concave formation. In the outer zone, the deviation pattern follows the one of the vertical case.

4.4.5 The effect of the modal reduction on the computational efficiency

Obviously, the computational load associated with the contact simulation algorithm exhibits a direct dependency on the discretisation degree. Two basic mechanisms contribute to this dependency. Firstly, the dimension of the belt related vectors (excitation, response and mode shapes) is equal to the total degrees of freedom. Having assigned two degrees to each of the belt nodes, the discretisation effect on the load associated with the calculation of the structural phenomena becomes obvious. The computational load increases further in the non linear sidewall case, where for each of the nodes the string geometry has to be derived by an iteration method. Secondly, the number of tread elements lying in the contact area depends on the degree of discretisation and as it is presented in fig. 4.39(a) the contact elements increase proportionally to the number of nodes. In this case, the computational load is related to the calculation of the tread response and the contact reaction forces. The combined effect of the discretisation degree on the relative computational time is presented in fig. 4.39(b) for a constant deformation and modal basis breadth. The computational time, which is regarded to be the computational load index, follows an exponential increase pattern with the number of nodes.

The modal reduction method is called to modulate the computation load, independently from the above discretisation effects. The computational time of the same contact calculation for a constant discretisation degree is presented in fig. 4.40. The time increases exponentially also with the frequency range, and characteristically the solution time of the complete model is almost 100 time longer than the $1000Hz$ reduced

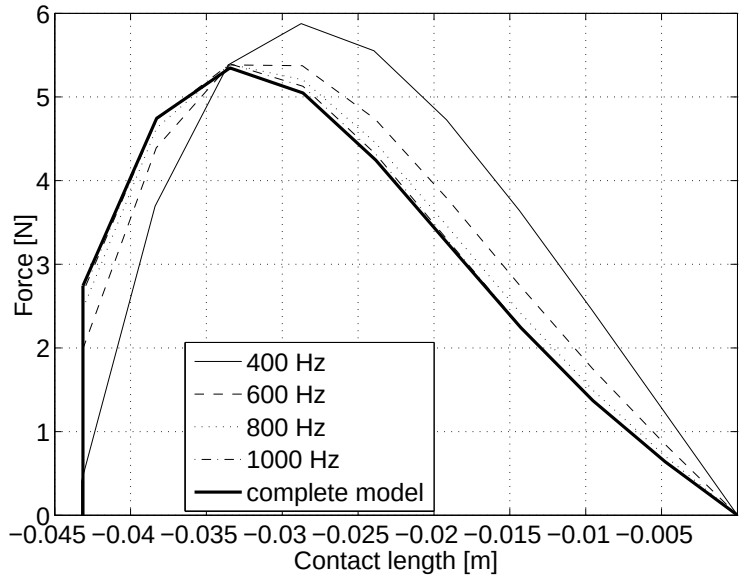

(a) $10mm$

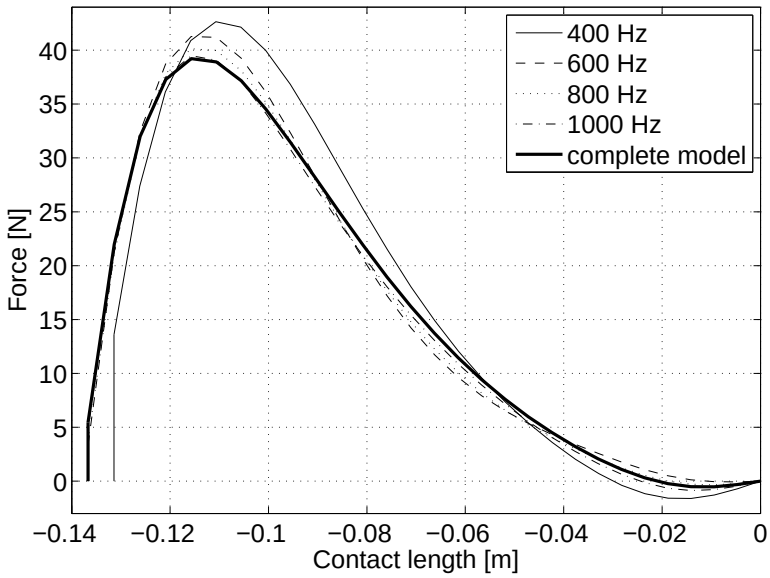

(b) $50mm$

Figure 4.38 – The horizontal force distribution for various levels of modal reduction.

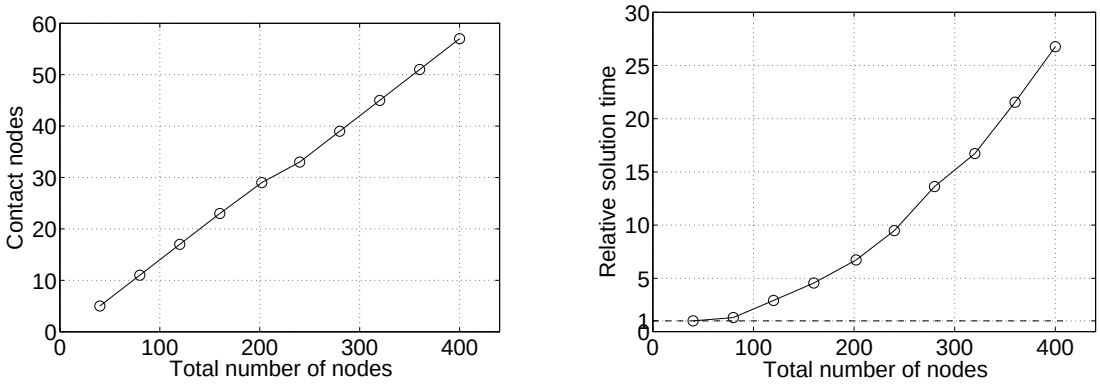

(a) The number of contact elements as a function of the total number of nodes.

(b) The relative computational time as a function of the total number of nodes.

Figure 4.39 – The discretisation effect on the computational load.

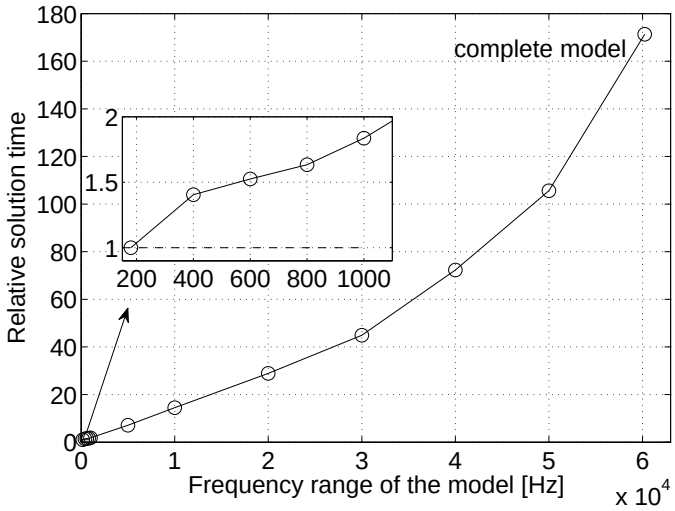

Figure 4.40 – The relative computational time as a function of the frequency range of the model.

model. The non linear increase of the calculation time does not result only from the higher number of the participating modes, but also from the requirement for the application of shorter time step to the numerical solution, which is associated with the presence of higher natural frequencies. Focusing in the reduced models which were examined in the previous section, the transition from the $180Hz$ (6 radial and 1 tangential mode) model to the $1000Hz$ (22 radial and 3 tangential modes) one magnifies the computational time by a factor of 1.8.

4.5 Summary of the chapter

A contact simulation algorithm was developed, able to represent the transient interaction phenomena between the tyre deformation and the tread frictional slip. The tyre tread was modelled as a discretised foundation of contact elements, each of them composed by a radial and a tangential Kelvin-Voigt element. The tread model

was found able to simulate the transient adhesion or slip shear motion, as imposed by the belt response, the frictional potential of the road and the viscoelastic properties of the elements.

The tread foundation was combined with the analytical ring on elastic foundation model, but here a space discretised form of this model was developed, in order to be coupled with the discretised tread foundation. The transient deformation of the belt structure was calculated in the modal-time domain, using as variables the participation factors of the modes in the response. The tread-road interaction was calculated in the space-time domain, as the non linear character of the friction force development prevents a common application of a modal expansion method on both the belt and the tread models.

The contact behaviour of the model was enhanced by the addition of a discretised foundation of inextensible string elements capturing the shape (buckling) non linear contact effects of the sidewall. The general contact behaviour of the model, in terms of total stiffness, was examined together with the effects of the imposed deformation and the inflation pressure on the predicted contact forces distribution fields. The model was found capable of predicting the increasing with the load contact stiffness, the sub-proportional increase of the contact pressure values with the load and their direct dependency on the inflation pressure. The typical evolution of the distribution shape from a parabolic into a trapezoidal one was acquired, while the non linear sidewall was found to support the formation of a radially inwards central section of belt deformation pattern, resulting in a corresponding central concave shape of the vertical pressure distribution.

Two contradicting to each other contact deformation mechanisms of the belt were identified: the solid disk-like one and the bending one supported by the relaxation of the, inflation-induced, radial stress. The first mechanism results in a horizontally expanding belt as its circular shape conforms to the plane surface, while the second one results in a horizontally shrinking belt as imposed by the formation of the concave pattern. The relative to each other degree of conformation to each of the mechanisms is depicted on the horizontal contact stress distribution of the tyre and associates it with the belt mechanical properties. The possible development of a radially inwards belt deformation, depending on the tyre properties, was found to have a crucial role in the direction of the horizontal contact pressure field and based on that the mechanism of interaction between the belt deformation, the friction potential and the resulting horizontal pressure field was identified.

Given that the modal reduction method is crucial for the accomplishment of an acceptable computational efficiency of the model, the modal content of the belt deformation was investigated as a function of the load conditions. The contact participation of the modes, of both the radial and tangential groups, decreases with the modal number, while the participation of the tangential modes is much lower than the participation of the radial ones. This pattern validates the applicability of a reduced model, based on the omission of the high frequency modes, for the simulation of the contact behaviour of the tyre. In parallel, the association of the contact deformation with the low and medium frequency range modes highlights the contribution of a number of physical properties (sidewall stiffness, inflation pretension, bending mechanism) and strain patterns (coupled radial and tangential deformations) that define the ring modal behaviour across the particular range.

The actual effect of the modal reduction on the computational accuracy was further investigated. The necessary modal range for the achievement of a certain degree of accuracy was found to decrease with the deformation level, as the extension of the contact induced deformation to an increasing portion of the belt circumference can be described by lower modal number mode shapes. In general the modal range was found

to be a function of both the circumferential length associated with the deformation response and the shape forms (e.g. the concave one) which are to be represented. For the contact with a plane road surface and including the prediction capability of the concave pattern, a $1000Hz$ model was found to offer a satisfactory accuracy for the typical belt and tread properties used in this study.

The participation of the modes corresponding to the contact equilibrium can be associated with the optimum representation of the belt deformation shape by the superposition of the mode shapes. In result, the solution accuracy depends on the extent to which the linear combination of the participating in the solution mode shapes is able to describe the belt conformity and the variations in its equilibrium deformation shape. The above examination of the tyre contact behaviour through the excitation of selected modes, though, is not a pure shape correlation process. It should be reminded that the contact equilibrium has been established through a contact dynamic process. The increasing with the modal number frequency corresponds to a higher energy level associated with the deformation described by the mode shape of the mode. In result, the higher the modal number of a mode the higher is the energy required for the participation of it to the belt response.

The above issue becomes more complicated when the modal participation factors are investigated in the case of higher frequency transient tyre operating conditions and the respective sufficient modal range is to be captured. The transient nature of the excitation magnifies the participation factor of certain modes, the natural frequency of which lies in the area of the excitation frequency. Furthermore, the effect of the damping coefficient of each mode is crucial for the derivation of the structural response. The modal damping coefficients should ideally be experimentally determined or derived through a space distribution model corresponding to a physical dissipation mechanism (as presented in section 3.10 of chapter 3), as the measurable modal range is usually shorter than the appropriate one for the modal expansion of the tyre model ($\simeq 1000Hz$). The effect of damping on the transient tyre performance and the possible differences between the modal range associated with the tyre contact behaviour and the transient rolling one will be examined in chapter 5, where the modelling of the rolling contact behaviour of the tyre will be investigated.

Chapter 5

The simulation of the transient rolling and slipping conditions

In this chapter, the tyre-road contact modelling approach (chapter 4) will be further developed so that transient rolling operating conditions may be accounted for, including the slipping behaviour and the shear force generation. The simulation of the physical mechanism of interaction between the tyre structural characteristics and the friction force generation along the contact area is the obvious advantage of the method.

The calculation of the belt deformation in the modal-time domain is retained and offers, apart from the apparent computational advantage, the modal participation content of the tyre response under usual operating conditions. Moreover, the method may offer an insight into the effect of the model's physical properties on its physical behaviour and performance through the sensitivity of the excited modes to them. The effect of the physical properties on the tyre modal characteristics has already been presented in section 3.4.1of chapter 3; the predicted modal range (as a function of the modal number) may be decomposed in successive sectors, and a physical property was found to have a dominant influence over each of them. Here, the variation in the modal participation factors from the static contact ones will be proposed as a method for the study of the above interaction mechanism.

Initially, the theoretical background of the simulation of transient rolling conditions will be extensively presented. This is the final step of the ring model transformation from a frequency domain modal model into a fully transient time domain tyre model, able to simulate both vibrational and frictional phenomena and to be embedded in a vehicle dynamics model. The simulation of large displacement conditions (in comparison to the small displacement modal deformation) will be identified as the main challenge for this transformation and a mathematical method for its overcome will be proposed.

Later, the model will be used for the study of the launch process and the effect of structural characteristics (damping) and interface properties (friction) on the dynamic transformation of the horizontal motion to the rotational one (and vice versa) will be discussed. Finally, a method for the application of steady state kinematic and slip operating conditions to the model will be prescribed and the predicted tyre shear force as a function of the macroscopic slip will be presented, together with the conclusions that may be drawn from its pattern.

5.1 The simulation of the large displacement conditions

The major conceptual difference between the simulation of the tyre contact and the tyre rolling and translational operating conditions, is that in the second case the displacement of the belt nodes,a combination of the tyre deformation and translation, cannot be regarded as small. In the case of the contact, though, assuming that it is kinematically imposed suspending the wheel degrees of freedom and moving the road surface, the displacement of the belt nodes is small and purely induced by its deformation. The latter, allowed for the application of a modal based method, given that the modal expansion of any structure is accomplished under the small deformation assumption. Obviously, this assumption is not valid in the general rolling case, as the wheel participates in the motion.

The capability to simulate transient large displacement operating conditions, imposed not kinematically but dynamically by external excitations, is a major enhancement of the proposed approach over existing modal based models and its theoretical background will be presented in detail. Moreover, the method could be applied on the simulation of any dynamic system which combines translational and deformational response. Firstly, the approach will be presented for a simple, two degrees of freedom, model and later will be applied to the tyre structure.

5.1.1 The two mass system

A simple two degrees of freedom system is presented in fig. 5.1. A respective mass is assigned to each of them and their dynamic interaction is in general prescribed by a stiffness and a viscous damping element, although the effect of the second one will be neglected in the following analysis. The system's motion is described by the following equations:

$$m_1 \cdot \ddot{x}_1 + k(x_1 - x_2) = F_1 \tag{5.1a}$$

$$m_2 \cdot \ddot{x}_2 + k(-x_1 + x_2) = F_2 \tag{5.1b}$$

where:

$m_1,\ m_2$	the mass assigned to each of the DOFs
$x_1,\ x_2$	the displacements of the DOFs
k	the internal stiffness of the system
$F_1,\ F_2$	the external excitation forces

The system may be loosely regarded as representing the wheel-belt interaction (m_1 and m_2 respectively) in a simplified way, along one dimension and neglecting the flexural deformation of the belt, while, the stiffness element accordingly represents the sidewall stiffness. Although the expression of the displacements in the stationary system (using their absolute values) may be used in the rectilinear motion case, it is not viable in the rotational motion one, given that a consistent from of the globally expressed equations of motion could not be retained. Apparently, a relative to each other expression of the equations has to be used. An obvious approach, which would retain the information of the global position of the system, could be the expression of the wheel (m_1) displacement in global (absolute) terms and the expression of the belt (m_2) response in a form relative to that. Designating the relative displacement as $\Delta x = x_2 - x_1$, the equations of

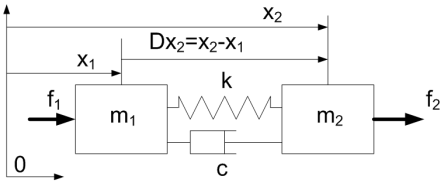

Figure 5.1 – The two degrees of freedom system.

motion are rewritten using x_1 and Dx as their variables:

$$m_1 \cdot \ddot{x}_1 - k \cdot \Delta\dot{x} = F_1 \tag{5.2a}$$

$$(m_2 - m_1)\ddot{x}_1 + m_2 \cdot \Delta\ddot{x} + 2 \cdot k \cdot \Delta x = F_2 - F_1 \tag{5.2b}$$

where $\Delta\dot{x}$ and $\Delta\ddot{x}$ are respectively the relative to m_1 velocity and acceleration of m_2:

$$\Delta\dot{x} = \dot{x}_2 - \dot{x}_1 \tag{5.3}$$

$$\Delta\ddot{x} = \ddot{x}_2 - \ddot{x}_1 \tag{5.4}$$

Obviously, the two forms of the system's equations of motion (5.1 and 5.2) are equivalent in physical terms.As the followed approach is based on the modal expansion of the system, possible differences in the modal basis, as emerging from the two forms, should be investigated. Starting from the global one, the equations are rewritten in a matrix form:

$$\begin{bmatrix} m_1 & 0 \\ 0 & m_2 \end{bmatrix} \cdot \begin{bmatrix} \ddot{x}_1 \\ \ddot{x}_2 \end{bmatrix} + \begin{bmatrix} k & -k \\ -k & k \end{bmatrix} \cdot \begin{bmatrix} x_1 \\ x_2 \end{bmatrix} = \begin{bmatrix} F_1 \\ F_2 \end{bmatrix} \tag{5.5}$$

$$\Rightarrow \mathbf{M} \cdot \ddot{\mathbf{x}} + \mathbf{K} \cdot \mathbf{x} = \mathbf{F} \tag{5.6}$$

where:

- **M** the mass matrix
- **K** the stiffness matrix
- **F** the excitation vector
- **x** the displacements' vector

The two natural frequencies of the system are calculated as:

$$\omega_{1,2} = \begin{cases} 0 \\ \sqrt{\dfrac{k}{m_1} + \dfrac{k}{m_2}} \end{cases} \tag{5.7}$$

and the corresponding mode shape matrix is:

$$\tilde{\mathbf{\Psi}} = \begin{bmatrix} \mathbf{\Psi_1} & \mathbf{\Psi_2} \end{bmatrix} = \begin{bmatrix} 1 & 1 \\ 1 & -\dfrac{m_1}{m_2} \end{bmatrix} \tag{5.8}$$

The first mode corresponds to the common, non-deformational, displacement of the two DOFs, rigid mode, while the second mode describes their out of phase, deformational, response (flexural mode). Obviously, the above eigenvectors matrix is a complete modal basis of the system and diagonalises the inertia ($\mathbf{M}$) and stiffness ($\mathbf{M}$) matrices of it:

$$\mathbf{M}^m = \tilde{\mathbf{\Psi}}^T \cdot \mathbf{M} \cdot \tilde{\mathbf{\Psi}} \tag{5.9}$$

$$\mathbf{K}^m = \tilde{\mathbf{\Psi}}^T \cdot \mathbf{K} \cdot \tilde{\mathbf{\Psi}} \tag{5.10}$$

where $\mathbf{M}^m$ and $\mathbf{K}^m$ are the diagonal matrices of modal mass and modal stiffness respectively. Applying the same process to eqns. 5.2, it may be written:

$$\begin{bmatrix} m_1 & 0 \\ m_2 - m_1 & m_2 \end{bmatrix} \cdot \begin{bmatrix} \ddot{x}_1 \\ D\ddot{x} \end{bmatrix} + \begin{bmatrix} 0 & -k \\ 0 & 2 \cdot k \end{bmatrix} \cdot \begin{bmatrix} x_1 \\ Dx \end{bmatrix} = \begin{bmatrix} F_1 \\ F_2 - F_1 \end{bmatrix} \tag{5.11}$$

$$\Rightarrow \mathbf{M}_{rel} \cdot \ddot{\mathbf{x}}_{rel} + \mathbf{K}_{rel} \cdot \mathbf{x}_{rel} = \mathbf{F}_{rel} \tag{5.12}$$

The application of the modal expansion method to the above matrix equation returns the same natural frequencies with eqn. 5.6 (given by eqn. 5.7) and the following eigenvectors:

$$\tilde{\mathbf{\Psi}}_{rel} = \begin{bmatrix} \mathbf{\Psi}_1^{rel} & \mathbf{\Psi}_2^{rel} \end{bmatrix} = \begin{bmatrix} 1 & 1 \\ 0 & -1 - \dfrac{m_1}{m_2} \end{bmatrix} \tag{5.13}$$

which obviously describe the same deformation patterns with the ones described by eqn. 5.8,from which they could be derived applying the transformation $Dx = x_2 - x_1$. Nevertheless, there is a significant difference between the two forms of the modal basis. The diagonalisation of the matrices corresponding to the relative form:

$$\mathbf{M}_{rel}^m = \tilde{\mathbf{\Psi}}_{rel}^T \cdot \mathbf{M}_{rel} \cdot \tilde{\mathbf{\Psi}}_{rel} \tag{5.14}$$

$$\mathbf{K}_{rel}^m = \tilde{\mathbf{\Psi}}_{rel}^T \cdot \mathbf{K}_{rel} \cdot \tilde{\mathbf{\Psi}}_{rel} \tag{5.15}$$

fails, as the emerging ones are not diagonal. The arbitrary response of the system, when it is described by the relative equations of motion, cannot be decomposed in the excitation of the distinctive modes. Moreover, as the rigid mode ($\mathbf{\Psi}_1$) cannot be decoupled from the flexural one ($\mathbf{\Psi}_2$), the response cannot be decomposed in a translational motion of the mass m_1 (which would be calculated in global coordinates in the space domain), and a relative to it deformation of the mass m_2 (which would be calculated in relative coordinates). Applying the above conclusion to the wheel-belt case, the system's response cannot be decoupled in the wheel's displacement and the, relative to that, belt deformation.

The above barrier is overcome by the adoption of a new, moving, system of reference, which does not

necessarily coincide with the wheel centre and an assigned to that degree of freedom (x_s) prescribes its response. Using that response as a reference value, the relative response of the system's degrees of freedom may be written as:

$$\Delta x_1^s = x_1 - x_s \tag{5.16a}$$

$$\Delta x_2^s = x_2 - x_s \tag{5.16b}$$

The translational motion of the system (x_s degree of freedom) is defined by the total inertial property of the system:

$$\sum m \cdot \ddot{x}_s = \sum f \Rightarrow (m_1 + m_2)\ddot{x}_s = F_1 + F_2 \tag{5.17}$$

and corresponds to the rigid body response of the system. Subtracting the above equation from the initial equations of motion (eqns. 5.1) and substituting the expressions 5.16 to them, it may be written:

$$m_1 \cdot \Delta\ddot{x}_1^s + k \cdot (\Delta x_1^s - \Delta x_2^s) = -F_2 + m_2 \cdot \ddot{x}_s \tag{5.18a}$$

$$m_2 \cdot \Delta\ddot{x}_2^s + k \cdot (\Delta x_2^s - \Delta x_1^s) = -F_1 + m_1 \cdot \ddot{x}_s \tag{5.18b}$$

The relative deformation vector is defined as:

$$\mathbf{\Delta x}^s = \begin{bmatrix} \Delta x_1^s \\ \Delta x_2^s \end{bmatrix} \tag{5.19}$$

and respectively the system of the equations of motion may be written as:

$$\begin{bmatrix} m_1 & 0 \\ 0 & m_2 \end{bmatrix} \cdot \begin{bmatrix} \Delta\ddot{x}_1^s \\ \Delta\ddot{x}_2^s \end{bmatrix} + \begin{bmatrix} k & -k \\ -k & k \end{bmatrix} \cdot \begin{bmatrix} \Delta x_1^s \\ \Delta x_2^s \end{bmatrix} = - \begin{bmatrix} F_2 \\ F_1 \end{bmatrix} + \ddot{x}_s \cdot \begin{bmatrix} m_2 \\ m_1 \end{bmatrix} \tag{5.20}$$

$$\Rightarrow \mathbf{M} \cdot \mathbf{\Delta\ddot{x}}^s + \mathbf{K} \cdot \mathbf{\Delta x}^s = \begin{bmatrix} F_1 \\ F_2 \end{bmatrix} - \begin{bmatrix} \sum F \\ \sum F \end{bmatrix} + \ddot{x}_s \cdot \quad \begin{bmatrix} \sum m \\ \sum m \end{bmatrix} - \begin{bmatrix} m_1 \\ m_2 \end{bmatrix} \Bigg) \tag{5.21}$$

Substituting eqn. 5.17 to the above, it is derived:

$$\mathbf{M} \cdot \mathbf{\Delta\ddot{x}}^s + \mathbf{K} \cdot \mathbf{\Delta x}^s = \mathbf{F} - \ddot{x}_s \cdot \begin{bmatrix} m_1 \\ m_2 \end{bmatrix} \tag{5.22}$$

The left part of the above equation is identical to the left part of the matrix form of the initial system of the equations of motion (eqn. 5.6), if the vector of the global degrees of freedom ($\mathbf{x}$) is substituted by the corresponding relative one ($\mathbf{\Delta X}^s$). Consequently, the application of the modal expansion method results in the same natural frequencies and modal basis with the global form of the system, which are obviously able to diagonalise the system's matrices and to decouple the corresponding modes. The right part of eqn.5.22 is derived from the excitation vector and the acceleration of the system, calculated by eqn. 5.17.

In general,the modal expansion method [169, 250] imposes the substitution of the degrees of freedom vector ($\mathbf{\Delta X}^s$) by the product of the eigenvectors matrix ($\tilde{\mathbf{\Psi}}$) and the vector of the modal participation

factors ($\tilde{\eta}$):

$$\mathbf{\Delta X}^s = \tilde{\mathbf{\Psi}} \cdot \tilde{\eta} \tag{5.23}$$

while the matrix form of the equations of motion (eqn. 5.22) is multiplied with the transpose of the eigenvectors matrix:

$$\tilde{\mathbf{\Psi}}^T \cdot \mathbf{M} \cdot \tilde{\mathbf{\Psi}} \cdot \ddot{\tilde{\eta}} + \tilde{\mathbf{\Psi}}^T \cdot \mathbf{K} \cdot \tilde{\mathbf{\Psi}} \cdot \eta = \tilde{\mathbf{\Psi}}^T \quad \mathbf{F} - \ddot{x}_s \cdot \begin{bmatrix} m_1 \\ m_2 \end{bmatrix} \Bigg) \tag{5.24}$$

$$\Rightarrow \mathbf{M}^m \cdot \ddot{\tilde{\eta}} + \mathbf{C}^m \cdot \tilde{\eta} = \mathbf{\Psi}^T \quad \mathbf{F} - \ddot{x}_s \cdot \begin{bmatrix} m_1 \\ m_2 \end{bmatrix} \Bigg) \tag{5.25}$$

Rewriting the right part of the above equation only for the rigid mode, it may be derived:

$$\begin{bmatrix} 1 & 1 \end{bmatrix} \quad \begin{bmatrix} F_1 \\ F_2 \end{bmatrix} - \ddot{x}_s \cdot \begin{bmatrix} m_1 \\ m_2 \end{bmatrix} \Bigg) = \sum f - \ddot{x}_s \cdot \sum m \equiv 0 \tag{5.26}$$

Apparently, the right part of eqn. 5.25 cancels out the corresponding to the rigid mode excitation of the system. Its rigid mode motion inheres solely in the time domain inertial equation of motion (eqn. 5.17).

Summarising the above, the described approach addresses the problem associated with the application of the modal expansion method on the relative form of the system's equations of motion, which is necessary for the capture of the non linear large displacements such as the ones imposed by the rotation. Instead of expressing the response of the system's degrees of freedom as relative values to the global displacement response of one of them, an additional degree of freedom is introduced, associated with the global rigid mode motion of the whole system and controlled by the total inertia of it. A moving system of reference is accordingly introduced and the system'e equations of motion are rewritten according to that.Their homogenous form is similar to the one of their global expression and in return the modal characteristics remain unchanged, something that allows for the decomposition of the relative response in the participation of individual modes. The excitation, corresponding to the relative form of the equations, is calculated using the system's rigid acceleration. Under this approach, the rigid mode is deduced from the equations of motion of the system and is described solely by the inertial differential equation. Apparently, the total response (translational and deformational) of a degree of freedom is composed by the superposition of the system's translation, calculated in the space-time domain, and the relative flexural response, calculated in the modal-time domain.

5.1.2 The wheel-tyre system

The above method will be here applied to the wheel and belt system, starting from the remission of the suspension of the wheel degrees of freedom. The modal characteristics of the combined wheel and belt system have been presented in section 3.8 of chapter 3, but herein the same characteristics will capture the modal behaviour as expressed in the moving system of reference (xOy). This is enabled by the initial coincidence of the position of the system's origin with the respective one of the stationary system of reference and the wheel centre.

The in-plane displacement of the moving system, stated in the stationary system of reference (XOY), is described by three inertial differential equations (two for the in-plane translational motion and one for the rotational motion). The global position of the wheel and the belt nodes will be calculated by the

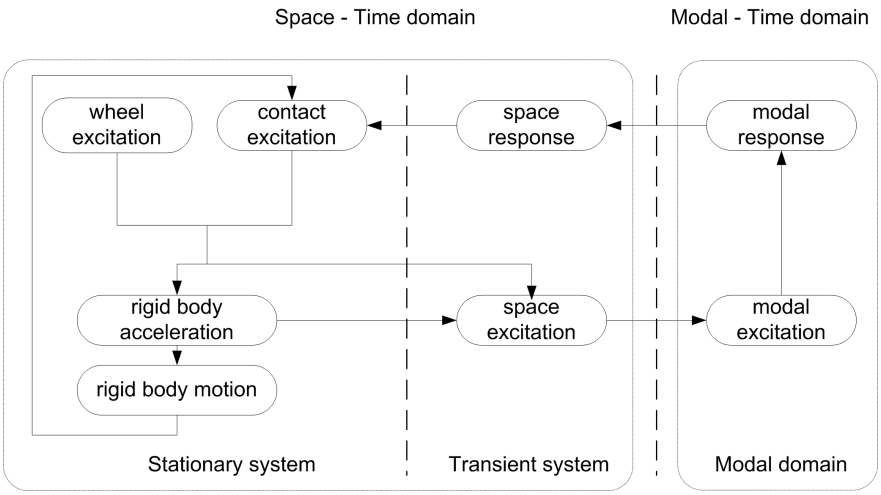

Figure 5.2 – An overview of the large displacement transient simulation algorithm.

superposition of their modal response on the system's motion. Using them, the contact interaction of the tyre with the road will be stated in the global stationary system, following the process described in chapter 4. The derived global forces and the total moment will be firstly used for the calculation of the global system's rigid motion; secondly, both global accelerations and external excitation forces will be transformed and projected to the transient system and the expression of the space domain local system excitation will be derived. The corresponding to that modal domain excitation will be calculated and the time domain differential equations of the modal participation factors will be numerically solved. The above procedure, summarised in fig. 5.2, is followed in every time step of the simulation, and will be analytically presented in the following.

The discretised belt and tread representations and the contact algorithm, developed in chapter 4, will be used for the investigation of the tyre-road interaction; in respect, the common stages of the modelling formulation will be excluded from the following analysis. A distributed external excitation will be used as a starting point for the analysis. In the linear sidewall case, which is initially examined, the excitation is composed by the contact forces, applied to the belt nodes, and the external forces and moment applied to the wheel.

It is worth mentioning that the incorporation of the effect of the inflation pressure through the superposition of an initial radius increase, instead of a steady radial excitation force, offers a significant computational advantage. The excitation vector incorporates non zero values only for the belt nodes which are in contact with the road and the computationally expensive transformation of the excitation forces from the stationary to the transient system of reference will only be accomplished for these nodes. The inflation pressure does not affect the wheel response, although it may be considered to be an external excitation, as the summation of the radial inflation forces along the wheel circumference results in a zero total resultant force.

The horizontal and vertical translational rigid body motion of the transient system of reference is de-

scribed by the following equations:

$$(m_w + m_b) \cdot \ddot{u}^s_X = \sum F_X \tag{5.27}$$

$$(m_w + m_b) \cdot \ddot{u}^s_Y = \sum F_Y \tag{5.28}$$

while the respective rotational rigid motion is given by:

$$(I_w + I_b) \cdot \ddot{u}^s_\Phi = \sum M \tag{5.29}$$

where:

$u^s_{X/Y}$	the horizontal/vertical displacement of the system
u^s_Φ	the rotational displacement of the system
$\sum F_{X/Y}$	the summation of the horizontal/vertical external excitation forces
$\sum M$	the summation of external moments of rotation
m_w	the wheel mass
m_b	the belt mass
I_w	the wheel moment of inertia
I_m	the belt moment of inertia

The total excitation force, along each of the dimensions, is composed by the contact forces applied to the belt nodes and the external forces applied to the wheel:

$$\sum F_{X/Y} = F^w_{X/Y} + \sum_{i=1,c_i=1}^{n_b} F^i_{tX/tY} \tag{5.30}$$

where:

$F^w_{X/Y}$	the horizontal/vertical external wheel forces
$F^i_{tX/tY}$	the horizontal/vertical contact forces applied to the ith node
n_b	the total number of nodes
c_i	the contact index of the ith node(c=0: no contact, c=1: contact)

The respective moment equation will be given at a later stage of the analysis, as its calculation necessitates the earlier calculation of the belt response.

In the preceding study of the modal and contact tyre behaviour (chapters 3 and 4 respectively), the centre of the fixed wheel was fixed at the origin of the stationary system of reference, an assumption followed here as an initial condition. As additionally the initial origin position and the orientation of the transient system coincide with the ones of the stationary system, the integration of the equations results in the global position and angular orientation of the transient system (respectively X_s, Y_s and Φ_s), measured in the stationary one.

Having calculated the rigid body motion of the system, the excitation is projected to the transient system:

$$\begin{bmatrix} F_{tx}^{i} \\ F_{ty}^{i} \end{bmatrix} = \mathbf{T}(\Phi_s) \cdot \begin{bmatrix} F_{tX}^{i} \\ F_{tY}^{i} \end{bmatrix} \tag{5.31}$$

while the projection of the wheel external excitation forces reads:

$$\begin{bmatrix} F_{x}^{w} \\ F_{y}^{w} \end{bmatrix} = \mathbf{T}(\Phi_s) \cdot \begin{bmatrix} F_{X}^{w} \\ F_{Y}^{w} \end{bmatrix} \tag{5.32}$$

where additionally $F_{tx/ty}^{i}$ are the contact forces applied to the ith belt node along the horizontal/vertical direction of the transient system and $F_{x/y}^{w}$ the external wheel forces along the same directions.

Prior to the composition of the space domain excitation vector in the transient system, the general form of the excitation and response vectors of the combined wheel and belt system will be discussed. The application of the modal expansion on the combined system has been presented in section 3.8 of chapter 3 and may be summarised in the following conclusions:

- The incorporation of the three wheel degrees of freedom (corresponding to the horizontal/vertical translations and the in-plane rotation) results in three distinctive modes, added to the modal basis of the fixed wheel model.
- In particular, three rigid -zero frequency- modes are predicted by the combined system, corresponding to the common wheel and tyre in-plane translations and their in-phase rotation. These modes may be regarded as having evolved from the radial n=1 and the tangential n=0 modes respectively.
- Examining the flexural modes, the radial $n = 0$ (torsional) and $n = 1$ modes are primarily affected by the wheel participation in the modal expansion and insignificantly the tangential n=1 modes. The corresponding mode shapes capture respectively the anti-diagonal (out of phase) relative wheel-tyre rotational ($n = 0$) and translational translational ($n = 1$) motion.
- All the $n > 1$ modes remain similar to the one of the fixed wheel model.

Given that the combined rigid body motion is not captured by the modal response but exclusively by the space domain inertial motion of the system, the rigid modes of the system may be subtracted from the modal basis. Consequently, the basis will differ from the one used in the contact study only in the $n = 1$ radial couple of modes (horizontal/vertical), the $n = 1$ tangential couple (horizontal/vertical) and the $n = 0$ radial (anti-diagonal torsional) modes, as the wheel-tyre (non rigid body) interaction is captured by these five modes. The discretised form of the belt model, proposed in chapter 4, is adopted and given that every mode shape vector must have the same length, each of them has to be extended in order to incorporate the three additional wheel DOFs, although non zero deformation amplitude values will be present only in the above mentioned five modes.

In compliance with eqn. 4.42, the mode shape vector of the jth mode can be written as:

$$\boldsymbol{\Psi}_j = \begin{bmatrix} U_x^{w,j} \\ U_y^{w,j} \\ U_\Phi^{w,j} \\ U_{x,i=1}^{j}(\theta_1) \\ U_{y,i=1}^{j}(\theta_1) \\ \vdots \\ U_{x,i}^{j}(\theta_i) \\ U_{y,i}^{j}(\theta_i) \\ \vdots \\ U_{x,i=n_b}^{j}(\theta_{n_b}) \\ U_{y,i=n_b}^{j}(\theta_{n_b}) \end{bmatrix} \tag{5.33}$$

where:

$U^{w,j}$	the wheel displacement predicted by the jth mode
U_i^j	the ith node deformation predicted by the jth mode
θ_i	the central angle of the ith node

Following the analysis of section 3.8 of chapter 3, such an orientation angle can be selected for the wheel-belt rectilinear interaction modes, that each of the two recurrences of each of them in the modal basis captures the horizontal or the vertical direction respectively:

$$U_x^{w,j} = \begin{cases} \dfrac{R \cdot \pi(k_r \cdot R_j^m - k_t \cdot T_j^m)}{\pi \cdot R(k_r + k_t) - \omega_j^2 \cdot m_w}, & j: \ n = 1, \text{ radial/tangential mode of horizontal displacement} \\ 0, & j: \text{ all the other modes} \end{cases} \tag{5.34}$$

$$U_y^{w,j} = \begin{cases} \dfrac{R \cdot \pi(k_r \cdot R_j^m - k_t \cdot T_j^m)}{\pi \cdot R(k_r + k_t) - \omega_j^2 \cdot m_w}, & j: n = 1, \text{ radial/tangential mode of vertical displacement} \\ 0, & j: \text{ all the other modes} \end{cases} \tag{5.35}$$

$$U_\Phi^{w,j} = \begin{cases} \Phi_j = \dfrac{2\pi \cdot R^2 \cdot k_t \cdot T_j^m}{2\pi \cdot R^3 \cdot k_t - \omega_j^2 \cdot I_w}, & j: n = 0, \text{ radial mode (torsional)} \\ 0, & j: \text{ all the other modes} \end{cases} \tag{5.36}$$

The force vector will follow the same space discretisation pattern with the eigenvectors and may be written

as:

$$\mathbf{F}(t) = \begin{bmatrix} F_x^w \\ F_y^w \\ M^w \\ F_{tx}^1 \\ F_{ty}^1 \\ \vdots \\ F_{tx}^i \\ F_{ty}^i \\ \vdots \\ F_{tx}^{n_b} \\ F_{ty}^{n_b} \end{bmatrix} \tag{5.37}$$

The derivation of the right part of the system's matrix equations (5.25) necessitates the subtraction from each of the above force terms of the global acceleration of the system multiplied by the inertia value assigned to the corresponding degree of freedom. The rotation of the transient system imposes some additional terms of global acceleration, further from the ones induced by the translational motion. These additional terms, in contrast to the translational ones, differ according to the examined node and depend on the circumferential position of it. The global acceleration of the transient system which corresponds to the ith node, will be calculated in the following. Firstly, the global acceleration of the ith node is expressed in the stationary system, starting from the general equation which transforms its coordinates from the one system to the other. Later, the system's global acceleration, as sensed by the particular node, is derived and finally this acceleration will be projected to the transient system, so that it can be used in the modal response calculation.

The global position of the ith node is given by the equation:

$$\begin{bmatrix} X_b^i \\ Y_b^i \end{bmatrix} = \begin{bmatrix} X^s \\ Y^s \end{bmatrix} + \mathbf{T}^T(\Phi_s) \cdot \begin{bmatrix} x^i \\ y^i \end{bmatrix} \tag{5.38}$$

where:

X/Y_b^i	the horizontal/vertical coordinates of the ith belt node in the stationary system of reference
X/Y^s	the horizontal/vertical coordinates of the transient system's origin in the same system
x/y^i	the horizontal/vertical coordinates of the ith node in the transient system of reference

A corresponding velocity expression emerges by the time derivation of the above equation:

$$\begin{bmatrix} \dot{u}_X^i \\ \dot{u}_Y^i \end{bmatrix} = \begin{bmatrix} \dot{u}_X^s \\ \dot{u}_Y^s \end{bmatrix} + \dot{\mathbf{T}}^T(\Phi_s) \cdot \dot{\Phi}_s \cdot \begin{bmatrix} x^i \\ y^i \end{bmatrix} + \mathbf{T}^T(\Phi_s) \cdot \begin{bmatrix} \dot{u}_x^i \\ \dot{u}_y^i \end{bmatrix} \tag{5.39}$$

and an expression for the global acceleration of the ith node is similarly derived:

$$\begin{bmatrix} \ddot{u}_X^i \\ \ddot{u}_Y^i \end{bmatrix} = \begin{bmatrix} \ddot{u}_X^s \\ \ddot{u}_Y^s \end{bmatrix} + \ddot{\mathbf{T}}^T(\Phi_s)\cdot(\dot{\Phi}_s)^2 \cdot \begin{bmatrix} x^i \\ y^i \end{bmatrix} + \dot{\mathbf{T}}^T(\Phi_s)\cdot\ddot{\Phi}_s \cdot \begin{bmatrix} x^i \\ y^i \end{bmatrix} + \dot{\mathbf{T}}^T(\Phi_s)\cdot\dot{\Phi}_s \cdot \begin{bmatrix} \dot{u}_x^i \\ \dot{u}_y^i \end{bmatrix} + \dot{\mathbf{T}}^T(\Phi_s)\cdot\dot{\Phi}_s \cdot \begin{bmatrix} \dot{u}_x^i \\ \dot{u}_y^i \end{bmatrix} + \mathbf{T}^T(\Phi_s)\cdot \begin{bmatrix} \ddot{u}_x^i \\ \ddot{u}_y^i \end{bmatrix} \tag{5.40}$$

The above acceleration expression can be simplified using the following identities:

$$\dot{\mathbf{T}}^T(\Phi_s) = \begin{bmatrix} -\sin\Phi_s & -\cos\Phi_s \\ \cos\Phi_s & -\sin\Phi_s \end{bmatrix} = \begin{bmatrix} \cos\Phi_s & -\sin\Phi_s \\ \sin\Phi_s & \cos\Phi_s \end{bmatrix} \cdot \begin{bmatrix} 0 & -1 \\ 1 & 0 \end{bmatrix} = \mathbf{T}^T(\Phi_s) \cdot \begin{bmatrix} 0 & -1 \\ 1 & 0 \end{bmatrix} \tag{5.41}$$

and

$$\ddot{\mathbf{T}}^T(\Phi_s) = \dot{\mathbf{T}}^T(\Phi_s) \cdot \begin{bmatrix} 0 & -1 \\ 1 & 0 \end{bmatrix} = \mathbf{T}^T(\Phi_s) \cdot \begin{bmatrix} 0 & -1 \\ 1 & 0 \end{bmatrix} \cdot \begin{bmatrix} 0 & -1 \\ 1 & 0 \end{bmatrix} = -\mathbf{T}^T(\Phi_s) \cdot \begin{bmatrix} 1 & 0 \\ 0 & 1 \end{bmatrix} = -\mathbf{T}^T(\Phi_s) \tag{5.42}$$

The global acceleration of the ith node can be now expressed as:

$$\begin{aligned} \begin{bmatrix} \ddot{u}_X^i \\ \ddot{u}_Y^i \end{bmatrix} = \begin{bmatrix} \ddot{u}_X^s \\ \ddot{u}_Y^s \end{bmatrix} &- \mathbf{T}^T(\Phi_s) \cdot (\dot{\Phi}_s)^2 \cdot \begin{bmatrix} x^i \\ y^i \end{bmatrix} + \mathbf{T}^T(\Phi_s) \cdot \ddot{\Phi}_s \cdot \begin{bmatrix} 0 & -1 \\ 1 & 0 \end{bmatrix} \cdot \begin{bmatrix} x^i \\ y^i \end{bmatrix} \\ &+ 2 \cdot \mathbf{T}^T(\Phi_s) \cdot \dot{\Phi}_s \cdot \begin{bmatrix} 0 & -1 \\ 1 & 0 \end{bmatrix} \cdot \begin{bmatrix} \dot{u}_x^i \\ \dot{u}_y^i \end{bmatrix} + \mathbf{T}^T(\Phi_s) \cdot \begin{bmatrix} \ddot{u}_x^i \\ \ddot{u}_y^i \end{bmatrix} \end{aligned} \tag{5.43}$$

The last four acceleration terms depend on the rotation of the transient system in respect to the stationary one and are referred in the literature as: centripetal, tangential, Coriolis and linear accelerations respectively. It should be considered that here an expression of the global acceleration of the transient system, as sensed by the ith node, is to be derived. Consequently, the terms of eqn. 5.43 referring to the acceleration of the node in the transient system (the Coriolis and the linear ones in particular) will be subtracted from the expression; their effect has been incorporated in the left (modal) part of the system's equations of motion. In conclusion, the global acceleration of the transient system will be composed by the translational terms (common for all the belt nodes) plus the centripetal and tangential terms, the values of which differ from node to node:

$$\begin{bmatrix} \ddot{u}_X^{s\to i} \\ \ddot{u}_Y^{s\to i} \end{bmatrix} = \begin{bmatrix} \ddot{u}_X^s \\ \ddot{u}_Y^s \end{bmatrix} - \mathbf{T}^T(\Phi_s) \cdot (\dot{\Phi}_s)^2 \cdot \begin{bmatrix} x^i \\ y^i \end{bmatrix} + \mathbf{T}^T(\Phi_s) \cdot \ddot{\Phi}_s \cdot \begin{bmatrix} 0 & -1 \\ 1 & 0 \end{bmatrix} \cdot \begin{bmatrix} x^i \\ y^i \end{bmatrix} \tag{5.44}$$

where $\ddot{u}_X^{s\to i}$ corresponds to the total global acceleration of the transient system, as sensed by the ith node of the belt.In order the above acceleration to be introduced in the equations of motion, it has to be projected

to the transient system:

$$\begin{bmatrix} \ddot{u}_x^{s\to i} \\ \ddot{u}_y^{s\to i} \end{bmatrix} = \mathbf{T}(\Phi_s) \cdot \begin{bmatrix} \ddot{u}_X^{s\to i} \\ \ddot{u}_Y^{s\to i} \end{bmatrix} \tag{5.45}$$

$$\begin{bmatrix} \ddot{u}_x^{s\to i} \\ \ddot{u}_y^{s\to i} \end{bmatrix} = \mathbf{T}(\Phi_s) \quad \begin{bmatrix} \ddot{u}_X^{s} \\ \ddot{u}_Y^{s} \end{bmatrix} - \mathbf{T}^T(\Phi_s) \cdot (\dot{\Phi}_s)^2 \cdot \begin{bmatrix} x^i \\ y^i \end{bmatrix} + \mathbf{T}^T(\Phi_s) \cdot \ddot{\Phi}_s \cdot \begin{bmatrix} 0 & -1 \\ 1 & 0 \end{bmatrix} \cdot \begin{bmatrix} x^i \\ y^i \end{bmatrix} \Bigg) \Rightarrow \tag{5.46}$$

$$\begin{bmatrix} \ddot{u}_x^{s\to i} \\ \ddot{u}_y^{s\to i} \end{bmatrix} = \mathbf{T}(\Phi_s) \cdot \begin{bmatrix} \ddot{u}_X^{s} \\ \ddot{u}_Y^{s} \end{bmatrix} - \mathbf{T}(\Phi_s) \cdot \mathbf{T}^T(\Phi_s) \cdot (\dot{\Phi}_s)^2 \cdot \begin{bmatrix} x^i \\ y^i \end{bmatrix} + \mathbf{T}(\Phi_s) \cdot \mathbf{T}^T(\Phi_s) \cdot \ddot{\Phi}_s \cdot \begin{bmatrix} 0 & -1 \\ 1 & 0 \end{bmatrix} \cdot \begin{bmatrix} x^i \\ y^i \end{bmatrix} \Rightarrow \tag{5.47}$$

$$\begin{bmatrix} \ddot{u}_x^{s\to i} \\ \ddot{u}_y^{s\to i} \end{bmatrix} = \mathbf{T}(\Phi_s) \cdot \begin{bmatrix} \ddot{u}_X^{s} \\ \ddot{u}_Y^{s} \end{bmatrix} - (\dot{\Phi}_s)^2 \cdot \begin{bmatrix} x^i \\ y^i \end{bmatrix} + \ddot{\Phi}_s \cdot \begin{bmatrix} 0 & -1 \\ 1 & 0 \end{bmatrix} \cdot \begin{bmatrix} x^i \\ y^i \end{bmatrix} \tag{5.48}$$

For the dynamic analysis, the wheel is modelled as a point with concentrated inertia properties. In respect, no rotation induced terms will be present in the corresponding to the wheel transient system's acceleration and consequently the system transformation deduces to a simple projection. Moreover, as an angular degree of freedom is assigned to the wheel, the system's angular acceleration can be directly transmitted to the wheel. The transformation reads:

$$\begin{bmatrix} \ddot{u}_x^{s\to w} \\ \ddot{u}_y^{s\to w} \end{bmatrix} = \mathbf{T}(\Phi_s) \cdot \begin{bmatrix} \ddot{u}_X^{s} \\ \ddot{u}_Y^{s} \end{bmatrix} \tag{5.49}$$

and

$$\ddot{u}_\Phi^{s\to w} = \ddot{u}_\Phi^{s} \tag{5.50}$$

The total excitation vector (following the pattern of eqn. 5.22) can be composed using the discretised force vector 5.62 and the above derived acceleration expressions(eqns. 5.48, 5.49 and 5.50):

$$\mathbf{F}^s = \begin{bmatrix} F_x^w \\ F_y^w \\ M^w \\ F_{x,i=1} \\ F_{y,i=1} \\ \vdots \\ F_{x,i} \\ F_{y,i} \\ \vdots \\ F_{x,i=n_b} \\ F_{y,i=n_b} \end{bmatrix} - \begin{bmatrix} \ddot{u}_x^{s\to w} \cdot m_w \\ \ddot{u}_y^{s\to w} \cdot m_w \\ \ddot{u}_\Phi^{s} \cdot I_w \\ \ddot{u}_x^{s\to i=1} \cdot \frac{m_w}{n_b} \\ \ddot{u}_y^{s\to i=1} \cdot \frac{m_w}{n_b} \\ \vdots \\ \ddot{u}_x^{s\to i} \cdot \frac{m_w}{n_b} \\ \ddot{u}_y^{s\to i} \cdot \frac{m_w}{n_b} \\ \vdots \\ \ddot{u}_x^{s\to i=n_b} \cdot \frac{m_w}{n_b} \\ \ddot{u}_y^{s\to i=n_b} \cdot \frac{m_w}{n_b} \end{bmatrix} \tag{5.51}$$

where $\mathbf{F}^s$ is the total excitation vector, including the terms corresponding to the acceleration of the transient system.

The modal mass of the model may be calculated by the addition of the concentrated wheel inertia

properties to the respective discretised belt modal mass expression (eqn. 4.51):

$$\mathbf{M}^m = \tilde{\mathbf{\Psi}}^T \cdot \begin{bmatrix} m_w & 0 & 0 & 0 & 0 \cdots & 0 & \\ 0 & m_w & 0 & 0 & 0 \cdots & 0 & \\ 0 & 0 & I_w & 0 & 0 \cdots & 0 & \\ 0 & 0 & 0 & \frac{m_b}{n_b} & 0 & \cdots & 0 \\ 0 & 0 & 0 & 0 & \frac{m_b}{n_b} & \cdots & 0 \\ \vdots & \vdots & \vdots & \vdots & \vdots & \ddots & \vdots \\ 0 & 0 & 0 & 0 & 0 & \cdots & \frac{m_b}{n_b} \end{bmatrix} \cdot \tilde{\mathbf{\Psi}} \tag{5.52}$$

The time differential equation of the participation factor of the jth mode may be written as:

$$\ddot{\eta}_j + \lambda_j \cdot \dot{\eta} + \omega_j^2 \cdot \eta_j = \frac{\mathbf{\Psi}_j^T \cdot \mathbf{F}^s}{\mathbf{M}^m(j,j)} \tag{5.53}$$

where $\mathbf{M}^m(j,j)$ is the (j,j) diagonal element of the matrix derived by eqn.5.52. The deformation and deformation rate response in the space-time domain are respectively calculated by the transformation:

$$\mathbf{u} = \tilde{\mathbf{\Psi}} \cdot \tilde{\eta} \tag{5.54}$$

$$\dot{\mathbf{u}} = \tilde{\mathbf{\Psi}} \cdot \dot{\tilde{\eta}} \tag{5.55}$$

The calculation of the global position of the belt nodes is processed in two steps; firstly, the deformation response is transformed into the stationary system of reference, using the rotation angle of the transient system (Φ_s):

$$\begin{bmatrix} u_X^i \\ u_Y^i \end{bmatrix} = T^T(\Phi_s) \cdot \begin{bmatrix} u_x^i \\ u_y^i \end{bmatrix} \tag{5.56}$$

where u_X^i and u_Y^i are the horizontal and vertical deformations of the ith belt node, projected to the global system of reference. Secondly,the transient system's global position and orientation is superimposed to the above deformation:

$$\begin{bmatrix} X_b^i \\ Y_b^i \end{bmatrix} = \begin{bmatrix} X_s \\ Y_s \end{bmatrix} + \mathbf{T}^T(\theta_i + \Phi_s) \cdot \begin{bmatrix} R \\ 0 \end{bmatrix} + \begin{bmatrix} u_X^i \\ u_Y^i \end{bmatrix} \tag{5.57}$$

The global velocity of the belt nodes is calculated by a similar process(eqn. 5.39).

The orientation of the tread elements in the stationary system can be calculated as a superposition of the system's rigid rotation and the belt's flexural deformational. Eqns. 4.58 and 4.59 respectively describe the rotation and torsional terms of the belt's contribution.

$$\alpha_i = \theta_i + \Phi_s + a_{rotation}^i + a_{torsion}^i \tag{5.58}$$

Having calculated the belt nodes' global position and the global orientation of the respective tread elements, the contact analysis presented in sections 4.2.2, 4.2.3, 4.2.4 and 4.2.5 may be applied and the contact forces are calculated.

For computational reasons, the contact induced moment is calculated in the transient system of reference.

Accordingly, the tangential component of each contact force is calculated by the transformation:

$$\begin{bmatrix} F_{r,i} \\ F_{t,i} \end{bmatrix} = \mathbf{T}(\theta_i) \cdot \begin{bmatrix} F_{x,i} \\ F_{y,i} \end{bmatrix} \tag{5.59}$$

while the respective moment is given by the equation:

$$M_i = F_t^i \cdot \sqrt{(R \cdot \cos\theta_i + u_{x,i})^2 + (R \cdot \sin\theta_i + u_{y,i})^2} \tag{5.60}$$

The total rotation moment of the system is calculated summing the above contact moments and the possible external moment applied to the wheel:

$$\sum M = M^w + \sum_{i=1,c_i=1}^{n_b} M_i \tag{5.61}$$

5.1.3 The non linear sidewall case

As it has been discussed in section 4.3.4 of chapter 4, the sidewall geometrical buckling imposes a geometry dependent non linearity to the respective stiffness. This behaviour was modelled using an analytical or discretised membrane foundation. Modal expansion,though, is a linear method (section 3.7.3 of chapter 3) and it cannot be applied on the simulation of the non linear behaviour. Consequently, the sidewall term was dropped from the modal model and its effect was captured by non linear excitation forces, calculated by the respective non linear equations (section 4.3.4, chapter 4). A similar approach will be followed in the rotation analysis. It should be highlighted that the non linear sidewall mechanism prevents the substitution of the inflation excitation by a constant radius increase. Consequently, the inflation pressure terms have to be retained in the right part of the equations and the breathing modal participation factor has to be calculated similarly to the rest of the modes.

The string forces are regarded as external excitations of both the belt nodes and the wheel and the calculation of the excitation of the latter one is accomplished summing them along the two directions of the transient system of reference. These forces are considered as internal ones of the wheel-belt system and in respect they do not participate in the rigid body motion of the combined system. In other words, the sidewall effect is captured in the transient system of reference and, similarly to the inflation pressure one, no projection to the stationary system is necessary.

The force vector in the non linear sidewall case is given by eqn. 5.62 with the addition of the sidewall

and the inflation terms, the latter ones obviously only for the belt nodes:

$$\mathbf{F}(t) = \begin{bmatrix} F_x^w + F_x^{b\to w} \\ F_y^w + F_y^{b\to w} \\ M^w + M^{b\to w} \\ Ftx^1 + T_{rx}^1 + F_{inf,x}^1 \\ F_{ty}^1 + T_{ry}^1 + F_{inf,y}^1 \\ \vdots \\ F_{tx}^i + T_{rx}^i + F_{inf,x}^i \\ F_{ty}^i + T_{ry}^i + F_{inf,y}^i \\ \vdots \\ F_{tx}^{n_b} + T_{rx}^{n_b} + F_{inf,x}^{n_b} \\ F_{ty}^{n_b} + T_{ry}^{n_b} + F_{inf,y}^{n_b} \end{bmatrix} \tag{5.62}$$

where:

$F_{x/y}^{b\to w}$	the total force applied from the belt to the wheel,
	through the discretised non linear sidewall foundation, along the x/y direction
$M^{b\to w}$	the total moment applied from the belt to the wheel
$F_{tx/y}^i$	the contact force applied to the ith node, along the x/y direction
$T_{rx/ry}^i$	the force applied from the wheel to the ith belt node,
	through the discretised non linear sidewall foundation, along the x/y direction
$F_{inf,x/y}^i$	the inflation force applied to the ith belt node, along the x/y direction

The total force applied from the belt nodes to the wheel is calculated as:

$$F_{x/y}^{b\to w} = -\sum_{i=1}^{n_b} T_{rx/ry}^i \tag{5.63}$$

It should also be mentioned that the moment applied to each of the wheel theoretical nodes is calculated assuming that the application point of the sidewall force is the belt node belt, similarly to eqn. 5.60 and not the respective wheel node. This computational simplification omits the sidewall geometry effect from any other part of the calculation apart from the force nonlinearity. The moment equation reads:

$$M^{b\to w} = -\sum_{i=1}^{n_b} T_{rt}^i \cdot \sqrt{(R\cdot\cos\theta_i + u_{x,i})^2 + (R\cdot\sin\theta_i + u_{y,i})^2} \tag{5.64}$$

where the force term T_{rt}^i is the tangential component of the in-plane string force applied to the ith node, which is calculated by the projection from the horizontal/vertical to the radial/tangential local system of reference:

$$\begin{bmatrix} T_{rr}^i \\ T_{rt}^i \end{bmatrix} = \mathbf{T}(\theta_i) \cdot \begin{bmatrix} T_{rx}^i \\ T_{ry}^i \end{bmatrix} \tag{5.65}$$

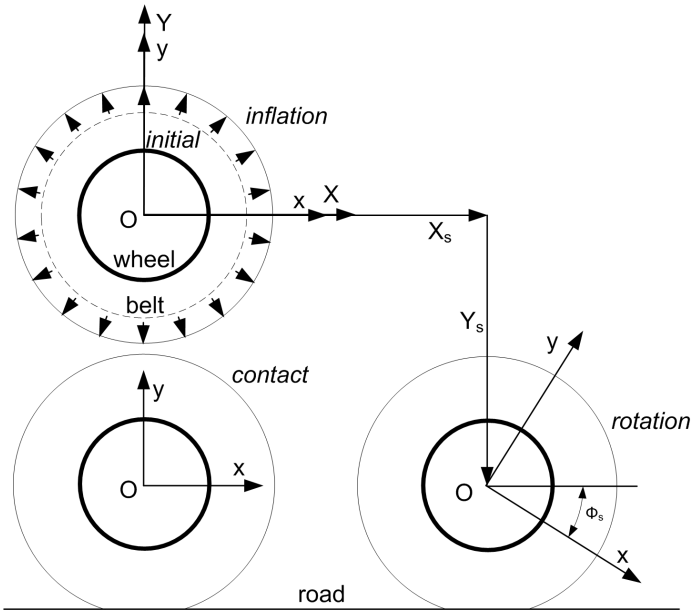

Figure 5.3 – The inflation and contact initial steps.

5.2 The tyre launch

The physical background of the model enables the simulation of the tyre launch process. Before that, the inflation and contact conditions are applied to the model, as characteristically presented in fig. 5.3, together with the respective transient system displacement. As it was highlighted in the algorithm analysis, the model interacts with the environment through the imposition of excitation forces and moments. Steady state kinematic conditions may be represented through the application of the corresponding forces and moments and the accomplishment of the equilibrium state with the time. Accordingly, the contact state is imposed through the application of a vertical load to the wheel and the respective equilibrium is gradually developed.

At the next stage, the rotation may be dynamically imposed to the wheel in two ways: either by the application of a rotational moment or the application of a horizontal force. The wheel responds developing an angular or horizontal motion which is transferred to the belt nodes by the sidewall foundation. The frictional interaction between the tread and the road surface is responsible for the transformation of them respectively into a horizontal or rotational motion which is in respect transferred through the sidewall back to the wheel. The moment imposed launch process represents a driving wheel, while the force imposed one corresponds to a driven wheel.

In terms of rotation, the interaction between the wheel and the belt is controlled by the tangential sidewall foundation while in terms of translation both the radial (along the direction of motion) and the tangential ones (vertical direction) contribute. Given that the magnitude of the radial stiffness is in general higher than the tangential one, especially taking into account its non linearity, the application of a horizontal force instantly results in steady rolling motion, while the application of a respective moment results in a significant rotational vibration (shuffle) of the translational velocity. Obviously, the above interaction and the equilibrium establishment depend on the frictional characteristics of the road surface and the structural

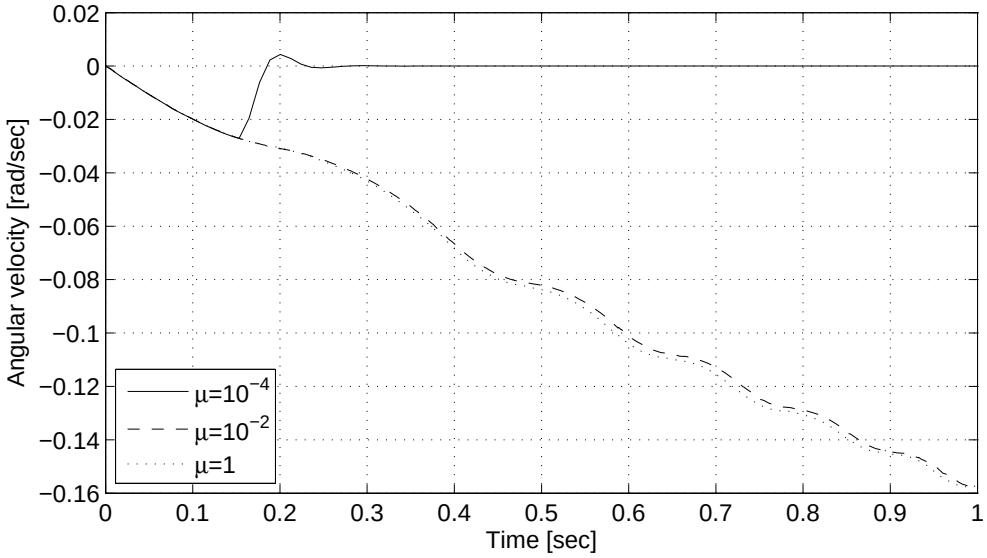

Figure 5.4 – The angular velocity response of the system to a horizontal step force excitation applied to the wheel, for various values of friction coefficient.

damping properties of the tyre. The existence of friction provokes the correspondence between the rotational and the translational motion of the system, while the damping factor controls to what extent the offered to the system energy will be transformed into motion or deformation. The above phenomena are summarised in figs. 5.4 to 5.7, where force and moment step excitations are applied to the wheel and the launch response of the system is monitored. In all the examined cases the non linear sidewall mode has been incorporated in the simulation.

In all the examined cases, the contact equilibrium imposed by a vertical load of $5000N$ is chosen as an initial condition, while both the wheel mass and moment of inertia are assumed to be equal to the respective belt values ($7.82kgr$ and $4.25 \cdot 10^{-3} kgr \cdot m^2$). The effect of the coefficient of friction on the launch process of a driven wheel, imposed by a horizontal step force of $1kgr \cdot m/sec^2$ applied to it, is presented in fig. 5.4. The history of the angular velocity response of the system is examined for three values of friction coefficient: $\mu = 10^{-4}$, 10^{-2} and 1. For the lowest one, the initial rotation of the system (supported by the initially high damping forces) diminishes and the tyre skids on the road surface without rotating. For the two higher friction coefficients an almost constant angular acceleration is developed and the magnitude of it slightly higher in the $\mu = 1$ case, given that the friction suspends the relative slip between the tread and the road that causes the discrepancy between the two motions.

The effect of the tyre damping on the driven wheel launch is depicted in fig. 5.5. A combined mass and stiffness proportional damping property is assumed (section 3.10.2 of chapter 3), with mass and stiffness proportionality coefficients of $\beta_d = 6 \cdot 10^{-5}$ and $\gamma_d = 400$ respectively. Arbitrary assigning these damping values to a medium damping case, a low one corresponds to half values of the above coefficient and a high one to double values of them. The step excitation force remains unchanged from the above driven wheel case. The difference between the damping cases is fond to be quantitative, as in all of them the development pattern of the angular velocity is the same. Obviously, the higher the damping effect, the slower is the

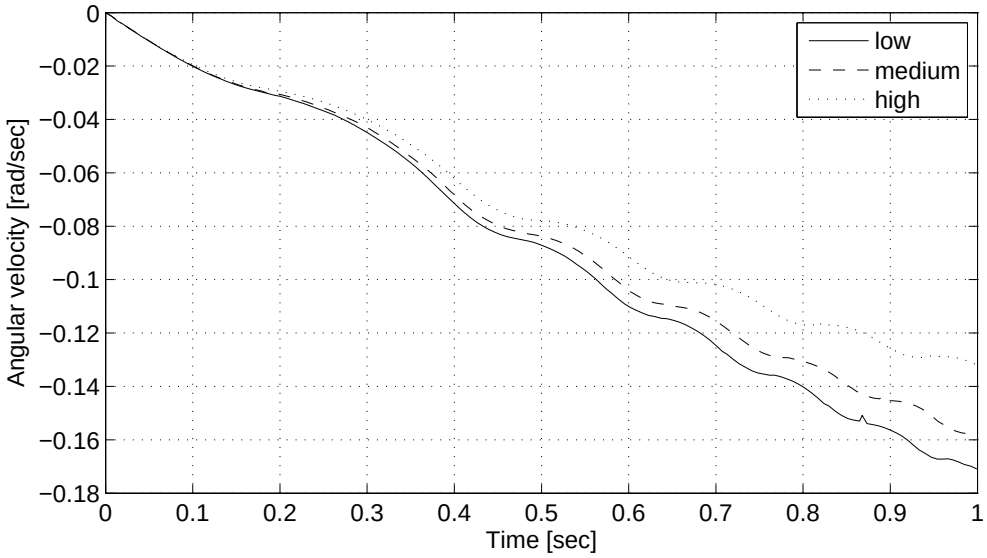

Figure 5.5 – The angular velocity response of the system to a horizontal step force excitation applied to the wheel, for various levels of damping.

velocity build up, given that the level of energy absorbed by the structural deformation (rolling resistance) accordingly increases.

Moving the discussion to the driving wheel case, the effect of the coefficient of friction on the launch process of the driving wheel is presented in fig. 5.6. A step moment excitation of $-10^{-3}kgr \cdot m^2/sec^2$ (clockwise) is applied to the wheel and the translational horizontal velocity of the system is monitored over the first two seconds for three values of friction coefficient. The lowest one fails to transform the rotational motion into a translational one and the wheel is practically spinning remaining at the same global position. For the other two higher friction coefficients, a forward motion may be developed but a large scale oscillation is observed (shuffle response) resulting in the velocity getting also negative values, in accordance to the simulation results published by Maurice and Savkoor in [261]. Interestingly, the higher coefficient of friction results in slightly higher oscillation amplitude, as the suspension of relative slip between the tread and the road magnifies the shuffle response. For similar reasons, the response predicted by the lower coefficient exhibits a slight time delay in comparison to the one predicted in the higher friction coefficient case.

The effect of the damping level on the shuffle behaviour of the driving wheel is presented in fig. 5.7. Obviously for all damping levels, the system exhibits a shuffle response with the same frequency but as the damping increases, the amplitude of the oscillation decreases, given that more energy is dissipated by the structural deformation. It is worth mentioning that in the above shuffle oscillations the frequency is very close to the damped one of the radial $n = 0$, mode revealing the torsional physical mechanism of the observed response.

Before moving from the launch to the examination of other rolling scenarios, the applicability of the approach to higher angular velocity cases should be mentioned. As it has been discussed in section 3.9 of chapter 3 there are two effects of the rotation on the belt modal characteristics. The centrifugal acceleration imposes a stiffening effect similar to the one of the inflation pressure, while the coriolis acceleration results

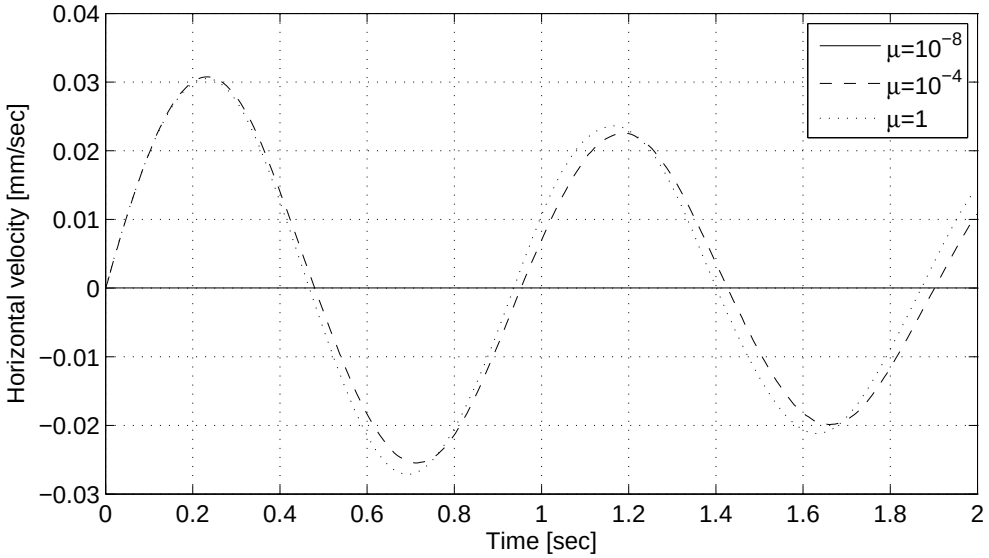

Figure 5.6 – The horizontal velocity response of the system to a step moment excitation applied to the wheel, for various values of friction coefficient.

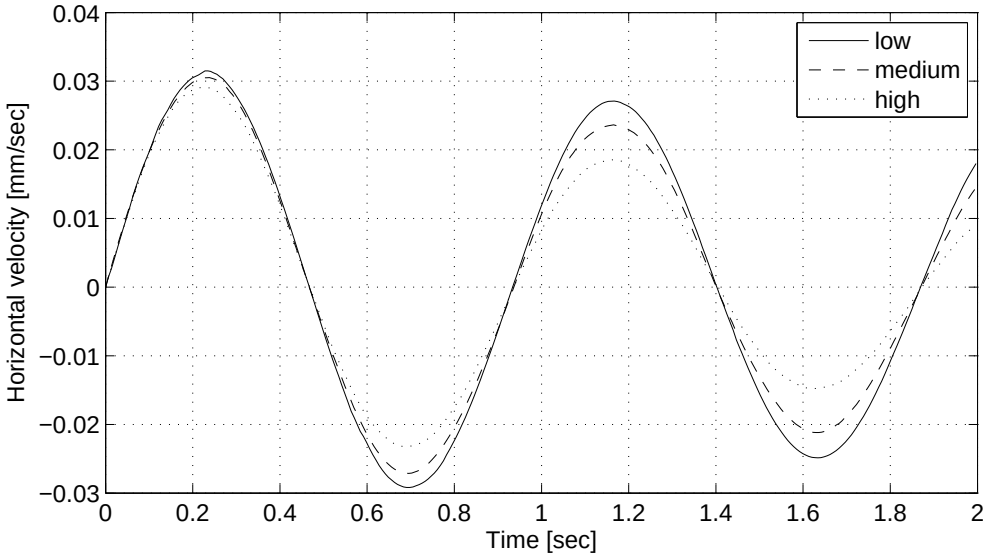

Figure 5.7 – The angular velocity response of the system to a step moment excitation applied to the wheel, for various levels of damping.

in a bifurcation of the modes. The intensity of both of them increases with the angular velocity and depends on the examined mode and the physical properties of the belt. These effects may be incorporated in the modal basis but their non linearity imposes the reapplication of the modal expansion process in order to be captured. Consequently, each modal basis corresponds to a single value of angular velocity but may be also associated with a range of it, for an acceptable error value. The zero angular velocity model which was used for the above launch analysis imposes a limit to the angular velocity at which the model is applicable, above which the modal expansion process should be reapplied.

5.3 The application of kinematic conditions

Although the described algorithm captures the dynamic response of the model, the simulation of certain kinematic conditions is not straightforward. Theoretically, certain steady state operating conditions, angular or horizontal velocity, may be simulated by the model through the application of the respective steady excitation and the provision of sufficient time for the equilibrium establishment. Usually, though, the respective excitation values are not known in advance since they are functions of a number of factors, such as the vertical load or the coefficient of friction. Consequently, the kinematic conditions could be only accomplished applying a closed-loop control system.

The direct assignment of certain velocity values to the degrees of freedom of the model is obstructed by the actual process of their calculation. The velocity and displacement of each of the model's degrees of freedom emerge as the superposition of the space (translational) and modal (vibrational) domain solutions. In accordance, a certain kinematic value may be obtained by an infinite number of combinations of the above values. Each of these combinations, though, corresponds to different physical stress and strain conditions of the model, resulting in a different behaviour and performance characteristics of it.

This problem may be overcome by the assignment of the desired kinematic values to the motion of the system and the drop of the respective differential equation. At the same time, though, the modal response of the degrees of freedom to which the values should be assigned to (usually the wheel ones) should be cancelled out, so that its global kinematic condition will be defined solely by the system's global displacement. The modal response cancellation is accomplished by dropping the excitation term associated with the particular degree of freedom from the right part of the equations of motion. Obviously, as the imposed kinematic condition is expressed in the stationary system of reference but the vibrational response of the system is expressed in the transient one, the response cancellation along a constant global direction incorporates a continuous (at every simulation step) transformation between the two systems of reference.

The global position of the wheel degrees of freedom is given by the equations (following the nomenclature of section 5.1):

$$\begin{bmatrix} X_w \\ Y_w \end{bmatrix} = \begin{bmatrix} X_s \\ Y_s \end{bmatrix} + \mathbf{T}^T(\Phi_s) \begin{bmatrix} u^m_{w,x} \\ u^m_{w,y} \end{bmatrix} \Rightarrow \tag{5.66}$$

$$\begin{bmatrix} X_w \\ Y_w \end{bmatrix} = \begin{bmatrix} X_s \\ Y_s \end{bmatrix} + \begin{bmatrix} u^m_{w,X} \\ u^m_{w,Y} \end{bmatrix} \tag{5.67}$$

Assuming that the system's global position (X_s/Y_s) or its derivative would be imposed, the cancellation of the respective modal response would be achieved by zeroing the line of the excitation vector which corresponds

to that:

$$\begin{bmatrix} F_x^{s,w} \\ F_y^{s,w} \\ M^{s,w} \end{bmatrix} = \begin{bmatrix} \cos\Phi_s & \sin\Phi_s & 0 \\ -\sin\Phi_s & \cos\Phi_s & 0 \\ 0 & 0 & 1 \end{bmatrix} \cdot \begin{bmatrix} F_X^{s,w} \\ F_Y^{s,w} \\ M^{s,w} \end{bmatrix} = \begin{bmatrix} \cos\Phi_s & \sin\Phi_s & 0 \\ -\sin\Phi_s & \cos\Phi_s & 0 \\ 0 & 0 & 1 \end{bmatrix} \left(\begin{bmatrix} F_X^w \\ F_Y^w \\ M^w \end{bmatrix} - \begin{bmatrix} \ddot{u}_X^s \cdot m_w \\ \ddot{u}_Y^s \cdot m_w \\ \ddot{u}_\Phi^s \cdot I_w \end{bmatrix} \right) \tag{5.68}$$

Obviously, the above step of the modal response cancellation may be omitted in case the desired kinematic characteristics are not strictly assigned to a particular degree of freedom but to the total motion of the model. In this case, the kinematic conditions may be applied to the system's motion as above, but the development of the modal response of the system is not suspended.

5.4 The effective radius concept

The tyre shear force evolves primarily as a non linear function of the tyre macroscopic slip and both simulation and experimental results prescribe this force across a range of steady state slip values. The definition of the slip value is based on the deviation of the rotational to the translational ratio from the value imposed by the theoretical non slipping single contact point rolling. Obviously, the tyre is a multi-degrees of freedom deformable system and the imposition of certain slipping positions is not possible, given that the actual kinematic conditions vary along the contact area. Following the analysis of section 5.3, the corresponding to a certain slip value kinematic conditions may be assigned to either the wheel or the combined wheel and belt system, with the second case corresponding to a computationally lighter method.

Apparently, the ratio between of the translational and the rotational velocity of a non slipping rolling tyre theoretically corresponds to the constant radius of the tyre. In the actual case, though, this radius is changing as a function of the load and the velocity and cannot be used for the relative to it definition of macroscopic slipping conditions. The issue is overcome by the definition of the effective radius, the value of which is assigned to certain free rolling operating conditions. For their establishment, a steady translational or rotational velocity value is imposed to the model while the complementary velocity is developed by the frictional interaction between the tyre and the road, given that sufficient time is provided for the equilibrium development. The ratio between the two velocities is the effective radius assigned to the particular free rolling conditions:

$$R_{ef} = \frac{\dot{X}_s^{fr}}{\dot{\Phi}_s^{fr}} \tag{5.69}$$

where the index ^{fr} refers to the free rolling operating conditions. Based on effective radius, the slip (sl) value may be alternatively defined by the deviation of either the angular or the translational horizontal velocity from the respective free rolling ones:

$$sl_{\dot{\Phi}} = 100\frac{\dot{\Phi}_s - \dot{\Phi}_s^{fr}}{\dot{\Phi}_s^{fr}}\% \tag{5.70}$$

$$sl_{\dot{X}} = 100\frac{\dot{X}_s - R_{ef}\cdot\dot{\Phi}_s^{fr}}{R_{ef}\cdot\dot{\Phi}_s^{fr}}\% = 100\frac{\dot{X}_s - \dot{X}_s^{fr}}{\dot{X}_s^{fr}}\% \tag{5.71}$$

Consequently, an accelerating wheel condition would be described by a positive slip value according to the

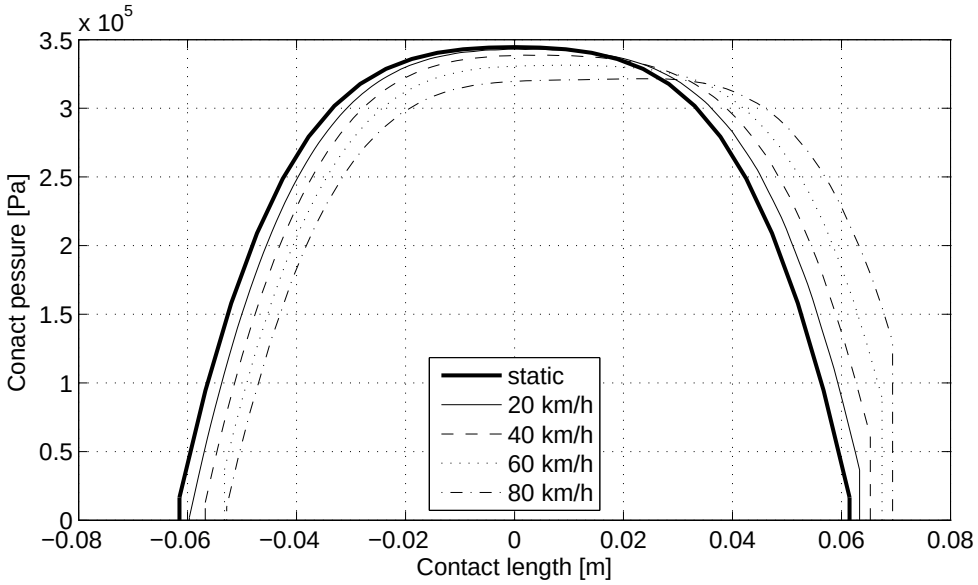

Figure 5.8 – The vertical pressure distribution for various values of free rolling velocity, in comparison to the static one.

angular velocity definition (eqn. 5.70) but by a negative slip value, if the latter is defined by the horizontal velocity values (eqn. 5.71). The slip definition according to the angular velocity values is the most common one in the bibliography (see for example [1]) and will be followed in the present analysis.

Some characteristic free rolling and slip steady state operating conditions will be examined in this section, together with the developed contact pressure distributions, the micro-slip development along the contact area and the predicted shear force. The application of a $5000N$ load to the wheel will be used, as previously, for the contact conditions generation, while all the results have been acquired by the non linear sidewall model. The tread-road interaction is assumed to be frictional, described by a with a coefficient of friction value of $\mu = 1$.

5.5 Free rolling cases examination

The vertical contact pressure distribution of a free rolling tyre for a range of horizontal velocities (up to $80km/h$), assigned to the system, is presented in fig. 5.8, in comparison to the static case. Although the general parabolic/trapezoidal shape of the contact pressure distribution is also retained in the rolling cases, its shape is not symmetrical any more. The whole contact area moves forward (towards the leading edge of the contact) as the velocity increases, while the pressure values at the initial phase of the contact increase significantly and in result the values along the biggest part of the contact slightly deduce. In terms of vertical equilibrium, the wheel load is primarily balanced at the front of the contact, generating a moment of opposite direction to the rotation. This contact reaction is imposed by the combined damping mechanism of the belt, the sidewall and the tread and offer a physical interpretation of the rolling resistance moment mechanism as a function of the rolling velocity.

The horizontal pressure distributions for the same range of horizontal velocity values are presented in fig. 5.9. A respective diversion from the symmetrical shape is developed as the velocity increases. The magnitude

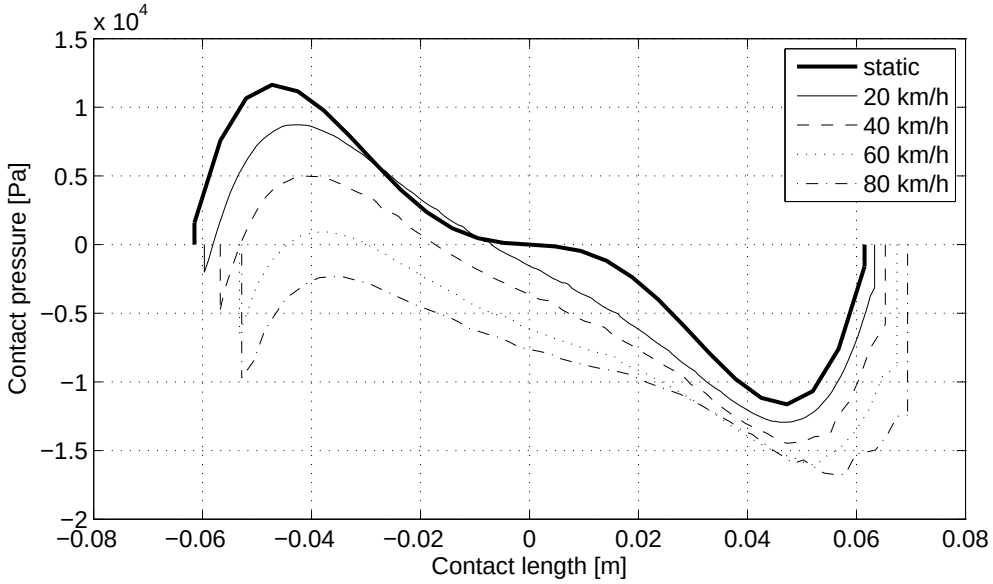

Figure 5.9 – The horizontal pressure distribution for various values of free rolling velocity, in comparison to the static one.

of the backwards directed pressures at the front of the contact area increases while the magnitude of the forwards directed pressures at the rear of the contact area decreases. Apparently, the total resultant force is backwards directed and is commonly referred as rolling resistance force. For velocity values exceeding a certain limit, the pressure values become backwards directed along the whole contact length area.

Following the analysis of section 5.4, the steady state free rolling conditions are used for the derivation of the effective radius (R_{ef} values, which are presented in fig. 5.10 for the examined velocity range. As it may be observed, the effective radius increases almost proportionally with the velocity. In physical terms, the rotating system balances along the vertical to the ground direction at a larger distance from it, corresponding to a decreased structural deformation. In other words and in comparison to the static contact case, a percentage of the vertical load of the wheel is now counterbalanced by the damping forces at the front of the contact area, deteriorating the stiffness (deformation induced) ones along the rest of the contact length.

5.6 Slip cases examination

Moving from the examination of the free rolling case to the steady state slip conditions, the $80km/h$ velocity case is selected for further analysis. The vertical pressure distributions for various values of positive slip (accelerating wheel) are presented in fig. 5.8, in comparison to the respective free rolling one. The effect of the positive slip is to a great extent similar to the one of the velocity, as the vertical load is primarily supported by the leading section of the contact, while the whole contact area is transposed to the same direction. In this case, though, the shape of the pressure distribution changes for trapezoidal to parabolic and a maximum pressure value (peak) may be obviously identified. This peak moves towards the leading edge of the contact as the slip increases, given that the damping forces are primarily excited at this section of the contact.

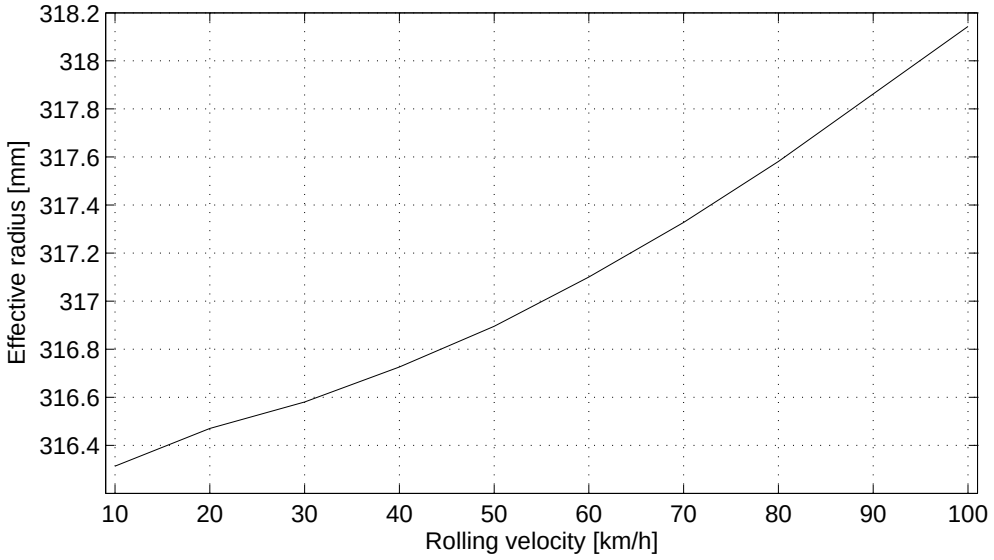

Figure 5.10 – The effective radius of the tyre, as a function of the rolling velocity.

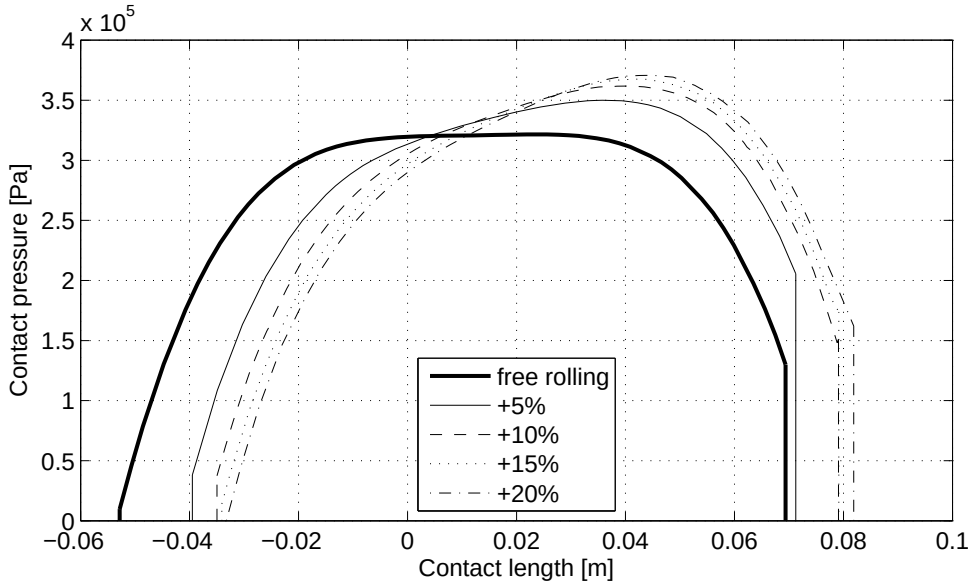

Figure 5.11 – The vertical pressure distribution for various values of positive slip (accelerating wheel), in comparison to the free rolling one.

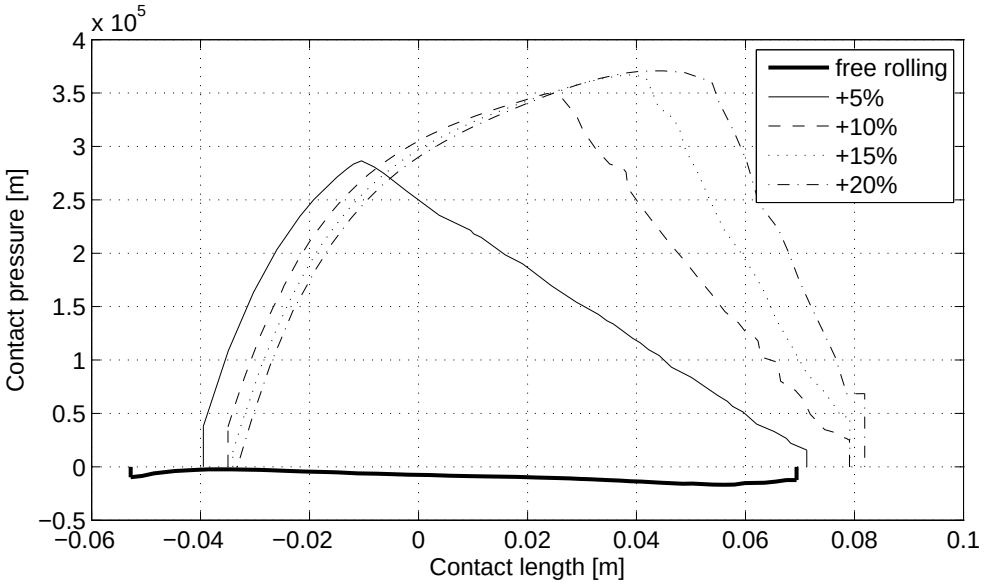

Figure 5.12 – The horizontal pressure distribution for various values of positive slip (accelerating wheel), in comparison to the free rolling one.

The horizontal pressure distribution for the same slip values is presented in fig. 5.12. Presumably, the negative pressure values of the free rolling case (also presented in the figure) have been transformed into positive ones. The pressure magnitude increases almost linearly from the leading edge of the contact along its length and reaches a maximum value (located towards the trailing edge), after which decreases parabolically. As the slip percentage increases, the peak magnitude value also increases and its position moves towards the front edge of the contact area, resulting in the shrinkage of the linear sector and the relative to that expansion of the parabolic one.Additionally, the pressure value developing at the leading edge of the contact increases. Above a slip value, although the peak position continues to move towards the leading edge of the contact, its value does not increase further, a behaviour that has a significant effect on the macroscopically observed shear force, as it will be later noticed.

The effect of the shear velocity of the tread on the development of the contact pressure distribution is examined in fig. 5.13. The sliding velocity of the tread along the contact area is presented for various values of slip and in comparison to the free rolling case. Starting from the latter one, it may be observed that the tread remains attached to the ground along the whole contact area as the particular operating conditions (vertical load and coefficient of friction) totally suspend its shear motion. In the accelerating wheel case, the tread develops a slip motion (backwards directed) at the front edge of the contact, the velocity of which, though, reduces further down the contact area and the tread sticks to the road surface. This behaviour is supported by the increase of the vertical pressure towards the centre of the contact area, which results in the proportional increase of the frictional force.

As the imposed slip increases further, the magnitude of the shear velocity increases accordingly and the shear slip suspension point moves towards the rear of the contact area. The point defines the relative dimensions of the slip and the stick sections (zones)of the contact area and the increase of the imposed slip level results in the magnification of the first zone and the shrinkage of the second one. Above a certain

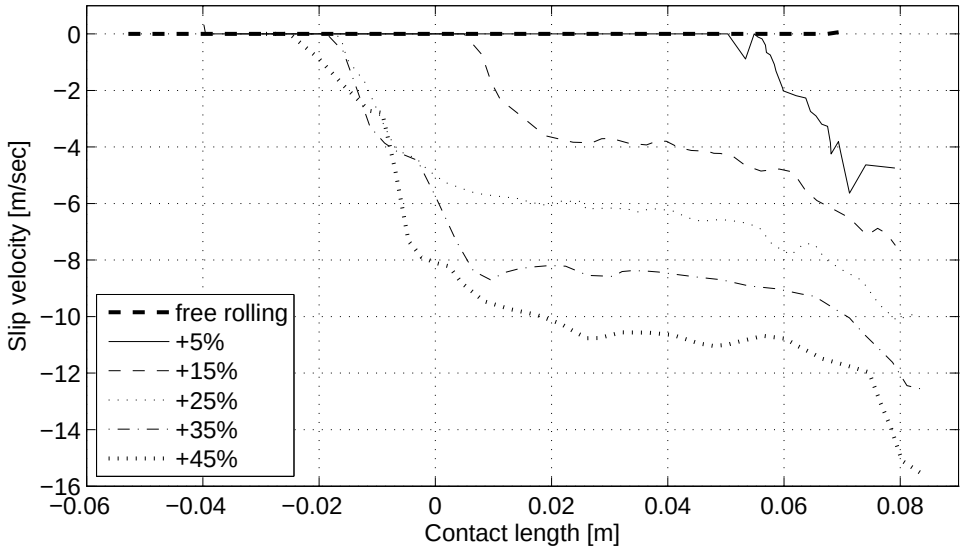

Figure 5.13 – The horizontal shear velocity distribution for various values of positive slip (accelerating wheel), in comparison to the free rolling one.

slip value, although apparently the slip velocity continues to increase (in magnitude) along the whole slip section, the relative dimensions of the two sectors remain constant. Examining together figs. 5.12 and 5.13 it may be concluded that the slip level which corresponds to the fixation of the zones' relative dimensions is also associated with the no further increase of the maximum pressure value.

The horizontal deformation of the tread along the contact area for the same slip cases is presented in fig 5.14. Although in the free rolling case a negative tread deformation may be observed along the whole contact area, in the accelerating wheel cases a positive tread deformation is observed. Starting from the leading edge of the contact, the deformation increases, reaches a positive value (maximum) and decreases towards the trailing edge. The displacement of the maximum deformation point towards the rear of the contact for increasing slip follows closely the displacement of the transition point between the stick and the slip zones. Apparently, though, as the tread shear velocity increases further with the slip (fig. 5.13), above a certain value it hardly affects the slip deformation magnitude.

The vertical contact pressure distribution of a braking wheel (negative slip values) is presented in fig. 5.15. The negative slip effects emerge as opposite ones to the positive slip effects. The contact area is transposed backwards and although the change from trapezoidal to parabolic distribution shape is again obvious, in this case the maximum value point moves towards the trailing edge of the contact. As the slip value increases, the maximum pressure is developed further down toward the trailing edge of the contact and the the whole contact area is displaced towards the same direction. It is worth mentioning that the pressure value at the initial contact phase remains higher at the leading edge of the contact (similarly to the accelerating wheel case), due to the significant effect of the damping reaction at the particular area.

The horizontal pressure distribution for the same slip conditions is presented in fig. 5.16. In contrast to the accelerating wheel case (fig. 5.12), the pressure is negative (instead of positive) along the whole contact area and a maximum value may be observed towards the trailing edge of the contact (instead of the

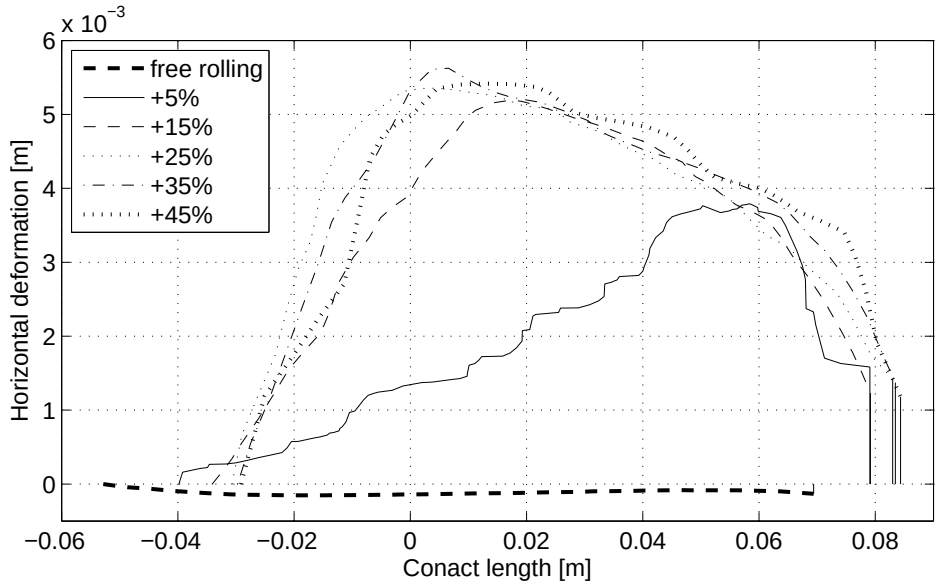

Figure 5.14 – The horizontal tread deformation distribution for various values of positive slip (accelerating wheel), in comparison to the free rolling one.

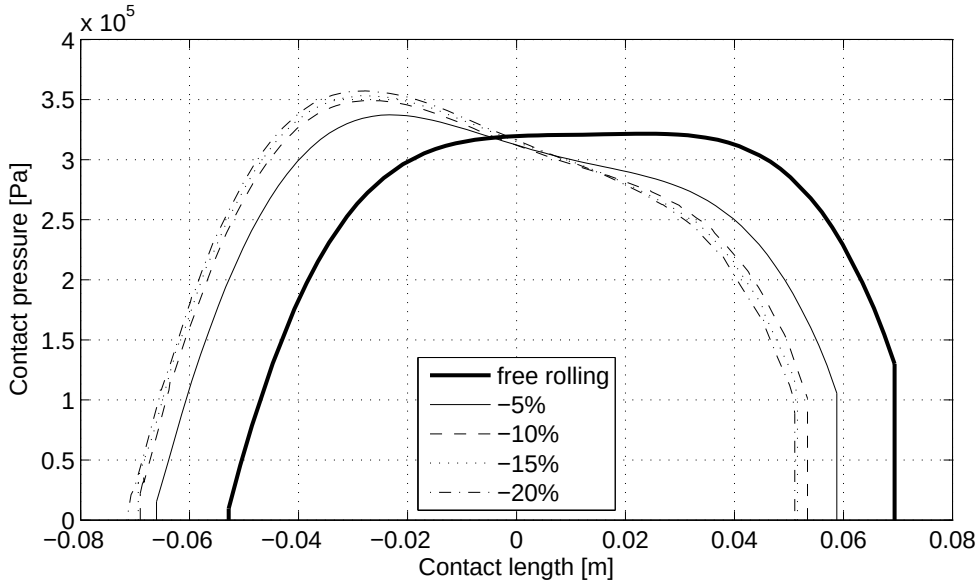

Figure 5.15 – The vertical pressure distribution for various values of negative slip (braking wheel), in comparison to the free rolling one.

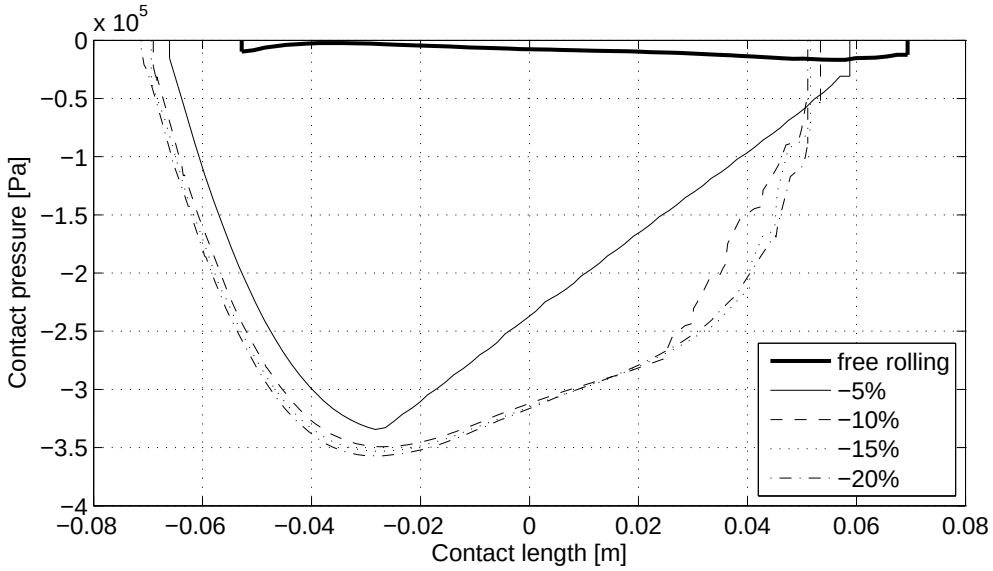

Figure 5.16 – The horizontal pressure distribution for various values of negative slip (braking wheel), in comparison to the free rolling one.

leading). For a modest slip value linear and parabolic sections may be identified but as the magnitude of the slip increases the distribution becomes parabolic-like along the whole contact area. Interestingly, comparing figs. 5.12 and 5.16 it may be observed that for conditions corresponding to the same slip magnitude but opposite signs of it, the contact distributions, apart form the obvious opposite directions, exhibit different shapes. This difference results form the fact that under the followed slip definition the physical effect of the free rolling is imposed to the predicted pressure distributions but is not included in the derivation of the slip value. For this reason , alternative slip definitions that take into consideration the free rolling effects (assuming a different effective radius definition) have been developed and can be found in the respective literature [1].

The tread shear velocity for the braking wheel case is examined in fig. 5.17. Similarly to the accelerating one, for small slip values shear motion is developed at the front of the contact area, in this case, though, having positive direction, and it is suspended towards the rear. Accordingly also, the increase of the slip magnitude increases the slip velocity of the tread and transposes the border between the slip and the stick sections towards the rear. Further increase of the slip magnitude above a certain value increases the shear velocity, retaining though the relative dimensions between the two zones. For the examined slip values, the slip zone extends to the whole contact area, a difference (from the accelerating case) which is justified by the above mentioned free rolling effect.

The horizontal tread deformation corresponding to the braking wheel cases is presented in fig. 5.18. Although negative deformation is developed along the whole contact, the development pattern follows the one observed in the accelerating wheel case. The maximum deformation position moves towards the rear of the contact as the slip magnitude increases, while its fixation along the contact (together with the no further increase of the deformation magnitude) are apparently justified by the extension of the slip zone to the whole contact area (fig. 5.17).

The parallel examination of the tread shear behaviour with the total shear force development, as a

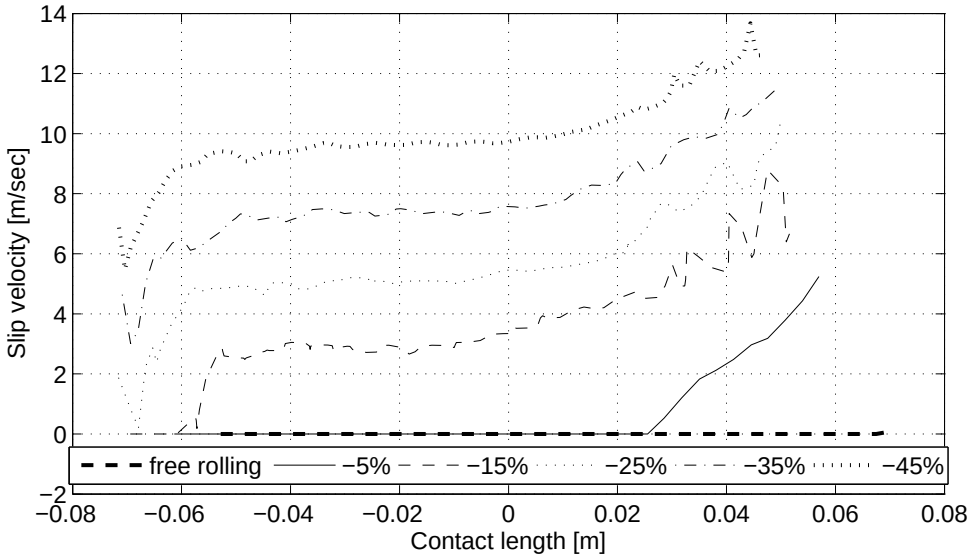

Figure 5.17 – The horizontal shear velocity distribution for various values of negative slip (braking wheel), in comparison to the free rolling one.

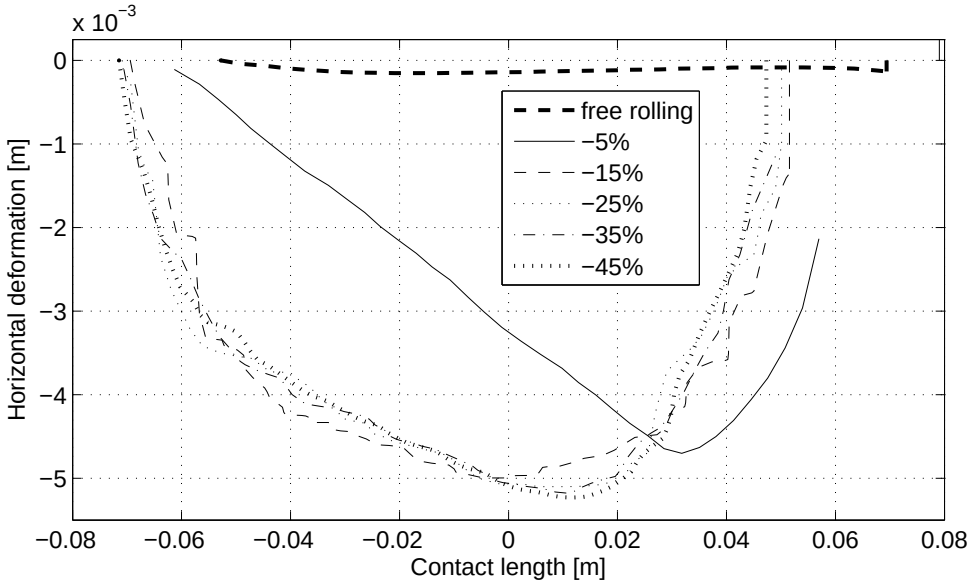

Figure 5.18 – The horizontal tread deformation distribution for various values of negative slip (braking wheel), in comparison to the free rolling one.

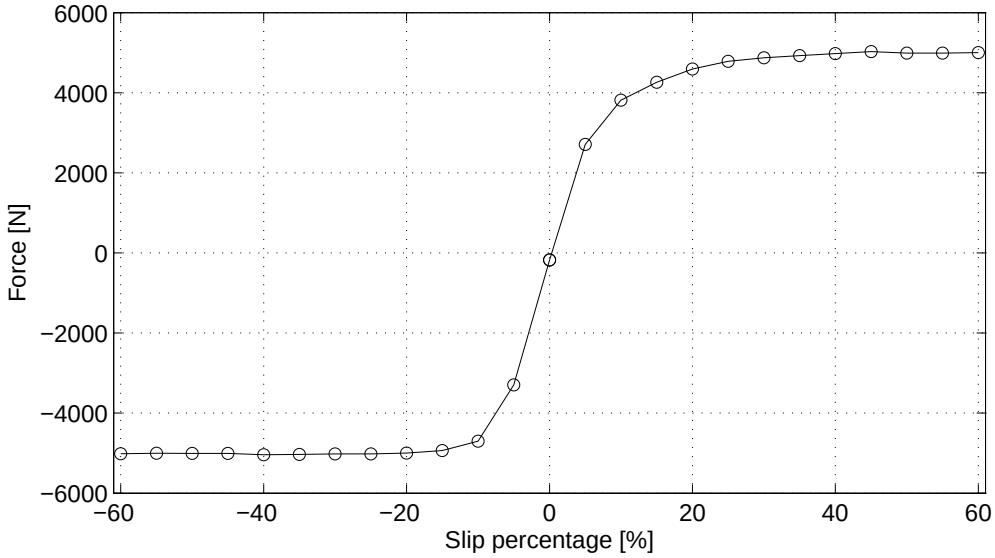

Figure 5.19 – The tyre traction force as a function of the slip percentage.

function of the macroscopic slip (fig. 5.19), leads to interesting conclusions. Typically, the force increases proportionally to the slip for small slip values but for higher slip values the force saturates, reaches a maximum value and remains constant for any further slip increase. Apparently, the initial linear behaviour corresponds to the slip values for which the relative length of the stick and slip zones varies while the saturation behaviour corresponds to the fixation of their relative dimensions. Apparently, the belt and tread damping mechanisms introduce a progressive transition of the force from the first zone to the second.

Incorporating in the same approach the capability of modelling the structural deformation, the damping mechanisms and the tread shear motion was found able to predict the experimentally observed nonlinear force development with the macroscopic slip, although an oversimplified friction law was used (Coulomb). The above conclusion supports the argument that the tyre forces nonlinearity should not be exclusively assigned to the tread viscoelastic friction characteristics but to a combination of structural and frictional phenomena.Obviously, the incorporation of a more realistic friction model (e.g. Savkoor [228], LuGre [42]) would improve the accuracy of the model, in case the coincidence with an experimental derived behaviour was to be enhanced. The qualitative agreement of the predicted pressure distributions, the tread slip development and the macroscopic tyre behaviour with a series of experimentally derived, published ones ([1], [18], [8]) is sufficient, though, for the purposes of this theoretical investigation.

5.7 The effect of the operating conditions on the modal participation

The use of a method based on the modal expansion for the simulation of the belt structural response, apart from the obvious computational advantage, also leads to the association of the tyre behaviour and performance with the participation of certain modes in its structural response. For this reason, the modal

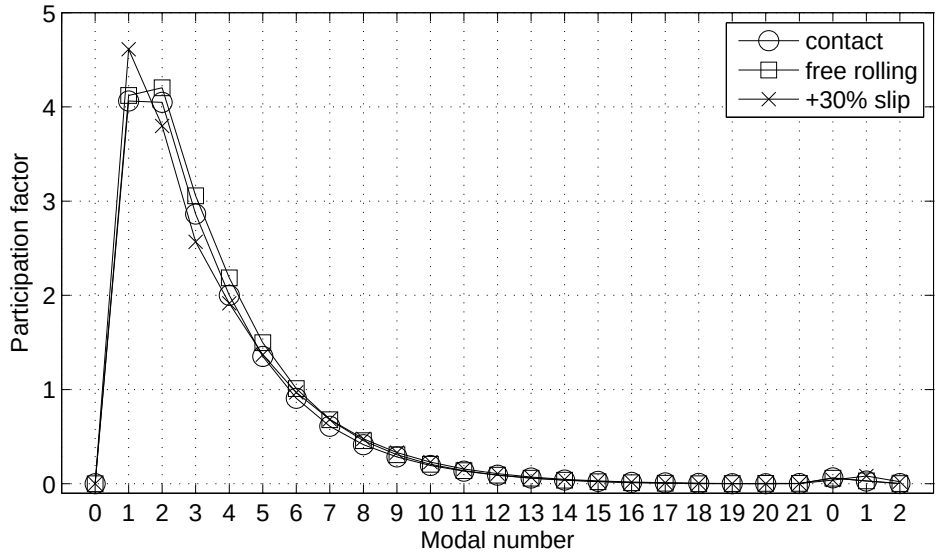

Figure 5.20 – The participation factors of the contact, free rolling and rolling under slip conditions.

participation factors corresponding to some of the above steady state operating conditions will be compared to the one corresponding to the contact equilibrium, derived in section 4.4.2 of chapter 4.

Following the respective analysis presented in chapters 3 (section 3.2) and 4 (section 4.4), every $n \geq 1$ mode is included in the modal basis twice (with a relative to each other angle of $\pi/2n$), so that any orientation of the mode shape may be represented through the linear combination of the participation of these two modes. Given that the global orientation of the two modes may be arbitrarily chosen, one of them may be chosen to be symmetrical to the perpendicular axis, for every modal number value. Contact imposes a symmetrical excitation and the respective structural deformation may be captured exclusively by these symmetrical modes. Consequently, the examination of the modal participation factors in the contact case (e.g. fig. 4.26), is a straightforward process given that participation of the symmetrical modes only is examined. In the rotation case, though, both modes participate in the non symmetrical response and the direct comparison of the participation factors with the contact case is not possible. For this reason a combined participation factor of every modal couple is derived using the equation:

$$\eta_n = \sqrt{(\eta_n^1)^2 + (\eta_n^2)^2} \tag{5.72}$$

Rolling operating conditions (both free and slip) do not impose radical changes to the contact induced structural response of the tyre. The decreasing with the modal number pattern of the participation factors, developed by the contact (fig. 4.26), may be also identified in the simulation results of the rolling cases, as comparatively presented in fig. 5.20.This result practically validates the application of a computational method based on the modal reduction on the simulation of the rolling operating conditions.

The percentage deviation of the modal participation factors from the contact equilibrium, induced by the free rolling conditions , is presented in fig. 5.21. Free rolling velocity values from 0 to $100km/h$ are examined, in $10km/h$ intervals. Two significant effects may be identified, the intensity of which increases

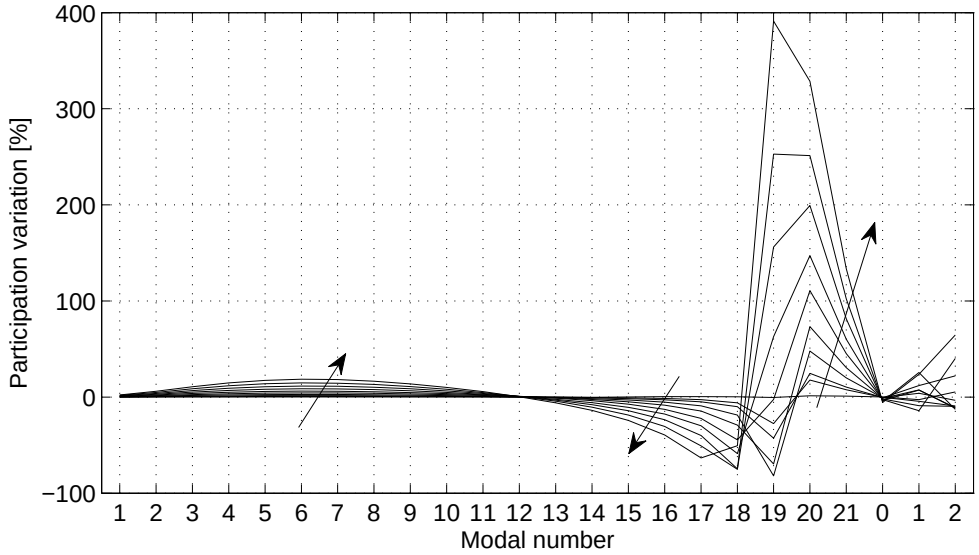

Figure 5.21 – The percentage variation of the participation of each mode from the respective static contact one, as a function of the free rolling velocity. The arrows indicate the increasing rolling velocity which covers the range from 0 to $100km/h$, in $10km/h$ intervals.

with the velocity. In the low modal number range a slight increase of the participation of the modes is observed, which becomes maximum for the $6th$ and $7th$ modes. In the high modal number range a decrease of the participation factor followed by a radical increase is the dominant effect of the rotation. For low values of the velocity this behaviour is developed in the region of the $19th$ and $20th$ modes, but as the rolling velocity increases it is transposed to the $18th$ and $19th$ modes.

The 80km/h case is chosen for further investigation under steady state slipping conditions and the percentage deviation of the participation factors from the free rolling respective ones is presented in fig. 5.22. The range up to 60% positive slip is examined, in 2.5% intervals. As it is expected, the tyre slip primarily results in the radical increase of the participation of the radial $n = 0$ mode, as the particular mode expresses the rigid torsional deformation of belt, relatively to the wheel. Examining the flexural modes, a slight participation decrease is noticed for the $n \geq 1$ modes and a local minimum is noticed for the $3rd$ mode. The most significant effect of the slip on the participation of the flexural modes, though, may be identified in the high modal number range, where a radical increase of the participation of the 18th mode is dominant.

Revisiting the discussion of section 4.4.2 of chapter 4, the drawn conclusion that the contact distribution shape may be associated with the mode shapes of the excited modes and their wavelengths, through the respective deformation of the belt, may be used for the analysis of the above participation factors variations. In the free rolling case, the trapezoidal distribution was retained but the pressure values decreased along its length, a shape variation matching the long wavelength of lower modal number modes (fig. 4.29). This change is depicted by the slight increase of the low modal number factors. Accordingly, the loss of symmetry and the increase of the pressure at the front section of the contact area are both, in terms of shape, highly localised changes, depicted by mode shapes of very short wavelength, such as the high modal number ones. These changes are associated with the radical variation of the participation factors which may be observed in the high modal range. The latter mechanism is also present in the slip rolling cases, given that the

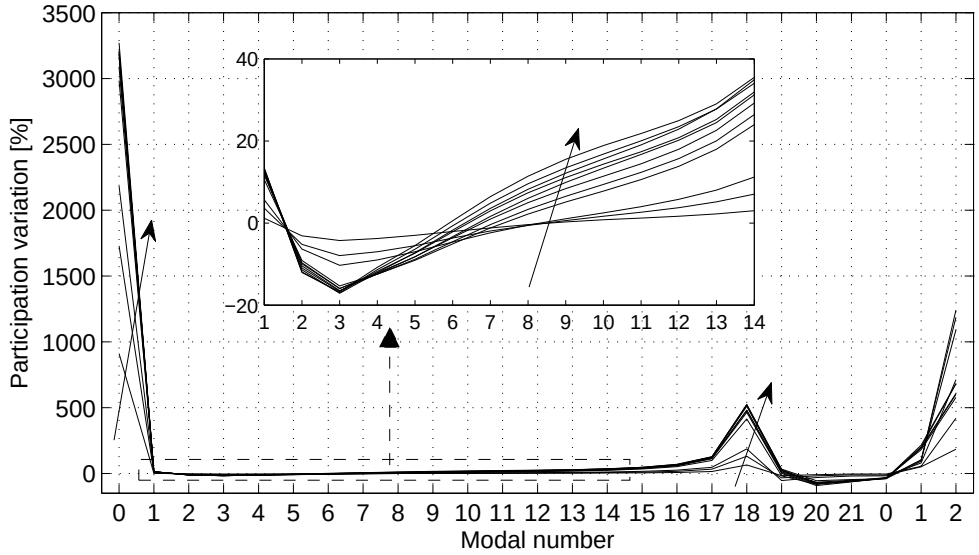

Figure 5.22 – The percentage variation of the participation of each mode from the respective free rolling one, as a function of the slip. The arrows indicate the increasing slip values, which cover the range from 0 to 60%, in 2.5% intervals.

respective distribution shapes also exhibit significant non symmetry. Moreover, the distribution shape was found to transform from a trapezoidal to a parabolic one, a distribution which corresponds to mode shapes of higher modal number. Accordingly, the participation of the very low modal number modes, which are responsible for the long wave length trapezoidal shape representation (such as the 3rd, the 4th and the 5th ones), decreases and the participation of the successive higher modal number modes, which are associated with shorter wavelength parabolic mode shapes,increases.

Furthermore, the concentration of the rolling effect in the high modal number range, in terms of percentage and not absolute effect, may be examined in combination with the sensitivity of the modes to the model's physical properties (section 3.4.1, chapter 3). In particular, it was found that each of the main physical properties of the model has a dominant effect on the modes across a certain modal number range: the radial sidewall on the low range, the inflation pretension on the medium range and the elastic modulus on the high one. The deviation of the rolling cases structural response from the respective contact one is captured by modes lying in the latter, elastic modulus dependent, zone. In respect, the effect of the structural properties on the tyre's shear force performance is primarily depicted by the one of the elastic modulus, in the same way that the corresponding effect on the contact behaviour was found to be depicted by the sidewall stiffness.

5.8 Summary of the chapter

In this chapter the simulation of the transient rolling operating conditions was investigated. Given that the small displacement assumption (on which the previous contact analysis was based) could not be justified, the wheel translational and rotational degrees of freedom were incorporated in the model. The large displacement

simulation was accomplished at two levels: the flexural response of the belt and the relative belt to wheel motion were captured by the modal response of the combined wheel and belt model, following the modal expansion method which was presented in chapter 3, expressed here in a moving system of reference. The translational and rotational rigid motions of the system were prescribed by the respective inertial equations of motion, calculated in the global (stationary) system of reference. The rigid motions were accordingly deduced from the modal motion calculations subtracting the corresponding to them force terms (composed as products of the respective accelerations and inertia terms) from the excitation expression of the transient system. The global system was also used for the calculation of the contact excitations and the expression of the external ones applied to the wheel.

The composed algorithm was used for the study of the launch process of a tyre, initially being in contact equilibrium under a constant vertical load applied to the wheel. The differences in the launch behaviour of the tyre, as imposed by the rotational or translational excitation, were analysed, corresponding to the driving or the driven wheel case respectively. In both cases, the roles of the friction and the damping mechanisms in the development of the respective horizontal or rotational velocity responses were found to be crucial.

Commonly, the tyre performance (at an experimental or simulation level) is investigated and expressed for steady state operating conditions. Theoretically, in order such conditions to be simulated by the dynamic algorithm, the respective excitation has to be known in advance and sufficient time for the equilibrium establishment should be provided. Both of these conditions, though, impose practical difficulties in their application to the model. Moreover, the assignment of certain kinematic values (e.g. global position or velocity) to certain degrees of freedom of the system is impossible as their kinematic conditions are calculated by the superposition of the modal vibrational response and the inertial motion of the system. Accordingly, the kinematic conditions could theoretically be prescribed by infinite combinations of the above responses. Two different methodologies were proposed for the tackling of the above problem. The kinematic conditions could be imposed to the wheel degrees of freedom while at the same time their respective modal response along the same global direction should be calculated and eliminated. Alternatively, the conditions could be applied to the total system's motion (instead of its degrees of freedom), omitting the respective inertial equations and allowing for the unrestricted development of the modal response.

Using the second method, which is also computationally more efficient, the free rolling of the tyre was examined, in terms of the two-dimensional contact pressure distribution development. Applying certain ratios of horizontal and angular velocity values to the system, steady state slipping conditions were simulated and the respective pressure distributions were derived. The saturation of the total shear force with the slip was found to be associated with the relative dimensions of the stick and slip zones along the contact area. Moreover, the prediction of the force saturation pattern using an oversimplified (non velocity dependent) friction model (Coulomb) proved that the the structural deformation and the damping mechanisms of the tyre certainly contribute to this characteristic behaviour, obviously in combination with the viscoelastic frictional properties of the tread.

The participation factors of the modes, excited by the rolling and slipping conditions, were investigated, in comparison to the ones corresponding to the static contact equilibrium conditions. Although the general, decreasing with the modal number pattern, was in general retained, in both rolling and slipping cases the participation of certain modes was found to increase radically. These modes belong to the high modal number range, which, as discussed in chapter 3, is mainly affected by the elastic modulus of the belt. In conclusion,

the respective effect of the structural deformation on the shear force performance was mainly assigned to the sensitivity of these modes to the elastic modulus property, in addition, obviously, to the obvious effect of the sidewall stiffness on the contact deformation and on the rigid body (relative to the wheel) torsional displacement of the belt.

Chapter 6

Conclusions and future work

6.1 Summary of the work

Following the initial brief presentation of the various tyre modelling approaches, the theoretical background for the development of a transient in-plane tyre model, able to capture the interaction between the structural response and the shear force development, was investigated. The proposed model was based on the modal representation of the tyre structural deformation for reasons associated with the computational efficiency of the method and the possible expression of the tyre response under varying operating conditions through the excitation of certain modes. The sensitivity of these modes to the model's physical properties was found to prescribe the effect of these properties on the performance characteristics and the behaviour of the tyre, something that the pure spatial modelling approaches cannot accomplish.

The investigation starts from the structural modal representation and progressively evolves to the simulation of the contact phenomena and later to the incorporation of the rolling and slipping conditions. These steps were respectively examined in the three basic chapters of the study and in each of them certain modelling enhancements to the initial vibrational model were proposed. In result, the effect of each of them on the accuracy and the simulation behaviour of the model was highlighted. Furthermore, having identified the key factors and mechanisms that define the tyre behaviour and the interaction of the structural response and the shear force development, the possible validity or not of various modal modelling approaches, which in many cases are a priori adopted and incorporated in the physical models, were critically examined. The basic findings of the study are briefly summarised in the following section.

6.2 Basic findings and conclusions

6.2.1 The simulation of the tyre modal behaviour

The modal prediction of both analytical (rectilinear or circular) and discretised modelling approaches was analysed across a broad modal range, as the sufficient breadth of the modal basis for the accurate capture of the structural mechanisms of the tyre behaviour is neither constant or a priori known. The analytical ring on elastic foundation model was used as a comparison basis, given that, at least in the low frequency

range, its correlation with the tyre modal behaviour has been experimentally established. The structural mechanisms that define the modal behaviour of the ring model and the physical properties that support their development were analysed. These factors were found to have a varying effect across the modal range and based on their possible capture or omission by the rest of the modelling approaches, their modal range of agreement with the ring one was identified, something that later defined their applicability or not on the particular study.

The primal vibration mechanism of a ring model is the circumferential bending deformation. Due to its circular shape, the respective strain is composed by both radial and tangential deformation contributions. It was found that both the radial and tangential groups predict a decreasing with the modal number participation in their mode shapes of the supplementary deformation to the one they are named after, which starts from an almost equal level to their primal one and progressively reduces with the modal number. Above a certain number, the radial modal group exhibits a pure radial deformation and the tangential modal group a pure tangential one. For this reason, the rectilinear modelling approaches were found to be insufficient for the capture of the low and medium modal range behaviour as they fail to predict such a deformation coupling. The low frequency range of the ring is primarily composed by the radial low and medium modal number modes and in respect the modelling capture of various mechanisms and properties' effects is necessary for the accurate simulation of the modal behaviour across this range. In contrast, the high frequency modal behaviour of the tyre is associated with a decoupled deformation pattern and pure bending or extensional deformation characteristics, that justify the use of simplified models. The modal prediction of the discretised models, was found to be in good correlation with the analytical ones as the deformation coupling in this case is induced by the angular transformation of the elements prior to their assembly. The modal characteristics of the modes that lie close to the upper limit of the available range deviate from the respective analytical ones, being usually significantly stiffer. In respect, the discretisation of the structure should be accomplished taking into consideration that not all the predicted modes correspond to modal behaviour of the structure, as induced by the respective physical mechanisms.

Using the ring model, the effect of three mechanisms across the predicted modal range was analysed: the non linear sidewall, the incorporation of the wheel in the modal expansion and the rotational phenomena. A membrane mechanism was proposed for the capture of the pressure and shape variation effects of the sidewall on the tyre behaviour, as an enhancement to the ring model. The incorporation of the wheel was found to affect only three modes of the ring model resulting in either an out of phase deformation response between the wheel and the belt, or an in-phase rigid mode one. Both the coriolis and centrifugal rotational phenomena were analysed. Given that they impose a non linear deviation to the ring model equations, the use of the modal basis, which is acquired for a particular value of the angular velocity, across a broader velocities range introduces a computational error. The magnitude of this error depends not only on the properties and the breadth of the range but also varies according to the modal number. It was found that the rotation phenomena primarily affect the low modal number modes and deteriorate in the high modal number range, a conclusion which supports the above stated argument that the low-medium range modal representation is more demanding in terms of mechanisms' and effects' consideration, compared to the high one. Finally, the effect of the common energy dissipation mechanisms on the predicted modal behaviour was also analysed. The correlation of the experimentally acquired damping characteristics with the respective ones predicted by some simplified modelling assumptions was investigated.

6.2.2 The simulation of the tyre contact behaviour

Based on the contact stiffness concept, a discretised foundation of tread elements was proposed for the simulation of the tyre contact behaviour. Each of the elements was composed by two, vertical to each other, Kelvin-Voigt elements, able to capture the slip displacement of the tread on the road surface, as imposed by the frictional conditions and its viscoelastic properties. This tread model was paired with a discretised form of the analytical ring model, decoupling the discretisation level from the modal range breadth and characteristics prediction. Assigning one tread element to each of the belt nodes, the physical mechanism of interaction between the belt deformation, the tread slip behaviour and the development of the two-dimensional contact pressure distribution field was identified.

The incorporation of the nonlinear, string based, sidewall mechanism to the model was found to have a significant effect on the predicted behaviour. Although for low deformation levels the vertical pressure distribution is a parabolic one independently from the sidewall mechanism, the actual buckling sidewall behaviour results in a concave (radial inwards) belt deformation as the load increases, which is not predicted by the linear sidewall model. This belt deformation pattern results in a similar pressure distribution shape, as opposed to a trapezoidal one for the linear model, and in a relative lower magnitude of the developed pressure field. In general, the conformation of the circular belt shape to a plane surface is associated with a horizontally outwards displacement, which is reacted by the friction force and results in an inwards directed horizontal pressure field. The radially inwards belt deformation was found to affect also the horizontal pressure distribution development as the respective belt points also move horizontally inwards. In this case, the respective friction force generates an outwards directed pressure field. The possible formation and the dimensions of the concave belt shape was found to affect the direction of the horizontal pressure field and also to justify a respective discrepancy between various experimental studies.

Examining the tyre contact from a computational point of view, it was found that the participation of both radial and tangential modes decreases with the modal number but also that the tangential modes participation is insignificant compared to the respective one of the radial modes. This conclusion theoretically validates the use of a reduced modal basis for the calculation of the contact induced structural deformation. Moreover, the reduction method may be based on the application of a frequency cut-off limit as the contact deformation was found to be accurately captured by a low and medium frequency range model. In particular, a modal basis reduced to $1kHz$, composed by 22 radial and 3 tangential modes, was found to offer a good combination of accuracy and computational efficiency, for typical tyre properties. The above conclusions justify the choice of the pretensioned ring model, as opposed to its simplified forms and the rectilinear representations, for the contact simulation modal basis construction, as the rest of them exhibit a significant modal characteristics deviation across the particular range of interest.

Interestingly, the increase of the deformation level was found to narrow the sufficient modal range for the achievement of a certain degree of accuracy. The profound belt deformation and contact length dimensions correlate better with the longer wavelength deformation patterns of the low modal number modes. In contrast, the study of moderate deformation cases requires shorter wavelength patterns associated with the mode shapes of the higher modal number modes.

6.2.3 The simulation of the tyre rolling and slipping conditions

The conceptual difference between the simulation of the contact and the rolling conditions is that in the second case the wheel and belt displacements cannot be assumed to be small, given that apart from the respective deformations a profound translational and rotational contribution to them develops. The small displacement assumption, though, is a necessary simulation requirement for any modal based method, given that the modal expansion is a linear transformation. A simulation methodology is proposed according to which a combined modal-time and space time-domain solution is accomplished. The belt deformation and the relative wheel to belt response are acquired using the respective modally expanded representation in a moving system of reference, while the rigid mode translation and rotation of the complete system is calculated in the space-time domain by the corresponding to it inertial equations. Using the above method, the tyre launch process was investigated and the differences between the driving and the driven wheel cases were identified. In both cases, the effect of the friction development and the damping characteristics (of both the tread foundation and the belt structure) were found to play a significant role in the development of the rolling conditions.

The problem of the application of steady state operating conditions to the model was examined, as in general the displacement superposition of the rigid and modal motion contributions imposes an infinite number of combinations resulting in the same macroscopically observed kinematic conditions of a degree of freedom. Applying, though, the steady state conditions to the system's motion, instead of the degree of freedom one, the free rolling conditions were imposed to the model. Based on them, the concept of the effective radius was derived in order the steady state slipping conditions to be defined using the macroscopic kinematic characteristics of the motion. The rolling and slipping conditions contact pressure distributions were found to lose their symmetry, compared to the static contact ones and the centre of pressure was found to move forward in the free rolling and accelerating wheel cases and backwards in the braking wheel ones. The relative length of the tread adhesion and slip zones varies as a function of the macroscopic slip and the shrinkage of the adhesion zone was found to be related to the force saturation for profound slip values. The prediction of the force saturation pattern of development using a simplified (non velocity dependent) Coulomb friction model proves the contribution of the structural deformation and damping mechanisms to the macroscopically observed tyre performance characteristics.

The participation of the modes in the contact and rolling deformation was found to follow the decreasing with the frequency pattern associated with the contact deformation. The loss of the deformation symmetry and the tangential excitation of the friction (in the case of slip) impose the radical increase of the participation of certain modes, lying in the high modal number zone. The actual mode associated with this behaviour depends on the model's physical properties and the imposed conditions. The modal basis of the model should be sufficiently broad so as to be able to capture such structural phenomena. Moreover, for the ring model, these modes were found to belong to the modal zone where the, elastic modulus dependent, bending stiffness is the predominant property. In respect, the association of the particular property with the shear force performance of the tyre may be proposed in addition to the already established sidewall mechanism dependent contact and torsional behaviour.

In general, the structural response of the tyre to contact and rolling -slipping operating conditions may be captured by a reduced modal basis, omitting the high modal number modes. Although this conclusion makes such models computationally superior to the pure space domain structural representations, at the

same time it imposes the necessary incorporation of certain physical mechanisms that may be neglected in the higher frequency range modal prediction. Low and medium frequency range phenomena associated with the coupling between the radial and the tangential deformations, the sidewall non linear behaviour, the pretension effects, the coriolis and centrifugal accelerations and the participation of the wheel in the modal behaviour cannot be neglected as they bear a significant effect on the tyre structural characteristics. This should be thoroughly considered when a modelling approach is to be proposed for the capture of the interaction between the modal behaviour and the shear force performance of the tyre, as usually the modal representations of the tyre structure are focused in the related NVH characteristics, primarily associated with the bending behaviour of it.

6.3 Future work

Apparently, the above work may be extended by the introduction of the lateral shear force and aligning moment development, together with the three-dimensional structural response of the belt. Such an approach would be able to offer a physical insight in the interaction between the frictional characteristics of the tyre along the two horizontal dimensions and would identify the actual mechanism and the structural contribution of the shear force reduction in the case of their coexistence.

The concept of using the participation factors of the excited modes for the study of the effect of the tyre physical properties on its performance characteristics may be further investigated. A respective study should be based on a more accurate tyre physical representation, than the ring model used here, offering a direct association of the modal characteristics with the used materials, the different tyre zones and the construction methods. A modal basis composed by such a model could lead to interesting conclusions regarding the possible operational tunning of certain modes of the tyre. Especially in the cases that the tyre performance under strictly defined conditions is to be investigated (e.g. anti-lock braking systems, launch process control, e.t.c.) the respective modes may be used for the optimisation of the tyre behaviour. Obviously, such an investigation should definitely include the experimental validation of the method and the possible conclusions.

The theoretical background of the combined space-time and modal-time domains simulation could be applied to a broader subsystem including the suspension of the vehicle. The interaction between the tyre shear force generation, its structural response and the suspension characteristics should be investigated. Although methods for the modal coupling of the tyre and the suspension have been proposed, they focus in the combined NVH characteristics and their effects on the vehicle's chassis. The inclusion of the transient shear force and slip development effects in the interaction necessitates a tyre modelling approach similar to the one developed in the present study.

Finally, the above, large-displacement but modal based, simulation methodology could be applied to various systems exhibiting an operational response following certain deformation patterns. The latter characteristic was found to promote the applicability of a modally reduced structural representation which offers a significant computational efficiency advantage compared to conventional space domain simulation methods.

Nomenclature

α	global angle of tread orientation
β_d	stiffness proportional viscous damping coefficient
ΔR_t	axial (radial) deformation of tread element
ΔT_t	tangential (vertical to axial) deformation of tread element
ΔX_t	horizontal deformation of tread element
ΔY_t	vertical deformation of tread element
ΔY_w	vertical relative approach between the road and the wheel, measured from the critical contact initial condition
$\frac{\partial}{\partial}$	partial derivative
$\dot{}$	time derivative
ϵ_{ss}	tension (membrane) strain of an arch
η	modal participation factor
γ_d	inertia proportional viscous damping coefficient
ι	complex value $\sqrt{-1}$
κ_{ss}	bending strain of an arch
λ	modal damping coefficient
$\mathbf{\Psi}$	eigenvector
$\mathbf{\Psi}^d$	damped eigenvector
$\mathbf{A}^{ss}$	matrix coefficient of the discretised state space model representation
$\mathbf{B}^{ss}$	matrix coefficient of the discretised state space model representation
$\mathbf{C}^m$	modal damping matrix
$\mathbf{F}$	vector of the belt nodes' excitation forces

$\mathbf{F}^s$	excitation vector of the discretised belt, including the acceleration terms corresponding to the transient system's acceleration
$\mathbf{F}_t$	vector of the contact forces applied from the tread elements to the corresponding belt nodes
$\mathbf{K}$	stiffness matrix
$\mathbf{K}^m$	modal stiffness matrix
$\mathbf{M}$	inertia matrix
$\mathbf{M}^m$	modal mass matrix
$\mathbf{T}$	global to local system of axis transformation matrix
$\mathbf{u}$	vector of the belt nodes' deformation response
$\mathbf{u}^{ss}$	vector of nodes' state space response
Ω	belt angular velocity of rotation
ω	natural frequency
ω_d	damped natural frequency
Ω_{ms}	angular propagation velocity of a mode shape of a rotating tyre
Φ_s	global orientation of the moving system of reference, measure in the stationary one
Φ_w^m	modal amplitude of the wheel angle of rotation
ρ	belt material density
$\mathbf{L}_{\mathrm{r/t}}^{\mathrm{d}}$	damping force partial differential operator
$\mathbf{L}_{\mathrm{r/t}}^{\mathrm{s}}$	stiffness force partial differential operator
t	time
Θ	central angle of rotating belt, in the stationary system of axis
θ	central angle of belt arch, used as a position variable along it's circumference
θ_n	the central angle of the mode shape wavelength of the nth mode
Θ_{ms}	global rotation angle of a mode shape of a rotating tyre
θ_{n_b}	the central angle of two successive belt nodes
$\tilde{\eta}$	vector of modal participation factors of the modal basis modes
$\tilde{\mathbf{\Psi}}$	eigenvectors' matrix (modal basis)
φ	orientation angle of mode shape analytical function

$\varphi_{g\to l}$ the global to local system of axis transformation angle of the rectilinear elements of a discretised belt model

ζ modal damping ratio

ζ^h hysteretic damping ratio (loss factor)

^{T} matrix transpose

A belt cross section area

b belt width

c contact indicator

c^m viscous modal damping coefficient

C^t axial viscous damping coefficient of tread element

D bending stiffness of an arch, normalised to its length

d belt cross section height (radial dimension)

D^* bending stiffness of an arch, normalised to its length and width

DOF degree of freedom

E belt material elastic modulus

$F(\mathrm{t})$ concentrated or total force, as a function of time (t)

$f(\theta, \mathrm{t})$ belt excitation force, as analytical function of time (t)and central angle (θ)

f^m modal force

$F^{b\to w}$ total force applied from the belt nodes to the wheel, through the non linear sidewall foundation

F_t contact force applied to the belt node from the tread element along its direction

F_t^d viscous damping contact force applied to the belt node from the tread element along its direction

F_t^s stiffness contact force applied to the belt node from the tread element along its direction

fr free rolling steady state tyre operating conditions

$G(\theta, \mathrm{t})$ energy dissipation analytical function

I belt cross section second moment of inertia

i belt node index

I_b belt moment of inertia

I_w wheel moment of inertia

j mode index

K tension stiffness of an arch, normalised to its length

k sidewall stiffness, normalised to circumference length

K^* tension (membrane) stiffness of an arch, normalised to its length and width

k^m modal stiffness

K^t axial stiffness of tread element

L wheel to belt distance

l length of the rectilinear element of a discretised belt model

l_s string arch circumferential length

l_t initial axial length of tread element

$local/global$ local/global system of axis index

$M(\mathrm{t})$ moment of rotation, as a function of time (t)

m^m modal mass

$M^{b\to w}$ total moment applied from the belt nodes to the wheel, through the non linear sidewall foundation

m_b belt mass

m_t mass of tread element

m_w wheel mass

M_{ss} bending moment of an arch, normalised to its length and width

n modal number

n_b number of nodes/elements of a discretised belt model

n_m number of modes of modal basis

N_{ss} tension (membrane) pressure of an arch

$p(\theta, \mathrm{t})$ belt excitation force, as analytical function of time (t)and central angle (θ), normalised to the circumferential length and belt width (b)

P_0 tyre inflation pressure

P_0^* discretisation normalised inflation pressure

$q(\theta, \mathrm{t})$ belt excitation force, as analytical function of time (t)and central angle (θ), normalised to the circumferential length

R	belt radius
r/t	radial/tangential index
R^m	radial deformation amplitude of a mode shape
R_s	radius of curvature of an arch
r_s	string or membrane profile radius of curvature
R_w	wheel radius
R_w^m	modal amplitude of the wheel displacement projected on the radial direction
R_{ef}	the effective rolling radius of the tyre
s	length variable of an arch along its central axis
sl	the macroscopic tyre slip
T	string tension force
T^m	tangential deformation amplitude of a mode shape
T_n	out of plane component of the string or membrane tension force
T_r	in plane component of the string or membrane tension force
T_w^m	modal amplitude of the wheel displacement projected on the tangential direction
$U(\theta)$	belt deformation, as analytical function of the circumferential position (θ)
$u(\theta, \mathrm{t})$	belt deformation, as an analytical function of the central angle (θ)and the time (t)
u^s	displacement of the moving system of reference
$u^w(\mathrm{t})$	wheel translational displacement, as a function of time (t)
$u_\Phi^w(\mathrm{t})$	wheel angle of rotation, as a function of time (t)
$u^{s.v.}$	generalised state variables for the damping force calculation
u_Φ^s	angular displacement of the moving system of reference
w	central angle of the string or membrane profile arc
X/Y	global horizontal/vertical index
x/y	local (moving) system horizontal/vertical index
X_s	horizontal global coordinate of the moving system of reference, measure in the stationary one
X_t	global horizontal coordinate of the tread element's tip

X_w global horizontal coordinate of the wheel

X_w^m modal amplitude of the horizontal wheel displacement

XOY global (stationary) system of reference

xOy local (moving) system of reference

Y_b vertical global coordinate of a belt point

Y_r vertical global coordinate of the road profile at the contact point

Y_s vertical global coordinate of the moving system of reference, measure in the stationary one

Y_t global vertical coordinate of the tread element's tip

Y_w global vertical coordinate of the wheel

Y_w^m modal amplitude of the vertical wheel displacement

Bibliography

[1] H. Pacejka, *Tyre and Vehicle Dynamics*. Butterworth-Heinemann, 2006.

[2] R. J. Reinalter, W. and A. Lutz, "TMPT–conclusions and consequences for the industry from the industry," *Vehicle System Dynamics*, vol. 45, no. supplement, pp. 217–225, 2007.

[3] P. Bösch, D. Ammon, and F. Klempau, "Reifenmodelle–Wunsch und Wirklichkeit aus der Sicht der Fahrzeugentwicklung (Tire models–wish and reality, seen from vehicle development needs)," *VDI progress report series*, vol. 12, pp. 87–101, 2002.

[4] J. Reimpell, H. Stoll, and J. Betzler, *The Automotive Chassis: Engineering Principles (Second Edition)*. Butterworth Heinemann, 2001.

[5] A. Sitchin, "Acquisition of transient tire force and moment data for dynamic vehicle handling simulations," *SAE Paper no. 831790*, 1983.

[6] H. Pacejka, "Study of the lateral behaviour of an automobile moving on a flat, level road, and of an analog method of solving the problem," *Cornell Aeronautical Laboratory Report YC-857-F-23*, 1958.

[7] H. S. Radt and W. F. J. Milliken, "Non-dimensionalizing tyre data for vehicle simulation," *In Proceedings of the Road Vehicle Handling Conference (IMechE)*, pp. 229 – 240, London, United Kingdom, 1983.

[8] W. Milliken and D. Milliken, *Race Car Vehicle Dynamics*. SAE, 1995.

[9] E. Bakker, L. Nyborg, and H. Pacejka, "Tyre modelling for use in vehicle dynamics studies," *SAE Paper no. 870421*, 1987.

[10] E. Bakker, H. Pacejka, and L. Lidner, "A new tire model with an application in vehicle dynamics studies," *SAE Paper no. 890087*, 1989.

[11] R. Sharp and M. Bettella, "Tyre Shear Force and Moment Descriptions by Normalisation of Parameters of the Magic Formula," *Vehicle System Dynamics*, vol. 39, no. 1, pp. 27–56, 2003.

[12] R. Sharp, "Testing and Improving a Tyre Shear Force Computation Algorithm," *Vehicle System Dynamics*, vol. 41, no. 3, pp. 223–247, 2004.

[13] K. Rao, R. Kumar, R. Mukhopadhyay, and V. Misra, "A study of the relationship between Magic Formula coefficients and tyre design attributes through finite element analysis," *Vehicle System Dynamics*, vol. 44, no. 1, pp. 33–63, 2006.

[14] D. Arosio, F. Braghin, F. Cheli, and E. Sabbioni, "Identification of Pacejka's scaling factors from full-scale experimental tests," *Vehicle System Dynamics*, vol. 43, no. 1, pp. 457–474, 2005.

[15] C. Lu and M. Shih, "An experimental study on the longitudinal and lateral adhesive coefficients between the tyre and the road for a light motorcycle," *Vehicle System Dynamics*, vol. 43, no. supplement, pp. 168 – 178, 2005.

[16] A. Higuchi and H. Pacejka, "The Relaxation Length Concept at Large Wheel Slip and Camber," *Vehicle System Dynamics*, vol. 27, no. supplement, pp. 50–64, 1996.

[17] H. Pacejka and I. Besselink, "Magic Formula Tyre Model with Transient Properties," *Vehicle System Dynamics*, vol. 27, no. supplement, pp. 234–249, 1996.

[18] S. Clark, *Mechanics of Pneumatic Tires*. National Highway Traffic Safety Administration (US Department of Transportation), 1981.

[19] E. Winkler, *Die Lehre von der Elastizitat und Festigkeit (The theory of elasticity and thickness)*. H. Dominicus, Prague, 1867.

[20] H. Pacejka and R. Sharp, "Shear Force Development by Pneumatic Tyres in Steady State Conditions: A Review of Modelling Aspects," *Vehicle System Dynamics*, vol. 20, no. 3, pp. 121–175, 1991.

[21] R. Sharp and M. El-Nashar, "A Generally Applicable Digital Computer Based Mathematical Model for the Generation of Shear Forces by Pneumatic Tyres," *Vehicle System Dynamics*, vol. 15, no. 4, pp. 187–209, 1986.

[22] G. Gim and P. Nikavresh, "An analytical model of pneumatic tires for vehicle dynamic simulations: Part 1. Pure slips," *International Journal of Vehicle Design*, vol. 11, no. 6, pp. 589–618, 1990.

[23] G. Gim and P. Nikavresh, "An analytical model of pneumatic tires for vehicle dynamic simulations: Part2. Comprehensive slips," *International Journal of Vehicle Design*, vol. 12, no. 2, pp. 19–39, 1991.

[24] G. Gim and P. Nikavresh, "An analytical model of pneumatic tires for vehicle dynamic simulations: Part3. Validation agianst experimental data," *International Journal of Vehicle Design*, vol. 12, no. 2, pp. 217–218, 1991.

[25] M. Levin, "Investigation of Features of Tyre Rolling at Non-Small Velocities on the Basis of a Simple Tyre Model with Distributed Mass Periphery," *Vehicle System Dynamics*, vol. 23, no. 1, pp. 441–466, 1994.

[26] M. Salaani, "Analytical Tire Forces and Moments with Physical Parameters," *Tire science and Technology*, vol. 36, no. 1, pp. 3–42, 2008.

[27] A. Sorniotti and M. Velardocchia, "Enhanced Tire Brush Model for Vehicle Dynamics Simulation," *SAE Paper no. 2008-01-0595*, 2008.

[28] F. Frank, *Theorie des Reifenschräglaufs*. PhD Thesis, Braunschweig, 1965.

[29] R. Sharp, "Tyre structural mechanisms influencing shear force generation: Ideas from a multi-radial-spoke model," *Vehicle System Dynamics*, vol. 21, pp. 145–155, 2004.

[30] J. Pauwelussen, "The Local Contact Between Tyre and Road Under Steady State Combined Slip Conditions," *Vehicle System Dynamics*, vol. 41, no. 1, pp. 1–26, 2004.

[31] C. Clover and J. Bernard, "Longitudinal Tire Dynamics," *Vehicle System Dynamics*, vol. 29, no. 4, pp. 231–260, 1998.

[32] G. Gim, Y. Choi, and S. Kim, "A semiphysical tyre model for vehicle dynamics analysis of handling and braking," *Vehicle System Dynamics*, vol. 45, no. supplement, pp. 169–190, 2007.

[33] G. Rill, "First order tire dynamics," *In Proceedings of the 3rd European Conference on Computational Mechanics Solids, Structures and Coupled Problems in Engineering*, Lisbon, Portugal, 2006.

[34] W. Hirschberg, "Tire model TMeasy," *Vehicle System Dynamics*, vol. 45, no. supplement, pp. 101–119, 2007.

[35] R. J. Lutz, A. and V. Reinalter, "Developments in vehicle dynamics and the tire model performance test," *Vehicle System Dynamics*, vol. 45, no. supplement, pp. 7–19, 2007.

[36] C. de Wit, H. Olsson, K. Astrom, and P. Lischinsky, "Dynamic friction models and control design," *In Proceedings of the American Control Conference*, San Franciso, USA, 1993.

[37] C. de Wit, H. Olsson, K. J. Astrom, and P. Lischinsky, "A new model for control of systems with friction," *IEEE Transactions on Automatic Control*, vol. 40, no. 3, pp. 419–425, 1995.

[38] P. Dahl, "A solid friction model," *The Aerospace Corporation Tech. Rep. TOR-158 (3107-18)-1*, 1968.

[39] C. de Wit and P. Tsiotras, "Dynamic tire friction models for vehicle traction control," *In Proceedings of the 38th Conference on Decision and Control (IEEE)*, Phoenix, USA, 1999.

[40] P. Tsiotras, E. Velenis, and M. Sorine, "A LuGre tire friction model with exact aggregate dynamics," *Vehicle System Dynamics*, vol. 42, no. 3, pp. 195–210, 2004.

[41] E. Velenis, P. Tsiotras, and M. Sorine, "Dynamic tyre friction models for combined longitudinal and lateral vehicle motion," *Vehicle System Dynamics*, vol. 43, no. 1, pp. 3–29, 2005.

[42] K. Åström and C. C. De Wit, "Revisiting the LuGre friction model," *Control Systems Magazine, IEEE*, vol. 28, no. 6, pp. 101–114, 2008.

[43] R. R. Liang W., Medanic J., "Analytical dynamic tire model," *Vehicle System Dynamics*, vol. 46, no. 3, pp. 197–227, 2008.

[44] B. v. Schlippe and R. Dietrich, "Das Flattern eines bepneuten Rades (The fluttering of an inflated wheel)," *Lilienthall Gessellschaft*, vol. 140, pp. 34–34, 1941 (english translation: NACA Report TM1365, 1954).

[45] I. Besselink, *Shimmy of aircraft main landing gears*. PhD Thesis, Delft, 2000.

[46] Q. Liu, J. Lee, and K. Guo, "Analysis of Non-Steady State Tire Cornering Properties Based on String-Concept Deformation and Geometric Relationship of Contact Patch," *SAE Paper no. 2007-01-1514*, 2007.

[47] E. Kuiper and J. Van Oosten, "The PAC2002 advanced handling tire model," *Vehicle System Dynamics*, vol. 45, no. supplement, pp. 153–167, 2007.

[48] H. Pacejka, *The wheel shimmy phenomenon.* PhD Thesis, Delft, 1966.

[49] H. Pacejka, "Analysis of the Dynamic Response of a Rolling String-Type Tire Model to Lateral Wheel-Plane Vibrations," *Vehicle System Dynamics*, vol. 1, no. 1, pp. 37–66, 1972.

[50] J. Zhou, J. Wong, and R. Sharp, "A Multi-Spoke, Three Plane Tyre Model for Simulation of Transient Behaviour," *Vehicle System Dynamics*, vol. 31, no. 1, pp. 35–45, 1999.

[51] G. Mastinu and M. Fainello, "Study of the Pneumatic Tyre Behaviour on Dry and Rigid Road by Finite Element Method," *Vehicle System Dynamics*, vol. 21, no. 1, pp. 143–165, 1992.

[52] G. Mastinu, S. Gaiazzi, F. Montanaro, and D. Pirola, "A Semi-Analytical Tyre Model for Steady-and Transient-State Simulations," *Vehicle System Dynamics*, vol. 27, pp. 2–21, 1996.

[53] B. Kao, "Tire Vibration Modes and Tire Stiffness," *Tire Science and Technology*, vol. 30, no. 3, pp. 136–155, 2002.

[54] J. Dunn, "Experimental and theoretical mechanical mobility characterising functions of rolling and non-rolling tyres," *In Proceedings of the 1st Symposium on Science and Motor Vehicles*, Belgrade, Serbia, 1972.

[55] O. Olatunbosun, "Generalized representation of the low frequency radial dynamic parameters of rolling tyres," *International Journal of Vehicle Design*, vol. 12, no. 5–6, pp. 513–524, 1991.

[56] H. Sugiyama and Y. Suda, "Modeling nonlinear flexible tire belt in the study of in-plane tire dynamics," *In Proceedings of the International Design Engineering Technical Conference (DETC–ASME)*, New York, USA, 2007.

[57] P. v. d. Jagt, H. Pacejka, and A. Savkoor, "Influence of tyre and suspension dynamics on the braking performance of an anti-lock system on uneven roads," *In Proceedings of the 2nd International Conference on New Developments in Powertrain and Chassis Engineering (EAEC–IMechE)*, Strasbourg, Austria, 1989.

[58] P. Zegelaar, *The dynamic response of tyres to brake torque variations and road unevennesses.* PhD Thesis, Delft, 1998.

[59] J. Maurice, *Short wavelength and dynamic tyre behaviour under lateral and combined slip conditions.* PhD Thesis, Delft, 2000.

[60] P. Zegelaar, S. Gong, and H. Pacejka, "Tyre Models for the Study of In-Plane Dynamics," *Vehicle System Dynamics*, vol. 23, pp. 578–590, 1994.

[61] P. Zegelaar and H. Pacejka, "The In-Plane Dynamics of Tyres on Uneven Roads," *Vehicle System Dynamics*, vol. 25, pp. 714–730, 1996.

[62] P. Zegelaar and H. Pacejka, "Dynamic tyre responses to brake torque variations," *Vehicle System Dynamics*, vol. 27, no. supplement, pp. 65–79, 1997.

[63] J. Maurice, P. Zegelaar, and H. Pacejka, "The influence of belt dynamics on cornerig and braking properties of tyres," *Vehicle System Dynamics*, vol. 29, pp. 299–311, 1998.

[64] S. Jansen, P. Zegelaar, and H. Pacejka, "The Influence of In-Plane Tyre Dynamics on ABS Braking of a Quarter Vehicle Model," *Vehicle System Dynamics*, vol. 32, no. 2, pp. 249–261, 1999.

[65] A. Schmeitz, "TNO MF-SWIFT," *Vehicle System Dynamics*, vol. 45, no. supplement, pp. 121–137, 2007.

[66] K. Guo, L. Ren, and Y. Hou, "A Non-Steady Tire Model for Vehicle Dynamic Simulation and Control," *In Proceedings of the 4th International Symposium on Advanced Vehicle Control (AVEC)*, Nagoya, Japan, 1998.

[67] K. Guo, "UniTire: unified tire model for vehicle dynamic simulation," *Vehicle System Dynamics*, vol. 45, no. supplement, pp. 79–99, 2007.

[68] A. Gallrein, "CDTire: a tire model for comfort and durability applications," *Vehicle System Dynamics*, vol. 45, no. supplement, pp. 69–77, 2007.

[69] F. Böhm, "Mechanik des gürtelreifens (Mechanics of the tyre belt)," *Ingenieur-Archiv*, vol. 35, no. 2, pp. 82–101, 1966.

[70] R. Hoppe, "The Bending Vibration of a Circular Ring," *Crelles Journal of Mathematics*, vol. 73, p. 158170, 1871.

[71] J. Tielking, "Plane vibration characteristics of a pneumatic tire model," *SAE Paper no. 6504925*, 1965.

[72] D. Dodge, "The dynamic stiffness of a pneumatic tire model," *SAE Paper no. 650491*, 1965.

[73] S. Clark, "Rolling tire under load," *SAE Paper no. 650493*, 1965.

[74] A. Chiesa, L. Obert, and L. Tamburini, "Transmission of tyre vibrations," *Automobile Engineer*, vol. 54, pp. 520–530, 1964.

[75] G. Potts, C. Bell, L. Charek, and T. Roy, "Tire vibrations," *Tire Science and Technology*, vol. 5, no. 1, pp. 202–225, 1977.

[76] P. Zegelaar, "Modal Analysis of Tire In-Plane Vibration," *SAE Paper no. 971101*, 1997.

[77] L. Yam, D. Guan, and A. Zhang, "Three-dimensional mode shapes of a tire using experimental modal analysis," *Experimental Mechanics*, vol. 40, no. 4, pp. 369–375, 2000.

[78] D. Guan, L. Yam, M. Mignolet, and Y. Li, "Experimental Modal Analysis of Tires," *Experimental Techniques*, vol. 24, no. 6, pp. 39–45, 2000.

[79] J. Perisse and J. Hamet, "A comparison of the 2d ring and 3d orthotropic plate for modelling of radial tire vibrations," *In Proceedings of the Internoise Conference*, Nice, France, 2000.

[80] Z. Geng, A. Popov, and D. Cole, "Measurement, identification and modelling of damping in pneumatic tyres," *International Journal of Mechanical Sciences*, vol. 49, no. 10, pp. 1077–1094, 2007.

[81] S. Clark, "Mechanics of Pneumatic Tyres: Tire in-plane dynamics," *National Bureau of Standards, Monograph 122*, 1971.

[82] J. Padovan, "On viscoelasticity and standing waves in tires," *Tire Science and Technology*, vol. 4, no. 4, pp. 233–246, 1976.

[83] W. Soedel, *Vibrations of Shells and Plates*. Marcel Dekker Inc., 2004.

[84] A. Leissa, *Vibration of Shells (NASA SP-288)*. US Government Printing Office, 1973.

[85] G. Bryan, "On the beats in the vibrations of a revolving cylinder or bell," *In Proceedings of the Cambridge Philosophical Society*, vol. 7, no. 1, pp. 101–111, 1890.

[86] G. Carrier, "On the vibrations of the rotating ring," *Quarterly of Applied Mathematics*, vol. 3, pp. 235–245, 1945.

[87] D. Johnson, "Free Vibration of a Rotating Elastic Body: The General Theory and Some Examples of Practical Cases," *Aircraft Engineering and Aerospace Technology*, vol. 24, no. 8, pp. 234–236, 1952.

[88] J. Padovan, "Natural frequencies of rotating prestressed cylinders," *Journal of Sound and Vibration*, vol. 31, no. 4, pp. 469–482, 1973.

[89] M. Endo, K. Hatamura, M. Sakata, and O. Taniguchi, "Flexural vibration of a thin rotating ring," *Journal of Sound and Vibration*, vol. 92, no. 2, pp. 261–272, 1984.

[90] W. Bickford and E. Reddy, "On the in-plane vibrations of rotating rings," *Journal of Sound and Vibration*, vol. 101, no. 1, pp. 13–22, 1985.

[91] T. Saito and M. Endo, "Vibration of finite length, rotating cylindrical shells," *Journal of Sound and Vibration*, vol. 107, no. 1, pp. 17–28, 1986.

[92] J. Lin and W. Soedel, "On general in-plane vibrations of rotating thick and thin rings," *Journal of Sound and Vibration*, vol. 122, no. 3, pp. 547–570, 1988.

[93] S. Natsiavas, "Dynamics and stability of non-linear free vibration of thin rotating rings," *International Journal of Non-linear Mechanics*, vol. 29, no. 1, pp. 31–48, 1994.

[94] R. Eley, C. Fox, and S. McWilliam, "Coriolis coupling effects on the vibration of rotating rings," *Journal of Sound and Vibration*, vol. 238, no. 3, pp. 459–480, 2000.

[95] W. Kim and J. Chung, "Free non-linear vibration of a rotating thinring with the in-plane and out-of-plane motions," *Journal of Sound and Vibration*, vol. 258, no. 1, pp. 167–178, 2002.

[96] S. Huang and W. Soedel, "Effects of coriolis acceleration on the free and forced in-plane vibrations of rotating rings on elastic foundation," *Journal of Sound and Vibration*, vol. 115, no. 2, pp. 253–274, 1987.

[97] J. Padovan, "On standing waves in tires," *Tire Science and Technology*, vol. 5, no. 2, pp. 83–101, 1977.

[98] S. Huang and W. Soedel, "Response of rotating rings to harmonic and periodic loading and comparison with the inverted problem," *Journal of Sound and Vibration*, vol. 118, no. 2, pp. 253–70, 1987.

[99] S. Huang and B. Hsu, "An approach to the dynamic analysis of rotating tire-wheel-suspension units," *Journal of Sound and Vibration*, vol. 156, no. 3, pp. 505–519, 1992.

[100] Y. Wei, L. Nasdala, and H. Rothert, "Analysis of forced transient response for rotating tires using REF models," *Journal of Sound and Vibration*, vol. 320, no. 1-2, pp. 145–162, 2009.

[101] L. Meirovitch, "A modal analysis for the response of linear gyroscopic systems," *Journal of Applied Mechanics*, vol. 42, pp. 446–450, 1975.

[102] R. Kennedy and J. Padovan, "Finite element analysis of steady and transiently moving/rolling nonlinear viscoelastic structure. II: Shell and three-dimensional simulations," *Computers & structures*, vol. 27, no. 2, pp. 259–273, 1987.

[103] W. Soedel, "On the dynamic response of rolling tires according to thin shell approximations," *Journal of Sound and Vibration*, vol. 41, no. 2, pp. 233–246, 1975.

[104] C. Dohrmann, "Dynamics of a tire–wheel–suspension assembly," *Journal of Sound and Vibration*, vol. 210, no. 5, pp. 627–642, 1998.

[105] S. Saigal, T. Yang, H. Kim, and W. Soedel, "Free vibrations of a tire as a toroidal membrane," *Journal of Sound and Vibration*, vol. 107, no. 1, pp. 71–82, 1986.

[106] J. Perisse, J. Clairet, and J. Hamet, "Modal testing of a smooth tire in low and medium frequency-estimation of structural parameters," *SPIE proceedings series*, pp. 960–967, 2000.

[107] J. Muggleton, B. Mace, and M. Brennan, "Vibrational response prediction of a pneumatic tyre using an orthotropic two-plate wave model," *Journal of Sound and Vibration*, vol. 264, no. 4, pp. 929–950, 2003.

[108] F. Wullens and W. Kropp, "A Three-Dimensional Contact Model for Tyre/Road Interaction in Rolling Conditions," *Acta Acustica united with Acustica*, vol. 90, no. 4, pp. 702–711, 2004.

[109] K. Larsson and W. Kropp, "A high-frequency three-dimensional tyre model based on two coupled elastic layers," *Journal of Sound and Vibration*, vol. 253, no. 4, pp. 889–908, 2002.

[110] W. Kropp, *Ein Modell zur Beschreibung des Rollgeräusches eines unprofilierten Gürtelreifens auf rauher Strassenoberfläche (A model for the descripton of the rolling noise of an non patterned tyre on a rough road)*. PhD Thesis, Düsseldorf, 1992.

[111] P. Dinkova and W. Kropp, "A model for the dynamic response of truck tyres based on two elastic layers," *In Proceedings of the 4th European Conference for Constitutive Models for Rubber (ECCMR)*, Stockholm, Sweden, 2005.

[112] R. Pinnington and A. Briscoe, "A wave model for a pneumatic tyre belt," *Journal of Sound and Vibration*, vol. 253, no. 5, pp. 941–959, 2002.

[113] R. Pinnington, "A wave model of a circular tyre. Part 1: belt modelling," *Journal of Sound and Vibration*, vol. 290, no. 1-2, pp. 101–132, 2006.

[114] R. Pinnington, "A wave model of a circular tyre. Part 2: side-wall and force transmission modelling," *Journal of Sound and Vibration*, vol. 290, no. 1-2, pp. 133–168, 2006.

[115] Y. Chang, T. Yang, and W. Soedel, "Dynamic analysis of a radial tire by finite elements and modal expansion," *Journal of Sound and Vibration*, vol. 96, no. 1, pp. 1–11, 1984.

[116] L. Kung, W. Soedel, and T. Yang, "Free vibration of a pneumatic tire-wheel unit using a ring on an elastic foundation and a finite element model," *Journal of Sound and Vibration*, vol. 107, no. 2, pp. 181–194, 1986.

[117] C. Mousseau and G. Hulbert, "The dynamic response of spindle forces produced by a tire impacting large obstacles in a plane," *Journal of Sound and Vibration*, vol. 195, no. 5, pp. 775–796, 1996.

[118] W. Soedel and M. Prasad, "Calculation of natural frequencies and modes of tires in road contact by utilizing Eigenvalues of the axisymmetric non-contacting tire," *Journal of Sound and Vibration*, vol. 70, no. 4, pp. 573–584, 1980.

[119] S. Huang, "Vibration of rolling tyres in ground contact," *International Journal of Vehicle Design*, vol. 13, no. 1, pp. 78–95, 1992.

[120] S. Huang and C. Su, "In-plane Dynamics of Tires on the Road Based on an Experimentally Verified Rolling Ring Model," *Vehicle System Dynamics*, vol. 21, no. 1, pp. 247–267, 1992.

[121] L. Kung, W. Soedel, and T. Yang, "On the vibration transmission of a rolling tire on a suspension system due to periodic tread excitation," *Journal of Sound and Vibration*, vol. 115, no. 1, pp. 37–63, 1987.

[122] S. Kim and A. Savkoor, "The Contact Problem of In-Plane Rolling of Tires on a Flat Road," *Vehicle System Dynamics*, vol. 27, no. supplement, pp. 189–206, 1997.

[123] E. Rustighi and S. Elliott, "Stochastic road excitation and control feasibility in a 2D linear tyre model," *Journal of Sound and Vibration*, vol. 300, no. 3-5, pp. 490–501, 2007.

[124] E. Rustighi, S. Elliott, S. Finnveden, K. Gulyás, T. Mócsai, and M. Danti, "Linear stochastic evaluation of tyre vibration due to tyre/road excitation," *Journal of Sound and Vibration*, vol. 310, no. 4-5, pp. 1112–1127, 2008.

[125] P. Andersson and W. Kropp, "Time domain contact model for tyre/road interaction including nonlinear contact stiffness due to small-scale roughness," *Journal of Sound and Vibration*, vol. 318, no. 1-2, pp. 296–312, 2008.

[126] I. Lopez, R. Blom, N. Roozen, and H. Nijmeijer, "Modelling vibrations on deformed rolling tyres a modal approach," *Journal of Sound and Vibration*, vol. 307, no. 3-5, pp. 481–494, 2007.

[127] A. Miège and A. Popov, "Truck tyre modelling for rolling resistance calculations under a dynamic vertical load," *Proceedings of the Institution of Mechanical Engineers, Part D: Journal of Automobile Engineering*, vol. 219, no. 4, pp. 441–456, 2005.

[128] R. Pinnington, "Radial force transmission to the hub from an unloaded stationary tyre," *Journal of Sound and Vibration*, vol. 253, no. 5, pp. 961–983, 2002.

[129] G. Mavros, *Tyre models for vehicle handling analysis under steady-state and transient manoeuvres.* PhD Thesis, Loughborough, 2005.

[130] S. Kim, P. Nikravesh, and G. Gim, "A two-dimensional tire model on uneven roads for vehicle dynamic simulation," *Vehicle System Dynamics*, vol. 46, no. 10, pp. 913–930, 2008.

[131] D. Guan, D. Liu, and L. Yu, "The tire experimental modal analysis & probe to establish tire model by using modal parameters," *In Proceedings of the 13th International Symposium of Dynamics of Vehicles on Roads and Tracks*, Chengdu, China, 1993.

[132] D. Guan, W. Wu, and A. Zhang, "Tire modeling for vertical properties by using experimental modal parameters," *SAE Paper no. 980252*, 1998.

[133] D. Guan and C. Fan, "Tire Modeling for Vertical Properties Including Enveloping Properties Using Experimental Modal Parameters," *Vehicle System Dynamics*, vol. 40, no. 6, pp. 419–433, 2003.

[134] D. Guan, C. Fan, and X. Xie, "A dynamic tyre model of vertical performance rolling over cleats," *Vehicle System Dynamics*, vol. 43, no. 1, pp. 209–222, 2005.

[135] D. Guan, J. Shang, and L. Yam, "A study on tire non-steady cornering charactristics using experimental modal parameters," *SAE Paper no. 2000-01-0362*, 2000.

[136] J. Shang, D. Guan, and L. Yam, "Study on Tire Dynamic Cornering Properties Using Experimental Modal Parameters," *Vehicle System Dynamics*, vol. 37, no. 2, pp. 129–144, 2002.

[137] J. Padovan and O. Paramadilok, "Transient and steady state viscoelastic rolling contact," *Computers and Structures*, vol. 20, pp. 545–553, 1985.

[138] L. Faria, J. Oden, B. Yavari, W. Tworzydlo, J. Bass, and E. Becker, "Tire Modeling by Finite Elements," *Tire Science and Technology*, vol. 20, no. 1, pp. 33–56, 1992.

[139] K. Danielson, A. Noor, and J. Green, "Computational strategies for tire modeling and analysis," *Computers and Structures*, vol. 61, no. 4, pp. 673–693, 1996.

[140] M. Gipser, "FTire: a physically based application-oriented tyre model for use with detailed MBS and finite-element suspension models," *Vehicle System Dynamics*, vol. 43, no. 1, pp. 76–91, 2005.

[141] M. Gipser, "FTire–the tire simulation model for all applications related to vehicle dynamics," *Vehicle System Dynamics*, vol. 45, no. supplement, pp. 139–151, 2007.

[142] C. Oertel, "On Modeling Contact and Friction Calculation of Tyre Response on Uneven Roads," *Vehicle System Dynamics*, vol. 27, no. supplement, pp. 289–302, 1996.

[143] C. Oertel and A. Fandre, "Ride comfort simulations and steps towards life time calculations: RMOD-K and ADAMS," *In Proceedings of the International ADAMS Users Conference*, Berlin, Germany, 1999.

[144] C. Oertel and A. Fandre, "Simulation: Das Reifenmodellsystem RMOD-K-ein Beitrag zum virtuellen Fahrzeug (Simulation: The tire model system RMOD-K contributes to the virtual vehicle)," *Automobiltechnische Zeitschrift*, vol. 103, no. 11, pp. 1074–1079, 2001.

[145] J. Pelc, "Towards realistic simulation of deformations and stresses in pneumatic tyres," *Applied Mathematical Modelling*, vol. 31, no. 3, pp. 530–540, 2007.

[146] A. Noor, K. Kim, and J. Tanner, "Analysis of aircraft tires via semianalytic finite elements," *Finite Elements in Analysis and Design*, vol. 6, no. 3, pp. 217–233, 1990.

[147] A. Burke and O. Olatunbosun, "New techniques in tyre modal analysis using MSC/NASTRAN," *International Journal of Vehicle Design*, vol. 18, no. 2, pp. 203–12, 1997.

[148] D. Bozdog and W. Olson, "An advanced shell theory based tire model," *Tire Sciences and Technology*, vol. 33, no. 4, pp. 227–238, 2005.

[149] J. Cho and B. Jung, "Prediction of Tread Pattern Wear by an Explicit Finite Element Model," *Tire Sciense and Technology*, vol. 35, no. 4, pp. 276–299, 2007.

[150] K. Kabe, K. Rachi, N. Takahashi, and Y. Kaga, "Tire Design Methodology Based on Safety Factor to Satisfy Tire Life (Simulation Approach to Truck and Bus Tire Design)," *Tire Science and Technology*, vol. 33, no. 4, pp. 195–209, 2005.

[151] S. Oida, E. Seta, H. Heguri, and K. Kato, "Soil/Tire Interaction Analysis Using FEM and FVM," *Tire Science and Technology*, vol. 33, no. 1, pp. 38–62, 2005.

[152] S. Shoop, K. Kestler, and R. Haehnel, "Finite Element Modeling of Tires on Snow," *Tire Science and Technology*, vol. 34, pp. 2–37, 2006.

[153] M. Ghoreishy, "A State of the Art Review of the Finite Element Modelling of Rolling Tyres," *Iranian Polymer Journal*, vol. 17, no. 8, pp. 571–597, 2008.

[154] K. Kabe and M. Koishi, "Tire Cornering Simulation Using Finite Element Analysis," *Journal of Applied Polymer Science*, vol. 78, no. 8, pp. 1566–1572, 2000.

[155] S. Chae, M. E-Gindy, M. Trivedi, I. Johansson, and O. F., "Dynamic response predictions of a truck tire using detailed finite element and rigid ring models," *In Proceedings of the International Mechanical Engineering Congress and Exposition (IMECE–ASME)*, Anheim, USA, 2004.

[156] S. Chae, J. Allen, F. Oijer, M. El-Gindy, M. Trivedi, and I. Johansson, "Dynamic Response Predictions of Quarter-Vehicle Models Using FEA and Rigid Ring Truck Tire Models," *In Proceedings of the Internstional Mechanical Engineering Congress and Exposition (IMECE–ASME)*, Chicago, USA, 2006.

[157] F. Braghin, F. Cheli, and R. Sangalli, "From Tread Design to Tread Stiffness Matrices," *Tire Sciense and Technology*, vol. 36, no. 3, pp. 227–241, 2008.

[158] F. Liu, M. Sutcliffe, and W. Graham, "Modeling of Tread Block Contact Mechanics Using Linear Viscoelastic Theory," *Tire Science and Technology*, vol. 36, no. 3, pp. 211–226, 2008.

[159] Y. Nakajima, "Numerical Simulation of Tire Traction on Various Road Conditions," *Rubber Chemistry and Technology*, vol. 80, no. 3, pp. 412–435, 2007.

[160] R. Mundl, M. Fischer, W. Strache, K. Wiese, B. Wies, and K. Zinken, "Virtual Pattern Optimization Based on Performance Prediction Tools," *Tire Science and Technology*, vol. 36, no. 3, pp. 192–210, 2008.

[161] P. Lugner and M. Plöchl, "Tyre model performance test: First experiences and results," *Vehicle System Dynamics*, vol. 43, no. 1, pp. 48–62, 2005.

[162] `http://tmpt.tuwien.ac.at/`.

[163] P. Lugner and M. Plöch, "Results," *Vehicle System Dynamics*, vol. 45, no. supplement, pp. 29–55, 2007.

[164] R. Mundl, "Tire data for TMPT: the point of view of the tire industry," *Vehicle System Dynamics*, vol. 45, pp. 57–68, 2007.

[165] P. Lugner, H. Pacejka, and M. Plöchl, "Recent advances in tyre models and testing procedures," *Vehicle System Dynamics*, vol. 43, no. 6, pp. 413–426, 2005.

[166] J. Ferry, *Viscoelastic properties of polymers.* Wiley, 1970.

[167] R. Crawford, *Plastics engineering.* Butterworth-Heinemann, 1998.

[168] J. Mark, B. Erman, and F. Eirich, *Science and Technology of Rubber.* Academic Press, 1994.

[169] D. Ewins, *Modal Testing: Theory and Practice.* Wiley, 1986.

[170] B. Persson, "Rubber friction: role of the flash temperature," *Journal of Physics, Condensed Matter*, vol. 18, no. 32, pp. 7789–7823, 2006.

[171] L. McKeen, *The effect of temperature and other factors on plastics and elastomers.* William Andrew, 2008.

[172] J. Aklonis and W. MacKnight, *Introduction to Polymer Viscoelasticity.* John Wiley and Sons, 1983.

[173] M. Williams, R. Landel, and J. Ferry, "The Temperature Dependence of Relaxation Mechanisms in Amorphous Polymers and Other Glass-forming Liquids," *Journal of the American Chemical Society*, vol. 77, no. 14, pp. 3701–3707, 1955.

[174] J. Rayleigh, *The Theory of Sound*. Macmillan, 1896.

[175] S. Adhikari, "Damping model uncertainty in Structural Dynamics," *In Proceedings of the International Conference on Noise and Vibration Engineering (ISMA)*, Leuven, Belgium, 2006.

[176] S. Adhikari and J. Woodhouse, "Identification of damping: part 1, viscous damping," *Journal of Sound and Vibration*, vol. 243, no. 1, pp. 43–61, 2001.

[177] S. Adhikari and J. Woodhouse, "Identification of damping: part 2, non viscous damping," *Journal of Sound and Vibration*, vol. 243, no. 1, pp. 63–88, 2001.

[178] A. Ribeiro, N. Maia, and J. Silva, "On the modelling of damping in structural vibrations," *In Proceedings of the International Conference on Noise and Vibration Engineering (ISMA)*, pp. 1097–1105, Leuven, Belgium, 2006.

[179] X. Lu and L. Segel, "Vehicular energy losses associated with the traversal of an uneven road," *In Proceeding of the 9th IAVSD Symposium on Dynamics of Vehicles on Roads and Tracks*, Linköping, Sweden, 1986.

[180] D. Stutts and W. Soedel, "A simplified dynamic model of the effect of internal damping on the rolling resistance in pneumatic tires," *Journal of Sound and Vibration*, vol. 155, no. 1, pp. 153–164, 1992.

[181] A. Popov and Z. Geng, "Modelling of vibration damping in pneumatic tyres," *Vehicle System Dynamics*, vol. 43, no. 1, pp. 145–155, 2005.

[182] J. Woodhouse, "Linear damping models for structural vibration," *Journal of Sound and Vibration*, vol. 215, no. 3, pp. 547–569, 1998.

[183] B. Kim, C. Chi, and T. Lee, "A study on radial directional natural frequency and damping ratio in a vehicle tire," *Applied Acoustics*, vol. 68, no. 5, pp. 538–556, 2007.

[184] D. Dowson, *History of tribology*. Longman, 1979.

[185] I. Newton, *Philosophiae naturalis principia mathematica*. 1687.

[186] G. Amontons, "On the resistance originating in machines," *In Proceedings of the French Royal Academy of Sciences*, pp. 206–222, 1699.

[187] C. Coulomb, "Theory of simple machines," *Mem. Math. Phys. Acad. Sci.*, vol. 10, pp. 161–331, 1785.

[188] L. Euler, "Sur le frottement des corps solides (On the friction of solid bodies)," *Mem. Acad. Sci. Berl*, vol. 4, pp. 122–132, 1748.

[189] L. Euler, "Sur le diminution de la resistance du frottement (On the reduction of the friction resistance)," *Mem. Acad. Sci. Berl*, vol. 4, pp. 133–148, 1748.

[190] B. Persson, *Sliding Friction: Physical Principles and Applications*. Springer, 2000.

[191] Y. Guo, Z. Qu, Y. Braiman, Z. Zhang, and J. Barhen, "Nanotribology and nanoscale friction," *IEEE Control Systems Magazine*, vol. 28, no. 6, pp. 92–100, 2008.

[192] F. Al-Bender and J. Swevers, "Characterization of friction force dynamics," *IEEE Control Systems Magazine*, vol. 28, no. 6, pp. 64–81, 2008.

[193] H. Hertz, "Über die Berührung fester elastischer Körper (On the contact of solid elastic body)," *Journal für die reine und angewandte Mathematik (Crelle's Journal)*, vol. 1882, no. 92, pp. 156–171, 1882.

[194] N. Adam, *The physics and chemistry of surfaces*. Oxford University Press, 1938.

[195] R. Holm, "The frictional force over the real area of Contact," *Wiss. Vereoff. Siemens Werken*, vol. 17, no. 4, pp. 38–42, 1938.

[196] F. Bowden and D. Tabor, "The Area of Contact between Stationary and between Moving Surfaces," *Proceedings of the Royal Society of London. Series A, Mathematical and Physical Sciences*, vol. 169, no. 938, pp. 391–413, 1939.

[197] F. Bowden and D. Tabor, *The Friction and Lubrication of Solids*. Clarendon, 1950.

[198] J. Archard, "Elastic Deformation and the Laws of Friction," *Proceedings of the Royal Society of London. Series A, Mathematical and Physical Sciences*, vol. 243, no. 1233, pp. 190–205, 1957.

[199] J. Archard, "Contact and rubbing of flat surfaces," *Journal of Applied Physics*, vol. 24, no. 8, pp. 981–988, 1953.

[200] J. Greenwood and J. Williamson, "Contact of Nominally Flat Surfaces," *Proceedings of the Royal Society of London. Series A, Mathematical and Physical Sciences*, vol. 295, no. 1442, pp. 300–319, 1966.

[201] D. Whitehouse and J. Archard, "The Properties of Random Surfaces of Significance in their Contact," *Proceedings of the Royal Society of London. Series A, Mathematical and Physical Sciences*, vol. 316, no. 1524, pp. 97–121, 1970.

[202] J. Greenwood, "A Unified Theory of Surface Roughness," *Proceedings of the Royal Society of London. Series A, Mathematical and Physical Sciences*, vol. 393, no. 1804, pp. 133–157, 1984.

[203] J. Greenwood and J. Wu, "Surface Roughness and Contact: An Apology," *Meccanica*, vol. 36, no. 6, pp. 617–630, 2001.

[204] P. Wriggers, *Computational Contact Mechanics*. Wiley, 2002.

[205] M. Ciavarella, V. Delfine, and G. Demelio, "A re-vitalized Greenwood and Williamson model of elastic contact between fractal surfaces," *Journal of the Mechanics and Physics of Solids*, vol. 54, no. 12, pp. 2569–2591, 2006.

[206] J. Perrin, "La discontinuité de la matière (The discontinuity of matter)," *Revue du mois*, vol. 1, pp. 323–343, 1906.

[207] N. Wiener, *I am a mathematician*. Garden City, 1956.

[208] R. Sayles and T. Thomas, "Surface topography as a nonstationary random process," *Nature*, vol. 271, no. 2, pp. 431–434, 1978.

[209] B. Mandelbrot, *The Fractal Geometry of Nature*. WH Freeman, 1982.

[210] B. Mandelbrot and J. Wheeler, "The Fractal Geometry of Nature," *American Journal of Physics*, vol. 51, no. 3, pp. 286–287, 1983.

[211] M. Ausloos and D. Berman, "A Multivariate Weierstrass-Mandelbrot Function," *Proceedings of the Royal Society of London. Series A, Mathematical and Physical Sciences*, vol. 400, no. 1819, pp. 331–350, 1985.

[212] A. Majumdar and C. Tien, "Fractal characterization and simulation of rough surfaces.," *Wear*, vol. 136, no. 2, pp. 313–327, 1990.

[213] A. Majumdar and B. Bhushan, "Fractal Model of Elastic-Plastic Contact Between Rough Surfaces," *Journal of Tribology*, vol. 113, pp. 1–11, 1991.

[214] I. Singer and H. Pollock, *Fundamentals of Friction: Macroscopic and Microscopic Processes*. Kluwer Academic Print on Demand, 1992.

[215] J. Krim, "Surface science and the atomic-scale origins of friction: what once was old is new again," *Surface Science*, vol. 500, no. 3, pp. 741–758, 2002.

[216] A. Roberts, "Theories of Dry Rubber Friction," *Tribology International*, vol. 9, no. 2, pp. 75–82, 1976.

[217] R. Ariano, "The Coefficients of Function between Rubber and Various Materials Part II – Gripping Friction of Rubber Belting," *Rubber Chemistry and Technology*, vol. 3, no. 2, pp. 286–292, 1930.

[218] R. Derieux, "The Coefficient of Friction of Rubber," *Rubber Chemistry and Technology*, vol. 8, no. 3, pp. 441–442, 1935.

[219] A. Schallamach, "The Velocity and Temperature Dependence of Rubber Friction," *Proceedings of the Physical Society Section B*, vol. 66, no. 5, pp. 386–392, 1953.

[220] A. Schallamach, "Friction and abrasion of rubber," *Wear*, vol. 1, pp. 384–417, 1957.

[221] B. Sabey, "Pressure Distributions beneath Spherical and Conical Shapes pressed into a Rubber Plane, and their Bearing on Coefficients of Friction under Wet Conditions," *Proceedings of the Physical Society*, vol. 71, no. 6, pp. 979–988, 1958.

[222] J. Greenwood and D. Tabor, "The Friction of Hard Sliders on Lubricated Rubber: The Importance of Deformation Losses," *Proceedings of the Physical Society*, vol. 71, pp. 989–1001, 1958.

[223] K. Grosch, "Rubber Friction and Its Relation to Tire Traction," *Rubber Chemistry and Technology*, vol. 80, no. 3, pp. 379–411, 2007.

[224] K. Grosch, "The Relation between the Friction and Visco-Elastic Properties of Rubber," *Proceedings of the Royal Society of London. Series A, Mathematical and Physical Sciences*, vol. 274, no. 1356, pp. 21–39, 1963.

[225] A. Schallamach, "How does rubber slide?," *Wear*, vol. 17, no. 4, pp. 301–312, 1971.

[226] K. Johnson, K. Kendall, and A. Roberts, "Surface Energy and the Contact of Elastic Solids," *Proceedings of the Royal Society of London. Series A, Mathematical and Physical Sciences*, vol. 324, no. 1558, pp. 301–313, 1971.

[227] M. Barquins, "Sliding friction of rubber and Schallamach waves - a review," *Materials Science and Engineering*, vol. 73, pp. 45–64, 1985.

[228] A. Savkoor, "Some aspects of friction and wear of tyres arising from deformations, slip and stresses at the ground contact," *Wear*, vol. 9, no. 1, pp. 66–78, 1966.

[229] K. Ludema, "Physical factors in tyre traction," *Physics in Technology*, vol. 6, no. 1, pp. 11–17, 1975.

[230] J. Cesbron, F. Anfosso-Lédée, D. Duhamel, H. Yin, and D. Le Houédec, "Experimental study of tyre/road contact forces in rolling conditions for noise prediction," *Journal of Sound and Vibration*, vol. 320, no. 1–2, pp. 125–144, 2009.

[231] O. Panagouli and A. Kokkalis, "Skid resistance and fractal structure of pavement surface," *Chaos, Solitons and Fractals*, vol. 9, no. 3, pp. 493–505, 1998.

[232] L. Zhixiong and Z. Lanying, "On fractal behavior of road surface roughness," *In Proceedings of the 2nd International Conference on Transportation Engineering (ICTE)*, Chengdu, China, 2007.

[233] M. Mannel and T. Beckenbauer, "Characterisation of road surfaces by means of texture analysis," *VDI Berichte*, vol. 2014, p. 223, 2007.

[234] M. Kuwajima, M. Koishi, and J. Sugimura, "Contact Analysis of Tire Tread Rubber on Flat Surface with Microscopic Roughness," *Tire Science and Technology*, vol. 34, no. 4, pp. 237–255, 2006.

[235] K. Hofstetter, C. Grohs, J. Eberhardsteiner, and H. Mang, "Sliding behaviour of simplified tire tread patterns investigated by means of FEM," *Computers and Structures*, vol. 84, no. 17-18, pp. 1151–1163, 2006.

[236] B. Persson, O. Albohr, U. Tartaglino, A. Volokitin, and E. Tosatti, "On the nature of surface roughness with application to contact mechanics, sealing, rubber friction and adhesion," *Journal of Physics: Condensed Matter*, vol. 17, pp. R1–R62, 2005.

[237] M. Kluppel and G. Heinrich, "Rubber friction on self-affine road tracks," *Rubber Chemistry and Technology*, vol. 73, no. 4, pp. 578 – 606, 2000.

[238] G. Heinrich and M. Klüppel, "Rubber friction, tread deformation and tire traction," *Wear*, vol. 265, no. 7–8, pp. 1052–1060, 2008.

[239] B. Persson, U. Tartaglino, O. Albohr, and E. Tosatti, "Rubber friction on wet and dry road surfaces: The sealing effect," *Physical Review B*, vol. 71, no. 3, p. 35428, 2005.

[240] B. Persson, "On the theory of rubber friction," *Surface Science*, vol. 401, no. 3, pp. 445–454, 1998.

[241] B. Persson and E. Tosatti, "Qualitative theory of rubber friction and wear," *The Journal of Chemical Physics*, vol. 112, p. 2021, 2000.

[242] B. Persson, O. Albohr, C. Creton, and V. Peveri, "Contact area between a viscoelastic solid and a hard, randomly rough, substrate," *The Journal of Chemical Physics*, vol. 120, no. 18, pp. 8779–8793, 2004.

[243] W. Weaver, S. Timoshenko, and D. Young, *Vibration Problems in Engineering*. Wiley-Interscience, 1990.

[244] A. Love, "The Small Free Vibrations and Deformation of a Thin Elastic Shell," *Philosophical Transactions of the Royal Society of London*, vol. 179, pp. 491–546, 1888.

[245] Y. H. Wijnant and A. De Boer, "A new approach to model tyre/road contact," *In Proceedings of the International Conference on Noise and Vibration Engineering (ISMA)*, Leuven, Belgium, 2006.

[246] J. Wilkinson, *The algebraic eigenvalue problem*. Oxford University Press, 1988.

[247] M. Bhatti, *Fundamental finite element analysis and applications*. John Wiley & Sons, 2005.

[248] O. Zienkiewicz and R. Taylor, *The FInite Element Method For Solid and Structural Mechanics*. Butterworth-Heinemann, 2005.

[249] F. Gauterin and C. Ropers, "Modal tyre models for road noise improvement," *Vehicle System Dynamics*, vol. 43, no. 1, pp. 297–304, 2005.

[250] N. Maia and J. Silva, *Theoretical and experimental modal analysis*. Research Studies Press, 1998.

[251] D. Guan, J. Shang, and L. Yam, "Modeling of tire cornering properties with experimental modal parameters," *SAE Paper no. 1999-01-0784*, 1999.

[252] D. Guan, L. Yam, A. Zhang, and J. Shang, "Modeling of Tire Rolling Properties By Using Experimental Modal Parameters," *SAE paper 2000–01–0361*.

[253] H. Shiobara, T. Akasaka, S. Kagami, and S. Tsutsumi, "One-dimensional contact pressure distribution of radial tires in motion," *Tire Science and Technology*, vol. 23, no. 2, pp. 116 – 135, 1995.

[254] D. Zimmer and M. Otter, "Real-time models for wheels and tyres in an object-oriented modelling framework," *Vehicle System Dynamics*, vol. 48, no. 2, pp. 189–216, 2010.

[255] T. Akasaka and K. Kabe, "Deformation and cord tension of a bias tire in contact with the road," *Tire Science and Technology*, vol. 5, no. 4, pp. 171 – 201, 1977.

[256] M. Pottinger, "Three-dimensional contact patch stress field of solid and pneumatic tires," *Tire Science and Technology*, vol. 20, no. 1, pp. 3–32, 1992.

[257] E. Sakai, "Measurement and visualization of the contact pressure distribution of rubber disks and tires," *Tire Science and Technology*, vol. 23, no. 4, pp. 238 – 255, 1995.

[258] W. Hall, J. Mottram, D. Dennehy, and R. Jones, "Characterisation of the contact patch behaviour of an automobile tyre by physical testing," *International Journal of Vehicle Design*, vol. 31, no. 3, pp. 354–376, 2003.

[259] T. Akasaka, M. Katoh, S. Nihei, and M. Hiraiwa, "Two-dimensional contact pressure distribution of a radial tire," *Tire Science and Technology*, vol. 18, no. 2, pp. 80–103, 1990.

[260] A. Tuononen, "Optical position detection to measure tyre carcass deflections," *Vehicle System Dynamics*, vol. 46, no. 6, pp. 471–481, 2008.

[261] J. Maurice and A. Savkoor, "Influence of flexibility properties and friction laws on tyre behaviour," *Vehicle System Dynamics*, vol. 37, no. supplement, pp. 107–124, 2002.